

The University of Sheffield



Advanced Non-Overlapping Winding Induction Machines for Electrical Vehicle Applications

Tayfun Gundogdu

A thesis submitted for the degree of Doctor of Philosophy

Department of Electronic and Electrical Engineering

The University of Sheffield

UK

July 2018

Abstract

This thesis presents an investigation into advanced squirrel-cage induction machines (IMs), with a particular reference to the reduction of the total axial length without sacrificing the torque and efficiency characteristics and analysis of recently found non-sinusoidal bar current phenomenon, which occurs under some certain design and operating conditions, and affects the overall performance characteristics of the IMs.

As a first step, the most convenient method is determined by utilizing a fractional-slot concentrated winding (FSCW) technique, which has advantages such as non-overlapping windings, high slot filling factor, and simple structure. After implementing this technique, it is found that due to the highly distorted magnetomotive forces (MMFs) created by the FSCWs, significant high rotor bar copper loss occurs. In order to reduce the MMF harmonics without increasing the size of the machine, a new technique titled “adapted non-overlapping winding” is developed. This technique consists of the combination of the auxiliary tooth and phase shifting techniques, resulting in a stator with concentrated windings of two-slot coil pitches but without overlapping the end-windings. Thanks to this method a large number of the MMF harmonics are cancelled. Thus, a low copper loss IM with significantly reduced total axial length is obtained. Influence of design parameters; such as stator slot, rotor slot, and pole numbers, number of turns, stack length, stator and rotor geometric parameters, etc. on the performance characteristics of the advanced IM is investigated and a comprehensive comparison of advanced and conventional IMs is presented.

This thesis also covers an in-depth investigation on the non-sinusoidal bar current phenomenon. It is observed that the rotor bar current waveform, usually presumed to be sinusoidal, becomes non-sinusoidal in some operation and design conditions, such as high speed operation close to synchronous speed, or fairly high electrical loading operation, or in the IMs whose air-gap length is considerably small, etc. Influences of design and operating parameters and magnetic saturation on the rotor bar current waveform and the performance characteristics of squirrel-cage IMs are investigated. The levels of iron saturation, depending on the design and operating parameters, in different machine parts are examined and their influences are also investigated, whilst the dominant part causing the non-sinusoidal rotor bar current waveform is identified. It is revealed that the magnetic saturation, particularly in the rotor tooth, has a significant effect on the bar current waveform.

Acknowledgements

I wish to express my deepest gratitude and appreciation to Professor Zi-Qiang Zhu for all the strong and continued help, support, advice, and encouragement which he has provided throughout this project and have been invaluable during my PhD study and in the completion of this thesis. His abilities as a teacher, thinker, and expert in electrical machines are truly unparalleled.

I would like to thank Associate Professor Dr Güven Kömürgöz at the Istanbul Technical University, Turkey, for granting me to pursue the PhD degree supervised by Professor Zhu at The University of Sheffield. Without her encouragement, I would not have this chance to study in the Electrical Machines and Drives Research Group, The University of Sheffield. Thanks are also due to all members of the Electrical Machines and Drives Research Group at the University of Sheffield for their useful and productive discussions, particularly Dr Yang Guan, Dr Zhongze Wu, Mr Srinivas S. Mallampall, and Mr James Dexter.

I also would like to thank VALEO France, Powertrain Electrical Systems for the financial support, particularly Dr Philippe Farah, Dr Jean-Claude Mipo, and Dr Sophie Personnaz for their very helpful supervision and advices.

I would like to thank my family, particularly my wife, Burcu Gündoğdu, whose love, care, and encouragement are the rock upon which all of my successes are built.

Finally, I would like to acknowledge everyone who has knowingly and unknowingly helped me and wished me the best in successfully accomplishing this research.

Content

Abstract	III
Acknowledgements	V
Content	VII
Nomenclature	XV
Abbreviation	XIX
1 General Introduction	1
1.1 Introduction	1
1.2 Induction Machines for EV/HEV Applications	1
1.2.1 Structure of the IMs	3
1.2.2 Working Principle of the IMs	3
1.3 Stator and Rotor Windings Used in Induction Machines	4
1.3.1 Integer Slot Windings	4
1.3.2 Fractional Slot Windings	6
1.3.3 Adapted Non-Overlapping Integer Slot Concentrated Windings	9
1.3.4 Rotor Windings Used in Induction Machines	10
1.3.5 Technical Issues with Induction Machines	11
1.4 Literature Review on Novel Induction Machines	13
1.4.1 Novel Stator and Winding Topologies	13
1.4.2 Novel Rotor and Cage Topologies	24
1.4.3 Double Stator and Rotor Topologies	28
1.4.4 Other Novel IM Topologies	32
1.5 PhD Research Scope and Contributions	33
1.5.1 Scope of Research	33
1.5.2 Contributions of Research	37

2	Analysis of Induction Machines with Different Coil Pitches	39
2.1	Introduction	39
2.2	Winding Harmonic Index	41
2.3	Design of Different Winding Configurations	46
2.3.1	9S/6P-DL ($\gamma c = 1$) Fractional-Slot Concentrated Winding (FSCW)	48
2.3.2	18S/6P-DL ($\gamma c = 1$) Integer-Slot Concentrated Winding (ISCW)	50
2.3.3	18S/6P-SL ($\gamma c = 3$) Integer-Slot Distributed Winding (ISDW)	51
2.3.4	18S/6P-DL ($\gamma c = 2$) ISDW	52
2.3.5	36S/6P-SL and DL ($\gamma c = 5$) ISDW	54
2.3.6	54S/6P-DL ($\gamma c = 9$) ISDW	56
2.4	General Performance Comparison of 6-pole IMs with Different Winding Configurations	58
2.4.1	Axial Length and Phase Resistance	61
2.4.2	Induced Voltage	62
2.4.3	Air-Gap Flux Density	63
2.4.4	Rotor Bar Current Density	65
2.4.5	Flux Distributions	65
2.4.6	Torque, Torque Ripple, and Output Power	65
2.4.7	Power Losses and Efficiency	68
2.5	Experimental Validation	68
2.6	Conclusion	73
3	Development of Advanced Induction Machines with Coil Pitch of Two Slot Pitches	75
3.1	Introduction	75
3.2	MMF Harmonic Cancellation	77
3.2.1	Conventional Phase Shifting Method	78
3.2.2	Phase Shifting with Auxiliary Tooth Method	81
3.2.3	Stator Slot Utilization	86
3.3	Comparison of Electromagnetic Performance Characteristics	89
3.3.1	Before Stator Slot Utilization	89
3.3.2	After Stator Slot Utilization	95

3.4	Influence of Design Parameters on Performance of Advanced Non-Overlapping Winding Induction Machine	97
3.4.1	Stator Slot and Pole Number	98
3.4.2	Rotor Slot Number.....	100
3.4.3	Stack Length	103
3.4.4	Number of Turns.....	112
3.4.5	Stator and Rotor Geometric Parameters	114
3.5	Optimization of Advanced Non-Overlapping Winding Induction Machines	121
3.6	Comparison between Advanced and Conventional Induction Machines.....	121
3.7	Conclusion.....	127
4	Comparison of Conventional and Advanced Induction Machines with Coil Pitch of Two Slot Pitches and Various Slot and Pole Number Combinations	129
4.1	Introduction	129
4.2	Comprehensive Performance Comparison between AIMS with Different Slot/Pole Combinations and Geometrical Parameters	131
4.2.1	Design and Analysis of CIM and AIMS	131
4.2.2	Electromagnetic Performance Comparison	133
4.2.3	Comparison According to Stack Length.....	141
4.2.4	Comparison Based on the Maximum Power-Speed Characteristics.....	149
4.2.5	Comparison of Efficiency Maps	150
4.3	Investigation of the Best Candidates.....	156
4.3.1	Electromagnetic Performance Comparison of the CIM and Selected AIMS	157
4.3.2	Flux-Weakening Performance Comparison.....	161
4.4	Performance of Advanced Non-Overlapping Winding Induction Machines with Different Rotor Topologies.....	164
4.4.1	Considered Squirrel-Cage Rotor Structures.....	168
4.4.2	Comparison of Electromagnetic Performance Characteristics	168
4.4.3	Comparison of Flux-Weakening Characteristics	175
4.4.4	Overall Comparison.....	185
4.5	Conclusion.....	186

5	Influence of Magnetic Saturation on Non-Sinusoidal Bar Current Waveform	189
5.1	Introduction	189
5.2	Analysis of Rotor Bar Current	190
5.3	Investigation of Bar Current	192
5.4	Investigation of Flux Density	195
5.5	Influence of Magnetic Saturation.....	199
5.6	Conclusion.....	204
6	Influence of Design Parameters on Non-Sinusoidal Bar Current Waveform	205
6.1	Introduction	205
6.2	Air-Gap Length	206
6.2.1	Importance of Air-Gap Length	208
6.2.2	Investigation of Air-Gap Length.....	209
6.2.3	Influence of Air-Gap Length on Electromagnetic Performance Characteristics	209
6.2.4	Influence of Air-Gap Length on Magnetic Characteristics.....	215
6.3	Rotor Slot Number	219
6.3.1	Determination of Rotor Slot Number	220
6.3.2	Influence of Rotor Slot Number on Performance Characteristics	221
6.3.3	Investigation of Rotor Tooth Flux Density	228
6.3.4	Investigation of Rotor Slot Flux Density	231
6.3.5	Investigation of Electromagnetic Force	233
6.4	Stator Slot and Pole Number Combination.....	235
6.4.1	Determination of Stator Slot and Pole Number Combination	236
6.4.2	Influence of Stator Slot and Pole Number on Performance Characteristics	237
6.4.3	Performance with Optimal Rotor Slot Numbers.....	241
6.4.4	Investigation of Tooth Flux Density	246
6.4.5	Influence of Core Saturation.....	247
6.5	Stator and Rotor Slot Geometric Parameters.....	251
6.5.1	Influence of Stator Slot Geometric Parameters.....	251
6.5.2	Influence of Rotor Slot Geometric Parameters	255

6.5.3	Investigation of Magnetic Saturation.....	258
6.6	Rotor Skew.....	263
6.6.1	Rotor Skew Angle.....	263
6.6.2	Influence of Rotor Skew on Performance Characteristics	264
6.7	Stator Coil Pitch	268
6.7.1	Design of IMs with Various Coil Pitches	268
6.7.2	Influence of Stator Coil Pitch on Performance Characteristics	269
6.8	Discussions and Conclusions	273
7	Influence of Operating Parameters on Non-Sinusoidal Bar Current Waveform.....	279
7.1	Introduction	279
7.2	Electric Loading	281
7.2.1	Influence of Electric Loading on Performance Characteristics	281
7.2.2	Influence of Electric Loading on Magnetic Characteristics.....	284
7.3	Slip	286
7.3.1	Influence of Slip on Electromagnetic Performance Characteristics	286
7.3.2	Influence of Slip on Magnetic Characteristics.....	290
7.4	Verification of Non-Sinusoidal Bar Current Waveform by Locked-Rotor Analysis ..	292
7.4.1	Constant Frequency and Variable Current.....	292
7.4.2	Constant Current and Variable Frequency.....	294
7.5	Conclusion.....	295
8	General Conclusions and Future Work.....	297
8.1	Summary	297
8.2	Importance of MMF Harmonics for Squirrel-Cage IMs.....	298
8.3	Developed Non-Overlapping Winding Topology.....	299
8.3.1	MMF Harmonic Reduction Method	299
8.3.2	Key Properties of the Developed Winding Topology.....	299
8.3.3	Design of IMs with Adapted Non-Overlapping Winding Topology	300
8.3.4	Influence of Design Parameters.....	301
8.3.5	Influence of Rotor Type/Slot Opening Effect.....	302

8.4	Comparison between CIM and AIM	303
8.5	Non-Sinusoidal Bar Current Phenomenon in IMs	303
8.5.1	Influence of Saturation.....	304
8.5.2	Influence of Design and Operating Parameters	305
8.6	Future Work	305
References		307
Appendix A	Modelling of Induction Machine in dq-axis Reference Frame and Calculation of Flux-Weakening Characteristic	331
A.1	Voltage Limit	331
A.2	Current Limit	332
A.3	Torque Limit.....	332
A.4	Optimal Flux for Maximum Torque.....	333
Appendix B	Drive Requirements and Lamination Specifications	335
B.1	Specification Limits	335
B.2	Lamination Specifications.....	335
Appendix C	Specifications and Winding Properties of IMs Designed for Valeo	337
C.1	Specifications of Conventional Induction Machine.....	337
C.2	Specifications of the Proposed AIMS	339
C.3	Winding Layout and Coil Connections of the 18S/6P AIMS	341
Appendix D	Specifications of Toyota Prius 2010 IPM Machine.....	345
Appendix E	Design Optimization of AIMS	347
E.1	Individual Optimization of AIM	348
E.1.1	Determination of Optimization Parameters.....	348
E.1.2	Determined Topology and Optimization Parameters	357
E.2	Single-Objective Global Optimization (SOGO) by GA.....	357
E.2.1	With the Restriction of Maximum Current Density	358

E.2.2 With the Restriction of Maximum Stator Copper Loss.....	358
E.2.3 SOGO Produced by GA.....	359
E.3 Multi-Objective Global Optimization (MOGO) by GA.....	360
E.3.1 Determination of Objectives and Goals.....	360
E.3.2 Justification of Objectives and Weights.....	361
E.3.3 Cost Function for MOGO.....	362
E.3.4 MOGO Procedure by GA.....	363
E.4 Design and Performance Comparison.....	364
E.4.1 Design Comparison.....	364
E.4.2 Electromagnetic Performance Comparison.....	366
Appendix F Influence of Rotor Slot Opening Parameters on the Electromagnetic and Flux-Weakening Performance Characteristics.....	369
G.1 Electromagnetic Performance Characteristics.....	370
G.2 Flux-Weakening Performance Characteristics.....	377
Appendix G Generator Mode Operating Characteristics.....	381
G.1 Circle Diagram of IMs.....	381
G.2 Motor and Generator Mod Operation Characteristics of the AIMs.....	382
Publications.....	387

Nomenclature

Symbol	Explanation	Unit
A_{Bar}	Cross-sectional area of bar	mm ²
A_{Rcore}	Cross-sectional area of rotor core	mm ²
A_{Ring}	Cross-sectional area of end-ring	mm ²
A_{Score}	Cross-sectional area of stator core	mm ²
A_c	Cross-sectional area of one coil-side	mm ²
A_s	Cross-sectional area of the stator slot	mm ²
$B_{g,avg}$	Average air-gap flux density	T
B_g	Instantaneous air-gap flux density	T
Br_r	Radial component of the rotor flux density	T
Br_t	Tangential component of the rotor flux density	T
Bs_t	Tangential component of the stator flux density	T
B_t	Total flux density	T
D_{CuR}	Mass density of rotor bar copper	kg/m ³
D_{CuS}	Mass density of stator winding copper	kg/m ³
D_{M330}	Mass density of M330-35A core material	kg/m ³
D_g	Average diameter of the air-gap	mm
D_{si}	Stator inner diameter	mm
D_{so}	Stator outer diameter	mm
I_M	Magnetizing current	A
I_R	Rotor current amplitude	A
I_S	Stator current amplitude	A
I_{bn}	Bar current of the n^{th} bar	A
I_{irn}	Inter-bar ring current	A
I_{sm}	Maximum stator current	V
J_r, J_R	Rotor bar current density	A/mm ²
J_s, J_S	Stator winding current density	A/mm ²
L_m	Mutual inductance between stator winding and rotor winding	mH
L_r	Rotor self-inductance	mH
L_s	Stator self-inductance	mH
MMF_{Rn}	Rotor magneto motive force	AT
MMF_{Sn}	Stator magneto motive force	AT
MMF_{gn}	Air-gap magneto motive force	AT
M_{Tot}	Total weight	kg
N_c	Number of coils per phase	—
N_j	Number of iteration for the j^{th} sub-goal	—
N_s	Number of conductors per pole per phase	—

N_{st}	Serial number of turns per phase	—
N_t	Number of turns per coil	—
P_{hyst}	Hysteresis loss	mW
P_C	Total core loss	kW
P_{Rcu}	Rotor bar copper loss	kW
P_{Scu}	Stator copper loss	kW
P_{Scu_end}	Stator end-winding copper loss	kW
P_{Scu_in}	Stator slot copper loss	kW
P_{eddy}	Eddy loss	mW
P_{fa}	Feasibly available active power	W
P_{out}	Electrical output power	kW
$P_{rcu(MOGO2)}$	Rotor bar copper loss justified for MOGO	W
$P_{rcu(Max_Sbar)}$	Maximum rotor bar loss obtained in case of maximum rotor bar Cross-sectional area	W
$P_{rcu(Min_Sbar)}$	Minimum rotor bar loss obtained in case of minimum rotor bar Cross-sectional area	W
$P_{scu(MOGO12)}$	Stator slot copper loss justified for MOGO	W
$P_{scu(SOGO-R1)}$	Stator slot copper loss obtained from the SOGO solution in case of maximum stator current density restriction	W
$P_{scu(SOGO-R2)}$	Stator slot copper loss obtained from the SOGO solution in case of maximum stator copper loss restriction	W
R_{bns}	Resistance of the n^{th} bar depending on the slip	Ω
R_{coil}	Resistance of one coil	Ω
R_{phase}	Phase resistance	Ω
R_s	Stator resistance	Ω
S_w	Diameter of one wire	mm
S_{fa}	Feasibly available apperent power	VA
T_{avg}	Time average torque at pullout slip	Nm
T_e	Electromagnetic torque	Nm
T_{e_t}	Maximum torque considering only the torque-limit boundary	Nm
T_{e_v}	Maximum torque considering only the voltage-limit boundary	Nm
$T_{e_v_m}$	Maximum torque of T_{e_v}	Nm
T_{fa}	Feasibly available electromangetic torque	Nm
V_{dc}	DC-link voltage	V
V_{sm}	Maximum stator voltage	V
X_{bns}	Reactance of the n^{th} bar depending on the slip harmonics	Ω
a_c	Electric loading	At

br_r	Rotor slot bottom width	mm
br_t	Rotor slot top width	mm
b_{tr}	Rotor slot body width	mm
e_i	Individual goal error at i^{th} iteration	—
f_r	Rotor frequency	Hz
f_s	Stator frequency	Hz
h_{shi}	Winding harmonic index	—
i_{ds}	d -axis component of stator current	A
i_{qs}	q -axis component of stator current	A
k_c	Stator copper loss coefficient	—
k_{dh}	Distribution factor for the h^{th} harmonic	—
k_{dh_FSCW}	Distribution factor for the h^{th} harmonic for FSCWs	—
k_{dh_ISDW}	Distribution factor for the h^{th} harmonic for ISDWs	—
k_f	Slot filling factor	—
k_{ir}	Rotor stacking factor	—
k_{ph}	Pitch factor for the h^{th} harmonic	—
k_{ph_FSCW}	Pitch factor for the h^{th} harmonic for FSCWs	—
k_{ph_ISDW}	Pitch factor for the h^{th} harmonic for ISDWs	—
k_{sat}	Saturation factor	—
k_{wh}	Winding factor for the h^{th} harmonic	—
k_{wh_final}	New winding factor for the h^{th} harmonic	—
$k_{wh_initial}$	Initial winding factor for the h^{th} harmonic	—
k_{wp}	Fundamental winding factor of any combination with p pole-pair number	—
l_{ring}	Axial length (thickness) of the one ring piece	mm
l_a	Total axial length including stack and end-winding axial lengths	mm
l_{av}	Average length of one coil	mm
l_{end}	End-winding length	mm
l_s	Stack length	mm
l_{total}	Total axial length	mm
m_r	Rotor phase number	—
n_{maxT}	Rotor speed delivering the maximum torque	rpm
n_r, n_s	Rotor speed, and synchronous speed	rpm
n_t	Number of overlays	—
r_w	Average winding radius	mm
v_{ds}	d -axis component of stator voltage	V
v_{qs}	q -axis component of stator voltage	V
w_i	Absolute weighted value at i^{th} iteration	—
w_j	Weight factor related with the j^{th} sub-goal	—
y_c, y_p	Coil pitch in slot number, and pole pitch in slot number	—

α_r	Phase shift between bars divided by pole pitch	deg
θ_e	Electrical angle	deg
λ_s	Split ratio	—
μ_0	Relative permeability of air	H/m
ρ_{Cu}	Resistivity of copper	S/m
σ_{Cu}	Conductivity of copper	Ωm
τ_r	Rotor slot pitch	mm
τ_s	Slot pitch	mm
ψ_{ds}	d -axis component of stator flux	Wb
ψ_{ds_c}	Critical flux	Wb
$\psi_{ds_opt1}^*$	Optimal flux reference one	Wb
$\psi_{ds_opt2}^*$	Optimal flux reference two	Wb
ω_c	Critical angular frequency	rad
ω_e	Excitation angular frequency	rad
ω_r	Angular speed	rad/s
ϕ_t	Total flux	Wb
h, h_p	Harmonic order, and harmonic order of the working harmonic	—
A	Integrated cross-sectional area (studied machine part's cross-sectional area)	mm^2
$Cost$	Actual cost function	—
G, N	Number of sub-goals, and iteration size	—
P	Pole number	—
R	Rotor slot number	—
S	Stator slot number	—
Z_2	Rotor impedance	Ω
a, a_{max}	Number of parallel branches, and maxium number of parallel branches	—
g, g_e	Air-gap length, and effective air-gap length	mm
k	An integer number	—
m	Stator phase number	—
p	Pole pair number	—
q	Stator slots per phase per pole number	—
s	Slip	—
x	Physical phase displacement in number of slots	—
t	Time	s
α	Phase winding shift angle	$^\circ\text{e}$
η	Efficiency	%
θ, θ_r	Mechanical rotor position (mechanical angle)	deg
τ_p	Pole pitch	cm
σ	Total leakage factor	—
ω	Angular frequency	rad

Abbreviation

2-D	Two dimensional
ANW	Adapted non-overlapping winding
AIM	Advanced induction machine (designed by adapted non-overlapping windings)
BH	Flux density versus field intensity
C#	Case number
CIM	Conventional induction machine
CRCS	Cast-rotor closed-slot
CROS	Cast-rotor open-slot
DL	Double-layer
FE	Finite-element
FEA	Finite element analysis
FSCW	Fractional slot concentrated winding
FSCWIM	Induction machine having fractional slot concentrated winding
GA	Genetic algorithm
GO	Global optimization
IB	Insert-bar
IM	Induction machine
IPM	Interior permanent magnet machine
IROS	Insert-rotor open-slot
ISCW	Integer slot concentrated winding
ISCWIM	Induction machine having integer slot concentrated winding
ISDW	Integer slot distributed winding
ISDWIM	Induction machine having integer slot distributed winding
L	Linear relative permeability
MO	Multi-objective
MOGO	Multi-objective global optimization
N	Non-linear relative permeability
RT	Rotor tooth
RTM	Middle of the rotor tooth body
RY	Rotor yoke
S/P	Stator slot/pole number
S/R/P	Stator slot number/rotor slot number/pole number
SL	Single-layer
SO	Single-objective
SOGO	Single-objective global optimization
ST/SY	Stator tooth/Stator yoke
THD	Total harmonic distortion
UMP	Unbalanced magnetic pull

1 General Introduction

1.1 Introduction

With the ever-increasing global economic and population growth, the worldwide demand for personal vehicles has increased. Therefore, the demand for fossil fuel is increasing significantly in order to satisfy the ever-increasing number of the vehicles. Consequently, due to the rising crisis in the petroleum supplies and CO₂ emission contributing to the greenhouse effect considerably, battery-powered electric vehicle (EV), hybrid electric vehicle (HEV), and fuel cell electric vehicle (FCV) are emerging as important areas of research.

An electrical machine is one of the key components of the EVs/HEVs. Although there are a number of different electrical machines used in the EV/HEV traction systems, permanent magnet (PM) and induction machines (IMs) are the most popular machines in these applications. Although a PM machine has better performance characteristics in such applications, particularly providing a high efficiency than an IM, because of the high cost and limited resource of the NdFeB PMs, the popularity of the IM in EV/HEV market has risen over a decade. High reliability, relatively high efficiency, simplicity, mature manufacturing technology and control methods, and much lower maintenance requirement of the squirrel-cage IMs have been the key features for industrial, automotive, and domestic applications for over 130 years.

With the concern of price and resource of rare earth PMs, electrical machines without rare earth magnets become very interesting research topics. IMs are clearly one of the best candidates, particularly following Tesla's use of IMs for its EV propulsion. In this thesis, advanced squirrel-cage IM topologies with improved performance will be developed and investigated for EV applications. In addition, the non-sinusoidal bar current waveform, a very important phenomenon occurring in the IMs, is also investigated in depth by considering the influence of magnetic saturation and design and operating parameters.

1.2 Induction Machines for EV/HEV Applications

Nowadays, EV/HEVs have gained increasingly attention each passing day because of the increasing concern on the global warming, reducing fuel-oil sources, energy conservation and efficiency, etc. Another reason is that the global CO₂ emission restrictions for new passenger vehicles, regulated by the international council on clean transportation, have increased each passing year in order to benefit public health and mitigate climate changes [DIA16]. Therefore, to be able to improve the environmental performance and energy efficiency of transportation, the focus on automotive electrification has seriously re-increased in the last decades. Since the electrical machines are the heart of the propulsion

system of the EVs, their improvements have received much attention, together with power electronics, controls and energy storage devices.

The origin of the HEVs dates back to 1890s. The first known HEV has been built by F. Porsche by using in-well (hub) motors [ONL17i]. After Porsche, other inventors built a number of EV/HEVs in the early 20th century. However, then the internal combustion engine (ICE) technology improved remarkably. Consequently, the EV/HEVs disappeared from the market for a long time. After revolutionary improvements in the fields of material science, power electronics, control systems, and battery technology, EV/HEV concepts returned strongly nearly a century later in the form of many research prototypes and commercial products such as Toyota Prius, Honda Insight, Nissan Leaf, Tesla all models, etc. In addition, a substantial support to research in this area has been provided by some government initiatives, such as the US Partnership for a new generation of vehicles [MAT01].

The electrical machines designed for propulsion applications should satisfy the following basic characteristics [ZHU07], [ZHU08]: (a) high torque, power, and efficiency; (b) high starting torque; (c) high torque at low speeds and hill climbing; (d) high power for high-speed cruising; (e) wide speed range; (f) wide constant torque region (approx. 3-4 times of the base speed); (g) intermitted overload capability, typically twice the rated torque for short durations; (h) low torque ripple and acoustic noise; (i) high reliability and robustness; (j) acceptable cost. The PM and IM can easily satisfy the following characteristics. Consequently, in the world's leading commercial hybrid electric vehicles (HEVs) and electric vehicles (EVs) such as Toyota/Prius, Nissan/Leaf, BMW/i3, Honda/Insight, Chevrolet/Volt, and several other vehicles, the interior-permanent magnet (IPM) machines are used [CHA07]. On the other hand, it is preferred to use the IMs in some other vehicles. IMs have been adopted in the transmission systems of a variety of automobiles from sport/luxury to light trucks such as Tesla/Roaster, Tesla/Model S, GM/EV1, Fiat/Seicento Elettra, Ford/Think City, BMW/X5, DaimlerChrysler/Durango, Chevrolet/Silverado, Renault/Kangoo ZE, etc. [ZER06], [ZHU07], [HAS08], [DOR12], [GOS13], [REF13], [BOL14], [YAN15], [GUA16], [EST16], [YAN17], [ONL17a], [ONL17b], [ONL17c], [ONL17d], [ONL17e], [ONL17f], [ONL17g], [ONL17h].

Recently, although the performance of electrical machine is significantly improved with the aid of permanent magnets (PM), the rising cost and limited resource of rare-earth PMs have renewed attention to using magnet-free machines. Currently, China produces 97% of the world's rare earth elements, therefore China may make reductions in export quotas because of the increasing global demand [XUE11], [GUN12]. Hence, considering all of these aspects together with the increasing concern of cost-effective design, the IM, the oldest and well-known type three-phase electrical machine, have become increasingly attractive in the use of industry and EV/HEV applications.

Consequently, since the IMs are preferred by a large number of EV/HEV manufacturers and it is also widely used in the other industrial applications, their improvement is of great importance in producing green and cheap energy in the world wide.

1.2.1 Structure of the IMs

The first commercial IM was invented by Nikola Tesla in 1888 [TES88], [ALG76]. The first invention had a stator with 4-poles comprising of tooth-concentrated windings and a wound rotor forming a squirrel-cage with short-circuited coils, which would start and run at a little below synchronous speed.

The former IMs were designed for the line-fed applications. Since the developments of solid-state inverters and control algorithms have reached maturity in the early 1990s, more attention started to give to the inverter-driven IMs [DAU91]. Due to high reliability, simple and rugged construction, relatively high efficiency, low cost, and mature manufacturing technology and control methods of IMs, they are favourable in a large number of different application areas. IMs still represent the largest market share despite of the wide variety of the electrical machines [ALM14].

In terms of number of phases, there are two basic types of IMs: single-phase and polyphase. In terms of rotor structure, there are two basic types: wound-rotor and cage-rotor. In terms of stator and winding topology, there are three basic types: integer-slot distributed winding (ISDW), fractional-slot distributed winding (FSDW), and fractional-slot concentrated winding (FSCW).

1.2.2 Working Principle of the IMs

In principle, an IM is an electrical machine in which the rotor receives its power not by conduction but by induction. A winding that receives its power exclusively by induction constitutes a transformer. Therefore, an IM is a transformer with a rotating secondary winding. Once the phase windings are properly connected to a 3-phase AC source, a magnetic field rotating at the synchronous speed is created. This is basically due to the Biot-Savart law which states that a magnetic field is created around the current-carrying wire. This field passes through the air-gap and causes inducing an EMF in the short-circuited rotor bars due to the Faraday's law of induction. In other words, since the bars in IM are short-circuited by a pair of end-rings and cut the stator rotating magnetic field, an EMF is induced in the rotor copper bar, and due to this EMF, a current flows through the rotor bar, in a manner similar to current induced in a transformer's secondary winding. Consequently, the induced currents in the rotor bars create magnetic fields in the rotor reacting against the stator field. The current induced in the rotor bars due to the rotating field is so directed as to oppose the change in flux due to the Lenz's Law. Consequently, to oppose the change in bar currents the rotor starts to rotate in the direction of the rotating stator magnetic field. The rotor accelerates until the amplitude of the bar current and torque balances the applied mechanical load. However, the rotor can never rotate at the synchronous speed since the rotation at the synchronous speed would result in no induced EMF in the bars. This is because the rotor bars would appear stationary with respect to the rotating field. When no EMF is induced in the bars, there would be no current in the rotor conductors, and consequently the force creating the torque would not be generated. Here, the relative speed between the rotating field (synchronous speed) and the rotor is the cause of current generation in the bars. The difference between the stator's rotating field and

rotor speed is called as the slip. As a summary, the rotor gains its power by induction only when there is a relative difference between the rotor speed and the stator's rotating field. That is why an IM is also called as an asynchronous machine.

1.3 Stator and Rotor Windings Used in Induction Machines

The IMs are designed by employing a rotating-field stator winding which is symmetrical, three-phase AC distributed or concentrated windings. At this point, there are basically two types of windings called integer slot and fractional slot windings. If the the stator slot per pole per phase number q is an integer number, then the winding called integer slot winding. If the q is a fractional number, then the winding called fractional slot winding. In addition, depending on the amount of q , these windings are grouped as distributed and concentrated windings. If $q \geq 1$, it is a distributed winding, else ($q < 1$) it is a concentrated winding. However, there is an exception for distributed windings. For $q = 1$ combination, it is possible to obtain both distributed and concentrated winding depending on the coil pitch number y_c . More details related with this exceptional winding, calling as integer slot concentrated winding, will be given in following section. The basic characteristics, such as winding factor, magnetomotive force (MMF) harmonics, etc. and merits and demerits of various winding configurations will be explained in Chapter 2, in detail.

1.3.1 Integer Slot Windings

Integer slot windings are know also as integral-slot windings. For inreger slot windings, q is any integer number and they can be configured as either distributed or concentrated depending on y_c . The winding layouts and key properties of these winding configurations with y_c from 1 to 5 are presented as follows.

A. Integer Slot Distributed Windings

Since the coils of the phases are distributed around the stator slots with the coil pitch larger than 2 slots ($y_c \geq 2$), the integer slot distributed windings (ISDWs) are overlapping windings as illustrated in Fig. 1.1. Furthermore, the stator slot per pole per phase number q of ISDWs is an integer number. They can be designed as double- or single-layer. The slots of the ISDWs are distributed uniformly among poles. The ISDWs are the most widely employed winding configurations for IMs because of their significant advantages over FSCWs are summarized as follows.

- High fundamental winding factor amplitude;
- High fundamental MMF amplitude per one-ampere and one-turn;
- High torque per ampere-turn;
- Very low MMF harmonics and relatively low rotor bar copper loss;

- Relatively low torque ripple, vibration, and acoustic noise.

On the other hand their major disadvantages are listed below.

- Very long-end windings and consequently long total axial length;
- Relatively low slot fill factor;
- Relatively high stator copper loss;
- Complex winding structure and difficulty in manufacturing.

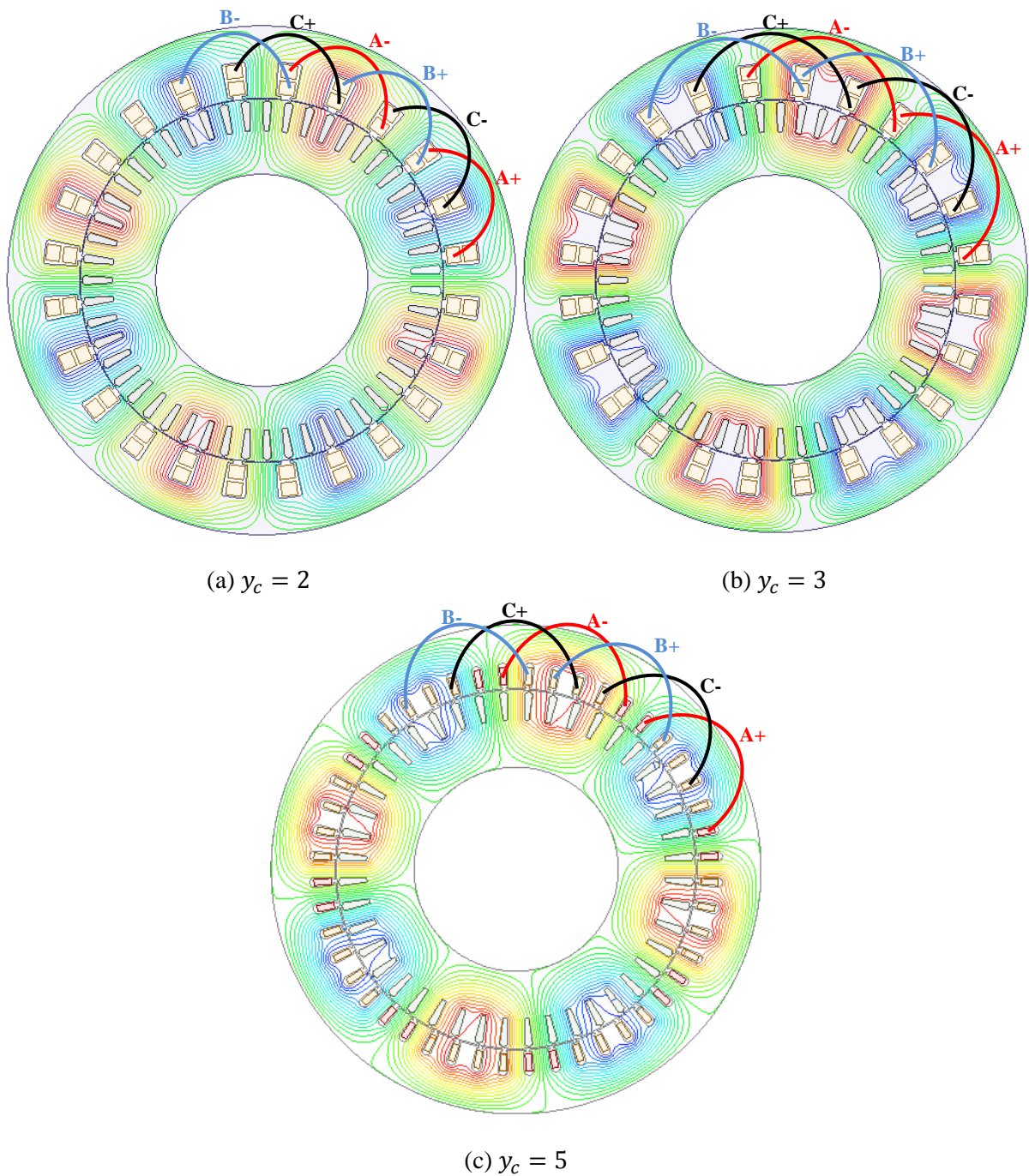


Fig. 1.1 Various ISDW configurations: (a) 24-slot and 8-pole, double-layer (24S/8P-DL) with $y_c = 2$ and (b) $y_c = 3$, (c) 48S/8P, single-layer (SL) with $y_c = 5$.

B. Integer Slot Concentrated Windings

Even though the integer slot concentrated windings (ISCWs) belong to the concentrated winding family since $y_c = 1$ is ensured (see Fig. 1.2), q is an integer number. The amplitude of the fundamental winding factor is dramatically low (i.e. 0.5). Therefore, this winding topology is not very common and not preferred by machine designers. Although there is no practical use of this kind of winding topology, in order to indicate the similarity between this winding and to be proposed winding topologies, this section has been presented. The physical properties of this winding structure are similar to FSCWs. However, the main differences between ISCWs and FSCWs are summarized as follows.

- They usually do not contain sub-harmonics;
- The fundamental winding factor is usually 0.5;
- Their fundamental MMF amplitude is lower than both ISDWs and FSCWs.

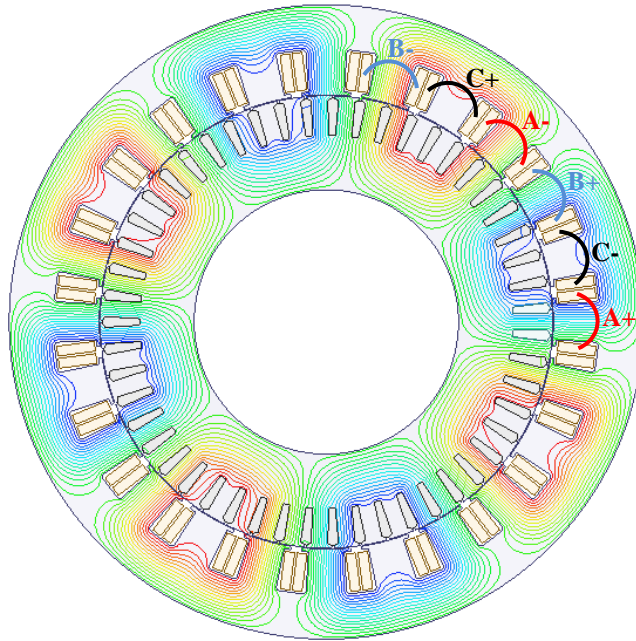


Fig. 1.2 The 24-slot and 8-pole, double-layer (24S/8P-DL) with $y_c = 1$ ISCW configurations.

1.3.2 Fractional Slot Windings

Fractional slot windings can also be configured as either distributed or concentrated depending on y_c . For this kind of windings, the q is always an inter number. The winding layouts and key properties of these winding configurations with y_c from 1 to 3 are presented as follows.

A. Fractional Slot Distibuted Windings

Since the coils of the phases are distributed around the stator slots with the coil pitch larger than 2 slots ($y_c \geq 2$), the fractional slot distributed windings (FSDWs) are overlapping windings as illustrated in Fig. 1.3. Furthermore, the q of ISDWs is a fractional number. They can be designed as double- or single-layer. However, since all the single-layer winding combinations of this family have MMF sub-

- The fundamental winding factor amplitude is slightly lower than that of the ISDWs for the same pole combinations;
- The fundamental MMF amplitude per one-ampere and one-turn is also slightly lower than that of the ISDWs for the same pole combinations;
- Relatively high torque per ampere-turn;
- Low MMF harmonics can be achieved only for $q = k + 0.5$ combinations with double-layer windings;
- Low rotor bar copper loss can be achieved only for $q = k + 0.5$ combinations with double-layer windings;
- All single-layer combinations have MMF sub-harmonics;
- Long-end windings and consequently long total axial length;
- Relatively low slot fill factor and relatively high stator copper loss;
- Complex winding structure and difficulty in manufacturing.

B. Fractional Slot Concentrated Windings

The FSCWs belong to the non-overlapping winding family since the coils of the phases are concentrated on only one stator tooth ($y_c = 1$) as illustrated in Fig. 1.4. In addition, the q of FSCWs is always lower than one. The winding factor of the FSCWs include both super- and sub-harmonics, except for $q = 0.5$ family. The family of $q = 0.5$ includes only super-harmonics of winding factor. Some advantages of the FSCWs are summarized as follows.

- Short end-winding;
- High slot fill factor, about 60% [STA05]; and it is possible to increase the slot fill factor to up to 78% by employing compressed coils with segmented stator [JAC00];
- High slot thermal conductivity due to higher slot fill factor;
- Easy manufacturing.

Despite of these advantages, the research on IM having FSCWs is still not popular due to the following drawbacks.

- 1) Lower fundamental MMF amplitude per one-ampere and one-turn;
- 2) Low torque per ampere-turn;
- 3) Very high MMF harmonics;
- 4) High harmonic leakage inductance;
- 5) Higher torque ripple, vibration, and acoustic noise;
- 6) Higher rotor bar loss [REF08] and higher magnetizing current necessity [GUN14];

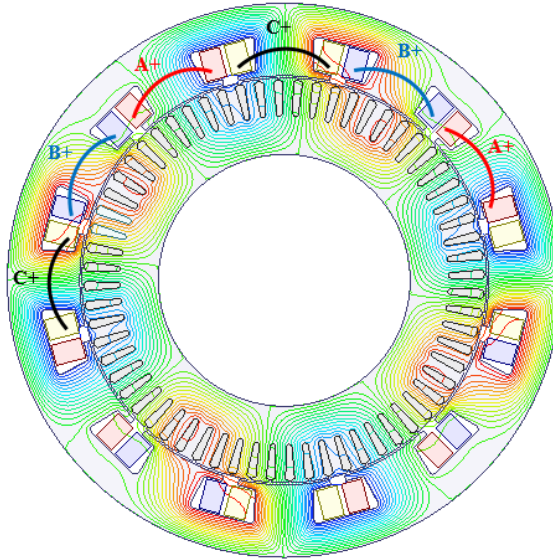


Fig. 1.4 12S/8P-2L with $y_c = 1$ FSCW configuration.

1.3.3 Adapted Non-Overlapping Integer Slot Concentrated Windings

In order to combine the advantages of ISDW and FSCW configurations, a new winding configuration called adapted non-overlapping winding (ANW), which belongs to the integer slot concentrated winding (ISCW) family, is developed in this thesis. The same winding topology has been intended to use in high-temperature superconductor (HTS) synchronous machine [ZHA16]. It is shown that the MMF harmonic content of the double-layer non-overlapping windings are low. Therefore, it is decided to adapt the winding topology proposed in [ZHA16] into an advanced IM. As seen in Fig. 1.5, the windings comprises of coils with $y_c = 2$. The windings are electromagnetically overlapped but there is no physically overlapping between the phase coils. This unique configuration has been modified to achieve shorter total axial length without sacrificing the torque and power density and efficiency. Some key advantages and disadvantages of the ANWs are summarized as follows. Design, analyses, investigations, and development of squirrel-cage IMs with ANWs have been presented in Chapters 2, 3 and 4.

- Relatively high fundamental MMF amplitude per one-ampere and one-turn;
- Relatively high torque per ampere-turn;
- Relatively low MMF harmonics and consequently, low rotor bar copper loss;
- Very short end-winding;
- Relatively high slot fill factor and high slot thermal conductivity due to higher slot fill factor;
- Easy manufacturing;
- Relatively high torque ripple, vibration, and acoustic noise;
- Moderate fundamental winding factor amplitude (0.866).

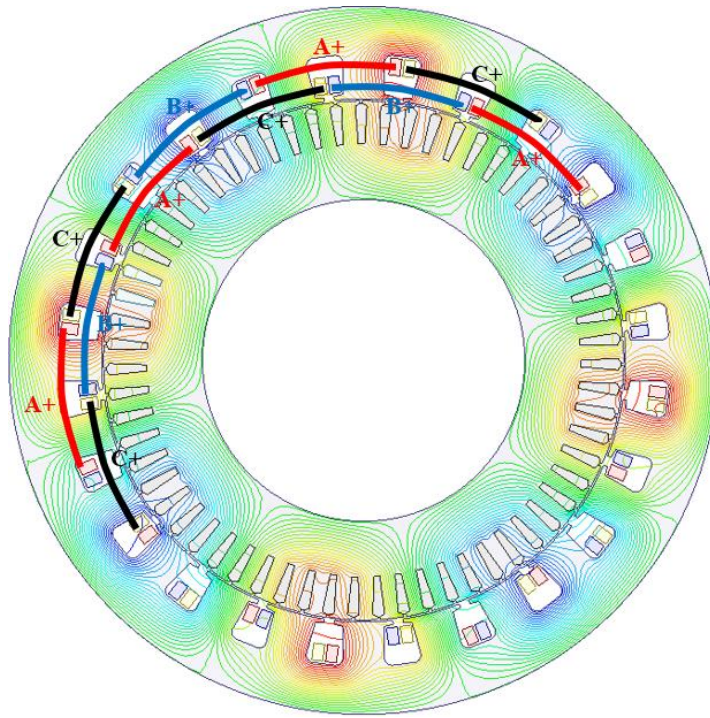
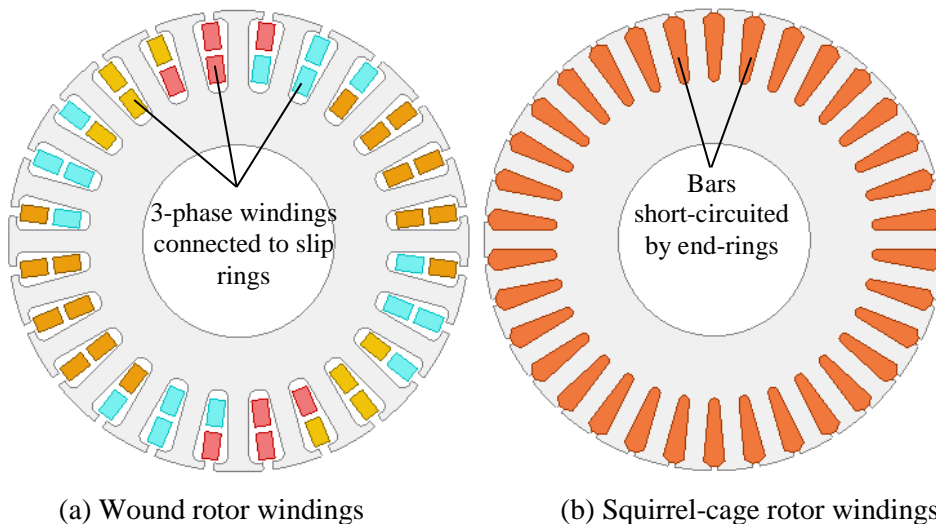


Fig. 1.5 24S/8P-2L with $y_c = 2$ ANW configuration.

1.3.4 Rotor Windings Used in Induction Machines

The rotor of an IM can be either squirrel-cage or wound rotor as shown in Fig. 1.6. Each structure has its own advantages and each one can be used in different application areas. The squirrel-cage consists of cylindrical laminated core having semi-closed or closed slots filled with die-casted or insert type aluminium or copper bars which are short-circuited at each end by copper or aluminium rings (see Fig. 1.6(b)). On the other hand, the wound rotor consists of laminated cylindrical core which has a semi-closed slot at the outer periphery and carries three-phase insulated winding similar to stator windings as seen Fig. 1.6(a). The rotor windings are wound for the same number of poles as the stator. Usually, the end terminals of phase windings are connected from a star point while the start terminals of each phase windings are connected to three copper slip rings fixed on the shaft.



(a) Wound rotor windings

(b) Squirrel-cage rotor windings

Fig. 1.6 IM rotor structures: (a) wound rotor and (b) squirrel-cage rotor.

A. Wound Rotor

For wound rotor IMs, it is possible to connect a resistance group or an inverter to rotor windings in order to change the starting or drive characteristics of the IMs whilst the stator winding is still connected to grid. They are extensively used in double fed induction generators for wind power application. More than 70% of the installed wind turbines employ wound rotor IMs [GOR14]. The wound rotor IMs have some advantages and disadvantages over their squirrel-cage counterparts, such as low required inverter capacity [BOG13], adjustable power factor in the stator side, complex rotor structure, low efficiency, and maintenance problem. Although the structure of the IMs having wound rotor is complicated (as seen in Fig. 1.6(a)) and they requires frequent maintenance due to the existence of the rotor windings, slip rings, and brushes, their starting characteristics are excellent: the high starting torque with low starting current.

B. Squirrel-Cage

A squirrel-cage IM is a singly-fed machine and its rotor structure is very simple as seen in Fig. 1.6(b). Therefore, it does not require a commutator, slip-rings, or brushes. In fact, there are no moving contacts between the stator and the rotor. This results in a machine that is rugged, reliable, and almost maintenance free. That is why the squirrel-cage IM is used widely in industrial and EV/HEV applications. The absence of brushes eliminates the electrical loss because of the brush voltage drop and the mechanical loss due to friction between the brushes and commutator or the slip-rings. Thus, a squirrel-cage IM has a relatively high efficiency.

Since the rotor bars are short-circuited via end-rings, it is not possible to make an external connections to change the starting or drive characteristics. In addition, in order to reduce the parasitic effects, such as torque ripple, acoustic noise, vibration, etc. and increase the starting performance, the squirrel-cage rotor of grid connected IMs is usually skewed.

1.3.5 Technical Issues with Induction Machines

There are a number of technical issues related with the IMs, namely, faults occurring in IMs, unbalanced or asymmetric operating of IMs due to the some certain faults, and recently revealed non-sinusoidal bar current waveform phenomenon. The accurate prediction of the degradation of the performance characteristics of the IMs under faulty operating conditions and an appropriate assumptions of the rotor bar current waveform, directly affecting the performance characteristics, are of substantial importance.

A. IM Faults

Although the IMs are rugged and reliable, they are subjected to some undesirable stresses, causing them some faults and eventually to failure as classified below [VAS93], [TOL95], [NAN99], [SID05], [BON08], [BEL08].

- Stator faults defined by one or more of a stator phase winding open or short circuited, or abnormal connection of the stator windings;
- Rotor faults defined by rotor winding open or short circuited for wound rotor and broken bar and/or cracked rotor end-rings for squirrel-cage;
- Mechanical faults defined by dynamic eccentricity, bearing damage, misalignment, bent shaft, etc.

These faults cause stresses, such as thermal, electrical, mechanical, and environmental resulting in one or more of the symptoms as classified follows.

- Decreased average torque;
- Increased torque ripples and pulsations;
- Increased bar current waveform distortion level;
- Increased power losses and consequently reduced efficiency;
- Excessive heating;
- Unbalanced air-gap flux distribution, stator voltage, and line currents;
- Large errors between the predicted and measured performance characteristics.

Among the specified faults, the bearing, the broken bar/end-ring, the eccentricity, and particularly the stator faults (35%-40% of IM failures) are the most prevalent faults [VAS93], [NAN99], [SID05]. The stator and rotor faults result in unbalanced operating situations.

B. Unbalanced or Asymmetric Operations of IMs

The wound rotor IMs with multi-phase winding configurations have the capability of running with one or more of its stator or rotor phase open- or short-circuited or abnormal connection of the stator windings. In the same manner, the squirrel-cage IMs with multi-phase winding configurations have also the capability of running with one or more of its stator phase open- or short-circuited or abnormal connection of the stator windings or broken rotor bar or end-ring. In this instance, the IM would have asymmetric stator and/or rotor winding connections. Once the IM is operated with such an unbalanced condition, the dynamic properties of the machine would change extremely [VAS75], [TOL95], [ZHA96], [TOL98].

Asymmetric operation of the IMs results in unbalanced phase current, unbalanced air gap field distribution, decreased average torque, decreased starting torque, increased torque ripple and pulsations, increased power losses and consequently decreased efficiency and excessive heating [TOL95], [ARA10]. In addition, control and drive strategies developed for an IM having balanced winding configuration would no longer work properly [ZHA96].

C. Non-Sinusoidal Bar Current Phenomenon

The rotor bar current of an IM plays an important role in generating of torque and output power, and accurate calculation of the power losses and consequently the efficiency [LAN77]. In a healthy squirrel-cage IM, fed with a balanced symmetrical 3-phase sinusoidal source, the induced EMF waveform on the rotor bars is generally presumed to be sinusoidal and consequently the bar currents are also presumed to be sinusoidal [WEI11], [HOO11], [BUC72]. It is shown that under non-sinusoidal source fed or faulty operating conditions, the bar current waveform can become non-sinusoidal [GYS00], [BOT04], [BRU07], [KUN12], [SUN13], [MES14]. However, as will be shown in this thesis, the bar current waveform of a healthy IM, fed with a balanced symmetrical 3-phase sinusoidal source, can also be non-sinusoidal under some certain design or operating conditions given below.

- Very low slip;
- Excessively high electric loading;
- Very short air-gap length;
- Excessively high rotor slot number;
- Inappropriate stator slot/rotor slot/pole number combinations;
- Not optimised/inappropriate stator/rotor slot geometries;
- Not optimised/inappropriate rotor skew angle;
- Very short coil pitches.

In Chapters 5, 6, and 7, the conditions for such non-sinusoidal rotor bar current to occur and the reasons behind this phenomenon will be investigated by FEA, with particular reference to the influence of the design and operating parameters given above.

1.4 Literature Review on Novel Induction Machines

In this section, a comprehensive literature review on the novel IMs is presented. Note that the discussed novel topologies in this section are on the improvement of performance characteristics of IMs by reducing or completely cancelling the MMF harmonics.

1.4.1 Novel Stator and Winding Topologies

In order to reduce the end-winding copper loss and also the total axial length, the FSCWs have been implemented to an IM having an unconventional squirrel-cage structure as shown in Fig. 1.7. In order to improve the starting characteristics of the IM, shaded pole structure has been employed in the stator. In addition, in order to reduce the undesirable effects of the heavily distorted MMF waveform; such as significantly high bar copper loss, a multi-cage rotor comprising of three-sets of bars and four different end-rings with different dimensions has been utilized. While the largest end-ring short-circuits

all the bars, the other rings short-circuit each set of bars separately. In other words, there is no electrical contact between the small end-rings. Although the rotor structure is quite complex, stator structure is quite simple. The rotor structure of this IM will be explained in the following section in more detail.

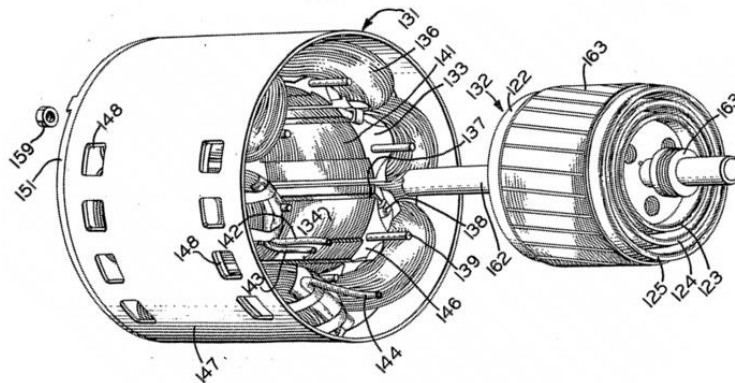


Fig. 1.7 Structure of the single tooth winding IM with multi-cage rotor [LIN76].

In order to reduce the higher order field harmonics, which may travel around the air-gap at different speed compared to the fundamental one, two stator sections at two different axial positions is proposed in [JAC04]. The structure of the proposed topology is illustrated in Fig. 1.8. Thus, the reductions and/or dips in the torque-speed characteristic and the extra rotor losses can be achieved. However, as seen in the figure, existence of the end-winding lengths and gaps between the IMs causes increasing in the total axial length reparably.

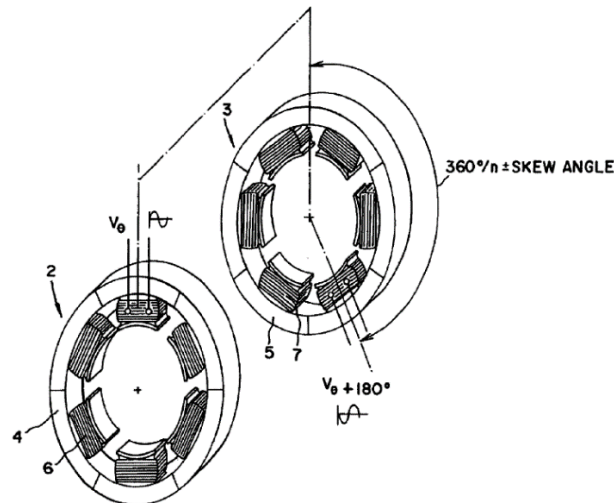


Fig. 1.8 Structure of the tooth winding IM with two stator sections at two different positions [JAC04].

A squirrel-cage IM's performance with FSCWs has been investigated and the obtained performance characteristics have been then compared with the ISDW version of the IM [REF08], [REF12], [GUN14], [BAC15]. Potential advantages and disadvantages of using FSCWs in the IMs have also been presented. According to the obtained results, it has been concluded that the IMs with ISDWs show a superior performance comparing to the FSCWs in terms of torque production and rotor bar losses. It has also been demonstrated that the higher the q , the better the performance in terms of torque and losses. On the other hand, FSCW IM is proven superior to CSDW IM in terms of higher power density, higher slot

fill factor, easier manufacture and lower manufacturing cost, and higher fault-tolerance. In addition, influence of stator and rotor slot parameters on the electromagnetic characteristics of an IM with FSCWs is discussed in [FUN15] and it is concluded that FSCW IM with closed slot rotor has lower air-gap flux density harmonic components. The feasibility of adopting a fractional-slot doubly fed induction generator in a direct-drive wind power generator has been investigated for the first time in [ALB09b]. Fractional slot windings are used in both stator and rotor as seen in Fig. 1.9. This study shows that with a suitable choice of the numbers of stator and rotor slots, it is possible to minimise the interaction between stator and rotor MMF harmonics, and hence, limit the losses and torque ripples. In addition, it is noticed that because of the very high magnetising current, the solutions with using a very low number of poles are not feasible. However, a direct-drive IM having FSCWs becomes attractive in the very low speed applications such as wind power.

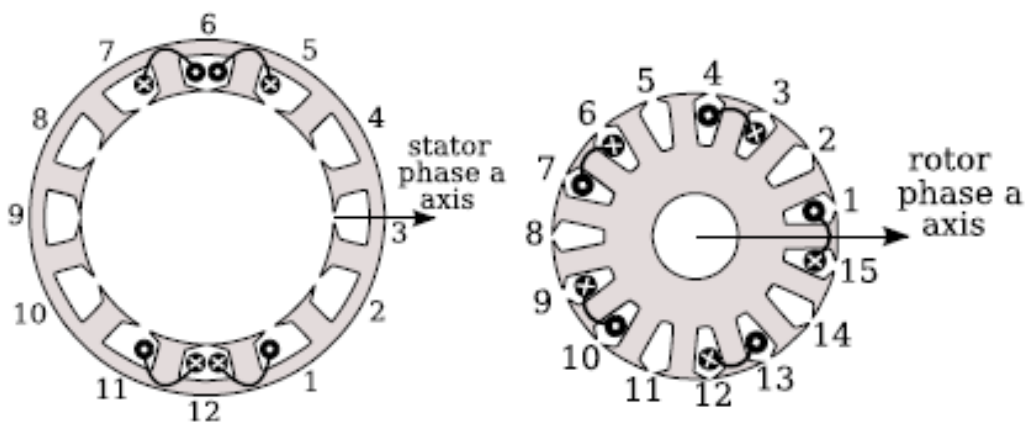


Fig. 1.9 FSCWs on both rotor and stator [ALB09b].

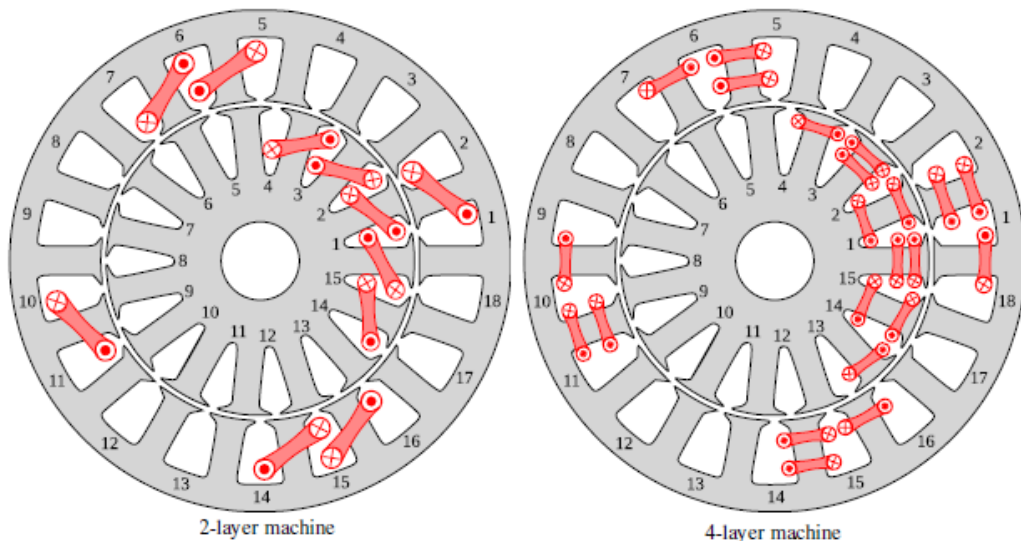


Fig. 1.10 Multi-layer windings on stator and rotor [ALB12].

In [ALB12] and [ALB13], the feasibility of the FSCW technique in IMs and the limits and difficulties have been highlighted. Multi-layer windings are used in the both stator and rotor as seen in Fig. 1.10 in order to reduce the MMF space harmonics amplitudes which lead to limit to the torque ripple. Due to the short end-winding of FSCWs, an increase in the efficiency and a reduction in the

weight/torque ratio can be achieved. However, FSCWs are characterised by a high MMF space harmonic content because of the low and fractional number of q . To be able to verify the simulation results, a small size IM prototypes one having 2- and other having 4-layer windings have been built. It is noticed that the large number of poles yield magnetization problems, and the high inductance reduces the maximum torque. Because of that reason authors suggested that the multi-layer windings could be attractive for low-speed high torque machines. In this study, a considerable reduction of the MMF harmonics and hence torque ripple are achieved by using multi-layer windings.

In [EAS10], in order to cancel the harmonics on linear IM (LIM) presented in [EAS08] (see Fig. 1.11(a)), a planar modular winding structure with two concentric coils in each coil group is proposed as shown in Fig. 1.11(b). In this study, as seen in single coil and two concentric coils in each group on the stator and also various pole slot combinations are investigated. In order to suppress the oppositional harmonic MMF waveform and reinforce the fundamental MMF waveform, a mechanically offsetted double-sided arrangement of stators is used. In a similar study presented in [COX11], in order to cancel unwanted MMF harmonics on a double-sided IM, simple and robust planar concentrated windings have been implemented. These windings can be multi-layer and made with different coil pitches as seen in Fig. 1.12. In this paper, a number of single-sided machines using multi-layered planar coils are developed and their performance are then analysed. It is concluded that the use of these planar concentrated windings in IMs gives significant advantages due to simplified production, reduced material requirements, reduced labour and material costs, and improved reliability and efficiency when compared to conventional double-layer type windings. In [POU15], a low-speed LIM with toroidal winding is proposed for providing a better performance and efficiency in space-constrained applications. The structure and winding layout of the proposed LIM are shown in Fig. 1.13. The obtained results of the LIM with toroidal winding is then compared with distributed winding LIM (DWLIM) and it is concluded that the proposed LIM has better performance and efficiency than DWLIM for every operating slip.

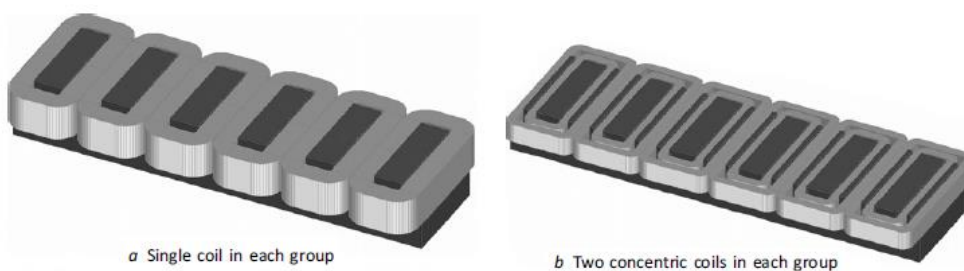


Fig. 1.11 Modular winding stators [EAS10].

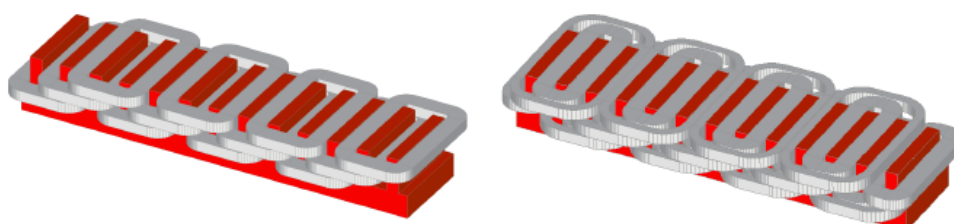


Fig. 1.12 Three-layer planar concentrated windings with different configurations [COX11].

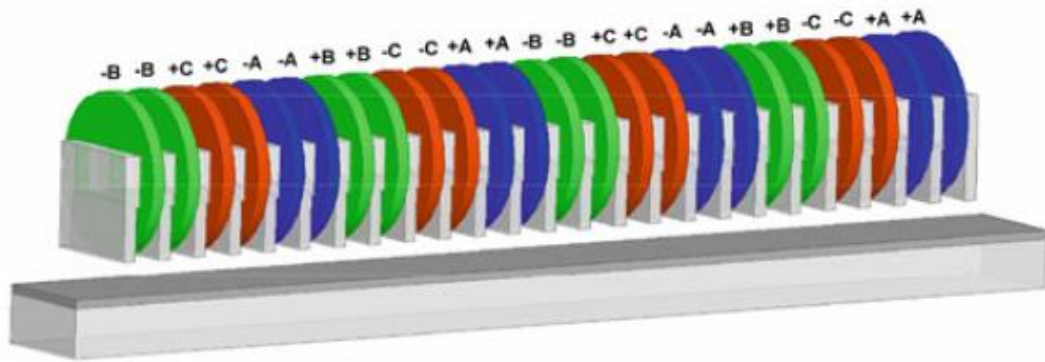


Fig. 1.13 Primary winding layout of the LIM [POU15].

A 20 kW high temperature superconducting induction-synchronous machine is designed and prototyped by introducing high temperature superconducting technology to EV drive motor (see Fig. 1.14) [SEK12]. In the paper, the design method, properties of used materials, winding method, fabrication, and test results of the prototype have been explained and a 112 Nm @ 1200 rpm synchronous torque with 92.3% efficiency is obtained.

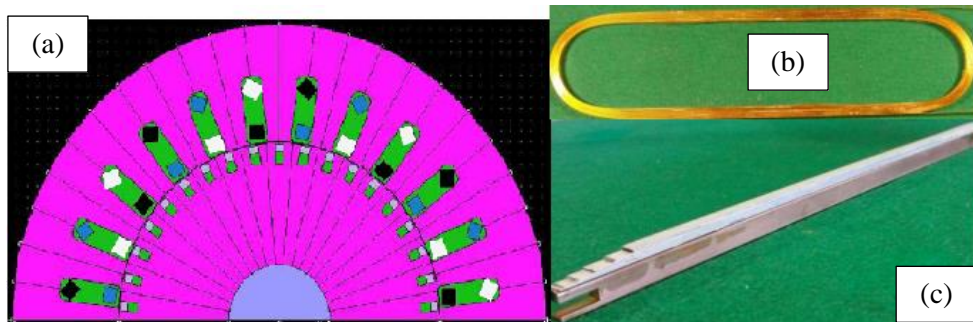


Fig. 1.14 Structure of the superconducting IM: (a) Analysis model of the HTS-ISM with 3-phase ISDWs; (b) Racetrack-shaped double pancake coil for stator windings; (c) rotor bar [SEK12].

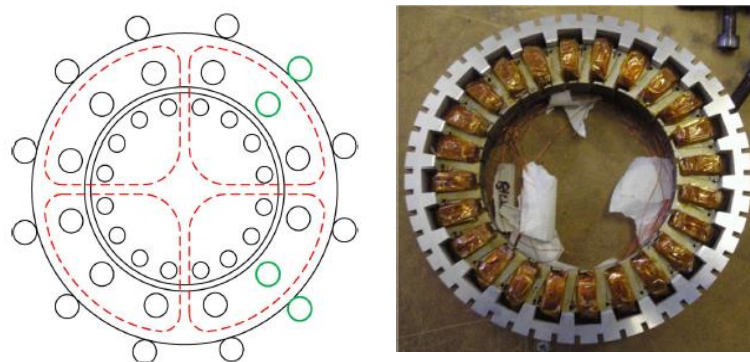


Fig. 1.15 Toroidally wound IM, principal scheme (left) and prototype (right) [JEN12].

In [JEN12], the authors designed and built a prototype of a four-pole toroidally wound IM, where the stator is constructed as a pre-wound foldable strip in order to achieve higher efficiency and cancel the even harmonics. Principle scheme and the prototype of the proposed IM are illustrated in Fig. 1.15. As seen in the figure, the windings are wound around the stator core back and hence are non-overlapped. It is shown that if the machine is axially restricted in length it can have substantially shorter stator end-

windings which leads to lower losses, and hence, higher efficiency when compared to the conventional wound IM with the same geometry. The construction of a toroidally wound IM prototype and the comparison of the experimental results to the estimated results for a conventionally wound IM having the same geometry and operating specifications are presented. Some important findings of this study can be summarised as:

- 31% shorter phase windings and 31% lower stator phase resistance;
- Significantly increased leakage inductance;
- Because of foldable strip, the final construction of stator contained distributed air-gaps on the stator yoke. These gaps appeared as reluctance in the magnetic circuit and result in a decrease in the magnetising current and magnetising reactance;
- Classic torque-speed characteristics is obtained.

In order to design high efficiency and low cost electrical machines for automotive applications, several improving methods for PMSM, IM and wound-rotor synchronous machine have been presented in [DAJ11a], [DAJ11b], [DAJ12a], [DAJ12b], [DAJ13a], [DAJ13b], [DAJ13c], [DAJ14a], [DAJ14b], [DAJ15]. These improving methods include use of concentrated winding technique, flux barriers on the stator core [JAC05], different number of turns per one coil side, series connected rotor bars [LIN76], doubled stator slot with shifted winding sub-system [KOM00], [ITO09], star & delta combined winding connection [KOR18], and stator cage winding concept. Note that the most of the topologies presented in these papers can be easily modified to the squirrel-cage IMs.

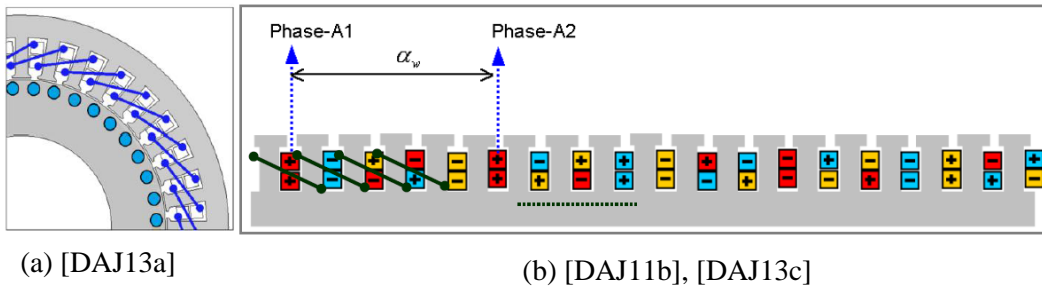


Fig. 1.16 Winding configuration for reducing MMF harmonic content: (a) short-pitch fractional-slot distributed windings and (b) auxiliary slots and winding sets shifted with a specific shift angle.

In order to improve the efficiency, short-pitch windings with $y_c = 2$ has been proposed in [DAJ13a]. The winding layout of the proposed winding topology has been shown in Fig. 1.16. In order to reveal the effectiveness of the proposed winding topology, efficiency of a squirrel-cage IM having 36-slot/10-pole double-layer ISDWs with $y_c = 2$ has been compared with its long-pitch counterpart having 90-slot/10-pole double-layer ISDWs with $y_c = 9$. Note that both IMs have the same geometric and operating specifications. The obtained results from FEA show that the efficiency of proposed IM having short-pitch windings is 3% higher than its long-pitch counterpart. On the other hand, if the machines are designed for the same efficiency condition, a weight-reduction up to 16% and length-reduction up

5% are reached. In a similar study, in order to minimise the MMF harmonics of 12-slots/10-pole winding, additional slots (by doubling the number of stator slot) and additional set of winding (by doubling the number of coils per phase) have been utilised. The reduction of MMF harmonics has been achieved by shifting the additional set of winding with a proposed shift angle (see Fig. 1.16(b)). However, it has been shown that it is not possible to reduce/cancel the winding harmonics without sacrificing the fundamental winding factor.

In order to increase the efficiency and reduce the size of an IM, a new winding structure with cage windings has been proposed [DAJ14a], [PAT14b], [DAJ15] (see Fig. 1.17). The proposed winding type is characterised with a simple construction and manufacturing, very low MMF harmonic content, short end-winding length, high fundamental winding factor, and good fault tolerance. The structure of the proposed winding type makes it possible to excite each stator bar separately. Thus, the IM can be driven at various modes, such as pole-pair number changing, multi pole-pair operation, active phase number changing, etc. In addition, the proposed winding construction offers a high thermal capability with a simple cooling mechanism [DAJ14a], [PAT14b], [DAJ15].

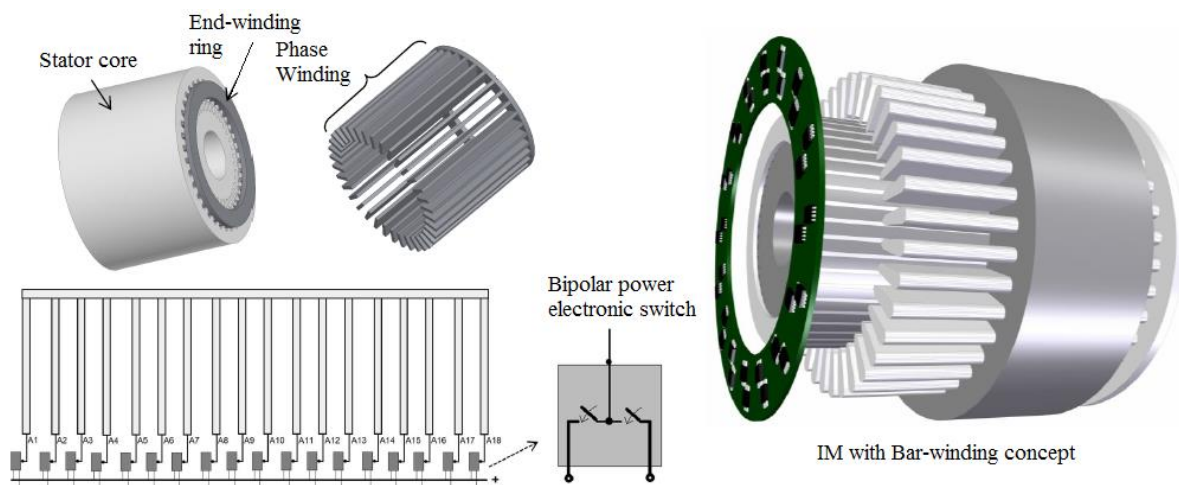


Fig. 1.17 Structure of the stator cage windings with multi-phase inverter drive concept [DAJ14a], [PAT14b], [DAJ15].

Effect of combined star-delta winding configuration on a three-phase IM's torque, space harmonics, losses and efficiency has been investigated in [MIS14]. The topology of the proposed winding arrangement is shown in Fig. 1.18(a). It is shown that by using that winding combination, lower stator and rotor copper losses, and hence higher efficiency, and higher fundamental winding factor and a lower harmonic content can be achieved. In similar studies, the same combined star-delta connection method is utilized for 18-slot/10-pole FSCW IM [MOR14] and [MOR15a]. In order to increase the performance characteristics and reduce the MMF space harmonics, 3-phase star-delta combination is illustrated in Fig. 1.18(a) and (b) has been utilized into a squirrel-cage IM. However, even if the some of the winding MMF super- and sub-harmonics are cancelled/reduced, the rotor bar copper loss is not reduced satisfactorily. A further study on the same combined star-delta connection method is utilized for 12-

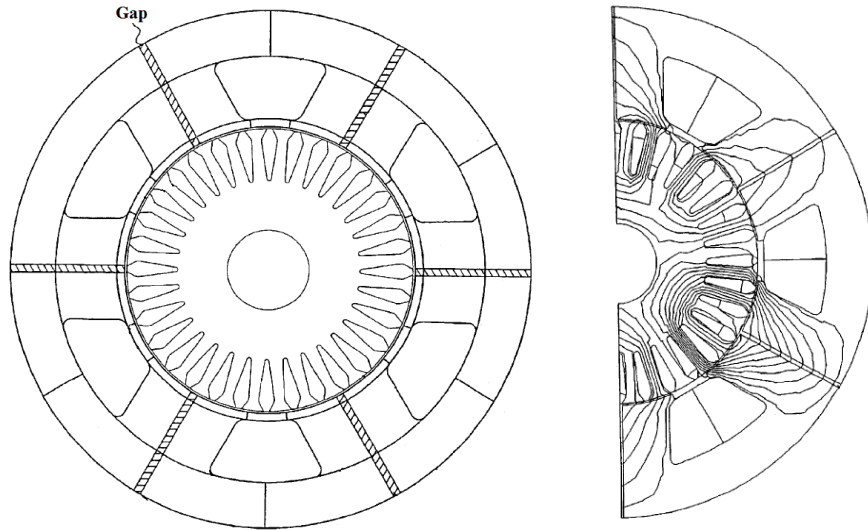


Fig. 1.19 FSCW IM with barriers (gaps) on the slot teeth [JAC05].

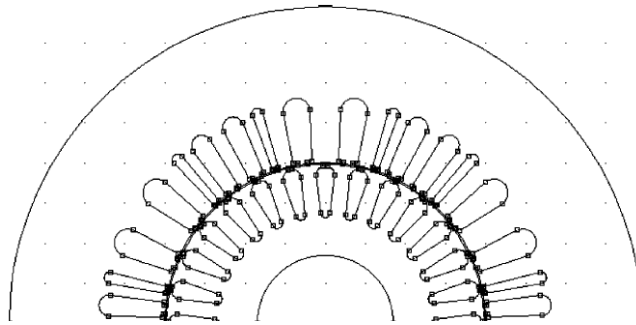


Fig. 1.20 Cross-section of the IM with asymmetric stator slots [KOC09].

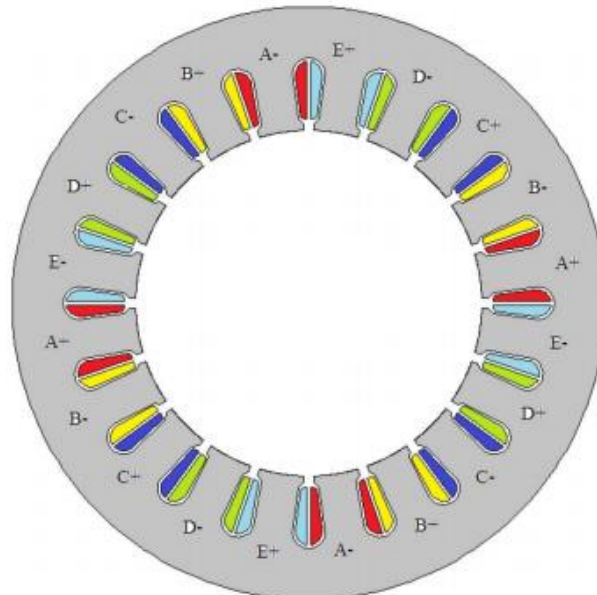


Fig. 1.21 Winding configuration of five-phase FSCW IM [ABD12].

In [ABD12], a five-phase 20-stator slot/4-pole ($q = 1$) modular winding squirrel-cage IM, whose winding layout is illustrated in Fig. 1.21, designed for reducing the effect of MMF harmonics is investigated through the simulations and experiments. Tradeoff, design considerations, and some

performance characteristics have been presented by comparing the three different IMs, namely, three and five-phase conventional, and five-phase modular. It has been concluded that with the 20% increase in the stator outer diameter, 30% increase in total weight, 24.5% decrease in the power density, and 0.64% decrease in the efficiency, it is possible to design a modular five-phase IM by keeping the stack length fixed with the conventional IMs. Considering the obtained experimental results, including lower winding factor, lower power density, higher space harmonics, higher torque ripples, higher core loss, lower efficiency and lower power factor, it seems that the proposed method is not suitable for five-phase FSCW IMs.

An outer-rotor IM with three-layer FSCWs and two-layers of stator slots has been designed and analysed through FEA [SUN15]. By utilizing this kind of winding, it has been intended to eliminate some sub- and higher-order space harmonics. The winding layout and the end-windings are shown in Fig. 1.22. Some performance characteristics of the designed machine have been presented by comparing the obtained results with an IM designed with conventional distributed winding. The obtained results have been summarised as below:

- FSCW IM has longer stack length but identical total axial length.
- Since very deep and remarkably narrow slot openings have been used, there is a very large amount of leakage flux all around the stator tooth and slot parts which cause increasing in core losses and decreasing in torque density.
- The achieved efficiency is 5.35% lower than that of the conventional IM.
- The same average torque with the conventional IM has been achieved in the FSCW IM with higher torque ripple and high magnetising current.

In [SAK17], in order to reduce the torque ripple of IMs with FSCWs, a new winding topology called full-slot distributed unequal-turn (FSUET) is proposed. Coils are wound around the teeth and the number of turns of each coil is different, but the number of turns per phase is the same. As shown in Fig. 1.23, the proposed winding method is utilized for tooth concentrated and toroidal IMs. It is shown that thanks to the utilized winding method, the torque ripple can be reduced considerably. In addition, it is suggested that the proposed winding topology is suitable for using in pole-changing machines with additional inverters. However, the most important issues of IMs with FSCW, which are the rotor bar copper loss and bar current density, have not been investigated. In addition, for the tooth concentrated winding (Fig. 1.23(a)), placing all the phase windings with different end-winding length causes unbalanced magnetic pull and parasitic effects because of the unbalanced phase resistance and inductance of the windings.

A new single tooth winding layout for a single-phase IM with segmented stator has been designed and prototyped in [ABD15b]. The proposed winding layout is based on dual two-phase windings shifted in space by 45° electrical degrees to completely cancel out both the third and fifth order harmonics. In

addition, different number of turns per slots have also been used for the same purpose of cancelling the harmonics as seen in Fig. 1.24. In the study, it has been shown that the efficiency of the machine is remarkably low. Since no performance comparison with a conventional IM has been conducted, it is not possible to mention about the advantages/disadvantages of using the proposed method.

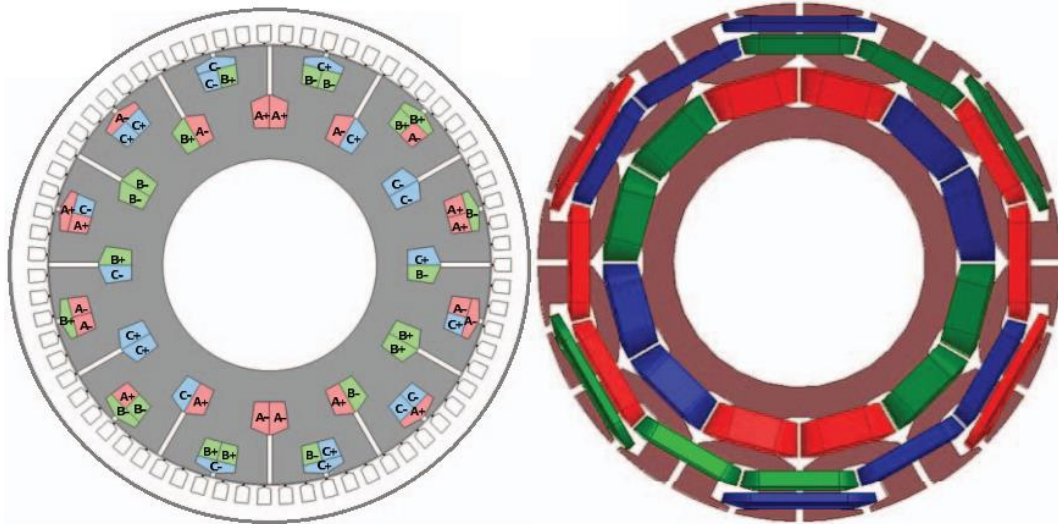


Fig. 1.22 Winding layout of the outer-rotor IM (left), and its end windings (right) [SUN15].

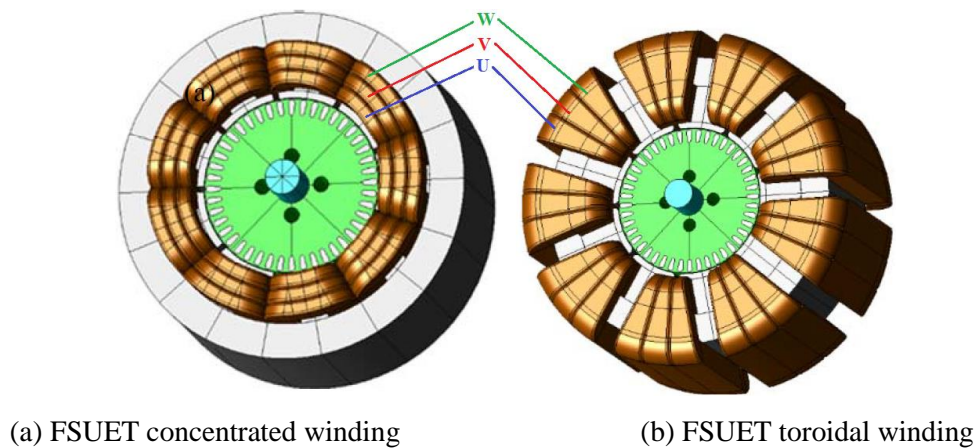


Fig. 1.23 Configurations of motors with FSUET windings [SAK17].

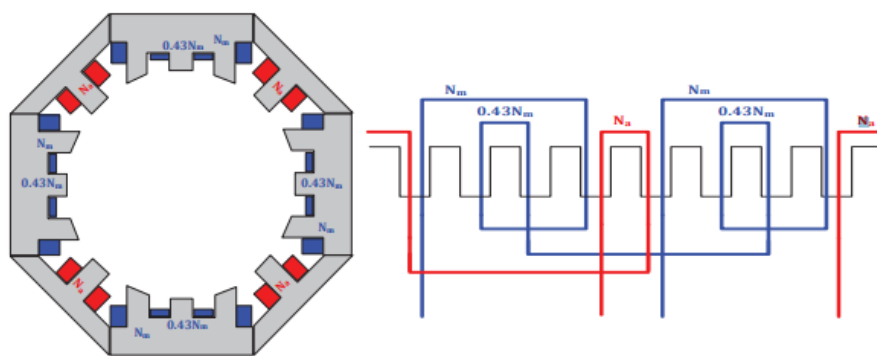


Fig. 1.24 Single-phase IM with segmented stator and single tooth windings (left), and its winding layout indicating the different number of turns per slot (right) [ABD15b].

1.4.2 Novel Rotor and Cage Topologies

This part includes the novel cage and rotor core designs. A large variety of papers have been focused on minimisation or elimination of rotor losses and parasitic effects due to the large air-gap flux density harmonics.

It has been claimed that by utilizing multi-cages in a single rotor, it is possible to reduce the harmonic currents [MOR34] (see Fig. 1.25). The key idea is to create a number of electrically independent circuits which enables to maintain the fundamental bar current with reduced harmonic content. Thus, the efficiency and torque of the IM can be improved and a lower starting current may be obtained. However, this concept causes increasing the manufacturing cost and effort remarkably. In a similar patent, in order to improve the performance of a three-phase IM in terms of efficiency, torque and power density, and harmonic contents, a new stator and rotor construction has been proposed [LIN76].

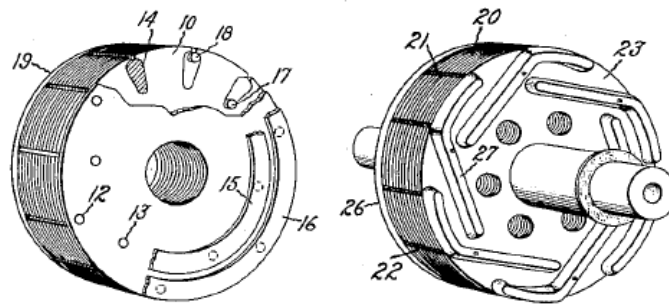
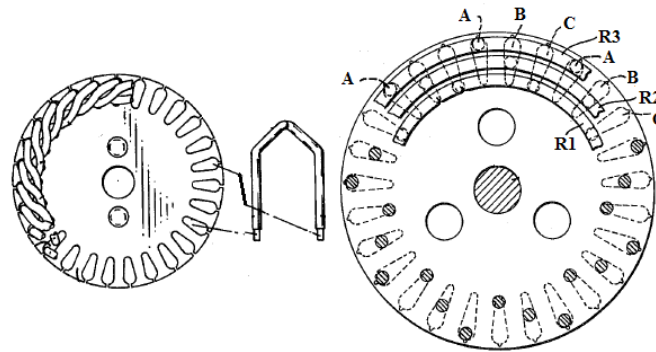
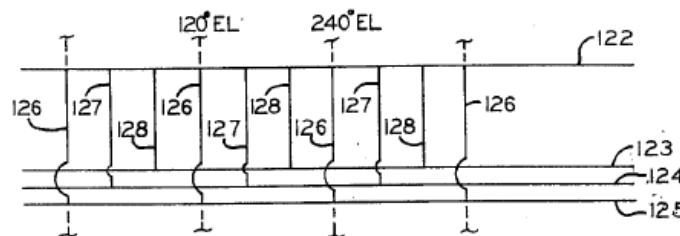


Fig. 1.25 IM cage-rotor members having a double and multi-end-rings [MOR34].



(a) Rotor bar structure and one side end-ring connections for multi-cage structure



(b) Rotor bar connection diagram

Fig. 1.26 Schematic representations of the rotor cage pattern and bar connections [LIN76].

Stator windings consist of 3-sets of FSCWs and closed loop shading coils are inserted on the each stator pole piece. By using this stator topology, stator copper losses are reduced because of the short-end

windings and EMF harmonics are reduced by using shading coils. The rotor consists of three-layer windings namely A, B, C and their rings namely R1, R2, and R3 as seen in Fig. 1.26(a). In addition, as shown in Fig. 1.26(b), other side of the multi-cages are short-circuited. Thanks to this rotor configuration, torque density increased significantly and torque ripples and cogging torques are reduced. It is concluded that by using this rotor and stator winding topology it is possible to increase the efficiency up to 33% more. In [ROS62], it is proposed that utilizing closed slot rotor structure with double-cage (see Fig. 1.27) enables to obtain a low starting current and low bar current harmonics which can improve the efficiency and thermal characteristics of the rotor bars.

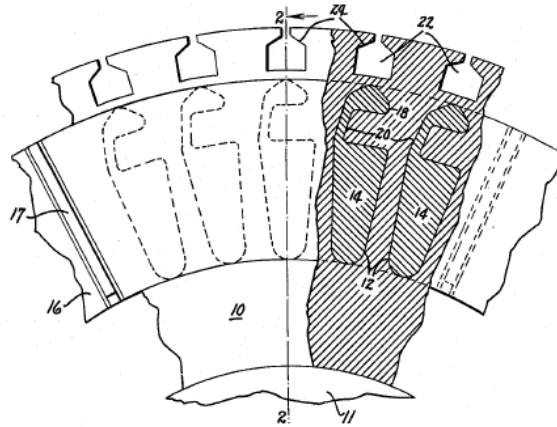


Fig. 1.27 Claimed rotor structure with die-cast winding for a squirrel-cage IM [ROS62].

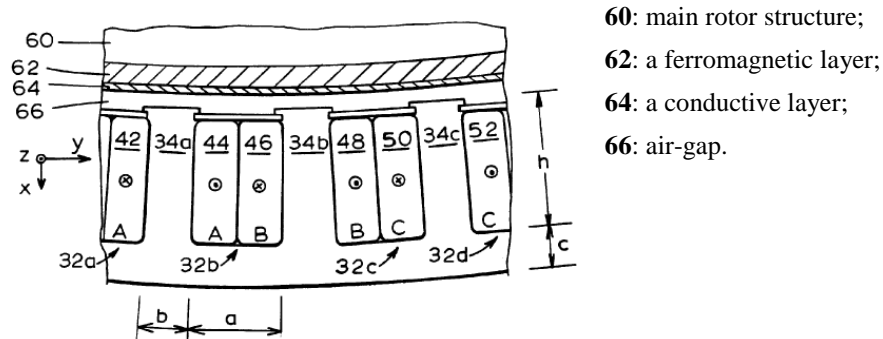
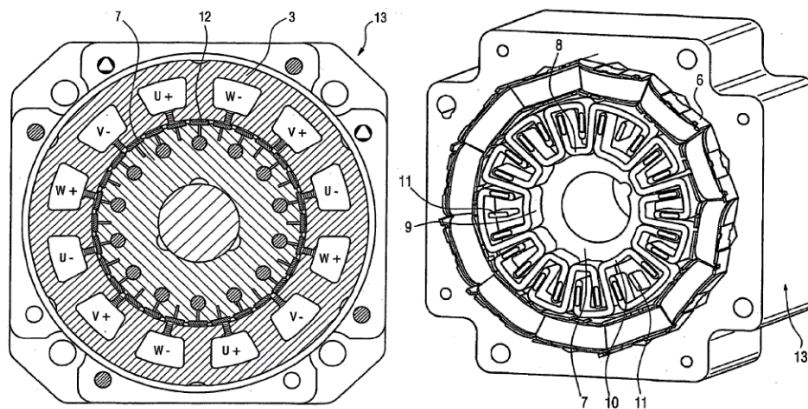


Fig. 1.28 Stator and rotor structure with ferromagnetic and conductive layers [BLA03].

In [BLA03], in order to improve the speed, torque and efficiency characteristics of an IM with FSCW, a simple rotor structure with ferromagnetic and conductive layer is proposed. The structure of the proposed IM is illustrated in Fig. 1.28. The main function of the proposed layers on the rotor is to diminish the Lorentz, Maxwell and hysteresis effect forces. Thus, the operational speed can be widened and both of the torque and efficiency can be improved by reducing the parasitic effects. In order to damp or eliminate disturbance on the rotor bars of an IM or line-start PM machine with FSCWs, the use of squirrel-cage windings with electrically isolated loops is proposed by [VOL07]. The structure of the proposed rotor is illustrated in Fig. 1.29. The method not only reduces the rotor losses but also reduce oscillating torques thanks to the additional null (not filled with conductor loops) slots provided in the rotor. In order to improve the thermal and electromagnetic performance characteristics of an conventional IM, a new rotor design with alloy on the top of the slot and cast-aluminium at the bottom

of the slot is proposed (see Fig. 1.30) [LI10]. It has been concluded that while the starting torque is increased, the starting current decreased, and the thermal characteristics, such as homogenous heat distribution, no influence from the change of the ambient temperature, etc. are obtained thanks to the proposed method.

To improve the spatial distribution of air-gap magnetic field from a harmonic point of view a new rotor configuration for doubly-fed IM is introduced [GOR13]. The schematic representation of nested loops and the prototyped cage-rotor are illustrated in Fig. 1.31. Some loops have been inserted between consecutive bars in order to decrease the value of rotor leakage reactance. A multi-circuit winding has been created by connecting these loops to the end-ring from one side. If a machine has lower leakage reactance on its rotor, motor's space harmonic levels will be lower. By using this technique, a 12.8% of improvement in the MMF harmonic distortion, a 11.67% reduced rotor leakage inductance, considerably reduced iron loss, significant reduction in rotor current amplitude and equal current amplitude in rotor bars have been obtained. The most prominent disadvantages of this rotor topology is the increased resistance of the rotor winding. However, it is shown that the reduction of rotor inductance has a more significant influence on the machine efficiency. Furthermore, it is also revealed that the lower the number of rotor bars, the higher the rotor leakage reactance and vice versa.



Stator 3; tooth wound coil 6; rotor 7; three squirrel-cage windings: 8, 9, 10, which are electrically isolated from one another; no contact is made with three slot conductors 11; PMs 12 are located on the external circumference of the rotor; synchronous or asynchronous machine 13.

Fig. 1.29 Proposed line-start FSCW IM with novel rotor cage [VOL07].

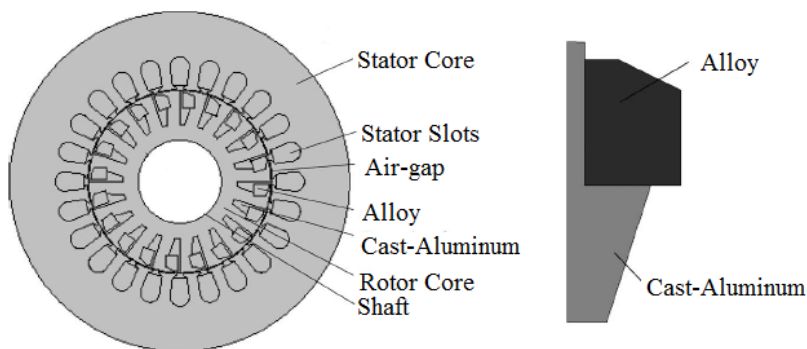


Fig. 1.30 IM cross-sectional view and structure of the rotor slot and bars [LI10].

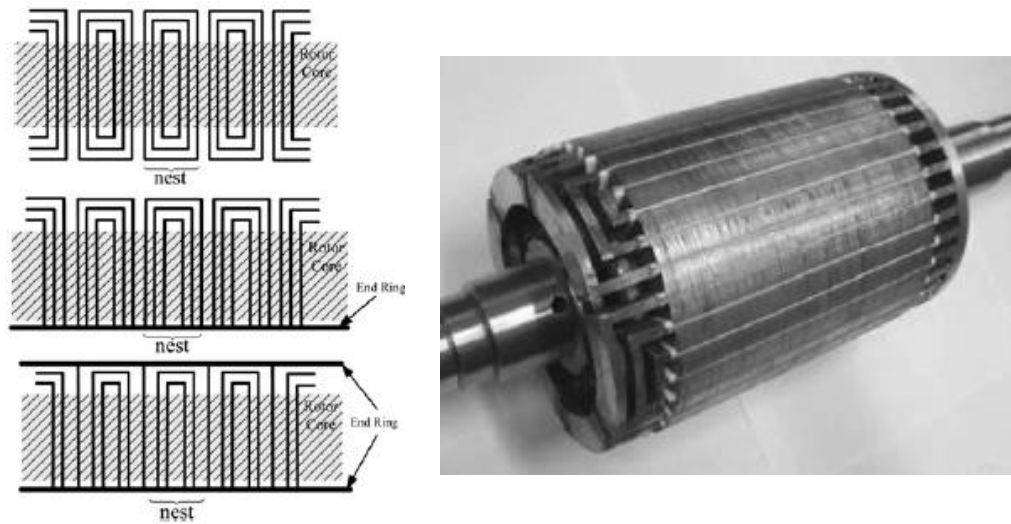


Fig. 1.31 Nested loop rotor: (left) three different arrangements of the nested loop rotor and (right) nested loop rotor prototype [GOR13].

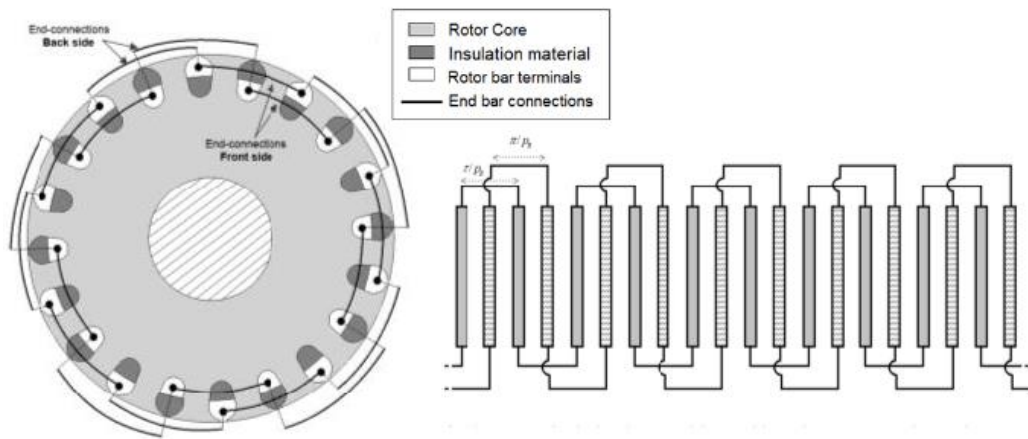


Fig. 1.32 IM rotor with series connected rotor bars and two winding systems [DAJ13a].

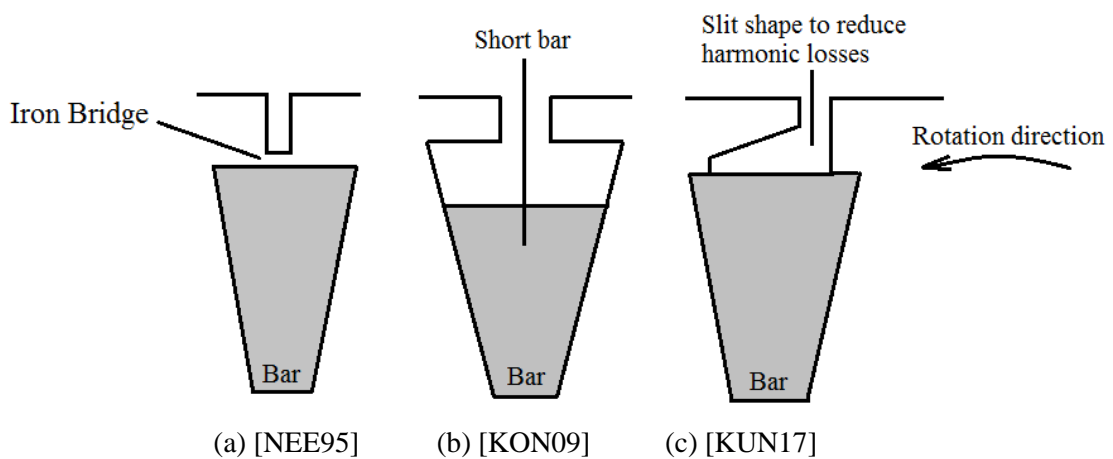


Fig. 1.33 Unconventional rotor slot shapes.

In [DAJ13a], in order to reduce the influence of MMF harmonics induced in the rotor bars and hence decrease the rotor losses and parasitic effects, a new cage structure consisting of electrically isolated

two-cages with serially connected bars (see Fig. 1.32) is proposed. It is shown that, thanks to the new rotor topology combined with FSCW technique with a proper slot/pole combination, it is possible to improve the torque and efficiency performances. In order to reduce the harmonic bar losses of the rotor to a minimum, a closed rotor structure with a u-shaped bridge is proposed (see Fig. 1.33(a)) [NEE93], [NEE95], [BOL10]. In addition, a rotor structure with short bars, as illustrated in Fig. 1.33(b), is proposed for a railway vehicle traction in [KON09] in order to improve the efficiency by reducing the harmonic losses of the rotor bars. In [KUN17], in order to reduce the time and space harmonics simultaneously, a new rotor structure with un-even tooth tips and narrower slot openings has been proposed (see Fig. 1.33(c)). The main idea behind these studies is to make the bar move away from the air-gap. Thus, the high-order air-gap flux density harmonics are diminished.

1.4.3 Double Stator and Rotor Topologies

This part covers the IMs designed with double stator and/or double rotors. In order to simplify the control, particularly eliminate the requirement of a controller, improve the performance characteristics by diminishing the field harmonics, and achieve a better utilization of the available space, or eliminate the differential used in the EV applications, a double stator and/or rotor topologies have been widely investigated by the researchers.

In order to simplify and increase the effectiveness of the control, a 3-phase one squirrel-cage IM with two independent identical sets of windings is designed as seen in Fig. 1.34. Designed machine is built and the results are also verified by the experimental test [SMI66]. Actually, in the study, the machine is not directly designed as a two stator one rotor configuration. Two similar IMs were set up side by side with their shafts mechanically connected via a chain and sprocket drive. It is explained that an inexpensive, simple and effective voltage control can be achieved by physically rotating one set of stator windings with respect to other or electrically rotating them by reconnect the phase orders (by using tapped 3-phase stator windings). By doing this relative phase and magnitude may be controlled without requiring any complex controllers. It is concluded that a negligible reduction in the efficiency and slight reduction in the power factor occur when compared to identical a pair of conventional IM.

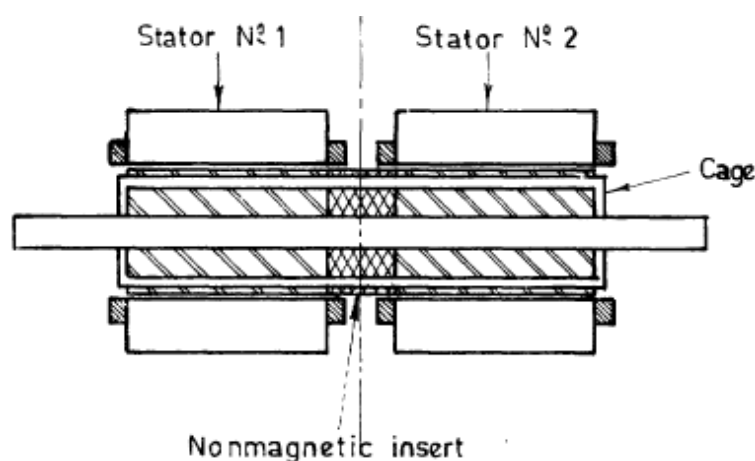


Fig. 1.34 Schematic of twin stator squirrel-cage rotor IM [SMI66].

In [JAN95], a detailed comparison of Linear IM (LIM) topologies, including the longitudinal-flux LIM and the transverse-flux LIM has been investigated in order to achieve the best design selection for very high performance systems. The general topology of the machine is a double-sided, short-moving-secondary and long-fixed-primary windings as seen in Fig. 1.35.

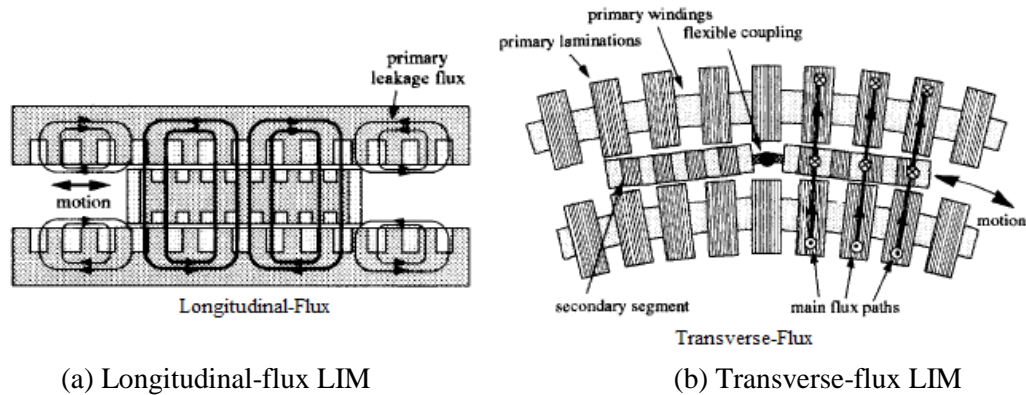


Fig. 1.35 Basic constructions of different LIMs [JAN95].

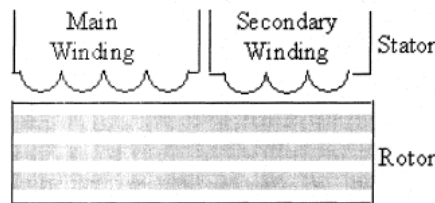


Fig. 1.36 Principle scheme of double winding IM [BU03].

A long pole pitch is required for longitudinal-flux machine because of the large leakage inductance due to the long-primary topology. In this machine, in order to decrease the end effects, the pole number of the machine should be increased. Longitudinal-flux machine is favourable for short pole pitch, wide geometries, whilst transverse-flux machine is favourable for long pole pitch, narrow geometries. One of the important advantages of the transverse-flux machine is that the self-containment of the flux eliminates all magnetic end effects in the both primary and secondary windings. In [BU03], a new energy recovery double winding cage-rotor IM is introduced. In the study, a double winding IM and its speed control methods have been proposed. As illustrated in Fig. 1.36, the machine consists of one cage rotor and two stator windings: one of them acts as a motor and the other acts as a generator. The rotor speed can be adjusted by controlling the voltage supplied to the secondary (generator winding). Some key findings can be summarised as: easy phase control that does not require a controller and the used power electronic circuit is much simpler and lower than the converter/inverter circuit which lead to reduce cost and harmonic injection to the supply system.

In order to drive the two wheels without the differential, a novel EV drive system has been introduced [PLA93]. In this study, an IM having a novel double rotor with cast squirrel-cage winding and single stator having two identical polyphase winding is proposed for using in an EV drive system without needing a differential. Some important advantages of the designed machine are as follows: both rotors produce equal armature reaction, independent shafts provide identical torques, magnetising

inductance, power factor and efficiency are maximised while leakage reactance, stator resistance, size and cost are minimised. Some disadvantages of the designed machine are: selection of stator yoke thickness is a design problem, generation of the torque depends on the saturation in the stator core and rotor slip parameters.

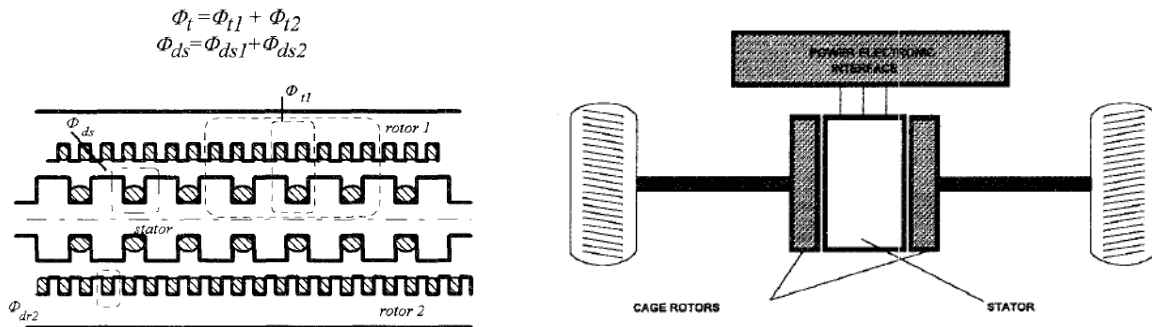


Fig. 1.37 Double rotor, single stator IM: (left) structure and (right) independent shaft driving system [CAR95].

In [CAR95], a novel axial-flux IM, which has a similar configuration (a single stator and two squirrel-cage rotors mounted on independent shafts driving two wheels of an EV) with that in [PLA93] as seen in Fig. 1.37, has been presented. Some of the key findings of the study can be summarised as: axial flux IM provides a very high torque density required in EV systems, small stator yoke dimension leads a reduction in core cost and core loss causing a high efficiency, wheels can be driven directly without the need of differential and gear box.

Another axial-flux IM has been designed in [PRO97]. In this study, design, comparison and control of axial flux IM and axial flux PM machine for EV applications have been presented. Designed machines consist of double rotor and single stator configuration as presented in [PLA93] and [CAR95]. The motor acts as a mechanical differential because double rotor can rotate at different speeds. According to the simulation results, it is concluded: double rotor axial-flux machines can allow saving copper and iron core, and hence, higher power density and efficiency can be achieved compared with those in the two-wheel individual motors.

A single stator with concentrated windings and a two squirrel-cages mounted on the same rotor in-wheel IM which has a dual air-gap, axial and radial flux configuration has been designed and also prototyped for an electric propulsion system [BEN98]. Rotor and stator configurations of the designed machine are given in Fig. 1.38. As seen in the figure, the rotor has both radial and axial cages. In this study, all calculations, magnetic and electric equivalent circuits of the designed machine have been derived by using FEA. A 1 kW axial and radial flux IM built and the obtained test results are then compared with a single air-gap axial IM whose rated values are identical. It is concluded that axial and radial cage rotor topology has substantial advantages over the conventional radial flux machine in terms of efficiency, volume, starting current and hence torque, and also fitness into the wheel. According to

the obtained experimental test results, axial and radial cage IM provides 5.43% higher efficiency while its weight is 19.10% heavier than that of single cage IM.

In an attempt to prevent the harmful leakage magnetic field produced by the double-side LIM with high current, which produces a strong electromagnetic coupling effect, a shielding structure, has been introduced in [ZHA14]. An equivalent circuit of double-sided LIM with shielding structure has been presented. The obtained analytical results showed that the coupling effect and shielding plate cause a decrease in both magnetising inductance and rotor resistance which reduces the produced force magnitude. A novel slotless double-sided long-stator LIM has been designed on the purpose of using in the electromagnetic launch applications [JIN14]. Total loss and temperature rise are decreased by enlarging the conductive area of the stator windings. In addition, in order to increase the effective cross-sectional area of the stator winding, 3-phase stator windings are arranged alternately along the longitudinal direction of the core. Considering the simulation results it is concluded that in the saturation state, the slip frequency is greater than that in linear state and if the slip frequencies are the same, the stator current increases with increasing the electromagnetic force. On the contrary, if the slip frequency is small in the saturation state, the motor power decreases.

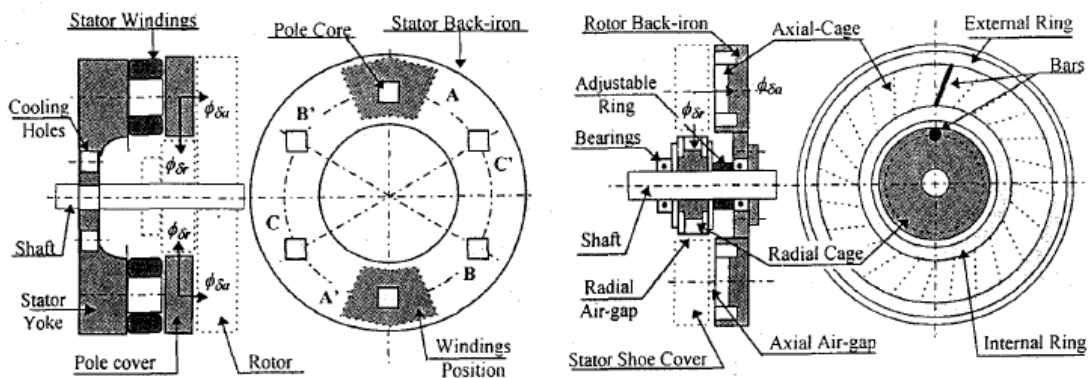


Fig. 1.38 Schematic view of the rotor and stator [BEN98].

In order to bring the advantages such as high torque density, wide torque-speed range, synchronous motor-like characteristics, robust rotor configuration and low cost of IM to a traction system of an EV/HEV, a doubly-fed, double stator-rotor configuration has been proposed [CHE14]. The designed machine can be counterpart to two wound-rotor IMs, one with inner rotor and one with outer rotor, which are aligned to the same axis as seen in Fig. 1.39. Some important key findings of the study can be summarised as follows:

- Simple structure, easy speed control and wide torque-speed operation range have been achieved.
- It is possible to connect the rotor windings in the same or reverse phase sequence.
- The proposed IM can operate in both motor and generator operation conditions at wide speed ranges that means the power flow can be bi-directional in both conditions.

A novel electromechanical converter-electrical variable transmission (EVT) consisting of two concentric IMs and two inverters suitable for HEVs is proposed in [CUI06]. In [CHE14], a double stator

and rotor concept has been introduced. Two separate cage rotors are mounted to each other through a non-magnetic support. Then, this rotor is sandwiched between two stators (see Fig. 1.39). The outer machine is a conventional squirrel-cage IM whilst the inner machine has its squirrel-cage winding on its outer part. The inner rotor of the IM is connected to the internal combustion engine's shaft and the outer rotor is connected to the final gear. It is concluded that the EVT can achieve the function of continuously variable transmission, starter and generator operation which optimises the operation of internal combustion engine and improves vehicle performance.

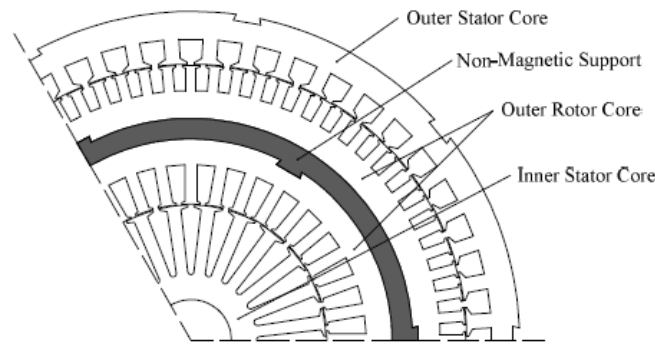


Fig. 1.39 The cross section of the doubler-rotor double-stator IM [CHE14].

1.4.4 Other Novel IM Topologies

Some other novel IM topologies are presented in this part as follows.

The use of the damper windings on the IM's stator has been brought forward in order to reduce the sideband flux waves and attenuate the unbalanced magnetic pull (UMP) [DOR13]. In this study, a method for reducing the UMP using additional stator windings with different pole numbers is addressed. Some of the key findings are summarised as below:

- Damper windings slow up torque response in an inverter controlled machine.
- The damping windings are effective under some circumstances such as light loading and dynamic eccentricity and for certain speed ranges for full load when there is static rotor eccentricity.
- Damper windings are not very effective in cage IMs, but it is effective for wound-rotor induction machines.

To be able to minimise the rotor resistance and optimise the leakage inductance which improves the power factor, and hence, the system efficiency and the peak torque, bar windings are used instead of stranded windings in the IM rotor as shown in Fig. 1.40 [JUR14]. It is shown that bar windings have major advantages in applications, requiring lower speed and high current demand. Some key findings summarising the several advantages of rotor bar windings over the stranded windings can be given as follows: (a) higher slot fill; (b) shorter end-turn which will enable longer active stack length of the machine improving the torque/ampere capability; (c) improved cooling performance due the larger

surface area in the end-turn which can be actively cooled, and better copper to steel path; (d) improved high voltage protection; (e) fully automated manufacturing process; (g) better torque ripple characteristics are obtained by 1 stator slot skew. The disadvantage of using bar windings is that it causes an increase in the rotor resistance with current and frequency due to eddy, skin and proximity effects.

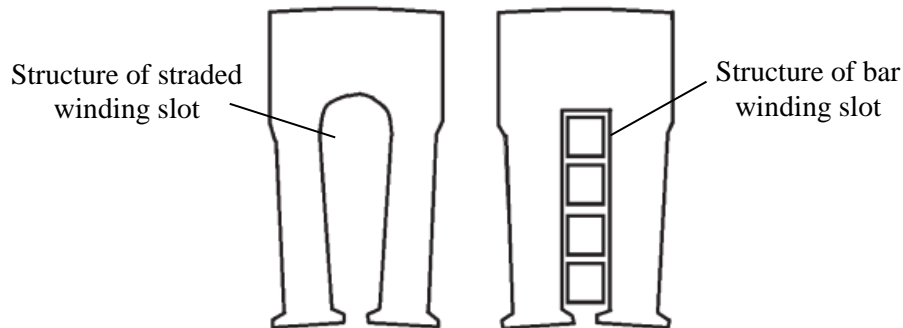


Fig. 1.40 Stranded and bar winding stator slot shape [JUR14].

In [DEM14], in order to reduce the stator core losses of a conventional IM, assignment of an amorphous material for the stator is proposed. It is shown that the use of the amorphous material leads to significant reduction in stator core losses compared to a conventional design with 0.5mm electric steel laminations. However, the main disadvantage of using amorphous material is that more complex technology of punching or cutting the material is required.

1.5 PhD Research Scope and Contributions

1.5.1 Scope of Research

The research presented in this thesis is mainly concerned with the following two topics:

- Development of advanced IMs for EV/HEV applications.
- Investigation of non-sinusoidal bar current in IMs.

To be able to overcome one of the major problems in the HEV applications, which is the reduction of the size of the traction machine without sacrificing the torque density, output power, and efficiency for mounting the traction machine into very limited place, an advanced topology with non-overlapping winding technique, whose basic schematic is shown in Fig. 1.41, has been developed and then globally optimised in order to meet the desired drive specifications. Furthermore, the second topic is to investigate the non-sinusoidal bar current phenomenon in IMs by considering the influence of design and operating parameters, such as slip, electric loading, magnetic saturation, air-gap length, rotor slot number, stator slot and pole number combinations, rotor slot geometry parameters, rotor skewing, and coil pitches.

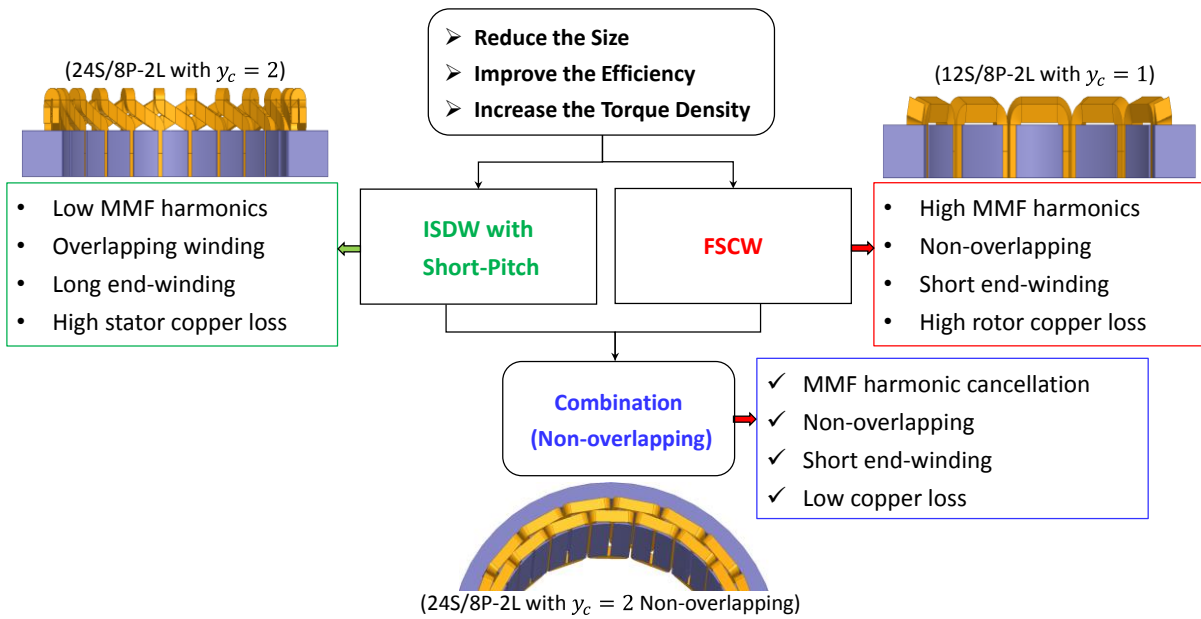


Fig. 1.41 Schematic of the proposed improvement methods for IMs.

The research scope and the contributions of this thesis are briefly illustrated in Fig. 1.42.

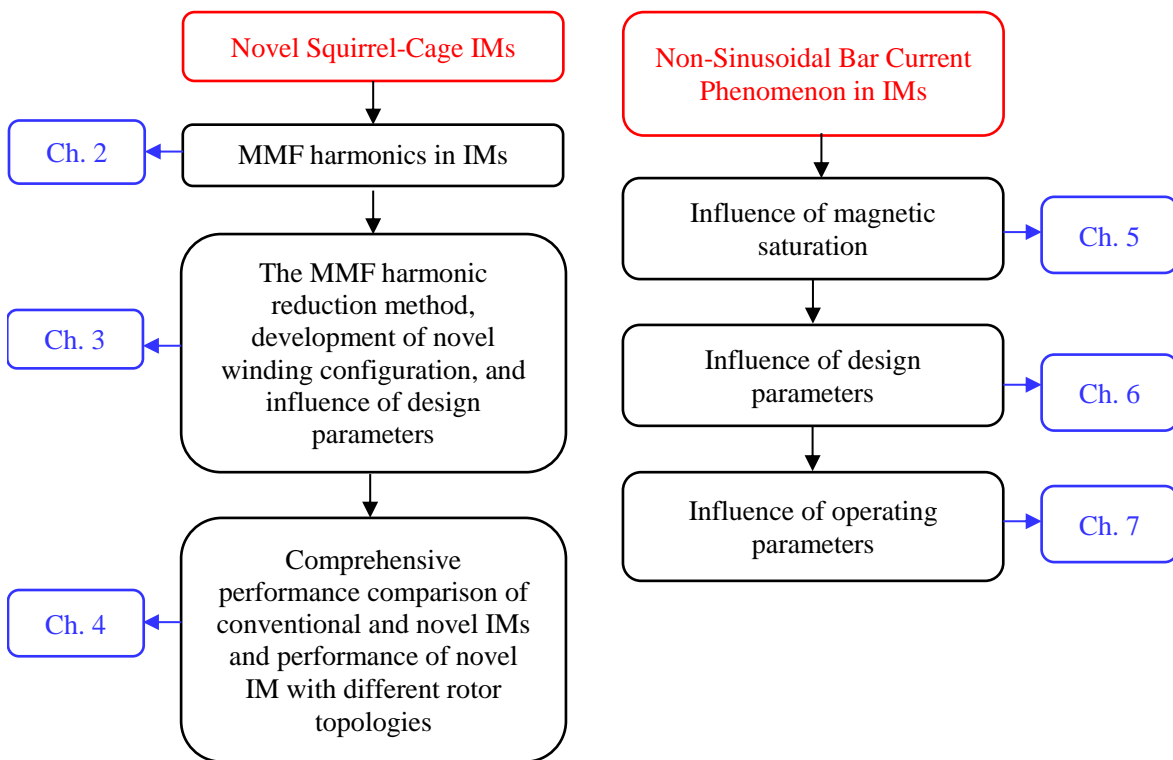


Fig. 1.42 Demonstration of research scope and contributions.

The contents of subsequent chapters are summarised as follows:

The research on the development of advanced IMs is presented in Chapters 2-4 and mainly divided into the following steps:

- Step 1: Chapter 2. Investigation of different conventional winding topologies to reveal the relationship between the end-winding length and the performance characteristics.
- Step 2: Chapter 2. Determination of suitable winding configurations for IMs for EV/HEV applications.
- Step 3: Chapter 3. Development of a new winding topology with very short end-windings but high quality MMF waveform.
- Step 4: Chapter 3. Investigation of the key design parameters on electromagnetic performance and comparison of performance characteristics of IMs having adapted windings designed by different specifications including the rotor, slot, and pole number combinations, stack length, number of turns, geometrical parameters, etc. in order to determine the best candidate meeting the desired drive specifications.
- Step 5: Chapter 4. Comprehensive performance comparison between conventional and advanced IMs.
- Step 6: Chapter 4. Performance of advanced IM with different rotor topologies.

The research on the investigation of non-sinusoidal bar current in IMs is presented in Chapters 5-7 and mainly divided into the following steps:

- Step 1: Chapter 5. Investigation of rotor bar current and verification of non-sinusoidal bar current waveforms under various operating conditions.
- Step 2: Chapter 5. Investigation of the reasons behind the non-sinusoidal bar current waveform. The levels of iron saturation in different parts, including stator and rotor back iron, tooth body and tooth tips etc., are examined and their influences are then investigated, while the dominant part which causes the non-sinusoidal rotor bar current waveform is identified.
- Step 3: Chapter 6. Investigation of the influence of design parameters on the non-sinusoidal bar current waveform.
- Step 4: Chapter 7. Investigation of the influence of operating parameters on the non-sinusoidal bar current waveform.
- Step 5: Chapter 7. Verification of non-sinusoidal bar current waveforms by numerical locked-rotor analyses.

Chapter 2

In this chapter, the influence of different winding configurations on the electromagnetic performance of squirrel-cage IM is investigated. These different winding topologies, namely integer-slot distributed winding (ISDW) with short- and long-slot pitches, integer-slot concentrated winding (ISCW), and fractional-slot concentrated winding (FSCW), are studied considering the number of winding layers

and slot/pole number combinations. In order to reveal the benefits and drawbacks of each winding topology, squirrel-cage IMs designed with one of these winding topologies are compared in terms of winding factor, winding factor harmonics, total axial length, average torque, torque ripple, machine losses, efficiency, etc. It has been revealed that because of very high MMF harmonics induced in the bar current, the bar copper loss of the IM designed with FSCW topology is significant. Therefore, it has been revealed that although the compactness is a vital issue for the electrical machines designed for Hybrid Electrical Vehicle (HEV) applications, it is not appropriate to use FSCW IMs because of the insufficient performance and unwanted high torque ripple and parasitic effect issues. In addition, it is also revealed that the parasitic effects of double-layer winding configuration is much lower than the single-layer winding configuration

Chapter 3

This chapter investigates the design and analysis of an advanced squirrel-cage IM with non-overlapping windings. The aim of this study is to improve a new winding and a stator topology for IMs which lead to reduce the total axial length without sacrificing the torque, power, and efficiency. In order to reduce the MMF harmonics, phase shifting method is employed for 2x9S/6P integer-slot distributed non-overlapping winding with 2 slot-pitch IM. By adopting this method, ~43% of the MMF harmonics have been reduced. The results show that according to conventional counterpart of the IM designed with developed windings, it is possible to shorten the total axial length by ~25% without sacrificing the torque, output power and efficiency. Moreover, the influences of some major design parameters, such as stator slot/pole number combinations, rotor slot number, stack length, number of turns, slot geometric parameters, etc., on the electromagnetic and flux-weakening performance characteristics of the advanced IM have also been investigated in this chapter.

Chapter 4

This chapter presents a comprehensive comparison on the performance characteristics of the advanced IMs designed with various stator slot/rotor slot/pole numbers, stack lengths, and number of turns. The various advanced IMs having different pole numbers with different stack lengths and number of turns, have been quantitatively compared with their conventional counterpart. Among the various advanced IMs, the best candidates for the EV/HEV applications are determined. Moreover, influence of various rotor types, such as insert-bar, open-slot cast-rotor, closed-slot cast-rotor with straight bridge, and closed-slot cast-rotor with u-shaped bridge on the electromagnetic and flux-weakening characteristics of the advanced IM have also investigated and then the obtained results have been compared.

Chapter 5

This chapter investigates the influence of magnetic saturation on the rotor bar current waveform and performance characteristics of a conventional IM. The levels of iron saturation in different parts are

examined and their influences on the electromagnetic performance characteristics and bar current waveform are investigated, whilst the dominant part which causes the non-sinusoidal rotor bar current waveform is identified. It has been revealed that the magnetic saturation, particularly in the rotor tooth, has a significant effect on the bar current waveform.

Chapter 6

In this chapter, the influences of a large number of design parameters on the electromagnetic performance characteristics of conventional IMs are examined in detail with particular reference to the bar current waveform. It has been revealed that each considered parameter has a significant effect on the bar current waveform and the key performance characteristics, such as torque, torque ripple, power losses, efficiency, etc. The conditions when the non-sinusoidal rotor bar current waveform occurs and the reasons behind this phenomenon are investigated by FEA.

Chapter 7

In this chapter, the influences of operating parameters on the electromagnetic performance characteristics and rotor bar current waveform of squirrel-cage IMs are investigated in detail. It is observed that after exceeding the certain slip rate and electric loading level, the rotor bar current waveform becomes non-sinusoidal even if the stator windings are fed with a symmetrical and balanced sinusoidal source. The conditions for such non-sinusoidal rotor bar current to occur and the reasons behind this phenomenon are investigated with particular reference to the numerical verification of the obtained non-sinusoidal bar current waveforms by locked-rotor analyses.

Chapter 8

This chapter contains the general conclusions of the thesis and potential future works in the development of IMs and non-sinusoidal bar current phenomenon areas.

1.5.2 Contributions of Research

The contributions of this thesis are summarised as follows:

- Development of an advanced squirrel-cage IM for EV/HEV applications by developing a non-overlapping winding technique in order to reduce the total axial length of a squirrel-cage IM without sacrificing the torque and power densities, and efficiency.
- Investigation of influence of the key design parameters, on electromagnetic and flux-weakening performance characteristics of advanced IM with reference to the conventional IM.
- Investigation of influence and identification of dominant parts, amongst the design parameters and operation parameters, of magnetic saturation on the non-sinusoidal bar current waveform and performance in IMs.

2 Analysis of Induction Machines with Different Coil Pitches

In this chapter, the influence of stator coil pitches on the electromagnetic performance of squirrel-cage IM is investigated. Three different winding topologies, obtained by changing the coil pitches, namely integer-slot distributed winding (ISDW), integer-slot concentrated winding (ISCW), and fractional-slot concentrated winding (FSCW), are studied considering the number of winding layers and slot/pole number (S/P) combinations. In order to reveal their merits and demerits, their performance are compared in terms of winding factor, total axial length, average torque, torque ripple, losses, efficiency, etc. It will be revealed that due to the very high MMF harmonics induced in the bar current, the bar copper loss of the IM with FSCW is significant. Therefore, although the FSCW topology provides very short end windings leading to more compact structures, which is desirable for the electrical machines for EV applications, it will be demonstrated that because of the parasitic effects, such as high torque ripple, high iron and bar copper losses, and low efficiency, it is not reasonable to use FSCWs in IMs. In addition, it will be revealed that the parasitic effects of the double-layer winding configurations are much lower than those of the single-layer winding configurations. Moreover, it is also revealed that for the combinations $q \leq 2$, the higher the coil pitch, the lower the parasitic effects and the higher the efficiency. As for the $q \geq 3$ combinations, although the MMF harmonics are reduced remarkably, the efficiency cannot be increased because of the significantly increasing stator copper loss due to the increased end-winding copper loss.

2.1 Introduction

The conventional integer-slot distributed windings (ISDWs) with long-slot pitch ($y_c > 3$) are excessively used in industrial and traction applications [DRI86], [LIA95], [BIA97a], [BIA97b], [WAN05], [AGA13], [GUA15a]. These types of windings are generally characterized by high-quality MMF waveform. However, they cause a significant increase in end windings, resulting in long total axial length of the machine and high stator copper loss and hence low efficiency. In order to improve the efficiency and reduce the end winding lengths, the conventional ISDWs with short-slot pitch ($1 \leq y_c \leq 3$) are proposed in [LAT18], [TOL91a], [TOL91b], [CHE98], [WAN14d], [PAT14c], [KAB16], [CHE17]. The length of end windings in such machines is still quite long due to overlapping windings. Therefore, in order to reduce the end winding length, FSCWs with one slot-pitch ($y_c = 1$) [LIN76], [JAC04], [REF08], [GUN14] could be utilized. The advantages and disadvantages of the integer and fractional slot windings are listed in Table 2.1. As clearly seen in the table, both winding topologies have their own advantages as highlighted in the yellow shaded boxes. Due to lower harmonic content, lower torque ripple, lower losses, and consequently higher efficiency, ISDWs are most extensively adopted for the electrical machines especially in EVs. On the other hand, the FSCWs have some advantages, such as high filling factor by using compressed coils with segmented stator (e.g. up to 78%

in [JAC99], [REF10]), relatively higher efficiency due to higher filling factor and shorter end windings, and simple manufacturing.

Table 2.1 Comparison of ISDW and FSCW

<i>Characteristic</i>	<i>Related design consideration</i>	<i>ISDW</i>	<i>FSCW</i>
Magnitude of fundamental MMF	Number of stator slot/phase/pole (q)	High	Low
MMF harmonic content	Slot-pitch number (y_c)	Low	High
Rotor copper loss	MMF harmonics	Low	High
Leakage inductance	Geometry of the slots and winding arrangement	Low	High
End winding	Space requirement	More	Less
	Total axial length for same stack length	Long	Short
	Stator end winding copper loss	High	Low
	Assembling	Difficult	Easy
Stator slot fill factor	Efficiency Current density Thermal conductivity	Low	High

Despite of these advantages, FSCWs for IMs exhibit some serious drawbacks; such as low pull-out (maximum) torque capability due to high leakage inductance, substantially high rotor bar copper loss, high torque ripple, high vibration, and acoustic noise. Therefore, the research on the IMs with FSCW is not as popular as that for PM machines with FSCW [CRO02], [ISH05], [SAL05], [REF05b], [MUN08], [WAN08], [TAN11], [CHE13]. However, in order to reduce or even cancel these unwanted characteristics, the research on IMs with FSCW has been gaining increasing attention in recent years [JAC04], [JAC05], [REF08], [BES09b], [EAS10], [COX11], [ALB12], [MOR14], [SUN15], [SAK17]. In order to reduce the effect of sub- and super-harmonics of the MMF on the performance of IMs, some proposed methodologies, presented in Chapter 1, are summarized as follows:

- Unconventional cage structures comprising of electrically isolated multi-cages with serial or parallel connected bars [MOR36], [LIN76], [GOR13], [DAJ13a];
- Unconventional rotor structures with closed slot [ROS62], [NEE93], [NEE95], short bars [KON09], and un-even toot tips with very narrow slot openings [KUN17];
- Stator comprising of at least two stator sections with circumferential angle shift [JAC04];
- Stator with radial flux barriers on each tooth [JAC05];
- Planer modular winding structure with two concentric coils in each coil groups [EAS10] and three-layer planar concentrated windings with different slot pitches and coil groups [COX11];

- Multi-layer windings on both stator and rotor supplied from double-fed source [ALB09b], [ALB12];
- Three-phase winding configuration comprising of combined star-delta configurations [MIS14], [MOR14], [MOR15a];
- Stator cage windings with multi-phase inverter drive concept [DAJ14a], [PAT14b], [DAJ15];
- Unconventional stator structure comprising of asymmetric stator slots [KOC09];
- Unconventional stator and winding structures comprising of multi-layer slots and multi-layer windings [SUN15], and multi-layer toroidal windings [JEN12], [SAK17].

In addition, in [CHA06], [REF11], [GUN14], and [BAC15], the performance of FSCW IM and ISDW IM are compared and the previously mentioned drawbacks, such as low pull-out torque capability, high rotor losses, and high torque ripple, are confirmed. However, in these studies, a few different winding configurations and very limited performance characteristics have been analysed and compared.

In this chapter, the electromagnetic performance of IMs with different slot pitches, in terms of total axial length, air-gap field and induced voltage harmonic distortions, stator and rotor current densities, torque, torque ripple, output power, slip, power losses, efficiency, etc., will be compared with due account for the influence of winding layer and S/P combination, with particular focus on the influence of MMF harmonics on the rotor bar copper loss.

2.2 Winding Harmonic Index

It is well-known that the performance of any electrical machine is heavily related to the S/P combinations. Therefore, it is critical to determine the most appropriate S/P combinations for the electrical machines used in EVs. For the traction electrical machines, there are many design considerations such as flux weakening performance, torque capability and quality, acoustic noise and vibration. As mentioned earlier, the MMF harmonics have significant impact on the IM performance. Therefore, a harmonic index [ALB12] is used to quantify the MMF harmonic content, as shown in (2.1).

$$h_{shi} = \frac{\sum_{h=1}^{\infty} \frac{k_{wh}}{h}}{\frac{k_{wp}}{h_p}} \quad (2.1)$$

where k_{wh} , k_{wp} , h , and h_p are the winding factor amplitude of the h^{th} order harmonic, the amplitude of the working (fundamental) harmonic, harmonic order, and the working harmonic which equals to pole pair number ($h_p = p$), respectively. Although (2.1) does not give any information about the direction of rotation of the MMF working harmonic, it gives useful information about the total harmonic content of any winding topology and consequently prediction of the rotor bar copper loss. Since there

is a direct correlation between the winding factor and MMF harmonics, the rotor bar copper loss rate can be predicted by using (2.1). Because the MMF harmonics content is induced in the air-gap flux density and then induced in the rotor bar induced voltage and consequently in the rotor bar current. These harmonics cause a considerable increase in the rotor bar copper loss. Since the effort given for the winding harmonic index calculation is quite short and the effectiveness of the rotor copper loss prediction is quite good, it is very useful to use (2.1). Hence, as shown in Table 2.2 and Table 2.3, considering h_{shi} for any S/P combination, the bar copper loss amount can be predicted easily. It can be deduced that the lower the h_{shi} , the lower the bar copper loss. The harmonic indices of different winding topologies can be calculated as listed in Table 2.2 and Table 2.3 for IMs having winding slot pitch $y_c = 1$ and 2, respectively. It should be noted that only these combinations resulting in symmetrical 3-phase balanced windings are considered. Furthermore, only the feasible windings ensuring $q \geq 0.5$ families having relatively low harmonic contents ($h_{shi} < 10$) with $y_c = 1$ and 2 combinations have been considered. From Table 2.2 and Table 2.3, it is possible to identify a suitable combination that minimizes the MMF harmonics. As the pole number increases, the minimum harmonic index decreases. The choice of S/P combination should consider the following factors:

- I. Low harmonic index h_{shi} ;
- II. High winding factor k_{w1} in order to improve the torque density;
- III. High Least Common Multiple LCM of stator slot number and pole number in order to reduce the torque ripple [REF05a];
- IV. High and even Great Common Divisor GCD of stator slot number and pole number in order to reduce the unbalanced magnetic force (UMF) and improve the radial symmetry [REF05a], [MAG07];
- V. $\frac{1}{2} < q \leq \frac{1}{3}$ ($k_{w1} > 0.9$) \longrightarrow Generally present higher performance than the other combinations of FSCWs [CRO02];
 $q = \frac{1}{2}$ ($k_{w1} = 0.866$) \longrightarrow No sub-harmonics, as ISDWs [REF08], [CRO02].

In addition, the torque-speed characteristics should also be considered in the determination of S/P combination. As will be shown in Chapter 4, at high speed operation, the higher the pole number, the lower the torque and hence the power, but also the higher the switching frequency of the inverter.

It is worth noting that the combinations with $GCD(S, P) = 1$ should usually be avoided since they exhibit asymmetric radial force distribution, i.e. UMF and potentially high acoustic noise and vibration [ISL10]. However, if the UMF is not of concern, it is possible to use $GCD(S, P) = 1$ combinations. In addition, as seen in the tables, among the considered S/P combinations, $q = 0.5$ with $y_c = 1$ and $q = 1$ with $y_c = 2$ families have the minimum h_{shi} due to the absence of sub-harmonics. On the other hand, there are a number of different S/P combinations, e.g. $q < 0.5$, having FSCWs with cancelled or very

low sub-harmonics as presented in [EAS10]. These configurations exhibit good compromise between the low space-harmonic index and the high fundamental winding factor. The variation of fundamental winding factor with respect to stator S/P for FSCW and ISCW, and fractional-slot distributed winding (FSDW) and ISDW are illustrated in Fig. 2.1 (a) and (b), respectively. As clearly seen in the figures, for each pole number there is an optimum stator slot number which provides the maximum fundamental winding factor. On the other hand, there is an optimum stator S/P combination delivering the minimum harmonic index as seen in Fig. 2.2.

Table 2.2 Harmonic Index h_{shi} for various S/P combinations
for IMs with FSCW with $y_c = 1$

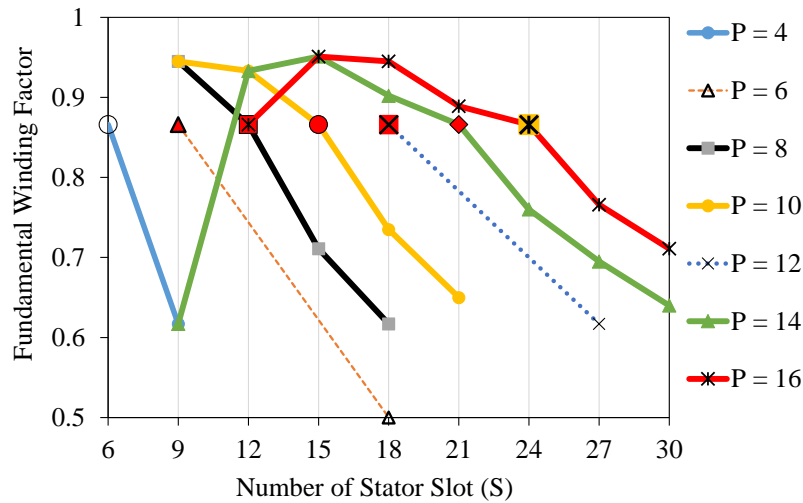
S	q	k_{w1}	h_{shi}	$LCM(S, P)$	$GCD(S, P)$
$P = 4$					
6	0.5	0.866	3.373	12	2
$P = 6$					
9	0.5	0.866	3.0822	18	3
18	1	0.5	3.0245	18	6
$P = 8$					
9	0.375	0.945	7.535	72	1
12	0.5	0.866	2.91	24	4
15	0.625	0.711	5.781	120	1
$P = 10$					
9	0.3	0.945	9.42	90	1
12	0.4	0.933	6.084	60	2
15	0.5	0.866	2.781	30	5
18	0.6	0.735	4.981	90	2
$P = 12$					
18	0.5	0.866	2.62	36	6
$P = 14$					
12	0.2857	0.933	8.517	84	2
15	0.357	0.9514	8.453	210	1
18	0.4285	0.902	5.863	126	2
21	0.5	0.866	2.557	42	7
24	0.571	0.76	5.061	168	2
27	0.643	0.695	5.84	378	1
$P = 16$					
15	0.3125	0.951	9.662	240	1
18	0.375	0.945	6.488	144	2
21	0.4375	0.889	6.821	336	1
24	0.5	0.866	2.41	48	8
27	0.5625	0.766	6.024	432	1
30	0.625	0.711	4.933	240	2

Table 2.3 Harmonic Index h_{shi} for various S/P combinations
for IMs with FSDW and ISDW with $y_c = 2$

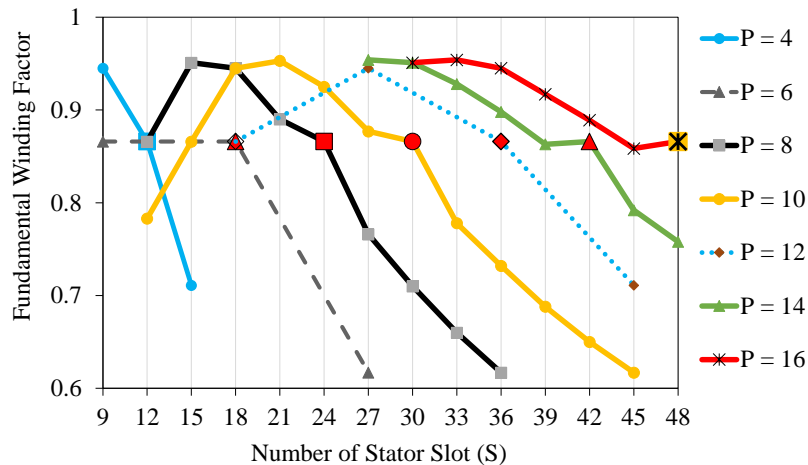
S	q	k_{w1}	h_{shi}	$LCM(S, P)$	$GCD(S, P)$
$P = 2$					
6	1	0.866	2.032	6	2
9	1.5	0.617	3.086	18	1
12	2	0.483	2.808	12	2
$P = 4$					
6	0.5	0.866	3.373	12	2
9	0.75	0.9452	4.225	36	1
12	1	0.866	1.917	12	4
15	1.25	0.711	3.3702	60	1
$P = 6$					
9	0.5	0.866	1.8662	18	3
18	1	0.866	1.772	18	6
$P = 8$					
12	0.5	0.866	2.91	24	4
15	0.625	0.951	5.5	120	1
18	0.75	0.945	3.663	72	2
21	0.875	0.89	3.85	168	1
24	1	0.866	1.7056	24	8
27	1.125	0.766	3.443	216	1
$P = 10$					
12	0.4	0.483	11.22	60	2
15	0.5	0.866	2.781	30	5
18	0.6	0.945	4.84	90	2
21	0.7	0.953	5.094	210	1
24	0.8	0.925	3.7	120	2
27	0.9	0.877	3.766	270	1
30	1	0.866	1.622	30	10
33	1.1	0.778	3.441	330	1
36	1.2	0.732	3.048	180	2
$P = 12$					
18	0.5	0.866	2.62	36	6
27	0.75	0.945	3.336	108	3
36	1	0.866	1.51	36	12
45	1.25	0.711	2.7	180	3
$P = 14$					
27	0.643	0.954	5.531	378	1
30	0.714	0.951	4.3	210	2
33	0.7857	0.928	4.322	462	1
36	0.857	0.898	3.456	252	2
39	0.928	0.863	3.63	546	1
42	1	0.866	1.51	42	14
45	1.072	0.792	3.438	630	1
$P = 16$					
30	0.625	0.951	4.75	240	2
33	0.687	0.954	5.204	528	1
36	0.75	0.945	3.16	144	4
39	0.8125	0.917	4.164	624	1
42	0.875	0.889	3.314	336	2
45	0.9375	0.8585	3.6111	720	1
48	1	0.866	1.4338	48	16
51	1.0625	0.7962	3.3915	816	1
54	1.125	0.7664	2.9915	432	2

At the points indicated with red markers in the figures, the minimum harmonic indices are obtained with the fundamental windings factor of 0.866. Therefore, it can be concluded that for any pole number there is an optimum stator slot number which provides the minimum harmonic index and consequently minimum rotor losses with a moderate fundamental winding factor. The key properties of the short-pitch ($y_c = 2$) ISDW configurations are compared to the FSDW, ISCW, and FSCW configurations, as summarised below:

- The higher and even GCD and consequently lower UMF;
- The lower harmonic contents and consequently rotor losses;
- The longer end winding (both radial and axial) lengths and consequently the longer total axial length and the higher the stator copper loss.

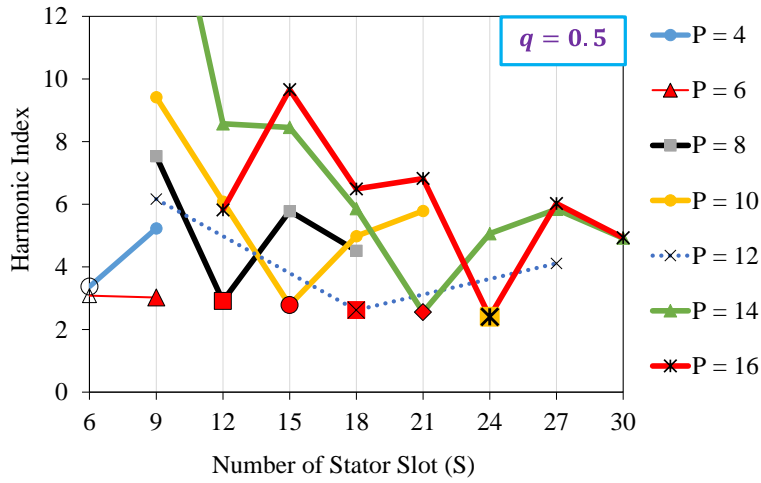


(a) FSCW and ISCW with $y_c = 1$

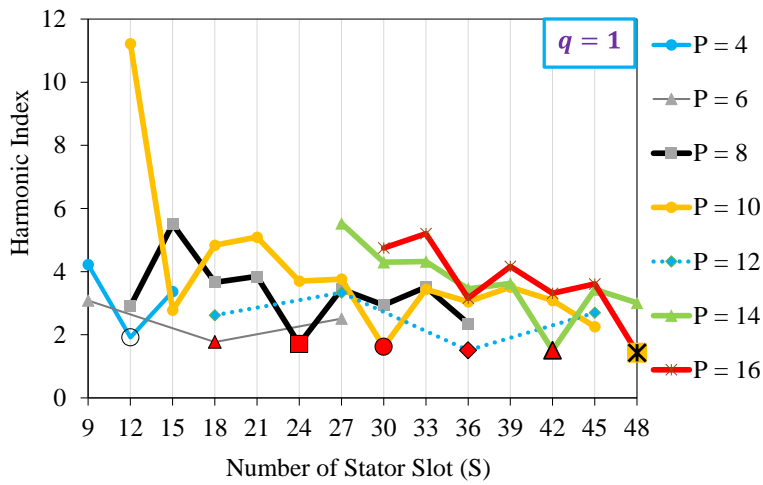


(b) FSDW and ISDW with $y_c = 2$

Fig. 2.1 Variation of fundamental winding factor with respect to slot and pole number.



(a) FSCW and ISCW with $y_c = 1$



(b) FSDW and ISDW with $y_c = 2$

Fig. 2.2 Variation of harmonic index with respect to S/P combinations.

2.3 Design of Different Winding Configurations

In this section, several S/P combinations and different winding configurations, which are determined by considering the fundamental winding factor, harmonic index, and GCD calculated in the previous section, have been analysed and compared. The corresponding winding layouts, winding factor harmonics, harmonic indices, and MMF harmonics are calculated for each combination. The winding factor k_{wh} consists of pitch k_{ph} and distribution k_{dh} factors, where there is no skewing on the stator slots. The winding factor harmonics for FSCW and ISDW are calculated separately by using the expressions given from (2.2) to (2.6) [BIA06], [FOR13], [YOK16].

$$k_{wh} = k_{ph} \cdot k_{dh} \quad (2.2)$$

$$k_{ph_ISDW} = \sin\left(h \frac{\pi}{S} y_c\right) = \sin\left(h \frac{\pi}{2} \cdot \frac{y_c}{y_p}\right) \quad (2.3)$$

$$k_{ph_FSCW} = \sin\left(h \frac{\pi}{S}\right) \quad (2.4)$$

$$k_{dh_ISDW} = \frac{\sin\left(h \frac{\pi}{P \cdot m}\right)}{\frac{S}{P \cdot m} \cdot \sin\left(h \frac{\pi}{S}\right)} \quad (2.5)$$

$$k_{dh_FSCW} = \frac{\sin\left(h \frac{\pi}{P \cdot m}\right)}{S \cdot \sin\left(h \frac{\pi}{S \cdot P \cdot m}\right)} \quad (2.6)$$

where h is the harmonic order, y_c is the slot-pitch (coil-pitch) in terms of slot number, y_p is the pole-pitch in terms of slot number, S , P , and m are the stator slot, pole and phase numbers, respectively. Once the winding layout is defined, the MMF created by the stator currents can be calculated. The parameter definitions of an MMF wave created by a single coil are described in Fig. 2.3. The MMF of order h for a coil fed with sinusoidal current, depending on the angular position θ (the space angle at a point of interest in the air-gap), the phase angle γ between the current vector and the rotor axis as shown in Fig. 2.3, the number of turns per phase N_s , the phase current I_s , the angular frequency ω , and the time t , is expressed by (2.7) [MAG03].

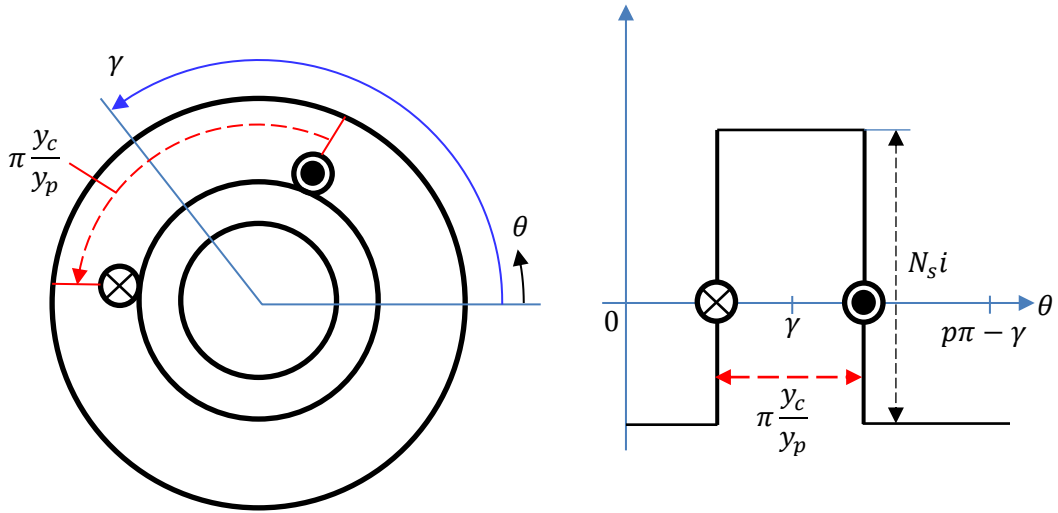


Fig. 2.3 A single coil inserted in slots of the stator (left) and a common representation of the air-gap MMF a single coil with N_s turns carrying the instantaneous current i (right).

$$\begin{aligned} MMF_s(\theta)_{(h)} &= \frac{4N_s}{hp\pi} k_{ph_ISDW} \cos[h(\theta - \gamma)] \cdot I_s \cos(\omega t) \\ &= \frac{4N_s I_s}{hp\pi} \sin\left(\frac{h\pi}{2} \cdot \frac{y_c}{y_p}\right) \cdot \frac{1}{2} \{\cos[\omega t - h(\theta - \gamma)] + \cos[\omega t + h(\theta - \gamma)]\} \end{aligned} \quad (2.7)$$

The equation given in (2.7) implies that the MMF can mathematically be separated into two waves, rotating in opposite directions. Due to the need of symmetry, the waveform pattern must be repeated at least once over the whole periphery of the machine, which means that the minimum harmonic order is $2/p$. Since the MMF pattern is not identical for each pole for FSDWs, an electrical displacement factor is used given by (2.8), where x is the physical phase displacement in number of slots. For any S/P combination, equations from (2.7) to (2.11) have been used for the calculation of the 3-phase MMF of order h for a machine with symmetrical phase windings. In (2.9), y_{cc} , N_c , MMF^+ , MMF^- , and γ_c are the coil span of the c^{th} coil, number of coils, forward and backward rotating MMF waves, and the phase angle of the c^{th} coil between the current vector and the rotor axis respectively. Note that the forward and backward MMF harmonics expressed in (2.10) and (2.11) can be used to predict any stator MMF harmonic of 3-phase winding configuration. In addition, it can be predicted that since 3-phase windings are uniformly displaced in space with respect to each other by 120° electrical degrees all triplen MMF harmonics are eliminated in $S/GCD(S, p)$ slots.

Note that the magnitudes of the MMF harmonics of any S/P combinations are normalized against that of the 3rd order working harmonics since only the pole number of 6 combinations have been considered in this section. In addition, the resultant MMF harmonics are calculated using (2.10) and (2.11) for any S/P combination, and in the plotted MMF spectrums, the forward and backward rotating harmonics are denoted by ‘F’ and ‘B’, respectively.

$$n_y = \frac{x}{6q} - \frac{1}{3} \quad (2.8)$$

$$MMF_s(\theta)_{3ph(h)} = \sum_{h=\frac{2}{p}}^{\infty} \sum_{c=1}^{N_c} \frac{4N_s}{hp\pi} \sin\left(h \frac{\pi}{2} \cdot \frac{y_{cc}}{y_p}\right) (MMF^+ + MMF^-) \quad (2.9)$$

$$MMF^+ = I_s \cos[\omega t - h(\theta - \gamma_c)] \cdot \left\{ \frac{1}{2} + \cos\left[\frac{2\pi}{3}(h-1) + 2\pi \cdot h \cdot n_y\right] \right\} \quad (2.10)$$

$$MMF^- = I_s \cos[\omega t + h(\theta - \gamma_c)] \cdot \left\{ \frac{1}{2} + \cos\left[\frac{2\pi}{3}(h+1) + 2\pi \cdot h \cdot n_y\right] \right\} \quad (2.11)$$

2.3.1 9S/6P-DL ($y_c = 1$) Fractional-Slot Concentrated Winding (FSCW)

A 9-slot/6-pole double-layer with one slot-pitch ($y_c = 1$) 9S/6P-DL FSCW configuration having 3 symmetrically distributed coils per phase has been examined in this section. Winding layout of this combination is illustrated in Fig. 2.4. The coils of the FSCWs are concentrated around the stator teeth and q is 0.5 for this winding configuration.

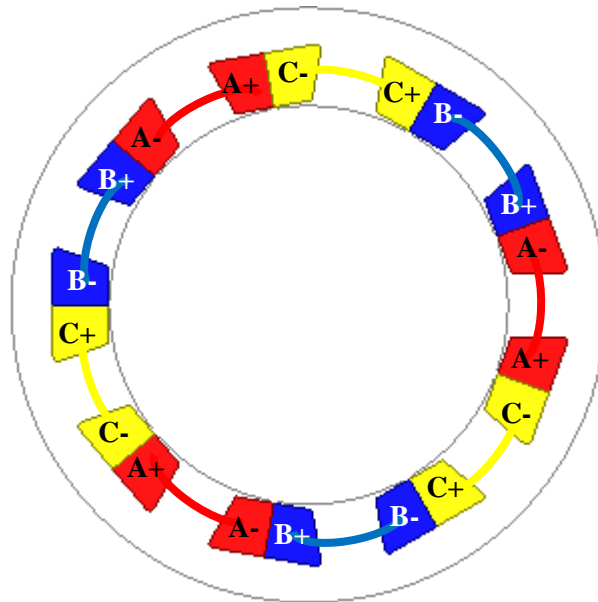
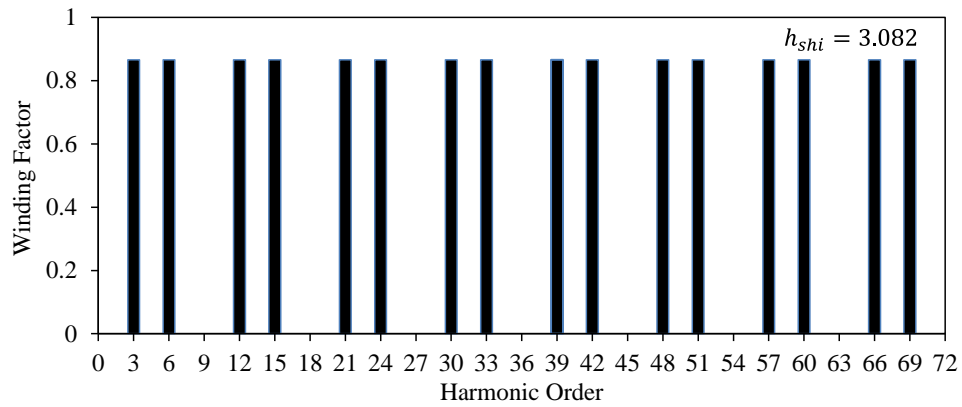
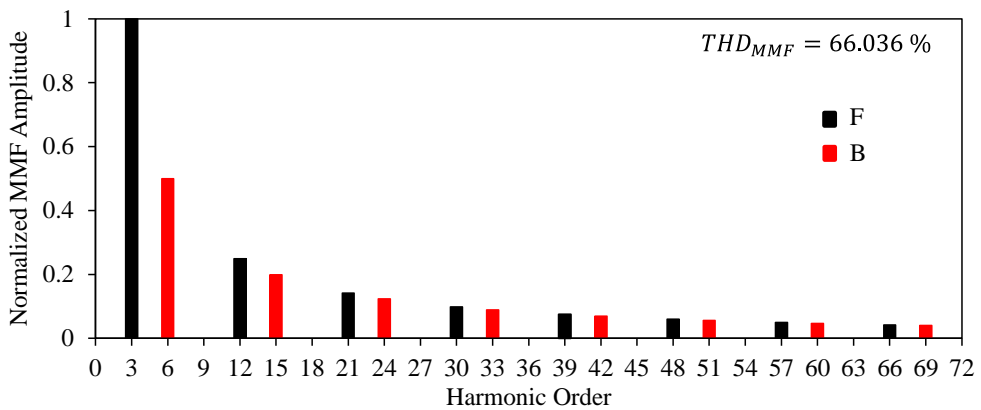


Fig. 2.4 Winding layout of 9S/6P-DL ($\gamma_c = 1$) FSCW IM.



(a) Harmonic winding factors and calculated h_{shi}



(b) MMF spectrum and its THD percentage

Fig. 2.5 Winding analyses of 9S/6P-DL ($\gamma_c = 1$) FSCW configuration: (a) harmonic winding factors and (b) normalized MMF harmonic spectrum.

The calculated harmonic winding factors, harmonic index, MMF harmonics, and MMF total harmonic distortion (THD) are shown in Fig. 2.5. Since the pole number is 6, the fundamental winding harmonic is 3 and the amplitude is 0.866. As clearly seen from the figures, harmonic index and THD

of the 9S/6P-DL combination are quite high. Therefore, it can be predicted that the rotor losses will be excessively high for the IM with this S/P combination and winding configuration.

2.3.2 18S/6P-DL ($y_c = 1$) Integer-Slot Concentrated Winding (ISCW)

In this section, an 18S/6P-DL ($y_c = 1$) ISCW configuration is investigated. This combination has 6 symmetrically distributed coils per phase as seen in Fig. 2.6. For this winding configuration, the fundamental winding factor is 0.5 and the real amplitude of the working MMF harmonic is 2.8643 At for 1-turn and 1-ampere and the magnitudes of the MMF harmonics are normalized against that of the 3rd order working harmonic. The calculated winding factor and normalized MMF harmonics are shown in Fig. 2.7. Since the winding factor of this combination is quite low, to be able to generate the same amount of torque as the other combinations, more number of turns are required. Therefore, it can be predicted that the stator copper loss of this combination will be higher than that of the other combinations.

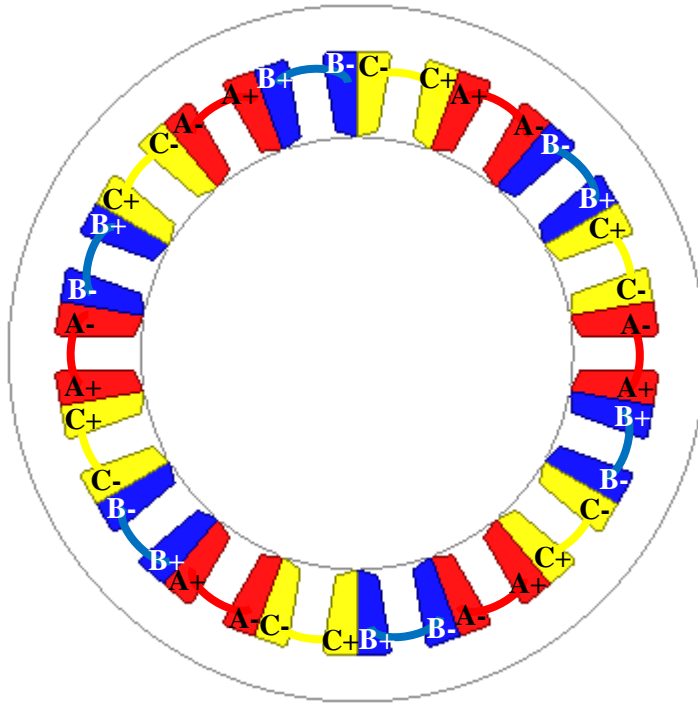
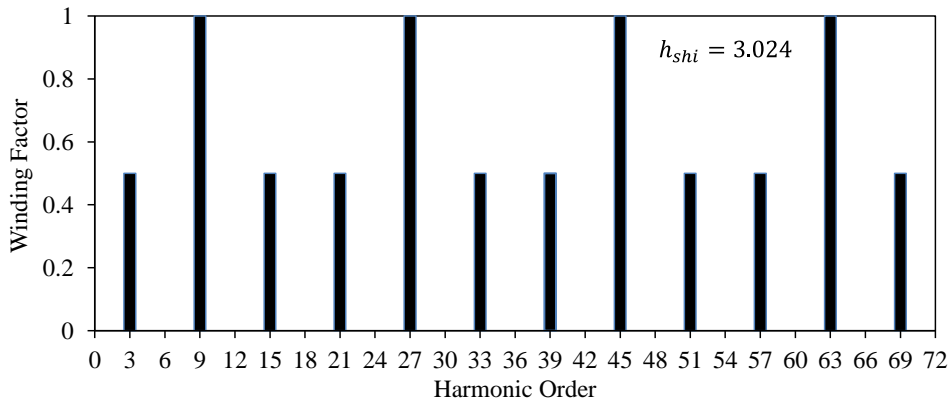
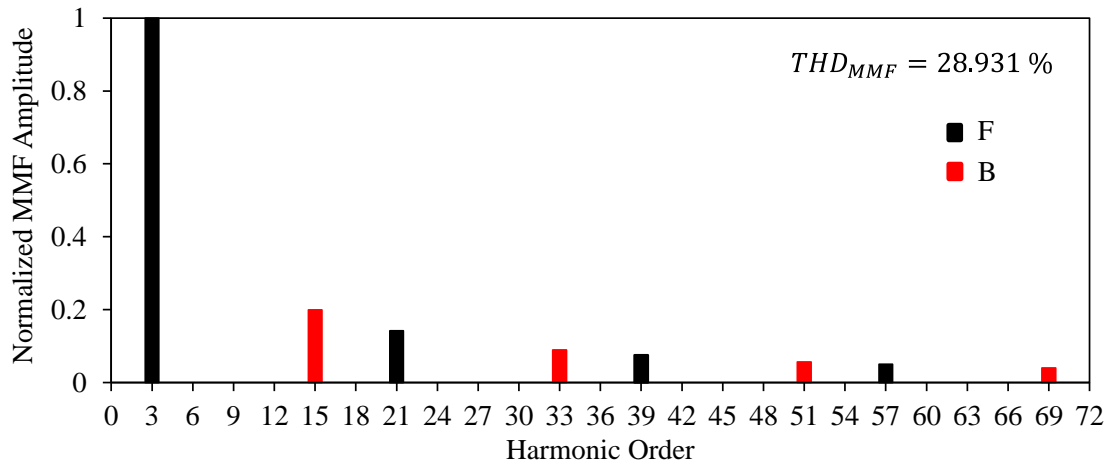


Fig. 2.6 Winding layout of 18S/6P-DL ($y_c = 1$) ISCW IM.



(a) Harmonic winding factors and calculated h_{shi}



(b) MMF spectrum and its THD percentage

Fig. 2.7 Winding analyses of 18S/6P-DL ($y_c = 1$) ISCW configuration: (a) harmonic winding factors and (b) normalized MMF harmonic spectrum.

2.3.3 18S/6P-SL ($y_c = 3$) Integer-Slot Distributed Winding (ISDW)

An 18S/6P-SL ($y_c = 3$) ISDW configuration is examined in this part. Winding layout, harmonic winding factors, and MMF harmonic spectrum of this combination are shown in Fig. 2.8 and Fig. 2.9, respectively. As seen in Fig. 2.8, this winding consists of 3 symmetrically distributed coils per phase. Since the distributed windings with $y_c = 3$ are used, it can be predicted that the both of the radial and axial lengths of the end windings will be longer, resulting in an increase in the end winding resistance and consequently copper loss.

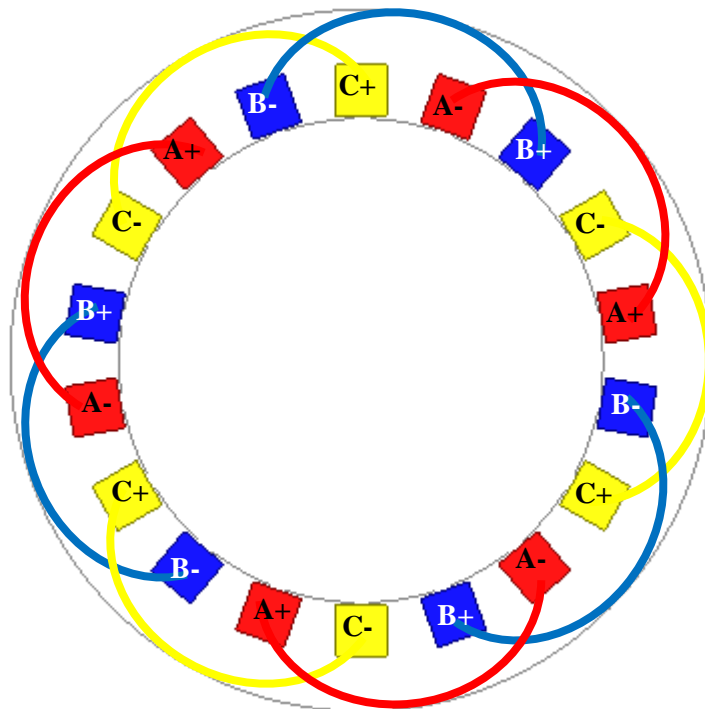
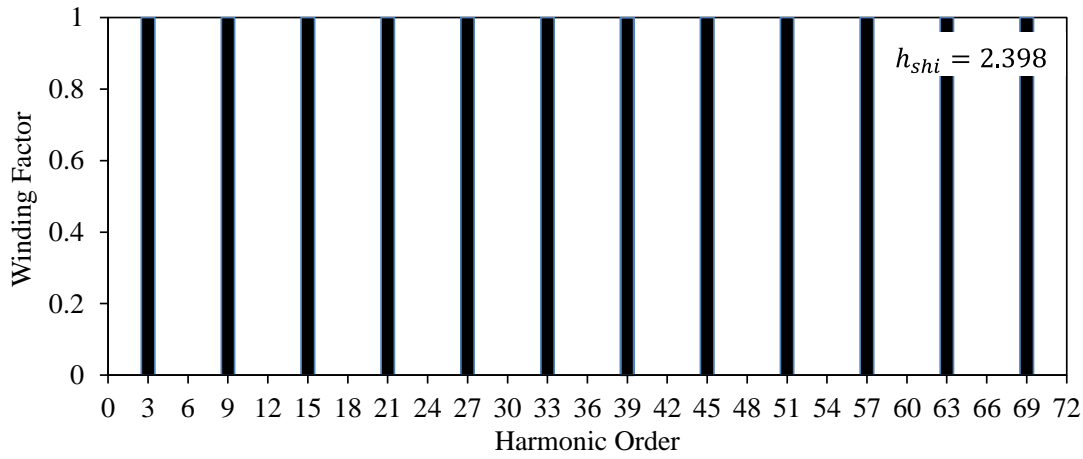
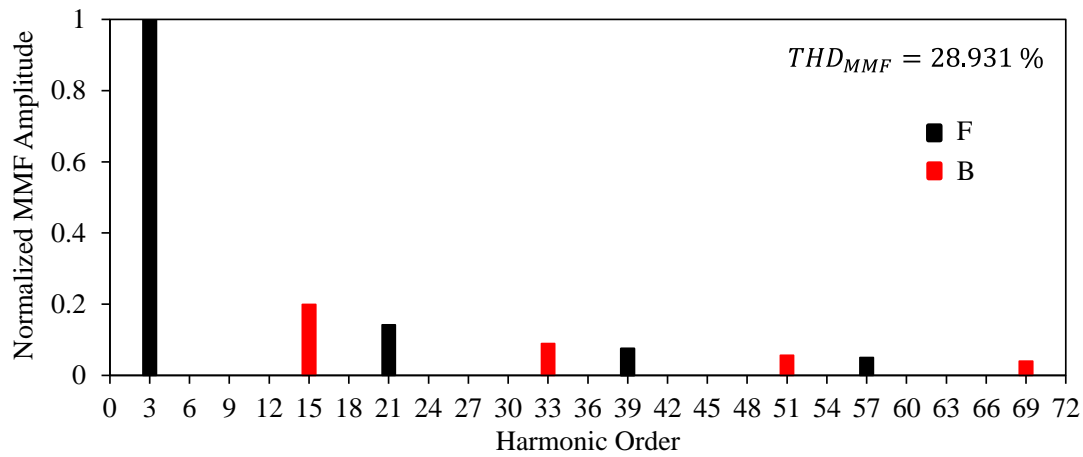


Fig. 2.8 Winding layout of 18S/6P-SL ($y_c = 3$) ISDW IM.



(a) Harmonic winding factors and calculated h_{shi}



(b) MMF spectrum and its THD percentage

Fig. 2.9 Winding analyses of 18S/6P-SL ($y_c = 3$) ISDW configuration: (a) harmonic winding factors and (b) normalized MMF harmonic spectrum.

2.3.4 18S/6P-DL ($y_c = 2$) ISDW

In this part, an 18S/6P-DL ($y_c = 2$) ISDW configuration, whose winding layout is shown in Fig. 2.10, is investigated. This winding structure consists of 6 symmetrically distributed coils per phase. Winding factor harmonics, winding harmonic index, normalized MMF harmonics, and MMF THD of this combination are illustrated in Fig. 2.11. The fundamental winding factor is 0.866 and it can be seen that the 6th, 9th, and multiples of these harmonics do not exist. Therefore, the harmonic index and the MMF THD are quite low and the amplitude of the fundamental MMF is quite high when compared to previous combinations. It can be predicted that the rotor bar copper loss of the IM designed with this S/P combination and winding configuration will be lower than the earlier combinations.

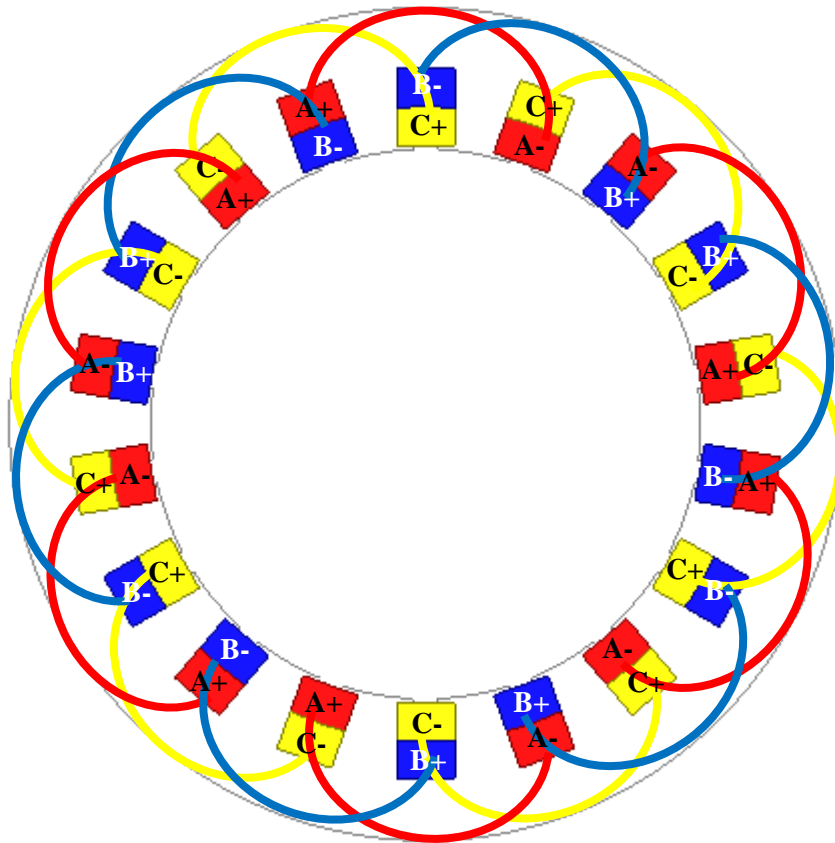
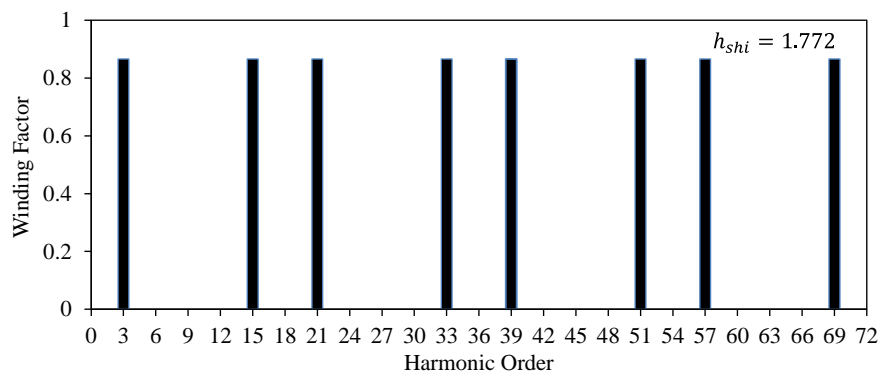
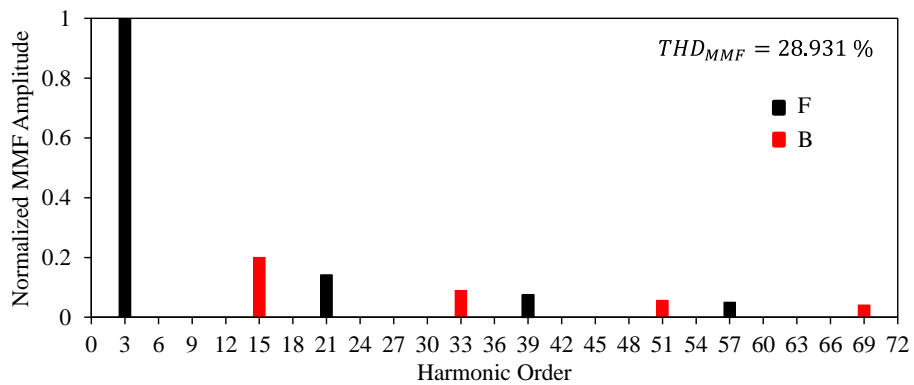


Fig. 2.10 Winding layout of 18S/6P-DL ($\gamma_c = 2$) ISDW IM.



(a) Harmonic winding factors and calculated h_{shi}



(b) MMF spectrum and its THD percentage

Fig. 2.11 Winding analyses of 18S/6P-DL ($\gamma_c = 2$) ISDW configuration: (a) harmonic winding factors and (b) normalized MMF harmonic spectrum.

2.3.5 36S/6P-SL and DL ($y_c = 5$) ISDW

A 36S/6P-SL ($y_c = 5$) ISDW configuration is investigated in this section. This combination consists of 6 symmetrically distributed coils per phase as seen in Fig. 2.12. Since the slot pitch is 5, the axial and radial lengths of the end windings are longer than those of the previous combinations. The winding factor and the MMF harmonics are shown in Fig. 2.13. As seen in the figure, the fundamental winding factor is very high (0.966). This indicates that the less number of turns will be adequate to generate the same average torque as the other combinations. In addition, since the fundamental MMF amplitude is quite high, the THD of the MMF is comparatively lower than the earlier combinations. Therefore, the high amount of stator copper loss will occur due to the long end-windings. However, remarkably low rotor losses will be achieved because of the lower harmonic content of the MMF.

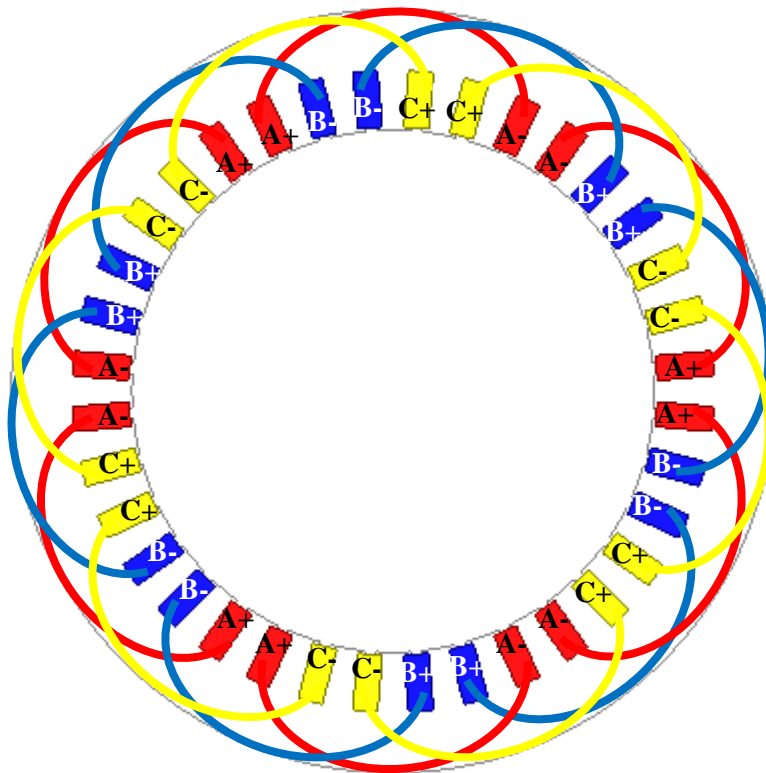
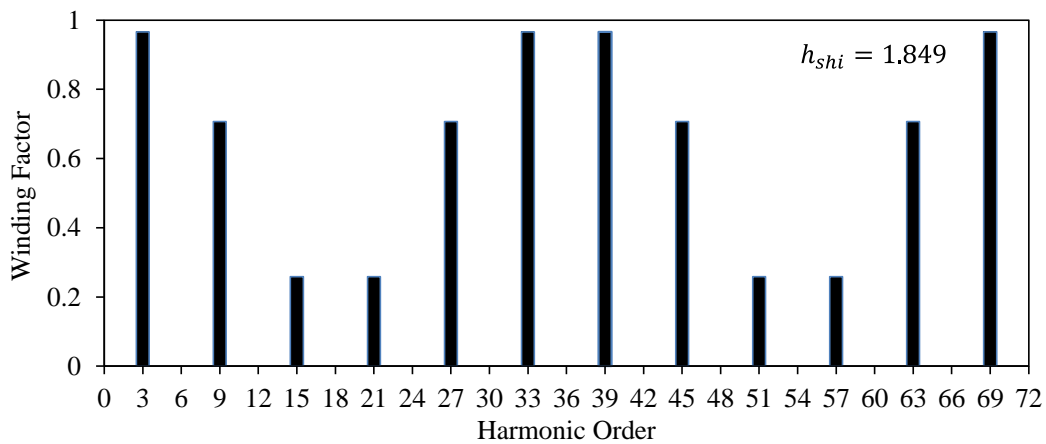
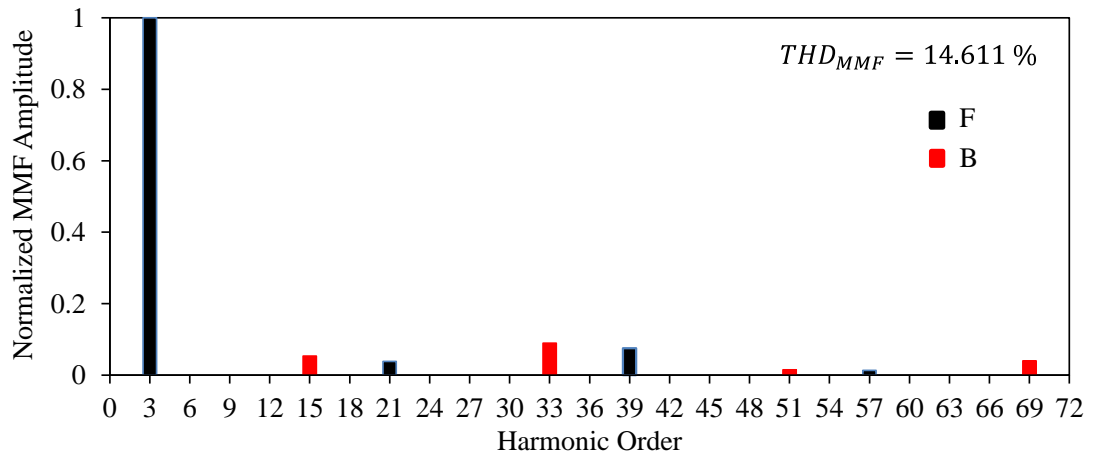


Fig. 2.12 Winding layout of 36S/6P-SL ($y_c = 5$) ISDW IM.



(a) Harmonic winding factors and calculated h_{shi}



(b) MMF spectrum and its THD percentage

Fig. 2.13 Winding analyses of 36S/6P-SL ($\gamma_c = 5$) ISDW configuration: (a) harmonic winding factors and (b) normalized MMF harmonic spectrum.

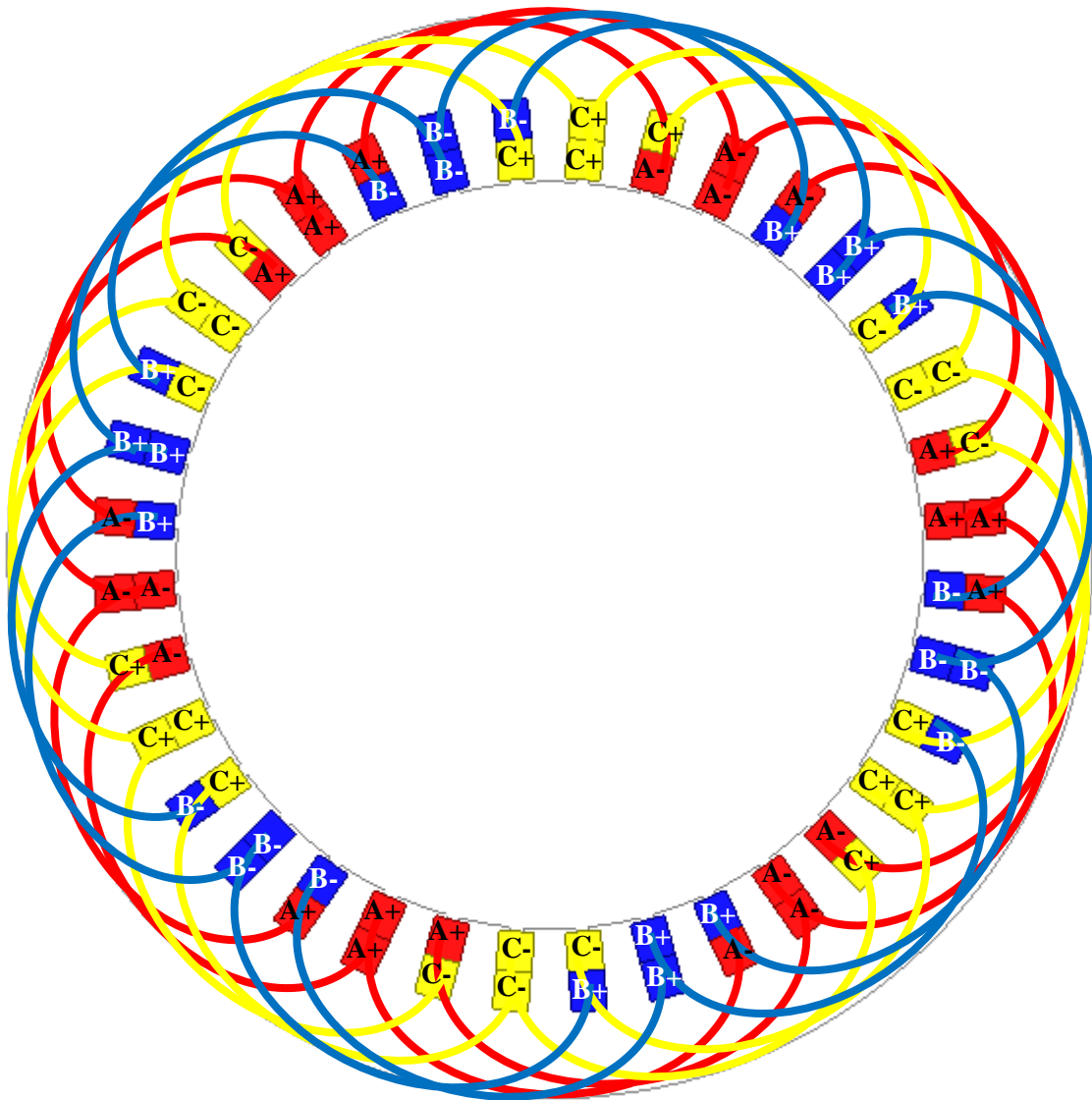
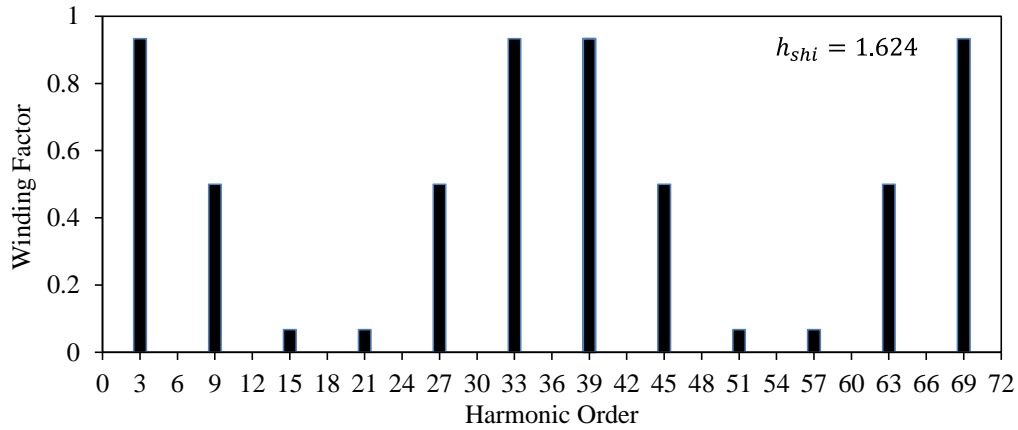


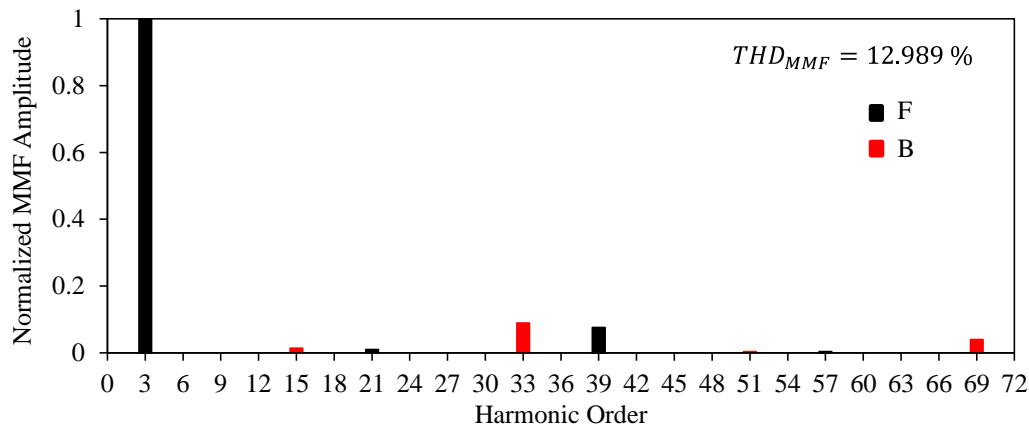
Fig. 2.14 Winding layout of 36S/6P-DL ($\gamma_c = 5$) ISDW IM.

The 36S/6P-DL ($\gamma_c = 5$) ISDW combination, which is the double-layer form of the 36S/6P-SL combination, is considered in this part. Winding configuration consists of symmetrically distributed 12

coils per phase as seen in Fig. 2.14. In comparison with the other investigated winding configurations, the complexity of this winding type is relatively high in terms of analysing and manufacturing. However, as seen in the winding and MMF harmonic distortion figures shown in Fig. 2.15, this winding configuration produces the most high quality MMF waveform. In addition, the fundamental winding factor is fairly high (0.933) and the real amplitude of the working MMF harmonic per 1-turn and 1-ampere is 5.345 At. Considering the lowest winding harmonic index and MMF THD of the 36S/6P-DL combination, it can be predicted that this combination will have the lowest rotor losses and the highest efficiency.



(a) Harmonic winding factors and calculated h_{shi}



(b) MMF spectrum and its THD percentage

Fig. 2.15 Winding analyses of 36S/6P-DL ($y_c = 5$) ISDW configuration: (a) harmonic winding factors and (b) normalized MMF harmonic spectrum.

2.3.6 54S/6P-DL ($y_c = 9$) ISDW

In this part, a 54S/6P-DL ($y_c = 9$) ISDW configuration, whose winding layout is shown in Fig. 2.16, is investigated. Note that, Fig. 2.16 is only for the illustration purpose. Only the winding layout of the 54S/6P-DL combination is shown. The real dimensions have been illustrated in Fig. 2.21(g) and the geometric specifications have been given in Appendix C.1. This winding structure consists of 9 symmetrically distributed coils per phase. Winding factor harmonics, winding harmonic index, normalized MMF harmonics, and MMF THD of this combination are illustrated in Fig. 2.17. The

fundamental winding factor is 0.96 and the real fundamental MMF amplitude is ~ 5.5 At. It can be seen that multiples of the 6th harmonic do not exist. Moreover, the 54S/6P combination has the least distortion among the other combinations. Therefore, it can be predicted that the rotor bar copper loss of the IM designed with 54S/6P-DL combination with $y_c = 9$ configuration will be the lowest.

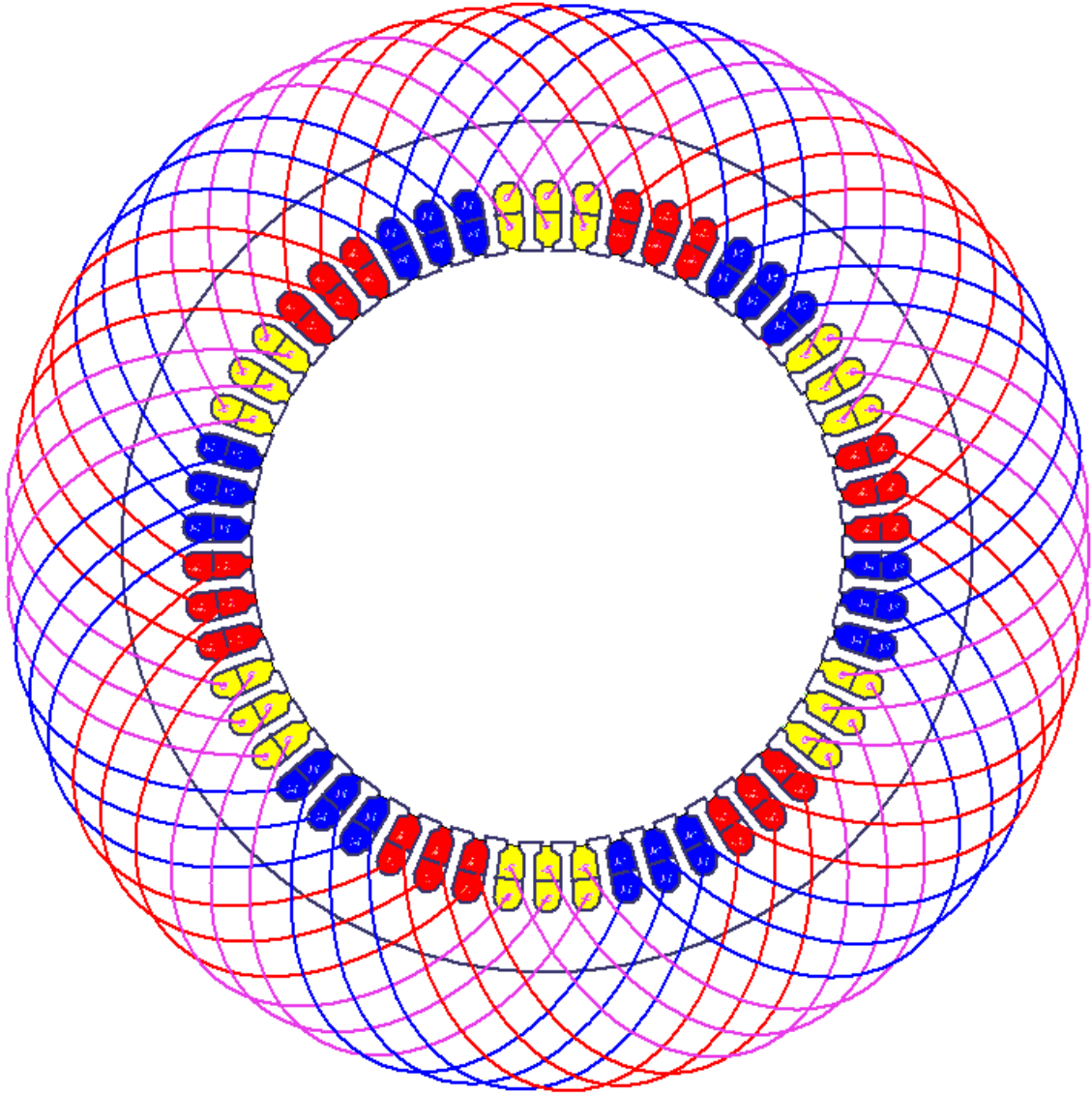
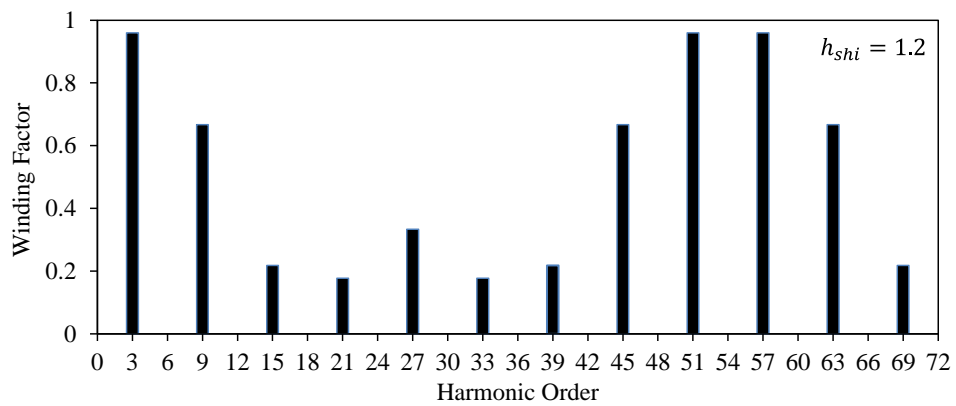
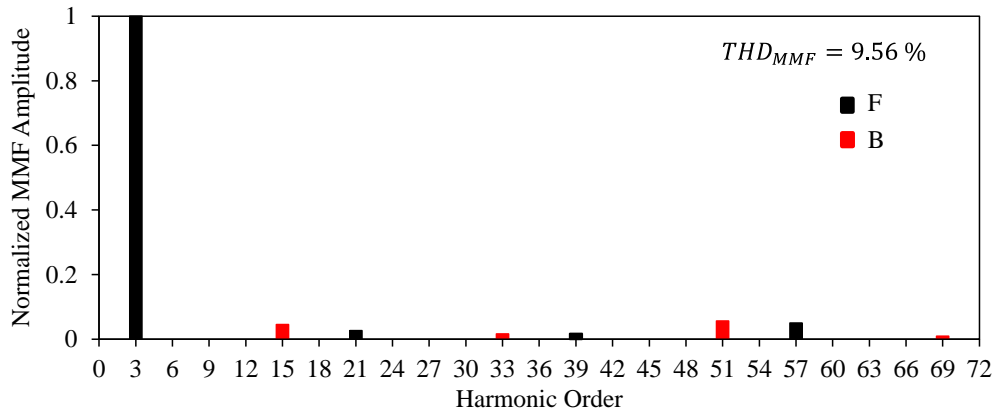


Fig. 2.16 Winding layout of 54S/6P-DL ($y_c = 9$) ISDW IM.



(a) Harmonic winding factors and calculated h_{shi}



(b) MMF spectrum and its THD percentage

Fig. 2.17 Winding analyses of 54S/6P-DL ($\gamma_c = 9$) ISDW configuration: (a) harmonic winding factors and (b) normalized MMF harmonic spectrum.

2.4 General Performance Comparison of 6-pole IMs with Different Winding Configurations

Seven different squirrel-cage IMs are designed by assigning the winding layouts given in the previous section and adopting the specifications listed in Appendix C.1. A 2-D FEA software is employed to simulate the designed IMs. During the analyses, the same geometrical and operational parameters have been assigned for all the IMs. The stator current, synchronous speed, and rated frequency are 500 Arms, 2 krpm, and 100 Hz, respectively. The rotor speed delivering the maximum torque has been parametrically determined for each machine. Each IM has been optimized by multi-objective global optimization by Genetic Algorithm (GA). The average torque, efficiency, and output power are then used as optimization objectives during the optimization, which ensures that the torque capability is maximized and copper losses are minimized. Note that in this thesis, the average torque defined as the time average torque at pullout slip. Optimization parameters are split ratio and stator and rotor slot geometric parameters indicated in Appendix C.1. During the optimization process the stator current density of all IMs is set to 23.4 A/mm^2 for a fair comparison. Note that the allowable current density is determined by available cooling equipment provided by Valeo Power-train [GUA15b]. In addition, typical continuous allowable current densities for IMs having liquid cooling in ducts have been specified as 23 to 31 A/mm^2 [LIP17]. Consequently, determined current density is chosen as to be within the allowable limits. More details about the optimization procedure will be presented in Appendix E. The obtained global optimum geometric parameters are summarized in Appendix C.1. Rotor slot numbers have been determined parametrically by conducting several parametric analyses. The estimation method of the rotor slot numbers including the considerations such as average torque, rotor bar current density, UMF, etc. and the general basic rules such as avoiding the multiples of phase and pole numbers, odd slot numbers, etc. will be explained in detail in Chapter 4 and Chapter 6. The specifications of the core material can be found in Appendix B.

Comparison of the fundamental winding factors of the considered combinations is shown in Fig. 2.18. It is obvious that the 18S/6P-DL ($y_c = 1$) combination has the minimum winding factor whilst the 18S/6P-SL ($y_c = 3$) combination has the maximum winding factor. The calculated winding harmonic index h_{shi} and the MMF THD rate are illustrated in Fig. 2.19. As clearly seen in the figure, at the same pole number, the higher the stator slot number, the lower the level of distortion. Therefore, it can be predicted that the lower the distortion, the lower the torque ripple, vibration, acoustic noise, and rotor losses.

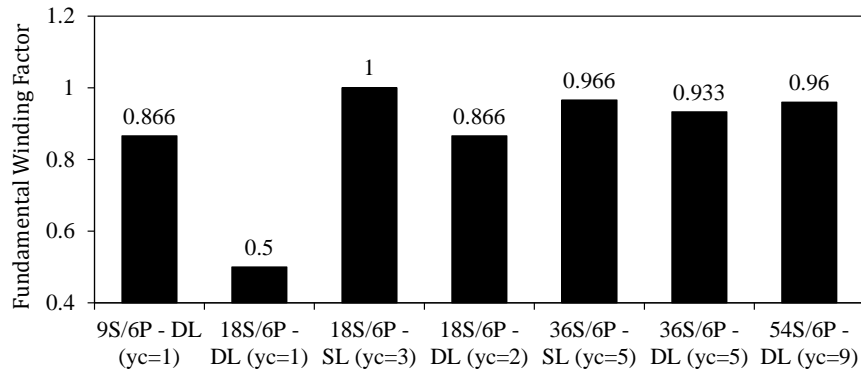


Fig. 2.18 Fundamental winding factors of the considered slot/pole and winding-layer combinations.

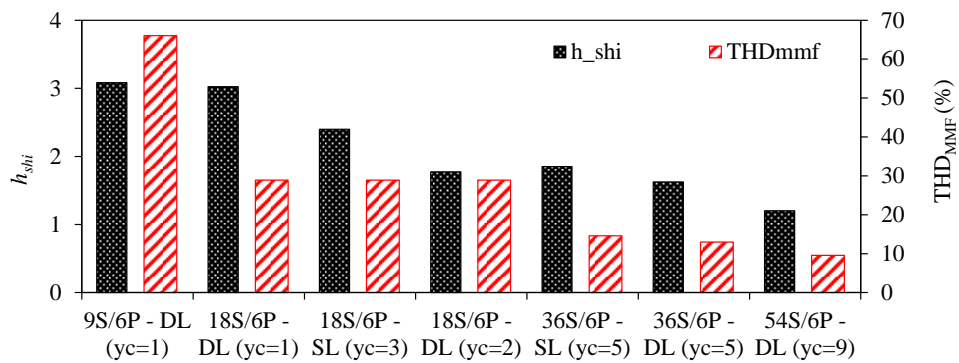


Fig. 2.19 Comparison of winding harmonic index (h_{shi}) and THD of winding MMFs of various winding structures.

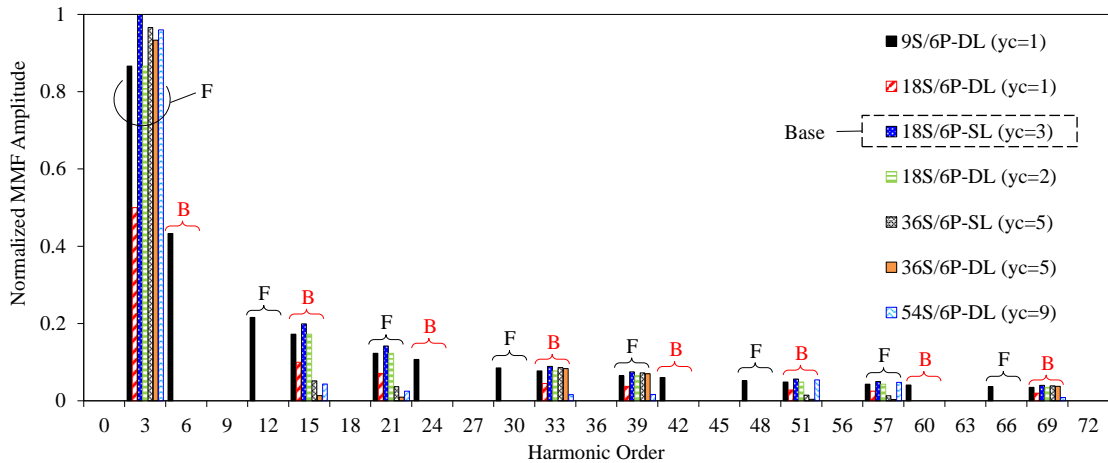


Fig. 2.20 Comparison of the normalized MMF amplitudes of different winding topologies having different S/P combinations.

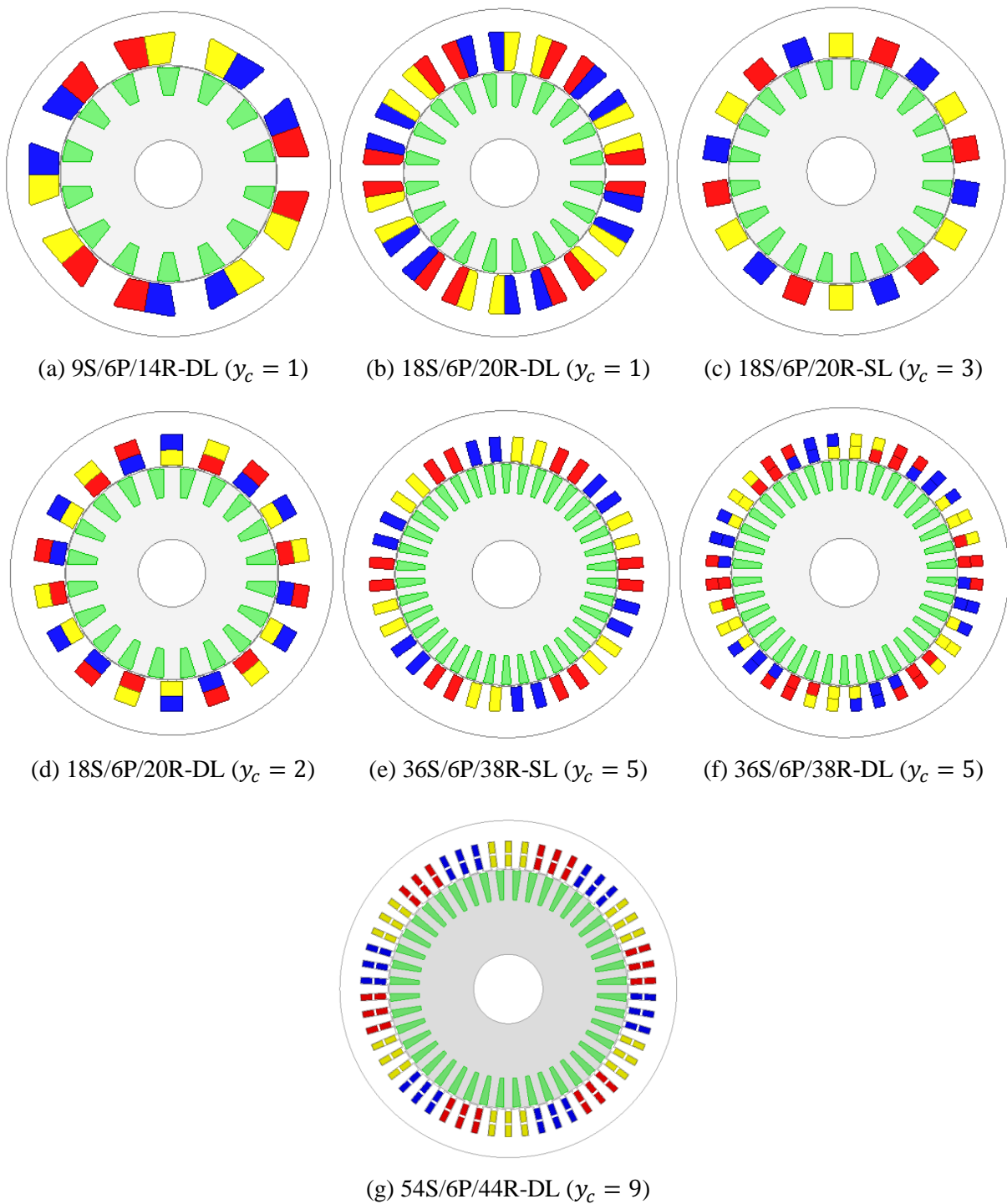


Fig. 2.21 Cross-sections of the IMs with various S/R/P combinations and winding layouts.

As seen from Fig. 2.19, adopting double-layer windings instead of single-layer windings leads to a decrease in the MMF THD rate. In addition, the magnitudes of the MMF harmonics are normalized against that of the S/P combination delivering the highest MMF amplitude of the 3rd order working harmonic, which is 5.7287 At of 18S/6P-SL ($y_c = 3$) and the obtained result is illustrated Fig. 2.20. As expected, exactly the same amounts with that of the fundamental winding factors have been obtained. Cross-sections of the optimized 6P IMs with different S/R combinations and winding configurations are illustrated in Fig. 2.21. In this study, a formula, $R = S + 2q$, is used to calculate the optimal rotor slot number for any stator slot/pole/phase number as seen in the figures. This empirical formula has

been proposed by adopting a large number of parametric analyses for a large number of S/P combinations. More details about the determination of the optimal rotor slot number can be found in Chapter 3 and 4. The geometric, electric, and electromagnetic performance of the considered IMs are presented in the following sections.

2.4.1 Axial Length and Phase Resistance

The average coil length of the low-voltage electrical machines with ISDWs and FSCWs having single-layer (SL) and double-layer (DL) windings composed of pre-fabricated round enamelled wires can be calculated by the following approximations from (2.12) to (2.15) in mm [MAG03].

$$l_{av_ISDW_SL} \approx 2l_s + \frac{2\pi^2 r_w y_c}{S} \quad (2.12)$$

$$l_{av_ISDW_DL} \approx 2l_s + \frac{6.4\pi r_w}{p} \quad (2.13)$$

$$l_{av_FSCW_SL} \approx 2l_s + \frac{5.44\pi r_w}{S} \quad (2.14)$$

$$l_{av_FSCW_DL} \approx 2l_s + \frac{3.72\pi r_w}{S} \quad (2.15)$$

where l_s is the stack length of the machine, y_c is the coil pitch number, r_w is the average winding radius, calculating as the distance from the centre of the machine to the middle of the slot, and S is the stator slot number. The stator phase resistance is calculated by using the following equations.

$$S_w = \frac{A_c}{N_t} \quad (2.16)$$

$$R_{coil} = \rho_{cu} N_t \frac{l_{av}}{S_w \cdot k_f} \quad (2.17)$$

$$\begin{aligned} R_{phase} &= R_{coil} N_c & \text{if } a &= 1 \\ R_{phase} &= R_{coil} \frac{1}{a} & \text{if } a &= N_c \\ R_{phase} &= R_{coil} \frac{N_c}{a^2} & \text{if } a &\neq 1 \text{ and } a \neq N_c \end{aligned} \quad (2.18)$$

where A_c is the cross-sectional area of one coil-side, N_t is the number of turns per coil, S_w is the diameter of one wire, k_f is the fill factor a is the number of parallel branch, R_{coil} and R_{phase} are the resistance of one coil and phase resistance, respectively, ρ_{cu} is the resistivity $(58 \cdot 10^6)^{-1}$ in Ωm , l_{av} is the average length of one coil, which is calculated according to winding type by using the approximations given from (2.12) to (2.14). The calculated total axial lengths ($l_{stack} + l_{end-winding}$) and phase resistance have been compared in Fig. 2.22 and Fig. 2.23. As expected, the total axial lengths

of the FSCW IMs are shorter. Moreover, the total axial length of the IMs designed with single-layer ISDWs are longer than those of their double-layer counterparts. It is interesting that the total axial lengths of the short slot-pitch IMs (18S/6P) are longer than those of the long slot-pitch IMs because of the more number of turns requirement of short slot-pitch configuration; compensating the low fundamental winding factor. In addition, the higher the number of stator slots, the higher the number of coils per phase and consequently the lower number of turns per slot and eventually the smaller winding diameter. Therefore, even if the radial length of the long-pitch winding is longer than that of the short slot-pitch winding, its axial length is shorter (see Fig. 2.21(d) and (f)). As seen in Fig. 2.23, since the current densities are kept at the same level ($\sim 23.4 \text{ A/mm}^2$) for each IM, the calculated phase resistances are similar except for the IM with 54S/6P. However, since the average coil radial length of the IM with 54S/6P-DL ($y_c = 9$) is the longest one among the other combinations (i.e. ~ 1.8 times longer than $y_c = 5$ combinations), its phase resistance is the highest. It is also noticeable that since the ISDW IMs within $q = 2$ family require less number of turns than those of $q < 2$ because of their high fundamental winding factor, their phase resistance are less than those of the other combinations.

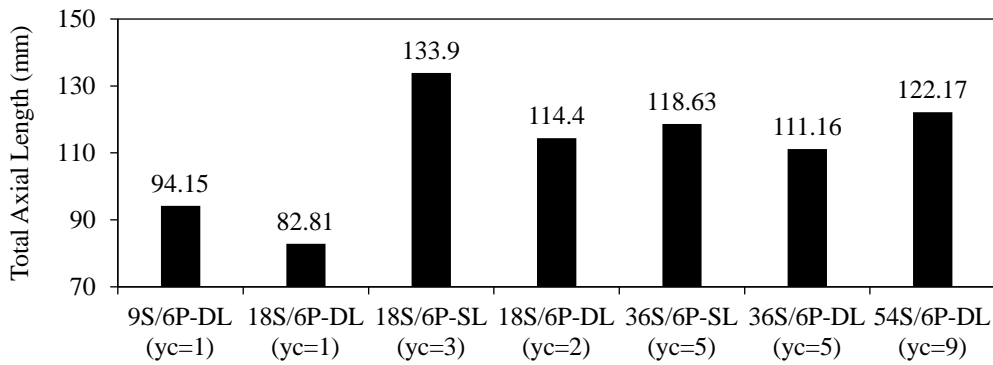


Fig. 2.22 Comparison of total axial lengths of designed IMs.

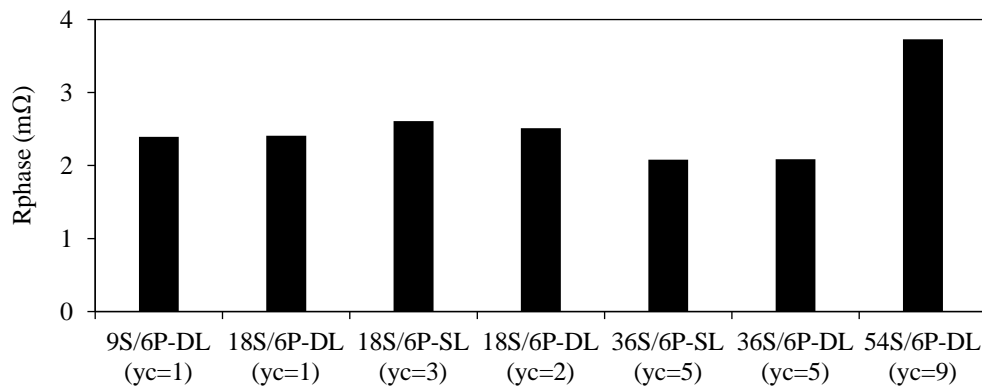


Fig. 2.23 Comparison of phase resistances.

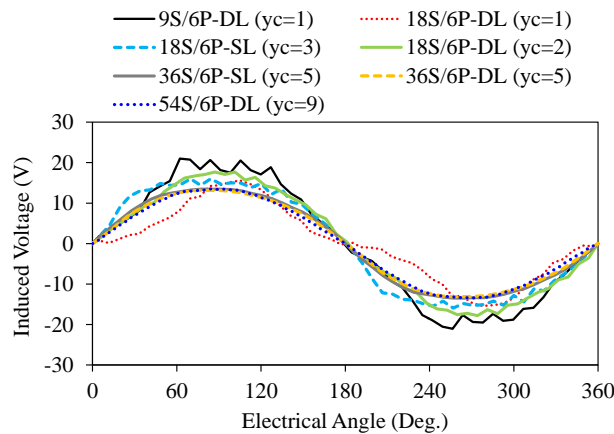
2.4.2 Induced Voltage

The waveform and harmonic spectra of the ‘Phase A’ induced voltage of the IMs are illustrated in Fig. 2.24. It appears from Fig. 2.24 that the 18S/6P-DL ($y_c = 1$) combination has the most distorted induced voltage waveform whilst the 18S/6P-DL ($y_c = 2$) combination has the least distorted waveform. It is interesting to note that, although the MMF harmonic distortion level of the 18S/6P-DL ($y_c = 2$)

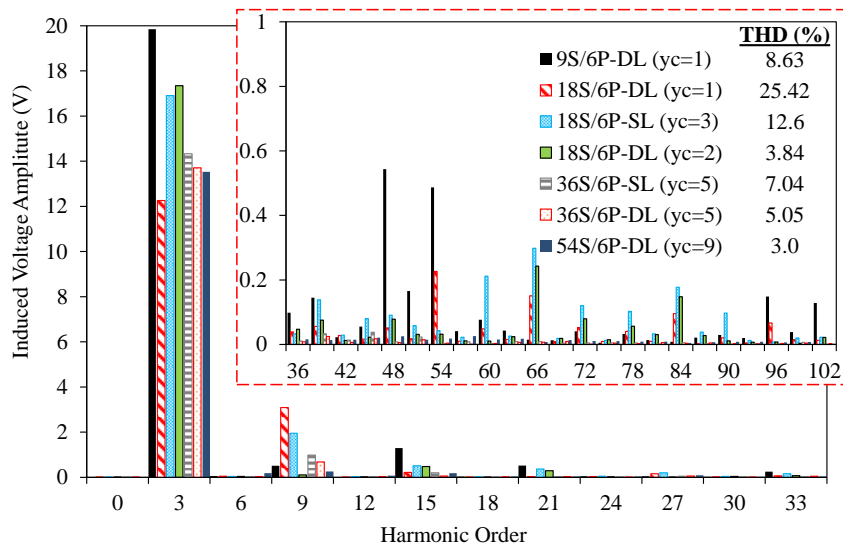
combination is much higher than that of the $y_c = 5$ combinations, its induced voltage THD appears lower. The reason for that is because the amplitude of the fundamental harmonic of the 18S/6P-DL ($y_c = 2$) is higher than that of the $y_c = 5$ combinations, its THD level appears much lower. As given in Appendix C.1, since the torque has been compensated by more number of turns for the S/P combinations having lower fundamental winding factor, their induced voltage amplitudes has increased due to the same stator current excitation. As clearly seen in Fig. 2.24(b), on the contrary of the FSCW IMs, only long-pitch ISDW combinations do not contain high order harmonics.

2.4.3 Air-Gap Flux Density

Comparison of the air-gap flux density waveforms is shown in Fig. 2.25. Note that the air-gap flux density waveforms given in this thesis are calculated by using the radial component of the resultant air-gap flux density. It is obvious that the higher the stator slot number, the lower the distortion in the air-gap flux density waveform. As clearly seen in the figures, the FSCW and ISDW combinations with short-pitch windings are highly distorted. In addition, the long-pitch ISDW combinations have higher air-gap flux density amplitudes than those of the other combinations.



(a) Induced voltage waveforms (Phase 'A')



(b) Induced voltage harmonics and THDs

Fig. 2.24 Phase 'A' induced voltage: (a) waveform and (b) harmonic spectra.

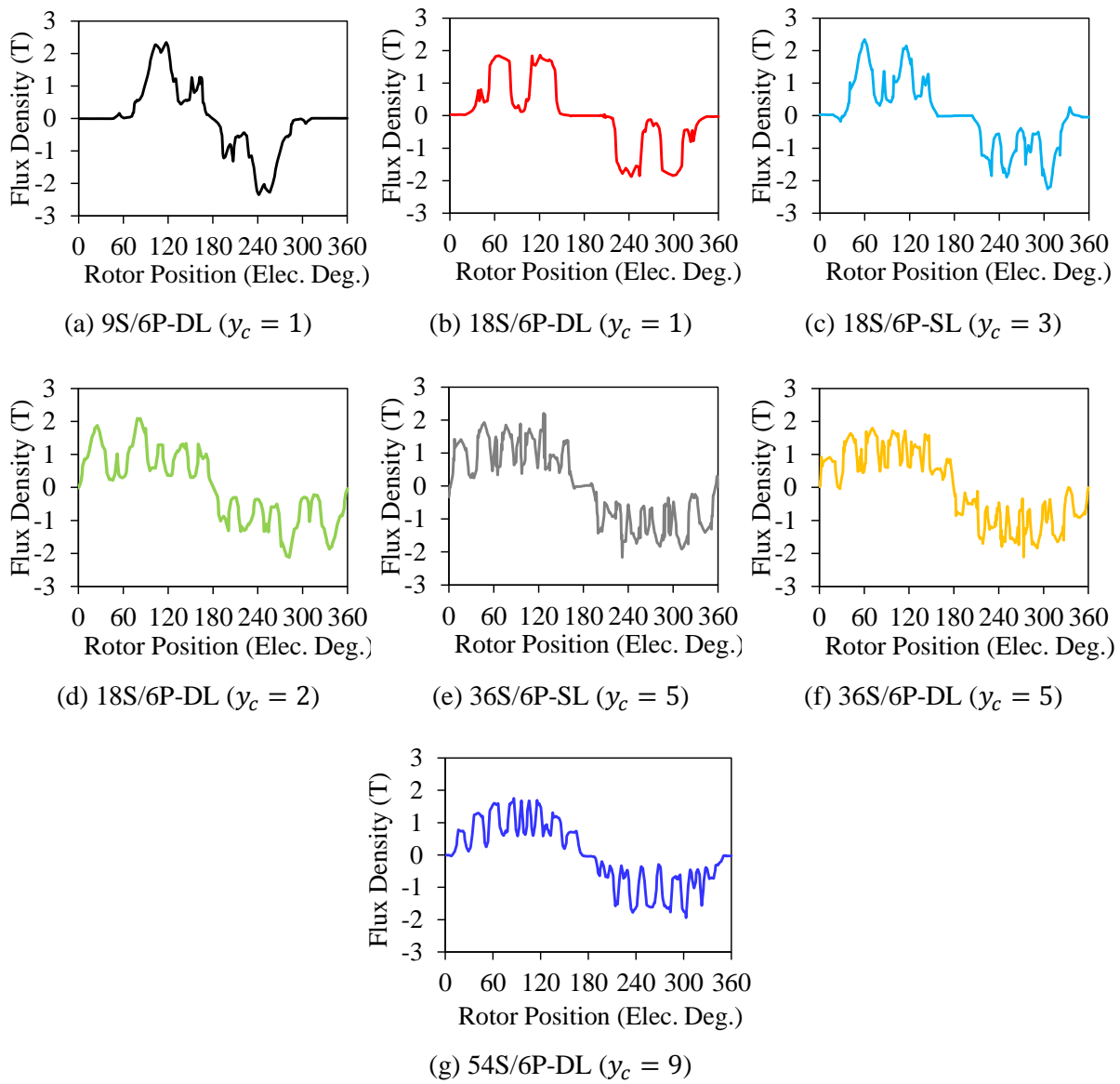


Fig. 2.25 Comparison of air-gap flux density waveforms.

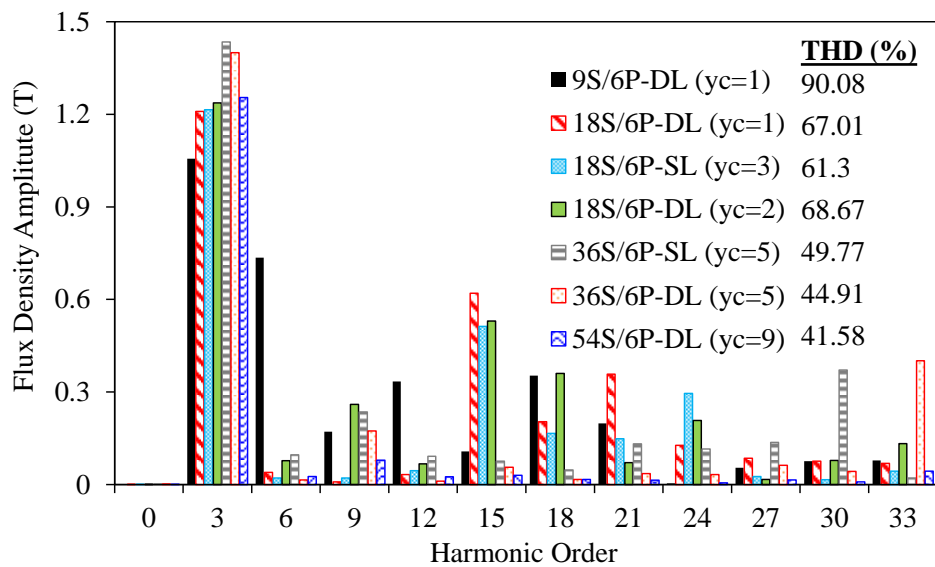


Fig. 2.26 Comparison of air-gap flux density harmonics and THDs.

2.4.4 Rotor Bar Current Density

The rotor bar current waveforms and their harmonic spectra are given in Chapter 6, Fig.6.79 and Fig.6.80. As seen in the figures, all the combinations have non-sinusoidal bar current waveform and among the various S/P combinations, the 9S/6P-DL has the most distorted bar current whilst the 36S/6P-DL has the least distorted one. The harmonics induced in the bar current cause an increase in the bar current density and rotor temperature. As seen in Fig. 2.27, the 9S combination, which has the most distorted bar current waveform, has the highest rotor bar current density. In addition, the 36S combinations have the least current density. Note that in this thesis, the rms value of the current has been used for the calculation of the bar current density. Therefore, it can be predicted that IMs designed with the FSCWs require more cooling equipment because of the very high bar current density. Moreover, the ISDW IMs with short-pitch windings require more cooling equipment than those with long-pitch windings.

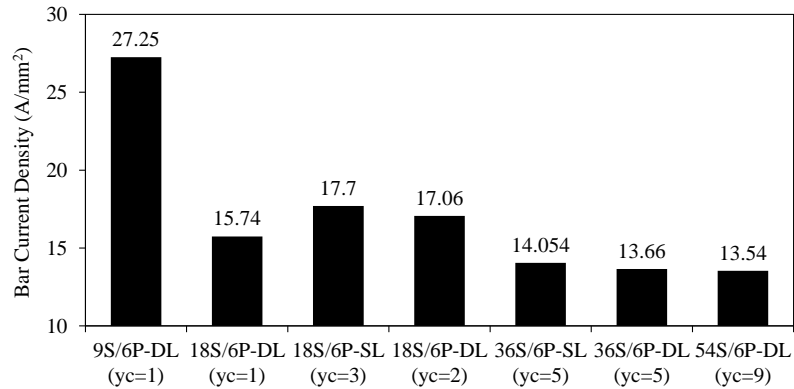


Fig. 2.27 Comparison of rotor bar current densities.

2.4.5 Flux Distributions

Flux line and flux density distributions of the IMs are illustrated in Fig. 2.28. It can be observed that as the stator slot number is increased, the saturation level decreases in the stator whilst it increases in the rotor. This is because of the fact that the MMF harmonics increase the saturation level of the stator parts due to the increase in the level of the leakage flux [REF08].

2.4.6 Torque, Torque Ripple, and Output Power

The comparison of the averaged torque and torque ripple percentage is shown in Fig. 2.29. As expected, the average torque of the IM with 18S6P-DL ($y_c = 1$) is the lowest among the other combinations because of its quite low fundamental winding factor. It has been revealed that the torque generating capabilities of the concentrated winding combinations are poorer than those of the distributed winding combinations. The reason behind this fact can be explained considering the torque equation given in (2.19) [ALB12].

$$T = \frac{9\mu_0 N_s I_s l_s D_g}{8\pi^2} \sum_{h=1}^{\infty} (N_s I_s k_{wh} + I_R) \int_0^{2\pi} \frac{\cos(h\theta - \omega t)}{h} \sin(h\theta - \omega t) d\theta \quad (2.19)$$

In (2.19), μ_0 is the relative permeability of air, N_s is the number of turns per phase, I_s is the stator current, l_s is the stack length, D_g is the average diameter of the air-gap, g is the air-gap length, I_R is the rotor bar current, ω is the angular frequency and θ is the angular rotor position. As detailed in Chapter 5, the increase in the saturation level of the rotor tooth body parts causes an increase in the 3rd harmonic of the bar current; where the sinusoidal waveform turns into a trapezoidal-like (flat-topped) waveform. From (2.19), it can be concluded that the lower winding factor and consequently smaller average air-gap diameter cause the FSCW IMs to generate lower torque than those of the ISDW IMs.

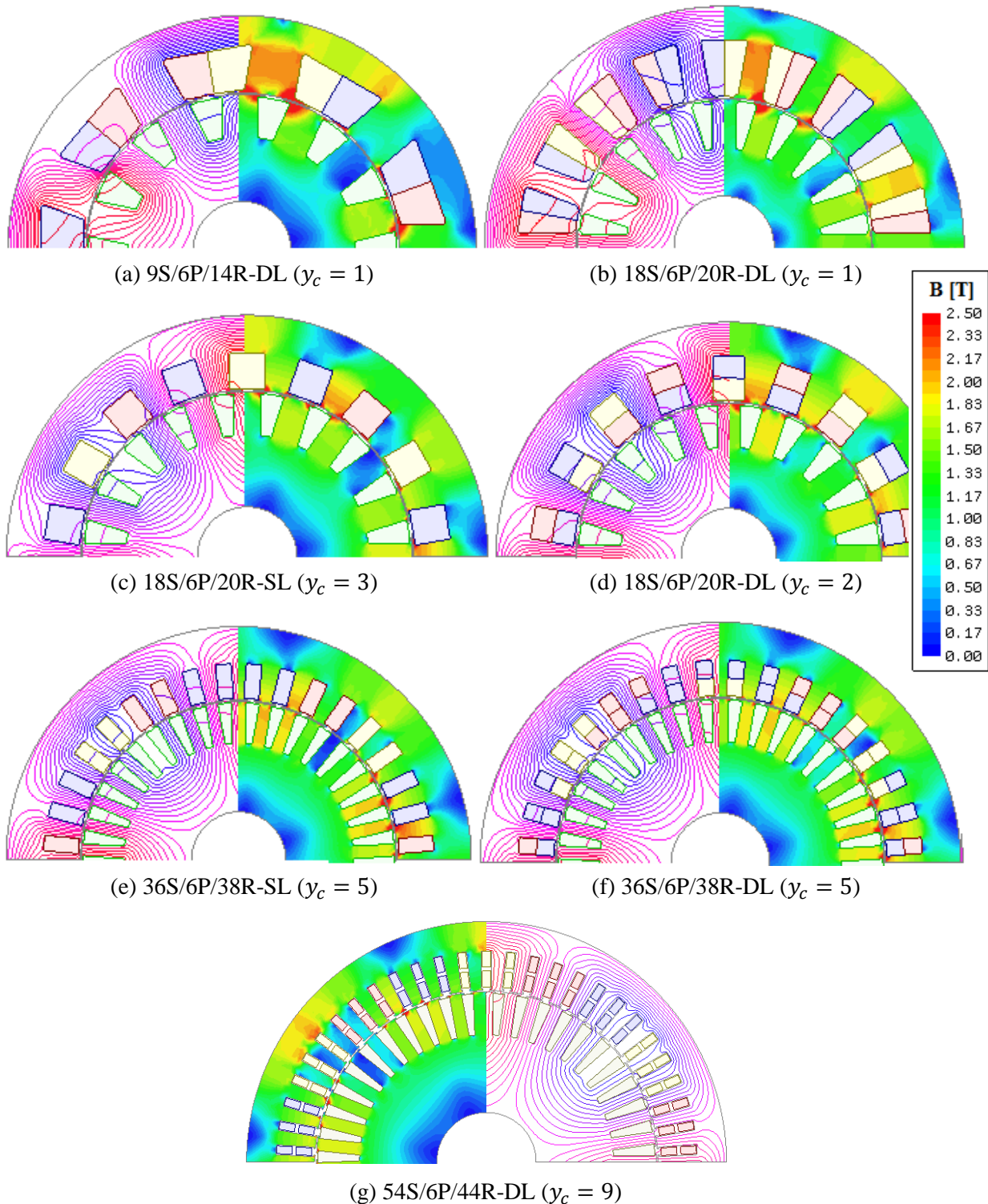


Fig. 2.28 Flux line and flux density distributions.

In other words, even though the same outer diameter, stack length, and operational specifications are adopted for FSCW and ISDW IMs, because of the more slot space requirement of the FSCW IM, the split ratio and consequently average air-gap diameter should be reduced substantially. Therefore, even if the number of turns of FSCW IM is increased, since the average diameter of the air-gap is reduced, torque cannot be increased remarkably. In order to increase the average torque of the FSCW IMs, the excitation current should be increased by keeping the wire diameter constant, i.e. the current density should be increased. That is why the FSCW IMs require more magnetizing current than those of the ISDW IMs. Therefore, the torque capability of ISDW IMs are much more satisfactory compared to the FSCW IMs. From Fig. 2.29, it can be seen that as the stator slot number is increased, the torque ripple rate reduces significantly. In addition, the double-layer configurations ensure the lower torque ripple than those of the single-layer counterparts.

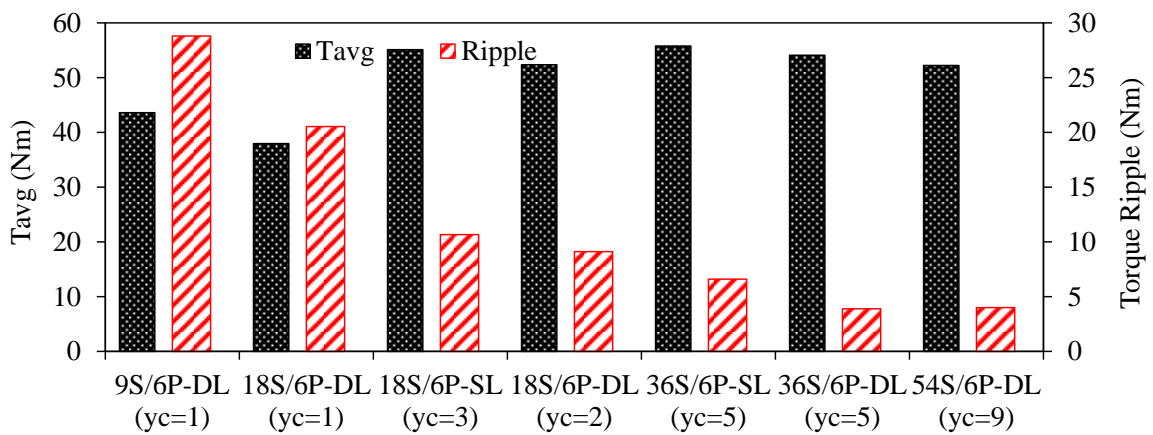


Fig. 2.29 Comparison of average torque and torque ripple percentages.

The comparison of the speed delivering the maximum torque (speed at pull-out torque) and output power is shown in Fig. 2.30. Note that the synchronous speed is 2000rpm and corresponding synchronous frequency is 100Hz. For the same pole number, the lower the stator slot number, the lower the speed and consequently the higher the slip. Therefore, the output powers of the ISDW IMs are considerably higher than those of FSCW IMs. As for the ISDW combinations, it can be concluded that the long-pitch winding combinations have better torque capabilities with lower torque ripple and higher power rates than those of short-pitch winding combinations.

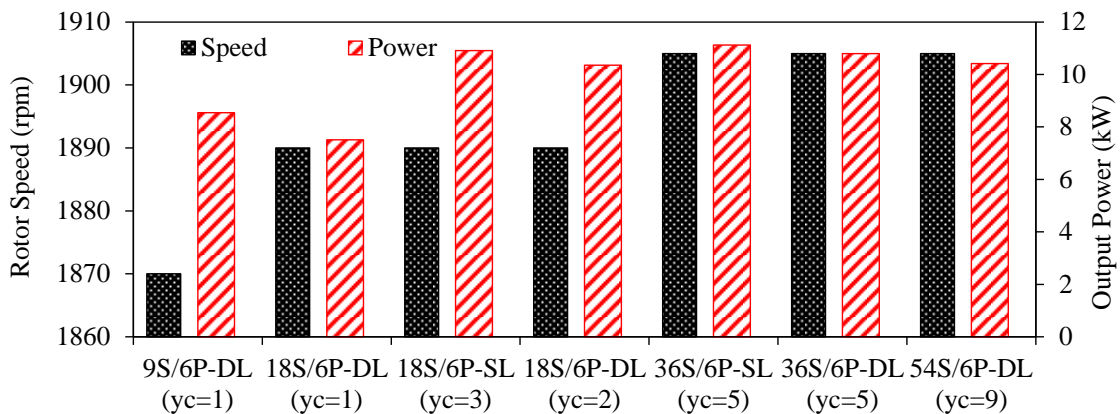


Fig. 2.30 Comparison of rotor speed giving the maximum torque and output power.

2.4.7 Power Losses and Efficiency

The copper and core losses are calculated and then compared in Fig. 2.31. The stator slot copper loss P_{Scu_in} and the end winding copper loss P_{Scu_end} are calculated separately in order to obtain the total stator copper loss P_{Scu} . P_{Rcu} indicates the rotor bar copper loss. It is well-known that the copper losses are the dominant loss components for IMs. As seen in Fig. 2.31, the levels of the total core losses P_c are ignorable.

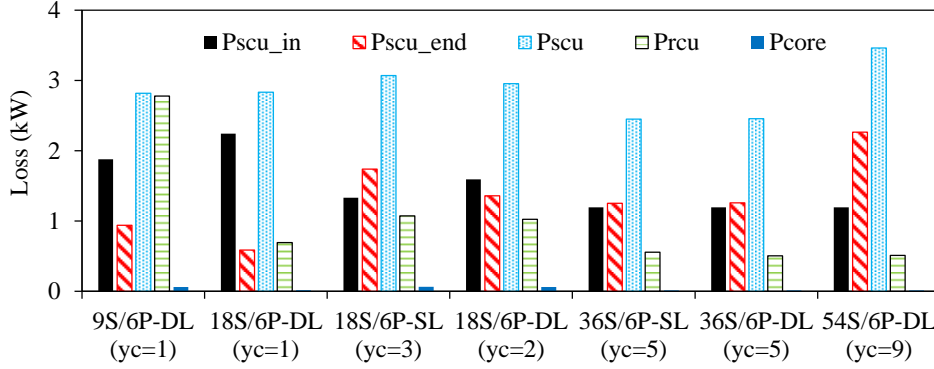


Fig. 2.31 Comparison of machine losses.

As predicted earlier, the bar copper loss P_{rcu} of 9S/6P-DL FSCW IM is significantly large because of the highly distorted MMF. On the other hand, since the fundamental bar current amplitude of the 18S/6P-DL ($y_c = 1$) ISCW IM is lower than those of $y_c = 2$, $y_c = 3$, and $y_c = 9$ counterparts (see Fig. 6.79), its bar copper loss is lower. Note that the rotor bar resistances of all IMs are almost the same. The comparison of total loss and efficiency is shown in Fig. 2.32. As seen in the figure, the higher the stator slot number, the higher the efficiency. As predicted previously, the IMs with long slot-pitch ISDWs have the lowest loss and the highest efficiency thanks to their high quality MMF capability.

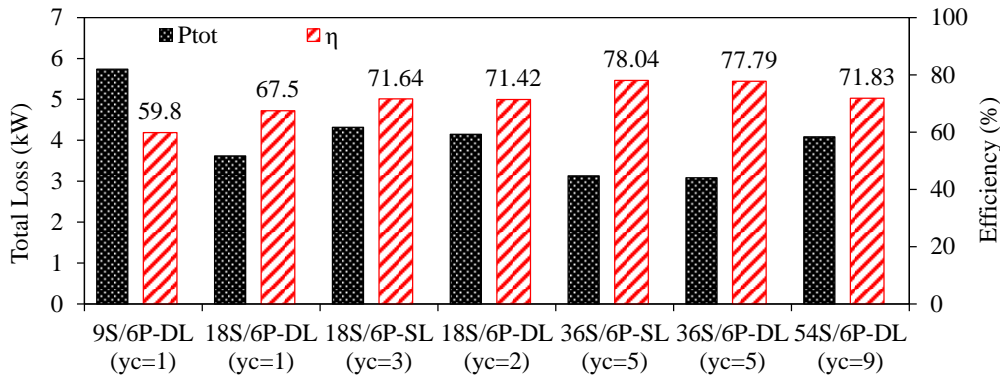
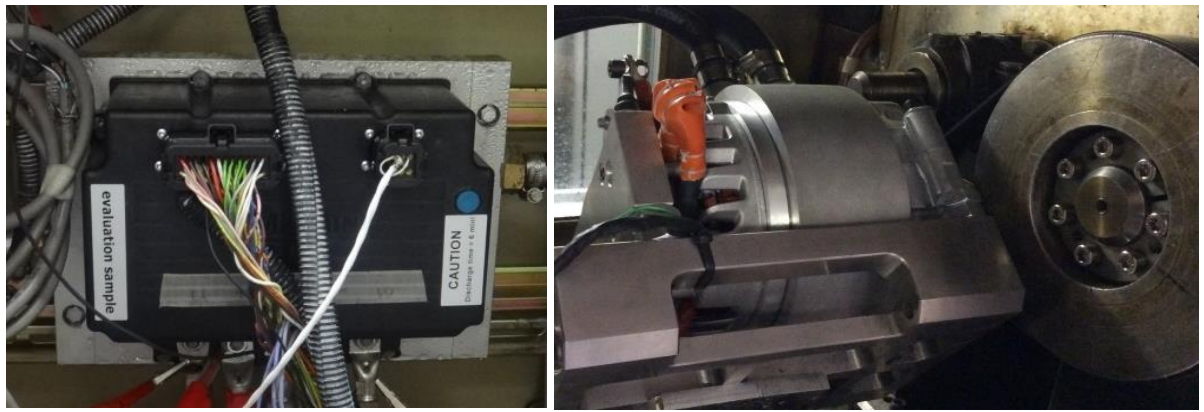


Fig. 2.32 Comparison of total loss and efficiency.

2.5 Experimental Validation

The numerically calculated electric loading and the flux-weakening characteristics of a 12kW conventional ISDW IM with 54S/44R/6P-DL ($y_c = 9$) are validated with measurements. The test results of the built IM is taken from [GUA15b] in order to validate the numerical calculations. The specifications of the tested IM are given in Appendix C.



(a) Inverter

(b) Tested IM and belt transmission



(c) Shaft joint and (d) Torque-speed sensors

(e) Dynamometer



(f) Power analyser

Fig. 2.33 Test rig components.

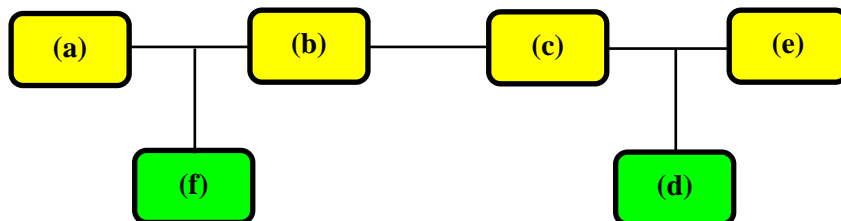


Fig. 2.34 Test rig connection schematic.

The winding temperatures are assigned as 120°C during the calculations and the winding temperatures are not beyond 120°C during the process of testing. Note that the cable resistance between the IM and inverter is measured as 3mΩ per phase which is considerably larger for a short connection

cable. In this section, in order to make an accurate comparison between FEA predicted and measured results, the cable is seen as part of the stator windings. The maximum inverter ratings are 707A phase current and 48V DC link voltage. The rotor speed is fixed at ~ 1 krpm during the electric loading test and its peak value for flux-weakening operating is ~ 6 krpm maximum. During the experiment, these limits have not been exceeded. Different current amplitudes are injected with different current angles which provide the maximum torque for each injected current amplitudes. Under these operating conditions, average torque, output power, power factor, and efficiency characteristics have been numerically calculated by FEA and validated by measurements. The test rig components and test rig connection schematic are shown in Fig. 2.33 and Fig. 2.34, respectively. As seen in the figure, the prototype machine is driven by the inverter and loaded by the dynamometer via belt transmission. The applied voltage and current, input power, power factor, current angle, etc. have been measured by the power analyser. In addition, torque and speed are measured by the torque and speed sensors placed between the belt transmission and dynamometer. The comparison between FEA predicted and measured torque- and power-current characteristics are illustrated in Fig. 2.35. Moreover, the variation of power factor and efficiency with respect to inverter current are illustrated in Fig. 2.36. As seen in the figures, although the power factor does not change considerably, the efficacy changes remarkably due to the increasing stator and rotor copper losses. As clearly seen in the figures, very good agreements between the predicted and measured results have been achieved.

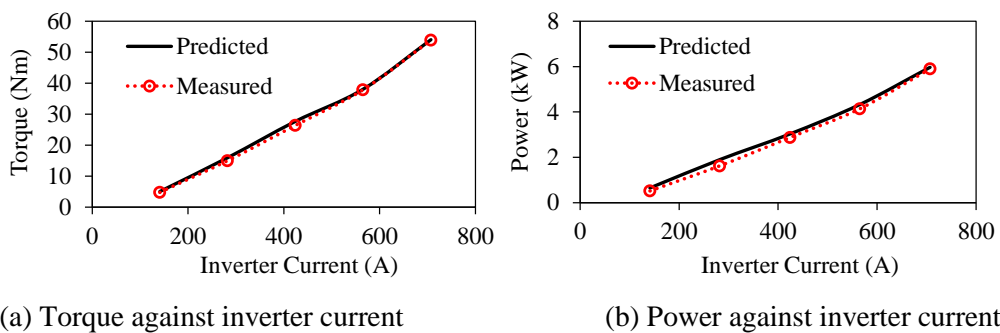


Fig. 2.35 Comparison of FEA predicted and measured (a) torque-current and (b) power-current characteristics for 21V inverter rating at ~ 1 krpm.

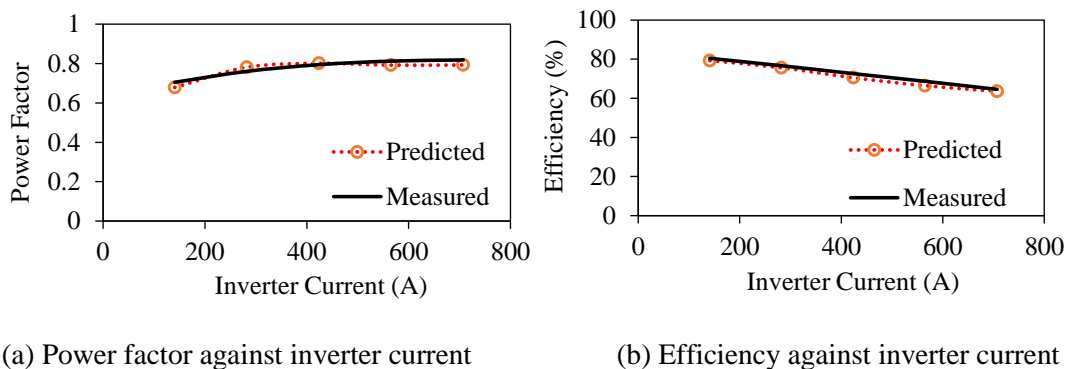


Fig. 2.36 Comparison of FEA predicted and measured (a) power factor and (b) efficiency against current for 21V inverter rating at ~ 1 krpm.

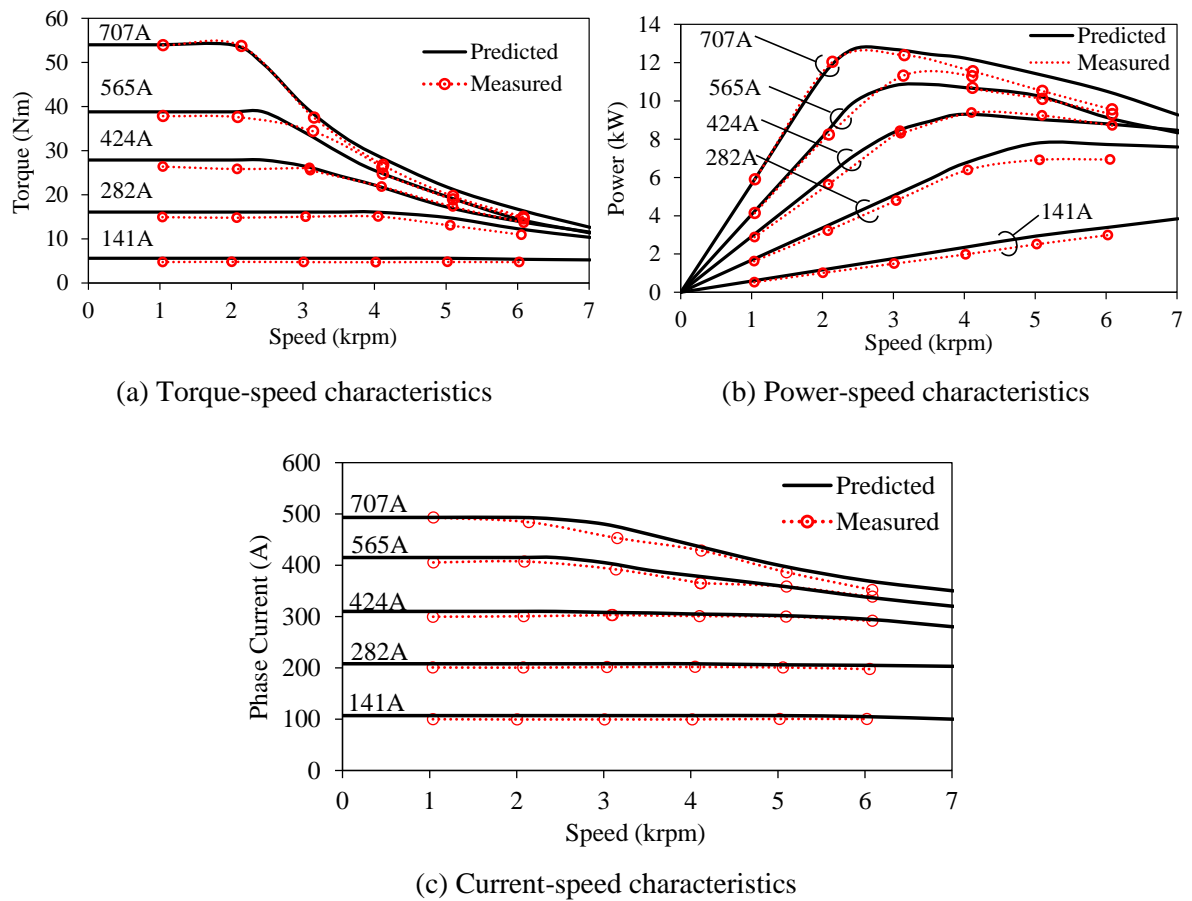
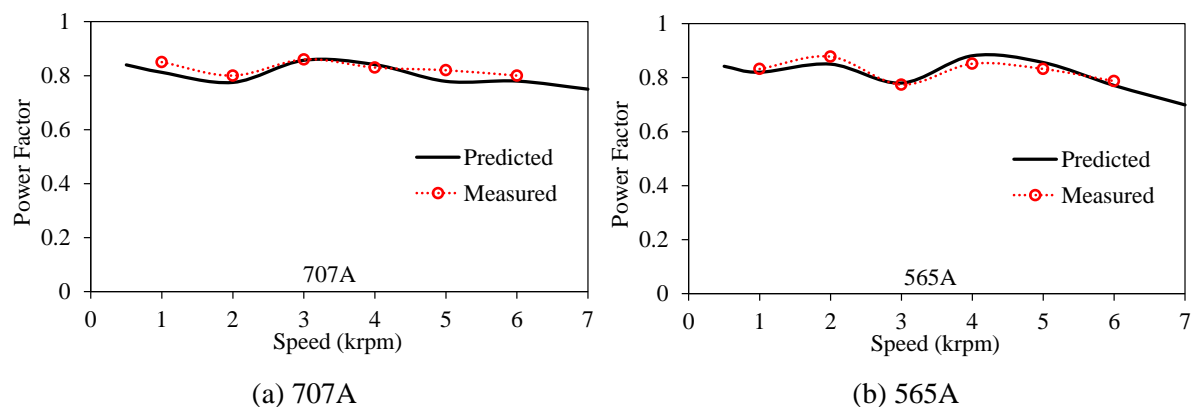
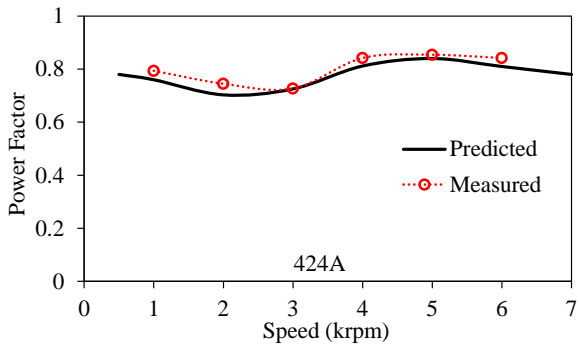


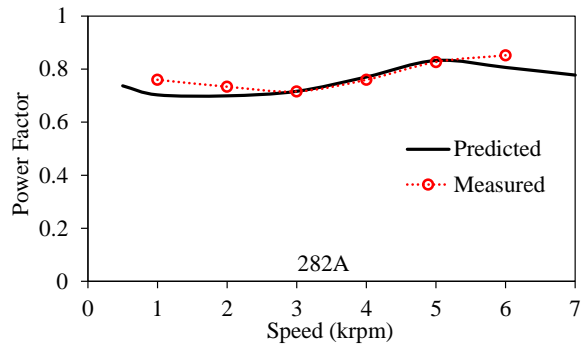
Fig. 2.37 Comparison of FEA predicted and measured flux-weakening characteristics for various phase current operations.

FEA calculated flux-weakening characteristics of the designed ISDW IM with 54S/44R/6P is validated by the measurements through built ISDW IM. The flux-weakening characteristics have been calculated by using a method that combining the calculated flux-linkage and power losses matrices for various I_d and I_q amplitudes by FEA and the current angle and speed loops by MATLAB®. The corresponding calculations are given in Appendix A. Comparison of the FEA predicted and measured torque- and power-speed characteristics for various phase current operations is illustrated in Fig. 2.37. As seen in the figures, good agreements between the FEA predicted and measured results have been achieved.

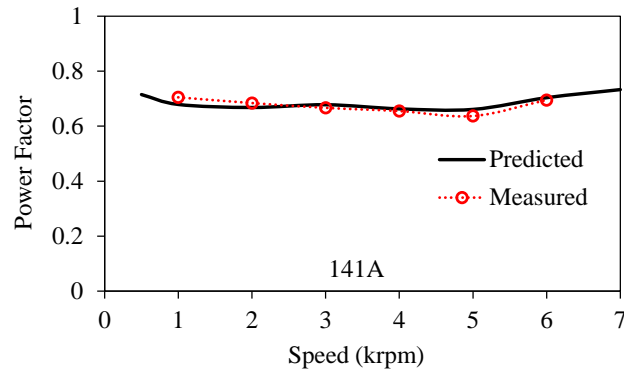




(c) 424A

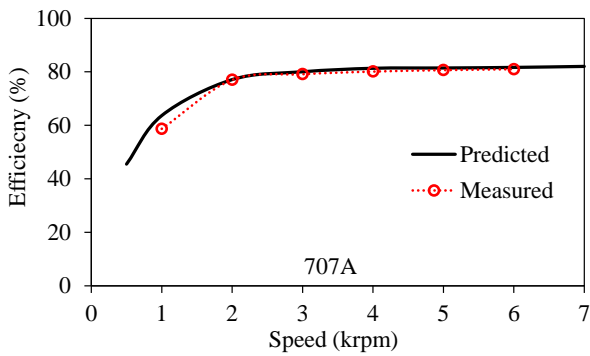


(d) 282A

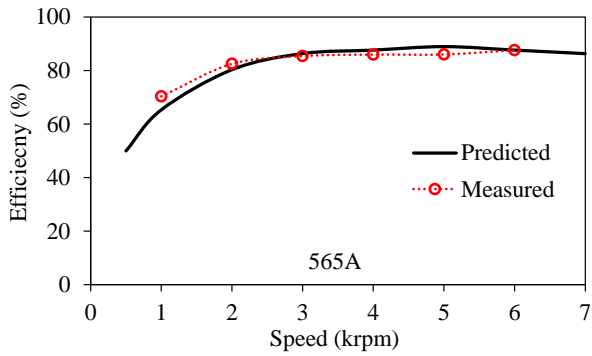


(e) 141A

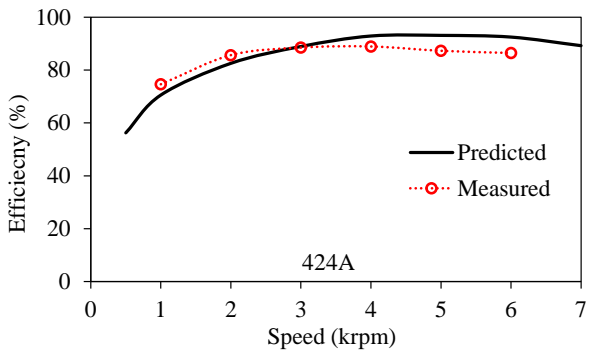
Fig. 2.38 Comparison of FEA predicted and measured power factor-speed characteristics for various phase current operations.



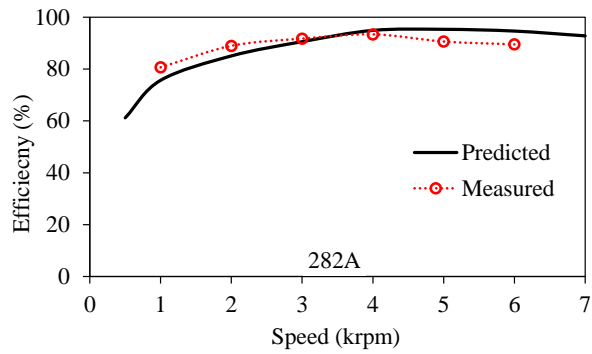
(a) 707A



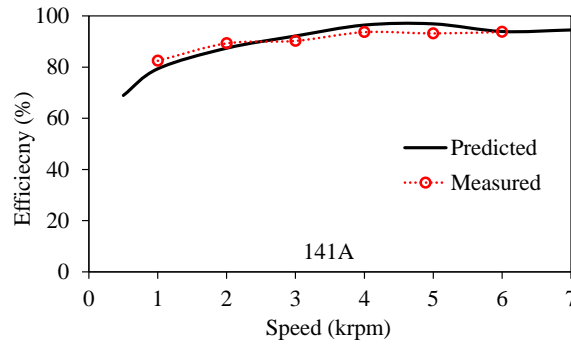
(b) 565A



(c) 424A



(d) 282A



(e) 141A

Fig. 2.39 Comparison of FEA predicted and measured efficiency-speed characteristics for various phase current operations.

Comparison of the FEA predicted and measured power factor and efficiency versus speed characteristics have been shown in Fig. 2.38 and Fig. 2.39, respectively. It is obvious that there is a difference between the previously predicted efficiency and the newly predicted efficiency after the consideration of the cable resistance between the IM and inverter. As seen from Fig. 2.32 and Fig. 2.39(a), because of the large resistance of the cable between the IM and inverter, there is a ~5% reduction in the efficiency at 2krpm operation. It is found that the higher the current level, the relatively higher the efficiency. On the other hand, the higher the current level, the lower the power factor. As seen, the FEA predicted and the measured results are agreed well.

2.6 Conclusion

In this chapter, the influence of stator coil pitch on the electromagnetic performance of squirrel-cage IMs is investigated in depth. The winding configurations, obtained by varying the coil pitch, are mainly divided into three different groups, namely, FSCW, ISCW, and ISDW. In addition, the number of winding layers has also been considered. Note that in order to avoid sub-harmonics, fractional slot distributed winding (FSDW) configurations have not been considered. To be able to reveal the advantages and disadvantages of different winding configurations, the performance of IMs designed with FSCW, ISCW, and ISDW are compared in terms of the serial number of turns per phase N_{st} , working (fundamental) winding factor k_{wp} , winding factor harmonic index h_{shi} , total axial length l_a , bar current harmonic distortion THD_{Ibar} , bar current density J_{bar} , the time average torque at pullout slip T_{avg} , torque ripple percentage ΔT , slip s , output power P_{out} , stator copper loss P_{Scu} , rotor bar copper loss P_{Rcu} , and efficiency η as given in Table 2.4. The low torque ripple, low power losses, high average torque, and high efficiency, which are essential characteristics for EVs, are chosen as comparison criteria. Therefore, since the 36S/6P-DL ($y_c = 5$) IM is the best candidate meeting these criteria, it has been chosen as the base for comparison. Considering the performance parameters given in Table 2.4, it can be concluded that the 9S/6P-DL IM designed with FSCW configuration has the worst performance characteristics among the other IMs. As seen, for the FSCW and ISCW

combinations with $y_c = 1$, even if the number of turns per phase have been increased substantially, their torque amounts could not have been compensated. As known well, the lower working winding factor can be compensated by more number of turns. Correspondingly, more space for stator slots is required. Therefore, because of the more slot space requirement of the concentrated windings, the split ratio and consequently the average air-gap diameter are reduced remarkably. Since there is a direct correlation between the torque and rotor outer diameter (corresponding to air-gap diameter), the more number of turns could not lead an increase in the torque although it causes a considerable decrease in the efficiency. In addition, because of the inadequate fundamental winding factor and significantly high harmonic index of 18S/6P-DL ($y_c = 1$) ISCW IM, the obtained average torque is ~30% lower and the bar copper loss is ~37% higher than that of the 36S/6P-DL ($y_c = 5$) IM. In addition, although the overall performance of the IM with $y_c = 9$ is very similar to that of $y_c = 5$ combinations, since its stator copper loss is much higher than that of the $y_c = 5$ combinations, its efficiency is quite low. As seen in the table, the total axial lengths of the FSCW and ISDW configurations are quite short when compared to other configurations. This is very favourable for the HEV applications since the space left for the electrical machine is quite limited. However, unfortunately they cannot be used in the EV/HEV applications because of their significantly high torque ripple and insufficient output power. In addition, the performance characteristics of the IMs with short slot-pitch ISDWs are not as bad as FSCW and ISCWs, yet not as good as the long-pitch ISDWs. It has also been revealed that the parasitic effects of the double-layer winding configuration are lower than those of the single-layer winding configuration. In conclusion, a new winding topology with short end windings and low MMF harmonics will be developed for the EV/HEV applications in Chapter 3.

Table 2.4 Performance Comparison as Percentage (Base: 36S/6P-DL ($y_c = 5$)).

	9S/6P - DL ($y_c = 1$)	18S/6P - DL ($y_c = 1$)	18S/6P - SL ($y_c = 3$)	18S/6P - DL ($y_c = 2$)	36S/6P - SL ($y_c = 5$)	54S/6P - DL ($y_c = 9$)
N_{st}	+35.72	+47.06	+10.00	+25.00	0	0
k_{wp}	-7.181	-46.409	+7.181	-7.181	+3.537	+2.9
h_{shi}	+89.767	+86.215	+47.667	+9.124	+13.853	-26.11
l_a	-15.297	-25.505	+20.46	+2.92	+6.721	+9.91
THD_{Ibar}	+553.722	+108.88	+114.13	+120.9	+29.125	-6.46
J_{bar}	+99.488	+15.227	+29.575	+24.89	+2.884	-0.878
T_{avg}	-19.39	-29.852	+1.876	-3.28	+3.096	-3.5
ΔT	+640.66	+428.06	+174.41	+134.41	+69.9	+2.9
s	+36.842	+15.79	+15.79	+15.79	0	0
P_{out}	-20.871	-30.404	+1.074	-4.04	+3.096	-3.46
P_{Scu}	+14.762	+15.414	+25.108	+20.345	-0.232	+77.93
P_{Rcu}	+448.5	+36.888	+112.0	+102.547	+9.934	-0.711
η	-22.506	-10.526	-7.002	-7.222	+0.127	-9.34

3 Development of Advanced Induction Machines with Coil Pitch of Two Slot Pitches

This chapter investigates the design and analysis of an advanced squirrel-cage IM with non-overlapping windings. The aim of this study is to develop a new winding and a stator topology for IMs, which lead to a decrease of total axial length without sacrificing the torque, power, and efficiency. In order to reduce the MMF harmonics, the conventional phase shifting method has been utilized for the FSCW IM with 9S/6P. Since the obtained results of the IM with 9S/6P are not satisfactory, auxiliary stator teeth are introduced and phase shifting method is re-employed for 2x9S/6P integer-slot distributed non-overlapping winding with 2 slot-pitch IM. By adopting this method, ~43% of the MMF harmonics have been reduced. As a natural consequence of the auxiliary tooth, the half of the stator teeth are left unfilled. However, in order to improve the electromagnetic performance by reducing the saturation level of the stator yoke parts, these unfilled slots have been filled by core material. The performance characteristics of the improved IM with 18S/6P having adapted non-overlapping windings (ANW) are compared with those of the 9S/6P FSCWIM, and the 18S/6P and 36S/6P ISDW IMs. The key electromagnetic performance characteristics such as induced voltage, air-gap flux density, rotor bar current, flux density distributions, torque, torque ripple, losses, output power, and efficiency, etc. are investigated by 2-D FEA. The results show that according to conventional counterpart of the IM designed with ANW, it is possible to shorten the total axial length by ~25% without sacrificing the torque, output power and efficiency by adopting the proposed ANW configuration.

In this chapter, the influences of some major design parameters, such as stator slot/pole number combinations, rotor slot number, stack length, number of turns, slot geometric parameters, etc., on the electromagnetic and flux-weakening performance characteristics of the advanced non-overlapping winding induction machine (AIM) will also be investigated. It will be shown that the major design parameters, particularly stator slot/pole number combination, stack length, and number of turns have a significant effect on both electromagnetic and flux-weakening performance characteristics.

3.1 Introduction

In conventional electrical machines, the windings are designed to achieve the maximum fundamental winding factor in order to maximize the torque density. However, as verified in Chapter 2, the short-pitch windings suffer from the high contents of MMF harmonics, resulting in high bar copper loss, torque ripple, acoustic noise, and vibration [TOL91a], [TOL91b], [TOL94], [FRE07], [BIA08], [WAN14b]. To be able to reduce the undesirable effects of the MMF harmonics in AC machines, a number of different methods such as multi-layer windings [GER05], [ITO09], [EAS10], [CIS10], [EAS08], [COX11], [RED11], [JEN12], [RED12], [RED14], [ALB12], [ALB13], [CHE14b], [SUN15], [SAK17], stator yoke and/or tooth flux barriers [JAC05], [HEI15], [DAJ12a], [DAJ12b], dual stator constructions or dual-layer windings [JAC04], [EAS08], [EAS10], [COX11], notches in the stator tooth

tips [GUO07], [YUB07], hybrid star-delta connections [MIS14], [LI14], [YON15], [ABD15], flux repeller (conductive solid bar that reduces the leakage flux) in the rotor/stator slot openings [GIE14], different number of turns per coil side [DAJ11a], [DAJ11b], [DAJ12b], [MOR14], [DAJ14], and the recently investigated 2 slot-pitch fractional winding topologies [DAJ13a], [WAN14a], [WAN14b], [WAN14c], [WAN14d] have been developed. In addition, the influence of slot number and pole number combination and winding configuration on the MMF quality of PM brushless motors has been investigated [ISH06], [WAN06].

In Chapter 2, it has been demonstrated that by using multi-layer windings, torque ripple and bar copper losses can be suppressed by sacrificing the average torque slightly. In addition, it is shown that the multi-layer windings cause a reduction in the amplitude of the MMF sub-harmonics whilst they have no influence on the super-harmonics [ALB12]. In addition, the same phenomenon has been verified by using flux barriers and different number of turns per coil sides [DAJ11a], [DAJ12a]. It is shown that only the sub-harmonics could have been suppressed by flux barriers and different number of turns per coil sides. In order to suppress some sub-harmonics induced in the rotor EMF, rotor tooth notches that leads to reduce the harmonic content of the air-gap flux density have been used in the tooth tips [GUO07], [YUB07]. However, the obtained results from these studies are not very satisfactory. Hybrid Wye-Delta phase connection technique has also been investigated as another alternative method to reduce some MMF harmonics by introducing three extra phases. By employing this technique, it is possible to reduce only some low-order harmonics [ABD15]. Nevertheless, the obtained results from the IM having 6-phase Wye-Delta connection are not satisfactory when compared to the results obtained from the conventional 3-phase counterpart with Wye connection.

In order to mitigate or cancel some MMF harmonics in the rotor, a double-fed IM with FSCWs is introduced [ALB09b], [ALB12]. In order to overcome the limited performance of squirrel-cage IM with FSCWs, the rotor is equipped with FSCW configuration and supplied by a converter. In order to further mitigate the MMF harmonics and increase the performance of the FSCW IM with wound-rotor, multi-layer windings have been introduced [ALB13]. In order to improve the performance of the FSCW IMs, some other different methods, such as single and multi-phase winding FSCWs [JUN07], [KHA12], [KHA15a], outer-rotor topology with modular stator windings [VIR12] and outer rotor IM with multi-layer FSCW wound around two and three layers of stator slots [SUN15], multi-layer toroidal windings [JEN12], [SAK17], stator cage windings [DAJ13], [DAJ14], combination of different number of turns per one coil side and combined star-delta connection [MOR14], and two sets of FSCWs with a dual slot-layer stator structure [DAJ16] have been used in the last decade. However, although the MMF harmonics are relatively mitigated by using various methods explained above, the obtained results are not satisfactory because of the newly arisen drawbacks, such as low torque per flux due to the relatively low winding factor and an increase in the total axial length and consequently in the copper loss due to the requirement of the extra number of turns. In addition, in order to increase the performance characteristics, such as slot fill factor, fault tolerant, simplicity, etc., FSCWs have been utilized for

linear IMs, and some feasible MMF reduction methods such as multi-layer modular/planar windings, dual stator structure, etc. have been investigated in [COX08], [EAS08], [EAS10], [COX11], [KHA15b].

A new winding technique, called stator cage winding, has been introduced in [DAJ14]. Instead of the conventional stranded windings, a solid cage winding, whose one-end side has been short-circuited and the other end-side is directly connected to a multi-phase inverter, has been utilized. The winding structure is characterized with high quality MMF distribution and very short end-winding length. It has been also shown that in order to reduce the MMF sub- and super-harmonics simultaneously, the number of stator slots is doubled but the number of poles is maintained the same in the PM motor with FSCWs [DAJ13a], [DAJ13b]. However, the fundamental harmonic winding factor and consequently the torque density are reduced when compared to PM motor with ISDWs. Therefore, the methods of harmonic cancellation in PM machines with FSCWs are further investigated by modifying the coil pitch of two, three, or four slot pitches which might reduce the sub- and super-harmonics simultaneously [KOM00], [DOR11], [ZHE11], [DAJ11b], [RED11], [DOG11], [WAN13], [CHE13].

In the previous chapter, it has been revealed that, the higher the slot pitch, the higher the winding factor, and the lower the MMF harmonics. Therefore, for the IMs with $q \geq 1$ combinations are advantageous in terms of lower torque ripple, copper loss, and consequently higher efficiency. It should be noted that increasing the coil pitch number will cause an increase in the length of end-windings, the total axial length and consequently the stator copper loss. As it is known, the space left for an electrical machine in the traction system of an EV/HEV is very limited. Therefore, compactness is a very important issue in the design of electrical machines for EV/HEV applications. Consequently, a new methodology needs to be developed in order to increase the slot-pitch number without increasing the end-winding length of the stator windings.

In this chapter, a new winding and stator topology for more compact IMs is introduced. In order to reduce the MMF harmonics, causing significantly high rotor bar copper loss and torque ripple, combination of the phase shifted multi-layer winding method and auxiliary stator tooth method have been developed. Moreover, in order to further improve the performance characteristics of the IMs by reducing the saturation and leakage flux amplitudes, the stator slots have been re-shaped by utilizing the unfilled slots. The steps of the performance improvement process have been explained in detail and the obtained performance characteristics have been compared with those of the IMs designed with FSCWs and ISDWs with short- and long-pitch windings. Moreover, the influence of some major design parameters on the flux-weakening and performance characteristics of the AIM have been investigated in detail.

3.2 MMF Harmonic Cancellation

In Chapter 2, some useful MMF cancellation or reduction methods implemented only in the IMs have been described. On the other hand, a large number of MMF cancellation or reduction methods

implemented in AC machines including PM machines and IMs have been reviewed in this chapter. In this section, an adapted MMF cancellation method comprising of the combination of the conventional phase shifting and auxiliary stator tooth methods will be introduced.

3.2.1 Conventional Phase Shifting Method

As validated in the previous chapter, the FSCWs are characterized by a high MMF harmonic content due to the unity slot pitch number and fractional number of slot per pole per phase q . As explained previously, in order to reduce these MMF harmonic contents, multi-layer winding method has been used extensively. In order to reveal the influence of the multi-layer windings on the performance characteristics, previously designed 9S/6P-DL (1sp) FSCW IM will be studied in this section. The winding layout of the studied combination and shifting method is illustrated in Fig. 3.1. Note that, the figure shows the initial case in which the shift angle is zero.

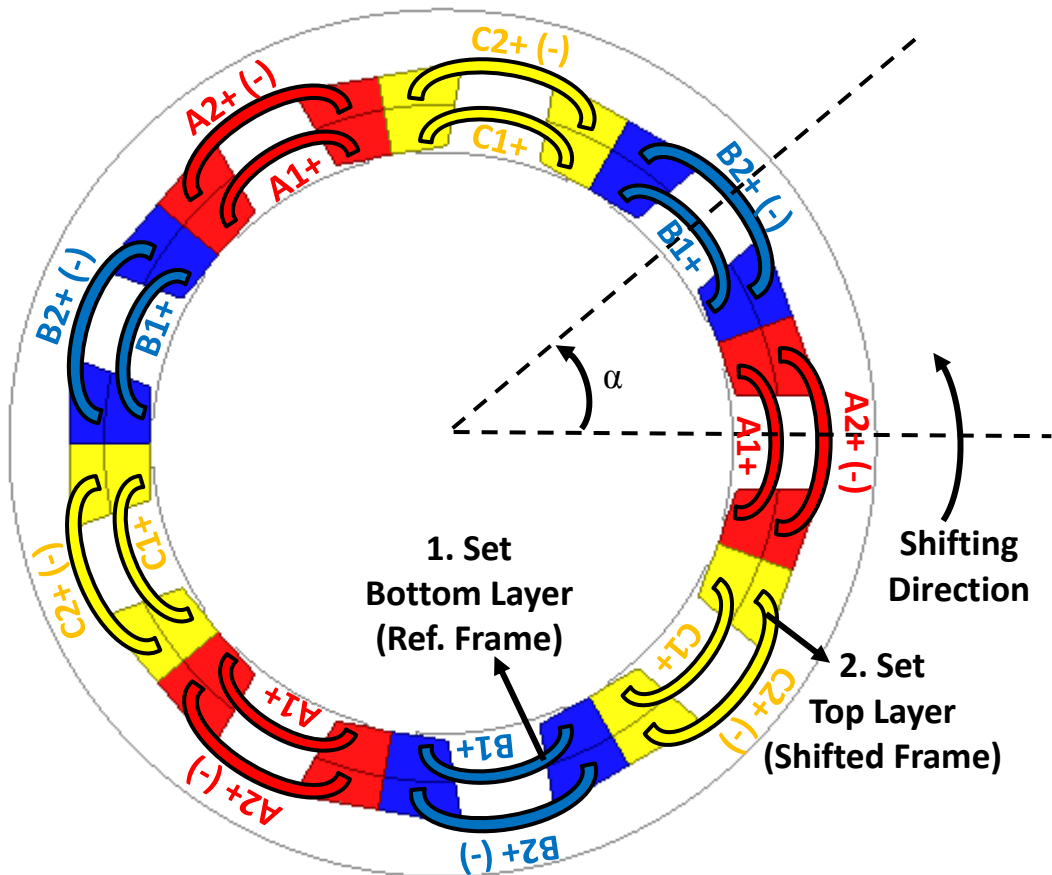
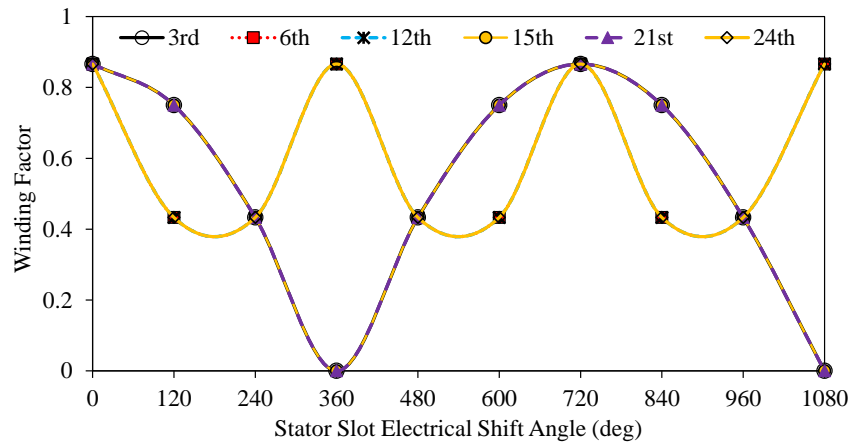


Fig. 3.1 Winding layout of the 9S/6P-4L combination: (+) is the base polarity and (-) is the opposite polarity.

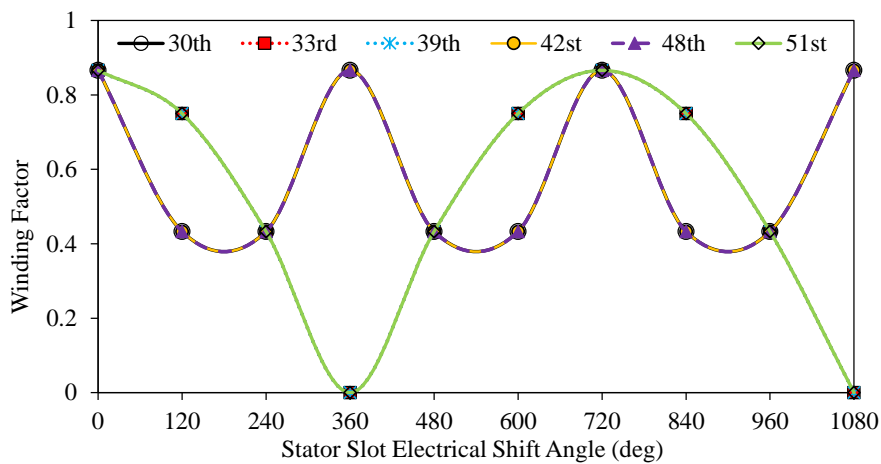
$$k_{wh_final} = k_{wh_initial} \cdot \left| \cos \left(h \frac{\alpha}{2 \cdot p} \right) \right| \quad (3.1)$$

As seen in the figure, each slot has 4-layer winding with the same 2 winding sets. The 1st set (bottom layer) has been chosen as reference (fixed) frame whilst the 2nd set of winding has been chosen as shifted frame. Since there are 9 slots in the stator the shifting angle α is $\frac{360}{s} \frac{p}{2} =$

120°e per slot. Initially, the polarity of all windings are positive (+), which is anticlockwise, and they are not changed during the shifting progress. After 1080°e of shift angle is completed, the polarity of the 2nd set of winding has been changed from positive (+) to negative (-), which is clockwise, and variations of torque, torque ripple and rotor bar current density characteristics are observed. The new winding factor k_{wh_final} depending on the initial winding factor $k_{wh_initial}$, the harmonic order h , the shift angle α in electrical degree, and the pole number P can be calculated by (3.1). The variation in the low- and high-order winding factor harmonics with respect to α is illustrated in Fig. 3.2. Since the winding factor harmonics of the 9S/6P combination have only sequential harmonics, whose amplitudes are 0.866 (see Fig. 3.8(a)), many of the harmonics vary with the same pattern, i.e. the first group 3rd, 15th, 21st and the second group 6th, 12nd, and 24th harmonics have exactly the same pattern. The same circumstance is valid for the higher-order harmonics. On the other hand, even if the 2nd winding set becomes (-), exactly the same waveform shown in Fig. 3.2 is obtained because of the symmetry of the winding configuration.

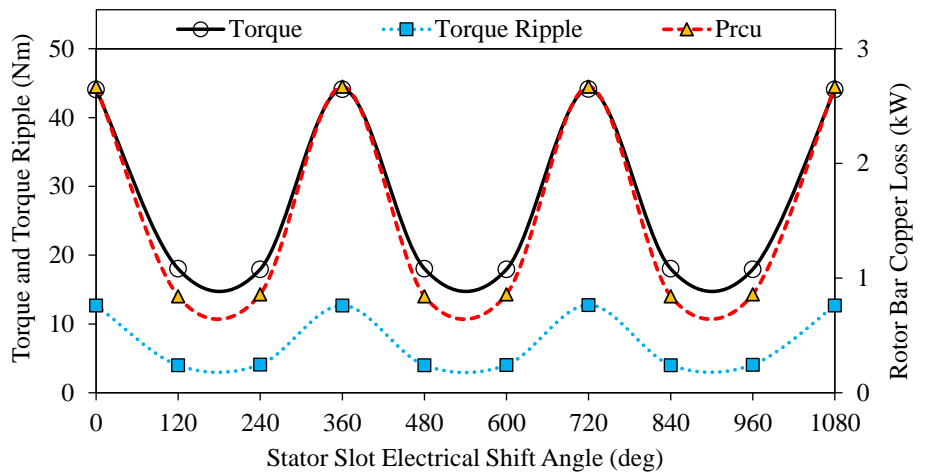


(a) Low-order harmonics

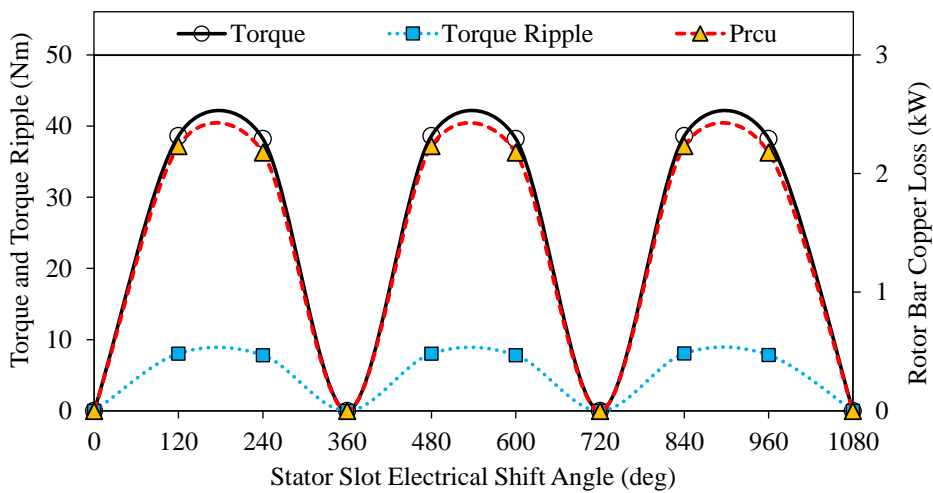


(b) High-order harmonics

Fig. 3.2 Variation of harmonics with respect to shift angle α : (a) low-order and (b) high-order.



(a) Positive polarization (+, +)



(b) Negative polarization (+, -)

Fig. 3.3 Variation of torque, torque ripple and rotor bar copper loss with respect to shift angle: (a) whilst the both of the winding sets are in (+) polarization and (b) while the 1.set is in (+) and 2.set is in (-) polarization.

The obtained results for both of the cases (+, + and +, -), are shown in Fig. 3.3. As seen in Fig. 3.3(a), the rotor bar copper loss, torque, and torque ripple have the similar waveform. Considering Fig. 3.2, it can be concluded that the working fundamental winding harmonic has been shifted from the 3rd to the 6th harmonic order. This is because the torque is maximised at 360°e of the shift angle. Once the polarity of the 2nd set of winding is changed from (+) to (-), the obtained performance characteristics are shown in Fig. 3.3(b). Since, to change the winding polarization results with the existing dead-slots, the zero-torque has been achieved at 0°e, 360°e, 720°e, and 1080°e of the shift angle. As in the previous case, the obtained curves have the similar trajectory. In addition, changing the polarizations causes a slight reduction in the average torque, torque ripple, and rotor bar copper loss as seen in Fig. 3.3. As clearly seen in the figures, torque ripple and the bar copper loss vary with the torque. This is a clear indicator that the winding factor harmonics cannot be cancelled or mitigated sufficiently. Therefore, it can be concluded that it is not possible to reduce the MMF harmonic contents by shifting the phases by 120°e for the 9S/6P combination.

3.2.2 Phase Shifting with Auxiliary Tooth Method

An innovative method for reducing the MMF harmonic content is presented in this section. The 9S/6P-4L combination, presented in the previous section, has been utilized here by forming auxiliary identical teeth. Therefore, the stator slot number has become 2x9S. Thus, an extra shifting angle has been provided that may cause reducing the winding harmonic content.

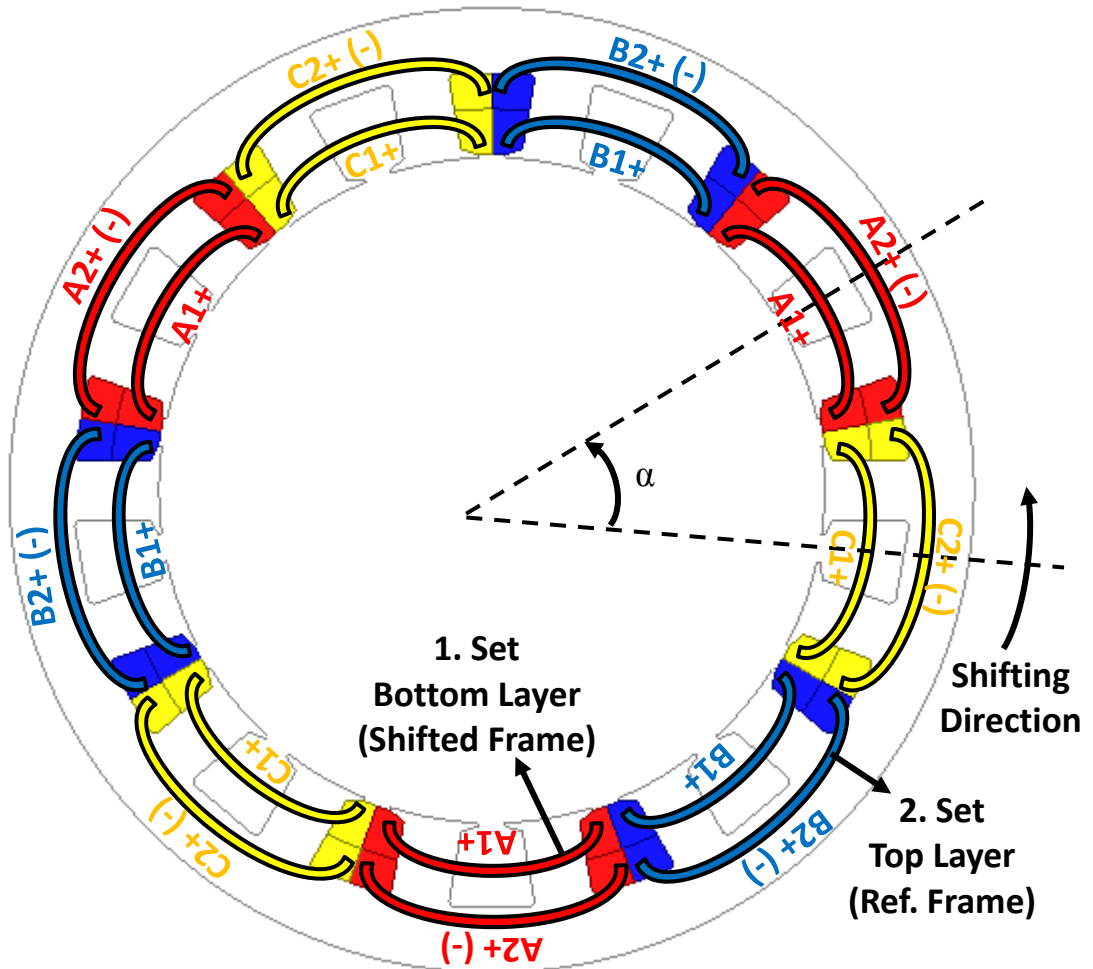


Fig. 3.4 Winding layout of the 2x9S/6P-4L combination.

As a consequence of doubling the slot number of the stator, the shifting angle α became $\frac{360}{S} \frac{P}{2} = 60^\circ$ electrical per slot. The winding layout and shifting scheme are illustrated in Fig. 3.4. Since the coils are not physically overlap each other, even if the slot pitch is two, each coil can be imagined as a single lap-coil as being in the FSCW topology. Therefore, by using this idea it is possible to design lap-coil windings with any slot pitch number without reducing the fundamental winding factor. However, this method cannot be used for each S/P combinations.

There are some specific rules for suitable combinations as expressed in (3.2) and (3.3). In order to utilize the lap-coils with multiple overlays, two-layer per slot windings, (3.3) should be satisfied. In (3.3), k is an integer and k_{wp} indicates the fundamental winding factor of any combination with p pole-pair number. For this kind of windings, the number of overlays n_t is consistently equal to number of slot-pitches y_c and the fundamental harmonic of the winding factor needs to be different from unity. On

the other hand, (3.4) is valid for the combinations whose fundamental winding factor equals to unity. The same shifting method, as explained in the previous section, has been utilized for 2x9S/6P combination with the halved shift angle.

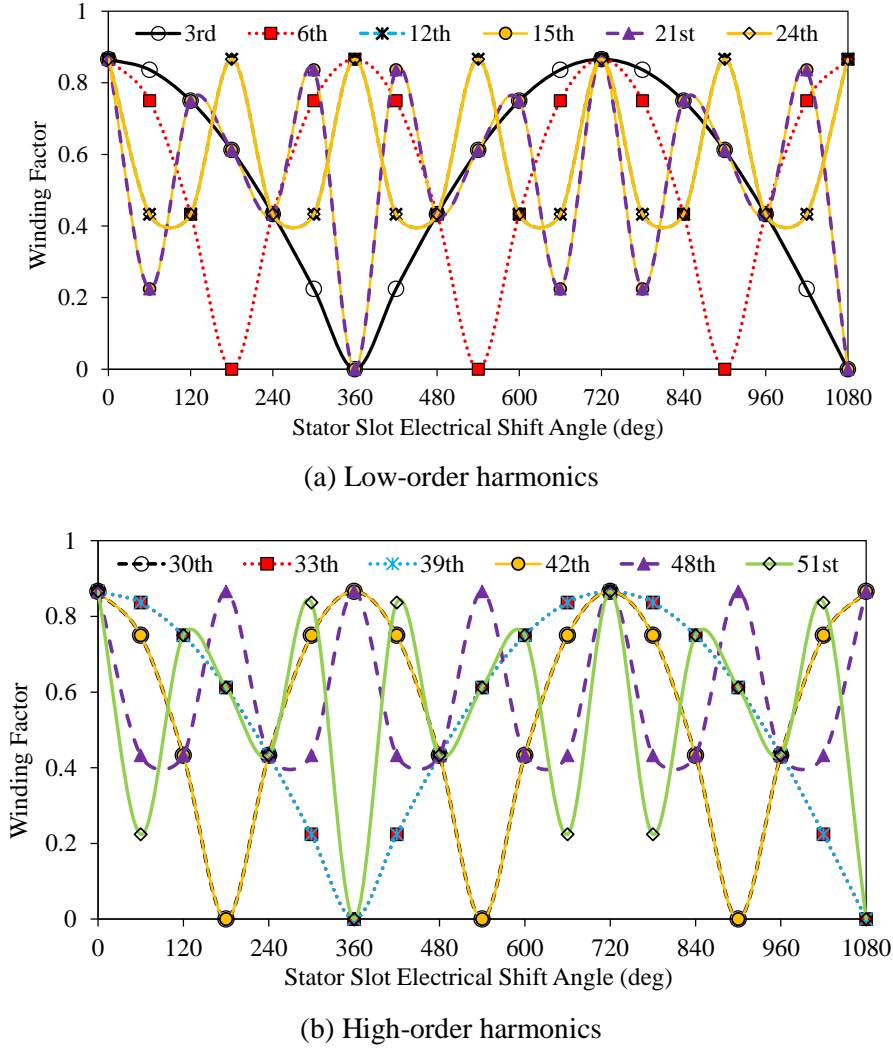


Fig. 3.5 Variation of harmonics with respect to shift angle α whilst the winding set polarizations are (+, +): (a) low-order and (b) high-order.

$$n_t = y \quad (k_{wp} \neq 1) \quad (3.2)$$

$$\frac{S}{\gcd\{S, P\}} = 3k \quad \text{and} \quad k_{wp} \neq 1 \quad (3.3)$$

$$n_t = y - 1 \quad \text{if} \quad k_{wp} = 1 \quad (3.4)$$

When the winding set polarizations are (+, +), variation of the winding factor harmonics with respect to shift angle is shown in Fig. 3.5. As clearly seen in the figure, introducing auxiliary identical teeth causes further reduction in the winding factor harmonics when compared to 9S/6P combination. Depending on the shifting angle some of the low- and high-order harmonics have been reduced and some of them have been completely cancelled, i.e. 6th, 30th, 42nd, 63rd, and so on harmonics are cancelled

at the 180° e (see Fig. 3.8(b)). However, the fundamental winding factor has been reduced at this shift angle. When the winding set polarizations are (+, -), the variation of the winding factor harmonics with respect to shift angle is illustrated in Fig. 3.6. As seen in the figure, by adopting negative polarity of the 2nd set of winding, 6th and all the multiply of 6th harmonics are completely cancelled at 180° e (see Fig. 3.8(b)). It can also be seen that the fundamental winding factor has been maximized at 180° e.

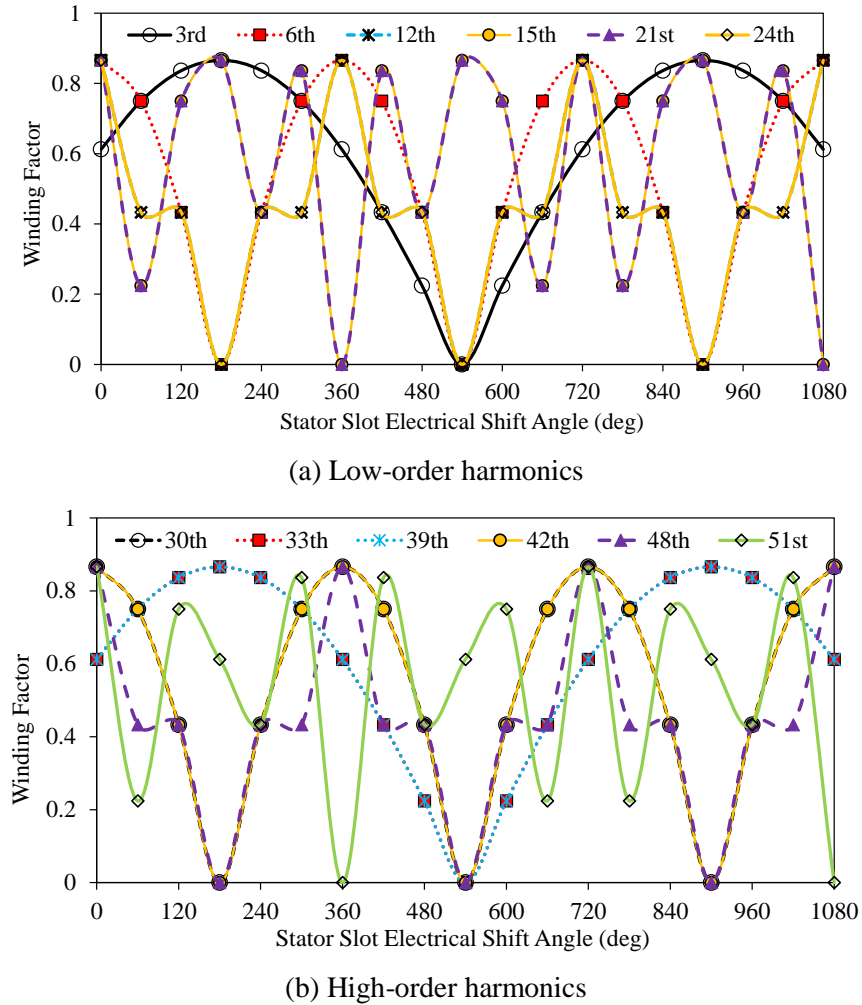


Fig. 3.6 Variation of harmonics with respect to shift angle α whilst the winding set polarizations are (+, -): (a) low-order and (b) high-order.

Therefore, the optimum shifting angle is 180° e for 2x9S/6P combination. After shifting 180° e (3 slot pitches) of the 2nd winding set and having the correct assignation of the winding polarizations, the final winding layout of the 2x9S/6P combination is shown in Fig. 3.7. As seen in the figure, half of each slot is empty. However, in order to improve the performance of the advanced IM, these empty slots will be utilized in the next section and the influence of using the slots will also be explained. On the other hand, the case that the full slot is utilized but the end winding overlapped will also be investigated in Section 3.6. Initial and final winding factor harmonics and the calculated harmonic interaction indexes are illustrated in Fig. 3.8. It is clearly seen that the winding harmonics are significantly reduced especially in case of 180° e shifting while the winding sets are polarized as (+, -). Therefore, it can be predicted that the rotor bar copper loss will be considerably low when compared to that of the 9S/6P combination.

In addition, since the magnitude of the fundamental winding factor has not changed, there will be no reduction in the average torque.

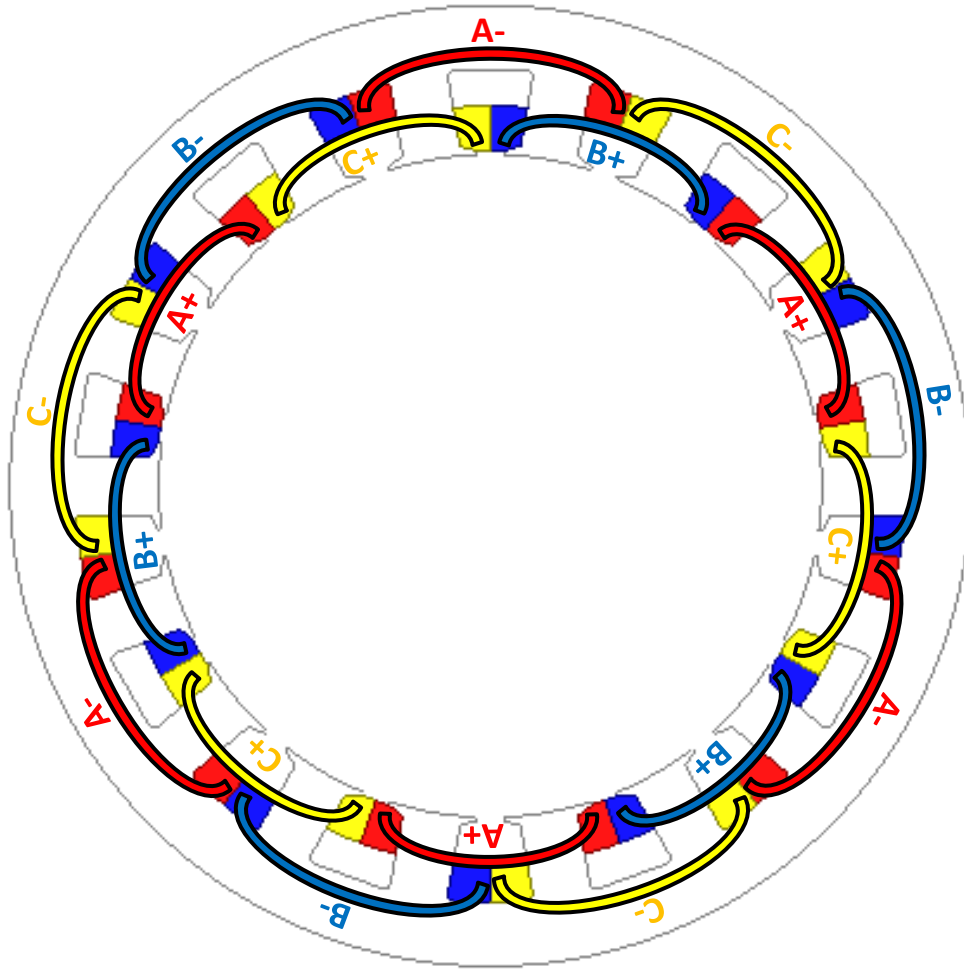
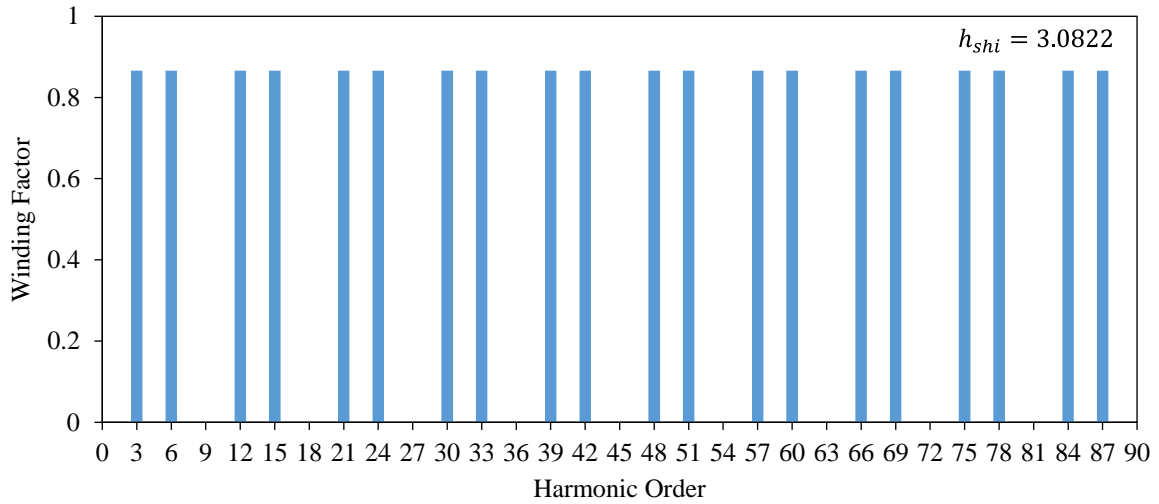


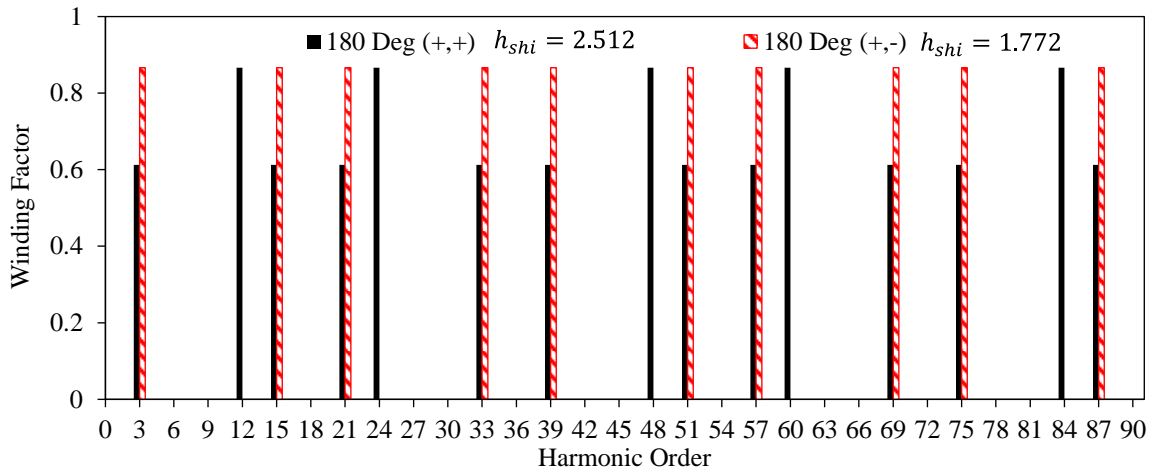
Fig. 3.7 Final winding layout of the 2x9S/6P combination.

The influence of the phase shifting in case of 2x9S/6P combination on the torque, torque ripple, and rotor bar copper loss are illustrated in Fig. 3.9 for both winding set polarizations. In the case of (+, +) polarization, although some of the winding harmonics are cancelled, the reduction of the rotor bar copper loss is not satisfactory as seen in Fig. 3.9(a). However, the rotor bar copper loss of the 2x9S/6P combination is substantially lower than that of the 9S/6P combination. It is obvious that almost more than half of the rotor bar copper loss have been cancelled by employing the proposed method (see Fig. 3.3(a) and Fig. 3.9(a)). On the other hand, if the polarization of the 2nd set of winding is reversed as (+, -), the reduction in the amount of rotor bar copper loss is significant as seen in Fig. 3.9(b). Once the shifting angle is 180°e, 540°e, or 900°e, the minimum rotor bar copper loss and torque ripple percentage, and the maximum average torque have been achieved. Therefore, it has confirmed that considering the winding set polarizations is of great importance. It is possible to predict the increase in the amount of rotor bar copper loss by observing the winding factor harmonics. Considering the 9S/6P-4L, 2x9S/6P-2L (+, +), and 2x9S/6P-2L (+, -), the dominant harmonics causing an increase in the bar copper loss are revealed as listed in Table 3.1. The findings in the table is obtained from the shifting angles delivering the maximum torque. In Table 3.1, the normalized values according to 9S/6P-4L configuration have

been given. It is obvious that if the 6th or/and 12th harmonics are cancelled, the reduction in the amount of bar copper loss is significant. It has been revealed that the 6th and 12th harmonics (as in 2x9S/6P (+, -)) are the dominant harmonics producing rotor bar copper loss. If the 6th harmonic is cancelled, the rotor bar copper loss decreases by ~ 2.5 times, and if the 6th and 12th harmonics are cancelled together, the rotor bar copper loss decreases ~6 times.



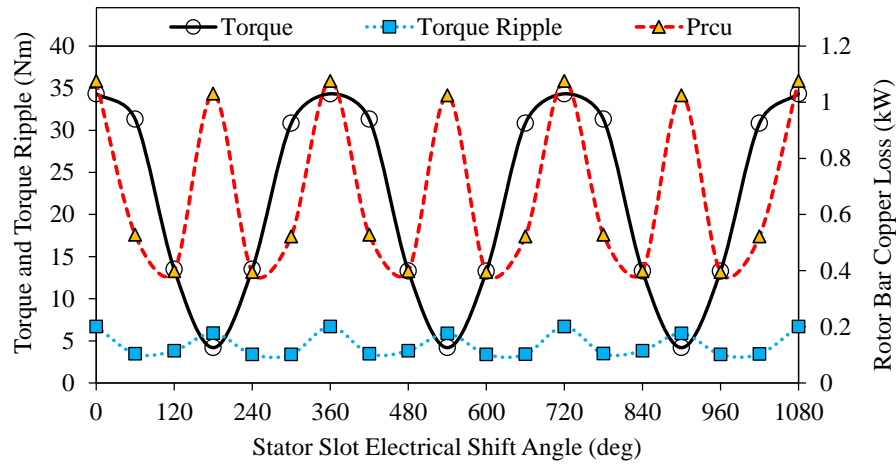
(a) Initial (original) winding factor



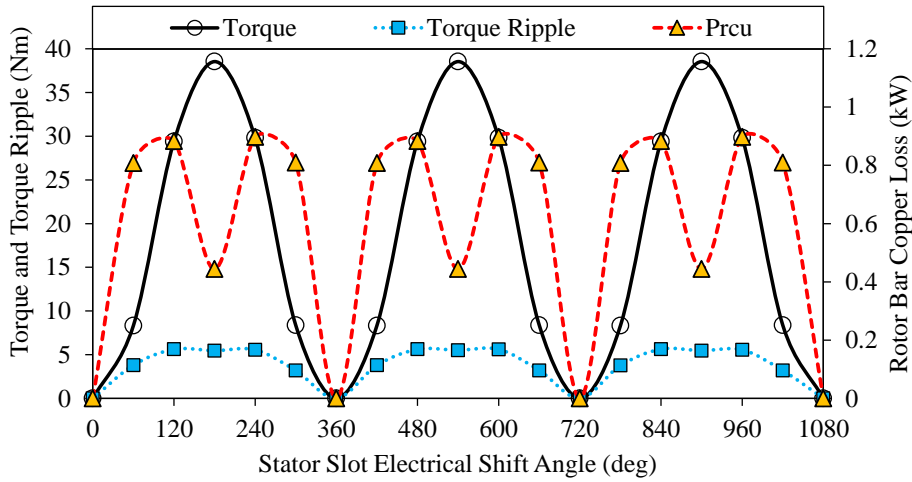
(b) Final winding factor

Fig. 3.8 Comparison of winding factors after phase shifting operation: (a) initial and (b) final.

Therefore, it can be predicted that the reduction or cancellation of low order harmonics has a significant impact on the rotor bar copper loss. In addition, as clearly seen in the table, the reduction of these harmonics also causes a reduction in the torque ripple. On the other hand, the average torque level decreases when the slot number is doubled. The reason behind this phenomenon can be explained for 2x9S/6P (+, +) and 2x9S/6P (+, -), separately. For the 2x9S/6P (+, -), since only half of the slots are filled, the saturation level causing a decrease in the average torque has increased. On the other hand, for the 2x9S/6P (+, +), in addition to the increase in the saturation level, the fundamental winding factor decreases due to the phase shifting. Therefore, average torque reduction rate of 2x9S/6P (+, +) configuration is 12.34% higher than that of the 2x9S/6P (+, -) configuration.



(a) Polarization of winding sets: (+, +)



(b) Polarization of winding sets: (+, -)

Fig. 3.9 Variation of torque, torque ripple and rotor bar copper loss with respect to shift angle: (a) both of the winding sets are in (+) polarization and (b) 1.set is in (+) and 2.set is in (-) polarization.

Table 3.1 Comparison of performance characteristics

Configuration	Winding Harmonic reduction/cancellation	Average torque	Torque Ripple	Bar Copper Loss
9S/6P	baseline	1	1	1
2x9S/6P (+, +)	3 rd – reduced	0.778	0.68	0.403
	6 th – cancelled			
	15 th – reduced			
2x9S/6P (+, -)	6 th – cancelled 12 th – cancelled	0.874	0.493	0.166

3.2.3 Stator Slot Utilization

After the phase shifting process, half of each stator slot has been left unfilled in order to not to overlap the phase windings as seen in Fig. 3.10. These unnecessary slot gaps cause an increase in the saturation level of the iron cores (see Fig. 3.11). By utilizing these gaps with core material, the performance of the IM can be improved. The improvement steps are illustrated in Fig. 3.10.

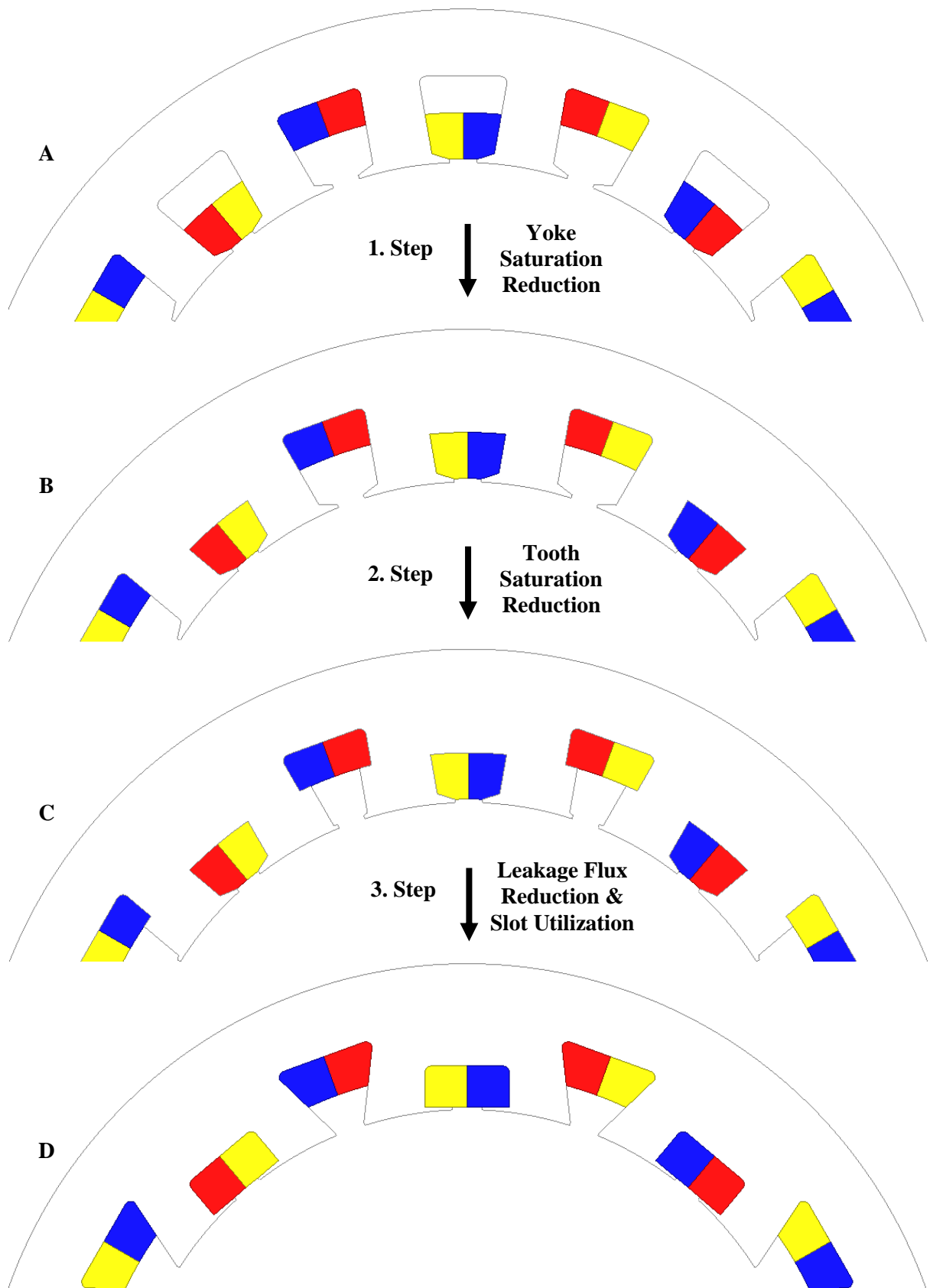


Fig. 3.10 Utilization progress of stator slots of the AIM.

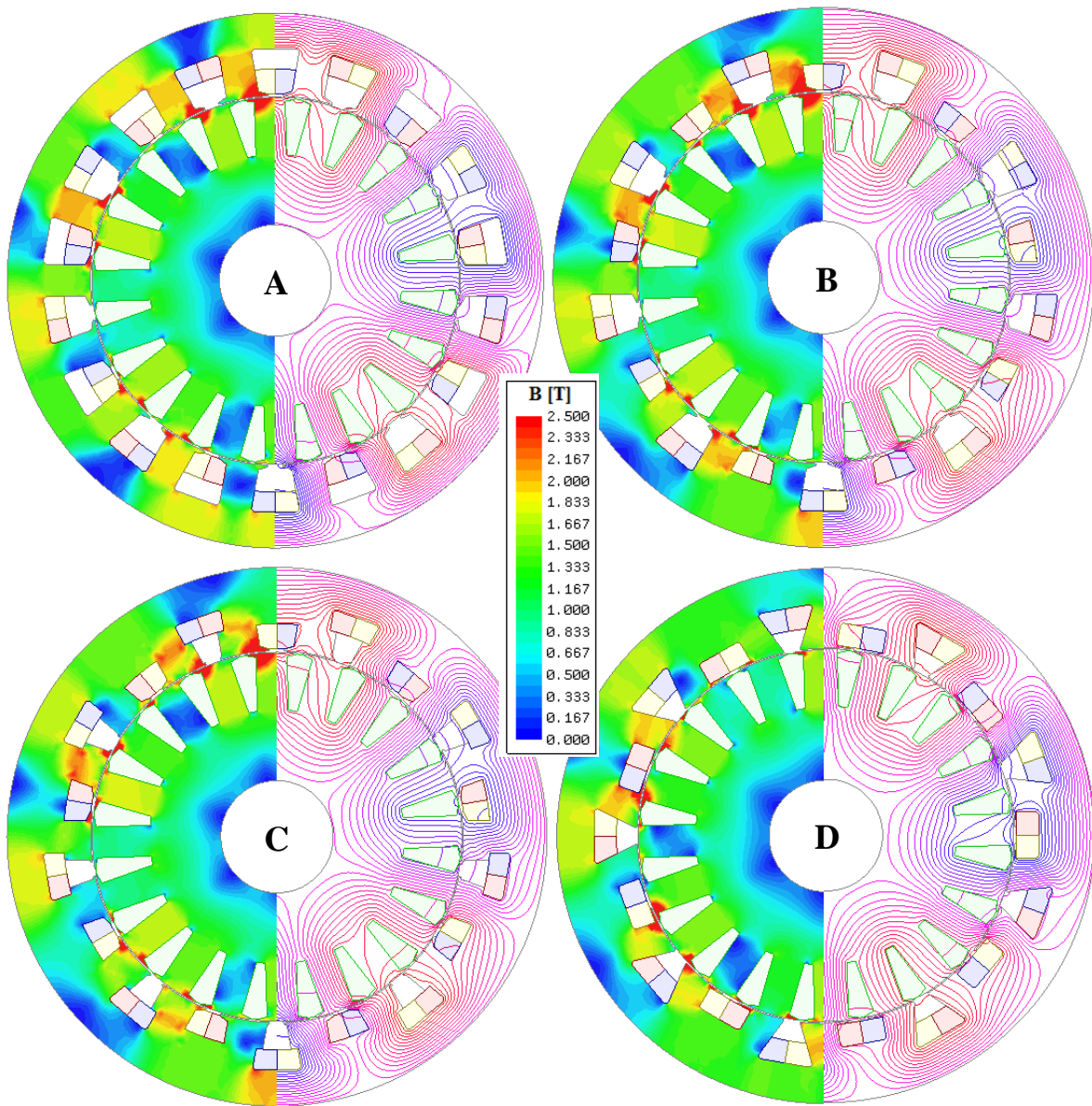


Fig. 3.11 Flux line and density distributions of the AIMs.

As explained previously, the main disadvantage of the proposed method is that only half of the slots can be filled. However, by utilizing the unfilled gaps between the slots, the saturation level can be decreased. As seen in Fig. 3.10(a) there are two unfilled gaps namely, one is at the yoke side and the other one is at the slot opening side. These two gaps can be utilized without overlapping the phase windings. In this way, more than half of the empty slots can be filled and hence the performance can be improved. On the other hand, these half unfilled slots are useful in terms of thermal issues. The unfilled slots if ventilated will help to reduce the temperature inside the stator slots. Thus, overloading capability of the IM can be increased considerably; or less cooling requirement might be needed comparing to its full-filled slot counterpart. The most significant advantage of this method is that it leads to reduce the total axial length of the machine without sacrificing the fundamental winding factor and hence the torque and power density. As seen in Fig. 3.10, in order to reduce the yoke saturation, the gaps between two adjacent slots close to the yoke have been bridged as a first step. As a second step, in order to reduce the saturation level of the stator tooth parts, the gaps between two adjacent slots at the air-gap side have

been reduced by enlarging the tooth width. The reduction of this gap causes some of the flux to be short circuited. Therefore, in order to avoid these short-circuited stator fluxes, the stator slots have been shaped with a special form as a third step. More details about the stator slot shaping can be found in Appendix F. Flux line and flux density distribution corresponding to each step is illustrated in Fig. 3.11. As clearly seen in the figures, reduction of saturation levels can be easily observed. From A→B: yoke saturation reduction, from B→C: stator tooth saturation reduction, and from C→D: further reduction of tooth saturation by avoiding the short-circuited flux has been achieved.

3.3 Comparison of Electromagnetic Performance Characteristics

3.3.1 Before Stator Slot Utilization

In order to realize the characteristics of the proposed method, design and performance characteristics of the 9S/6P-4L FSCW IM and 2x9S/6P-2L advanced non-overlapping (ANW) IM have been compared. The shift angles, delivering the maximum torque and minimum harmonic content, are determined as $0^\circ\text{e}/(+, +)$ and $180^\circ\text{e}/(+, -)$ for 9S/6P-4L FSCWIM and AIM, respectively. Cross-sectional views of the IMs are illustrated in Fig. 3.12.

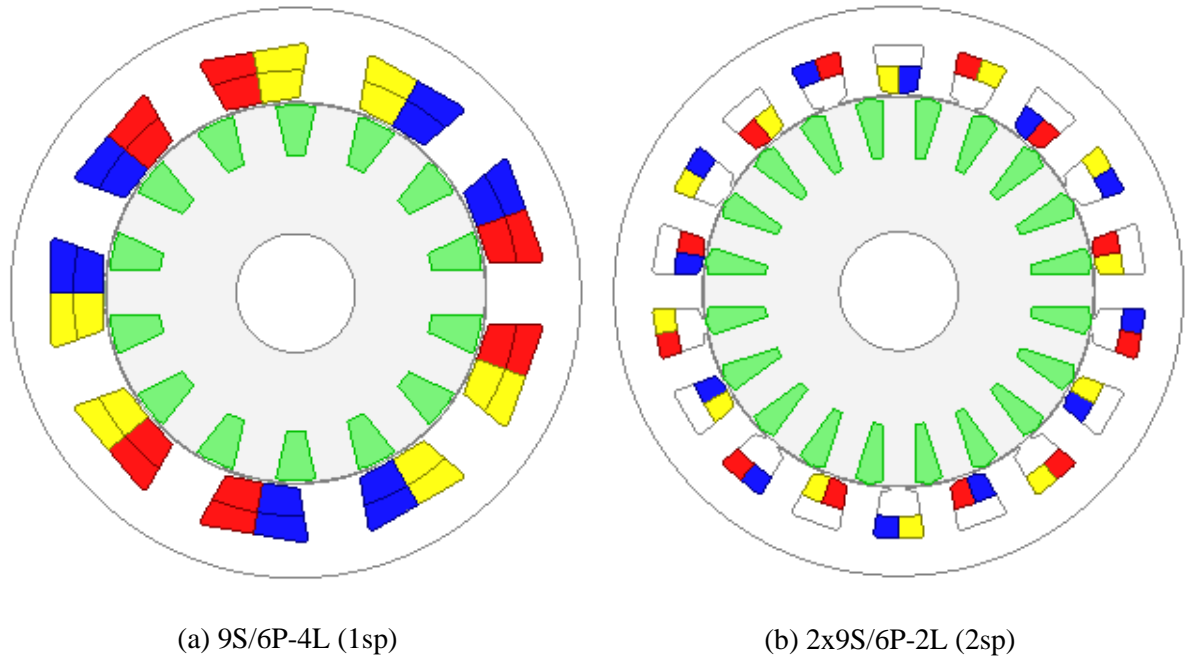


Fig. 3.12 2-D views of IMs: (a) FSCWIM and (b) primitive AIM.

As seen, all slots of the FSCWIM are filled whilst the half of the each slots of primitive AIM are unfilled. The specifications of the compared IMs are given in Table 3.2. Both IMs are operated at 500Arms excitation and the obtained steady state results are then compared. The speed delivering the maximum torque has been parametrically determined as 1870rpm and 1905rpm for FSCWIM and AIM, respectively.

Table 3.2 Specifications of the FSCWIM and AIM

Parameter	9S/6P-4L (1sp)	2x9S/6P-2L (2sp)
Number of turns per phase	14	9
Stator outer radius (mm)	144	144
Split ratio	0.67	0.69
Air-gap length (mm)	0.35	0.35
Rotor outer radius (mm)	95.78	98.66
Stator tooth width/ height (mm)	15.577/11.7	8.73/10.3
Stator/Rotor slot opening width (mm)	8/5.5	4/1.4
Rotor tooth width/ height (mm)	11.128/11.9	8.266/14
Stack length (mm)	70	70
Slot numbers S/R	9/14	18/20

A. Axial Length and Phase Resistance

The total axial length and the phase resistances are calculated by using the equations between (2.9) and (2.13) expressed in Chapter 2 and the obtained results are illustrated in Fig. 3.13. As seen, since the number of turns per phase of AIM is 36% lower than that of the FSCWIM, it is 14% shorter. On the other hand, since the slot area of the AIM is smaller than that of the FSCWIM, its wire diameter is smaller, and therefore, it has higher phase resistance and higher stator current density.

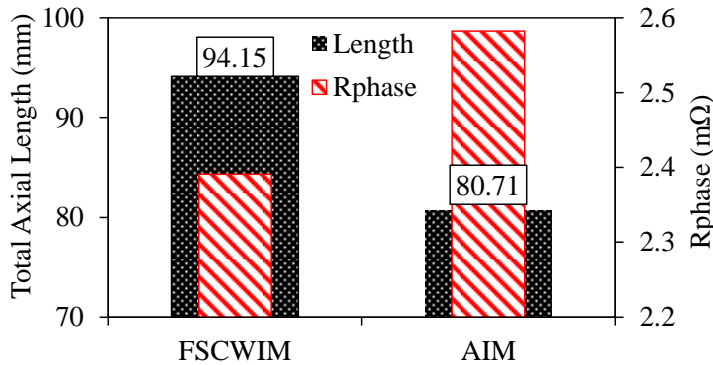


Fig. 3.13 Comparison of total axial length and phase resistance.

B. Induced Voltage

The induced voltage waveforms and harmonic spectra of the FSCWIM and AIM under 500Arms stator current excitation are shown in Fig. 3.14. As seen in the figure, since more number of turns is required for the FSCWIM in order to compensate the torque, the induced voltage amplitude is higher than that of the AIM. As clearly seen in Fig. 3.14(b), the level of high order harmonics of the FSCWIM are considerably higher than that of the AIM. Although the FSCWIM has more distortion because of the heavily distorted MMF waveform, its induced voltage THD is lower than that of the AIM. This is because the amplitude of induce voltage of the FSCWIM being quite higher than that of the AIM.

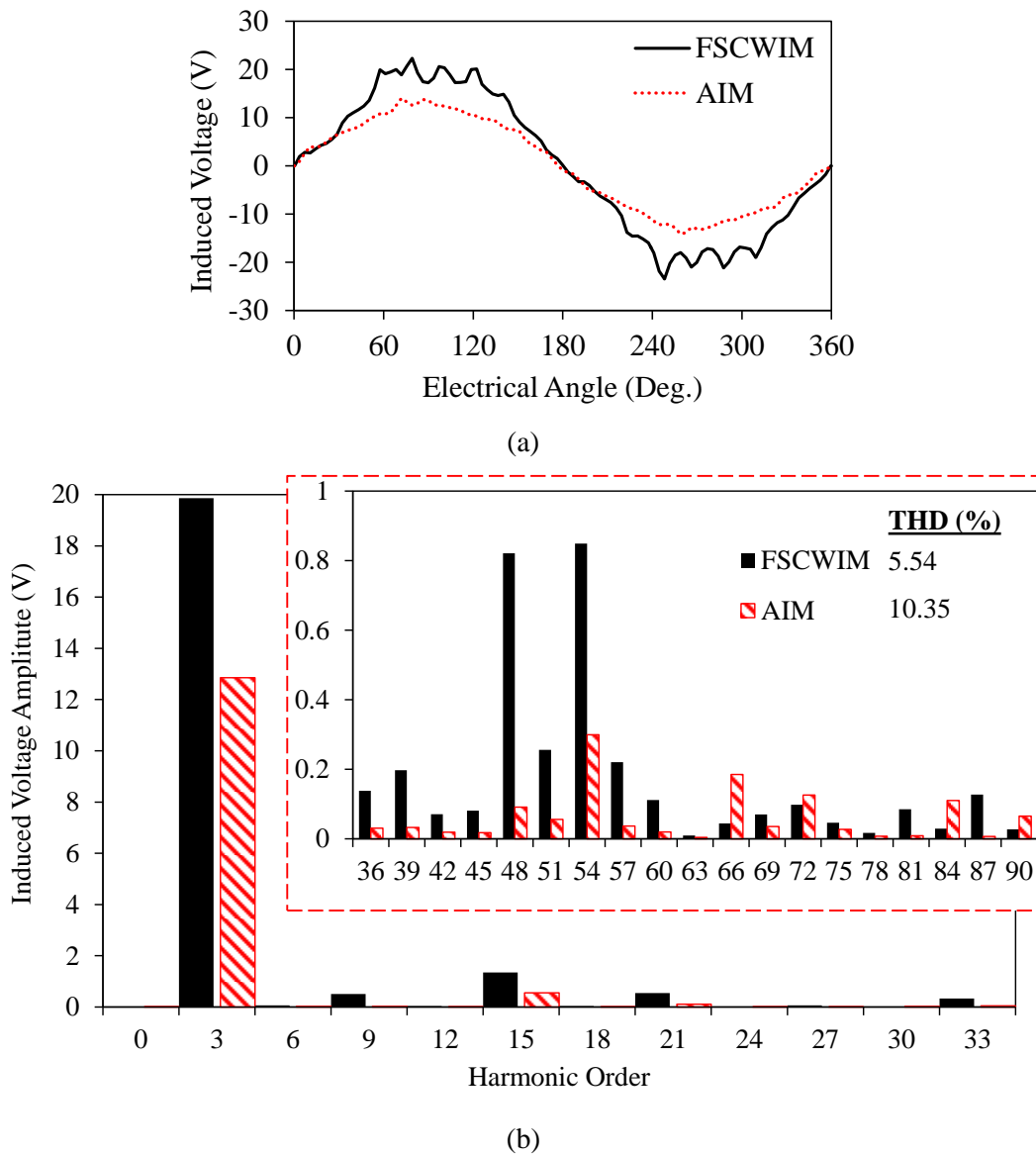
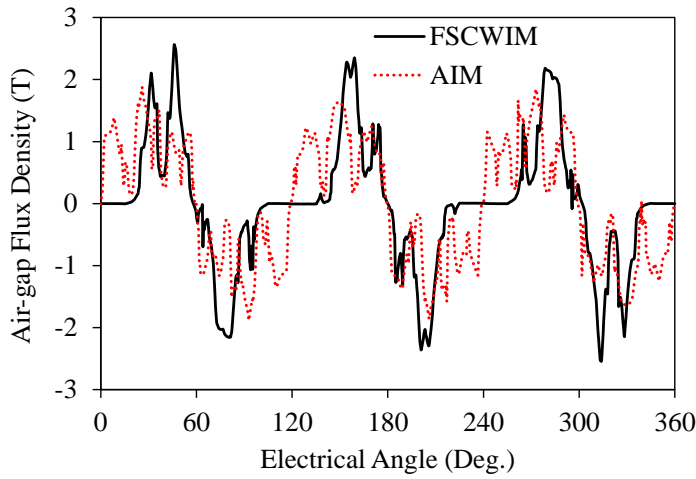


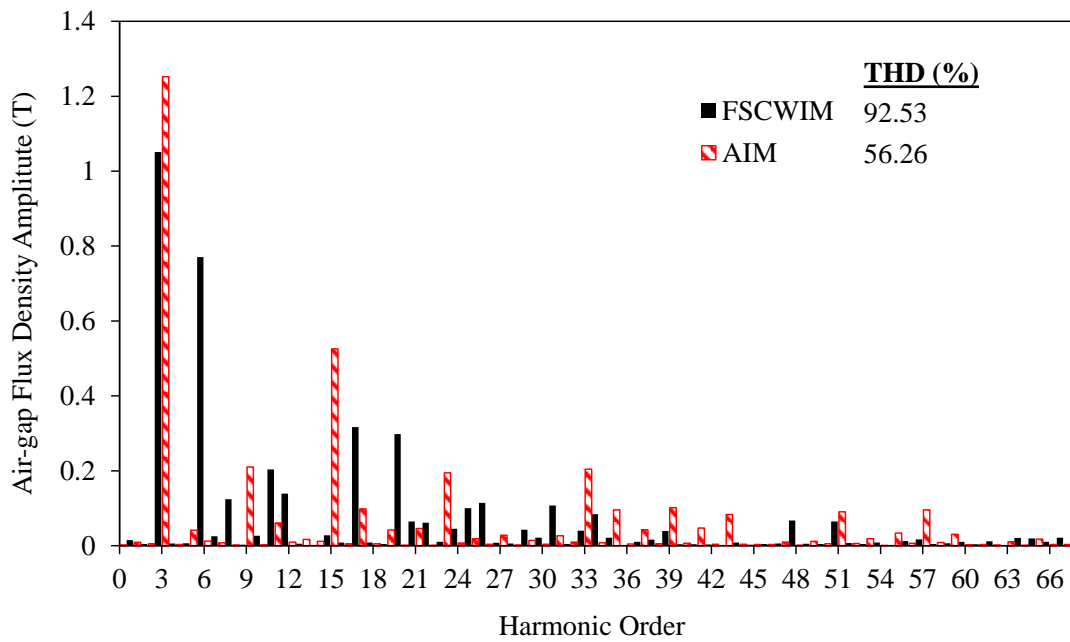
Fig. 3.14 Phase 'A' induced voltage: (a) waveform and (b) harmonic spectra.

C. Air-gap Flux Density

The variation of the radial component of the air-gap flux density with respect to rotor position is shown in Fig. 3.15(a). It is clear that the air-gap flux density of the FSCWIM is much more distorted than that of the AIM. This is because that each coil of the FSCWIM is concentrated on one stator tooth. On the other hand, as for the AIM, although the windings are not overlapped, one coil is not concentrated on the one stator slot as seen in Fig. 3.12(b). Since the coil pitch is two slot pitches, one phase winding is positioned on two adjacent stator teeth. Thus, more sinusoidal distribution of the windings has been designed. The harmonic spectra of the air-gap flux density waveforms are illustrated in Fig. 3.15(b). By employing the proposed method, ~ 40% of the air-gap flux density THD has been reduced. In addition, although the FSCWIM has 36% more number of turns than that of the AIM, its fundamental air-gap flux density amplitude is 20% lower.



(a)



(b)

Fig. 3.15 Air-gap flux density: (a) waveform and (b) harmonic spectra.

D. Rotor Bar Current

Bar current waveforms and their harmonic spectra are illustrated in Fig. 3.16. As seen, the bar current waveforms have rich harmonics. These harmonics are originated from the combination of stator and rotor slot harmonics, forward and backward MMF harmonics, and also magnetic saturation harmonics. In general, the low-order harmonics are originated from the forward and backward MMF and magnetic saturation harmonics while the high-order harmonics are originated from slot harmonics due to the S/P/R combinations. More explanations about the bar current waveforms and their harmonics can be found in Chapter 5. The significant level of distortion of the FSCWIM can be clearly seen from the figure. These bar current harmonics cause increasing level of rotor bar copper loss and temperature of the rotor bars, remarkably. By employing the proposed method, the distortion level has been decreased significantly. The amplitudes of the harmonics, particularly the high-order harmonics of the FSCWIM

are quite high. The bar current THD of AIM is ~261% lower than that of FSCWIM. Therefore, it can be predicted that the rotor bar copper loss of the AIM will be significantly lower than that of the FSCWIM. On the other hand, the waveforms of the bar currents seem like trapezoidal or flat-topped. The reason behind this phenomenon will be explained in Chapter 5 and 6.

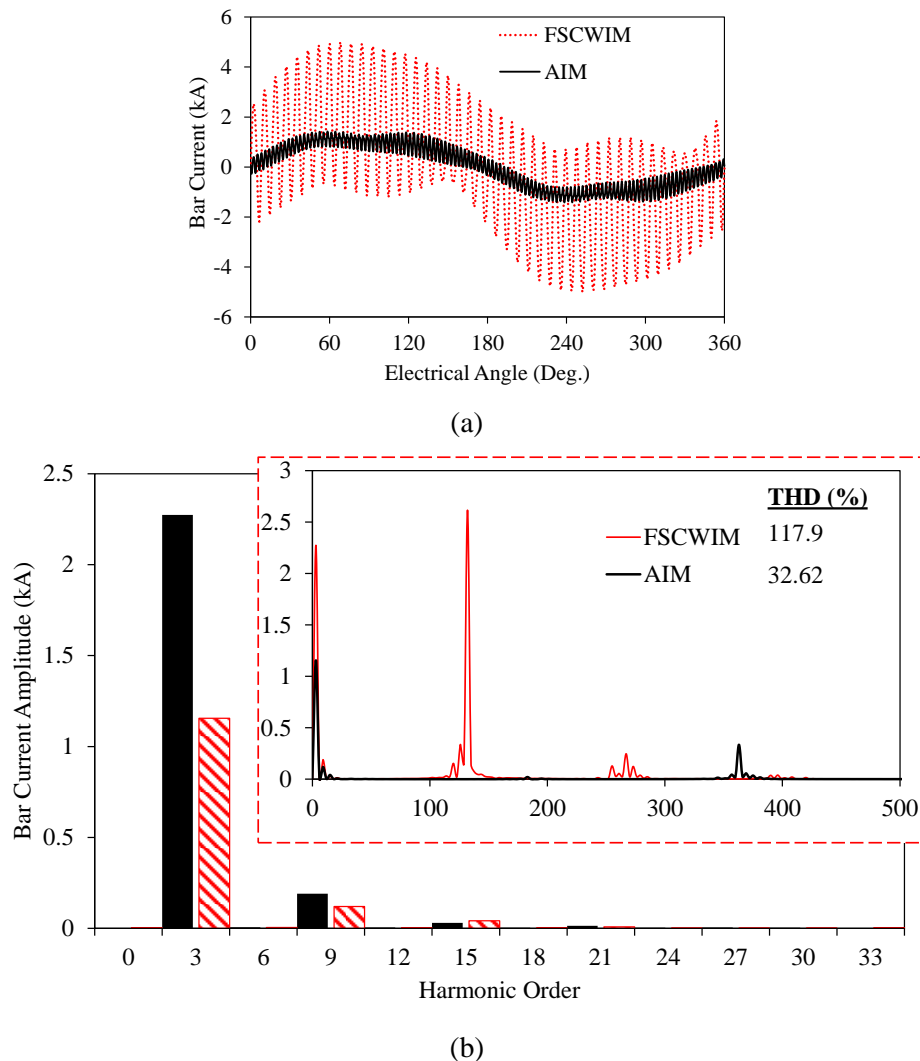


Fig. 3.16 Rotor bar current: (a) waveform and (b) harmonic spectra.

E. Flux Distributions

Flux line and flux density distributions of the considered IMs are illustrated in Fig. 3.17. As clearly seen, the saturation level of the FSCWIM is higher than that of the AIM. Stator tooth parts of both IMs are saturated highly. As known, the MMF harmonics cause partly local and variable saturations. The higher the MMF harmonics, the higher the saturation level of the machine cores. It can also be predicted that these local and variable saturations cause a decrease in the average torque and an increase in the torque ripple and core loss levels.

F. Torque and Torque Ripple

The variation of the torque is shown in Fig. 3.18. Due to the unfilled slots of the AIM, ~11% lower torque has been obtained than that of the FSCWIM. Considering that the studied AIM is the primitive

version (neither developed nor optimized), it can be deduced that the obtained torque level is acceptable. It can be also realized that using the proposed method, ~ 52% lower torque ripple has been obtained. In order to improve the performance of the AIM, the unfilled slots will be utilized and the obtained geometry of the stator will be globally optimized in the following section.

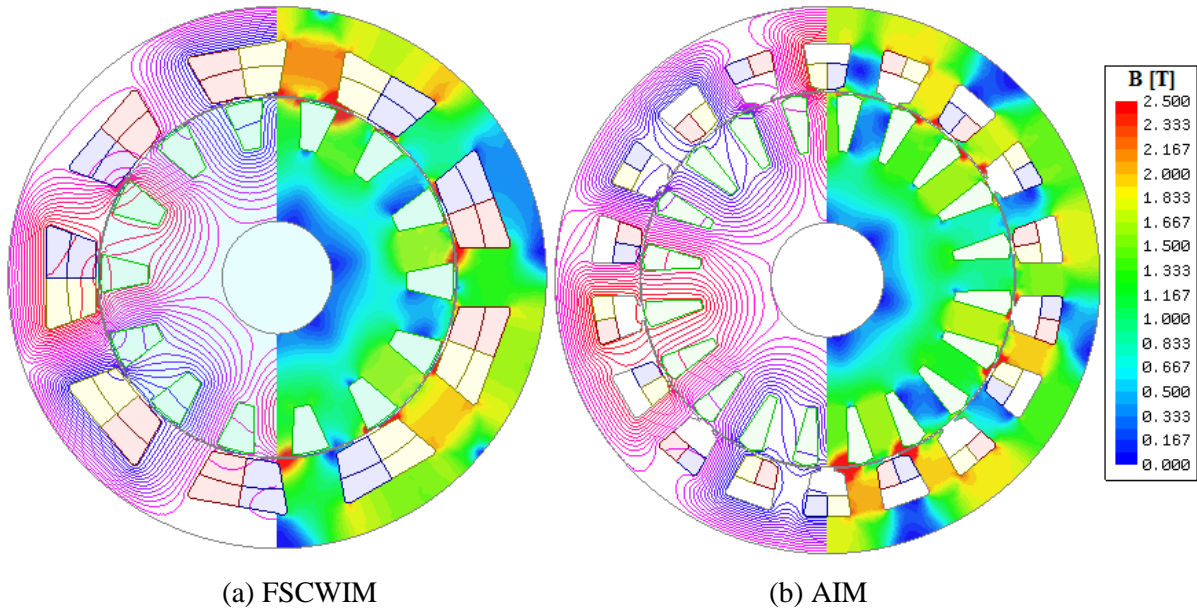


Fig. 3.17 Flux line and density distributions of the considered IMs.

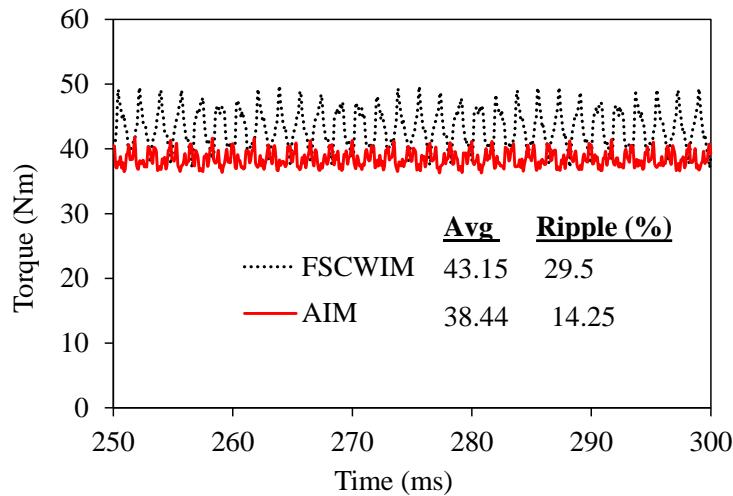


Fig. 3.18 Torque variations with respect to time.

G. Machine Losses and Efficiency

Calculated power losses including the stator copper slot P_{scu_in} , stator end-winding copper loss P_{scu_end} , total stator copper loss P_{scu} , rotor bar copper loss P_{rcu} , and total core loss P_c are shown in Fig. 3.19(a). As clearly seen in Fig. 3.19(a), although the total stator copper losses are quite similar, the rotor bar copper loss of the FSCWIM is ~517% higher than that of the AIM. Moreover, the total core loss of the FSCWIM is ~300% higher than that of the AIM. The total loss and efficiency comparison of the considered IMs is shown in Fig. 3.19(b). Thanks to the proposed method, the total power loss

level reduces from ~5kW to ~2.5 kW. Therefore, the output power and overall efficiency of the AIM are ~21% and ~15.7% higher than that of the FSCWIM, respectively.

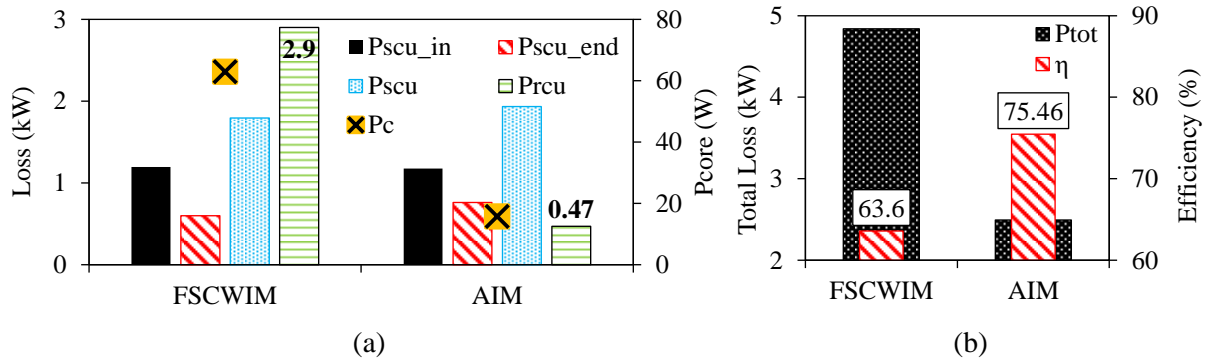


Fig. 3.19 Loss and efficiency comparison: (a) power losses and (b) total loss and efficiency.

In conclusion, it is verified that the proposed method works successfully. To combine the doubled stator slot topology with the phase shifting method leads to achieve more homogeny distributed winding layout with significantly reduced MMF harmonic content. Thanks to the proposed method, more compact and more efficient IM can be designed. It is obvious that by improving and optimizing the primitive design, further performance improvement might be achieved.

3.3.2 After Stator Slot Utilization

The influence of each performance improvement process step (see Fig. 3.20) on the performance characteristics have been investigated in this section. Numerically calculated key performance characteristics have been compared as shown in Fig. 3.21. For a fair comparison, the same geometric (144mm outer diameter and 70mm stack length) and operational parameters (500Arms excitation current and 2krpm synchronous speed) have been assigned during the improvement process. It is clear from Fig. 3.21 that the average torque is increased considerably from the initial design (A) to the final improved design (D). In addition, although the average torque is increased by ~19%, the torque ripple level is changed. The power losses including the stator copper loss P_{scu} , rotor bar copper loss P_{rcu} , and total iron core loss P_c have been compared in Fig. 3.21(b). As clearly seen in the figure, by utilizing the unfilled stator slots, the stator copper loss decreases by 15% and the total core loss also is decreased by ~28%. On the other hand, even if the average torque is increased, the amount of rotor bar copper loss is not increased. Comparison of the total power loss P_{tot} , output power P_{out} , and efficiency η are shown in Fig. 3.21(c). By utilizing the unfilled stator slots, from A to D; whilst the output power of the IM increases by ~19%, the total loss decreases by 8.8%, and consequently the efficiency increases by 7.3%.

As a conclusion, thanks to developed method allowing better slot utilization, the average torque, power, and efficiency characteristics of the AIM have been improved significantly. As seen in Fig. 3.20(D), there is still some unfilled slots left consistently. In essence, these gaps help to reduce the level of the short-circuited flux and also to improve the thermal characteristics of the AIM by introducing extra air-cooler canals into the stator.

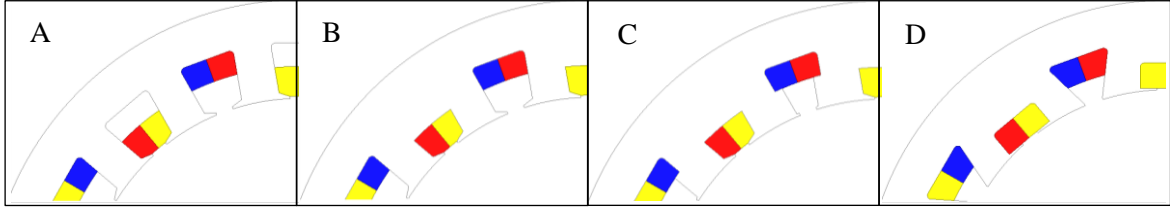
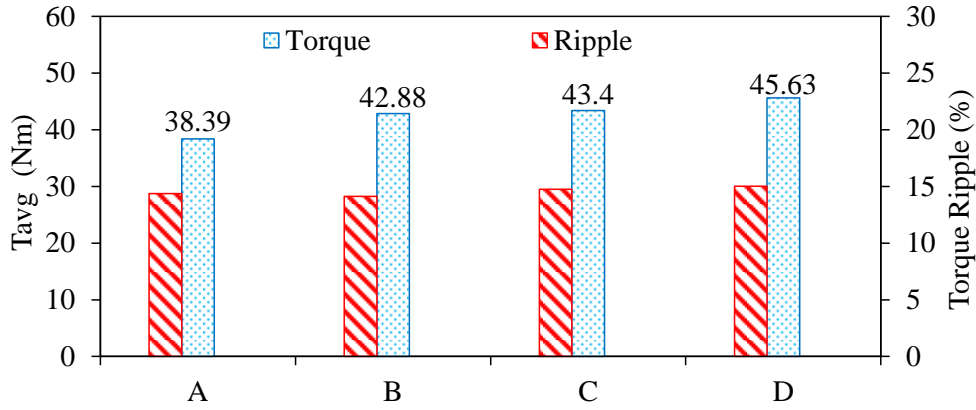
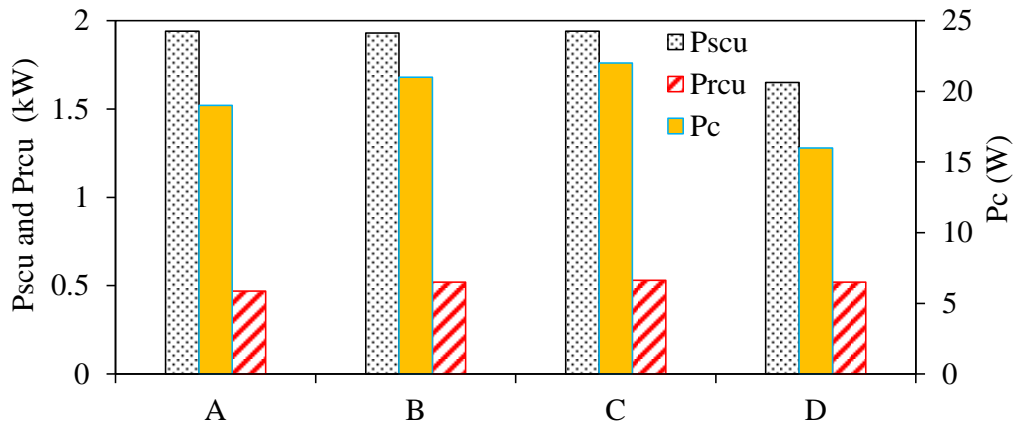


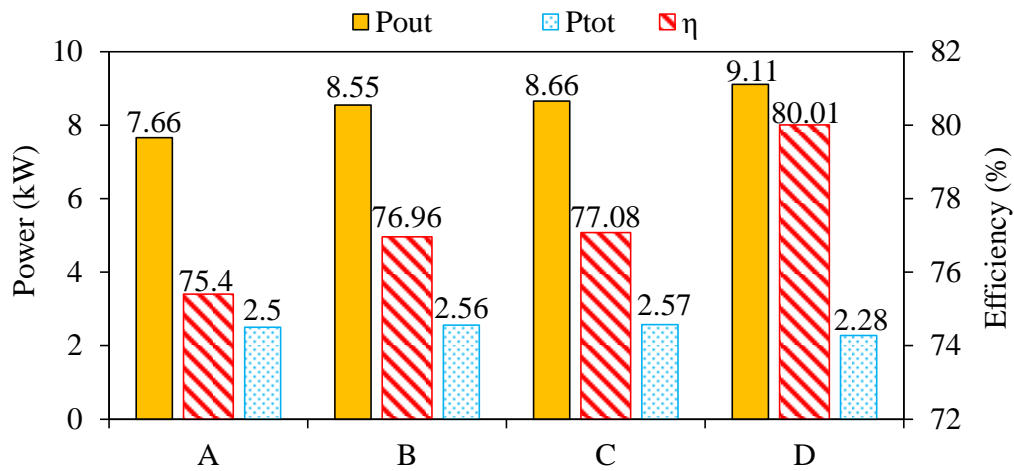
Fig. 3.20 Step by step stator slot utilization progress.



(a) Torque and torque ripple



(b) Stator copper Pscu, rotor copper Prcu, and core Pc losses



(c) Output power Pout, power losses Ptot, and efficiency η

Fig. 3.21 Comparison of some performance characteristic of the AIMs.

3.4 Influence of Design Parameters on Performance of Advanced Non-Overlapping Winding Induction Machine

In this section, the influences of the major design parameters on the electromagnetic and flux-weakening performance characteristics of AIM are investigated by FEA. The considered design parameters and their ranges are summarised as follows.

- Stator slot/pole number combinations: 18S/6P, 24S/8P, 30S/10P, and 36S/12P;
- Rotor slot numbers: from 14 to 62;
- Stack length: from 70mm to 110mm;
- Number of turns per phase: from 7 to 13;
- Geometric parameters: split ratio, slot and slot opening widths and heights.

Among these parameters, pole number, number of turns, and stack length have a major impact on the flux-weakening performance. As will be shown in the following sections and Chapter 4, IMs having higher pole numbers or shorter stack lengths requires more number of serial turns per phase in order to maintain the torque at constant torque region. Correspondingly, the higher the number of serial turns per phase, the higher the phase inductance. Considering the d - and q -axis equivalent circuit of an IM, the d - and q -axis voltage equations can be derived as expressed in (3.5) and (3.6), respectively, where i_{is} stator current, i_{ir} rotor current, p is the pole-pair number, L_s equivalent stator winding inductance and L_m is the mutual inductance between stator windings and rotor bars or magnetizing inductance.

$$V_{ds} = i_{ds}(R_s + pL_s) + i_{qr}(pL_m) \quad (3.5)$$

$$V_{qs} = i_{qs}(R_s + pL_s) + i_{dr}(pL_m) \quad (3.6)$$

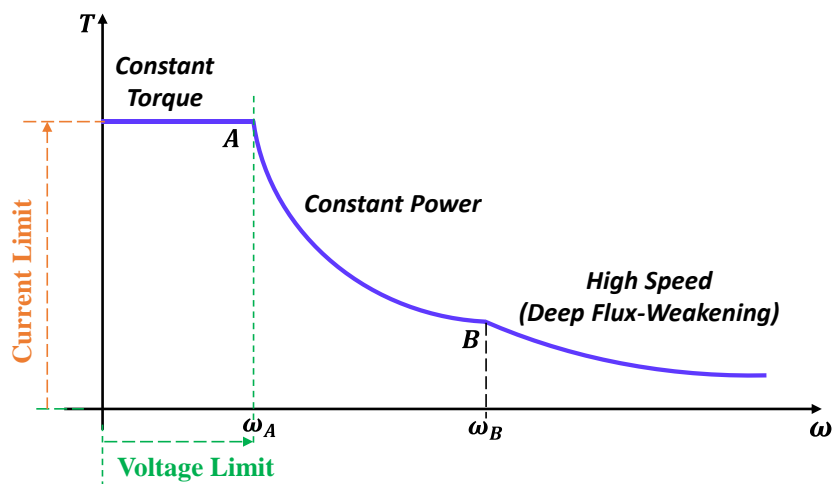


Fig. 3.22 Flux-weakening characteristics of an IM showing inverter voltage and current limits.

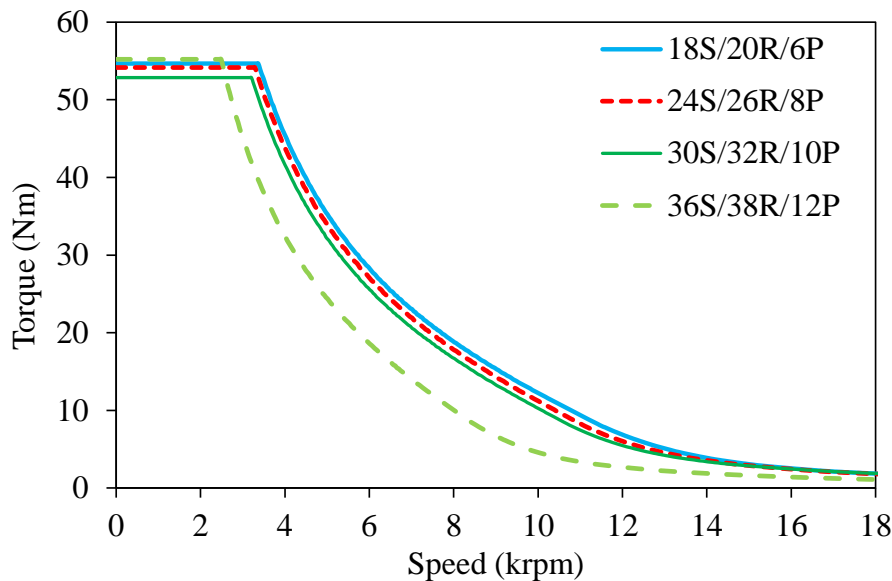
As can be seen from (3.5) and (3.6), the increase in the phase inductance causes an increase in the terminal voltage. As illustrated in Fig. 3.22, the length of the corner speed of an IM depends on the voltage limit. Considering that the inverter voltage is limited, the increase in the terminal voltage of the

IM mean is that the voltage requirement of the IM is increased. In other words, since the maximum terminal voltage of the inverter cannot be exceeded, the corner speed of the IM will be moved from high speed to low speed region. As a consequence, poorer flux-weakening performance can be predicted for the IMs with higher pole number or shorter stack lengths which require more serial turns per phase.

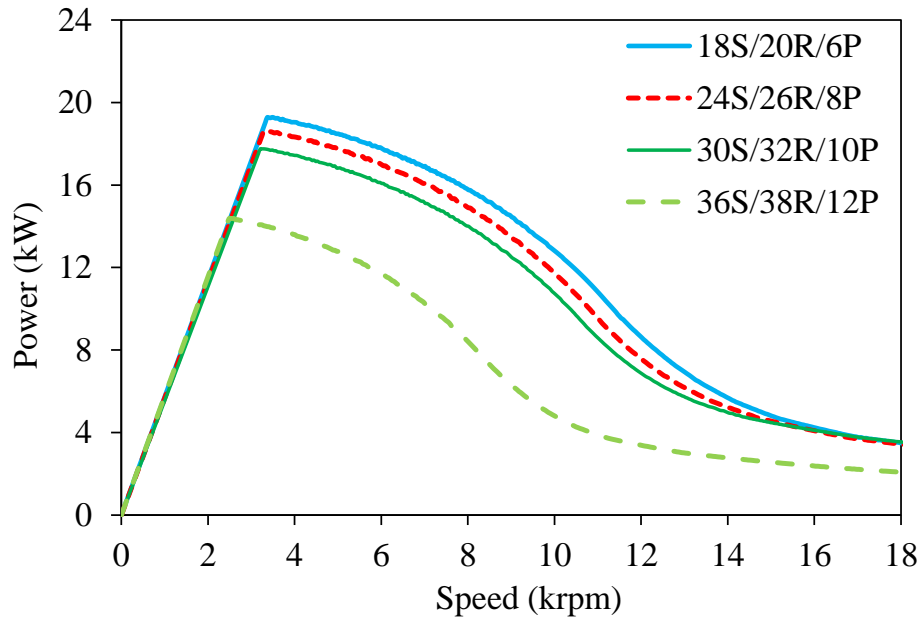
Note that all machines are designed by using 144mm of outer diameter. In addition the maximum current and voltage limits of the inverter employed in this section are 500Arms and 48V, respectively.

3.4.1 Stator Slot and Pole Number

In Chapter 2, it has been shown that the minimum harmonic index can be achieved in case of $q = 0.5$ for $y_c = 1$ and $q = 1$ for $y_c = 2$ winding topologies. For various S/P combinations satisfying these conditions, the higher the stator slot number, the lower harmonic index. In other words, in the case of $y_c = 2$, the harmonic index of the 72S/24P combination is 25.2% lower than that of the 18S/6P combination. Considering this finding, it can be predicted that the rotor bar copper loss of the 72S/24P combination will be lower than that of the 18S/6P combination under the same geometric and operating specifications. On the other hand, it should be considered that the higher the pole number, the higher the synchronous frequency requirement and consequently the increased core losses at high speed operations. Therefore, an optimum balance between the rotor bar copper loss and total core losses is required. On the other hand, since there is no PM in the design of IMs, the most dominant machine loss is the copper loss. Another important issue needs to be considered carefully before determining the S/P is the flux-weakening characteristics. Generally, the lower the pole number, the better the flux-weakening capability. In other words, higher torque at the constant power region can be obtained by designing IMs with lower number of stator slot and pole combinations. The AIMs with various S/P combinations and all having the optimal rotor slot numbers, estimated by $R \approx S + 2q$, are designed. The obtained torque- and power-speed characteristics are illustrated in Fig. 3.23.



(a) Torque-speed characteristic comparison for 80mm AIMs



(b) Power-speed characteristic comparison for 80mm AIMs

Fig. 3.23 Torque- and power-speed characteristics comparison for 80mm AIMs designed with different S/R/P combinations.

The details related with the calculation of the flux-weakening characteristics can be found in Appendix A. Clearly, the 6P AIM has the highest torque at constant power region whilst the 12P has the lowest torque. In the same manner, the 6P AIM has the highest power at constant power region whilst the 12P AIM has the lowest. Furthermore, as seen in Fig. 3.23 there is a big reduction in torque and power when P increases from 10 to 12. This is because of that the different serial number of turns per phase and consequently the different phase inductances of the IMs. As known, the higher the number of turns, the higher the phase inductance, and consequently the higher the voltage requirement. Since the inverted voltage is fixed at a constant amount, it causes a reduction in the power in the machines requiring more voltage. The serial number of turns per phase are 7, 8, 9, and 13 for IMs with 6P, 8P, 10P, and 12P, respectively. These number of turns have been parametrically determined in order to maintain the torque between 52Nm and 56Nm at the constant torque region. Because of the more stator slot number of the 12P IM, more stator tooth and yoke saturation have been occurred. That is why the 12P IM requires more number of turn than other combinations. Therefore, because of the large serial number of turns per phase difference between 10P and 12P IMs, there has been a big reduction in torque and power. More details about the influence of number of turns on the flux-weakening characteristics can be found in Section 3.4.4. In addition, the efficiency maps of the AIMs are compared as shown in Fig. 3.24. Since the AIMs with 6P, 8P, and 10P have a similar power level in the constant power region, their efficiency maps are similar.

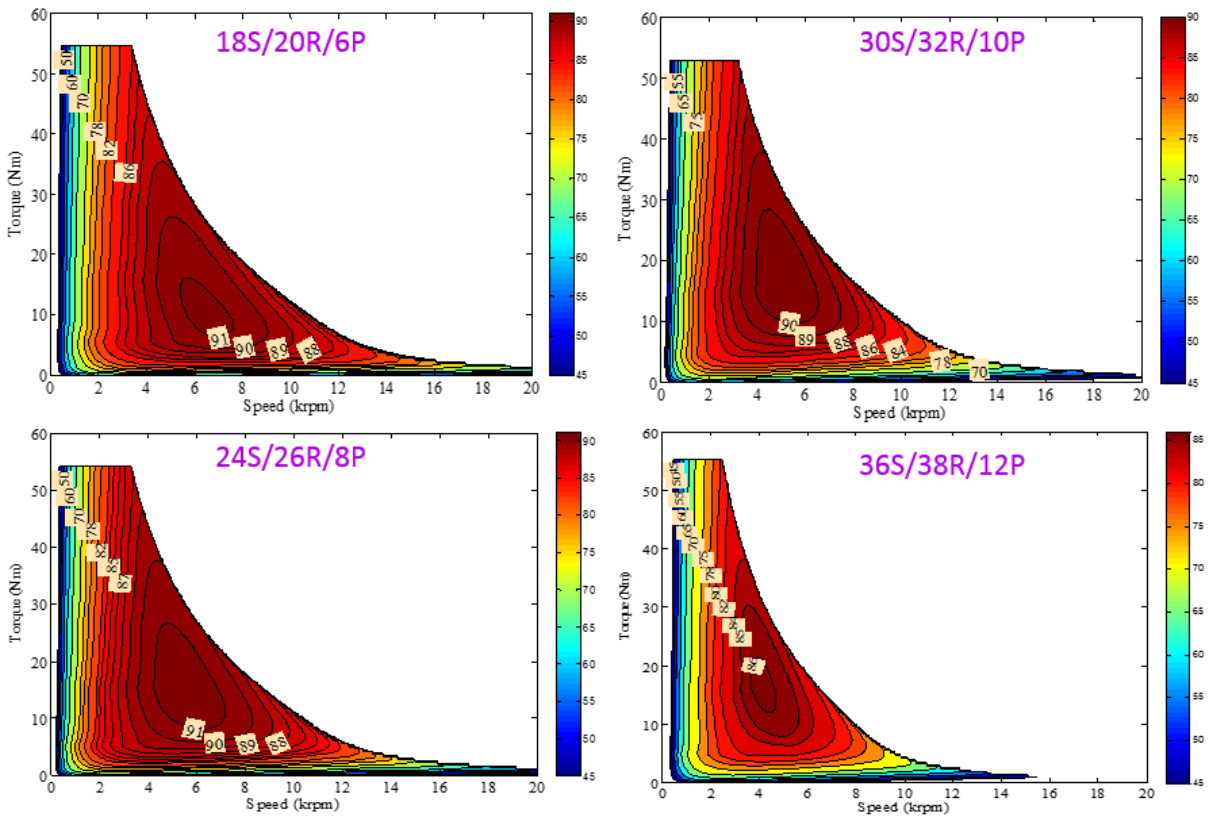


Fig. 3.24 Comparison of the efficiency maps of the AIMs with different S/P combinations.

3.4.2 Rotor Slot Number

In the rotor design stage of a squirrel-cage IM, the determination of the number of rotor slots and their geometries are some of the most important aspects determining the noise, vibration, torque density and torque ripple characteristics. In order to determine the accurate rotor slot number for IMs, some empirical rules will be presented in Chapter 6. In addition to these rules, based on the analysis results of the AIMs with $\gamma_c = 2$ presented in this section, the following rules have been derived to determine the optimal rotor slot number:

- a) In order to avoid the torque ripples, acoustic noise and unbalanced magnetic pull (UMP), the rotor slot number (R) should not be:
 - Multiples of phase number (m) $\rightarrow R \neq a \cdot m$;
 - Multiples of pole number (P) $\rightarrow R \neq a \cdot P$;
 - Multiples of stator slot number (S) $\rightarrow R \neq a \cdot S$;
 - Odd numbers.
- b) In order to avoid the high rotor bar copper loss and bar current density, R should be as low as possible;
- c) The rotor slot numbers close to the stator slot numbers are good candidates;

- d) The optimum slot number, in terms of torque, torque ripple, bar copper loss, and current density can be determined as $R \approx S + 2q$.

Several parametric analyses for the 18S/6P, 24S/8P, 30S/10P, and 36S/12P AIMs have been performed in order to investigate the influence of the rotor slot number on the performance characteristics and determine the best rotor slot number. Note that, odd rotor slot numbers have not been taken into account during the analyses. In order to conduct a fair comparison, all the parameters are kept constant and the ratio of rotor slot width b_{r12} to rotor tooth width t_{r12} has been also kept constant for all S/P combinations (see Fig. 3.25). For each combination, the influences of rotor slot number on the electromagnetic performance characteristics; such as torque, torque ripple, rotor bar copper loss, rotor bar current density, and slip are investigated.

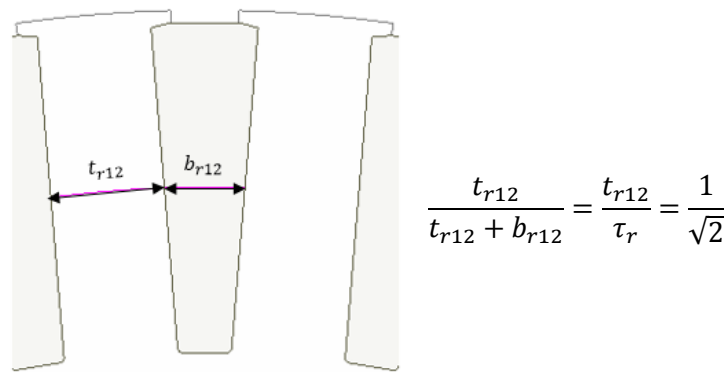


Fig. 3.25 Rotor geometry.

The variation of the torque, torque ripple, rotor bar copper loss, and bar current density with respect to rotor slot number for 18S/6P AIM is illustrated in Fig. 3.26. As expected, the torque ripple level is extremely high for multiples of phase, pole and stator slot numbers. On the other hand, the average torque does not show significant deviations (see Fig. 3.26(a)). Furthermore, it is clear that from Fig. 3.26(b), the rotor bar copper loss and bar current density increase significantly as the rotor slot number increases. The best rotor slot number can be determined by considering the maximum torque and minimum torque ripple, bar copper loss, and current density in the rotor bars. Consequently, the best rotor slot number for the 18S/6P AIM determined is 20. In the same manner, the variation of average torque, torque ripple, bar copper loss, and bar current density with respect to rotor slot number is calculated for 24S/8P, 30S/10P, and 36S/12P, respectively, as illustrated from Fig. 3.27 to Fig. 3.29. Considering these figures, 26, 32, and 38 rotor slot numbers have been determined as the best candidate for the 24S/8P, 30S/10P, and 36S/12P AIMs, respectively.

It has also been revealed that increasing the rotor slot number causes an increase in the maximum torque slip. Therefore, it can be predicted that the higher the rotor slot number, the lower the power factor and consequently the lower the efficiency. As seen from Fig. 3.26(b) to Fig. 3.29(b), the higher the rotor slot number, the higher the rotor bar copper loss.

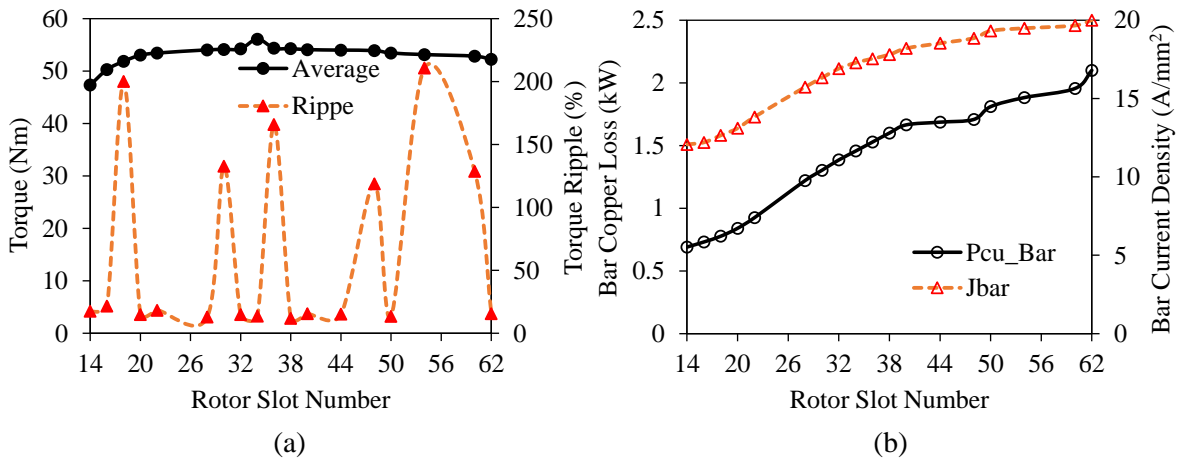


Fig. 3.26 Influence of rotor slot number on the performance characteristics of the 18S/6P AIM: (a) Torque and torque ripple, (b) Bar copper loss and bar current density.

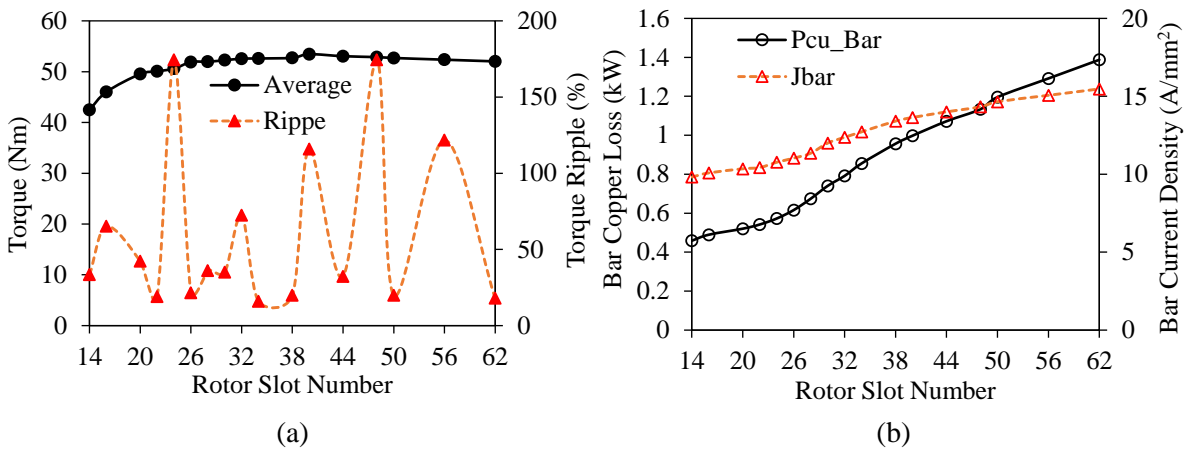


Fig. 3.27 Influence of rotor slot number on the performance characteristics of the 24S/8P AIM: (a) average torque and torque ripple, and (b) bar copper loss and bar current density.

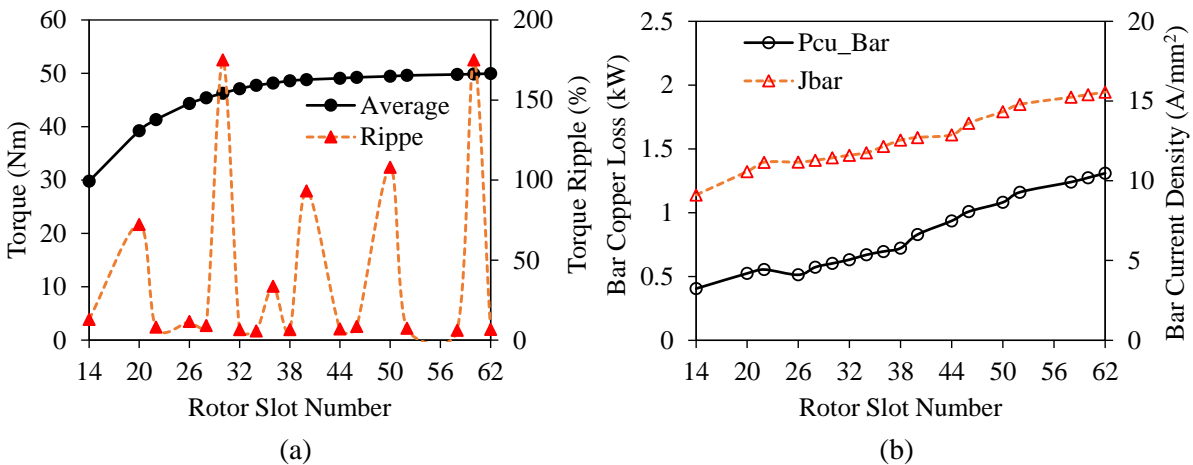


Fig. 3.28 Influence of rotor slot number on the performance characteristics of the 30S/10P AIM: (a) average torque and torque ripple, and (b) bar copper loss and bar current density.

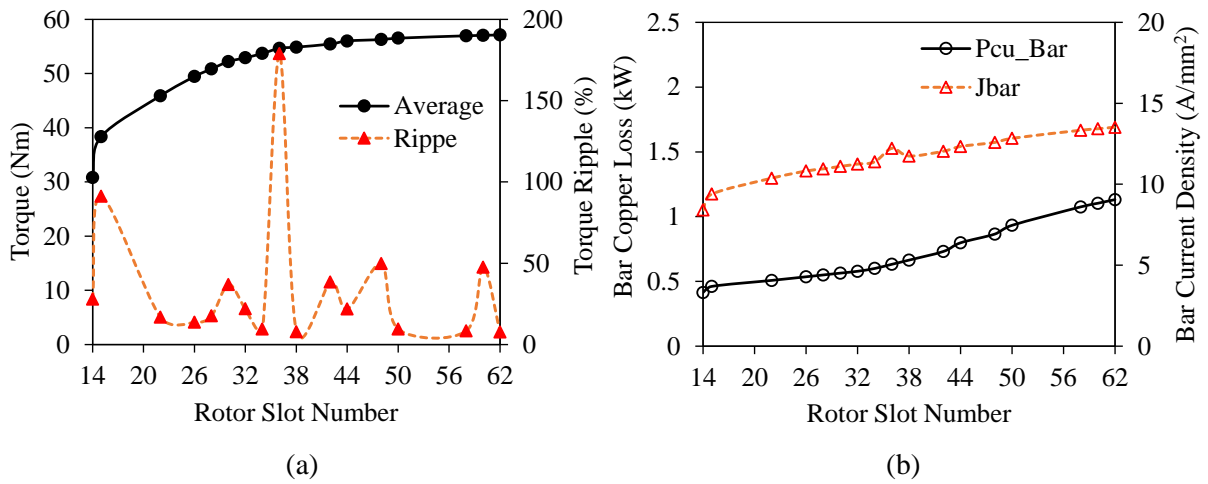


Fig. 3.29 Influence of rotor slot number on the performance characteristics of the 36S/12P AIM: (a) average torque and torque ripple, and (b) bar copper loss and bar current density.

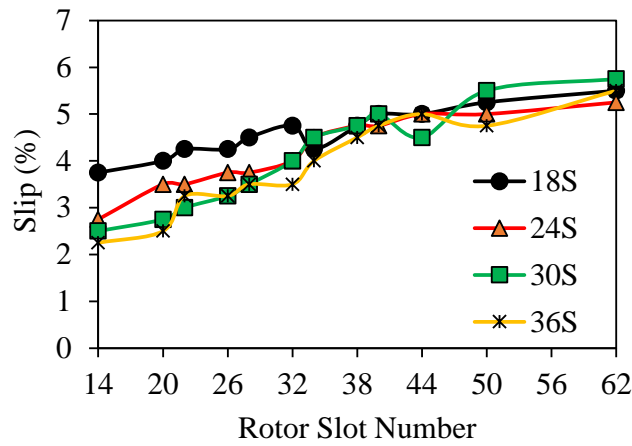


Fig. 3.30 Variation of slip delivering the peak torque with respect to rotor slot number for different stator slot/pole number combinations.

Considering the figures from Fig. 3.26 to Fig. 3.30, some key findings can be summarized as follows:

- The winding harmonics, inducing in the air-gap and hence the rotor bars, cause an increase in the bar copper loss and bar current density;
- Since the winding harmonic indices of higher pole combinations are lower, bar copper loss and bar current density of these combinations are lower than those of the other combinations with lower pole number.
- The torque ripple level of the AIMS having high pole number are lower than that of the AIMS having low pole number.

3.4.3 Stack Length

The design of the stack length is very critical issue, especially for the HEV applications, since the space for electrical machine is quite limited. The stack length of an IM can be determined by considering

the number of turns, stator winding current density, and required flux-weakening characteristic. Influence of the number of turns on the stack length can be investigated under the constant and variable number of turn per phase cases. The determination of the stack length for different design aspects, such as different stator current density and number of turns, has been investigated together with the flux-weakening characteristics in the following section.

a) *Constant Number of Turns per Phase Case*

In order to determine the best combination of stack length and number of turns, a scenario for adjusting the stack length by retaining the number of turns constant is developed by considering the 36S/38R/12P AIM design with 8-turns, 9-turns, and 13-turns per phase. The obtained parametric analysis results are illustrated from Fig. 3.31 to Fig. 3.33 for different number of turns. As clearly seen in the figure, increasing stack length always helps to increase the electromagnetic performance under the constant number of turn condition. The higher the stack length, the higher the torque, the higher the efficiency, and the lower the stator current density. It is also clearly seen from the figures that the longer the stack length, the lower the number of turns requirement for generating the same torque. The efficiency is calculated for only the torque levels between 54 Nm and 56 Nm. Furthermore, since a large slot area is required for the lower current density, the saturation levels of the stator tooth parts are quite high. In other words, the lower the stator current density, the higher the saturation level and consequently the lower the torque density. Therefore, as seen in the figures, the designs having the higher current densities generate higher torque than designs having lower current densities. Some important findings have been revealed for the IMs having lower number of turns, as given as follows:

- Longer stack length required for maintaining the torque;
- Lower current density and higher efficiency;
- Higher power at high speed operations (constant power regions).

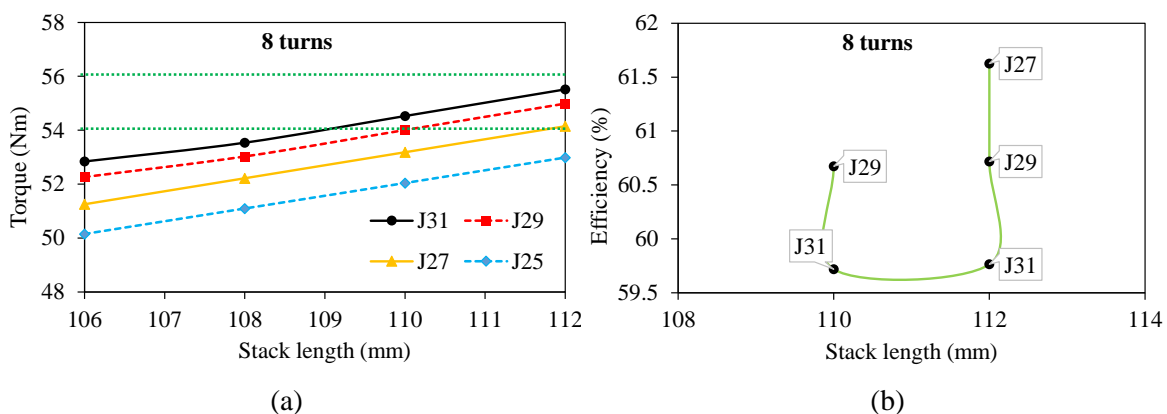


Fig. 3.31 Electromagnetic performance variations with respect to stack length for 8-turns per phase and different stator current density levels: (a) torque and (b) efficiency.

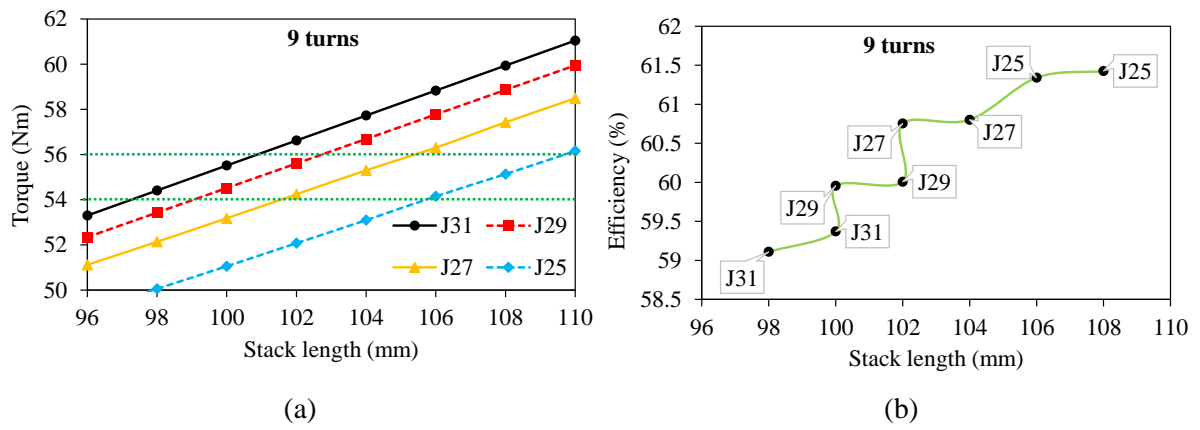


Fig. 3.32 Electromagnetic performance variations with respect to stack length for 9-turns per phase and different stator current density levels: (a) torque and (b) efficiency.

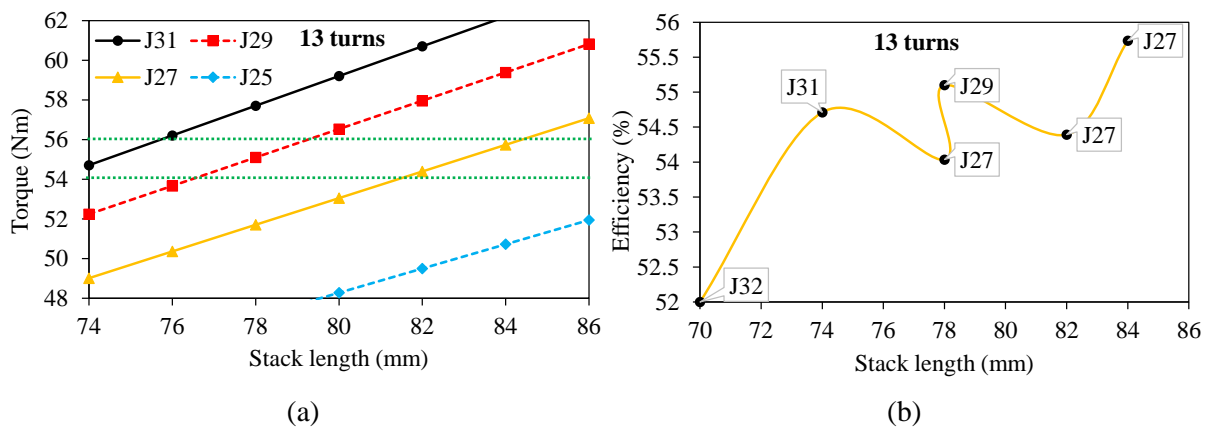


Fig. 3.33 Electromagnetic performance variations with respect to stack length for 13-turns per phase and different stator current density levels: (a) torque and (b) efficiency.

b) Variable Number of Turns per Phase Case

The variation of the number of turns per phase (N_s) and slip, delivering the peak torque is investigated for the 36S/38R/12P AIM. As illustrated in Fig. 3.34, since the stack length is increased, the required number of turns for maintaining the torque is reduced as expected. Furthermore, as the stack length is increased, the slip range is reduced. Therefore, it can be predicted that the power factor and hence efficiency are increased as the stack length is increased.

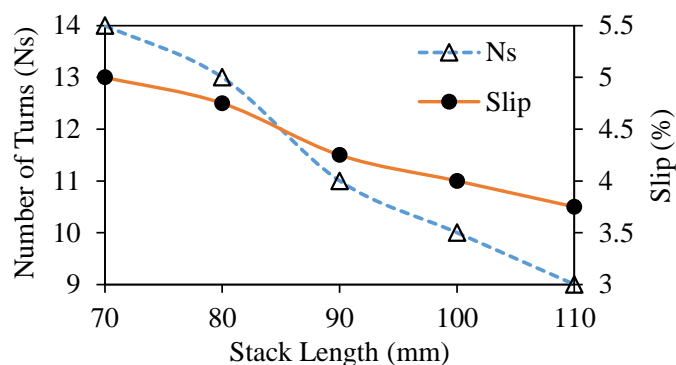


Fig. 3.34 Variation of the number of turns per phase and slip with respect to stack length.

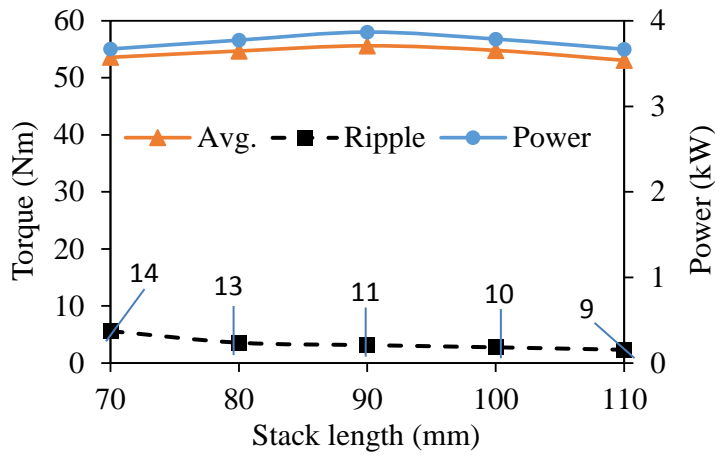


Fig. 3.35 Torque and power variations with stack length.

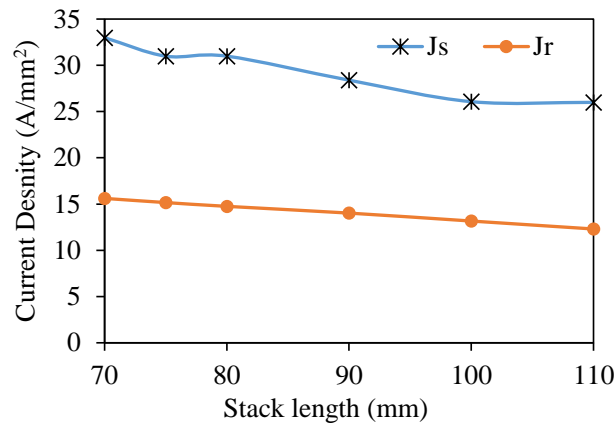


Fig. 3.36 Stator (J_S) and rotor (J_R) current density variations with stack length.

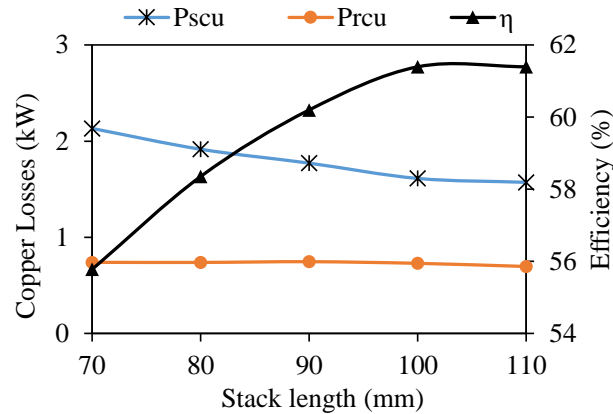


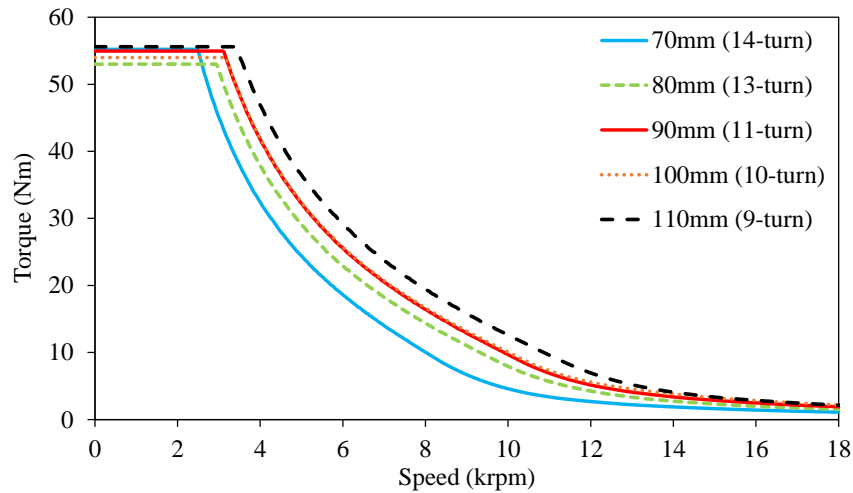
Fig. 3.37 Copper loss and efficiency variations with stack length.

The variations of the torque, torque ripple, and output power as a function of stack length and number of turns are illustrated in Fig. 3.35. As expected, increasing the stack length does not always lead to increase in the torque and power in case of different length and number of turns per phase design. Note that, all the calculations are considered under the different current densities (see Fig. 3.36). As seen in Fig. 3.35, it has been revealed that there is an optimum number of turns for a specific stack length that leads machine to deliver the maximum torque and power. Under the current conditions, the reduction

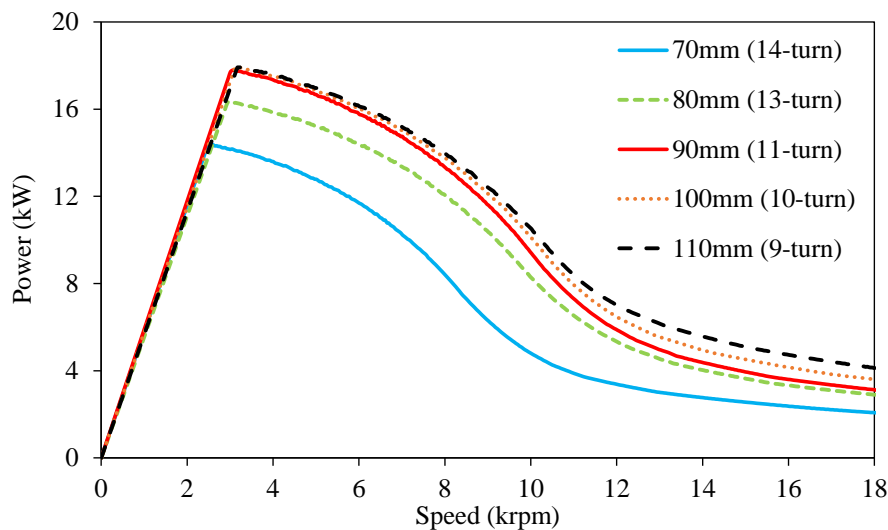
of stator current density is possible in case of the constant stator slot area. Therefore, since the number of turns per phase is decreased with increasing stack length, the total winding resistance is decreased. As a result, as seen in Fig. 3.37, since the stator copper loss P_{scu} is reduced with increasing stack length, the efficiency is increased. In order to determine the optimal number of turns considering the stack length, the torque- and power-speed characteristics of the 36S/38R/12P AIM should be investigated for the different number of turns and stack length parameters. The same criteria are valid for the other S/P combinations.

c) Demanded Torque- and Power-Speed Characteristics

Generally, the stack length and number of turns of a traction motor for EV/HEV applications are determined by considering the maximum flux-weakening capability. For instance, the torque- speed and power-speed characteristics of the 36S/38R/12P AIM are illustrated in Fig. 3.38. As clearly seen in the figure, at the constant torque region, all the combinations deliver similar amount of torque.



(a) Torque-speed characteristics of the 36S/38R/12P AIM with different stack length



(b) Power-speed characteristics of the 36S/38R/12P AIM with different stack length

Fig. 3.38 Torque- and power-speed characteristics of the 36S/38R/12P AIM for various stack lengths and number of turns.

On the other hand, at the constant power region, the IM with 110mm has the highest torque whilst the 70mm machine has the minimum. As well known, for an IM with a specific pole number, the lower the number of turns per phase, the better the flux-weakening performance. In the same manner, in order to determine the stack length and number of turns per phase for other S/P combinations, the torque- and power-speed characteristics need to be calculated. Considering Fig. 3.38, it can be concluded that at the flux-weakening region, the IMs having longer stack length generate higher torque due to the low number of turns required. The reason behind this phenomenon has been explained in detail in Section 3.4. As seen in Fig. 3.38, for each stack length a specific number of turns is determined. On the other hand, it is possible to investigate the behaviour of the IM with a specific stack length and different number of turns at constant current density. This method is used for the determination of the number of turns of an IM with a specific stack length used for EV/HEV applications. The influences of the number of turns on the torque- and power-speed characteristics of the AIMS with different S/P combinations are investigated in the next section.

d) Power Losses and Efficiency Maps

In order to investigate the influence of the stack length on the flux-weakening performance of the AIM, the previously designed 18S/20R/6P combination has been employed. The flux-weakening performance of the proposed AIM with 70mm, 90mm, and 105mm have been calculated and then compared by considering the copper loss and efficiency maps as follows. Note that the 105mm stack length is the maximum stack length not exceeding the total axial length restriction of 120mm.

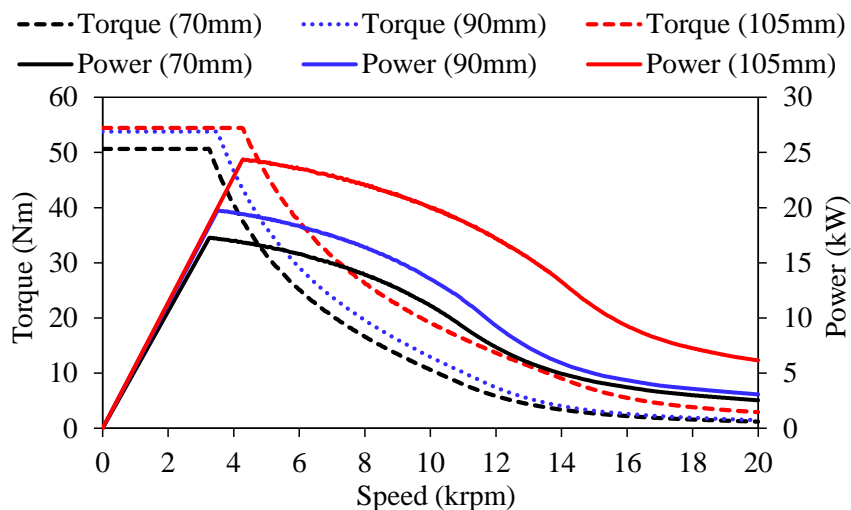
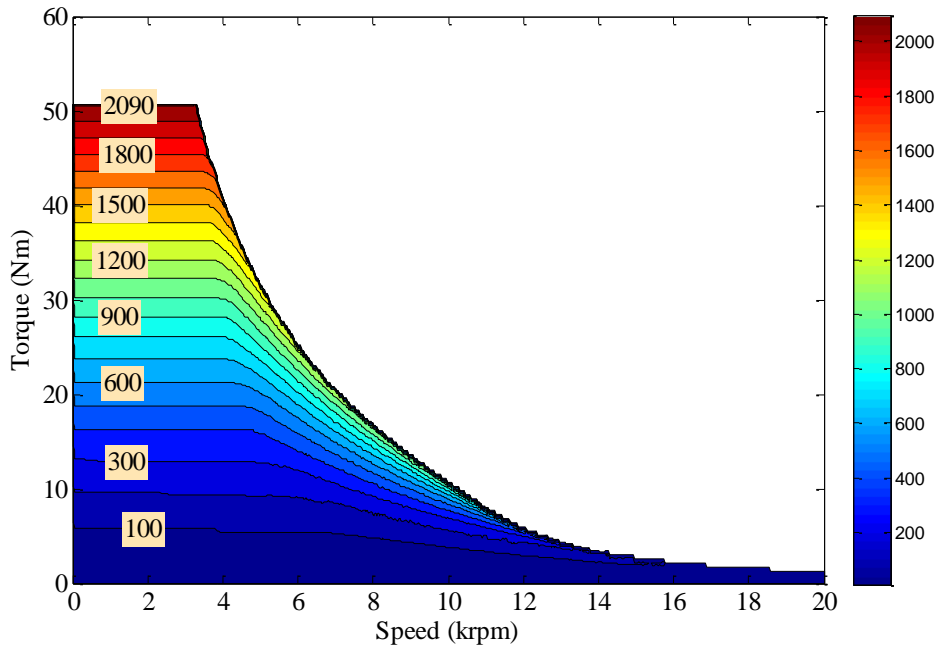


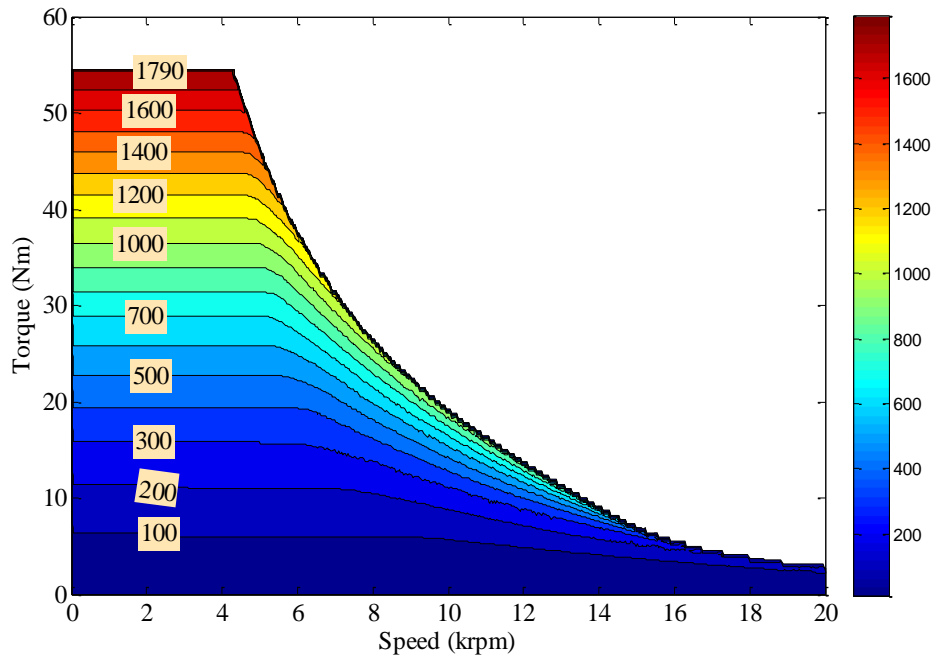
Fig. 3.39 Comparison of the torque- and power-speed characteristics.

The flux-weakening performance of the considered AIMS with different stack lengths have been calculated under the 500Arms and 27Vrms of inverter ratings. The number of turns per phase of 70mm, 90mm, and 105mm are 12, 9, and 8, respectively. The obtained torque- and power-speed characteristics

and power loss and efficiency maps are presented as follows. Torque- and power-speed characteristics of the AIM with 70mm, 90mm, and 105mm have been illustrated in Fig. 3.39. As seen, the flux-weakening characteristics are improved significantly with increasing stack length. It is obvious that the longer the axial length and correspondingly the lower the number of turns per phase, the higher the power at the high-speed operation region. Increasing the stack length from 70mm to 105mm leads to a 41.55% increase in the peak power at the constant power region. Furthermore, the peak power at the deep-flux weakening region (i.e. 20krpm) has been increased by 407.76% once the stack length is increased from 70mm to 105mm.

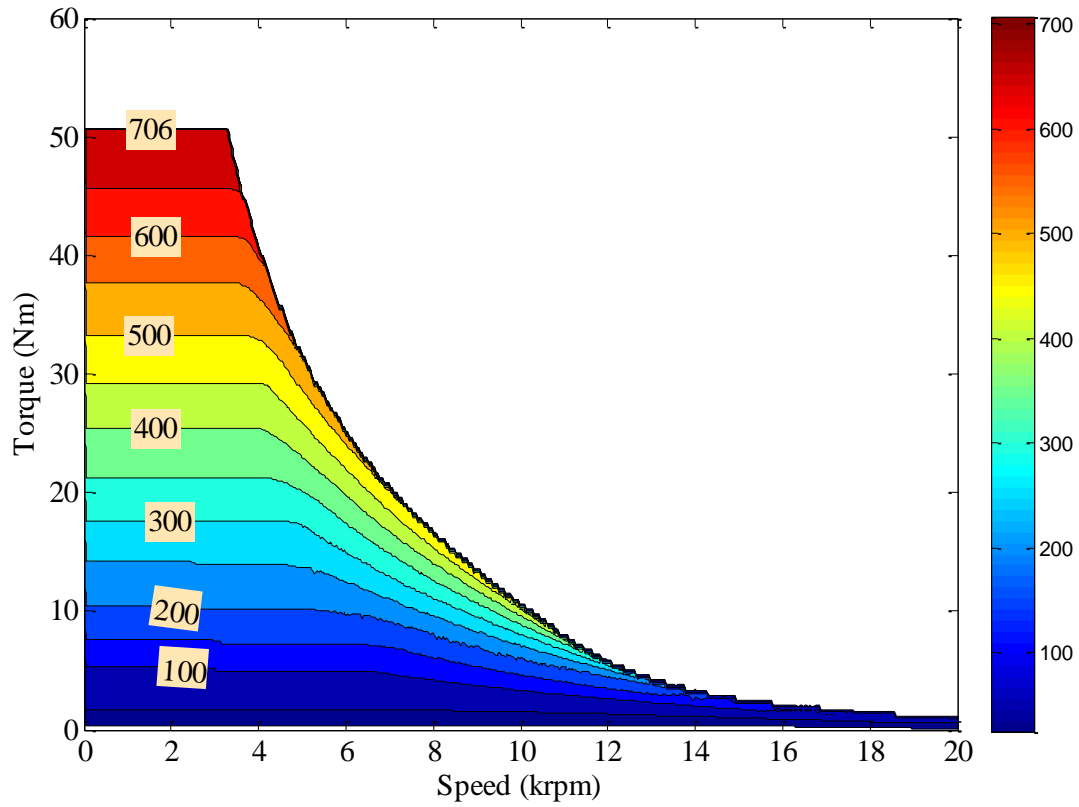


(a) 70mm

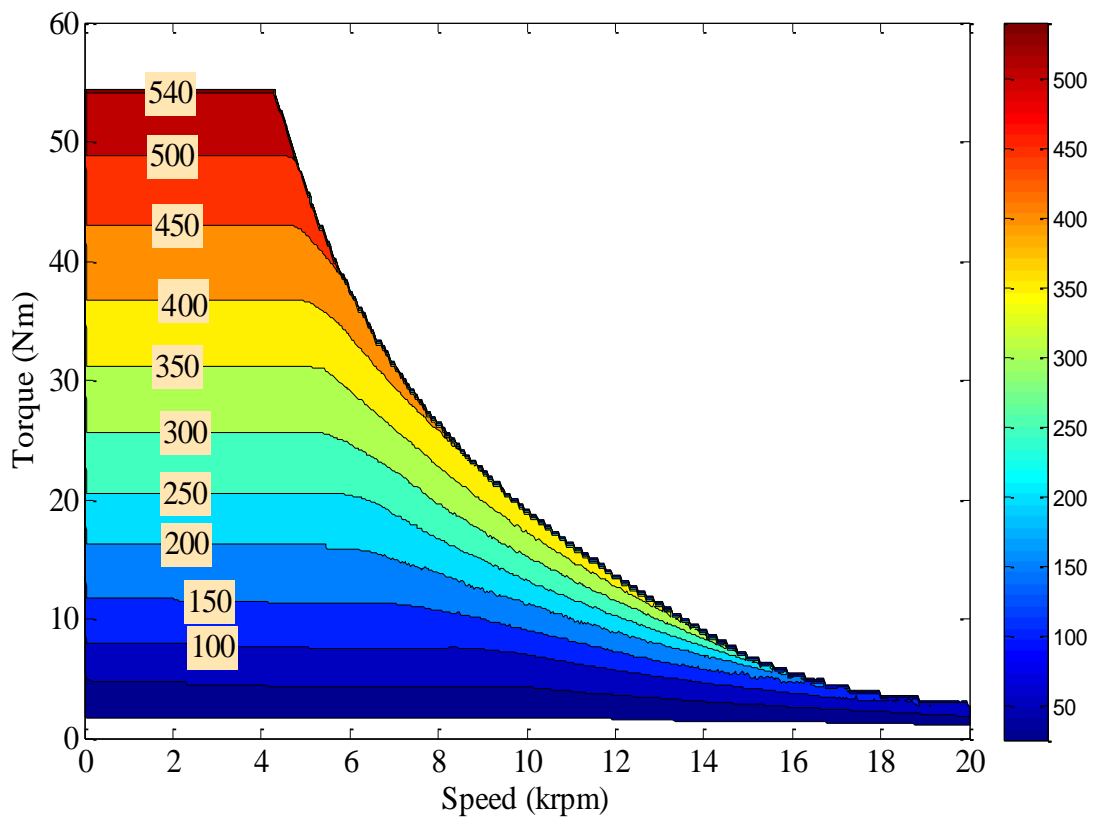


(b) 105mm

Fig. 3.40 Stator copper loss maps of AIMS having different stack length: (a) 70mm and (b) 105mm.

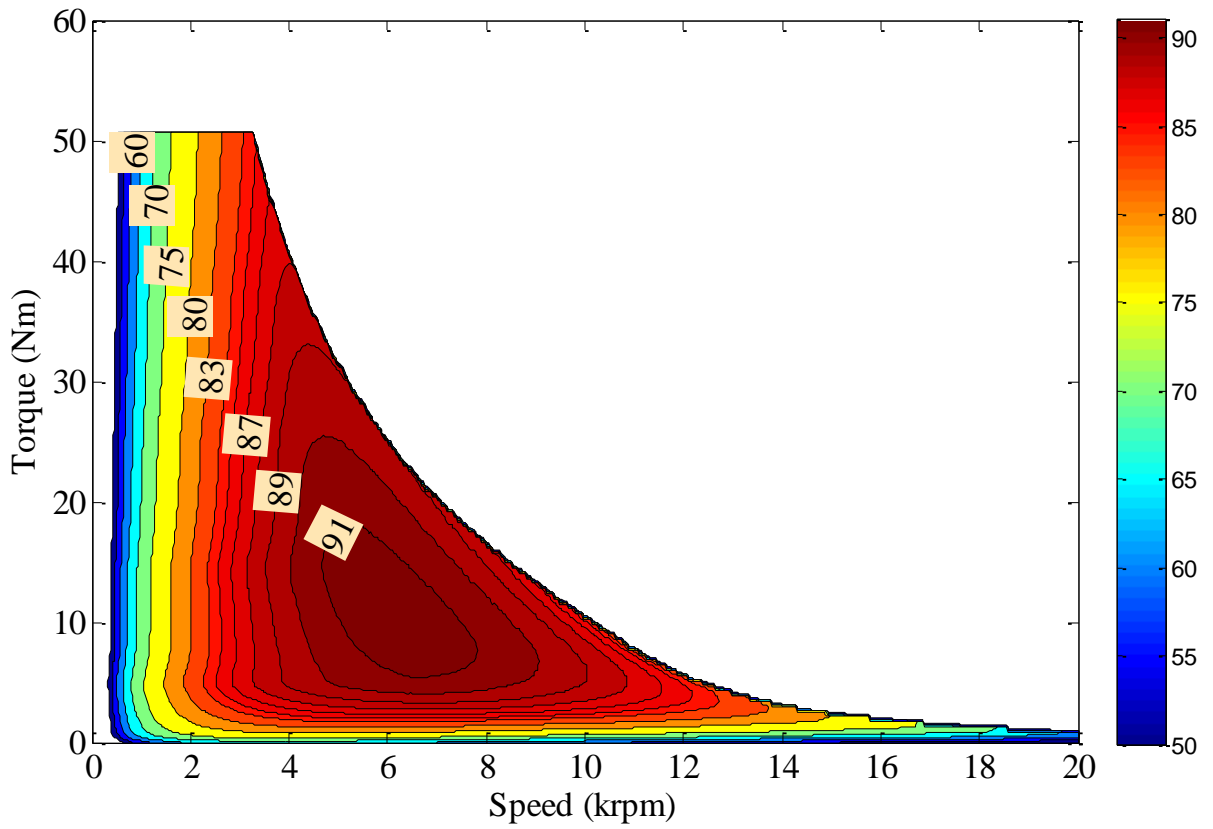


(a) 70mm

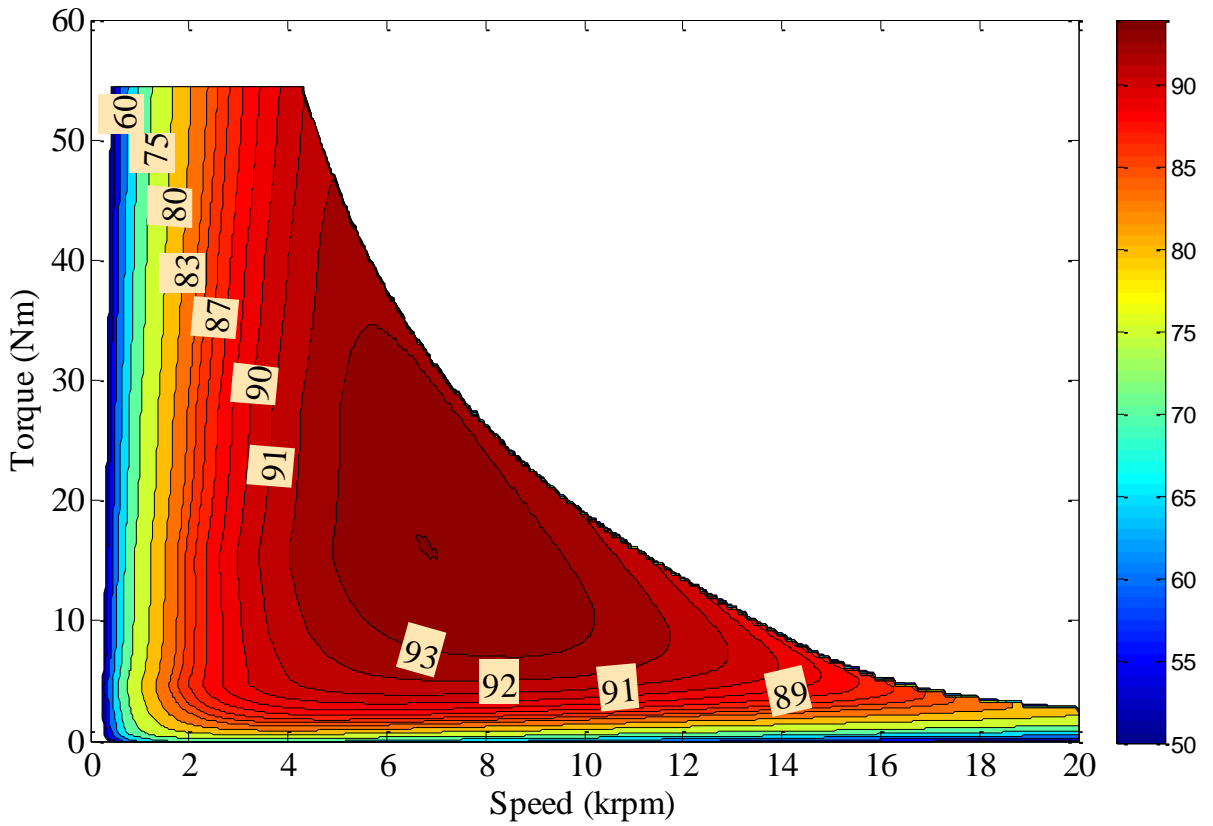


(b) 105mm

Fig. 3.41 Rotor copper loss maps of AIMs having different stack length: (a) 70mm and (b) 105mm.



(a) 70mm



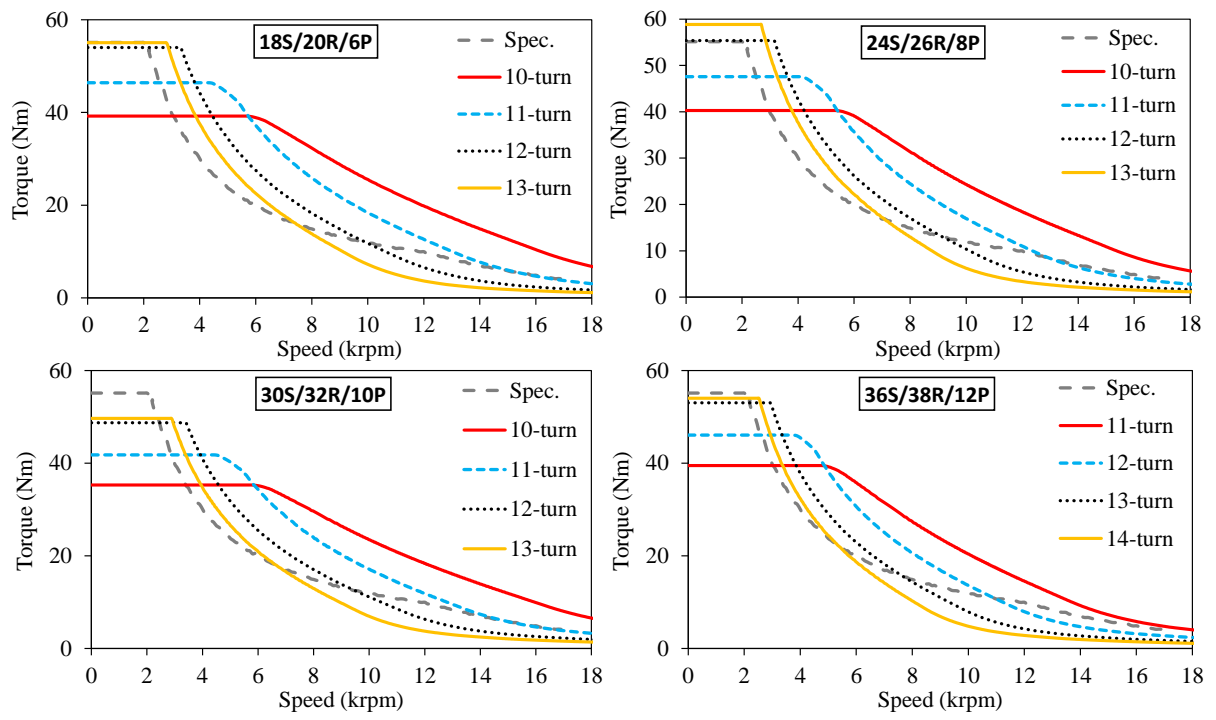
(b) 105mm

Fig. 3.42 Efficiency maps of AIMs having different stack length: (a) 70mm and (b) 105mm.

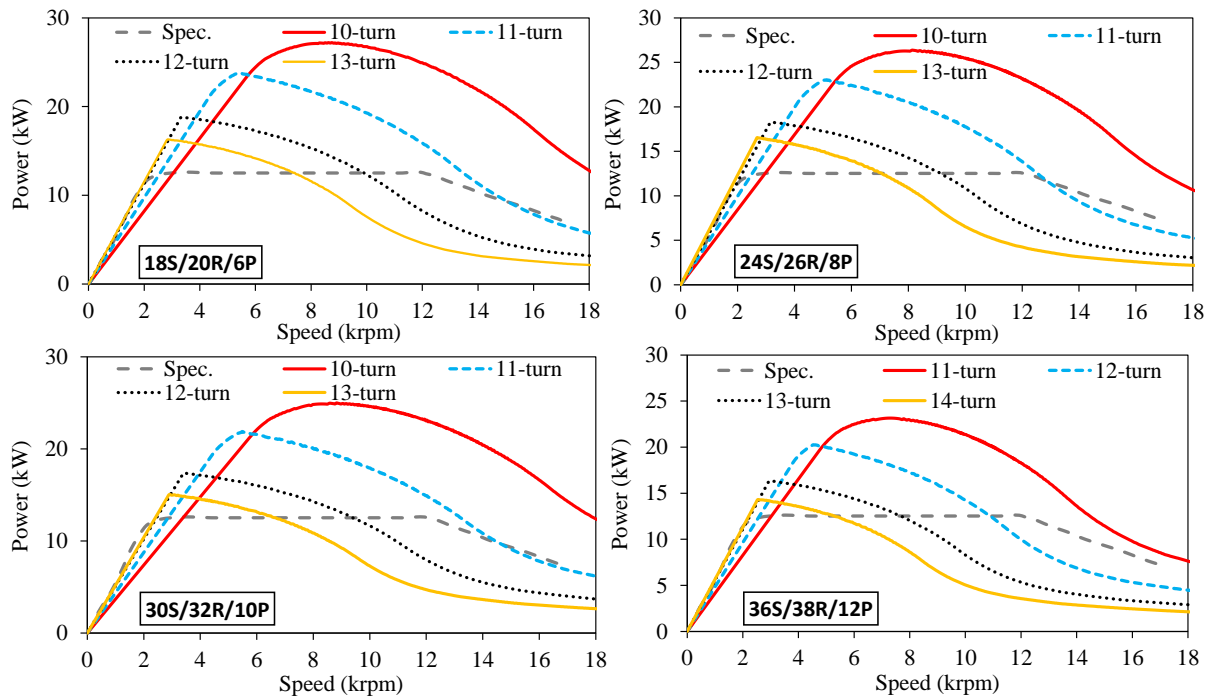
The calculated stator copper loss maps for the minimum (70mm) and maximum (105mm) stack length are illustrated in Fig. 3.40. Note that the stator copper loss maps have been calculated by considering the windings in the stator slots and end-windings. It is obvious from the figure that since the number of turns per phase is reduced, the maximum stator copper loss decreases by 14.35% when the stack length is increased from 70mm to 105mm. The rotor bar copper loss maps are illustrated in Fig. 3.41. As seen, since the high-order bar current harmonics are reduced with increasing stack length, the maximum rotor bar copper loss of the AIM with 105mm of stack length became 23.5% lower than that of the NWIM with 70mm of stack length. The comparison of the efficiency maps is shown in Fig. 3.42. As seen, the overall efficiency is increased significantly by increasing stack length. As seen in Fig. 3.42(a), the peak efficiency of the AIM with 70mm of stack length is 91% between ~5 and ~8krpm. Moreover, the efficiencies above 75% are spread over a large area of the operation region. On the other hand, the maximum efficiency of the AIM having 105mm of stack length is 94% between ~6 and ~8krpm. In addition, the efficiencies above 80% are spread over a large area of the operation region (see Fig. 3.42(b)).

3.4.4 Number of Turns

The number of turns per phase might be determined by considering the stack length, flux-weakening characteristics, and the maximum stator current density allowed. The torque- and power-speed curves of the AIMS with various S/P combinations, number of turns per phase and stack length are calculated by maintaining the stator current density at 31A/mm^2 . In the calculations, previously given current and voltage limits have not been exceeded. In this section, the AIMS having 70mm and 90mm stack lengths have been considered and all the obtained curves have been compared to the torque/power-speed curves specified by Valeo Powertrains Company. Torque/power-speed characteristics of the 70mm and 90mm AIMS with different S/P combinations and number of turns per phase are illustrated in Fig. 3.43 and Fig. 3.44, respectively. As seen, the designs having low number of turns have higher torque at high-speeds. It can be observed from the figures that the longer the stack length, the better the flux-weakening performance. Considering the 70mm AIMS, the best candidate meeting the specified torque- and power-speed characteristics is 18S/20R/6P with 12-turns per phase (see Fig. 3.43). In addition, considering the 90mm AIMS, the best choice meeting the specified torque- and power-speed characteristics is 18S/20R/6P with 9-turns per phase (see Fig. 3.44). Furthermore, comparing the fitness degree between the AIMS with 70mm and 90mm and specified curves, the 90mm design's characteristics fit better than those of the 70mm counterpart.

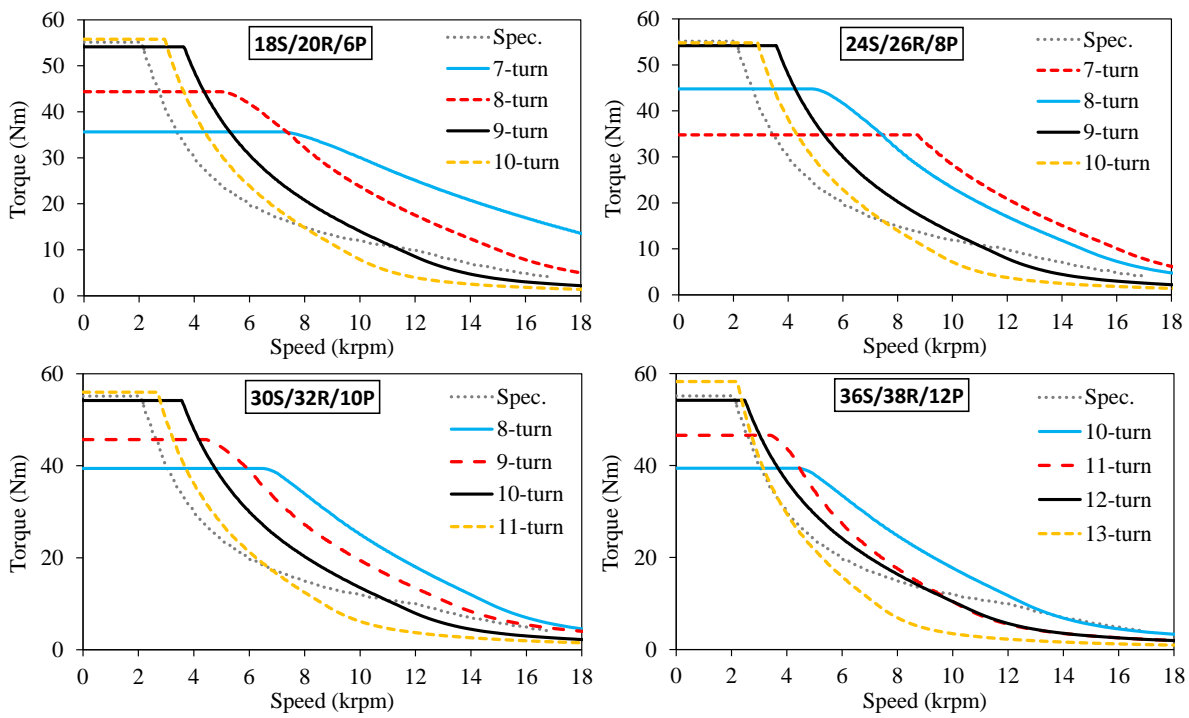


(a) Torque-speed curves for the 70mm AIMs

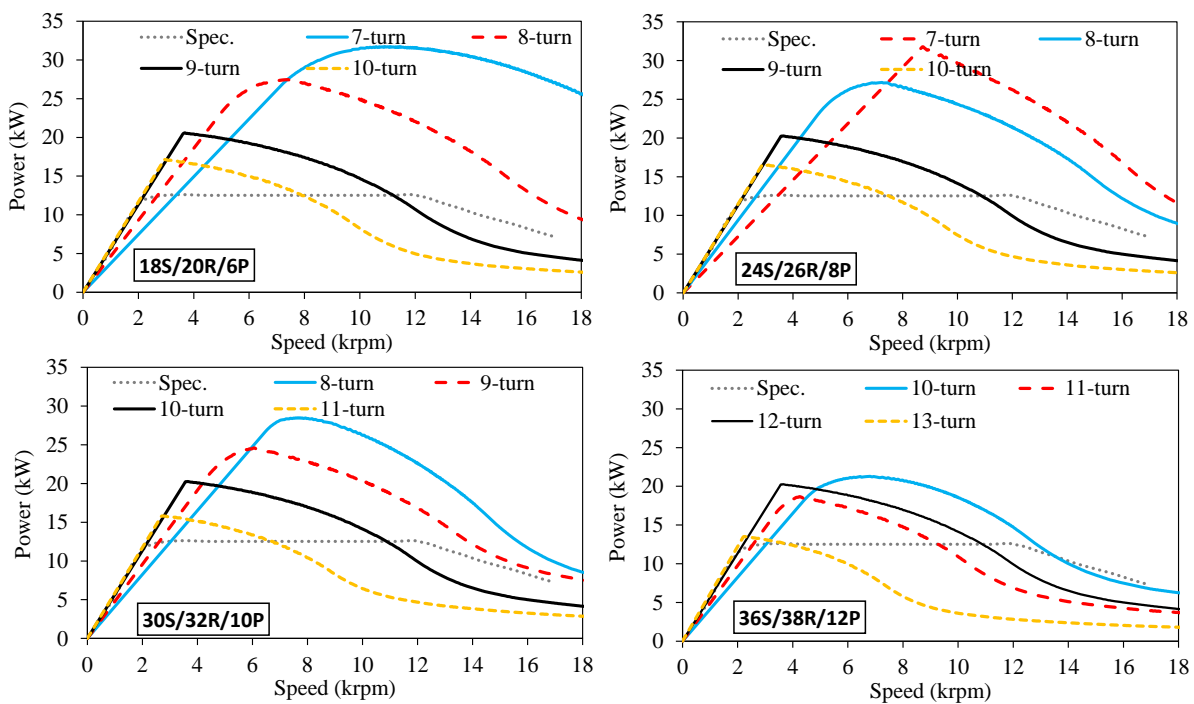


(b) Power-speed curves for 70mm AIMs

Fig. 3.43 Torque- and power-speed characteristics of the 70mm AIMs with different slot/pole number combinations and number of turns per phase.



(a) Torque-speed curves for the 90mm AIMs



(b) Power-speed curves for 90mm AIMs

Fig. 3.44 Torque- and power-speed characteristics of the 90mm AIMs with various slot/pole number combinations and different number of turns per phase.

3.4.5 Stator and Rotor Geometric Parameters

After determining the basic specifications such as S/P combination, rotor slot number, stack length, and number of turns, the influence of the machine geometric parameters on the electromagnetic performance of the machine is investigated. Each parameter, indicated in Fig. 3.45, has been analysed

parametrically and the constraints for the IMs to deliver the maximum available torque has been chosen as the initial geometric parameters. In essence, this progress is very important step before beginning the global optimization progress. Before presenting the details of the investigation into the geometric parameters, some important conditions; such as order or sensitivity, limits of the constraints and parameters, etc. need to be justified [ZHU11]. Therefore, among the geometric parameters, the split ratio λ_s , identified as the ratio of stator inner diameter D_{si} to stator outer diameter D_{so} as given in (3.7), has the first order in sensitivity. The second sensitivity belongs to the stator slot width b_{s12} . As seen in (3.8), b_{s2} parameter is a function of b_{s1} parameter because, for each slot, the slot filling factor is kept constant. In addition, as the type of the winding configuration is non-overlapping, the coil on the top layer should not be overlapped with the coil on the bottom layer. Therefore, the ratio between the top and bottom stator slot heights is defined as given in (3.9). The third sensitivity belongs to the stator slot height. And the fourth and fifth belong to rotor slot width and height parameters, respectively. The other parameters, i.e. slot opening width and height, are the parameters mainly responsible from the flux density harmonics, torque ripple, vibration and acoustic noise. Therefore, if the torque and power density is more important than the parasitic effects, the order of these parameters became less important. During the analyses, the parallel rotor tooth shape are retained. Therefore, as expressed in (3.10) the rotor slot parameters are correlated to each other.

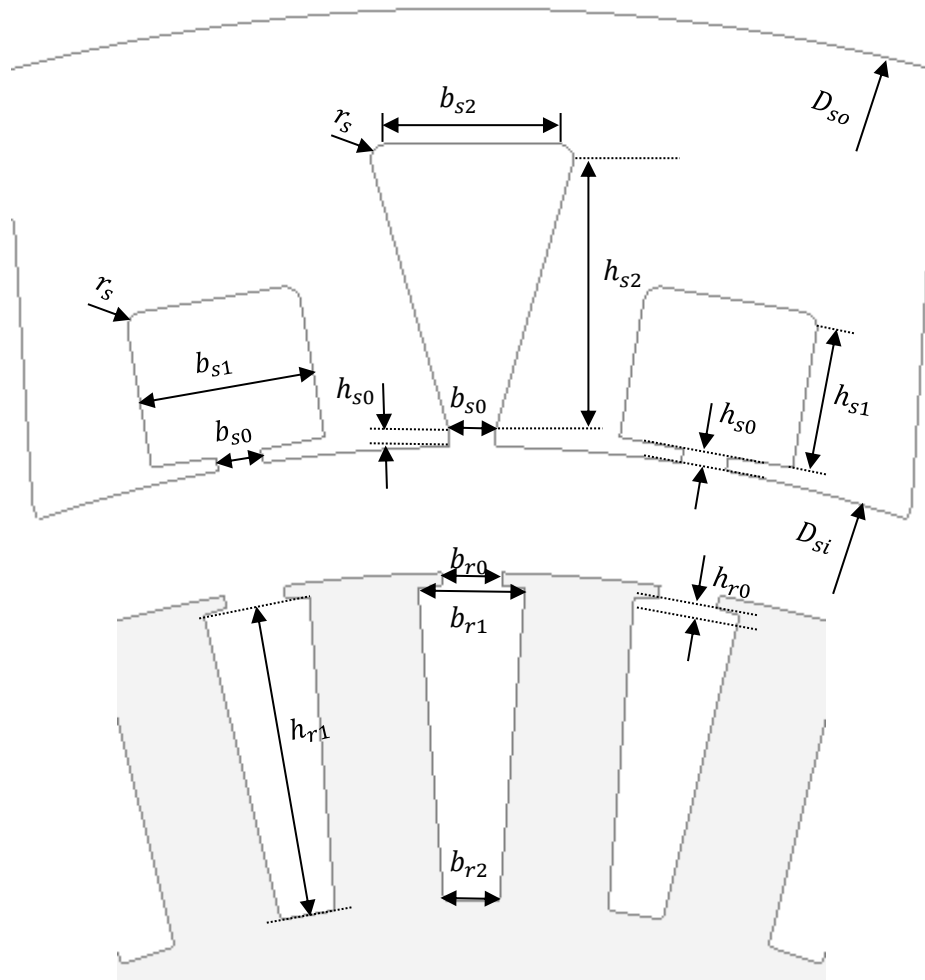


Fig. 3.45 Stator and rotor geometric parameters.

$$\lambda_s = \frac{D_{si}}{D_{s0}} \quad (3.7)$$

$$b_{s12} \rightarrow b_{s1} = f(b_{s2}) \rightarrow b_{s1} = k_s \cdot b_{s2} \quad (3.8)$$

$$\frac{h_{s1}}{h_{s2}} = \frac{1}{2} \quad (3.9)$$

$$b_{r12} \rightarrow b_{r1} = f(b_{r2}) \rightarrow b_{r1} = k_r \cdot b_{r2} \quad (3.10)$$

The influence of the geometric parameters on the electromagnetic performance of all considered AIMs are investigated by 2-D FEA. However, for simplicity, only the results of the 36S/38R/12P NWIM with 110mm is presented in this section. More details related with the geometric parameters and their justifications for optimising can be found in Appendix E.

a) Parametric Analysis of Split Ratio

The variation of the average torque and torque ripple with respect to split ratio is illustrated in Fig. 3.46. As seen in the figure, the peak torque is obtained at 0.753 of the split ratio. Therefore, for the 36S/38R/12P AIM, the initial value of the split ratio can be chosen as 0.753. Moreover, the influence of the split ratio on torque ripple can be negligible.

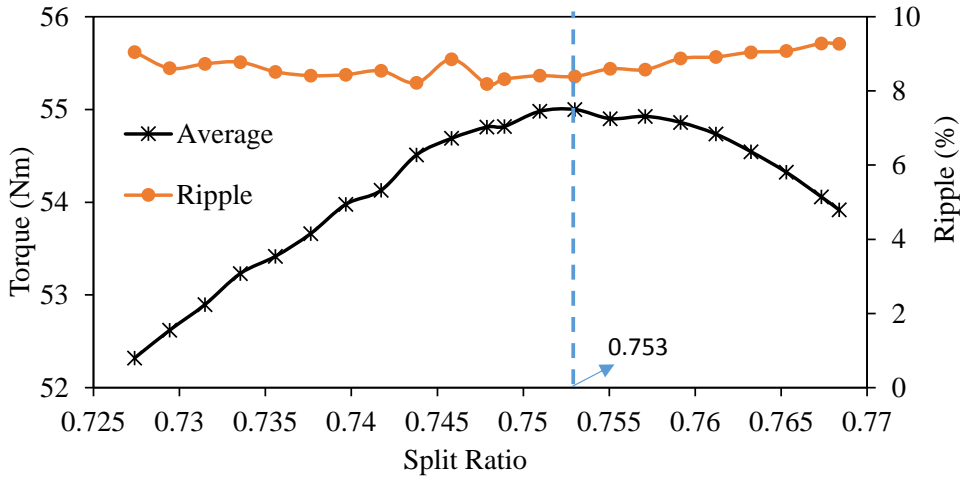


Fig. 3.46 Average torque and torque ripple against split ratio.

b) Parametric Analysis of Stator Geometric Parameters

The influence of the stator and rotor geometric parameters on the average torque, torque ripple, copper loss, and current density are parametrically investigated by 2-D FEA under steady-state operating condition. The influence of the stator slot opening parameter b_{s0} on the average torque, torque ripple, stator copper loss and current density is illustrated in Fig. 3.47. As seen in the figure, the peak torque is achieved at 1.8mm. On the other hand, the torque ripple range reduces considerably whilst the slot opening width increases. Moreover, the influence of the slot opening on the stator copper loss and

current density is negligibly low since the stator slot area is kept constant. The slight reduction in the stator copper loss is due to the slightly reduced harmonic content amplitudes of the stator current.

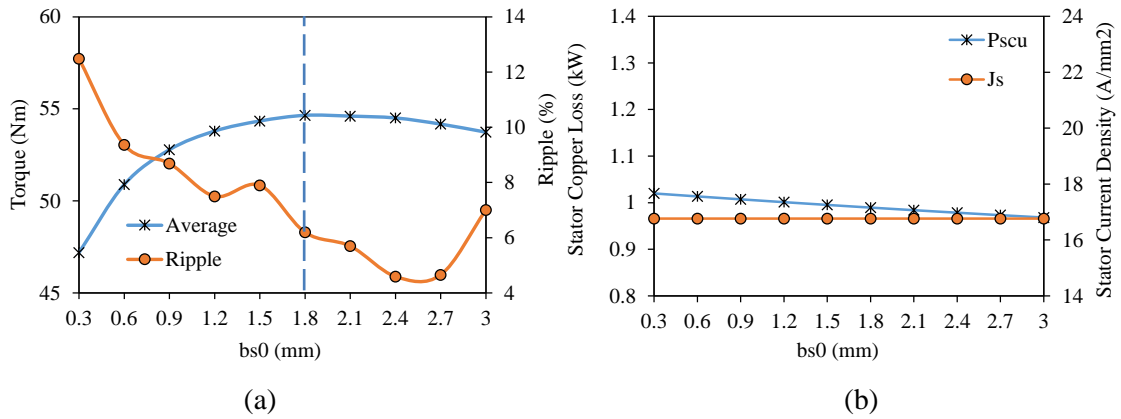


Fig. 3.47 Variation of performance characteristics with respect to b_{s0} : (a) average torque and torque ripple, and (b) stator copper loss and current density.

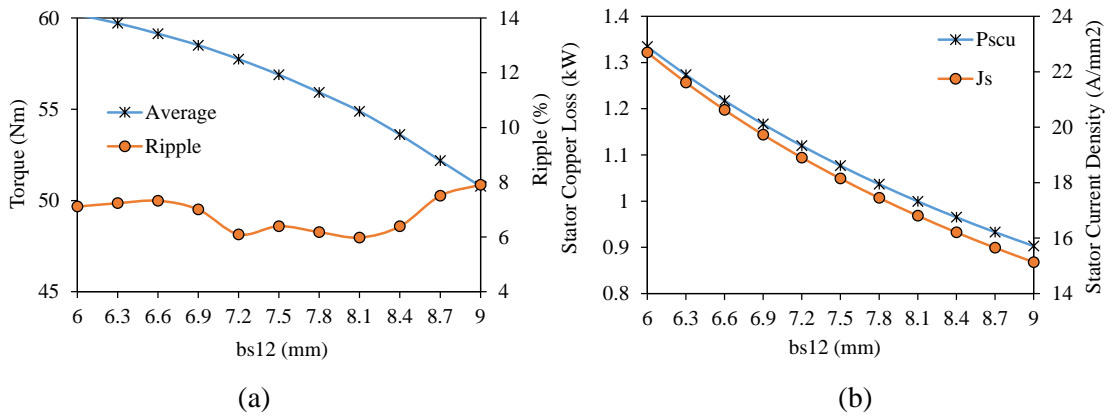


Fig. 3.48 Variation of performance characteristics with respect to b_{s12} : (a) average torque and torque ripple, and (b) stator copper loss and current density.

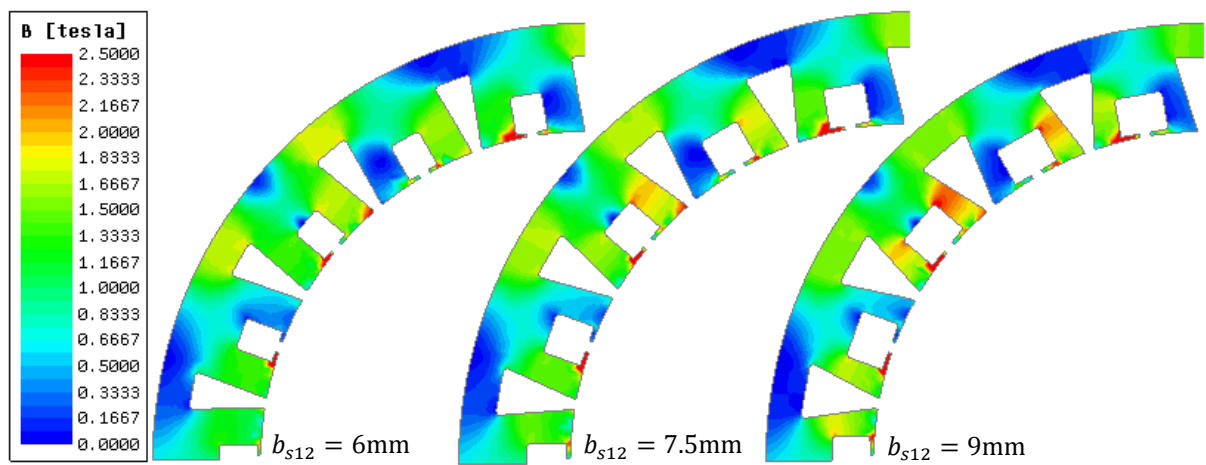


Fig. 3.49 Variation of flux density with stator slot width b_{s12} .

The influence of the stator slot width b_{s12} on some key performance characteristics is illustrated in Fig. 3.48. As seen in Fig. 3.48(a) the narrower the stator slot, the higher the average torque. This is

because of the reduction of the saturation level of the stator tooth parts as seen in Fig. 3.49. On the other hand, the variation of torque ripple range is not considerably high. Since the slot area is changed significantly, the variation of stator copper loss and current density is significantly high as seen in Fig. 3.48(b). As expected, the larger the slot area, the lower the winding resistance and the lower the copper loss. As seen in Fig. 3.50(a), the stator slot-opening height parameter h_{s0} has also a considerable effect on the torque and torque ripple. On the other hand, since the stator slot area is not changed, the stator copper loss and current density do not change (see Fig. 3.50(b)). Influences of the stator slot height parameter h_{s12} on key performance characteristics are illustrated in Fig. 3.51. For the dimensions larger than 5mm of h_{s12} , the average torque starts to reduce whilst the torque ripple range starts to increase. The torque reduction is due to the increase in the level of rotor tooth saturation. On the other hand, as seen in Fig. 3.51(b), since the slot area is increased, the stator copper loss and current density decreases as the stator slot width parameter increases.

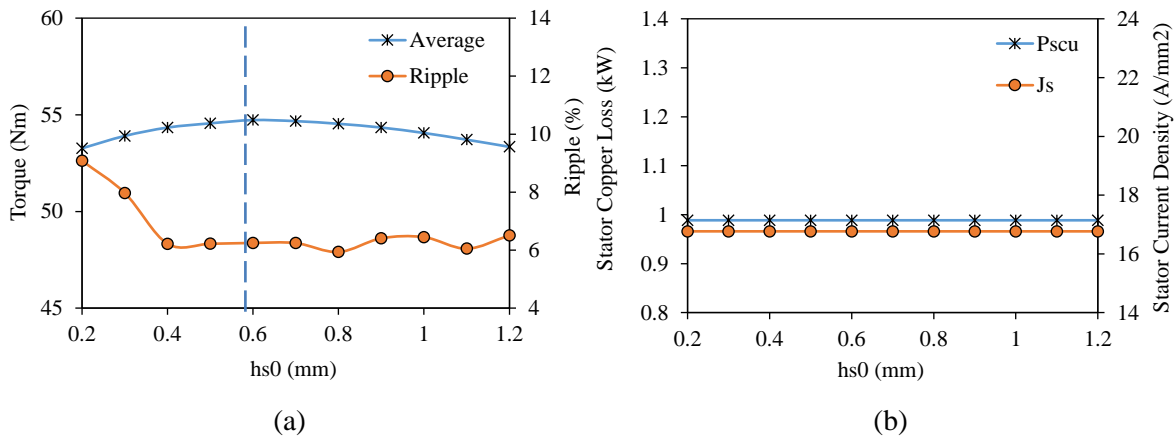


Fig. 3.50 Variation of performance characteristics with respect to h_{s0} : (a) average torque and torque ripple, and (b) stator copper loss and current density.

The influence of rotor geometric parameters on some key performance characteristics of the 36S/38R/12P AIM with 110mm is investigated by 2-D FEA under steady-state operating condition. After several parametric analyses, the obtained results are presented between Fig. 3.52 and Fig. 3.55. The influence of rotor slot opening width parameter b_{r0} on the average torque, torque ripple, bar copper loss and bar current density is illustrated in Fig. 3.52. As seen, the rotor slot-opening parameter has a significant influence on the torque and torque ripple. As seen in Fig. 3.52(b), the larger the rotor slot width, the higher the rotor bar copper loss and the bar current density. The reason behind this phenomenon will be explained in Chapters 5 and 6 in detail. Since the rotor tooth parts act as filter, the smaller the slot-opening width, the more the high-order harmonics are cancelled. On the other hand, since smaller slot opening causes an increase of the magnitude of short-circuited flux, the level of the average torque decreases as seen in Fig. 3.52(a). Therefore, 2.2mm rotor slot opening width is chosen as the initial value.

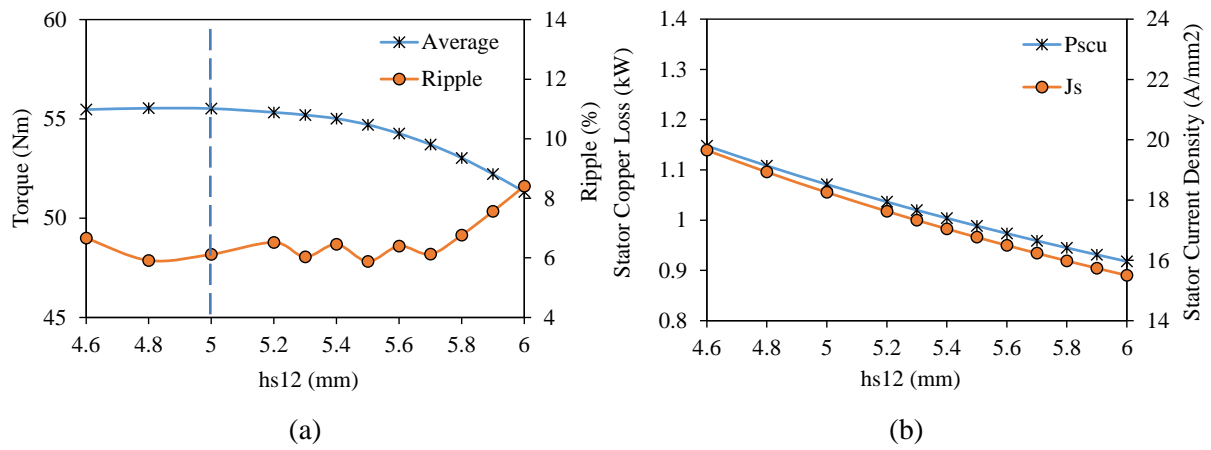


Fig. 3.51 Variation of performance characteristics with respect to h_{s12} : (a) average torque and torque ripple, and (b) stator copper loss and current density.

c) Parametric Analysis of Rotor Geometric Parameters

The influence of rotor slot width b_{r12} on the average torque and torque ripple is significant as shown in Fig. 3.53(a). The larger the rotor slot width, the lower the torque ripple. Since the induced bar current has not changed considerably, the rotor bar copper loss has also not changed significantly (see Fig. 3.53(b)), although the bar current density decreases as the rotor slot width and hence the slot area is increased. b_{r12} is selected as 3.8mm as indicated in Fig. 3.53(a). The rotor slot-opening height h_{r0} has also a considerable influence on the average torque and torque ripple as shown in Fig. 3.54(a). Whilst the average torque reduces as the slot-opening height is enlarged, the torque ripple decreases. On the other hand, as the slot-opening height is enlarged, the rotor bar copper loss decreases significantly whilst the bar current density decreases slightly. Although the slot area and the magnitude of the bar current are not changed considerably, the bar current harmonics are changed significantly as explained previously during the investigation of b_{s0} . The determined initial rotor slot-opening height is indicated in Fig. 3.54(a).

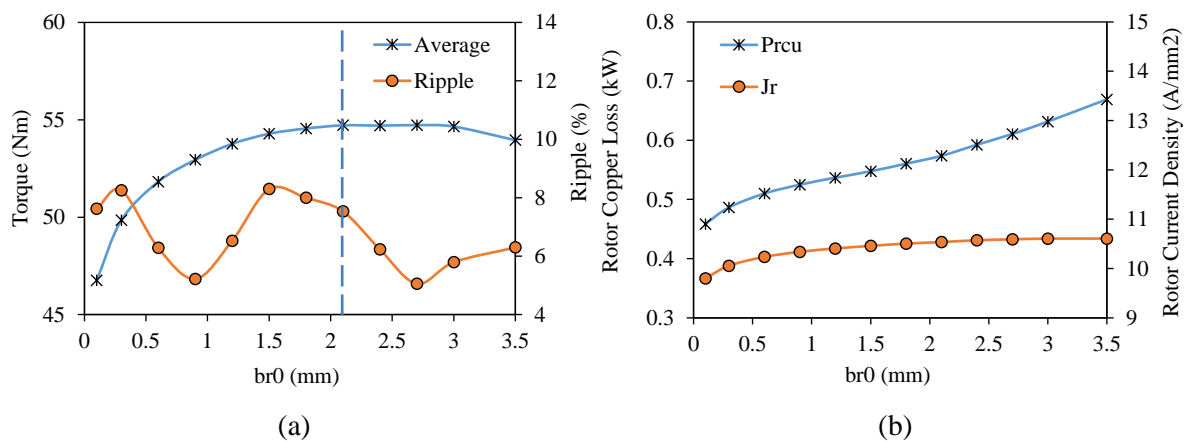


Fig. 3.52 Variation of performance characteristics with respect to b_{r0} : (a) average torque and torque ripple, and (b) stator copper loss and current density.

The influences of rotor slot height h_{r1} on the performance characteristics are illustrated in Fig. 3.55. As seen, as the rotor slot height is increased, the torque ripple reduces significantly. The peak torque is achieved at 9.5mm of the slot depth (see Fig. 3.55(a)). The influence of the rotor slot depth on the bar copper loss is not remarkable as seen in Fig. 3.55(b). On the other hand, as the slot height is increased, the current density decreases since the slot area is increased. This is because of the fact that although the magnitude of the bar current is kept almost constant, the current harmonic content is increased significantly. Therefore, even if the bar resistance is decreased with increased slot area, the bar copper loss has not changed significantly whilst the current density decreases considerably. It is possible to change the type of the rotor by changing the rotor slot opening parameters. For instance, if b_{r0} equals to zero, then the rotor type will be closed slot cast-rotor. The influence of rotor type on the performance and flux-weakening characteristics will be investigated in Chapter 4. In addition, for various rotor types, the influences of rotor slot opening parameters on the electromagnetic and flux-weakening characteristics are investigated in Appendix F.

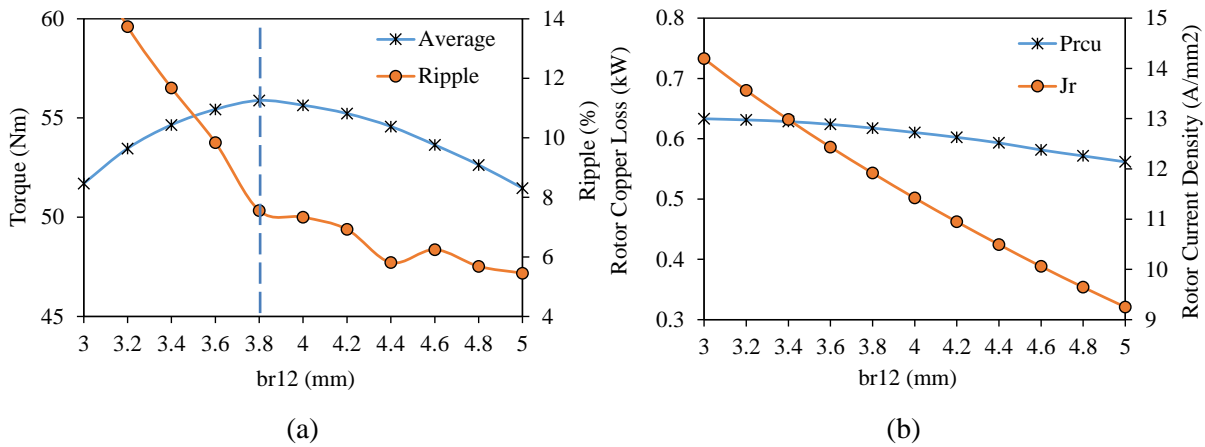


Fig. 3.53 Variation of performance characteristics with respect to b_{r12} : (a) average torque and torque ripple, and (b) stator copper loss and current density.

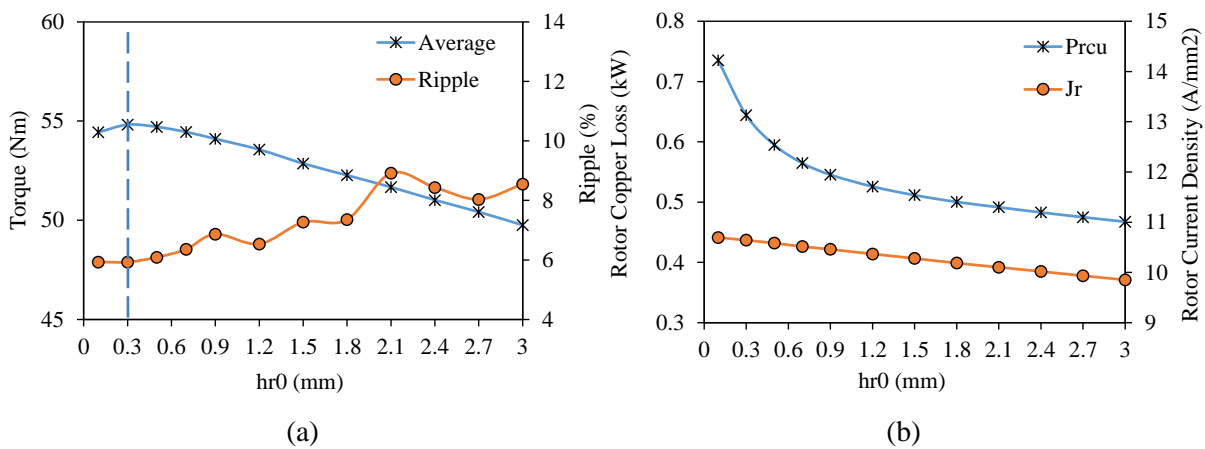


Fig. 3.54 Variation of performance characteristics with respect to h_{r0} : (a) average torque and torque ripple, and (b) stator copper loss and current density

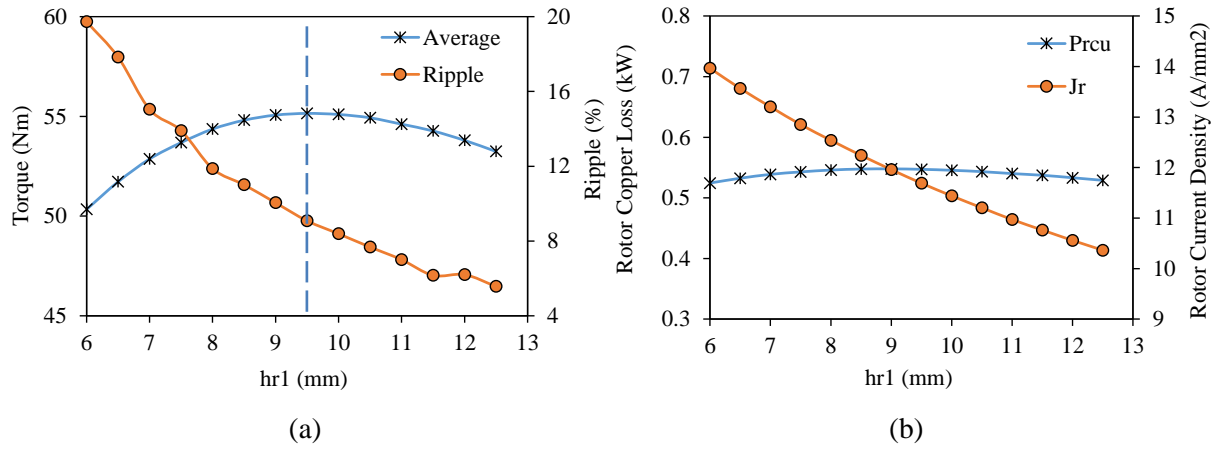


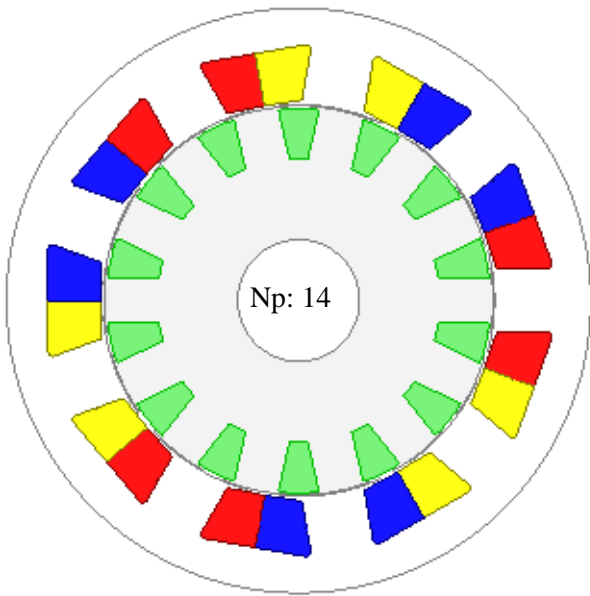
Fig. 3.55 Variation of performance characteristics with respect to h_{r1} : (a) average torque and torque ripple, and (b) stator copper loss and current density.

3.5 Optimization of Advanced Non-Overlapping Winding Induction Machines

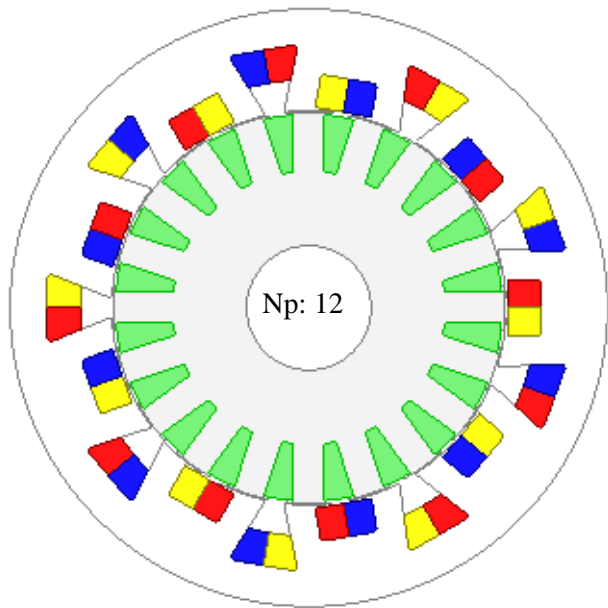
A comprehensive design optimization guidelines for AIMs by considering different optimization approaches, namely individual optimization, global optimization with single- and multi-objective analyses are presented in Appendix E in detail. The Genetic Algorithm (GA) approach, an effective optimization tool extensively used for the optimization of IMs, has been employed for global optimization. Note that an alternative stator slot structure, namely zig-zag slot, has also been considered for the optimization. The AIMs with straight and zig-zag stator slot structures are initially designed and a 2-D FEA based optimization program has been employed in order to perform the optimizations and evaluate the optimal solutions. The effectiveness of each optimization approach has been compared in terms of time consumption, error cost, restrictions, etc. After the optimization procedures, the key performance characteristics of the initially designed IMs and IMs with optimal solutions will be compared.

3.6 Comparison between Advanced and Conventional Induction Machines

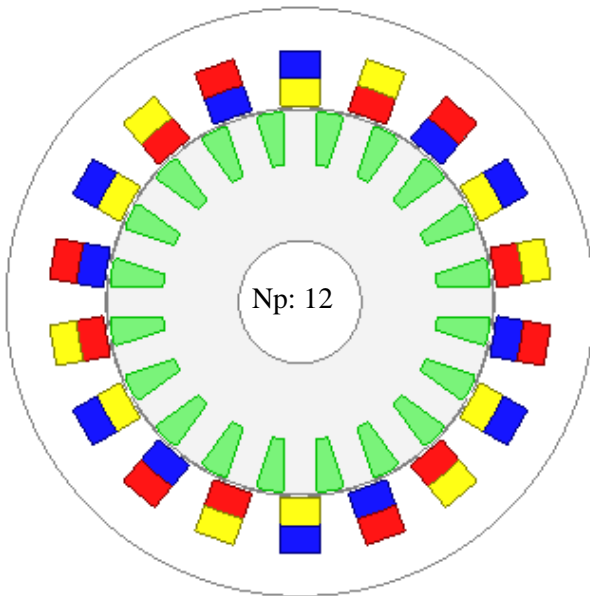
In order to reveal the advantages/disadvantages of the proposed method, IMs designed with different winding topologies such as; FSCW, ISDW with short- and long-slot pitches have been compared to the proposed ANW topology. For a fair comparison, the improved AIM (indicated as “D” in the previous section) has been optimized globally by using the multi-objective optimization method explained in Appendix E. In addition, as presented in Chapter 2, all other machines have been globally optimized. All machines designed by using the same geometric specifications i.e., 144mm outer diameter and 70mm stack length and also using the same operation specifications i.e., 500Arms (100Hz) current excitation and 2krpm synchronous speed. Furthermore, the determined turn number per phase N_p for each IM is given in Fig. 3.56.



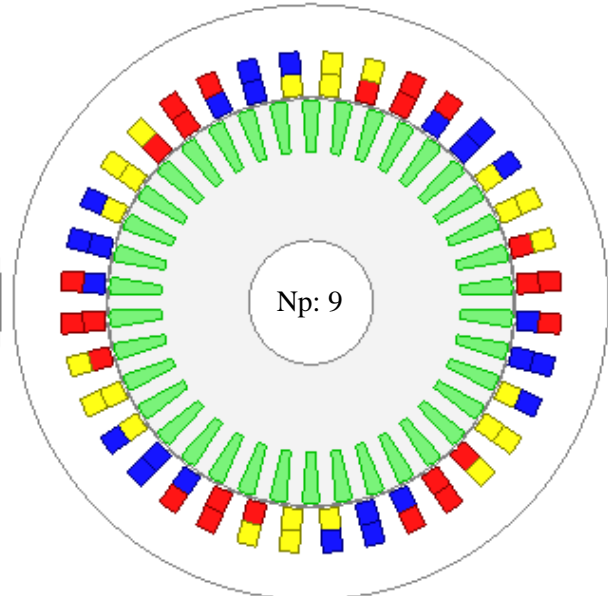
(a) 9S/6P/14R-DL ($y_c = 1$)



(b) 18S/6P/20R-DL ($y_c = 2$ -ANW)

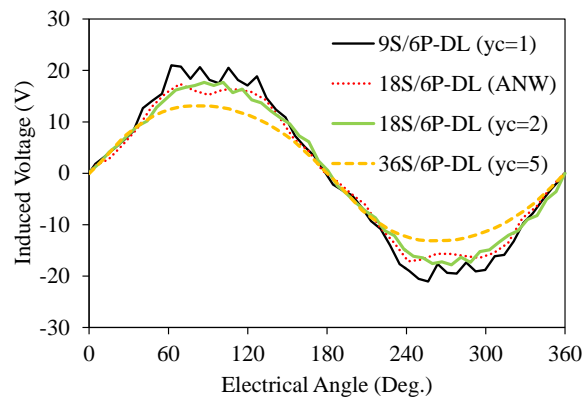


(c) 18S/6P/20R-DL ($y_c = 2$)

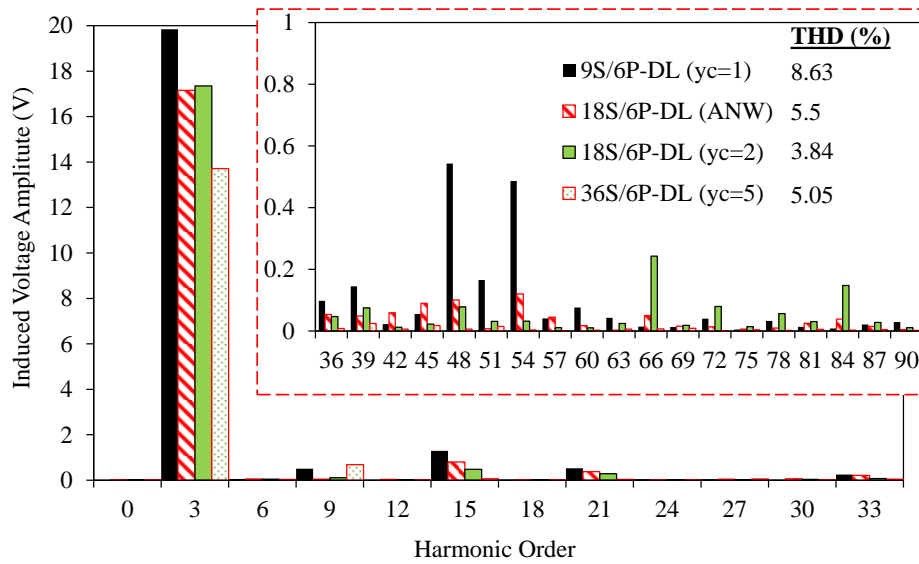


(d) 36S/6P/38R-DL ($y_c = 5$)

Fig. 3.56 Comparison of the IMs designed with the FSCW, ANW, and ISDWs.

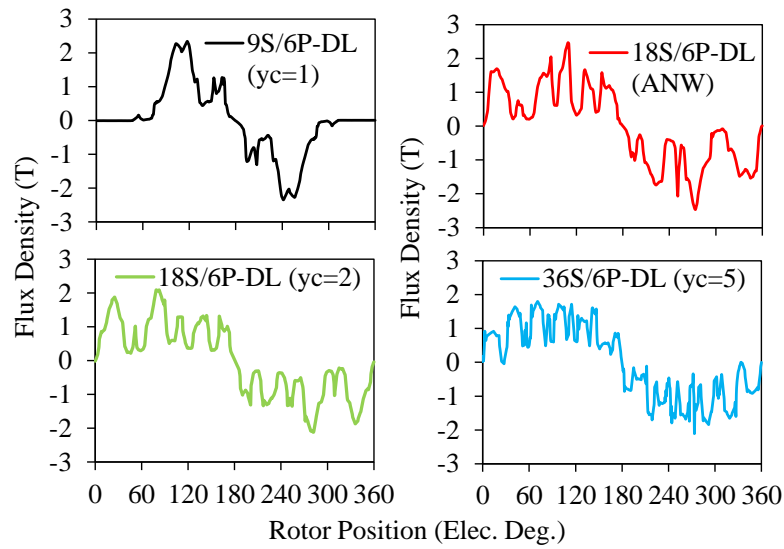


(a)

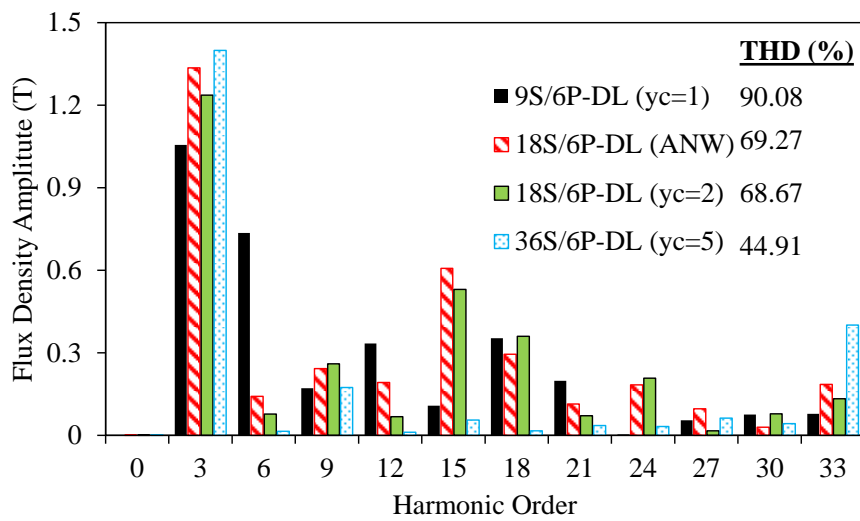


(b)

Fig. 3.57 Phase 'A' induced voltage: (a) waveform and (b) harmonic spectra.



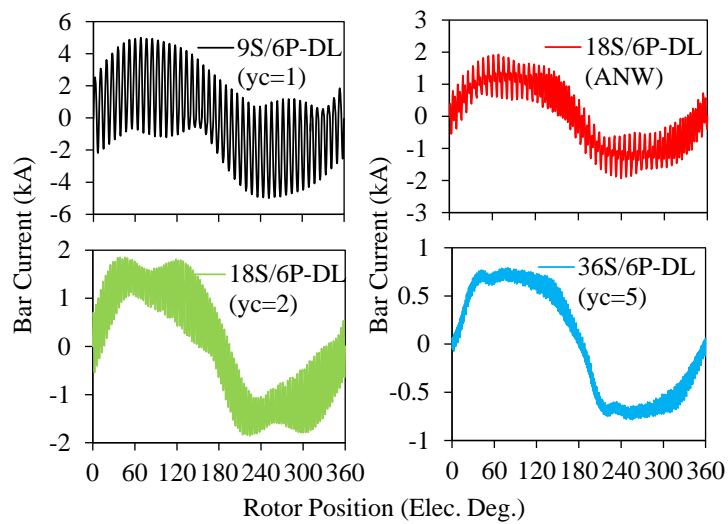
(a)



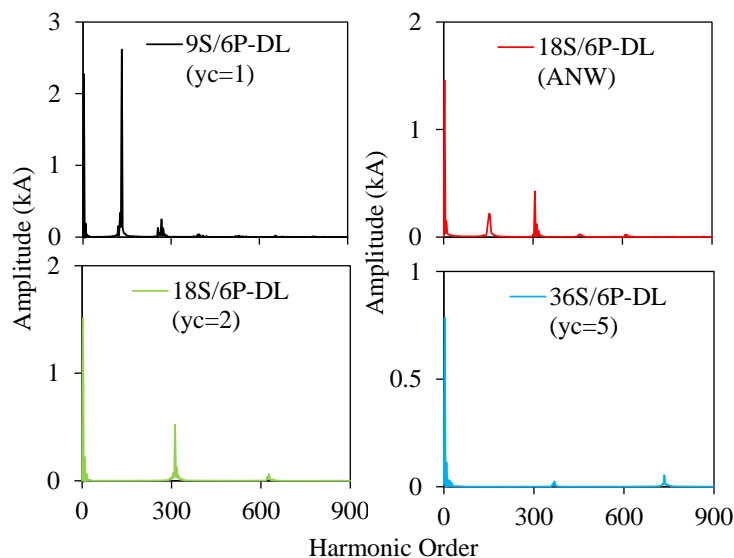
(b)

Fig. 3.58 Air-gap flux density: (a) waveform and (b) harmonic spectra.

As seen in Fig. 3.56, the winding structures of (a) and (b) consist of non-overlapping double-layer windings whilst (c) and (d) consist of overlapping double-layer windings. In essence, the full slot area is utilized in (c) but it is the end winding overlapped version of (b). When q is considered, (a) belongs to the FSCW family whilst the others belong to the ISDW family. The rotor slot numbers have been estimated by $R \approx S + 2q$. In order to numerically calculate the performance characteristics of the considered IMs, a 2-D FEA model of each IM has been built and the time-stepped analyses have been employed. The obtained steady-state characteristics have been presented as follows. Induced voltage waveforms for stator phase 'A' winding are illustrated in Fig. 3.57(a). As clearly seen in the figure, since the 9S/6P IM's turn number per phase is larger than the other IMs', its induced voltage amplitude is higher as seen in Fig. 3.57(b). However, as clearly seen in Fig. 3.57(b), the 9S/6P IM's waveform contains a large number of higher order harmonics because of the highly distorted MMF waveform. Therefore, its induced voltage THD is larger than that of the other IMs. The induced voltage distortion levels of the ISDWIMs are similar to each other.



(a)



(b)

Fig. 3.59 Rotor bar current: (a) waveform and (b) harmonic spectra.

The variation of air-gap flux density with rotor position is illustrated in Fig. 3.58(a). As seen in the figure, since the 9S/6P IM has quite high space harmonic index, its air-gap flux density is the most distorted one. On the other hand, the air-gap flux density waveforms of the 18S/6P IMs are similar to each other but also more distorted than the 36S/6P IM. The air-gap flux density harmonic spectra and THD levels are shown in Fig. 3.58(b). As seen in the figure, even if the 9S/6P IM has the highest number of turns per phase, due to the increased saturation level because of the high space harmonic index, the magnitude of the air-gap flux density is lower than the other IMs. On the other hand, since the space harmonic index of 36S/6P IM is lower than the IMs, its THD level is the lowest. Therefore, it can be predicted that since the air-gap flux density induces voltage in the rotor bars and hence the bar current due to the short-circuited conductor bars, the distortion level of the bar current will be the maximum for 9S/6P FSCW IM whilst being minimum for the 36S/6P ISDW IM. The rotor bar current waveforms are illustrated in Fig. 3.59(a).

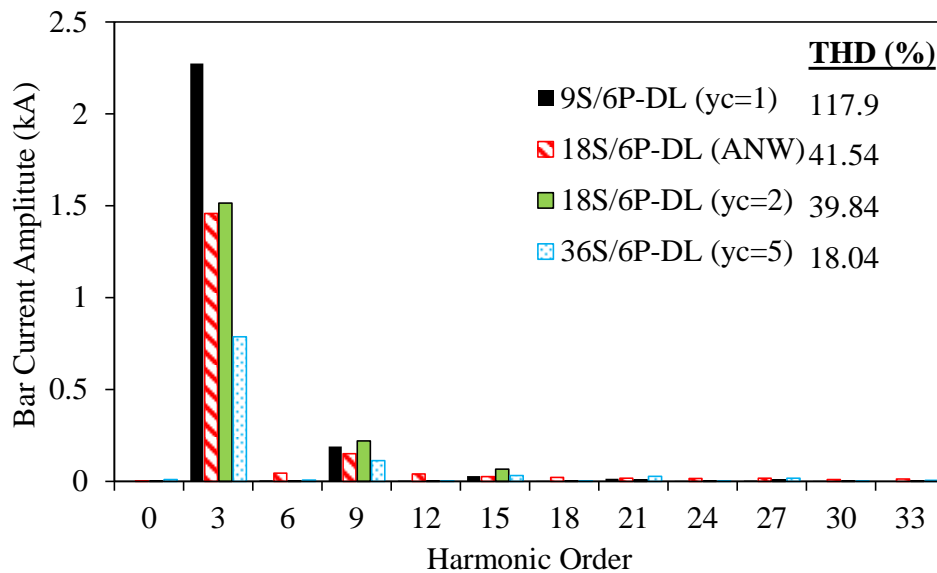


Fig. 3.60 Low order harmonics of bar current waveforms.

As predicated from the air-gap flux density waveforms, the distortion level of the 9S/6P FSCW IM is significant because of the very large number of MMF harmonics. On the other hand, the level of distortion is reduced in the ISDW IMs because of the lower MMF harmonics. As clearly seen from the waveforms and harmonic spectra (see Fig. 3.59(b)), bar current contains very high order harmonics. This is because of the recursive induction phenomenon occurred on the rotor bars. On the other hand, as seen in Fig. 3.59(a), the waveforms of the 18S/6P IMs and 36S/6P IM seem like trapezoidal or flat tapped. Generally, under the health operation conditions, the bar current waveform of an IM is assumed as sinusoidal. However, as seen in the figures, the obtained bar current waveforms are non-sinusoidal. The reason behind this phenomenon will be investigated and explained in Chapters 5, 6, and 7. The harmonic spectra of bar current waveform showing the high order and low order harmonics are illustrated separately in Fig. 3.59(a) and Fig. 3.60(b), respectively. As seen from the harmonic spectra of the 9S/6P IM, because of the highly distorted MMF waveform, the magnitude of the 132nd harmonic

order is larger than that of the fundamental harmonic. The amplitude of the fundamental harmonic and THD levels of the IMs are compared to each other in Fig. 3.60. As expected, whilst the 36S/6P ISDWIM has the minimum bar current THD, the 9S/6P FSCWIM has the maximum bar current THD. Moreover, the 18S/6P IMs show similar characteristics in terms of bar current waveform distortion. In addition, the amplitude of the bar current of the 9S/6P FSCWIM is 3 times larger than that of the 36S/6P ISDWIM. Therefore, it can be predicted that assuming the rotor bar resistance is similar, the rotor bar copper loss of the 9S/6P FSCWIM will be almost 6 times higher than that of the 36S/6P ISDWIM. In the same manner, it will be ~ 3 times larger than that of the 18S/6P ISDWIMs. The flux line and density distributions of the considered IMs are illustrated in Fig. 3.61. It can be seen that the saturation level of the non-overlapping winding IMs is higher than that of the IMs having overlapping windings. Especially, the stator tooth parts have been saturated highly.

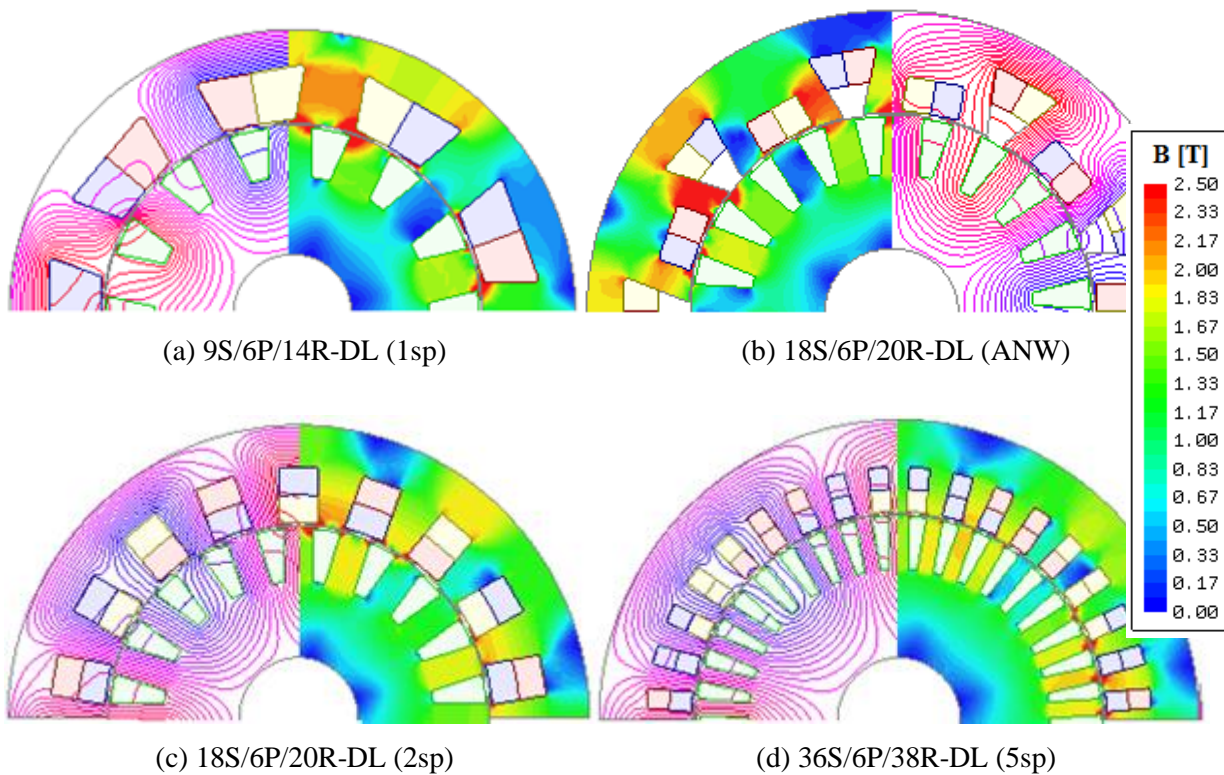


Fig. 3.61 Flux line and density distributions.

Other calculated performance characteristics are summarised in Table 3.3. As shown previously, the 18S/6P IMs have quite similar characteristics. Considering the winding-layout of these IMs, it can be realized that their coil distributions and polarizations are the same (see Fig. 3.56(b) and (c)). Therefore, it is reasonable to imagine that the 18S/6P/20R-DL ($y_c = 2$) IM is the fully filled slots version of the 18S/6P/20R-DL (ANW). It is found that by adopting the ANW topology, $\sim 27.1\%$ reduction in the total axial length has been achieved without sacrificing the torque, power, and efficiency according to its overlapping counterpart.

The main disadvantage of the proposed method is that it causes a very high torque ripple. However, the torque ripple can be reduced significantly by changing the rotor slot structure as presented in Chapter

4. In addition, thanks to proposed method, a significant reduction in stator end-winding copper loss, rotor bar copper loss and rotor bar copper density has been achieved. It is also validated that since the 36S/6P/39R-DL ($y_c = 5$) ISDWIM has the lowest MMF distortion, its overall performance is the best. The main disadvantage of this IM is that because of the very short end-windings, the total axial length is significantly long. Considering the limited space in the EV/HEV applications, the compactness is of great importance. Therefore, if a slight reduction in torque, power and efficiency is acceptable, it is possible to shorten the total axial length $\sim 25\%$ according to 36S/6P/38R ($y_c = 5$) thanks to the proposed NWW method.

Table 3.3 Comparison of the performance characteristics of the considered IMs

Parameter	9S/6P/14R- DL ($y_c = 1$)	18S/6P/20R- DL (ANW)	18S/6P/20R- DL ($y_c = 2$)	36S/6P/38R- DL ($y_c = 5$)
Number of turns per phase	14	12	12	9
Fundamental winding factor	0.866	0.866	0.866	0.933
Total axial length (mm)	94.15	83.4	114.4	111.16
Phase resistance (m Ω)	2.391	2.367	2.5094	2.0836
Torque (Nm)	43.613	54.01	52.33	54.1
Torque ripple (%)	28.8	18.14	9.11	3.88
Stator in-slot copper loss (kW)	1.195	1.09	1.0145	0.7614
Stator end-winding copper loss (kW)	0.598	0.684	0.8657	0.801
Rotor bar copper loss (kW)	2.788	0.86	1.026	0.506
Total core loss (W)	60.7	20.937	62.25	134.6
Output power (kW)	8.54	10.7	10.357	10.79
Rated speed (rpm)	1870	1890	1890	1905
Efficiency (%)	64.61	79.46	77.123	83.12
Stator copper density (A/mm ²)	23.42	23.5	23.44	23.45
Rotor bar copper density (A/mm ²)	27.25	16.21	17.06	13.66

3.7 Conclusion

In this chapter, an adapted non-overlapping winding configuration has been developed for a squirrel-cage IM in order to reduce the total axial length and improve the performance characteristics at the same time. The combination of the multi-layer phase winding shifting method with the auxiliary slot method leads to create more homogeny distributed winding layout with the significantly reduced MMF harmonic content. The half-unfilled slots, compromising of the consistence of the non-overlapping

winding concept, help to improve the thermal characteristics of the IM by introducing extra air-cooler canals into the stator. It has been revealed that thanks to the proposed method, ~43% of the MMF harmonics are reduced. In addition, more than 25% reduction in the total axial length is also achieved. Furthermore, torque and power densities are increased remarkably.

The influences of some major machine design parameters on the electromagnetic and flux-weakening characteristics of the newly developed AIM are also investigated in detail. Some important key findings of the study on the influence of design parameters can be summarised as follows.

- The lower the pole number, the higher the power at constant power region;
- There is a critical rotor slot number, which is estimated by $R \approx S + 2q$, for any stator slot/pole number combinations at which the maximum available average torque with relatively low torque ripple can be achieved;
- The higher the rotor slot number, the higher the bar current density, slip, bar copper loss, and consequently the lower the efficiency;
- The higher the stack length, the lower the number of turns requirement for maintaining the torque;
- The higher the stack length, the better the flux-weakening characteristics and the higher the efficiency;
- Each geometric parameter has a significant effect on the performance characteristics, individually.

A comprehensive performance comparison between the conventional IM and advanced IMs with coil pitch of two slot pitches and various stator slot/rotor slot/pole numbers, stack lengths, number of turns, etc. will be presented in Chapter 4.

4 Comparison of Conventional and Advanced Induction Machines with Coil Pitch of Two Slot Pitches and Various Slot and Pole Number Combinations

This chapter presents a comprehensive comparison on the performance characteristics of the advanced non-overlapping winding IMs (AIMs) designed with various stator slot/rotor slot/pole numbers, stack lengths, and number of turns. The aim of the comparison is to find out the best candidate meeting the specific requirements determined by considering the size and flux-weakening characteristics. Therefore, various AIMs having 6, 8, 10, and 12-poles with different stack lengths and number of turns, have been quantitatively compared in terms of torque, torque ripple, power losses, efficiency, current densities, axial length, flux-weakening characteristics, etc. by 2-D FEA. Among the various AIMs, the best candidates for the EV/HEV applications are determined. Furthermore, a conventional IM (CIM) having double-layer 9-slot pitch integer slot distributed windings (ISDWs) has been designed by using the same specific dimensions as the AIM and the obtained FEA results are compared quantitatively. Moreover, the AIMs equipped with various rotor structure types, such as insert-bar, open-slot cast-rotor, closed-slot cast-rotor with straight bridge, and closed-slot cast-rotor with u-shaped bridge have also investigated and the obtained results have also been compared.

4.1 Introduction

As known, electrical machine performance heavily depends on the stator slot, rotor slot, and pole number (S/R/P) combinations. This becomes a very critical issue when there are very strict restraints on the flux-weakening capability, torque quality, acoustic noise, and vibration characteristics. Therefore, the selection of the accurate combination of the S/R/P is essential for the systems, such as EVs/HEVs, aerospace, wind turbines, etc., which require high performance with low parasitic effects.

The influence of design parameters on conventional IMs (CIMs) are presented extensively in literature. A comparative study on the selection of the proper pole number of an inverter-driven IM is presented by involving numerous factors and trade-offs, many of which are identified and their influence on parameters and performance described [LIA95]. In order to minimise the harmonic winding losses of the rotor, the conventional rotor slot geometry is modified by using bridge with u-shapes on the rotor slot opening of squirrel-cage IMs [NEE93], [NEE95]. In order to reduce the various leakage reactance components and consequently improve the flux-weakening performance of the CIMs, some design suggestions, such as adopting open rotor slots and increased stator slot openings, increased air-gap length, unskewed rotor slots, and reduced number of turns are presented in [HAR95]. To be able to increase the speed of a squirrel-cage IM, multiple sub-phase windings are proposed in order to change the pole number of the machine [BAR56]. In attempt to further improve the constant power operation region of a CIM, a six-phase pole-changing IM is proposed with a new control strategy for reducing torque fluctuations during changing the pole [MOR97]. In a similar study, a pole-phase modulation method adopting for adjusting the pole-phase ratio of an IM is proposed in [KEL03]. Some major design

considerations including the machine dimensions and modified rotor slot shape especially for the inverter-driven IMs, and some design strategies for improving the output power without sacrificing the size and performance are presented in [ZHA00]. In [WAN05], a lot of useful design guidelines are given for inverter-driven IMs. It was suggested that the IMs with shallow and wide rotor slot is more suitable for HEV applications. In order to reduce the skin effect losses, stranded wires in parallel for stator windings and shallow slot for rotor is suggested. In addition, in order to restrain the influence of the harmonics, the magnetic wedges for both stator and rotor slots are suggested. Moreover, the number of rotor slots should be close to the number of stator slots in order to decrease the undesired effects of harmonics. In [LIW05], three different rotor slot shapes that commonly used for variable-frequency operations of squirrel-cage IMs are compared in terms of flux-weakening performance, leakage reactance, torque capability, machine losses, and efficiency. As a similar study, the influence of rotor slot shape on the flux-weakening performance and the influence of rotor slot number combinations on efficiency, power factor, torque capability, and torque ripple of a CIM are investigated in [SHU06]. An analytic model for investigating the influence of the design and inverter parameters on the flux-weakening performance of a CIM is presented in [DUA11]. As a similar study, the influence of machine design parameters, such as the mutual and leakage inductances, iron saturation, stator and rotor resistances, etc., on flux-weakening performance of a CIM is presented for EV applications in [GUA15]. In a recently published paper, a simplified analysis on the influence of the pole number on the steady-state behaviour of an IM is presented [AGA16]. In order to reduce the copper and core losses and hence increase the efficiency, the feasibility of adopting magnetic wedges in IMs with semi-closed slots is studied, and it is then concluded that by employing shorter wedges, it is possible to achieve a better performance [VER17]. In [MUT17], the influence of the various winding configurations on torque ripple production of a CIM having 5-phase 30S/2P is investigated. Moreover, influences of the air-gap length, S/P combinations, rotor slot number, and stator and rotor geometric parameters on the rotor bar current waveform, and electromagnetic performance of a CIM are investigated in Chapter 6.

In this chapter, the comparison of a CIM and AIMs having various stator slot/rotor slot/pole number (S/R/P) combinations with different number of turns and stack length will be presented. The best combinations having good flux-weakening capability and the highest power and efficiency with minimum torque ripple and total axial length are determined. After performing numerous parametric analyses by FEA, the 18S/20R/6P AIMs with 70mm and 90mm stack lengths are proposed for prototyping. In addition, the generator mode operating characteristics of the proposed IMs have also been investigated in Appendix G with particular reference to the difference between the motor and generator operating modes.

4.2 Comprehensive Performance Comparison between AIMs with Different Slot/Pole Combinations and Geometrical Parameters

In this section, steady-state electromagnetic and flux-weakening performance characteristics of the 18S/20R/6P, 24S/26R/8P, 30S/32R/10P, and 36S/38R/12P AIMs will be comprehensively compared with those of the CIM having 54S/44R/6P to reveal the advantages and disadvantages of the proposed method. All the IMs have the same outer diameter (144mm) and operational specifications (synchronous speed of 1500rpm and current excitation of 500Arms). Other geometric parameters have been globally optimized for different stack lengths. The best candidates have been chosen among a large number of different AIMs by considering the demanded torque/power-speed characteristics, efficiency, and total axial length.

4.2.1 Design and Analysis of CIM and AIMs

All the AIMs, i.e. 18S/6P, 24S/8P, 30S/10P, and 36S/12P, have the same winding configuration with $y_c = 2$ double-layer non-overlapping windings (ANWs) and the CIM with 54S/6P has $y_c = 9$ double-layer integer-slot distributed windings (ISDWs). The harmonic winding factors and winding MMF harmonics are compared in Fig. 4.1. As seen, none of the combinations contains sub-harmonics. It can be predicted that since the fundamental winding factor of the CIM is higher than that of the AIMs, the AIMs will require more number of turns in order to maintain the torque. However, it should be considered that with more number of turns, the torque is not necessary increase significantly due to saturation. In addition, as explained in the previous chapter, the more number of turns requires more space for stator slots. In order to avoid the saturation, the split ratio and consequently the rotor outer diameter should be reduced. Since there is a direct correlation between the torque and rotor outer diameter, the more number of turns could not lead an increase in the torque. In addition, since the MMF THD of the AIMs are much higher than that of the CIM (see Fig. 4.1(b)), the more rotor bar copper losses of the AIMs might also be predicted. As seen in Fig. 4.1(b), the higher the S/P, the lower the MMF THD of the AIMs. The details related with the S/P combinations and their influence on the machine performance can be found in Chapter 2.

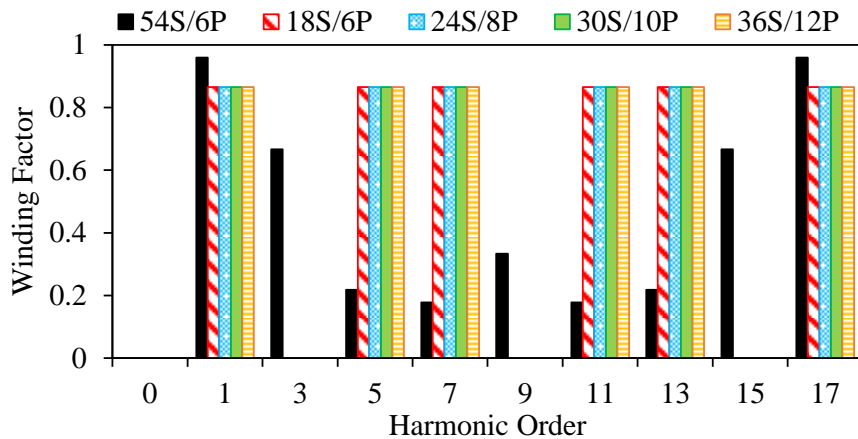
The total axial length of the CIM with 70mm stack length is estimated to be 122mm by (2.9). The total axial length of the CIM is assumed as the maximum axial length limit. Therefore, various stack lengths, i.e. 70mm, 80mm, 90mm, 100mm, 105mm, and 110mm, have been adopted for each S/P combinations without exceeding the total axial length limit of 122mm. In this section, it is intended to reveal the followings.

- a) Influence of the stack length on the electromagnetic and flux-weakening characteristics;
- b) If the AIM is designed with the same stack length of the CIM, what are the merits and demerits of the proposed method?

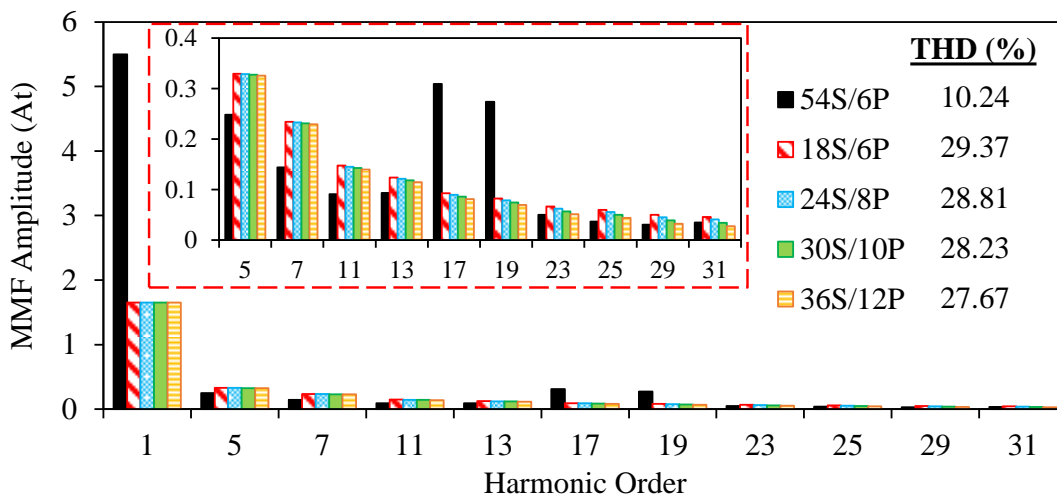
- c) If the AIM is designed with the same total axial length of the CIM, what are the merits and the demerits of the proposed method?

To be able to investigate the stack length of the AIMS with various S/R/P combinations, the number of turns, number of parallel branches, and stator current density should be considered. Various design options are summarised as follows.

- 1) Considering the torque-speed characteristics, there are two different design options:
 - (a) The higher number of turns for high torque at constant torque region;
 - (b) The lower number of turns for high torque at constant power region.
- 2) Considering the efficiency, there are two different design options:
 - (a) The shorter total axial length for compact but low efficiency design;
 - (b) The longer total axial length for bulky but high efficiency design.



(a) Harmonic winding factors



(b) MMF harmonic spectra for 1-ampere 1-turn

Fig. 4.1 Winding analyses: (a) harmonic winding factors and (b) MMF harmonics.

The possible parallel branch number a for different number of turns per phase N_t is listed in Table 4.1. In fact, since the injected peak phase current is quite high (707A_{peak}), parallel branches should be used in order to investigate the influence of number of turns in much larger scale. Moreover, the maximum parallel branch a_{max} is determined by the maximum coil per phase number N_c as given in (4.1). Therefore, a large number of turns can be adopted for any S/P combinations. Since there is a direct correlation between total flux and serial number of turns per phase N_{st} , any combination ensuring (4.1) will have the same electromagnetic performance characteristics. For instance, the ratios of 3x column, i.e. 3/4, 6/8, 9/12, ... have exactly the same characteristics since the total flux remains constant for all those ratios.

$$N_{st} = \frac{N_t \cdot N_c}{a} \quad \text{and} \quad a_{max} = N_c \quad (4.1)$$

On the other hand, it is obvious that the lower the number of turns, the lower the total equivalent flux. Therefore, the stack length l_s has been increased in order to maintain the torque. Furthermore, as seen in the table, since the IMs with longer stack lengths require less number of turns, their stator current density levels are lower than those of the IMs with shorter stack lengths. The CIM and AIMs are designed following these guidelines and all designed IMs are globally optimized by GA (see Appendix E for the optimization details). The 2-D cross-sectional views and the flux density and flux line distributions of the designed IMs are illustrated between Fig. 4.2 and Fig. 4.8. The numbers inside of the bracket indicate the turns-per-phase and the stack lengths, respectively: i.e. (9-70) mean is 9-turns per phase and 70mm stack length. Different from the Table 4.1 the CIM has 18-coils with 2-parallel branches and 1-turn per coil and hence 9-turns per phase.

Table 4.1 IMs design options with different parallel branch and number of turn

$\begin{matrix} N_t \\ a \end{matrix}$	3x	5x	11x	2x, 3x, 4x, 6x, 12x	13x	7x, 14x
l_s (mm)	113	102	90	80	75	70
3	–	–	–	3/3	–	–
4	3/4	–	–	4/4	–	–
6	3/6	5/6	–	6/6	–	7/6
8	6/8	10/8	11/8	12/8	13/8	14/8
10	6/10	10/10	11/10	12/10	13/8	14/10
12	9/12	10/12	11/12	12/12	13/12	14/12
J_s (A/mm ²)	23	26	28	31	31	32

4.2.2 Electromagnetic Performance Comparison

The calculated steady-state electromagnetic performance characteristics such as torque, torque ripple, power losses, efficiency, current densities, etc. have been listed for each IM from Table 4.2 to Table

4.4. In the tables, N_s , R , l_s , l_{end} , l_{total} , k_{w1} , R_{phase} , n_{maxT} , T , ΔT , P_{out} , P_{Scu_in} , P_{Scu_end} , P_{Scu} , P_{Rcu} , P_{hyst} , P_{eddy} , J_s , and J_R indicate the number of turns per phase, number of rotor slots, stack length, end-winding axial length, total axial length, fundamental winding factor, phase resistance with 0.63 slot filling factor, rotor speed delivering the maximum torque, average torque, torque ripple, output power, stator slot copper loss, stator end-winding copper loss, total stator copper loss, rotor copper loss, hysteresis loss, eddy current loss, stator winding current density, and rotor bar current density, respectively. To be able to compare the results of AIMs' with those of the CIM, each table's column starts with the performance characteristics of the CIM. As seen in Table 4.2, there is a 70mm AIM designed by utilizing the rotor of a previously prototyped CIM's specifications. In order to verify that the rotor slot combination of the existing (previously manufactured) rotor is not suitable for the 18S/6P AIM, calculated results of 18S/44R/6P (11-70e) have also been presented. As seen in Table 4.2, since the rotor slot number of the manufactured rotor (70e) is not suitable for all S/P combinations, the obtained performance characteristics are poor. As for the freely optimized designs with 70mm, 33% shorter IM can be designed without sacrificing the average torque and efficiency thanks to the proposed non-overlapping winding topology. It can be deduced that for the stack lengths longer than 70mm (see Table 4.3 and Table 4.4) the longer the stack length, the better the electromagnetic performance (average torque, torque ripple, and efficiency) and the lower the stator and rotor current densities. The results of the 90mm AIMs are promising, because the total lengths of the AIMs are ~13% shorter than those of the CIM. Rotor current density levels are acceptable. However, torque ripple levels are still high. The AIMs, whose stack lengths are longer than 90mm, show also promising results. In general, the rotor bar copper losses, current density, and the torque ripple levels of the AIMs are quite high comparing to the CIM. Since the liquid cooling system will be used, the maximum stator current density should not exceed 31A/mm². Therefore, stator current density limit is set to 31A/mm². Because of the unfilled stator slots, the stator current density of the AIMs is higher than that of the CIM. This is the main disadvantage of the proposed winding topology. The rotor current densities of the AIMs, whose stack lengths are shorter than 90mm, have exceeded the CIM's rotor current density. Therefore, it can be predicted that more cooling requirement is needed for those that exceed the CIM's rotor current density. Flux density and flux line distribution of the designed machines are illustrated in Fig. 4.2 to Fig. 4.8. As can be seen, there are some local saturated parts on the stator yoke, stator and rotor tooth tip parts. It is clear that the level of the saturation in the longer machines is lower than that in shorter machines.

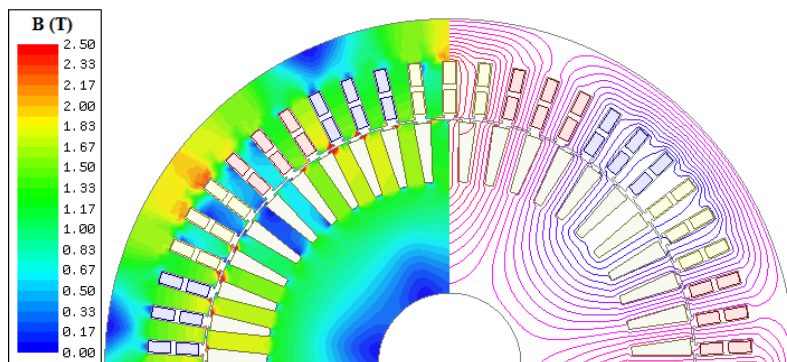


Fig. 4.2 Flux density and flux line distribution of the CIM.

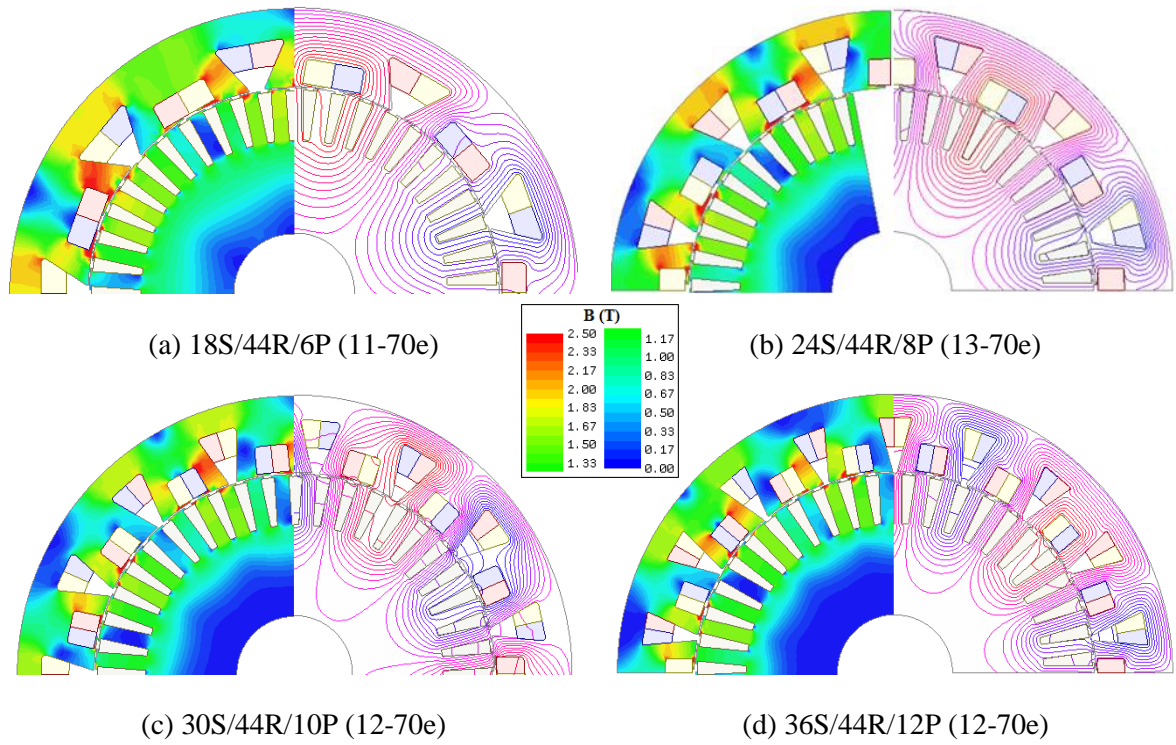


Fig. 4.3 Flux density and flux line distributions of the AIMs designed by using the dimensions of the manufactured rotor with 70mm stack length.

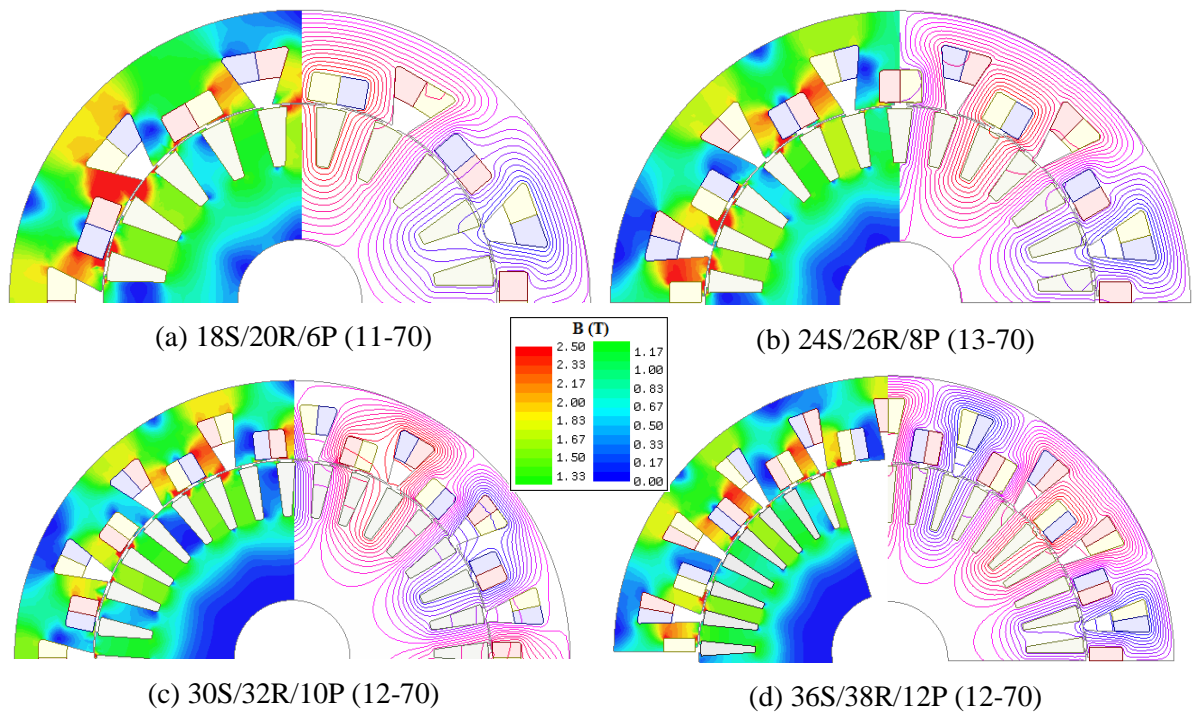


Fig. 4.4 Flux density and flux line distributions of the AIMs with 70mm stack length (with freely optimized rotor).

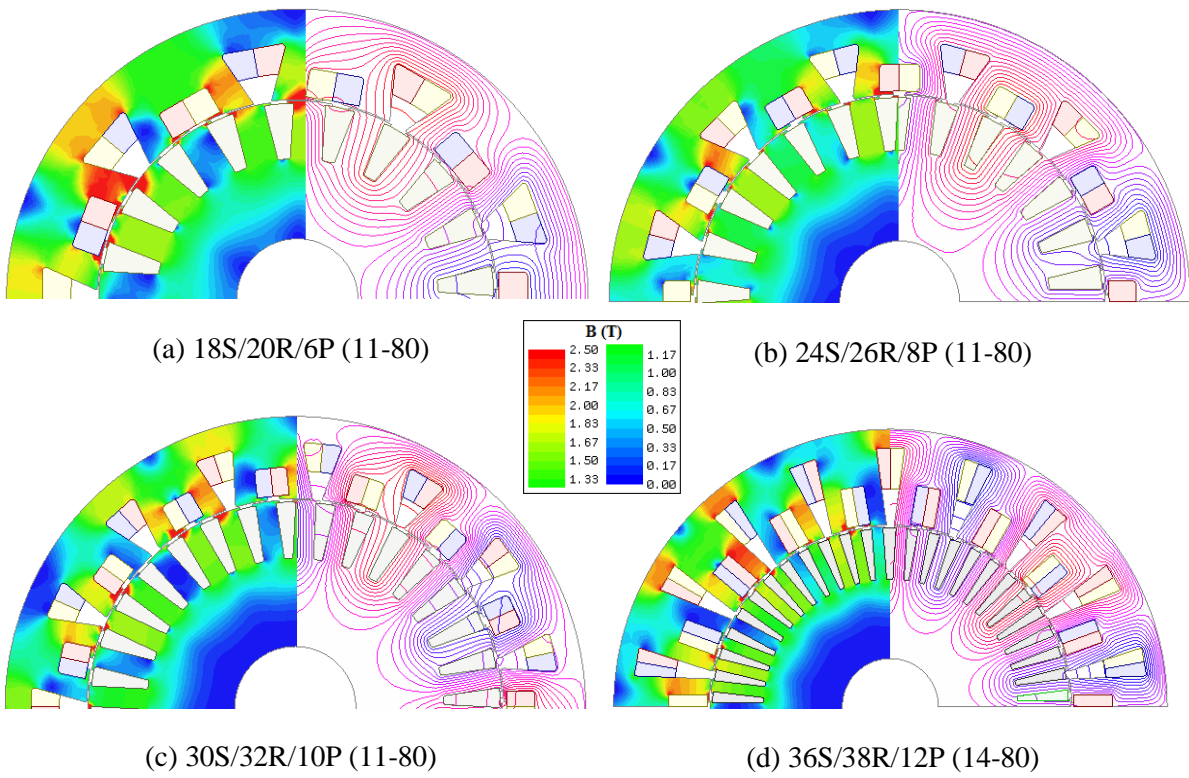


Fig. 4.5 Flux density and flux line distributions of the AIMs with 80mm stack length.

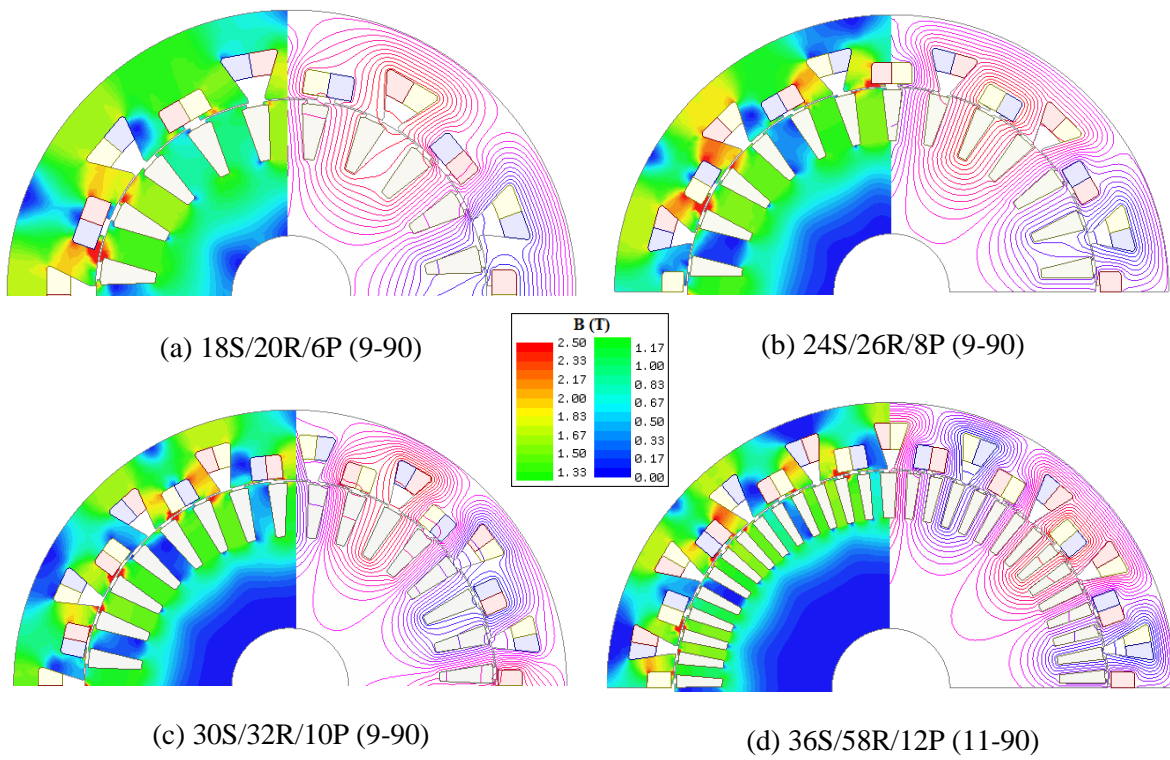


Fig. 4.6 Flux density and flux line distributions of the AIMs with 90mm stack length.

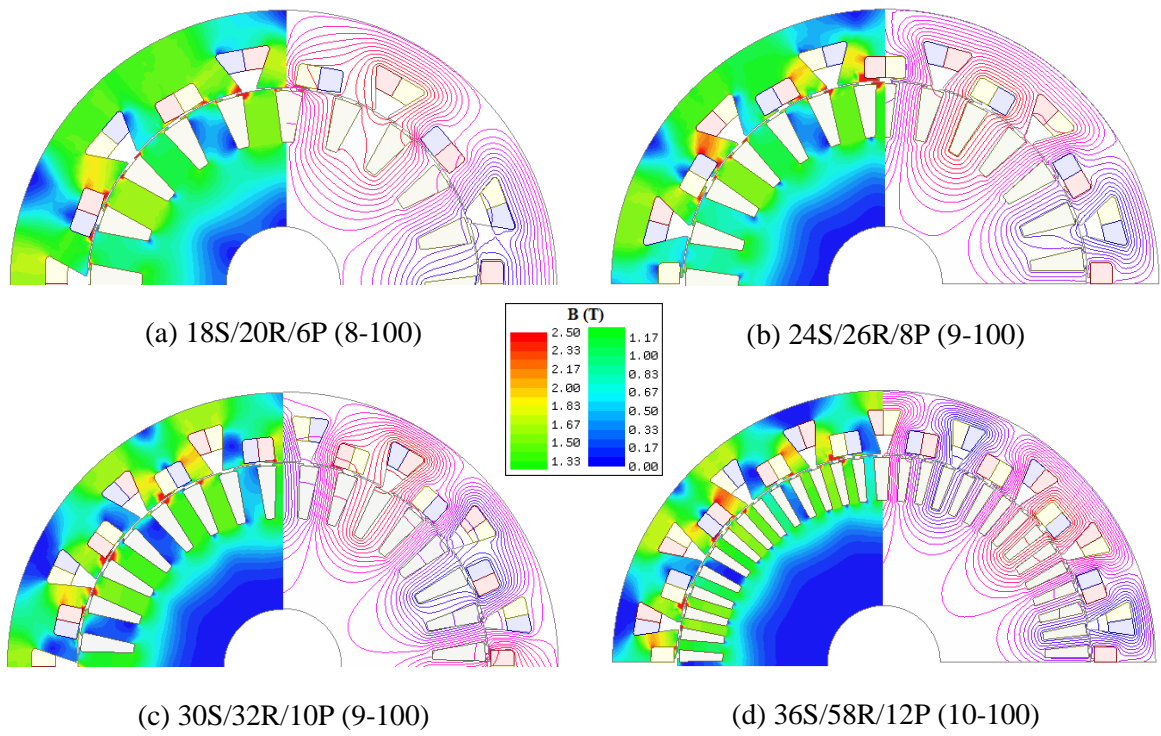


Fig. 4.7 Flux density and flux line distributions of the AIMs with 100mm stack length.

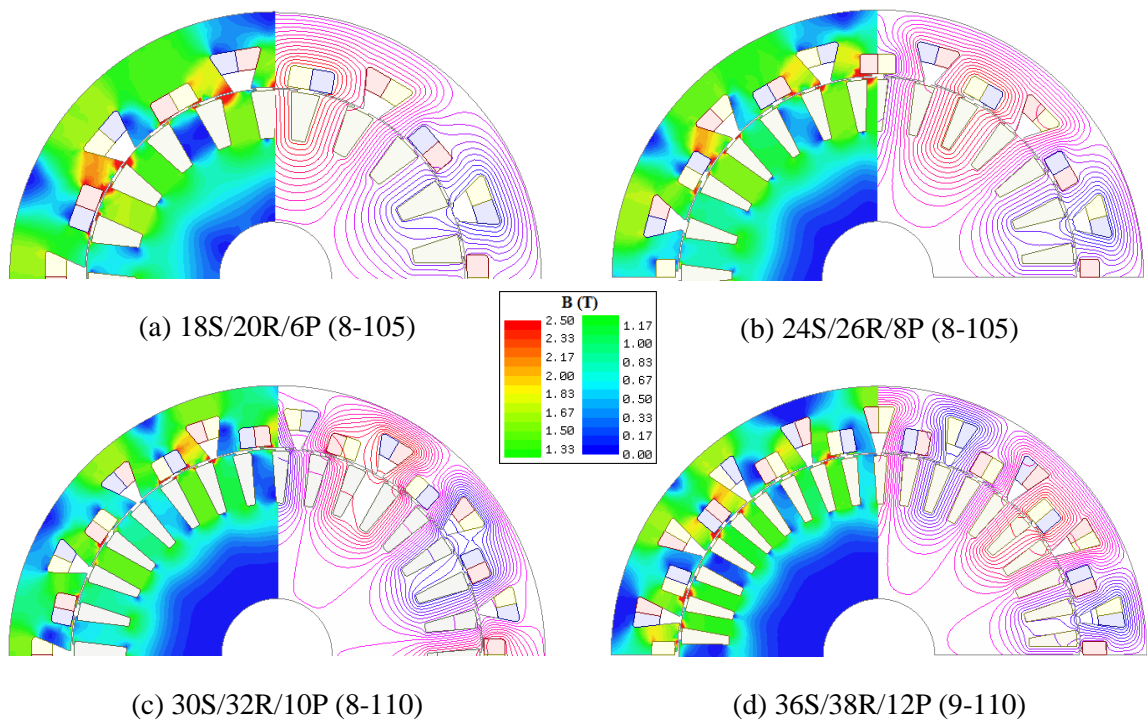


Fig. 4.8 Flux density and flux line distributions of the AIMs with 105mm and 110mm stack lengths.

Table 4.2 Steady-state performance characteristics (70e and 70mm)

	CIM 54S/44R/6P	18S/44R/6P (11-70e)	24S/26R/8P (12-70e)	30S/32R/10P (12-70e)	36S/44R/12P (12-70e)	18S/20R/6P (12-70)	24S/26R/8P (13-70)	30S/32R/10P (12-70)	36S/44R/12P (14-70)
N_s	9	11	12	12	12	12	13	12	13
l_s (mm)	70	70	70	70	70	70	70	70	70
l_{end} (mm)	52	19.255	14.84	11.8	10.08	18.5	14.356	11.44	11.58
l_{total} (mm)	122.17	89.41 (-26.84%)	84.62 (-30.75%)	81.98 (-32.96)	80.24 (-34.36%)	88.64 (-27.5%)	84.5 (-30.85%)	81.59 (-33.24%)	81.71 (-33.13%)
k_{w1}	0.96	0.866				0.866			
R_{phase} (mΩ)	3.7261	2.6202	2.1786	2.487	2.3618	2.8187	2.806	2.4736	3.0167
n_{maxT} (rpm)	1905	1875	1890	1885	1900	1880	1885	1900	1895
T (Nm)	52.21	45.92	49.96	49.83	46.66	50.8	52.764	48.68	55.15
ΔT (%)	4	16.25 (+281.3%)	34.928 (+773.2)	10.355 (+158.87)	16.502 (+312.55%)	18.827 (+370.67%)	21.046 (+426.15%)	10.8 (+170%)	20.35 (+408.75%)
P_{out} (kW)	10.42	9.016	9.888	9.836	9.283	10	10.415	9.685	10.944
$P_{Scu_{in}}$ (kW)	0.7273	1.2347	1.3467	1.4	1.346	1.347	0.9338	1.35	1.592
$P_{Scu_{end}}$ (kW)	2.067	0.7313	0.6861	0.507	0.425	0.768	0.4137	0.505	0.398
P_{Scu} (kW)	2.79	1.966	2.033	1.866	1.772	2.115	1.3475	1.856	1.99
P_{Rcu} (kW)	0.51	1.7174	1.3535	1.17	0.827	1.0273	0.9336	0.728	1.063
P_{hyst} (mW)	10.89	13.11	14.32	15.166	16.6	19.9	18.752	15.86	14.86
P_{eddy} (mW)	1.7	1.6775	2.41	2.95	3.754	2.178	2.89	3.16	3.23
η (%)	75.367	70.496	73.94	75.835	77.521	75.518	81.366	78.322	77.582
J_S (A/mm ²)	22.32	31 (+38.88%)	31 (+38.88%)	31 (+38.88%)	31 (+38.88%)	31 (+38.8%)	31 (+38.8%)	31 (+38.8)	31 (+38.8%)
J_R (A/mm ²)	13.54	20.1 (+48.45%)	18.48 (+36.48%)	17.81 (+31.53%)	15.5 (14.475%)	16.37 (+20.9%)	17.28 (+27.62%)	14.49 (+7.016%)	17.53 (+29.47%)
Split Ratio	0.723	0.723	0.723	0.723	0.723	0.66	0.676	0.717	0.742

Table 4.3 Steady-state performance characteristics (80mm and 90mm)

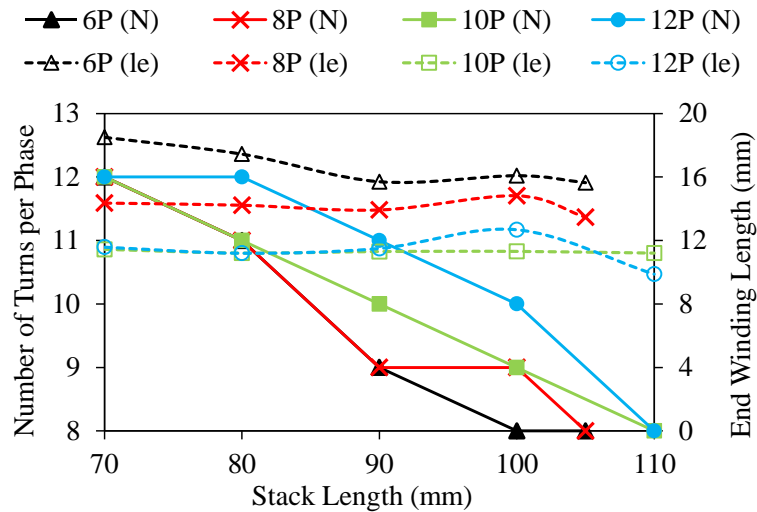
	CIM 54S/44R/6P	18S/20R/6P (11-80)	24S/26R/8P (11-80)	30S/32R/10P (11-80)	36S/38R/12P (14-80)	18S/20R/6P (9-90)	24S/26R/8P (9-90)	30S/32R/10P (10-90)	36S/58R/12P (11-90)
N_s	9	11	11	11	14	9	9	10	11
l_s (mm)	70	80	80	80	80	90	90	90	90
l_{end} (mm)	52	17.44	14.22	11.2	11.2	15.7	13.92	11.3	11.5
l_{total} (mm)	122.17	97.7 (-20.13%)	94.38 (-22.77%)	91.36 (-25.25%)	91.36 (-25.25%)	105.84 (-13.36%)	104.06 (-14.81%)	101.42 (-16.97%)	101.62 (-16.8%)
k_{w1}	0.96	0.866				0.866			
R_{phase} (m Ω)	3.7261	2.757	2.233	2.5024	2.7917	2.5242	2.3558	2.4946	2.5393
n_{maxT} (rpm)	1905	1890	1905	1910	1885	1905	1930	1920	1915
T (Nm)	52.21	54.74	54.25	52.87	55.27	54.66	51.27	54.46	56.22
ΔT (%)	4	17.5 (+337.5%)	19.67 (+391.75%)	10.63 (+165.75%)	10.11 (+152.75%)	17.15 (+328.75%)	24.66 (+516.5%)	8.226 (+105.65%)	9 (+125%)
P_{out} (kW)	10.42	10.83	10.52	10.57	10.91	10.9	10.36	10.95	11.27
$P_{Scu_{in}}$ (kW)	0.7273	1.3692	1.411	1.41	1.69	1.2976	1.2986	1.443	1.56
$P_{Scu_{end}}$ (kW)	2.067	0.7	0.3097	0.46	0.405	0.596	0.4685	0.428	0.344
P_{Scu} (kW)	2.79	2.0687	1.721	1.877	2.095	1.8936	1.7671	1.871	1.904
P_{Rcu} (kW)	0.51	1.0472	0.8607	0.751	1.262	0.789	0.6805	0.748	1.005
P_{hyst} (mW)	10.89	21.6	18.975	17.4	21.55	19.542	19.7626	18	15.806
P_{eddy} (mW)	1.7	2.447	3.15	3.62	4.34	2.71	3.468	3.785	3.542
η (%)	75.344	77.063	80.094	79.5	75.89	79.617	80.243	80.052	78.863
J_s (A/mm ²)	22.32	30 (+34.4%)	31 (-38.88%)	31 (-38.88%)	29 (-29.92%)	30.96 (+38.7%)	30.99 (+38.84%)	31 (-38.88%)	30.47 (+36.51)
J_R (A/mm ²)	13.54	16.34 (+20.68%)	15.21 (+12.33%)	13.98 (+%)	17.3 (+27.76%)	13.71 (+1.25%)	12.44 (+8.12%)	12.32 (-9.01%)	13.53 (-0.074%)
Split Ratio	0.723	0.688	0.711	0.718	0.655	0.69	0.741	0.746	0.766

Table 4.4 Steady-state performance characteristics (100mm, 105mm and 110mm)

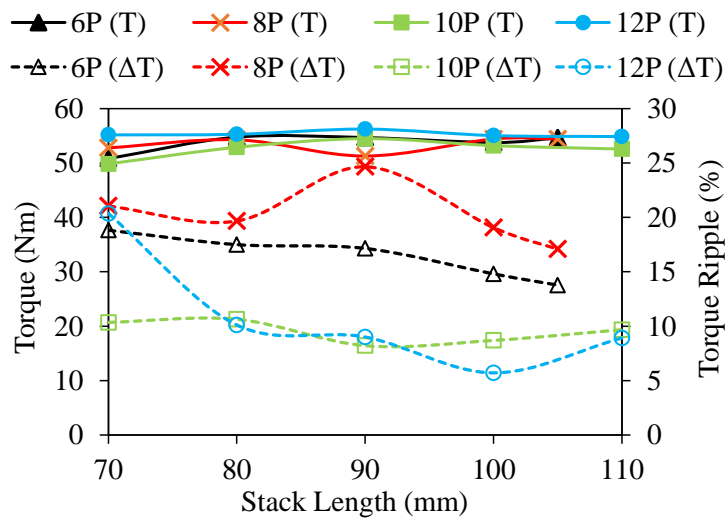
	CIM 54S/44R/6P	18S/20R/6P (8-100)	24S/26R/8P (9-100)	30S/32R/10P (9-100)	36S/38R/12P (10-100)	18S/20R/6P (8-105)	24S/26R/8P (8-105)	30S/32R/10P (8-110)	36S/38R/12P (8-110)
N_s	9	8	9	9	10	8	8	8	8
l_s (mm)	70	100	100	100	100	105	105	110	110
l_{end} (mm)	52	16.08	14.82	11.3	12.68	15.64	13.46	11.2	9.88
l_{total} (mm)	122.17	116.24 (-4.85%)	114.98 (-5.88%)	111.32 (-8.9%)	112.84 (-15.83)	120.8 (-1.11%)	118.62 (-2.9%)	121.38 (-0.655%)	119.98 (-1.73%)
k_{w1}	0.96	0.866				0.866			
R_{phase} (mΩ)	3.7261	2.3566	2.077	2.2013	2.34	2.412	2.0633	2.1421	2.1389
n_{maxT} (rpm)	1905	1920	1925	1930	1920	1925	1935	1935	1925
T (Nm)	52.21	53.75	54.4	53.18	55.03	54.6	54.4	52.55	54.85
ΔT (%)	4	14.8 (+270%)	19.061 (+376.52%)	8.7 (+117.5%)	5.71 (+42.75%)	13.77 (+244.25%)	17.103 (+372.57%)	9.67 (+141.75%)	8.91 (+122.75%)
P_{out} (kW)	10.42	10.807	10.966	10.748	11.064	11.006	11.023	10.648	11.056
$P_{Scu_{in}}$ (kW)	0.7273	1.241	1.35	1.302	1.463	1.2913	1.345	1.288	1.33
$P_{Scu_{end}}$ (kW)	2.067	0.526	0.237	0.346	0.291	0.518	0.2302	0.32	0.274
P_{Scu} (kW)	2.79	1.768	1.5871	1.651	1.763	1.8093	1.5759	1.607	1.604
P_{Rcu} (kW)	0.51	0.772	0.733	0.675	1.039	0.8584	0.634	0.612	0.6286
P_{hyst} (mW)	10.89	22.28	20.15	18.87	15.048	23.13	22.342	19.46	20.17
P_{eddy} (mW)	1.7	2.88	3.57	4	3.408	2.87	3.475	4.27	5.02
η (%)	75.367	80.319	81.862	81.539	79.161	79.848	82.612	82.075	82.514
J_S (A/mm ²)	22.32	30 (+34.41%)	29 (+29.93%)	28.07 (+25.76%)	28.3 (+26.79%)	29.72 (+33.15%)	31 (+38.88%)	28.62 (+28.22%)	25.73 (+15.27%)
J_R (A/mm ²)	13.54	12.33 (-8.93%)	11.5 (-15.06)	10.4 (-23.19%)	12.28 (+9.305%)	11.6 (-14.32%)	10.82 (-20.08%)	10.82 (-20.08%)	10.81 (-20.16%)
Split Ratio	0.723	0.718	0.74	0.747	0.765	0.716	0.752	0.769	0.753

4.2.3 Comparison According to Stack Length

The influences of stack length on some performance characteristics of the globally optimised AIMs are summarised in this section. The number of turns (N) and end-winding length (le) versus stack length for the 6P, 8P, 10P, and 12P AIMs are shown in Fig. 4.9(a). It is obvious that the higher the S/P, the shorter the end-winding length. In addition, since less number of turns requires longer stack length, the end-winding length reduces as the stack length increases.



(a) Variation of turn number and end-winding length with stack length

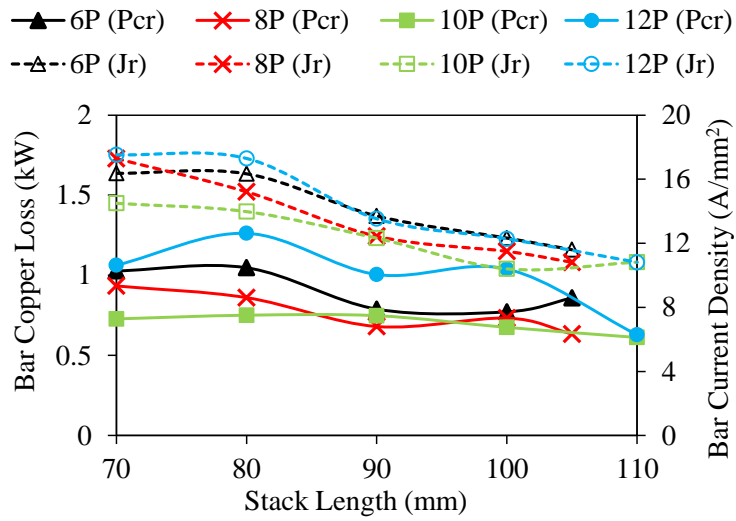


(b) Variation of torque and torque ripple percentage with stack length

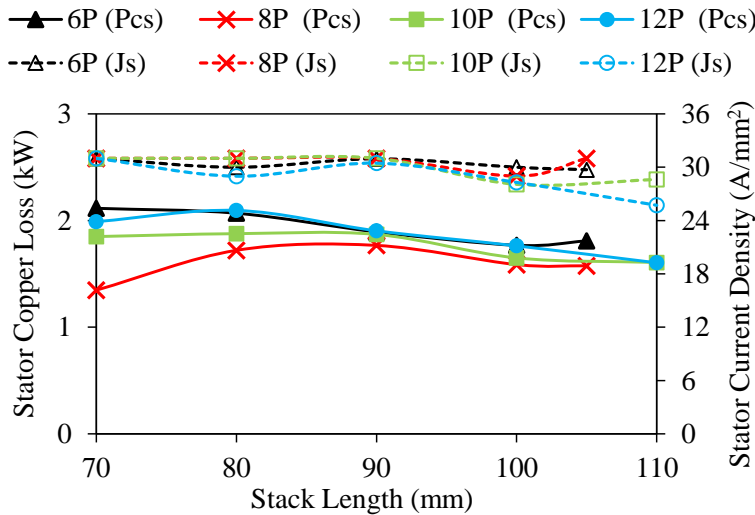
Fig. 4.9 Variation of winding properties and performance characteristics of 6P, 8P, 10P, and 12P AIMs with respect to stack length: (a) number of turns and end-winding length, and (b) average torque and torque ripple.

The variation of the averaged torque and torque ripple with stack length is illustrated in Fig. 4.9(b). As seen in the figure, similar torque levels have been obtained. On the other hand, there are significant differences between the torque ripples. The 8P AIM has the highest torque ripple regardless of stack length while the 12P AIM has the minimum. It is obvious that the higher the stack length, the relatively

lower the torque ripple percentage. Therefore, it can be deduced that the impact of the slotting effect and armature reaction change considerably with S/R/P combination.



(a) Variation of bar copper loss and bar current density with stack length



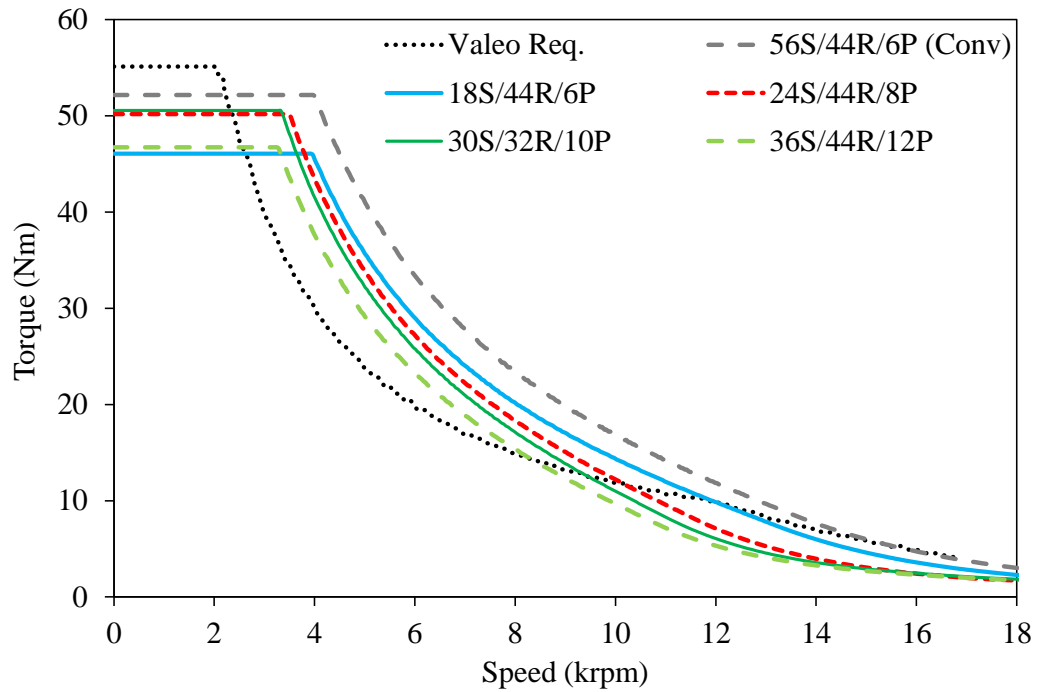
(b) Variation of stator copper loss and stator current density with stack length

Fig. 4.10 Variation of performance characteristics of 6P, 8P, 10P, and 12P AIMs with respect to stack length: (a) bar copper loss and current density, and (b) stator copper loss and current density.

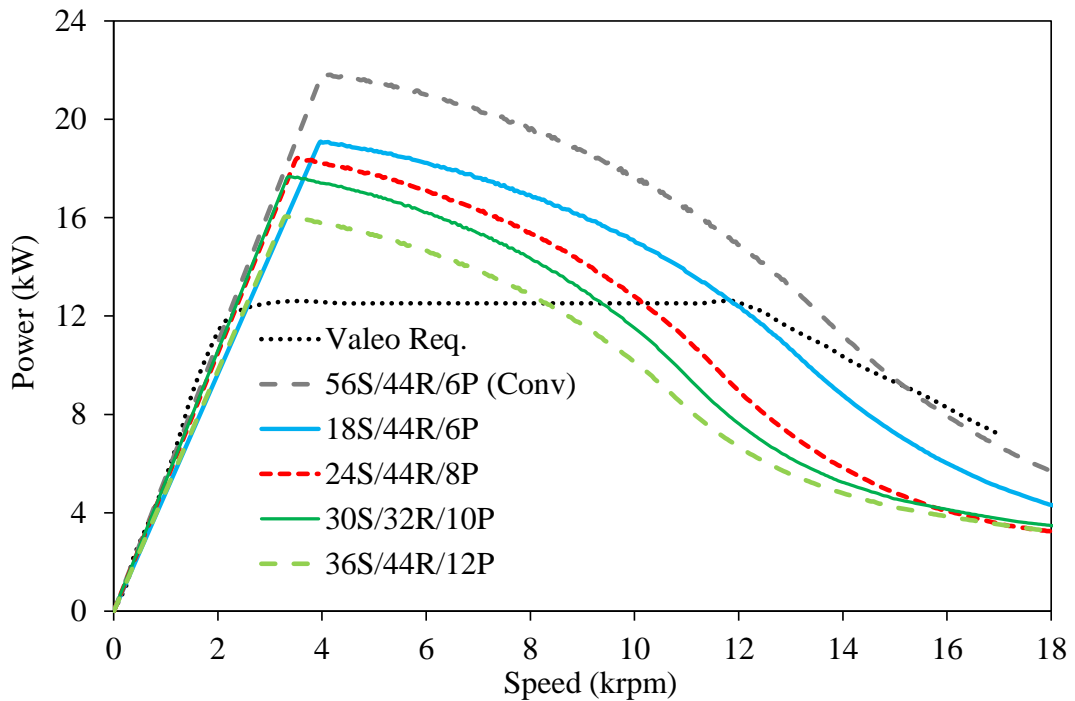
The variations of stator and rotor copper losses and current density with stack length are shown in Fig. 4.10. Since the stator winding current densities are kept constant, the variations of the stator copper loss are not significant. On the other hand, as the stack length increases, the rotor bar copper loss reduces significantly. This is because of the reduction of the air-gap flux density amplitude and consequently the amplitude of the bar current as the stack length increases. Therefore, it can be predicted that the longer the stack length, the lower the serial number of turns per phase, and the lower the stator and rotor copper losses and consequently the higher the efficiency regardless of the operating speed.

The Flux-weakening characteristics of the designed AIMs are calculated and the obtained results are then compared with those of the CIM as illustrated from Fig. 4.11 to Fig. 4.16. Note that, the flux-

weakening characteristics of the machines are grouped by considering their stack lengths. The inverter current and voltage limits are 500Arms and 48Vmax, respectively. None of the AIMs with any stack length can completely satisfy the desired torque/power-speed characteristics. However, it is obvious that the AIMs with the stack length longer than 90mm (including 90mm) show better results.

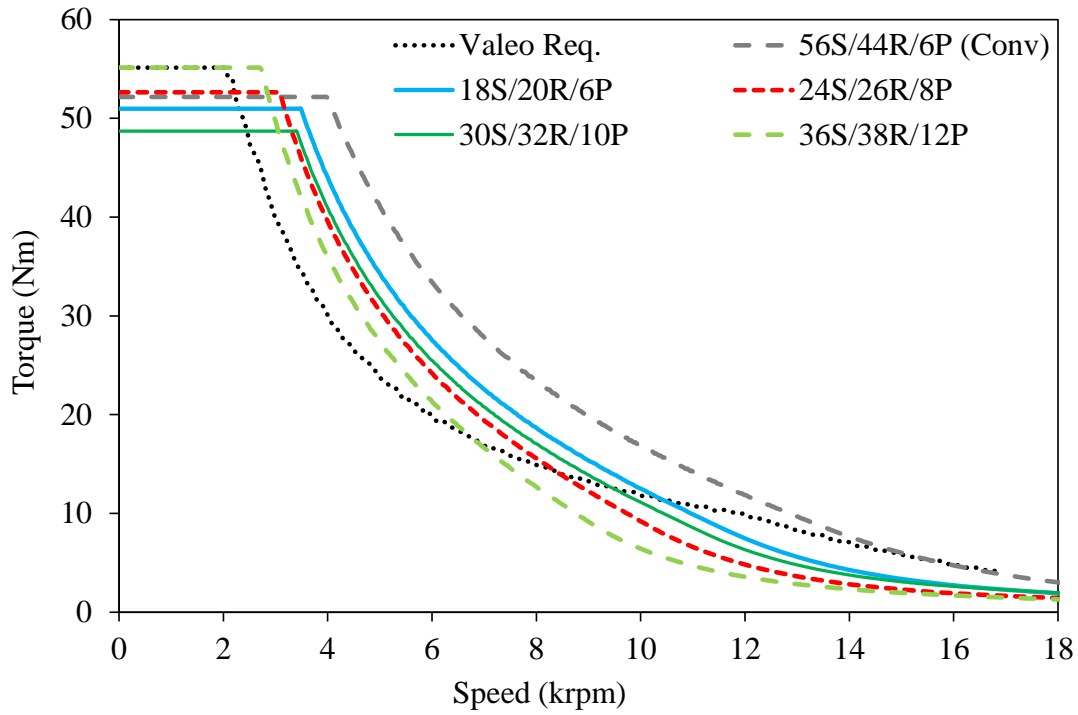


(a) Torque-speed curve of the 70mm AIMs with different pole numbers (70e)

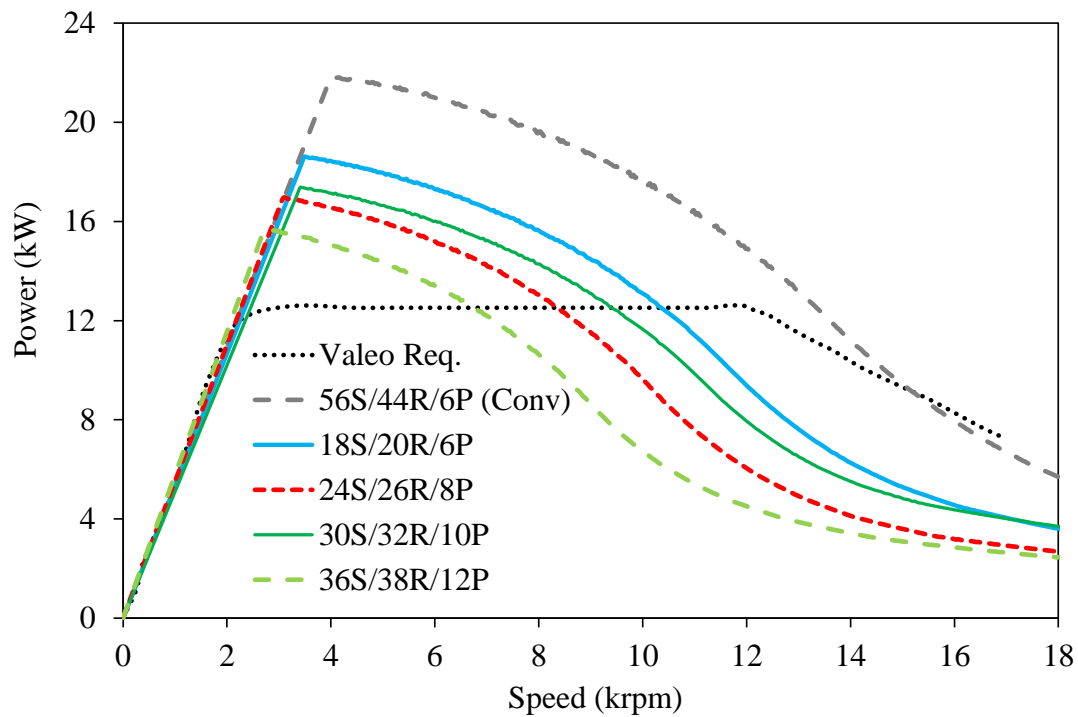


(b) Power-speed curve of the 70mm AIMs with different pole numbers (70e)

Fig. 4.11 Torque- and power-speed curves of the AIMs designed by using the dimensions of the manufactured rotor with 70mm stack length.

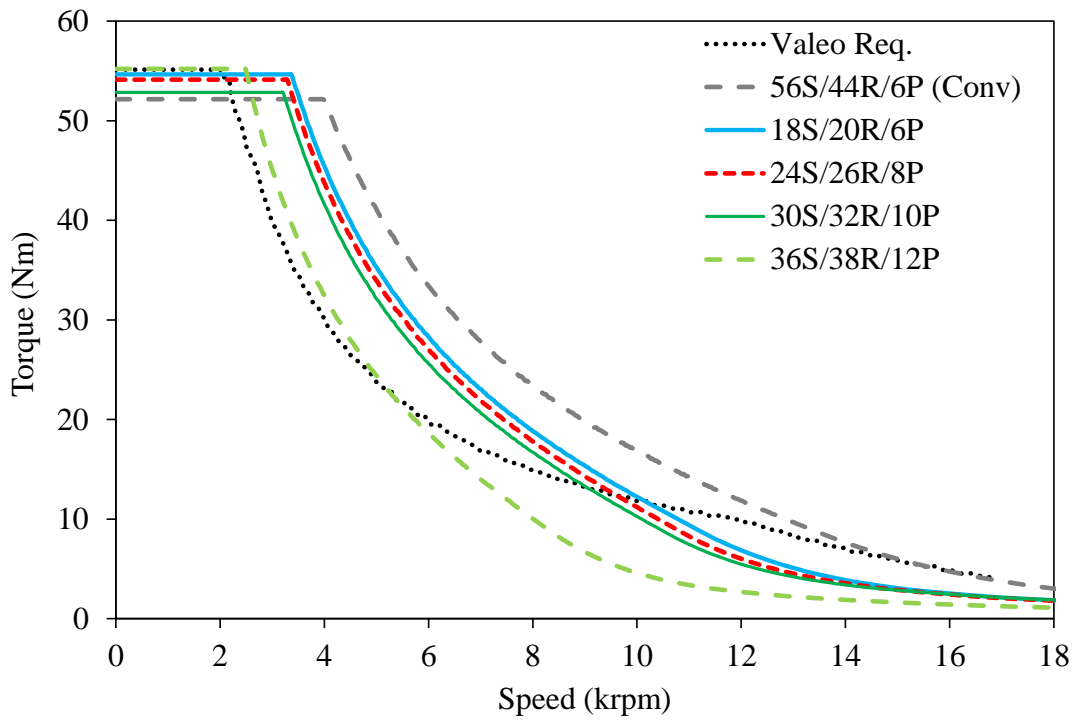


(a) Torque-speed curve of the 70mm AIMs with different pole numbers

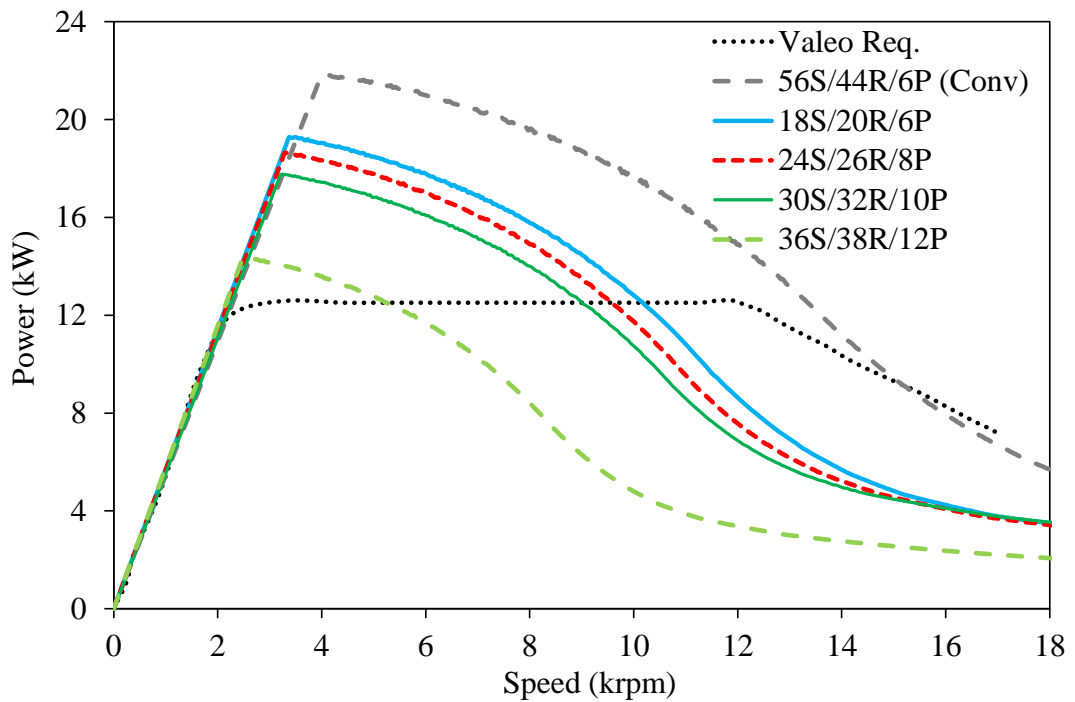


(b) Power-speed curve of the 70mm AIMs with different pole numbers

Fig. 4.12 Torque- and power-speed curves of the 6P, 8P, 10P, and 12P AIMs with 70mm stack length.

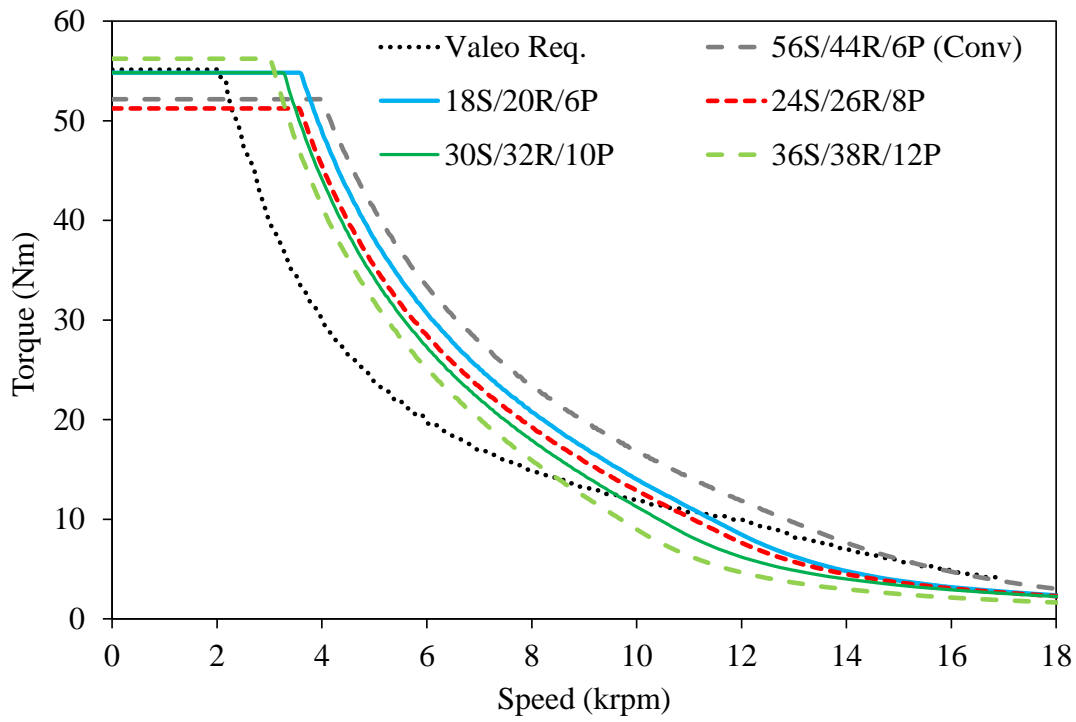


(a) Torque-speed curve of the 80mm AIMs with different pole numbers

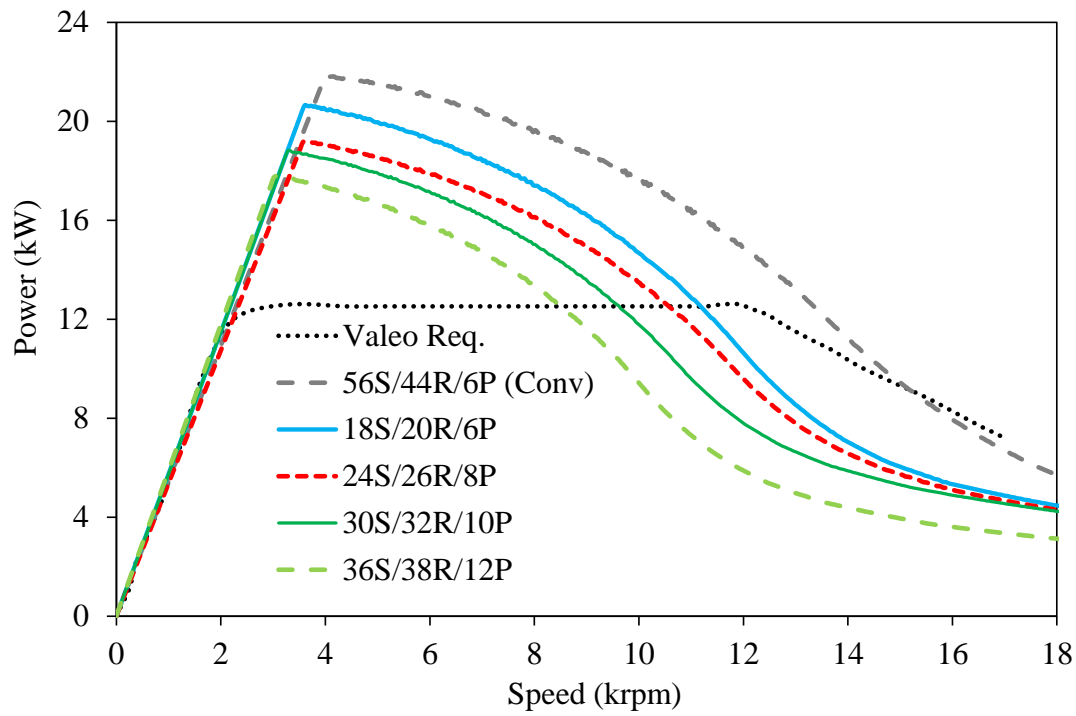


(b) Power-speed curve of the 80mm AIMs with different pole numbers

Fig. 4.13 Torque- and power-speed curves of 6P, 8P, 10P, and 12P AIMs with 80mm stack length.

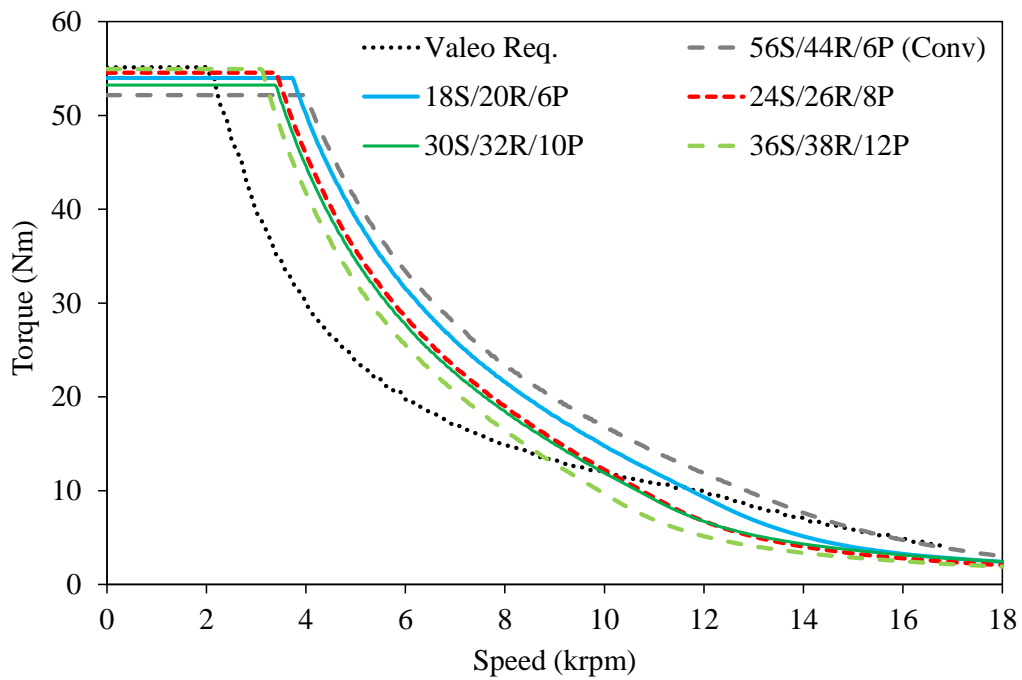


(a) Torque-speed curve of the 90mm AIMs with different pole numbers

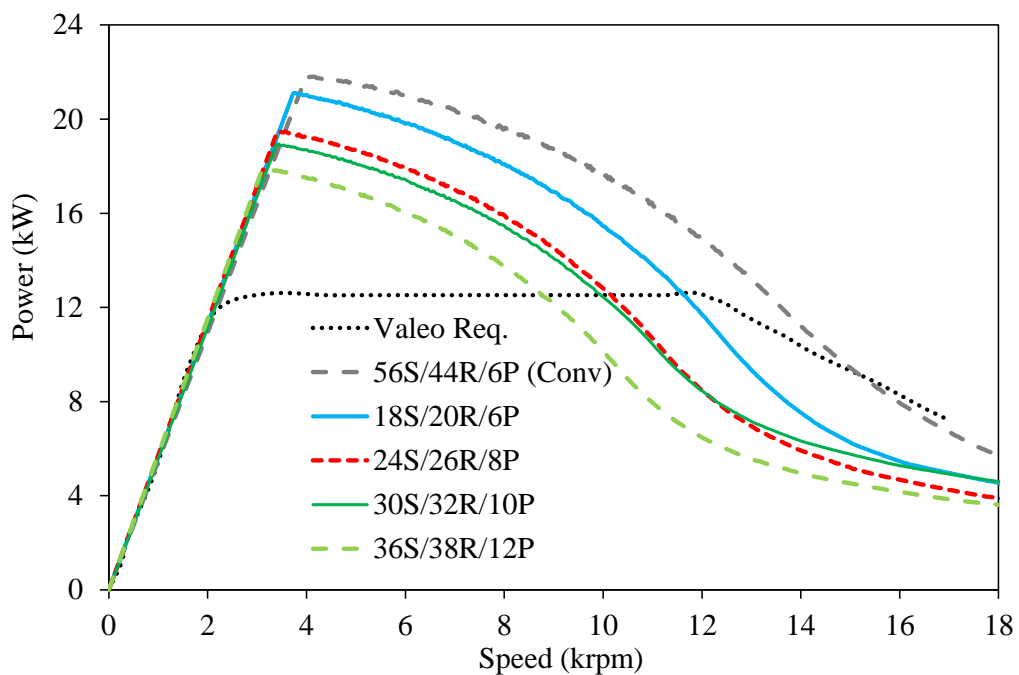


(b) Power-speed curve of the 90mm AIMs with different pole numbers

Fig. 4.14 Torque- and power-speed curves of 6P, 8P, 10P, and 12P AIMs with 90mm stack length.



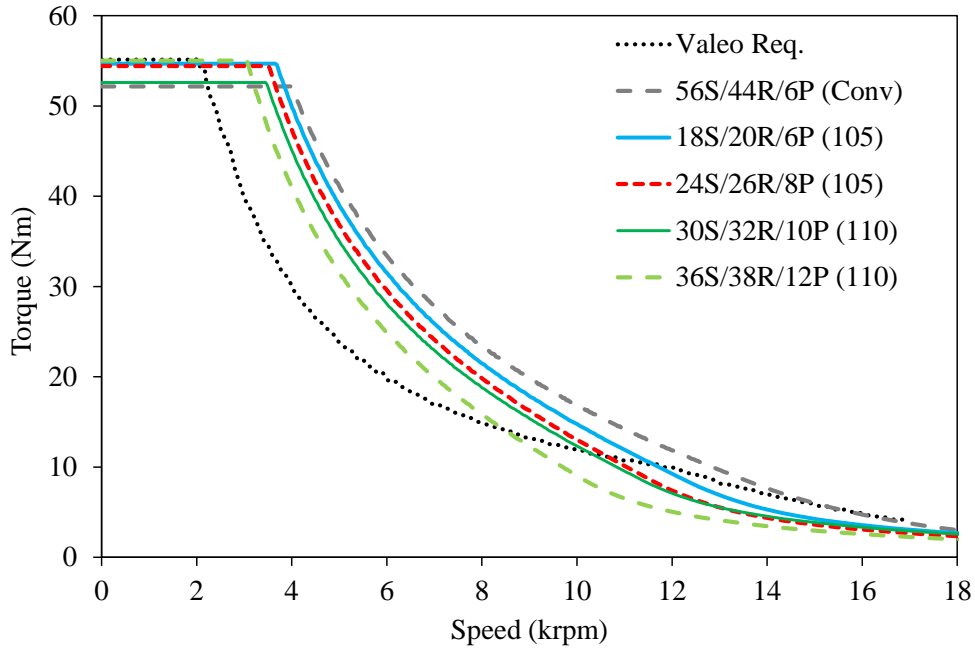
(a) Torque-speed curve of the 100mm AIMs with different pole numbers



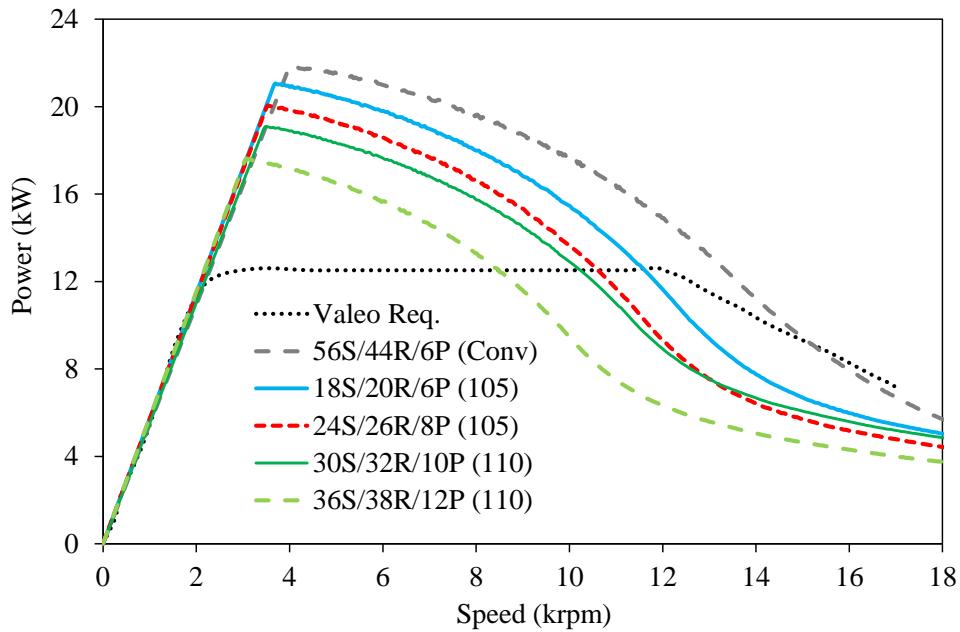
(b) Power-speed curve of the 100mm AIMs with different pole numbers

Fig. 4.15 Torque- and power-speed curves of the 6P, 8P, 10P, and 12P AIMs with 100mm stack length.

Among them, the 6P machine is the best candidate in terms of satisfying the desired torque-speed characteristics. It is obvious that the 18S/20R/6P AIM with 105mm stack length is the best candidate for the torque-speed curve (see Fig. 4.16). However, considering the compactness the 18S/20R6P AIM with 90mm design is also a promising candidate (see Fig. 4.14). It is clear that although the constant torque and constant power regions are good, the performance at high speed (deep flux-weakening) region is poor.



(a) Torque-speed curve of the 100mm and 105mm AIMs with different pole numbers



(b) Power-speed curve of the 100mm and 105mm AIMs with different pole numbers

Fig. 4.16 Torque- and power-speed curves of 6P, 8P, 10P, and 12P AIMs with the 105mm and 110mm stack lengths.

Furthermore, considering the flux-weakening characteristics of all candidates, it has been revealed that the longer the stack length, the better the flux-weakening performance. In addition, for the same stack length, the lower the pole number, the better the flux-weakening performance. As presented in Section 4.3, the underlying reasons why IMs having longer stack length or lower pole is related to the lower serial turns per phase and consequently the lower winding inductance. As a consequence of lower inductance, since the voltage requirement of IM will decrease, the corner speed will move into the

higher speed region. Thus, more power at higher speed region can be achieved. The key findings achieved from this study are summarised as follows:

- 70mm designs with the previously manufactured rotor (70e) - Fig. 4.11: The 6P AIM shows promising results in the deep flux-weakening region, whilst 8P AIM shows better characteristics in the constant torque region. Moreover, 6P AIM has the best power-speed characteristics.
- 70mm freely optimized designs - Fig. 4.12: Although the 6P AIM shows poor performance in the constant torque region, its performance in constant power and deep flux-weakening regions is acceptable. In addition, 6P AIM's power-speed characteristics are better than the other AIM's.
- The designs longer than 80mm (including 80mm) – fromn Fig. 4.13 to Fig. 4.16: Among the AIMs, 6P designs show the best flux-weakening performance characteristics in any region.

4.2.4 Comparison Based on the Maximum Power-Speed Characteristics

In this section, the AIMs ensuring the maximum power-speed characteristic for different stack lengths are compared to determine the best candidate for the desired torque/power-speed characteristics. As expected, the best power-speed characteristics have been obtained from the designs of 6P AIMs. Considering Fig. 4.18 and Fig. 4.17, it can be concluded that designs with the stack lengths longer than 90mm (including the 90mm) show almost similar characteristics with acceptable curve trends. As seen in Fig. 4.18, the 70mm and 80mm AIMs can deliver the required torque up to 10krpm, whilst 90mm machine can deliver the required torque up to 11.5krpm and 100mm-105mm machine can deliver that up to 12krpm. Accordingly, considering the limited space of the traction machine, it is reasonable to choose the 18S/20R/6P with 90mm stack length.

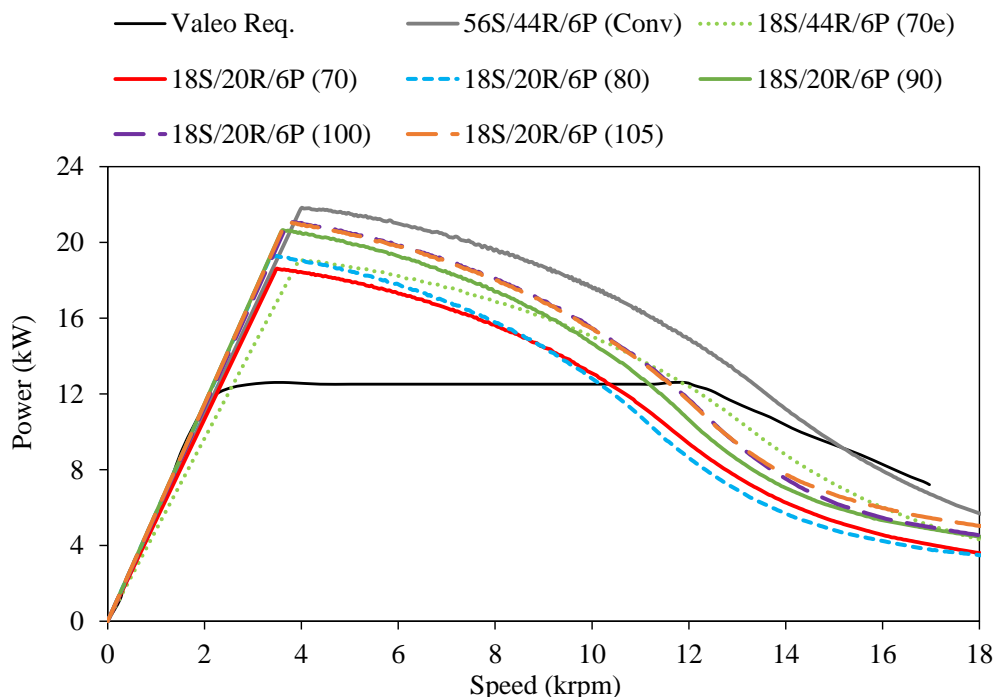


Fig. 4.17 Power-speed curve of the 6P AIMs designed with different stack lengths.

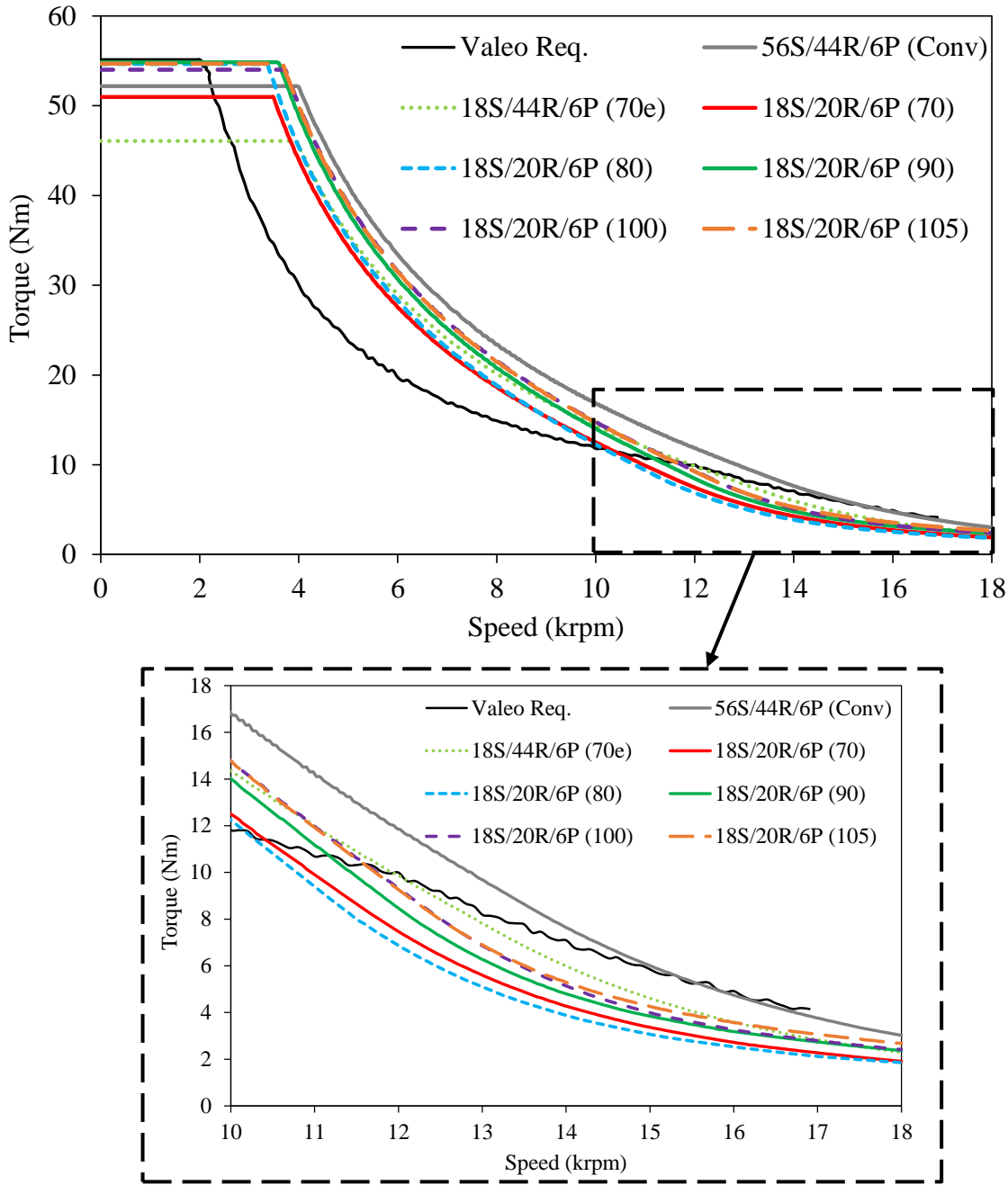


Fig. 4.18 Torque-speed curve of the 6P AIMs designed with different stack lengths.

4.2.5 Comparison of Efficiency Maps

Efficiency maps of the designed IMs have been calculated by using a combined FEA and analytical calculation method. The obtained results are illustrated from Fig. 4.19 to Fig. 4.25. Considering all efficiency maps, some important findings can be summarised as follows:

- For AIMs, the highest efficiency can be obtained between 5krpm to 9krpm, and it changes from the minimum 87% to the maximum 93%;
- The longer the stack length, the higher the efficiency;
- The longer the stack length, the higher the efficiency at low speed and low torque regions.

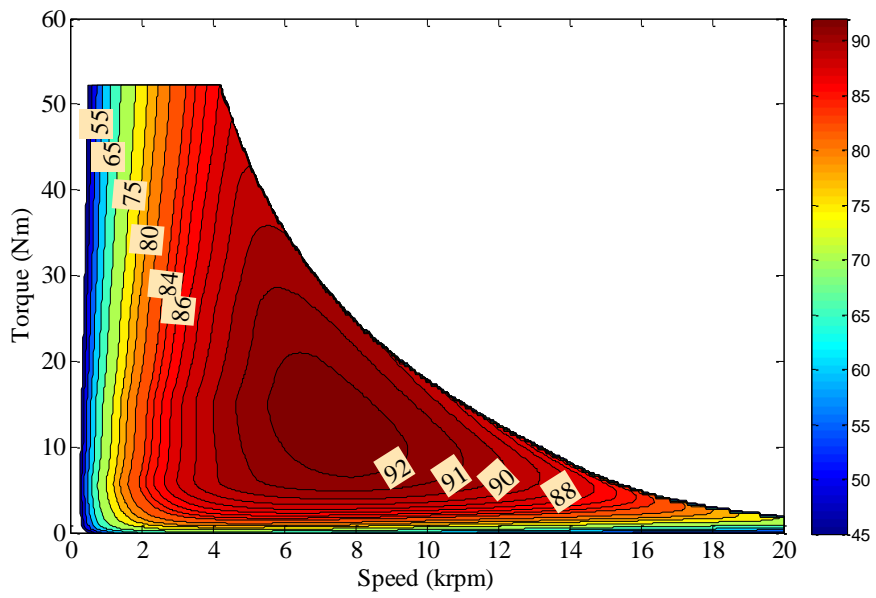
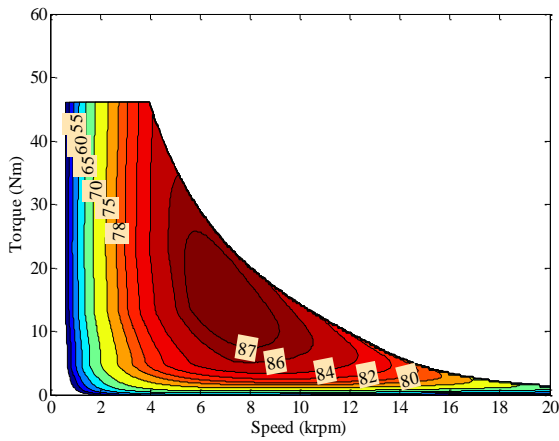
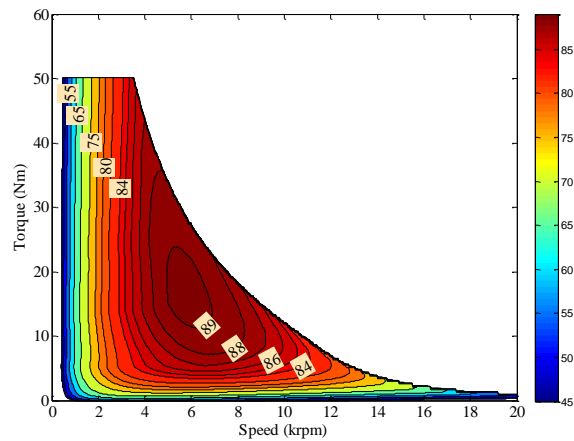


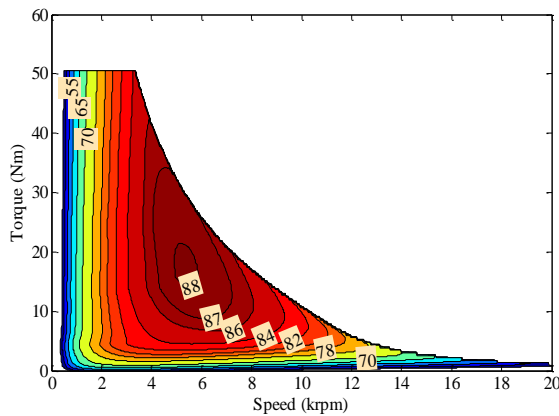
Fig. 4.19 Efficiency map of the CIM (9-70).



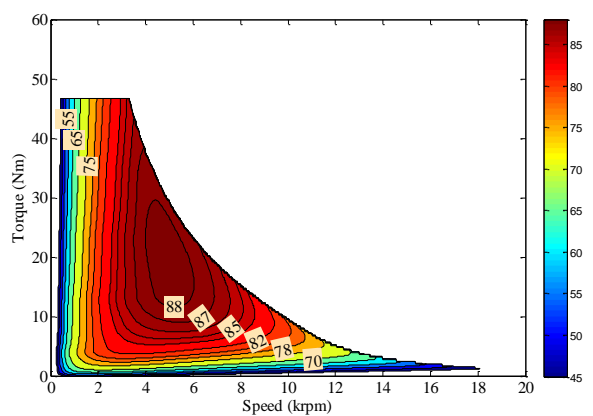
(a) 18S/44R/6P (6-70e)



(b) 24S/44R/8P (8-70e)



(c) 30S/44R/10P (10-70e)



(d) 36S/44R/12P (12-70e)

Fig. 4.20 Efficiency maps of the AIMs designed by using the dimensions of the manufactured rotor (70e).

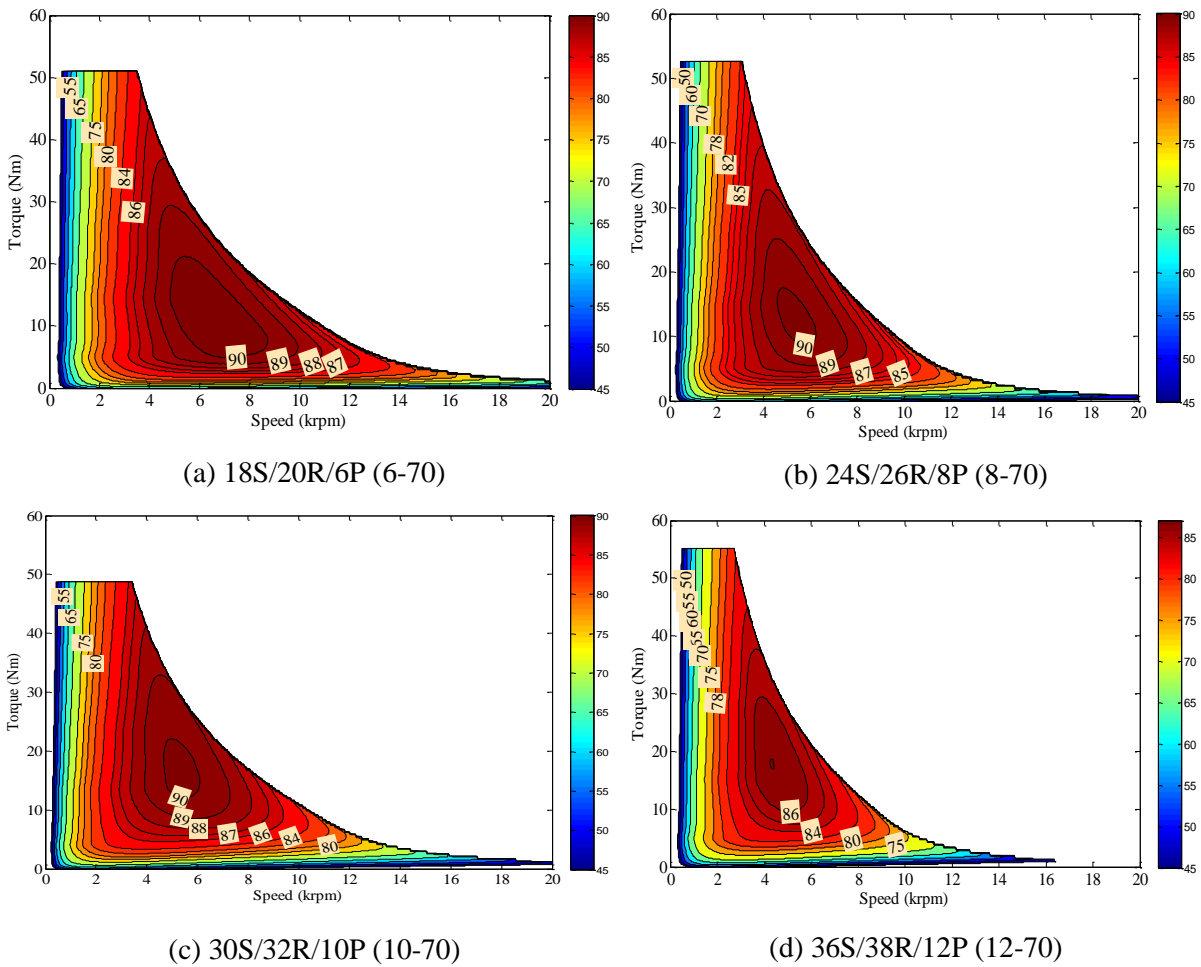
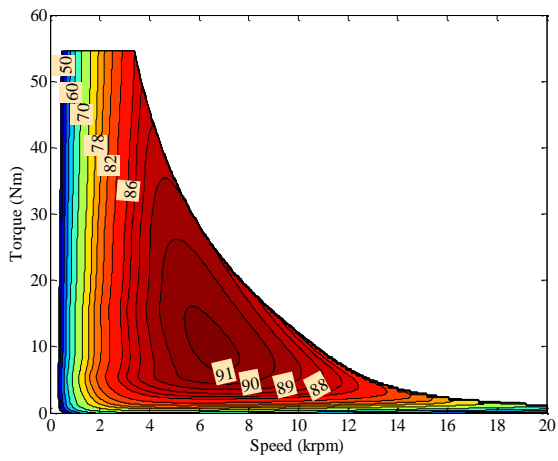
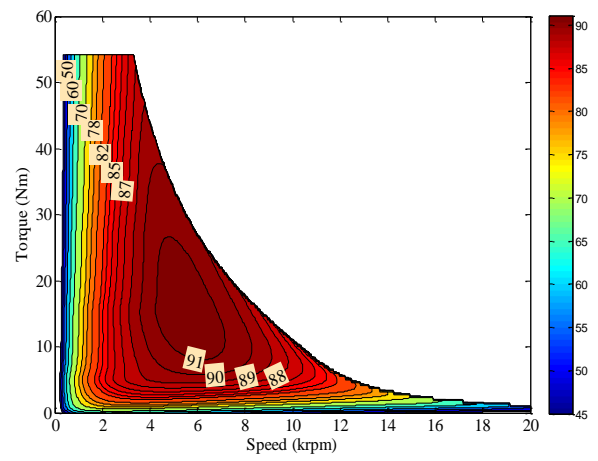


Fig. 4.21 Efficiency maps of the AIMs with 70mm stack length.

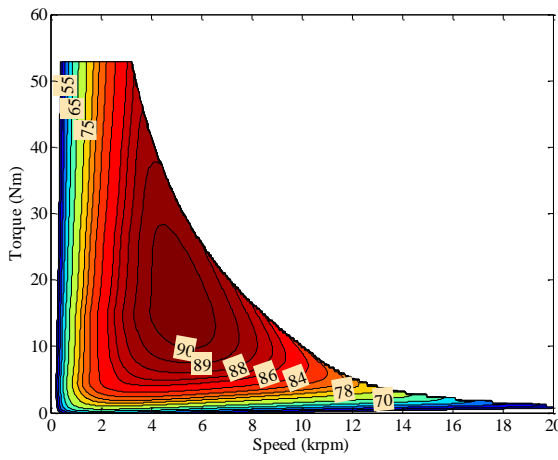
As seen in Fig. 4.19, the highest efficiency of the CIM is 92% between 6krpm and 9.5krpm. As explained previously and presented in Table 4.2 to Table 4.4 because of the lower MMF harmonics, lower bar current harmonics are induced in the bars, and consequently lower bar copper loss is obtained from the CIM. In the same manner, since the MMF harmonics and hence the bar current harmonics of the AIMs designed with $q = 1$ combinations are quite high, they have high bar copper losses. Therefore, as a consequence of this phenomenon, the highest efficiencies of the AIMs with the same stack length of the CIM are lower than those of the CIM as seen in Fig. 4.20 and Fig. 4.21. On the other hand, it has also shown that the efficiency of the designs with the previously manufactured rotor (44-rotor slots) can be improved by properly choosing and globally optimizing the geometry parameters as shown in Fig. 4.21. Since the rotor bar copper loss has been reduced, the maximum efficiency levels are increased up to 90% for 6P and 8P AIMs with 70mm stack length. On the other hand, it is shown that it is possible to obtain a comparable even higher efficiency than that of the CIM with the AIMs designs having ≥ 90 mm stack lengths. Nevertheless, the total axial length of the AIMs with 90mm is still ~ 13.5 shorter than that of the CIM (see Table 4.3).



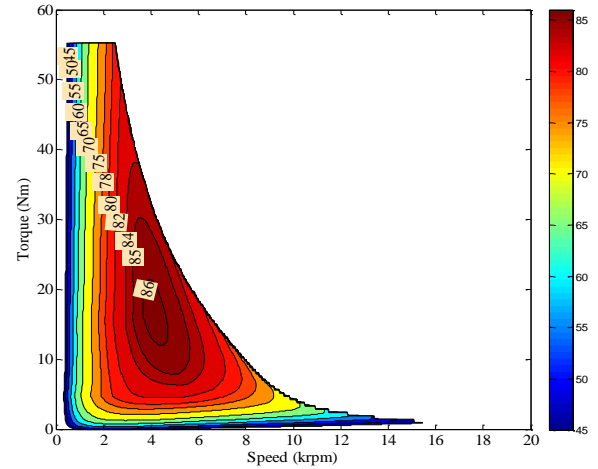
(a) 18S/20R/6P (6-80)



(b) 24S/26R/8P (8-80)

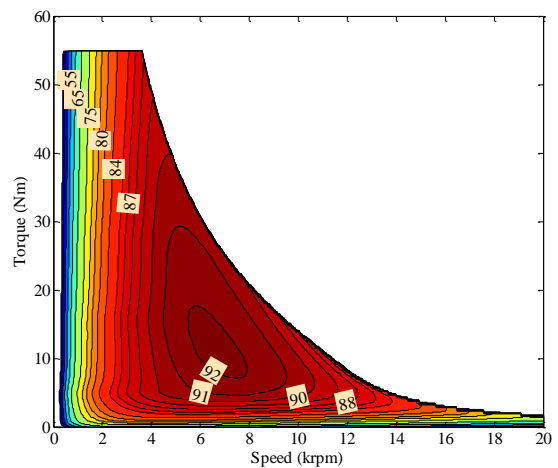


(c) 30S/32R/10P (10-80)

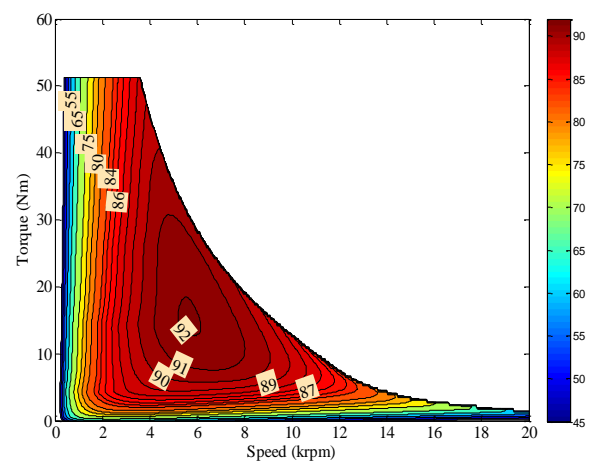


(d) 36S/38R/12P (12-80)

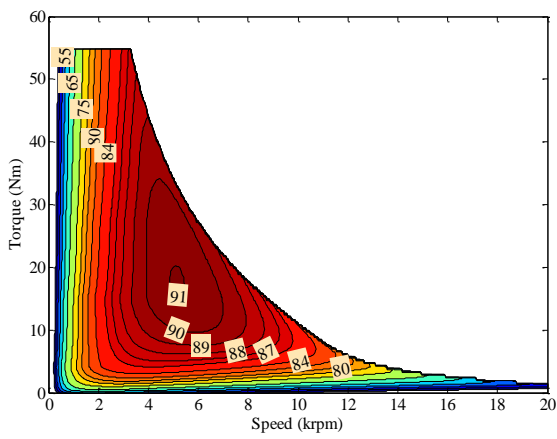
Fig. 4.22 Efficiency maps of the AIMs with 80mm stack length.



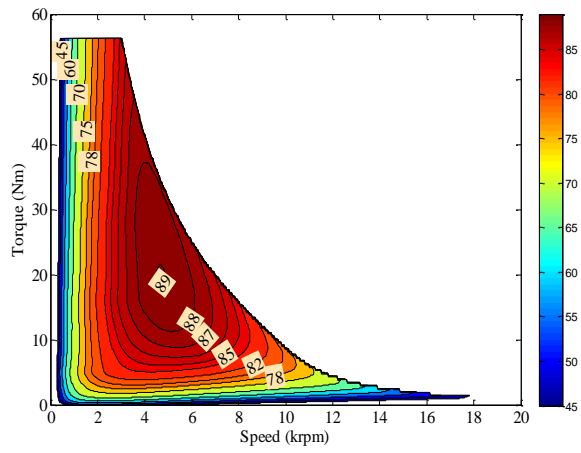
(a) 18S/20R/6P (6-90)



(b) 24S/26R/8P (8-90)

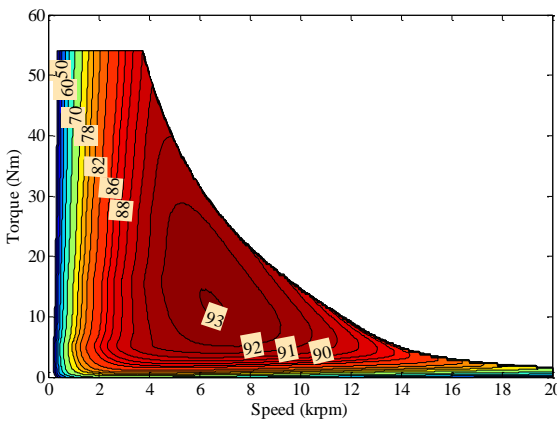


(c) 30S/32R/10P (10-90)

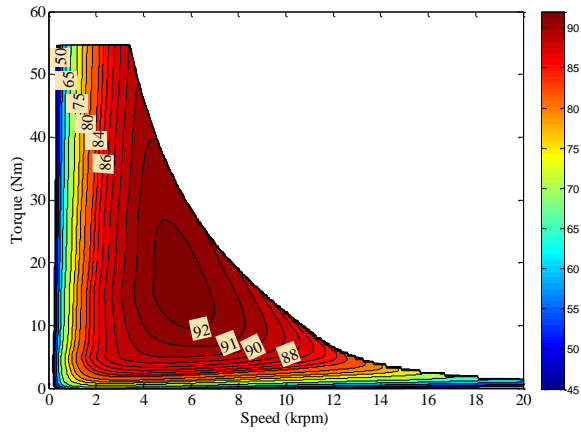


(d) 36S/38R/12P (12-90)

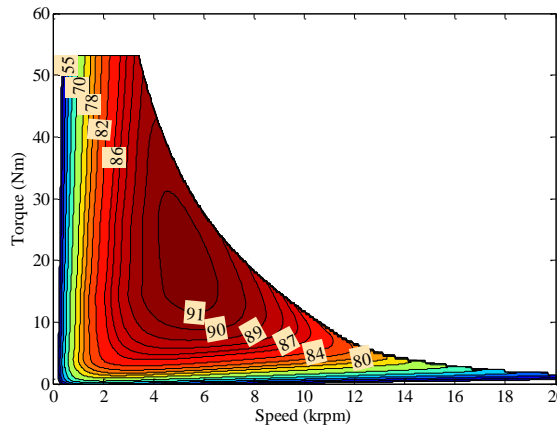
Fig. 4.23 Efficiency maps of the AIMs with 90mm stack length.



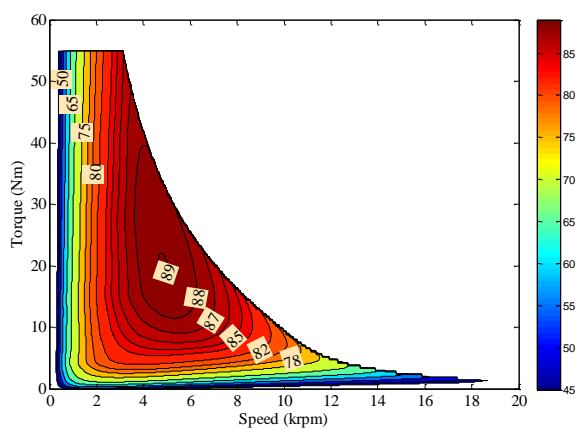
(a) 18S/20R/6P (6-100)



(b) 24S/26R/8P (8-100)



(c) 30S/32R/10P (10-100)



(d) 36S/58R/12P (12-100)

Fig. 4.24 Efficiency maps of the AIMs with 100mm stack length.

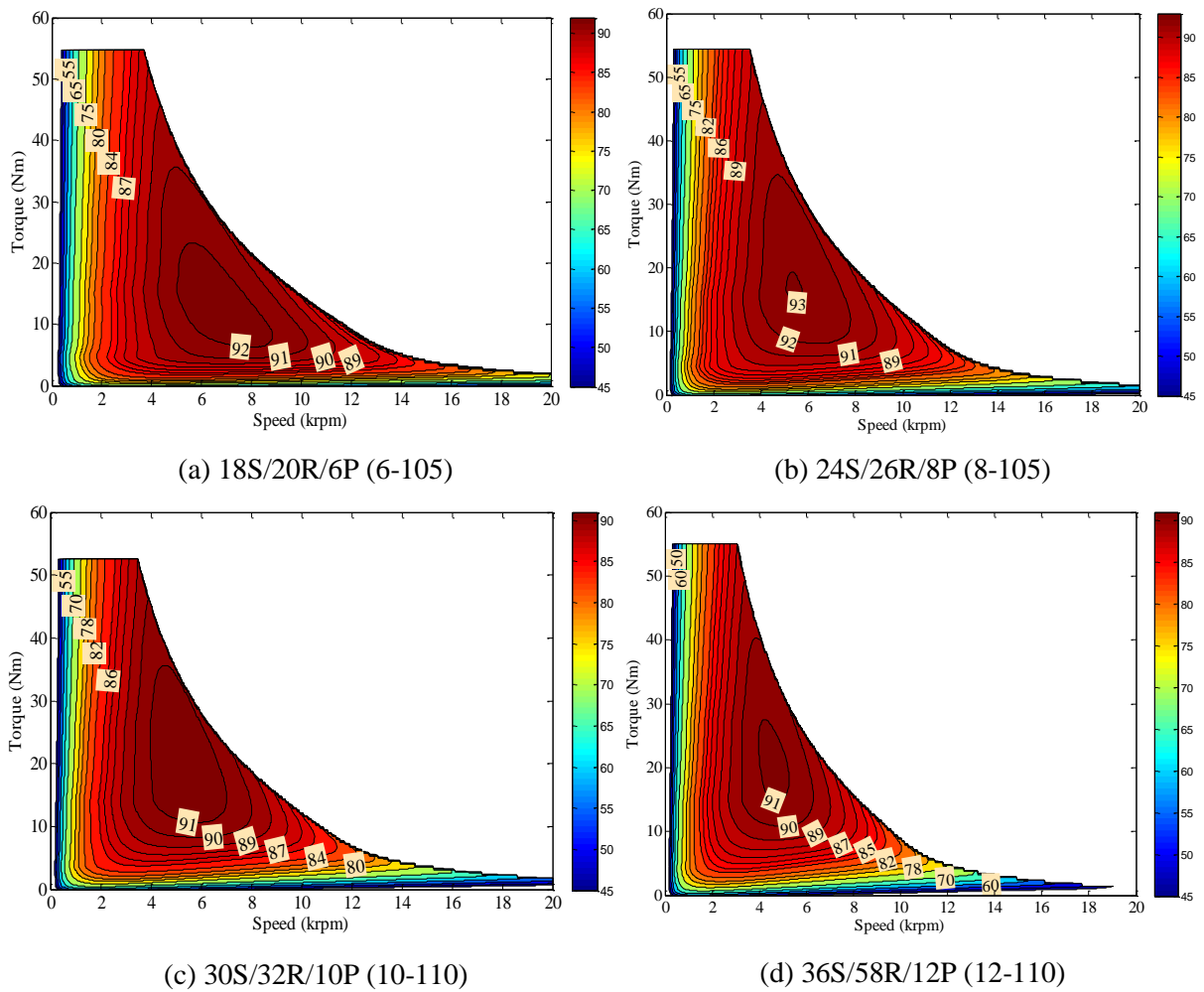


Fig. 4.25 Efficiency maps of the AIMs with 105mm and 110mm stack lengths.

Considering the findings from the comparison study, the discussions on the influence of the S/P combinations, number of turns, stack length, current density and flux-weakening capability, are summarised in Table 4.5.

In conclusion, the 18S/20R/6P AIM with 90mm can be chosen as a good candidate for the given specifications and requirements. The advantages and disadvantages of the proposed winding topology is summarised as follows:

- ☒ Advantages of using non-overlapping windings instead of conventional windings:
 - Relatively high efficiency;
 - Short total length;
 - Simplicity in manufacturing;
- ☒ Disadvantages of using non-overlapping windings instead of conventional windings:
 - Relatively high torque ripple;

- Relatively high current density;
- Low winding factor (0.866).

The high stator current density can cause an increase in the cooling requirement. However, additional cooling can be tolerated by extra air-cooling provided by the unfilled slots of the stator. It is also revealed that in terms of compactness, the proposed topology is more favourable for the high pole number and low speed (≤ 10 krpm) applications.

Table 4.5 Summary and discussion

Case#	Designs	Discussions
1	AIMs ensuring the best curve match (100 mm - 110mm)	<ul style="list-style-type: none"> • The lower the number of turns, the longer the stack length (for maintaining the torque in constant torque region), and the higher the power at high speeds; • Good T-S curve match; • Relatively high efficiency; • Moderate stator and rotor current densities.
2	AIMs designed by using the dimensions of the manufactured rotor (70mm)	<ul style="list-style-type: none"> • Stator winding and rotor bar current densities are very high; • Poorer torque-speed characteristic; • Lower efficiency.
3	Re-designed AIMs by using the dimensions of the manufactured rotor for low current density (70mm)	<ul style="list-style-type: none"> • Poorer torque-speed characteristic; • Lower power in constant power region, • Lower torque in constant torque region, • Lower efficiency.
4	Improved AIMs (70mm)	<ul style="list-style-type: none"> • Poor torque-speed characteristic; • Low power in constant power region, • Low torque in constant torque region, • Low efficiency.
5	Influence of S/P combination and stack length on the torque-speed characteristics	<ul style="list-style-type: none"> • 6-pole combination is the best candidate in terms of torque-speed characteristic and efficiency

4.3 Investigation of the Best Candidates

Considering the electromagnetic and flux weakening performance characteristics of the compared AIMs, the 18S/20R/6P AIM with 90mm stack length has been chosen as the best candidate. In addition, in order to utilize the previously manufactured squirrel-cage rotor with 44-rotor slot and 70mm stack length, the 18S/44R/6P (11-70e) design has also been selected to be prototyped. Therefore, the shortest and the moderate length (90mm) AIMs can be compared with the 54S/6P CIM having 70mm stack length. As given previously, the 54S/6P CIM has double-layer ISDWs with $y_c = 9$. However, in order to obtain low winding factor harmonic content and short end-winding, it is possible to design 54S/6P CIM double-layer ISDWs with short-pitch $y_c = 7$ by substantially sacrificing the working winding

factor from 0.966 to .0.902. However, the reason why the CIM with $y_c = 9$ has been chosen for comparison is that this CIM has already been made prototype and tested previously. And the test results of this machine has been validated by FEA in Chapter 2. The electromagnetic performance characteristics, including the back-EMF, air-gap flux density, rotor bar current, torque, torque ripple, machine losses, output power, efficiency, etc. have been compared. Note that for simplicity, the 18S/44R/6P (11-70e) and 18S/20R/6P (9-90) have been indicated as AIM1 and AIM2, respectively.

4.3.1 Electromagnetic Performance Comparison of the CIM and Selected AIMs

Flux density and flux line distributions of the selected machines are illustrated in Fig. 4.26. As clearly seen in the figure, there are some local saturated parts in the yoke, stator and rotor tooth parts.

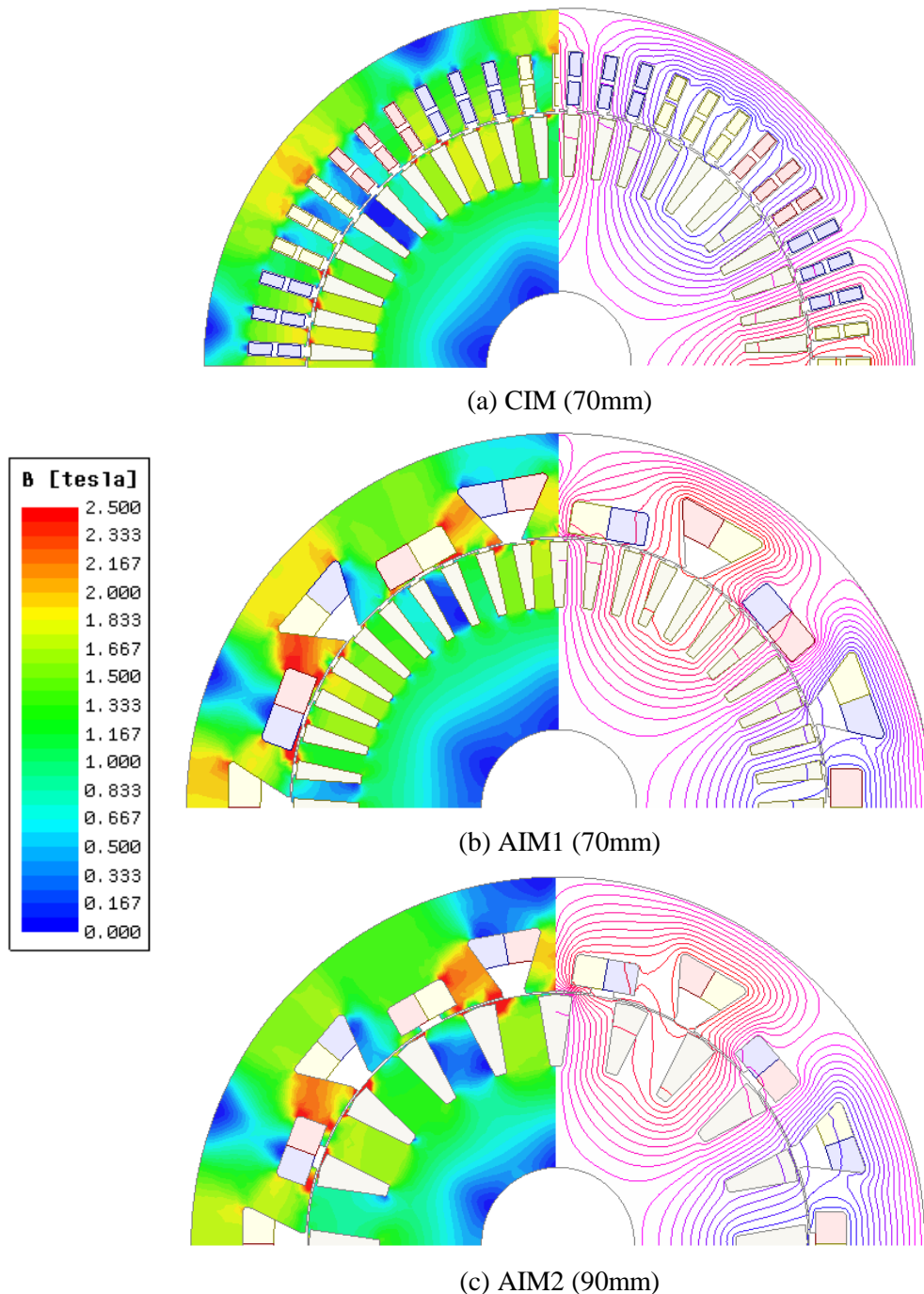


Fig. 4.26 Flux density and flux line distributions.

Especially, the stator tooth parts of the AIMs are saturated heavily. These heavily saturated parts may cause an increase in the harmonic distortion level of the air-gap flux density, rotor tooth flux density, back-EMF, and bar current [GUN16b]. The overall saturation level of the AIMs are higher than that of the CIM. In addition, the saturation level of the AIM2 is slightly lower than that of the AIM1. The back-EMF waveforms for Phase ‘A’ winding and their harmonic spectra are illustrated in Fig. 4.27. As seen, the AIM2’s waveform is the most distorted one, whilst the waveform of the CIM is the least distorted one. This might be resulted from the slotting effect, saturation, and the combined effect of stator and rotor field harmonics due to the winding MMF harmonics.

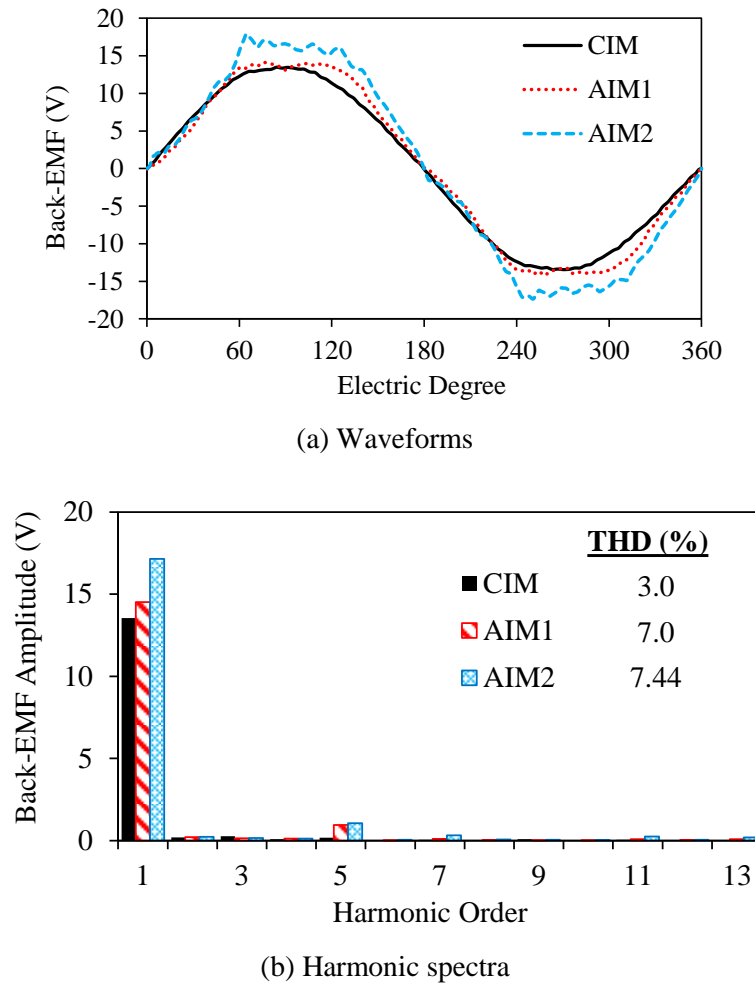


Fig. 4.27 Back-EMF: (a) waveform and (b) harmonic spectra.

The air-gap waveforms and their harmonic spectra are shown in Fig. 4.28. As seen, all waveforms have been heavily distorted. The THD levels of the air-gap flux density has revealed that the AIM1 is the most distorted one. Therefore, as seen in Fig. 4.29(a), its bar current waveform is the most distorted one. Correspondingly, as seen in Table 3.1, its rotor bar copper loss is the highest. In the same manner, the CIM, having the least distorted waveforms, has the least bar copper loss. As seen in Fig. 4.29(a), the waveforms seem like trapezoidal or top-flatted. The reason behind this phenomenon is explained in Chapter 5. It is obvious that the AIM1 has the most distorted waveform, and hence it has the highest THD. As seen in Fig. 4.29(b), all IMs have high-order harmonics, particularly the AIM1 has the high-

order harmonics at the highest amplitudes. This is because of the innate conclusion of the rotor phase number, which equals to the rotor slot number, slip harmonics, and induction principle occurring several times.

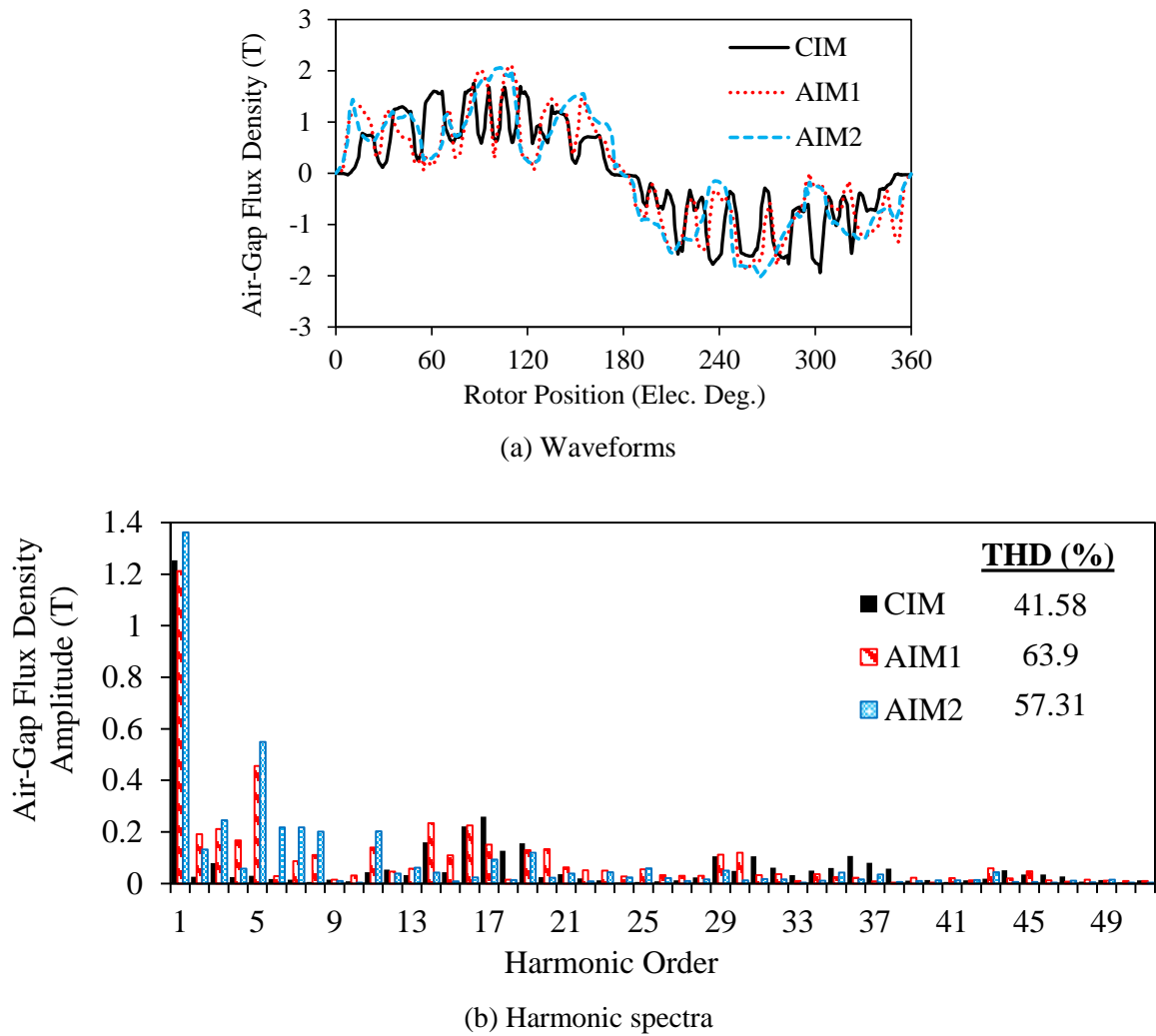
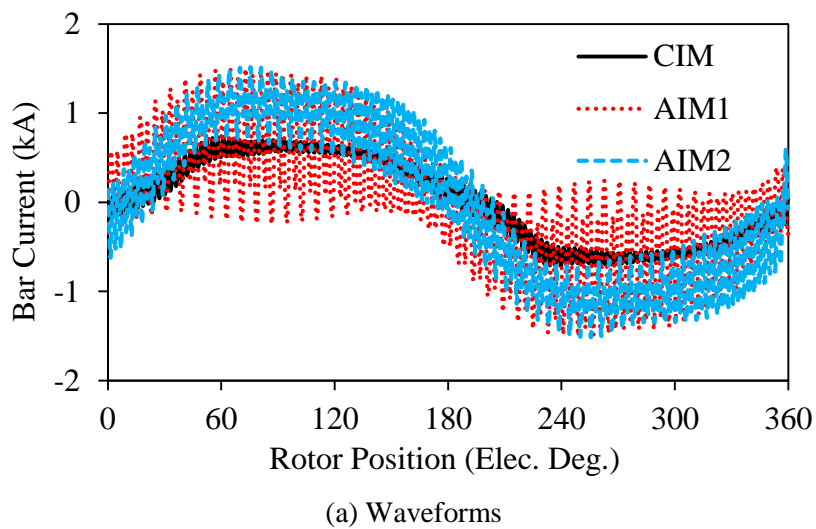
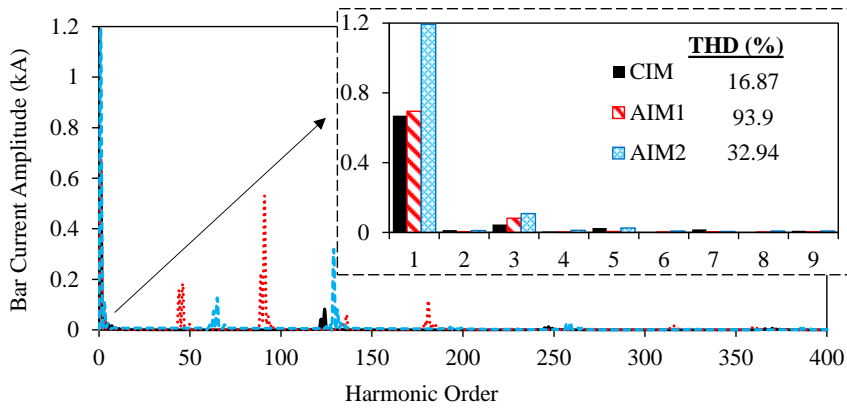


Fig. 4.28 Air-gap flux density: (a) waveform and (b) harmonic spectra.





(b) Harmonic spectra

Fig. 4.29 Bar current: (a) waveform and (b) harmonic spectra.

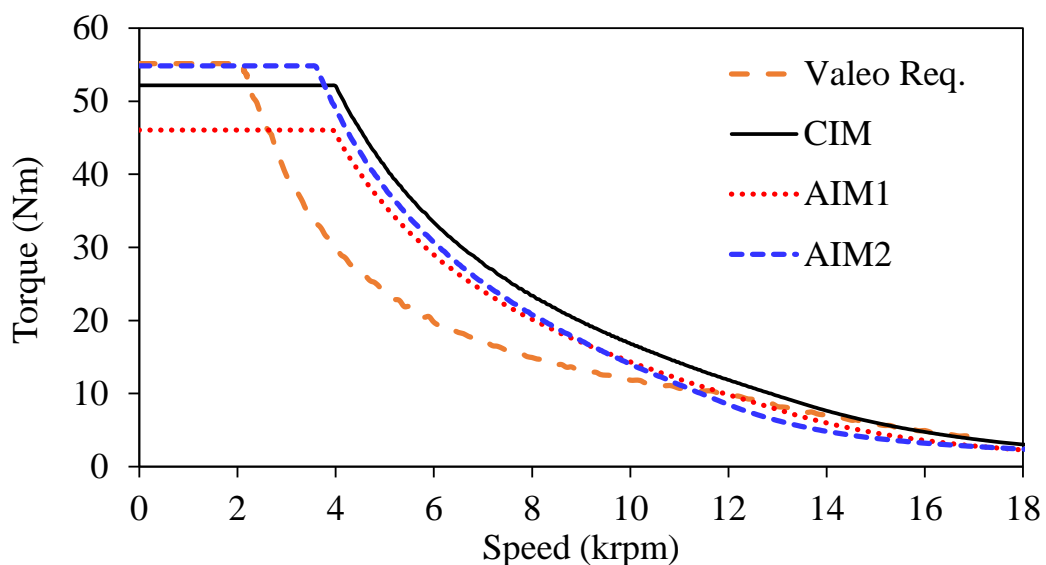
Table 4.6 Performance characteristics comparison

	CIM	AIM1	AIM2
N_{pp}	9	11	9
l_s (mm)	70	70	90
l_{end} (mm)	52	19.255	15.7
l_{total} (mm)	122.17	89.38 (-26.84%)	105.85 (-13.36%)
k_{w1}	0.96	0.866	
R_{phase} (mΩ)	3.7261	2.62023	2.524225
n_{maxT} (rpm)	1905	1875	1905
T (Nm)	52.21	45.92	54.66
ΔT (%)	4.26	16.25 (+281.36%)	17.15 (+328.75%)
P_{out} (kW)	10.95	9.016	10.9
P_{Scu_in} (kW)	0.728	1.235	1.298
P_{Scu_end} (kW)	2.07	0.733	0.6
P_{Scu} (kW)	2.798	1.968	1.898
P_{Rcu} (kW)	0.53	1.7174	0.925
P_{hyst} (mW)	10.89	13.11	19.542
P_{eddy} (mW)	1.7	1.6775	2.71
η (%)	75.343	70.497 (-6.43%)	79.618 (+5.67)
J_S (A/mm²)	22.32	31 (+38.88%)	30.96 (+38.7%)
J_R (A/mm²)	13.54	20.1 (+48.45%)	13.71 (+1.25%)
Split Ratio	0.723	0.723	0.69

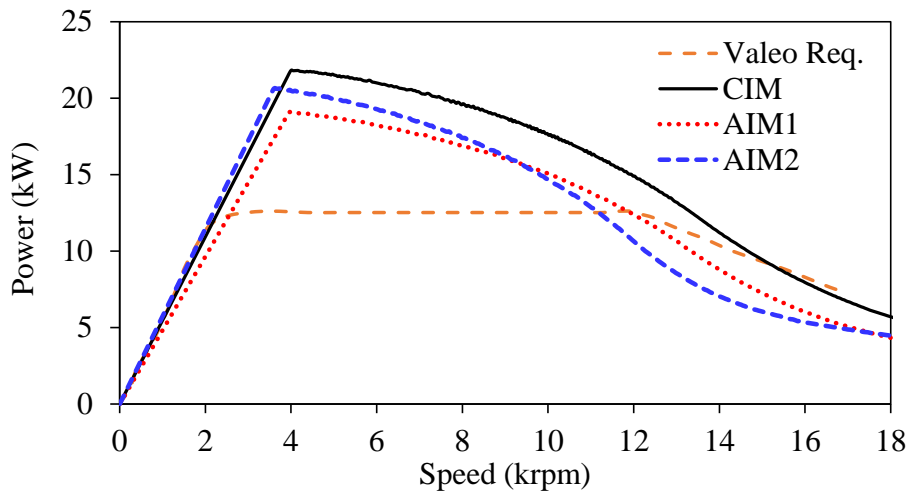
The calculated electromagnetic performance of the considered IMs are listed in Table 4.6. Although the axial length of the AIM1 is 26.8% shorter than that of the CIM, its average torque is 12% lower than that of the CIM. Since the 44-rotor slot number of the AIM1 is not suitable for the 18S/6P combination, the overall electromagnetic performance is not satisfactory. On the other hand, thanks to the proposed method and the properly selected rotor slot number, according to the CIM, the AIM2 has 4.7% and 5.67% higher torque and efficiency, respectively with 13.36% shorter total axial length. The torque ripple levels of the AIMs are much higher than those of the CIM. However, a design approach compromising of closed rotor slots with u-shaped bridges, which reduces the torque ripple and bar copper loss levels significantly, will be presented in following section. Furthermore, the stator and rotor current densities are within the acceptable limits. Note that almost similar slot fill factors 0.61 and 0.64 have been used for conventional and adapted winding IMs, respectively. However, as seen the stator current density of the AIMs are 38.88% higher than that of the CIM. The main reason is that the AIMs have some unfilled slots. This is why the AIMs have a bit higher slot fill factor. It can be predicted that because of the higher stator current density, the AIMs may require more cooling equipment or higher fluid flow rate or a much better fluid material. On the other hand, it should be considered that the unfilled stator slots will help cooling system for cooling the IM faster or to reduce size of cooling equipment or fluid flow rate.

4.3.2 Flux-Weakening Performance Comparison

The flux-weakening performance of the considered IMs under the 500Arms and 27Vrms operating condition are compared in Fig. 4.30. Although all machines show different characteristics at the constant torque region, they show similar characteristics in the constant power and deep-flux weakening regions. It is obvious that the overall flux-weakening characteristics of the AIMs are not as good as those of the CIM. However, the flux-weakening characteristics of the AIM2 is quite satisfactory since it meets the desired flux-weakening characteristics.

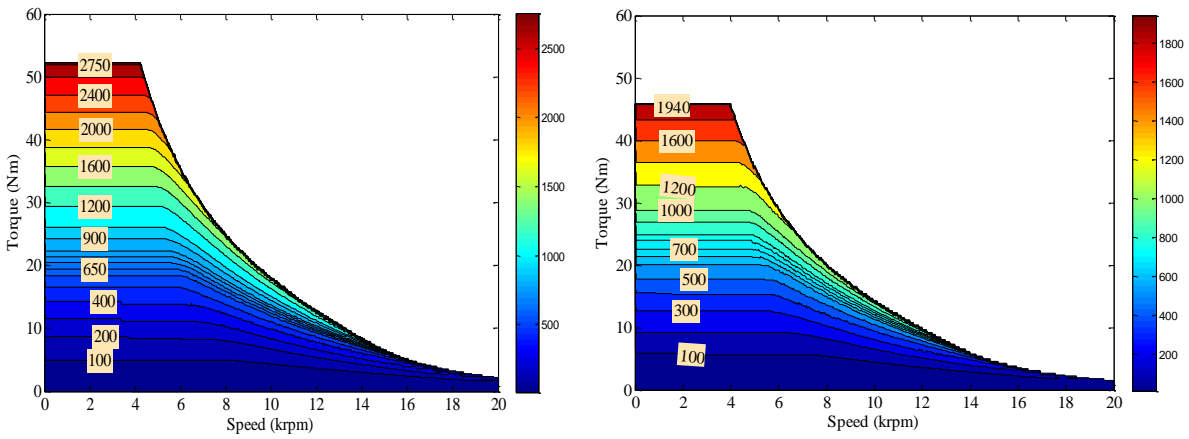


(a)



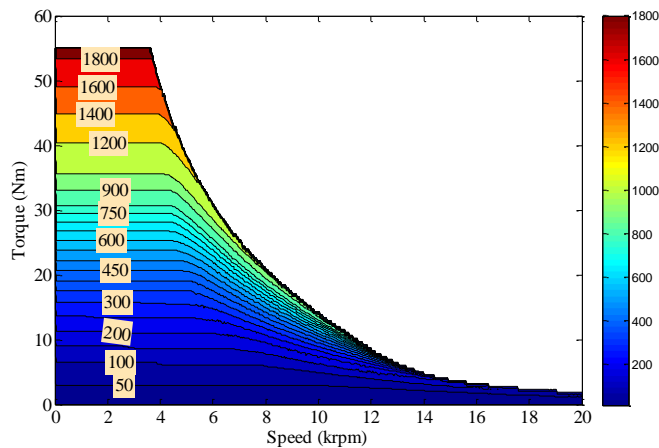
(b)

Fig. 4.30 Comparison of the flux-weakening characteristics of the investigated IMs.



(a) CIM

(b) AIM1



(c) AIM2

Fig. 4.31 Stator copper loss maps of the investigated IMs.

In general, the most dominant power loss components of an IM are the stator and rotor copper losses. Since there is no PM or constant flux component, the core loss are almost negligible. Therefore, although the core loss contributions have been taken into account in the efficiency calculations, only

the stator and rotor copper loss maps have been illustrated in this section. The comparison of stator copper losses are illustrated in Fig. 4.31. Because of the very long (9-slot pitch) end-winding length of the CIM, its stator copper loss is the highest. On the other hand, there is no significant difference in the stator copper losses of the AIMS. The squirrel-cage IMs suffer from the low power in the high-speed operation region due to the more voltage requirement of the leakage inductances increasing with speed and frequency and the low efficiency through all operation regions because of the existence of the copper loss on the rotor bars when compared to their competitors for the EV applications [WIE92], [SOO02], [ZER06], [BOL10], [BOL14], [GUA14], [GUA16]. The rotor bar copper loss maps have been compared as illustrated in Fig. 4.32. As expected, because of the very low winding MMF harmonic content of the CIM, its bar copper loss is the lowest, whilst the AIM1 has the highest bar copper loss. As seen in Fig. 4.32(a) and Fig. 4.32(c), the maximum bar copper loss of the AIM2 is 0.4kW higher than that of the CIM. As shown in the next section, it is possible to reduce this difference to 0.18kW by changing the rotor slot shape.

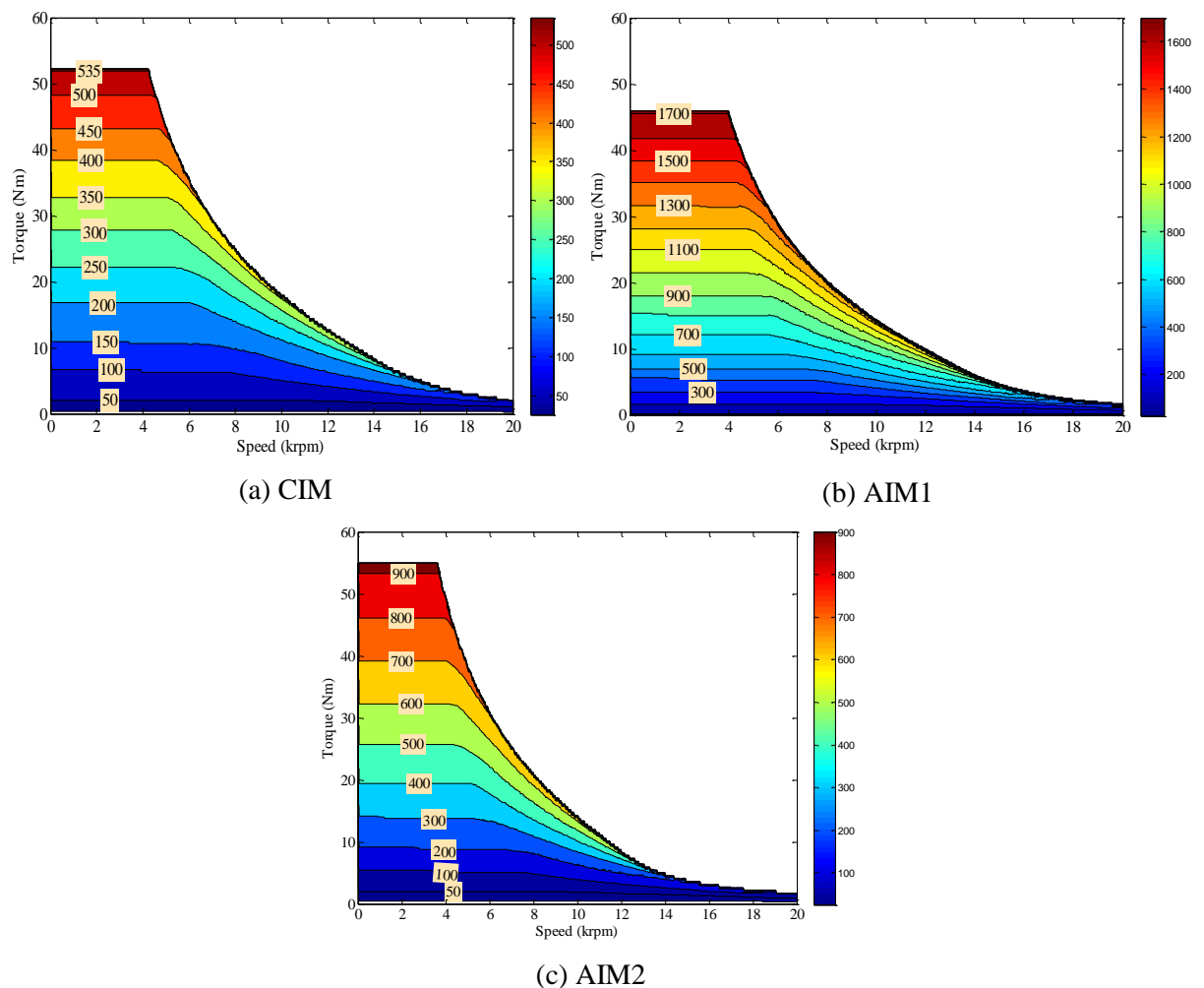


Fig. 4.32 Rotor bar copper loss maps of the investigated IMs.

The efficiency maps of the considered IMs are illustrated in Fig. 4.33. The CIM and AIM2 have quite similar efficiency maps, whilst AIM1 has a poor efficiency map. In the following section, it is shown that by utilizing a closed rotor slot with u-shaped iron bridges, it is possible to reduce the torque

ripple and bar copper loss substantially. Therefore, the efficiency of the AIM2 can be further increased. The influence of the rotor topology on the electromagnetic and flux-weakening performance characteristics will be investigated in the following section.

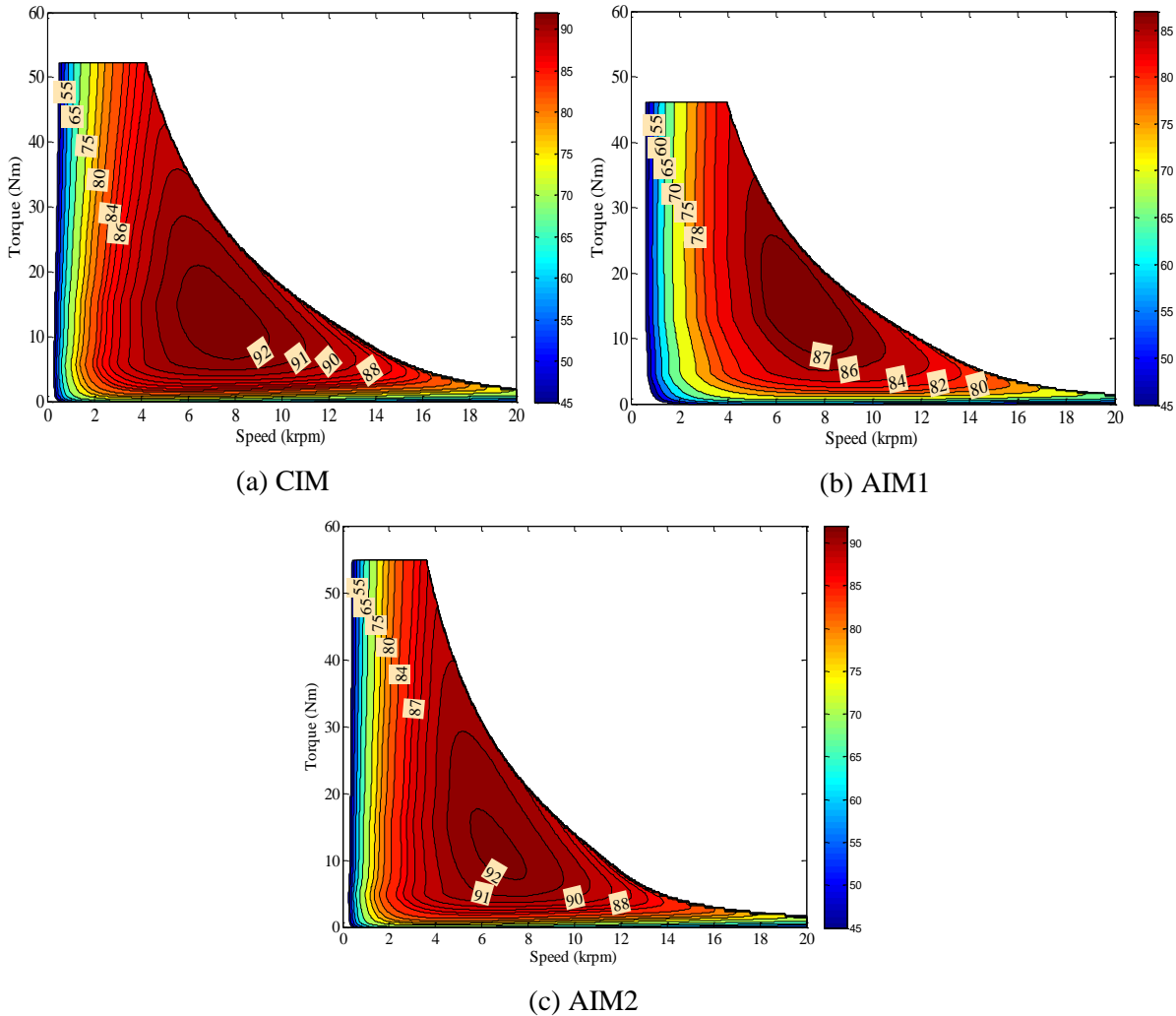


Fig. 4.33 Efficiency maps of the investigated IMs.

4.4 Performance of Advanced Non-Overlapping Winding Induction Machines with Different Rotor Topologies

It has been shown that the IMs have the high order frequency components in the air-gap, at the stator tooth tip parts, and dominantly at the rotor tooth tip parts arising from the slotting effect, saturation effect, winding MMF, and slip harmonics [GUN16b], [GUN17a], [LI16], [GUN17b], [KUN17]. The conventional rotor structure design with open-slot cast rotor (OS) is not a good candidate for adopting in the HEV application in terms of efficiency because of the significant bar copper loss and consequently overheating due to the air-gap flux density harmonics [LI10], [NEE95], [LI16], [KUN17]. In order to reduce the parasitic effects arising from the rotor part of the IM and consequently the bar losses, torque ripple, acoustic noise, etc. a number of different methods has been proposed. These methods can be classified as follows.

- Using copper bars instead of aluminium bars: [PET03], [COW03], [KIR07], [PET07];
- Using skewed rotor: [MCC98], [KAW09];
- Determining optimal rotor shape: [DIA72a], [DIA72b], [DIA72c], [NEE93], [NEE95], [FIR07], [PAR08], [KON09], [BOL10], [GER11], [MAU13], [LEE13], [KIM15], [LI16], [KUN17];
- Determining the best stator and rotor slot number/pole number combination: [KOB97], [HUA02];
- Adopting new control methods: [TAN02], [BEE08], [LIA11];
- Modulated rotor slots: [CHI08], [STE12].

Moreover, in order to improve the IM's performance characteristics such as efficiency and output power, the power factor correction method has been utilized widely [LAI82], [MUL89], [TAM99], [SPE92], [YAO16], [YAO17]. To be able to improve the power factor, different methods such as utilizing novel stator winding arrangements together with moving-coil regulator concept [LAI82], employing an auxiliary three-phase stator winding together with a PWM inverter [MUL89] or employing an auxiliary stator winding in conjunction with a PWM voltage inverter and a single capacitor on the DC side of the inverter [TAM99], using terminal capacitors which is proposed as the cost-effective and reliable means of power factor improvement, and utilizing a wound rotor with converter-fed rotor windings [YAO16], [YAO17] have been proposed.

It is shown that utilizing semi-magnetic wedges can reduce the negative effects caused by the open rotor slots, and consequently improve the performance characteristics of the IM [PET16]. Another improvement method, utilizing a mixed different winding configurations, has been proposed [MUT12]. It is shown that the combination of double and triple layer windings can provide a reduction in torque ripple without sacrificing the average torque. In some papers, in order to reduce the stray loss, skewed rotor is proposed to use [MCC98], [KAW09]. In addition, in order to increase the efficiency and improve the thermal characteristics, using copper material instead of conventional aluminium for the squirrel-cage is proposed [PET03], [COW03], [KIR07], [PET07]. Moreover, for high-speed applications of inverted-fed IMs, solid-rotor structures are proposed as a good candidate because of their rigid constructions which allow operating at much higher speeds than a squirrel-cage IM. It has been shown that the solid-rotor IM shows favourable performance characteristics such as high power density, high efficiency, high starting torque-to-starting current ratio, and high tip speed [GIE12], [UZH17a], [UZH17b].

In this section, influence of the rotor topology on the performance characteristics of the AIM has been investigated. The proposed 18S/22R/6P NWIM with 90mm stack length has been employed for investigating the effect of the rotor structure. In order to reveal the influence of rotor structure on the electromagnetic and flux-weakening performances, four different rotor structures, namely, insert-bar

(IB), open-slot cast-rotor (OS), closed-slot cast-rotor with straight bridge (SB), and closed-slot cast-rotor with u-shaped bridge (uB) have been considered. It has been reported that the most significant improvements can be achieved by changing the rotor slot geometry, which can reduce the bar losses of the rotor to the minimum [NEE93], [NEE95], [BOL10]. In this study, the short-bar method proposed in [KON09], [LI16], [LI17], and [KUN17] has not been considered in this study because of the significantly increased rotor bar current density due to the remarkably reduced slot fill factor [LI16]. On the other hand, the closed-rotor slot structure proposed in [NEE93], [NEE95], and [BOL10] is considered here.

The parameters of an initial rotor slot geometry is illustrated in Fig. 4.34(a). In addition, by assigning additional parameters as shown in Fig. 4.34(b) for the straight bridge (SB) rotor, it is possible to obtain a closed-slot cast-rotor with u-bridge (uB) rotor structure (see Fig. 4.37(d)). The initial slot geometry belongs to the insert-bar (IB) structure. By changing the rotor slot fill factor of the IB structure, it is possible to obtain open-slot cast-rotor (OS) structure as shown in Fig. 4.37(b). As seen in Fig. 4.34(a), it is possible to change the rotor type by changing the slot opening parameters, particularly b_{r0} , e.g. if b_{r0} is assigned as zero, then the slot structure will be turned into closed-slot cast rotor with SB as shown in Fig. 4.37(c). The influence of the slot opening width parameter b_{r0} on the steady-state performance characteristics of IMs having IB and OS rotors have been investigated as follows.

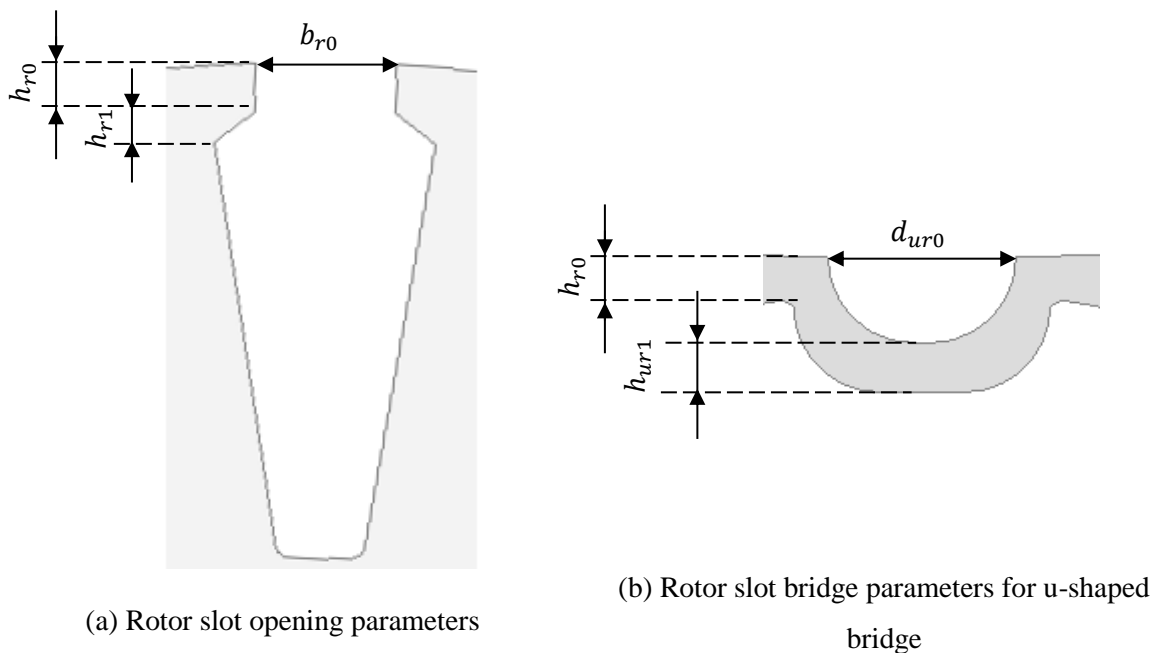


Fig. 4.34 Rotor slot dimensional parameters.

The variation of the average torque T , torque ripple ΔT , rotor bar copper loss P_{rcu} , and bar current density J_r with respect to b_{r0} parameter is illustrated in Fig. 4.35. As seen in the figures, the average torque and rotor current density amplitudes are not changed significantly with b_{r0} . However, the torque ripple and bar copper loss are increased considerably with increasing b_{r0} .

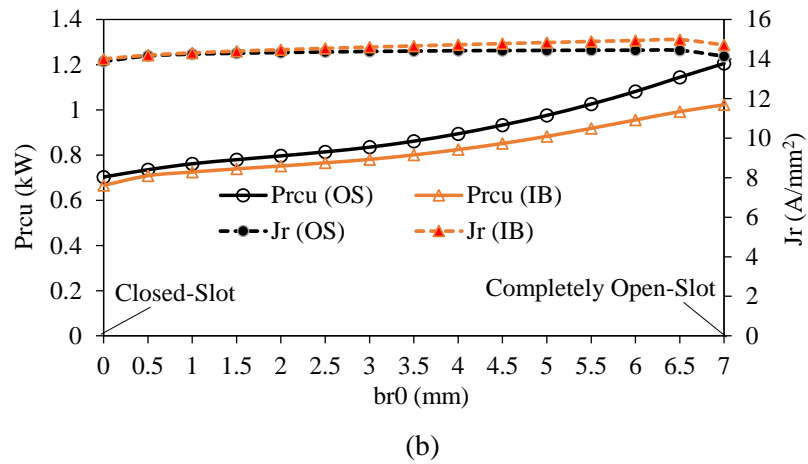
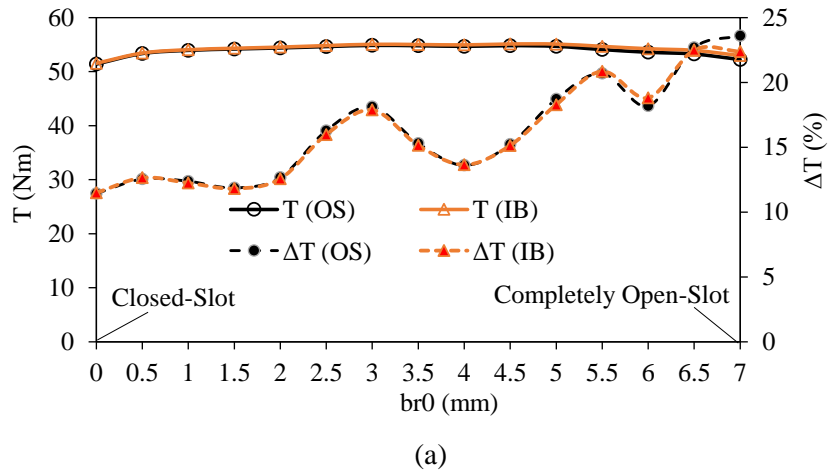


Fig. 4.35 Variation electromagnetic performance characteristics with respect to b_{r0} : (a) average torque and torque ripple, and (b) rotor bar copper loss and bar current density.

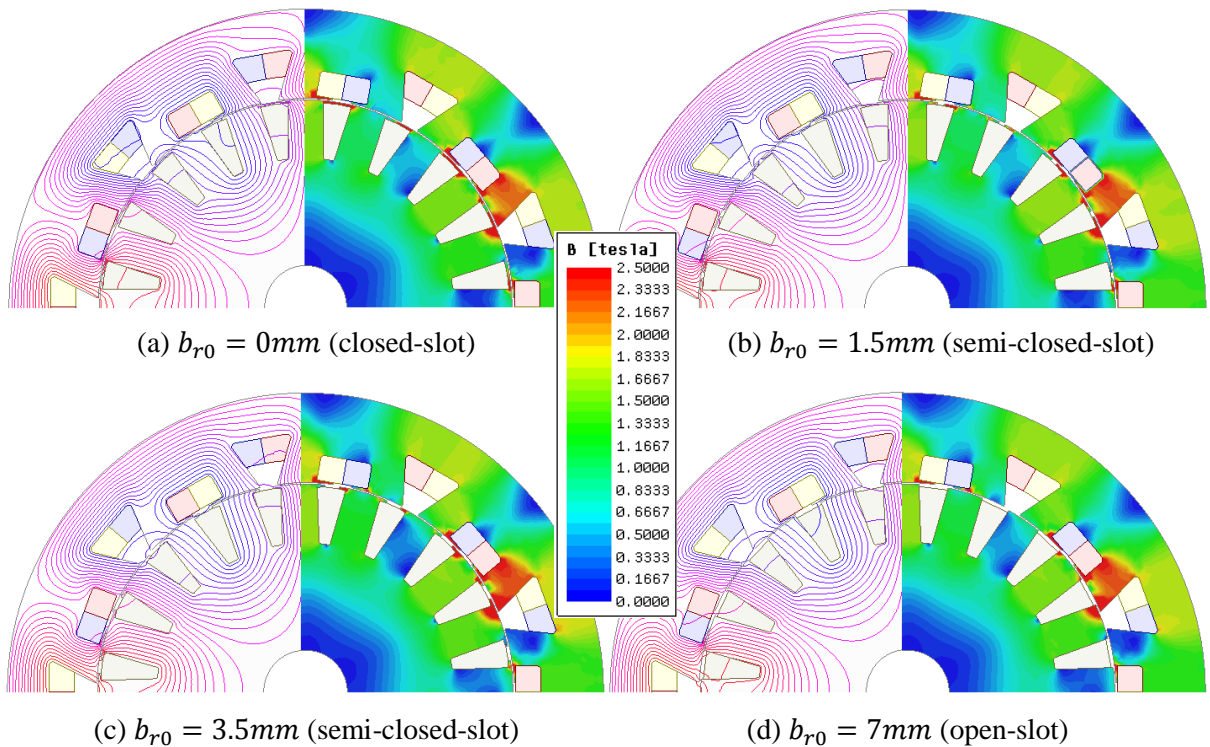


Fig. 4.36 Flux line and flux density distributions for various widths of b_{r0} .

Considering the obtained results, it can be concluded that it is favourable to keep b_{r0} at the minimum in order to keep the bar copper loss and the torque ripple percentage at minimum. The flux line and flux density distributions for various values of b_{r0} are shown in Fig. 4.36. As seen, stator and rotor tooth tip parts are highly saturated. As seen in Fig. 4.36(a), some of the flux are short-circuited through the bridges. On the other hand, since the open-slot rotor cannot collect flux as much as the semi-closed-slots, the flux density on its rotor reduced (see Fig. 4.36(d)). As a consequence, as shown in Fig. 4.35(a), the average torque has reduced for the closed- and open-slot rotors. Note that the influence of other slot opening parameters, including h_{r0} and h_{r1} , on the steady-state and flux-weakening characteristics is investigated in Appendix F.

4.4.1 Considered Squirrel-Cage Rotor Structures

According to rotor manufacturing type, it is possible to design the rotor in different ways as illustrated in Fig. 4.37. Constitutively, there are two different ways for manufacturing the rotor: insert-bar and cast-rotor. Manufacturing of cast-rotor type squirrel-cage rotor is simpler than that of the insert-bar. Basically, the cast-rotor type can be manufactured as open-slot and closed-slot as shown in Fig. 4.37(b) and (c), respectively. The rotor of the AIM is designed by using six-different rotor structures shown in Fig. 4.37. Note that, all the specifications kept at their optimum dimensions except for b_{r0} , h_{r0} , and h_{r1} and additional slot bridge parameters shown in Fig. 4.34(b). The electromagnetic and flux-weakening performances of the AIMs designed by using the rotor slot types shown in Fig. 4.37 have been compared with those of the CIM having IB rotor structure.

4.4.2 Comparison of Electromagnetic Performance Characteristics

In this section the steady-state electromagnetic performance characteristics including the flux-linkage, phase back-EMF, air-gap flux density, rotor bar current, flux density and flux line distributions, and torque waveforms for the AIM equipped with different rotor structures and the CIM equipped with the IB rotor structure have been investigated through a comparison study. The 18S/20R/6P AIM with 90mm stack length and the 54S/44R/6P CIM with 70mm stack length have been employed for investigating the influence of the rotor types. The excitation specifications are 500Arms and 100Hz. The rotor slot parameters are listed in Table 3.1 and the cross-sectional views are shown in Fig. 4.37. Other geometric specifications of the CIM and AIMs can be found in Appendix C.

a) Flux-Linkage

The flux-linkage waveforms and their harmonic spectra are illustrated in Fig. 4.38. As seen in the figure, since the CIM has low number of turns, its flux linkage amplitude is lower than that of the AIMs equipped with different rotor structures. It is also clear that there is no significant difference between the distortion levels of the IMs.

Table 4.7 Rotor slot parameters

Spec. (mm)	IMs	CIM			AIM		
		IB	IB1	IB2	OS	SB	uB
Rotor slot opening width b_{r0}		2	4.4	1.5	4.4	0	0
Rotor slot opening height h_{r0}		0.5	0.8	0.5	0.8	0.2	0.2
Rotor slot opening chamfer h_{r1}		0	0.4	0.3	0.4	0.6	0.6
Rotor slot width b_{r12}		2.68	6	6	6	6	6
Rotor slot opening height h_{r2}		12.6	12.58	12.58	12.58	12.58	12.58
u-bridge d_{ur0} / h_{ur1}		—	—	—	—	—	12 / 0.5

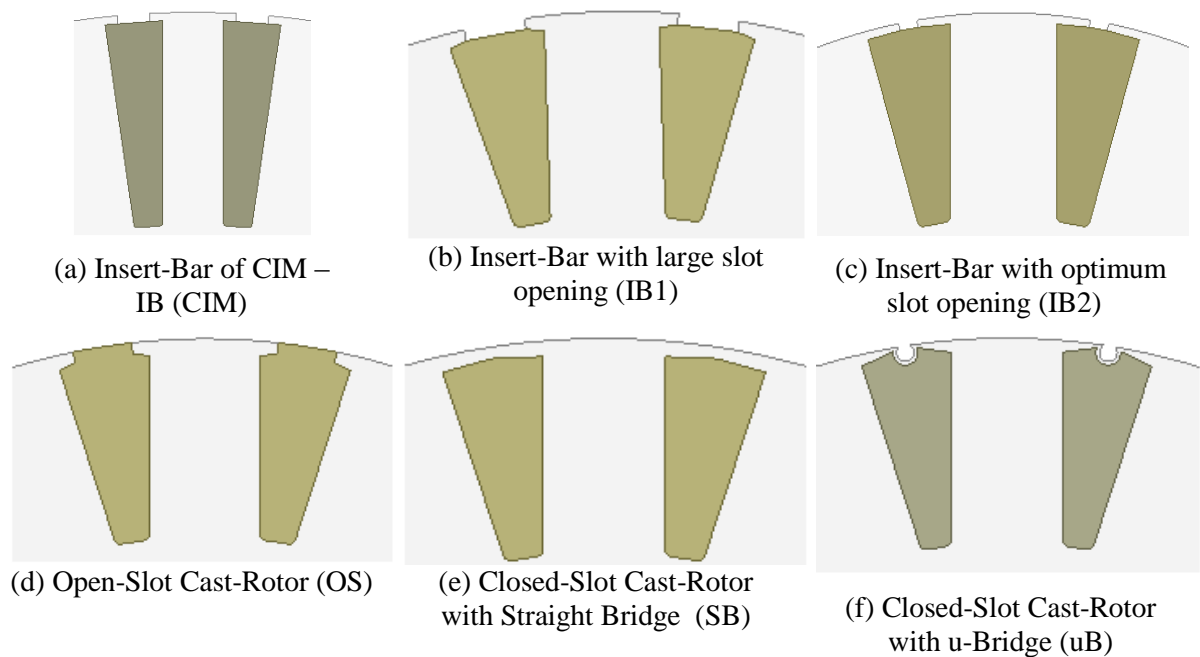


Fig. 4.37 Various rotor slot types having different shapes.

b) Back-EMF

The back-EMF waveforms and their harmonic spectra are illustrated in Fig. 4.39. As seen in the figure, the waveforms of the designs with non-overlapping winding topology are more distorted than those of the CIM because of the large winding MMF harmonics. As seen in Fig. 4.39(b), the THDs of the AIMs are much higher than those of the CIM. Moreover, the THD levels of the AIMs with closed slot rotor structure are higher than those of the open slot counterparts.

c) Air-Gap Flux Density

The air-gap flux density waveforms and their harmonic spectra are shown in Fig. 4.40. The air-gap flux density waveforms are highly distorted for all IMs. Nevertheless, since the AIMs have highly distorted MMF waveforms, their THD levels are much higher than that of the CIM. Furthermore, as clearly seen from Fig. 4.40(b), the THD level of the AIM with closed rotor structure has been reduced considerably owing to the filtering effect of the bridges. The more explanations about the filtering effect of the tooth parts can be found in Chapter 5.

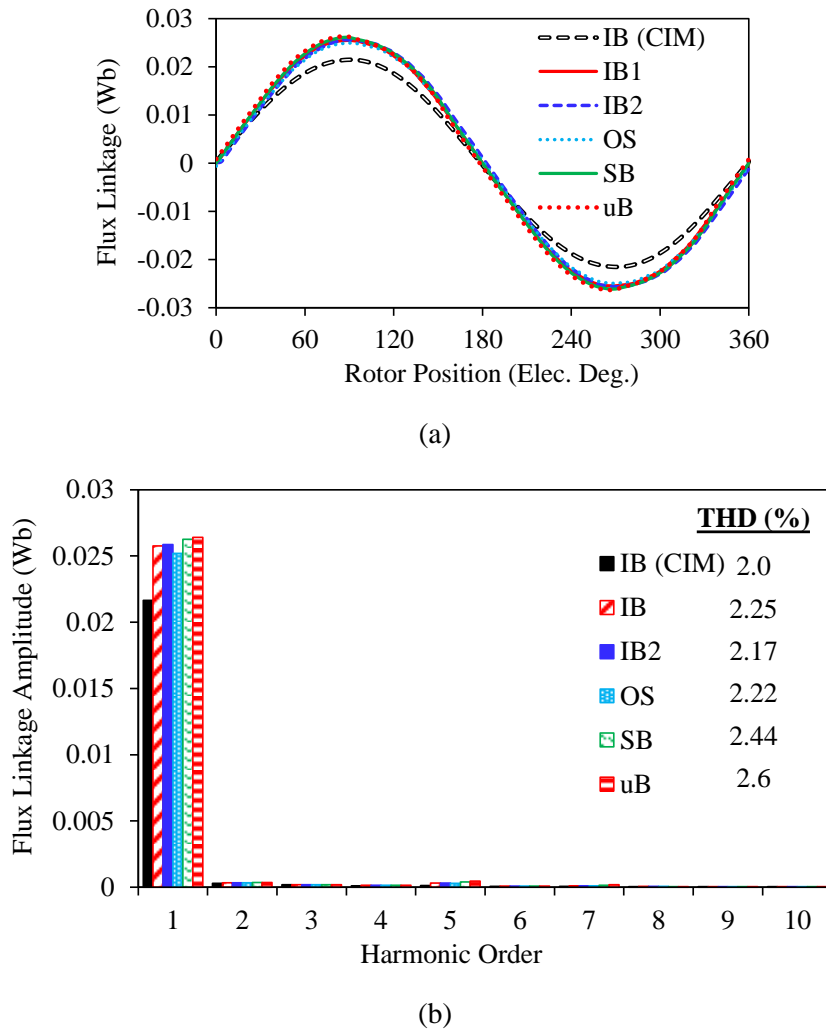
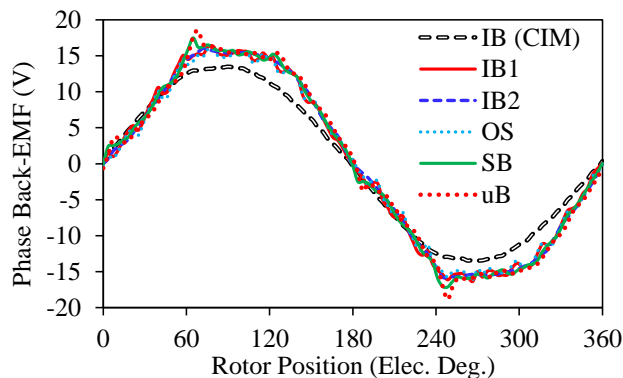
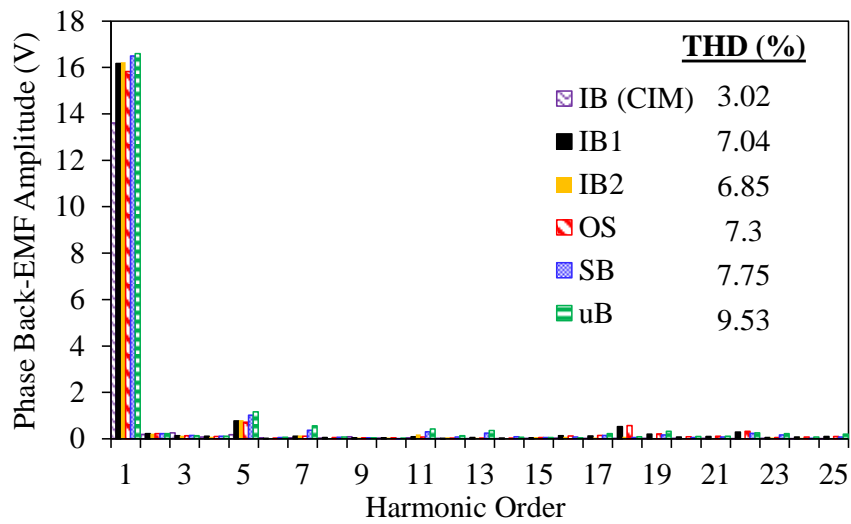


Fig. 4.38 Flux-linkage: (a) waveform and (b) harmonic spectra.

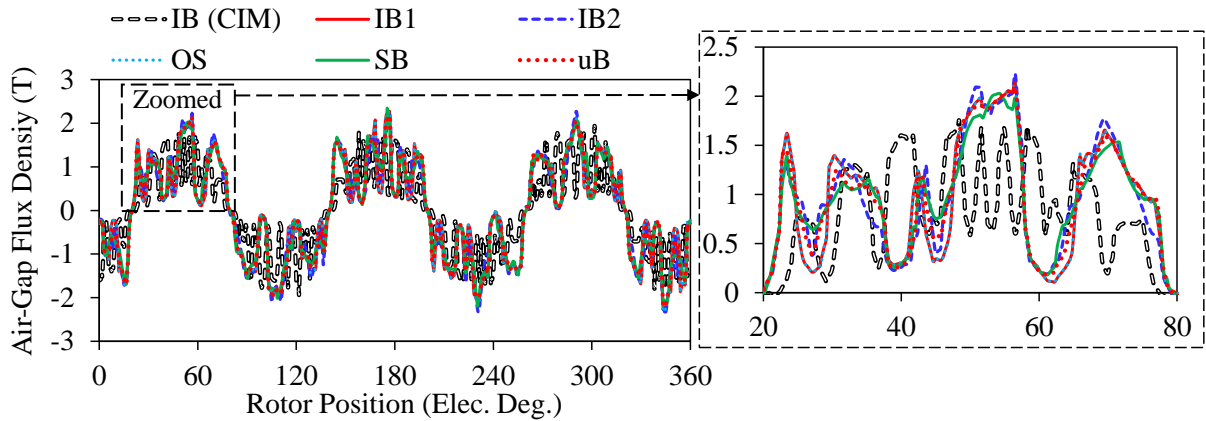


(a)

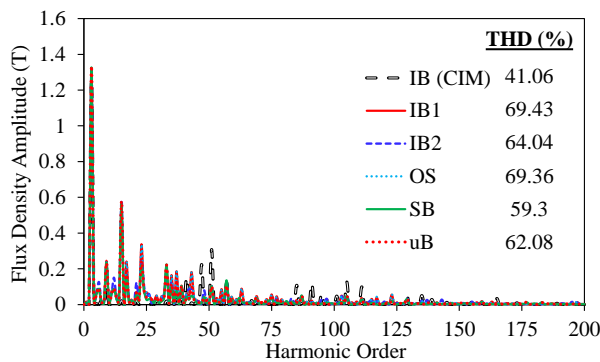


(b)

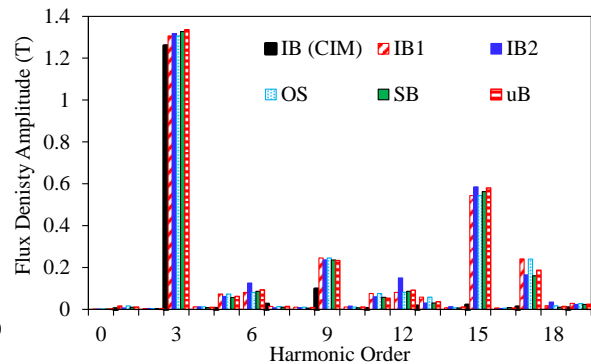
Fig. 4.39 Phase back-EMF: (a) waveform and (b) harmonic spectra.



(a) Waveforms: whole 360° (left) and zoomed in 60° (right)



(b) Low- and high-order harmonics



(c) Low-order harmonics

Fig. 4.40 Air-gap flux density: (a) waveforms and (b, c) harmonic spectra.

d) Bar Current

The bar current waveforms and their harmonic spectra are illustrated in Fig. 4.41. As seen, the AIMS have heavily distorted waveforms when compared to those of the CIM. These heavily distorted MMF harmonics are also induced in the bars. As a consequence, the distortion level of the bar current of the

AIMs are much higher than that of the CIM (see Fig. 4.41(b)). Furthermore, it is obvious that the bar current THD levels of the designs equipped with closed rotor slots are much lower than those of the designs equipped with open rotor slots. As clearly seen in Fig. 4.41, both of the low- and high-order harmonics have been reduced by employing the slot bridges. Besides, as explained previously, these bar current harmonics cause an increase in the rotor bar copper loss.

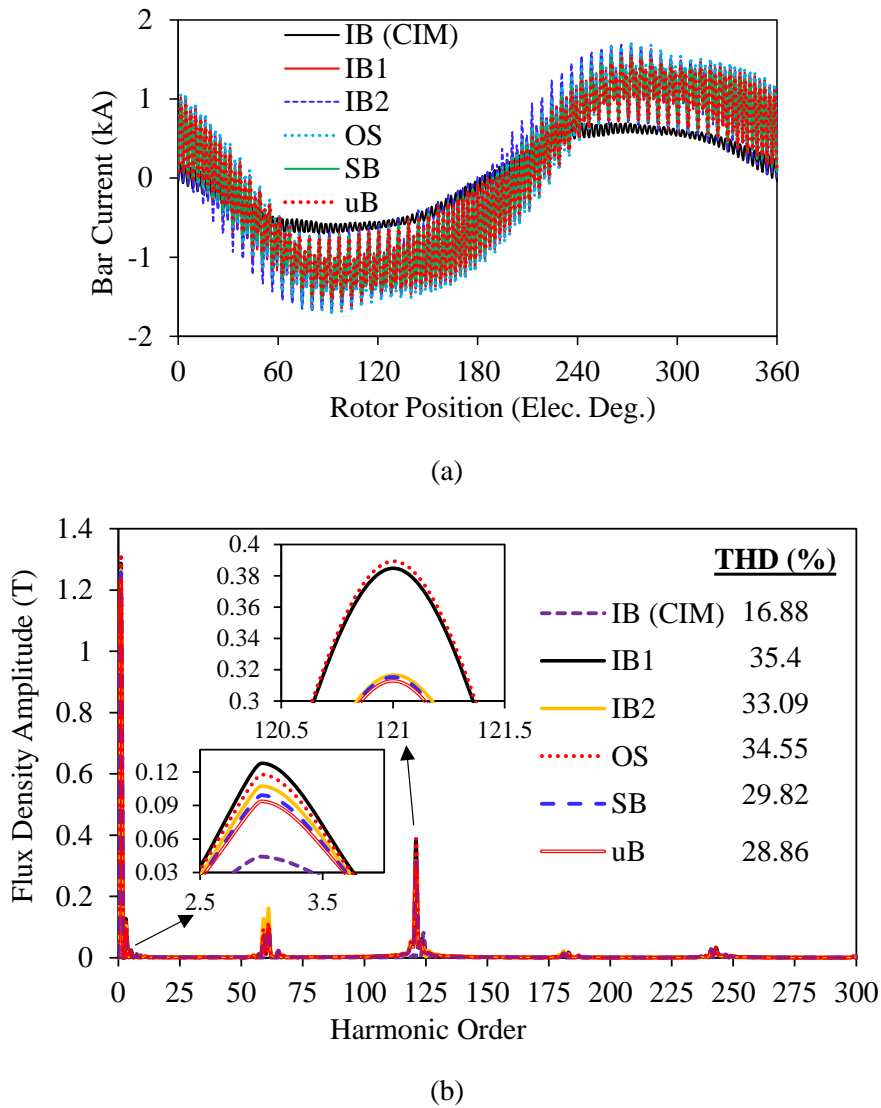


Fig. 4.41 Rotor bar current: (a) waveform and (b) harmonic spectra.

e) Field and Loss Distributions

The flux density and flux line distributions of the IMs are compared in Fig. 4.42. There are some highly saturated local parts, e.g. middle and tooth tip parts of the stator slot, stator yoke parts, and tips of the rotor tooth parts. It is visible that utilizing u-Bridge leads a reduction on the saturation level of the stator tooth parts. Moreover, short-circuited fluxes through the bridges are also visible in Fig. 4.42(d) and (e). That is the reason behind the lower torque amounts of the designs with closed slot rotors (see Fig. 4.44). The total loss distributions of the rotor bars are compared in Fig. 4.43. Note that the calculated total loss includes the copper and eddy current losses. As clearly seen from the loss

distributions, the losses are concentrated on the top parts of the bars. This is due to the combined effect of the deep slot, skin effect of the solid conductor bars, and highly distorted air-gap flux density. Since these high-distorted air-gap flux density harmonics are induced in the top region of the bars, they increase the amount of copper loss. As seen in Fig. 4.43(a), since air-gap flux density harmonics of the CIM are lower than those of the AIMS, their total losses are lower. Moreover, as seen in Fig. 4.43(d) and (e), the total loss level has been reduced owing to the slot bridges. It is also obvious that the total loss of the design with u-bridge (uB) is lower than that of the design with straight-bridge (SB). Due to the higher reactance of the lower part of the bar, the current density reaches its maximum at the top of the bar and diminishes to its minimum at the bottom.

In IB rotor slots, the air-gap flux density harmonics induce eddy currents in the copper bars in the slot necks. By providing a bridge in the rotor tip parts (see Fig. 4.43(d) and (e)), the rotor conductor is moved away from the air-gap and hence the additional cage losses are reduced. Using u-bridge instead of straight-bridge leads to bar conductors moving further away from the air-gap leading more reduction in the bar loss. On the other hand, the mechanical resilience of the rotor structure is somewhat reduced that might prevent the use of slot-bridge designs in the super-high speed IMs.

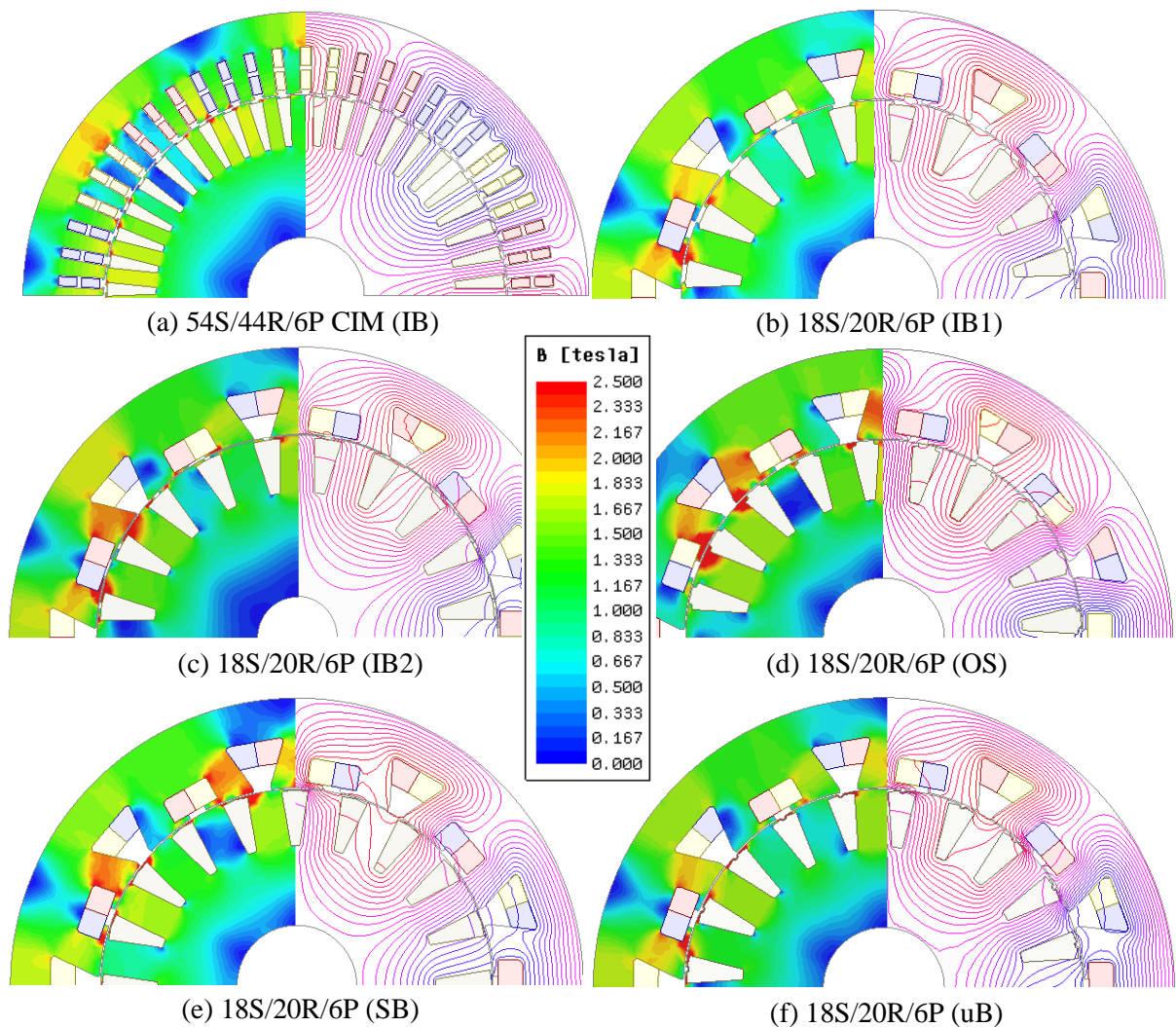
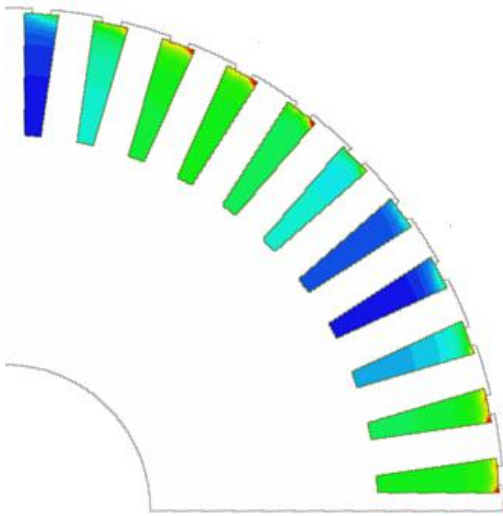
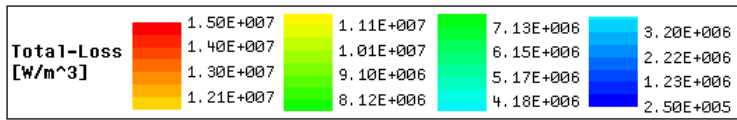
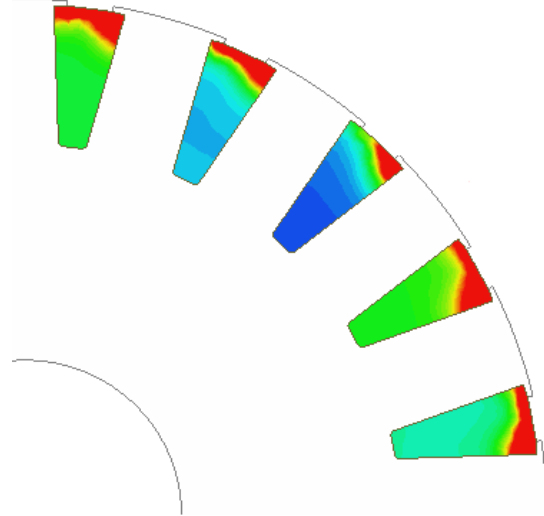


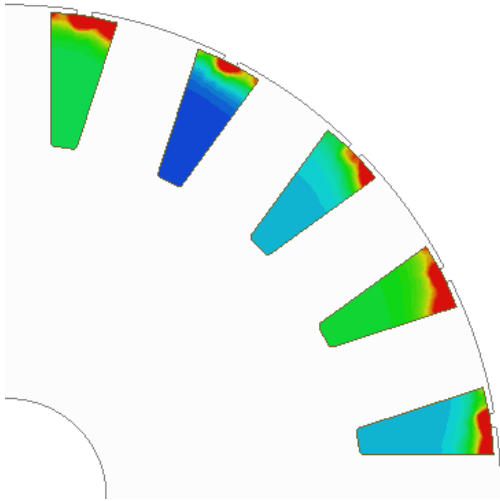
Fig. 4.42 Flux density and flux line distributions.



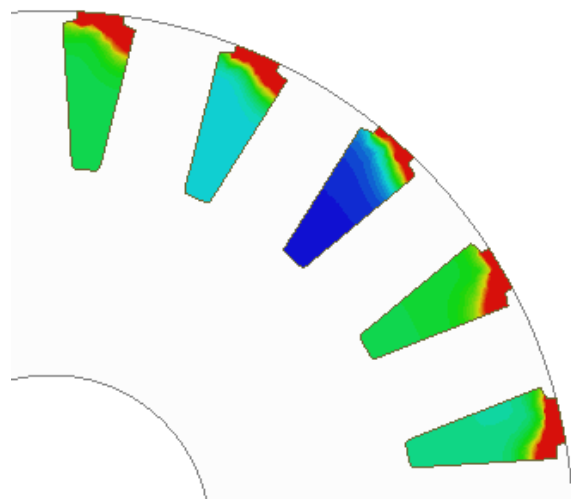
(a) 54S/44R/6P CIM (IB)



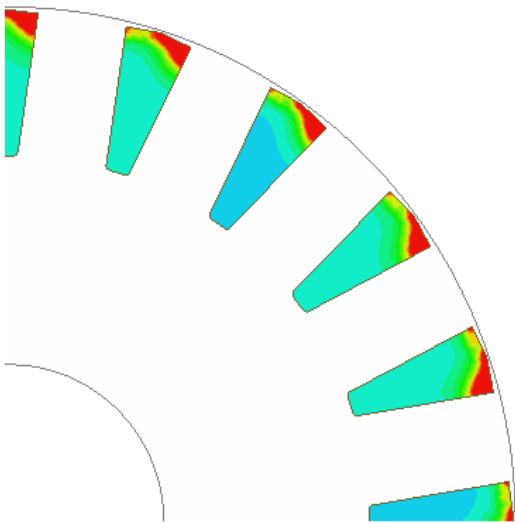
(b) 18S/20R/6P (IB1)



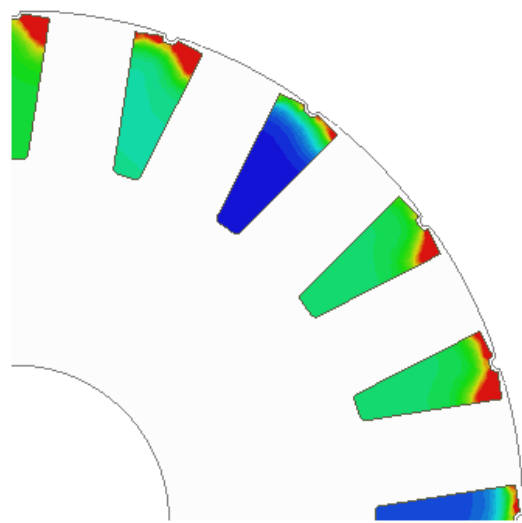
(c) 18S/20R/6P (IB2)



(d) 18S/20R/6P (OS)



(e) 18S/20R/6P (SB)



(f) 18S/20R/6P (uB)

Fig. 4.43 Total loss distributions on the rotor bars.

f) *Torque, Torque Ripple, and Power Losses*

The calculated electromagnetic torque against the rotor position is illustrated in Fig. 4.44. Although there are no significant differences between the average torque values, there are substantial differences between the torque ripple ranges.

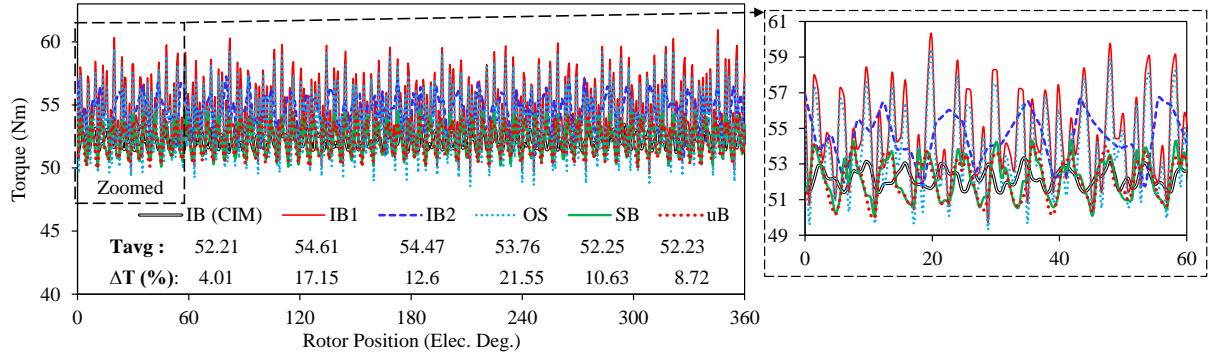


Fig. 4.44 Torque against rotor position.

However, as explained previously, due to the increase in the short-circuited flux through the rotor slot bridges, the average torque is slightly reduced for the AIMs with the slot bridges. On the other hand, the slot bridges cause a significant reduction in the torque ripple. As seen in the figure, more than half of the torque ripple is cancelled by employing the rotor slot bridges. When compared to the SB rotor structure, a further torque ripple reduction of ~18% has been obtained by employing the uB rotor structure.

4.4.3 Comparison of Flux-Weakening Characteristics

The flux-weakening characteristics of the considered IMs are compared in this section. The flux-weakening characteristics have been calculated by using a method that combines the calculated flux-linkage and power losses matrices by FEA and the current angle and speed loops by MATLAB®. The corresponding calculations are given in Appendix A. The calculated torque/power-speed, rotor and stator copper loss maps, and efficiency maps are presented as follows.

a) *Torque-Speed Performance*

Torque-speed characteristics of the CIM with IB and the NWIMs with IB, OS, SB, and uB have been illustrated in Fig. 4.45. Although the performance of the CIM at the constant torque region is low, its performance at the constant power region is quite high. On the other hand, it has been revealed that the influence of the rotor structure on the flux-weakening performance is not significant. As seen in the figure, the overall performances of the rotors with bridges are slightly poorer than those of the open slot rotor structures.

b) *Power-Speed Performance*

The power-speed characteristics of the considered machines have been compared in Fig. 4.46. It is clear that the CIM has the highest power for whole operational speed range. As seen in the figure, rotor

structures with bridges show slightly poorer power-speed characteristics than those of the rotor structures with open-slots.

c) Stator Copper Loss Map

Stator copper loss maps of the CIM and AIMs are illustrated in Fig. 4.47. Note that, since only the rotor structure has been changed by keeping all the other parts at their optimal dimensions, the stator copper losses of the AIMs with different rotor structures are quite similar as seen in Fig. 4.47(b). Due to the very short end-winding lengths of the AIM, their maximum copper losses at the constant torque region are 32.15% lower than those of the CIM.

d) Rotor Copper Loss Map

The calculated rotor bar copper loss maps are illustrated in Fig. 4.48. Although the open-slot rotor structure is utilized for the CIM, as a result of low MMF and consequently low air-gap flux density harmonic content, its bar copper loss is lower than those of the AIMs as seen in Fig. 4.48(a). As seen in Fig. 4.48(b-e), although the design with the OS has the highest bar loss at the constant torque region, the design with the uB has the lowest. Since the slot bridges act as a low-pass filter, some high-order air-gap flux density harmonics have been cancelled eventually. Therefore, some additional copper losses due to the MMF harmonics on the bars have been cancelled. The laminations have been modelled by considering the stacking factor as 0.97. Therefore, depending on the laminations' stacking factor the shielding effect could be much less in reality. In addition, since a small piece of copper bar has been removed from the slot of the IM equipped with uB rotor structure, the bar copper loss is further reduced (see Fig. 4.43(e) and Fig. 4.48(e)).

e) Efficiency Map

The efficiency maps of the considered IMs have been calculated by taking into account the additional losses such as stray current loss, mechanical losses, etc. The additional losses are assumed as 1% of the output power [LIP17], [BOL10]. The maximum efficiency of the CIM is 92%, that has been achieved between 5-9krpm. Moreover, the lowest efficiency (<55%) region is between 0-0.75krpm (see Fig. 4.49(a)). The efficiency maps of the AIMs with IB, OS, SB, and uB have been shown in Fig. 4.49(b-e), respectively. It is obvious that the designs with slot bridges have higher efficiency than the designs without slot bridges. The areas of the maximum efficiency are narrower for designs with open-slots (see Fig. 4.49(b) and (c)). However, as seen in Fig. 4.49(d) and (e), the maximum efficiency regions are larger. Furthermore, thanks to the u-shaped bridge, the maximum efficiency is increased from 92% to 93% between 5-8krpm. In addition, the highest efficiency region is much larger than that of CIM. Comparing the CIM and AIM with uB, it can be deduced that the efficiency of the NWIM with uB is quite higher. As known, an EV spends most of its time at the cruise/city operating mode (low-torque and low-speed operating region). Therefore, it is desirable to achieve high efficiency at the cruise mode operation. Considering Fig. 4.49(a) and Fig. 4.49(e), it can be concluded that the AIM with uB is more

advantageous than the CIM in terms of efficiency and consequently the fuel/energy economy concerns. Furthermore, the AIM with uB is also favourable in terms of compactness since its total axial length is ~15% shorter than that of the CIM (see Table 4.8).

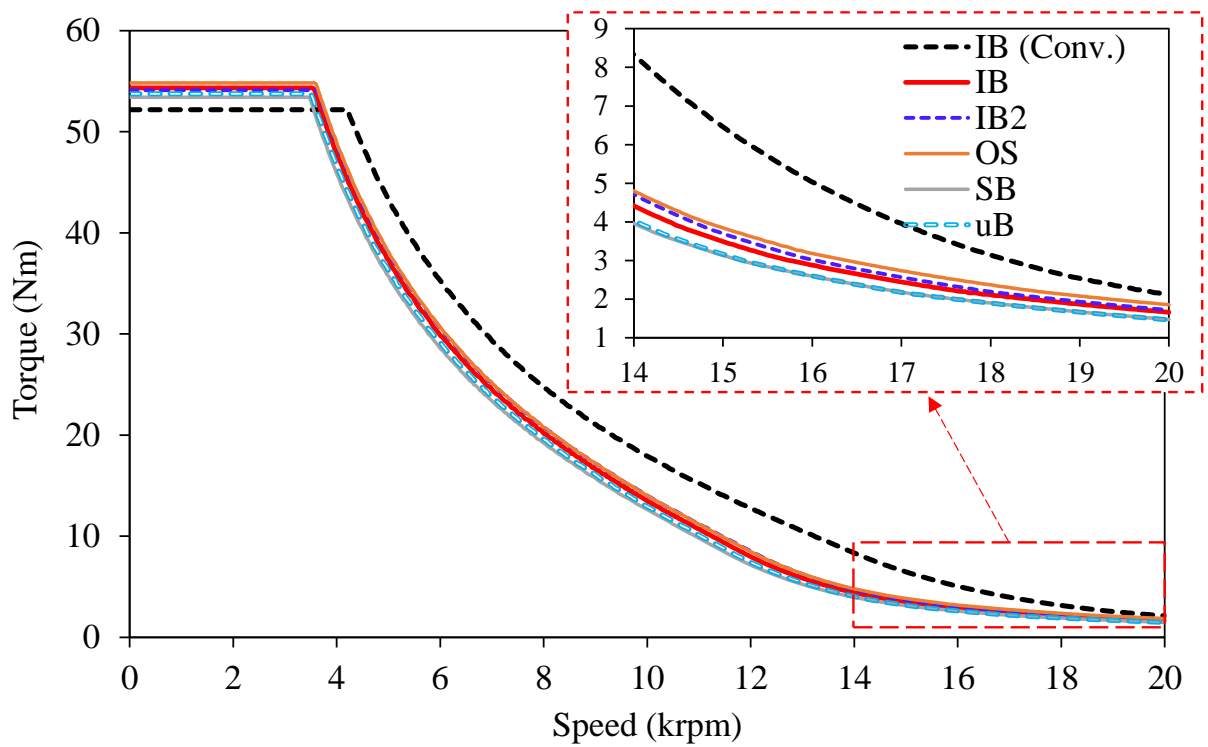


Fig. 4.45 Torque-speed characteristics.

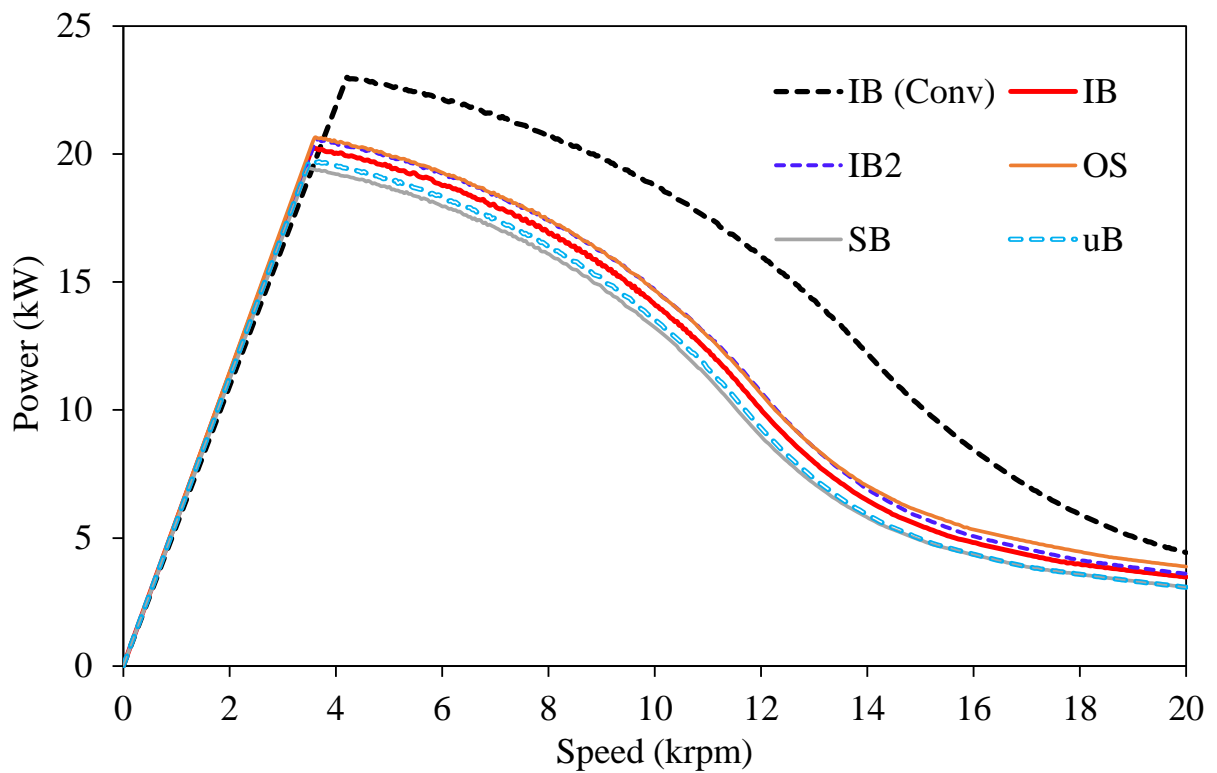
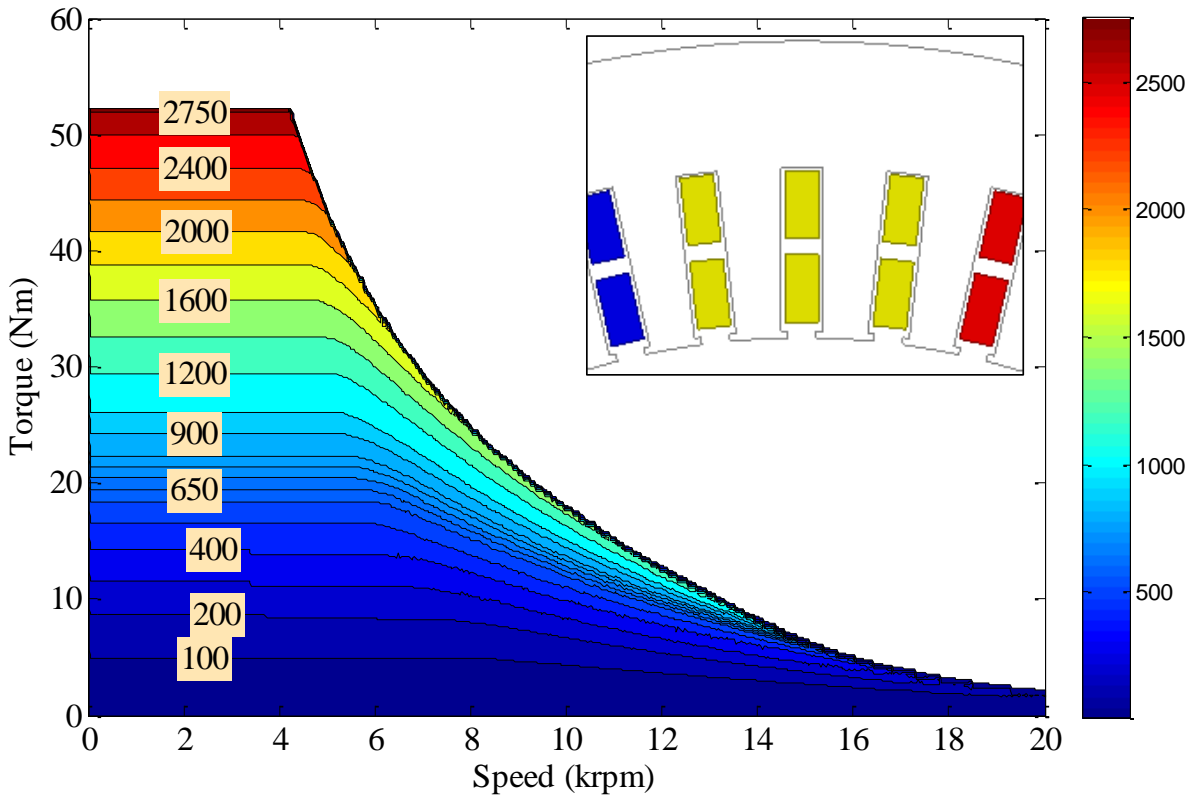
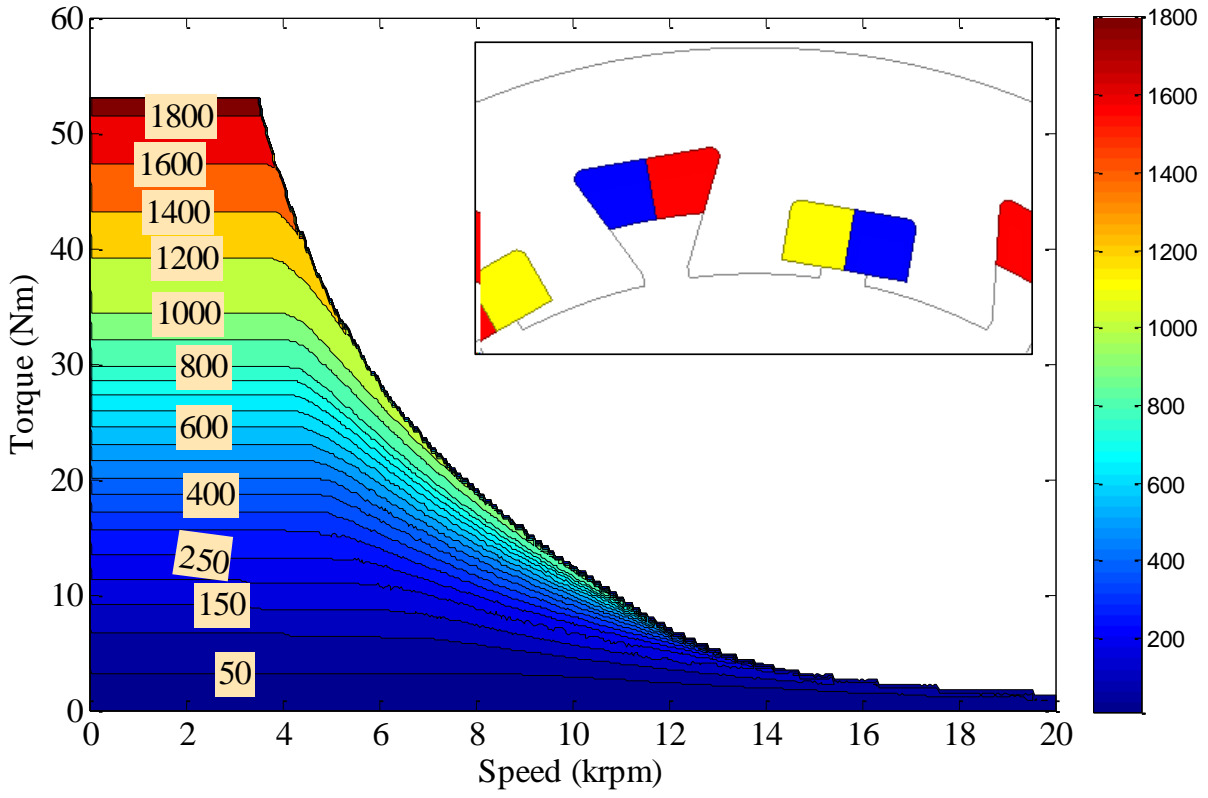


Fig. 4.46 Power-speed characteristics.

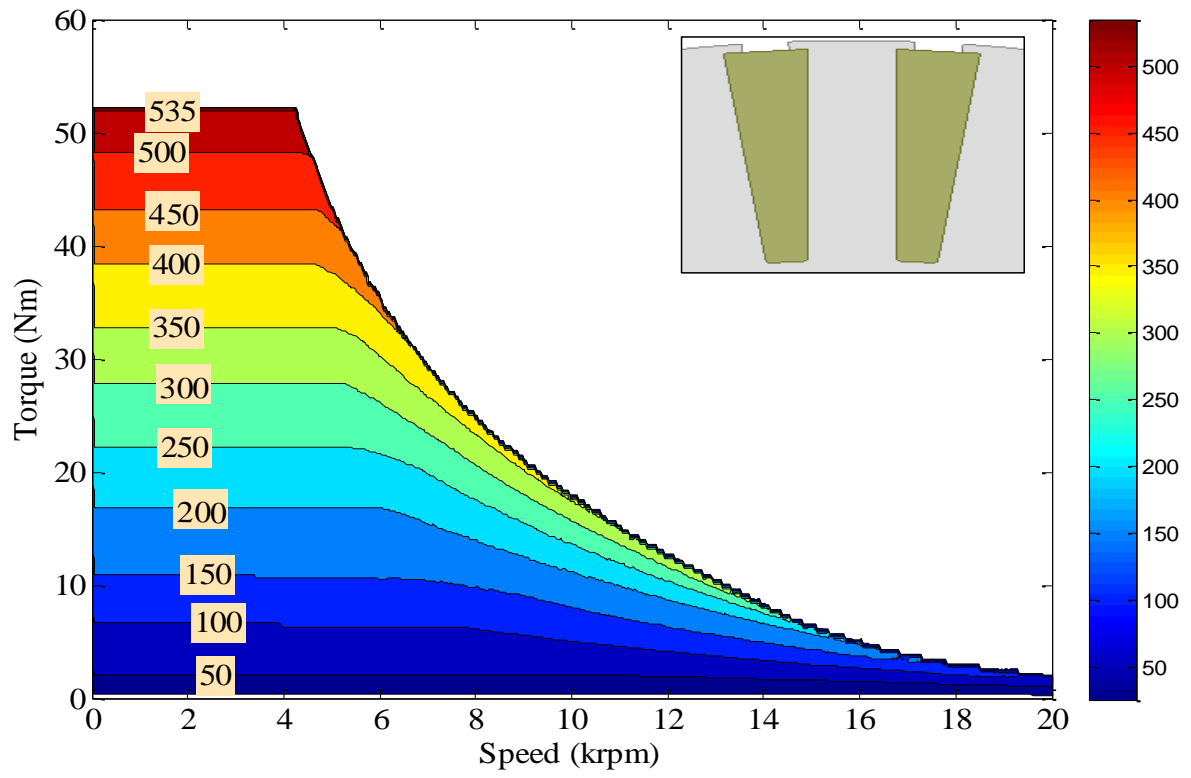


(a) CIM with IB rotor - IB (CIM)

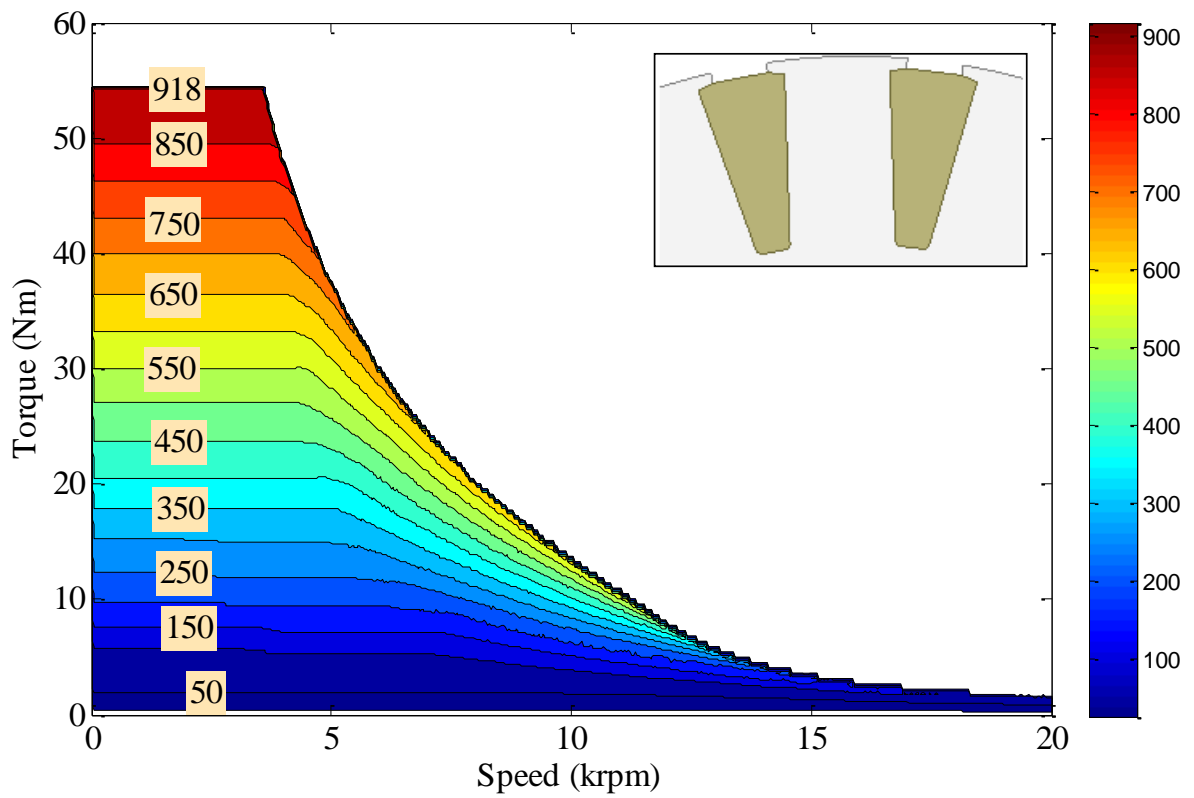


(b) AIMs with IB1, IB2, OS, SB, and uB

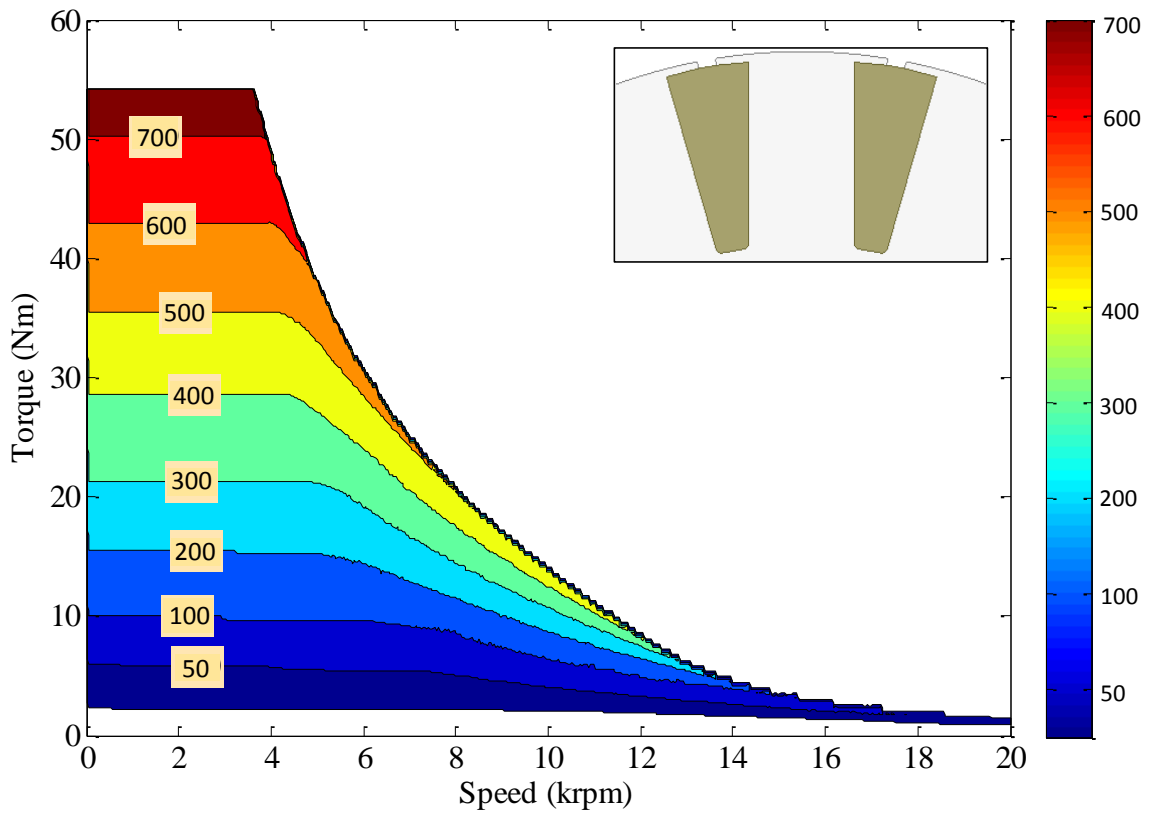
Fig. 4.47 Stator copper loss maps.



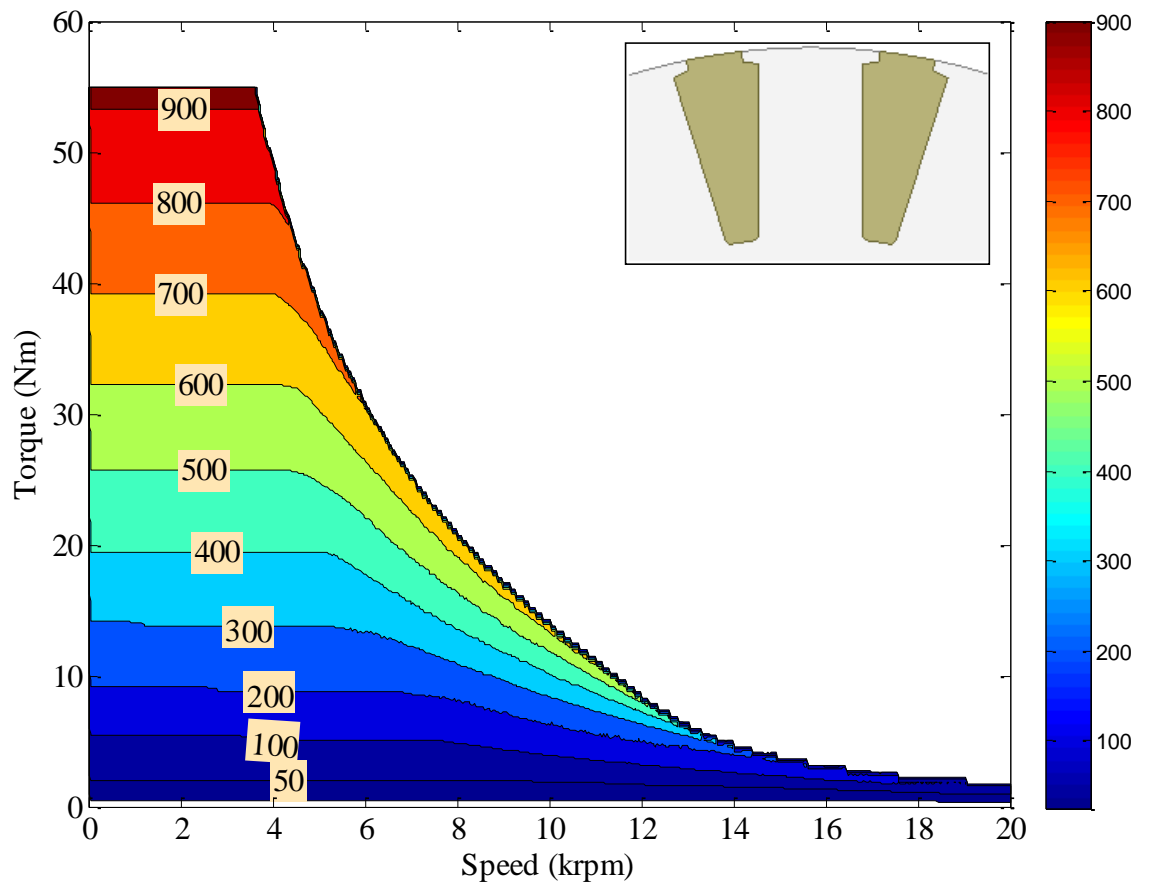
(a) 54S/44R/6P IB (CIM)



(b) 18S/20R/6P (IB1)



(c) 18S/20R/6P (IB2)



(d) 18S/20R/6P (OS)

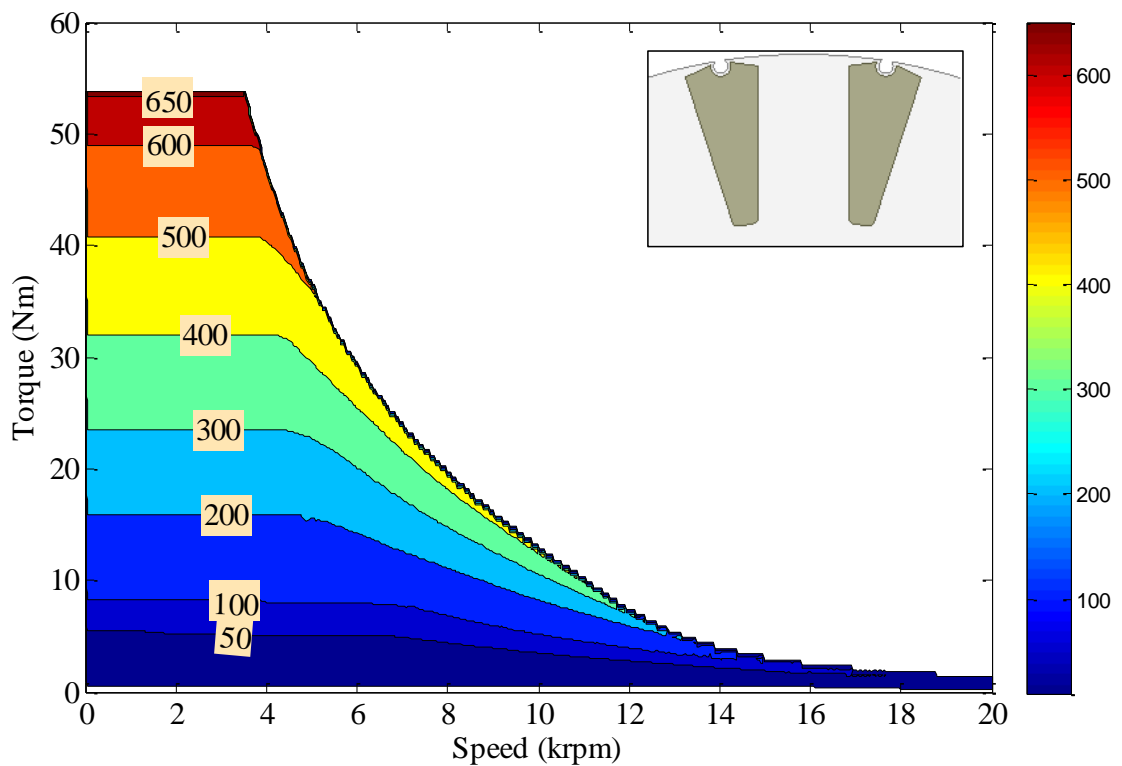
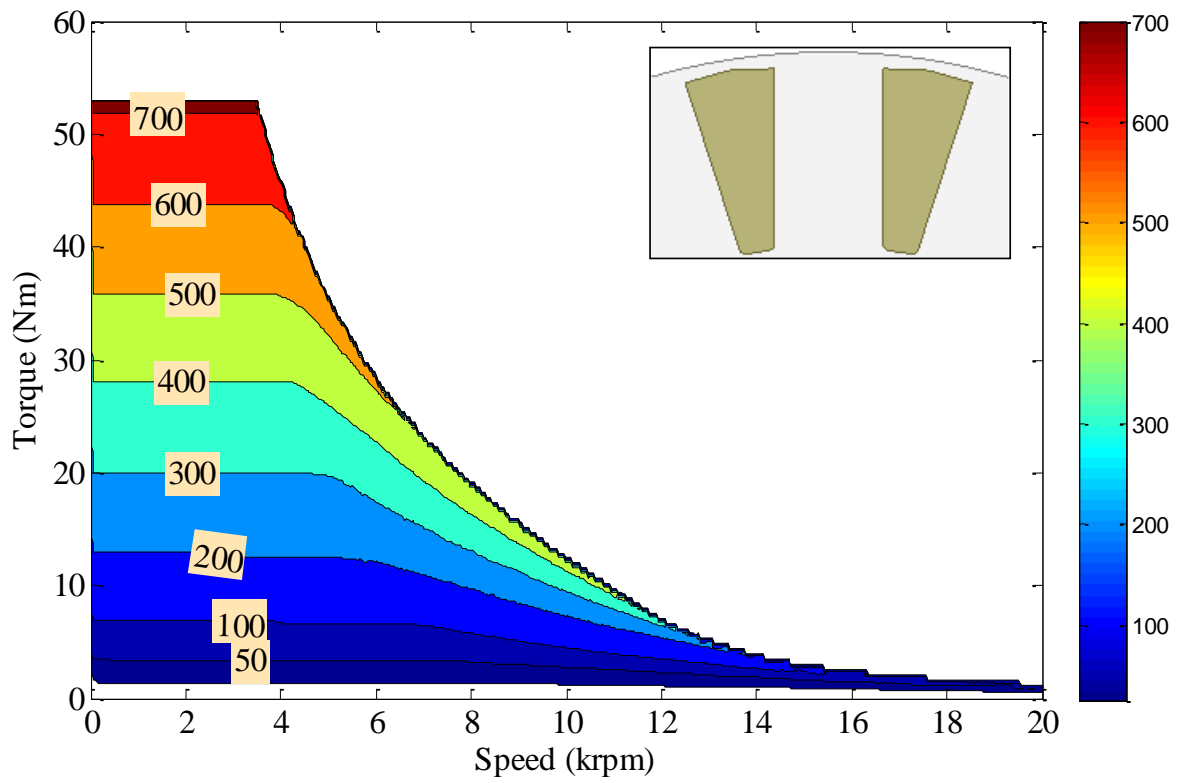
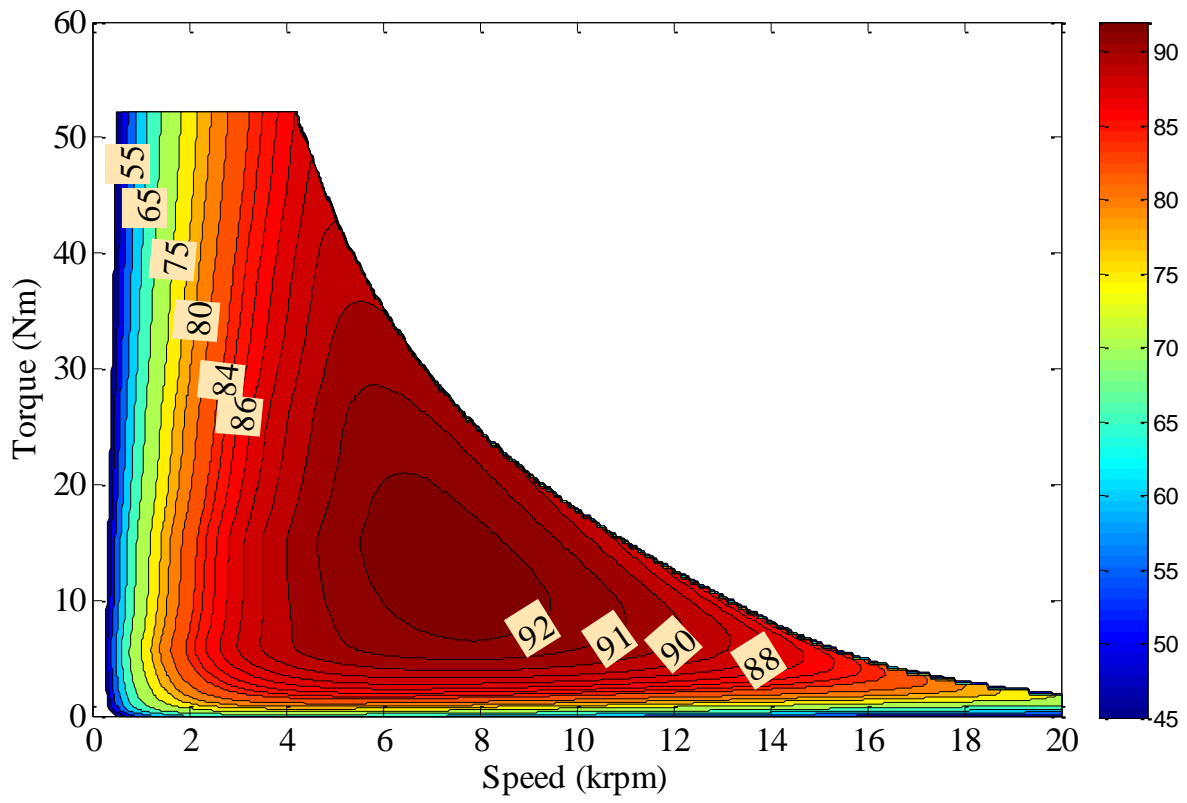
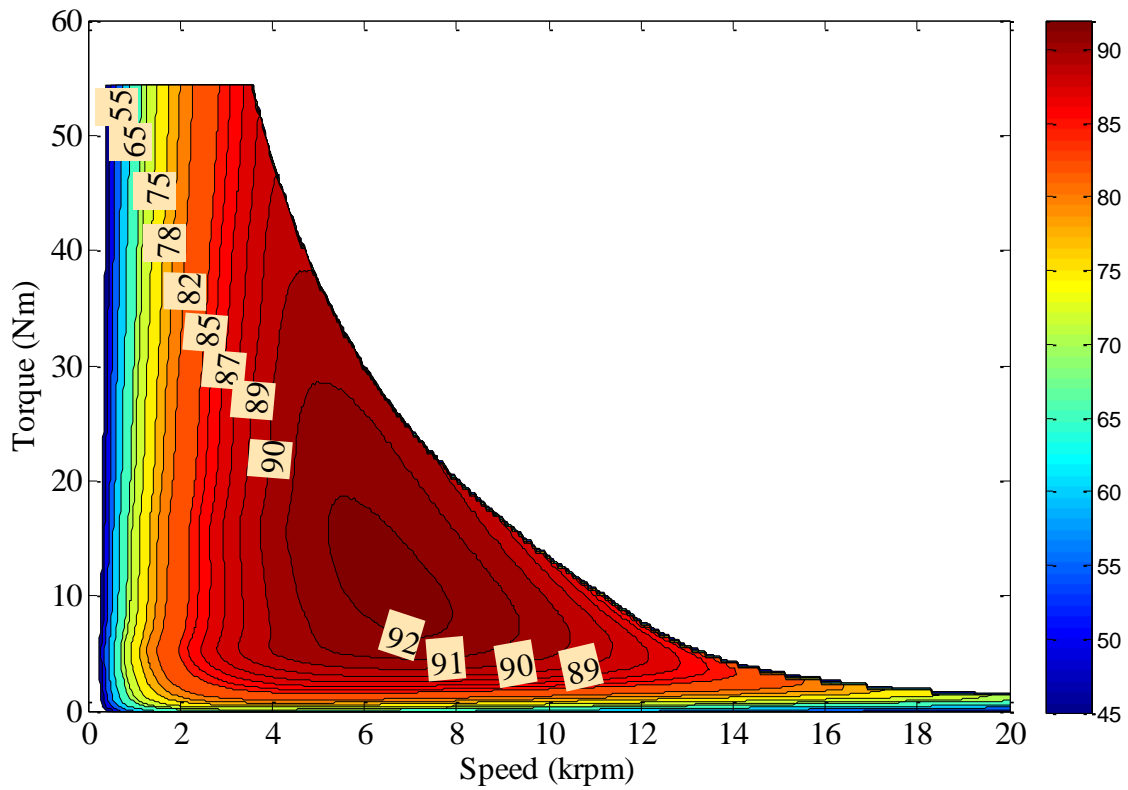


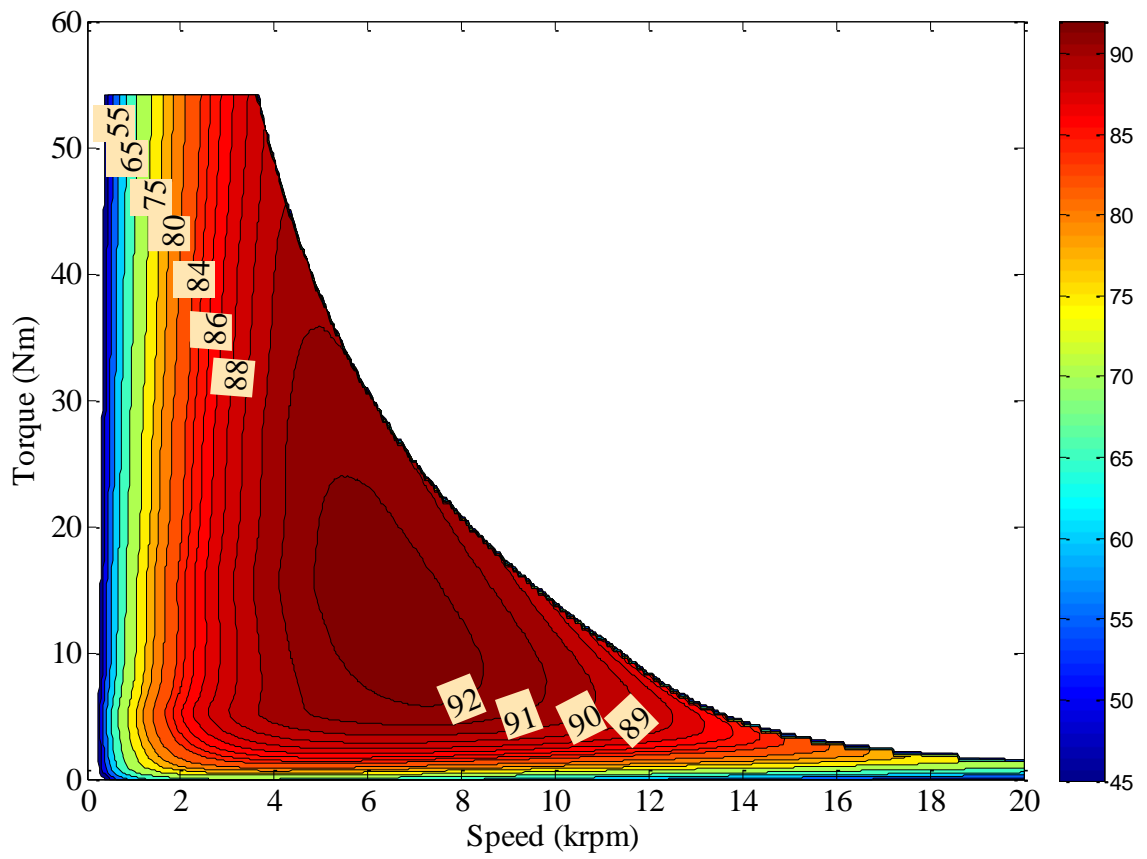
Fig. 4.48 Rotor bar copper loss maps of the CIM and AIMs with different rotor types.



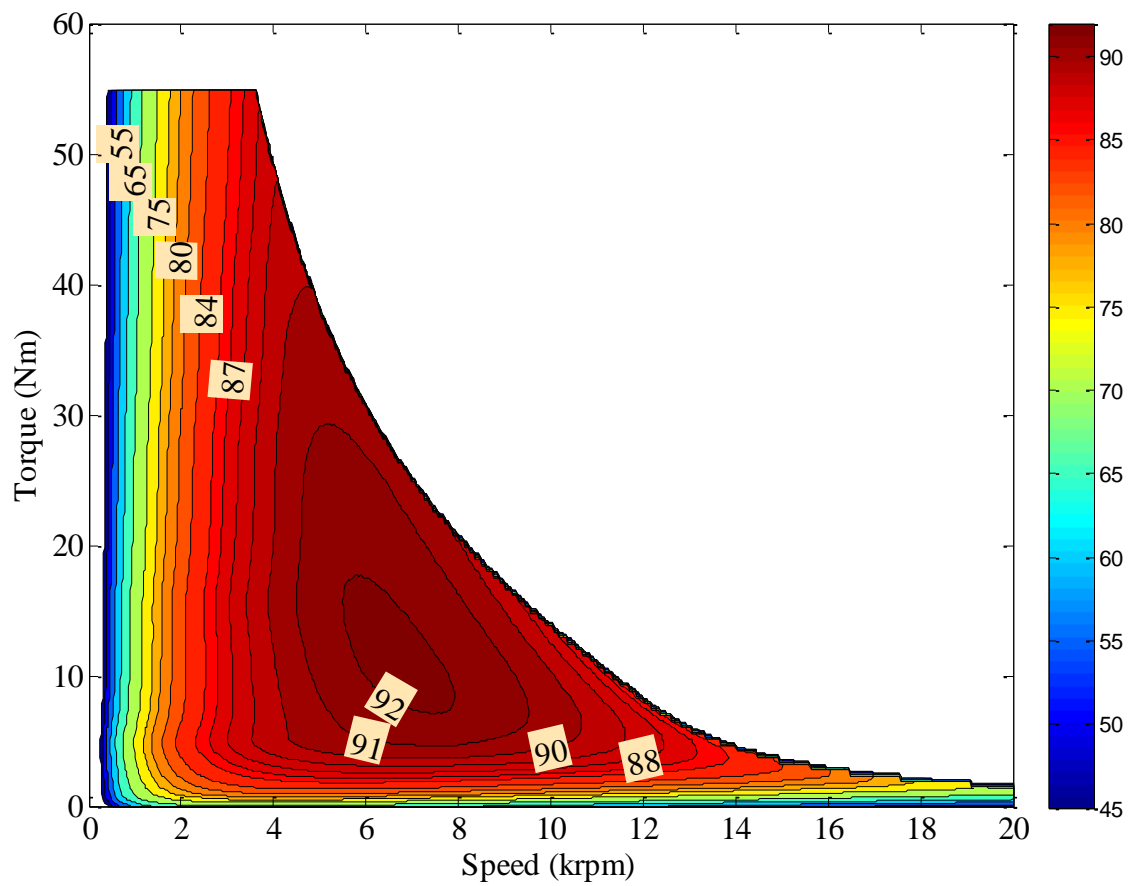
(a) 54S/44R/6P IB (CIM)



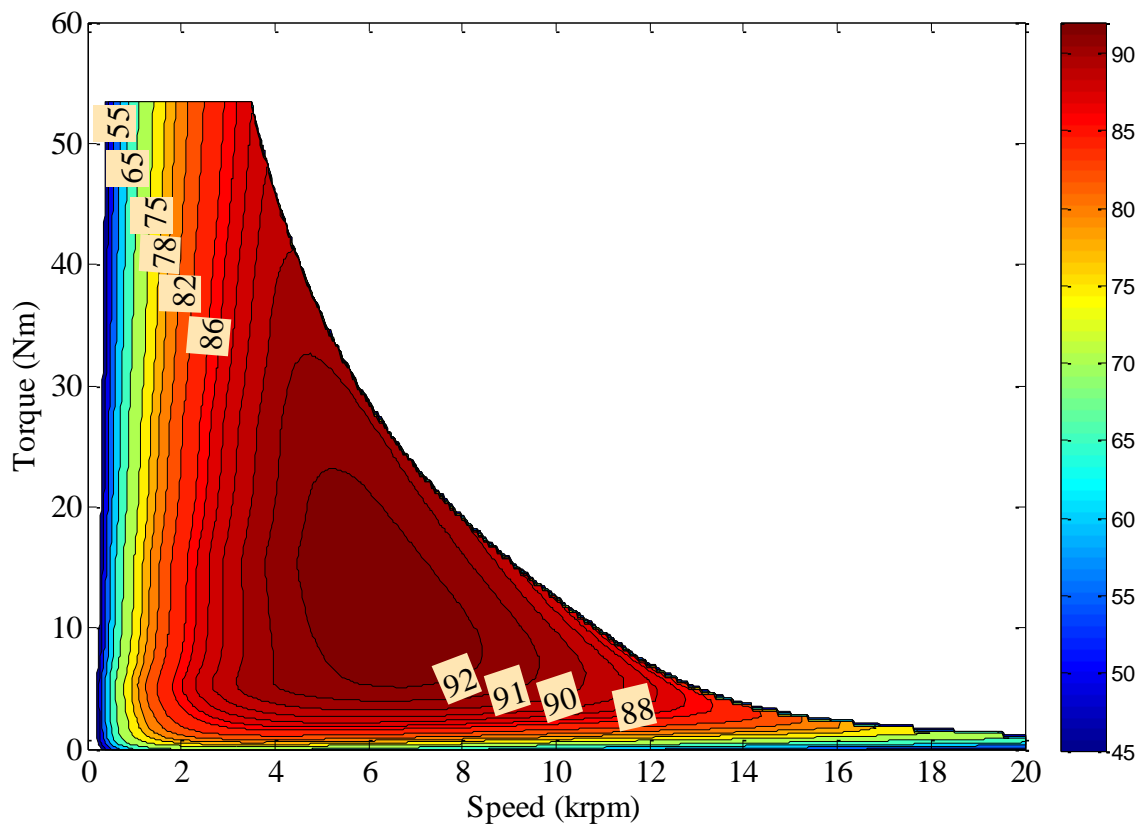
(b) 18S/20R/6P (IB1)



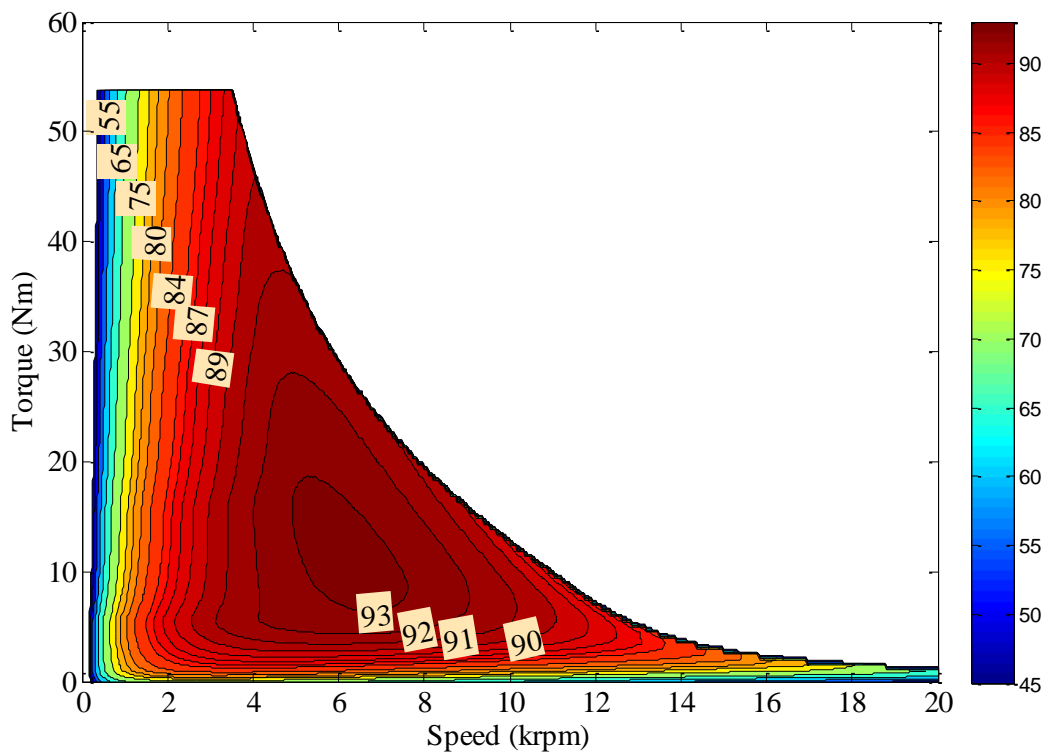
(c) 18S/20R/6P (IB2)



(d) 18S/20R/6P (OS)



(e) 18S/20R/6P (SB)



(f) 18S/20R/6P (uB)

Fig. 4.49 Efficiency maps of the CIM and AIMs with different rotor types.

4.4.4 Overall Comparison

In order to compare the overall electromagnetic performance characteristics of the considered IMs, Table 4.8 has been presented. Open-slot (OS) design has some advantages such as higher torque and higher efficiency. However, its torque ripple and bar copper loss are remarkably high. In addition, it should be also considered that manufacturing of insert-bar is quite difficult than that of the cast-rotor.

Table 4.8 Performance characteristics in constant torque region

	CIM 54S/44R/6P	18S/20R/6P (IB1)	18S/20R/6P (IB2)	18S/20R/6P (OS)	18S/20R/6P (SB)	18S/20R/6P (uB)
N_s	9			9		
R	44			20		
l_s (mm)	70			90		
l_{end} (mm)	52			13.92		
l_{total} (mm)	122.17			104.07 (-14.82%)		
k_{w1}	0.96			0.866		
R_{phase} (m Ω)	3.7261			2.5242		
n_{maxT} (rpm)	1905	1905	1905	1905	1910	1915
T (Nm)	52.21	54.61	54.47	54.14	53.4	52.5
ΔT (%)	4	17.15 (+328.75%)	12.6 (+215%)	21.55 (+438.75%)	10.63 (+165.75%)	8.72 (+118%)
P_{out} (kW)	10.41	10.9	10.87	10.8	10.68	10.53
$P_{Scu_{in}}$ (kW)	0.727	1.297	1.297	1.297	1.297	1.297
$P_{Scu_{end}}$ (kW)	2.067	0.596	0.596	0.596	0.596	0.596
P_{Scu} (kW)	2.79	1.893	1.893	1.893	1.893	1.893
P_{Rcu} (kW)	0.51	0.925	0.741	0.988	0.718	0.652
P_{hyst} (mW)	10.89	19.54	21.34	28.11	29.41	23.21
P_{eddy} (mW)	1.7	2.71	2.26	3.15	2.65	2.26
J_S (A/mm ²)	22.32	30.96 (+38.7%)	30.96 (+38.7%)	30.96 (+38.88%)	30.96 (+38.88%)	30.96 (+38.88%)
J_R (A/mm ²)	13.54	13.71 (+1.25%)	14.75 (+8.93%)	14.39 (+2.36%)	13.86 (+2.36%)	12.9 (-4.72%)
Power factor	0.658	0.682	0.683	0.654	0.683	0.687

On the other hand, it has been revealed that it is possible to improve the performance of the AIMs by employing closed rotor slots. Considering all the findings shown in Table 4.8, the advantages of using closed slots can be summarised as follows:

- ✓ Lower torque-ripple;
- ✓ Lower rotor bar copper loss;
- ✓ Higher efficiency;

- ✓ Cast-rotor availability (ease of manufacturing);
- ✓ Lower slip and consequently higher power factor;
- ✓ Low current density;
- ✓ Smaller cooling equipment.

On the other hand, some disadvantages of using closed slots can be summarised as follows:

- Since the bridges make an increase in the short-circuited flux level, the average torque decreases slightly;
- The closed-slot structure causes a slight reduction in the flux-weakening performance;
- The mechanical resilience of the rotor equipped with quite tin slot-bridges is somewhat reduced.

4.5 Conclusion

In this chapter, electromagnetic and flux-weakening performance characteristics of various AIMs having different S/R/P combinations, stack lengths, and numbers of turns have been comprehensively compared. In order to reveal the advantages and disadvantages of the proposed winding topology, all the obtained results have been quantitatively compared with those of the CIM equipped with 9-slot pitch double-layer ISDWs and 70mm stack length. Among the investigated AIMs, the 18S/20R/6P with 90mm of stack length is determined as the best candidate, meeting the requirements of a traction machine for the EV/HEV applications, including high efficiency, high torque, wide constant power region, low torque ripple, etc. Moreover, the performance of the AIM with different rotor topologies is investigated in detail. It has been concluded that adopting the closed-slot rotor structures, particularly with u-shaped slot bridges, provides reduced parasitic effects, lower bar current density, lower bar copper loss, and consequently the higher efficiency.

The key findings of this study have been summarised as follows in constant torque and constant power operating regions of the IMs.

In constant torque region:

- If the AIM is designed by using the same stack length as the CIM, 33.13% shorter total axial length can be achieved without sacrificing the average torque, output power, and efficiency;
- If the AIM is designed by using the same total length as the CIM, 9.5%, 5%, 6.2% higher efficiency, higher average torque, and higher output power can be achieved;
- If the optimum AIM is compared with the CIM, 5.7% higher efficiency, 4.7% higher average torque, 4.6% higher output power can be achieved with 13.36% shorter total axial length;

- For all the S/R/P combinations of the AIM, the higher torque ripple is inevitable comparing to the CIM. However, as shown, the torque ripple can be reduced significantly by employing the closed slot rotor structure;
- The higher the pole number, the better the performance in terms of higher torque, higher output power, higher efficiency, and lower torque ripple;
- The longer the stack length, the higher the output power, the lower the bar copper loss, the lower the bar current density, and the higher the efficiency;
- The undesired consequences of the parasitic effects can be suppressed by employing the closed slot rotor structures, as a result of this a higher efficiency with lower torque ripple might be achieved.

In constant power region:

- Regardless of the S/R/P combinations and stack length, the powers of AIMS at high-speed are lower than that of the CIM;
- The lower the pole number, the higher the power at high-speed regions;
- The longer the stack length, the better the flux-weakening capability;
- The IMs equipped with open slot rotors have slightly better flux-weakening characteristics than those of the IMs equipped with closed-slot rotors.

5 Influence of Magnetic Saturation on Non-Sinusoidal Bar Current Waveform

In this chapter, the influence of magnetic saturation on the rotor bar current waveform and performance characteristics of a conventional IM is investigated. The levels of iron saturation in different parts, including the stator and rotor back iron, tooth body and tooth tips etc., are examined and their influences are investigated, whilst the dominant part which causes the non-sinusoidal rotor bar current waveform is identified and the phenomenon is explained in depth. It has revealed that the magnetic saturation, particularly in the rotor tooth, has a significant effect on the bar current waveform.

5.1 Introduction

Due to the rugged, reliable, and almost maintenance free construction and relatively high efficiency, the performance and operating characteristics of induction machines (IMs) have been under investigation since their first invention in 1888 [TES88], [ALG76]. The rotor bar current of an IM plays a crucial role in generation of torque and output power, and accurate calculation of efficiency [LAN77]. In IMs which are fed with a 3-phase balanced sinusoidal source and run under the healthy operating condition, induced voltage and hence current on the rotor bars are usually assumed to be sinusoidal in accordance with the commonly used equivalent one phase circuit and other analytic models. In addition, a number of previous studies showed that the rotor bar current may be non-sinusoidal, since the rotor bar current is a summation of the various frequencies induced in the rotor circuit by the stator MMF harmonics. However this section is important since it examines the relationship between the bar current waveform and cross saturation. Therefore, the design and operating parameters concerning the magnetic saturation have also been investigated in Chapter 6 and 7, respectively.

The previous studies have revealed that the bar current may be non-sinusoidal under some specific design and operating conditions such as very low slip ranges [LUN36], [BRU07], [BLA09] or lower frequencies than the rated synchronous frequency [BOG03] or significantly high electrical loading operating conditions [BRA74], [GUN16a]. Furthermore, it might also be non-sinusoidal in case of fairly short air-gap lengths [GUN16c]. It has been proven that the level of the bar current distortion highly depends on the slot number/pole number combinations [GUN17a]. In addition, significant effect of rotor slot number on the bar current waveform has been shown in [GUN17b]. It has been revealed that the rotor and stator geometric parameters have also a considerable effect on the bar current waveform [GUN18a]. Furthermore, in existing literature, although there are a lot of studies on the stator current waveform, there are only a few studies on the rotor bar current waveform of a squirrel-cage IM [WEI11], [HOO11], [GAU41], [BUC72], [PRE89], [MUK89], [BOT04], [BOT05], [DON05], [BEL06], [GRA09]. However, in these studies, the explanations related with the non-sinusoidal bar current have not given or are insufficient. Therefore, the first aim of this chapter is to fill this gap and the second aim is to reveal which part of the machine causes the bar current to become non-sinusoidal.

In this chapter, the influence of more general magnetic saturation, which may occur due to the factors explained above, will be investigated. The saturation of the cores on the main flux path induces some lower order harmonics in the air-gap flux [LEE61], [MOR92]. These harmonics are called as saturation harmonics since they are produced directly by the saturation of the cores [LEE61]. Furthermore, these saturation harmonics vary with the operating conditions and also affect the leakage reactance of the IM [CHA69]. The lower the leakage reactance, the higher the saturation of the flux leakage paths in the stator and rotor [ANG63]. Therefore, the saturation of the main flux path components has a considerable effect on the rotor magnetic circuit [MOR92]. A 3rd harmonic flux component exists as a consequence of the saturation [CHA71], and this 3rd harmonic always exists notwithstanding the number of phases [PER12]. The non-linear characteristics of the core materials causes the equivalent distortion on the air-gap, which leads to the appearance of space harmonics in the main flux density distribution and consequently the distorted induced voltage in the rotor, and subsequently generates flat-topped rotor currents [CHA71], [FRE03]. Furthermore, saturation phenomenon also has a significant effect on the starting performance of wound-rotor IMs [JAB07] and other performance characteristics such as motor start-up, slot-leakage [OJO90], [IKE07], torque quality, vibration and acoustic noise, and stabilizing effect [SAL94], [MEL83], [DON99], [MON13]. In addition, it has been proven that the saturation is a very important parameter which should be taken into consideration at modelling stage of IMs [LIP84], [LIA94], [DON99], [XIA08], [BOL10].

In this study, an IM has been designed by using the same geometrical and operating parameters as the Toyota Prius 2010 IPM machine. The influence of the saturation on the induced voltage, air-gap flux density, rotor bar current, rotor and stator tooth flux densities, torque quality and also efficiency will be revealed. The levels of iron saturation in different parts, including the stator and rotor back iron, tooth body and tooth tips etc., are examined and their influences are investigated, while the dominant part which causes the non-sinusoidal rotor bar current waveform is identified.

5.2 Analysis of Rotor Bar Current

As well known, the operating of an IM is based on the interaction between the stator and rotor magnetic fields. Both of these fields have radial and tangential components. The tangential component of the rotor field B_{r_t} is the rotor slot leakage component and can be calculated as given in (3.1) [BOL10], [LIP17], where μ_0 , I_{bn} , br_t , br_r , and θ_r are the relative permeability of the air, the bar current of the n^{th} bar, the rotor slot width close to air-gap, the rotor slot width at slot bottom, and the rotor position, respectively. The leakage fluxes produced by the stator and rotor currents depend on the slot geometry and winding structure. These leakage fluxes are visible in Fig. 5.1(b). The radial component of the air-gap field B_{r_r} is the torque producing component that is produced by the stator currents in the rotor tooth parts and can be evaluated by using the average air-gap flux density given by (5.2) [LIP17], where $B_{g,avg}$, D_{is} , P , l_s , g , k_{ir} are the average air-gap flux density, the stator inner diameter, the pole number, the stack length, the air-gap length, and the rotor stacking factor, respectively.

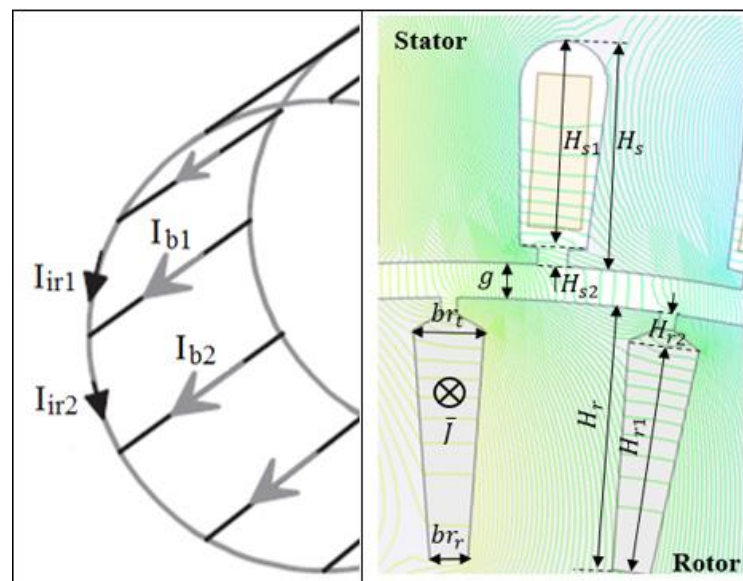
$$Br_t(\theta_r) = \frac{2\mu_0 I_{bn}(\theta_r, t)}{br_t + br_r} \quad (5.1)$$

$$Br_r(\theta_r) = B_{g,avg}(\theta_r) \frac{2\pi D_{is}}{P(br_t + br_r)} \frac{(l_s + 2g)}{k_{ir} l_s} \quad (5.2)$$

In addition, when considering the air-gap field, it should be taken into account that the air-gap flux density contains four different harmonics originated from slot, phase belt or space, saturation, and slot MMF combined with rotor slot permeance ripple harmonics that have a correlation with pole, rotor, and stator slot numbers [XIA08], [BOL10]. The bar current I_R is calculated by using (5.3), where I_M , f_r , Z_2 , k_{sat} , m , l_s , R , p , g_e , N_{st} , k_{wpp} , θ , x_n and τ_p are the magnetizing current, rotor frequency, rotor impedance, number of phase, stack length, number of rotor slots, pole pair number, effective air-gap length, serial number of turns per phase, working winding factor, the space angle at a point of interest in the air-gap, angle between the rotor position and space angle, and pole pitch length, respectively. As seen, (5.3) comprises of one variable term, which is the second term, and two constant terms, which are the first and the third term, and one angle term, which is the fourth term. In this thesis, influence of the variable terms on the bar current waveform have been investigated in depth.

$$I_R = \left(\frac{2\sqrt{2}}{5} 10^{-8} \right) \cdot \left(I_M \frac{f_r}{Z_2 \cdot k_{sat}} \right) \cdot \left[\frac{\tau_p \cdot m^2 \cdot l_s}{R \cdot p \cdot g_e} (N_s \cdot k_{wpp})^3 \right] \cdot \sin \left(\pi \frac{x_n}{\tau_p} - \theta \right) \quad (5.3)$$

$$I_{bn}(\theta_r) = Br_r(\theta_r) \left[\frac{0.37(n_s - n_r)l_s^2}{\sqrt{R_{bns}^2 + X_{bns}^2}} \right] \left[\frac{2\pi(l_s + 2g_e)}{P(br_t + br_r)k_{ir}} \right]^{-1} \quad (5.4)$$



(a) Rotor bar and inter-bar ring currents. (b) Rotor slot parameters and flux lines.

Fig. 5.1 Squirrel-cage rotor: (a) construction and (b) slot parameters (b).

$$I_{b1} = I_{ir2} - I_{ir1} \quad (5.5)$$

By subtracting end-ring current and simplifying (5.3), the bar current can be derived in terms of rotor tooth flux density as given in (5.4), where R_{bns} and X_{bns} are the resistance and reactance of the n^{th} bar depending on the slip, respectively and k_{ir} is the rotor stacking factor. $Br_r(\theta_r)$ in (5.4) is the torque producing component of the main reaction field. As seen from (5.4), the bar current depends on the torque producing component of the rotor flux, slip, bar impedance, pole number and other geometrical parameters such as air-gap length, slot dimensions, stacking factor and also stack length. Among these parameters, the rotor tooth flux density and the slip, and hence the impedance of the bar conductor change with respect to the speed. Therefore, these two parameters should be investigated in detail in order to reveal the reason behind the distortion of the bar current waveform. A simplified squirrel-cage with the bar and inter-bar ring currents denoted by the arrows is illustrated in Fig. 5.1(a). As clearly seen from Fig. 5.1(a), the relation between the bar I_{b1} and inter-bar ring currents I_{ir1} and I_{ir2} can be calculated by (5.5).

5.3 Investigation of Bar Current

Generally, an IM is designed as to be operated under slightly moderate saturated conditions during normal operating [LIA94]. However, under some extreme operating conditions such as fairly low slip or very significantly high electric loadings or quite low frequencies, the iron cores of the IM can be saturated. As to be explained in the followings, the saturation limits the flux in the main path and hence it tends to induce considerably high 3rd order harmonic in the air-gap flux. Furthermore, while these saturation harmonics affect only the starting and overload performance of the IM, they diminish to minimum under rated operating conditions [GUN16b].

In this section, the influence of saturation on the bar current waveform is investigated by time-stepping, non-linear 2-D finite element analysis (FEA) with transient magnetic solver under steady state operating condition at 950 rpm (maximum torque) and 102 V maximum supply voltage which generates 250 A stator current. The material composition and the direction of the lamination stacking have also been considered in the 2-D FEA modelling. The material compositions of the core materials are assigned as laminated with 0.97 stacking factor. The studied IM is designed by using the same outer diameter, stack length, slot/pole number, winding properties and rated operating conditions such as excitation current, speed, etc, as the Prius 2010 interior permanent magnet machine (IPM). Note that the rotor slots have not been skewed in this section.

To be able to validate the results of simulation, the rotor bars and end-rings have been modelled by the FEA with two different design approaches: (a) by using a default end-connection tool (as a ring short-circuiting the both side of bars) and (b) by building an equivalent squirrel-cage circuit consists of bars and rings. In order to reveal which part causes more distortion on bar current waveform; the components on the main flux path such as yokes, tips, teeth of the stator have been separated from each

other and assigned as Linear (un-saturable) material (see Fig. 5.2) by using the sequence in Table 5.1. By using a linear material on some parts of the IM, the saturation in the specific regions can be avoided while other parts with non-linear BH curve may be saturated by supplying the peak excitation voltage. In order to examine the saturation levels, the obtained analysis results, summarised in Fig. 5.3, have been compared with the original IM which has been designed by using W330 material which has a non-linear BH curve as shown in Fig. 5.2. The non-linear BH iron parts are shaded with red color as seen in Fig. 5.3 and the THDs of the bar currents are also given for each case. As clearly seen in Fig. 5.3, the rotor bar current has been significantly distorted in W330 (original) case and Case#3 in which the rotor teeth are assigned with non-linear (saturable) material. In Case#2, when only the stator teeth are saturated, the waveform of the bar current has not been distorted as in W330 case and Case#3 but it has been much distorted than the other cases.

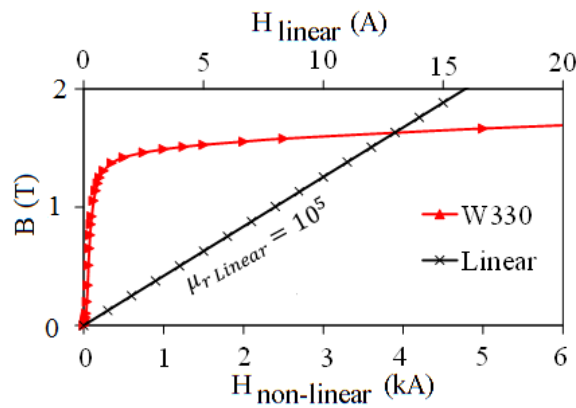


Fig. 5.2 BH curve of the linear and non-linear (W330_35) material.

Considering Fig. 5.3, it is obvious that the yokes have the minimum influence on the bar current waveform distortion while teeth especially rotor teeth have the maximum. Fig. 5.3 has revealed that the focus should be given on the rotor and stator tooth parts in order to explain the reason behind the non-sinusoidal bar current phenomenon.

Table 5.1 Comparison of properties of winding configurations

		Case#					
Assigned Region		W330	Linear	C1-SY	C2-ST	C3-RT	C4-RY
Permeability	Stator Yoke	N*	L*	N	L	L	L
	Stator Tooth Body	N	L	L	N	L	L
	Stator Tooth Tip	N	L	L	N	L	L
	Rotor Tooth Tip	N	L	L	L	N	L
	Rotor Tooth Body	N	L	L	L	N	L
	Rotor Yoke	N	L	L	L	L	N

*L: Relative Permeability is Linear ($\mu_r = 10^5$)
*N: Relative Permeability is Non-Linear: (W330_35) sat. point is 1.48 T

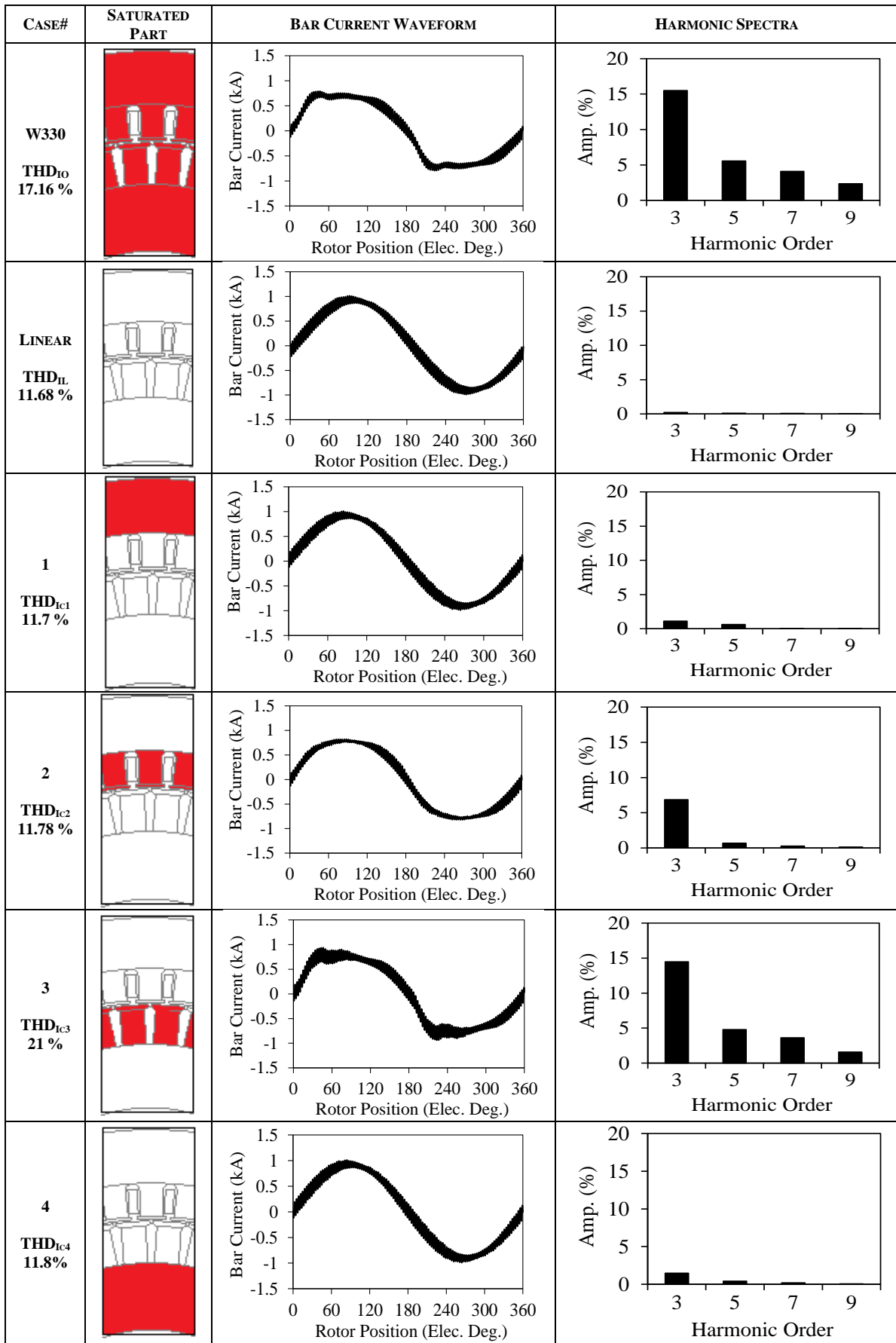


Fig. 5.3 Bar current waveforms, harmonic spectra, and THD in percentage for each case.

5.4 Investigation of Flux Density

The tangential component of the rotor and stator fields are the rotor and slot leakage components, respectively, and they can be calculated by (5.2) [BOL10]. As expressed in (5.2), they depend on the slot geometry (see Fig. 5.1(b)), stator and bar current [BOL10]. According to the Kirchhoff's first law, the current in a bar is the difference between the currents in adjacent inter-bar rings (see Fig. 5.1(a)). Since the rotor and stator tooth bodies have the most significant effect on the bar current distortion, the analysis results of linear Case, C#2 and C#3 have been compared as follows. The phase 'A' induced voltage waveforms and their harmonic spectra and THDs for all cases are illustrated in Fig. 5.4. Since the stator core material is highly saturated in case of C#2, the induced voltage is highly distorted. In linear case, only the high order harmonics seem very high. This is due to the slotting effect and MMF harmonics of the winding configuration. It is obvious that the saturation of the stator or rotor teeth cause to increase the 3rd harmonic significantly.

Owing to the distribution of the windings in discrete numbers of slots which causes an increase in the harmonics of the distortion factor, the flow of sinusoidal currents in a winding produces flux distributions in the air-gap, which contains a series of harmonic components in addition to the fundamental (see Fig. 5.5(a)). As seen in Fig. 5.5(b), the saturation of the rotor tooth parts (C#3) has more contribution to the distortion of the flux density waveform. Since the higher order harmonics increase as the available maximum current increases, the THD of the Linear case is the highest. However, the saturation affects only the 3rd order harmonic component. In order to obtain the relationship between the bar current and the air-gap flux density, the flux density waveform of the rotor tooth should be investigated by considering (3.1) and (5.4).

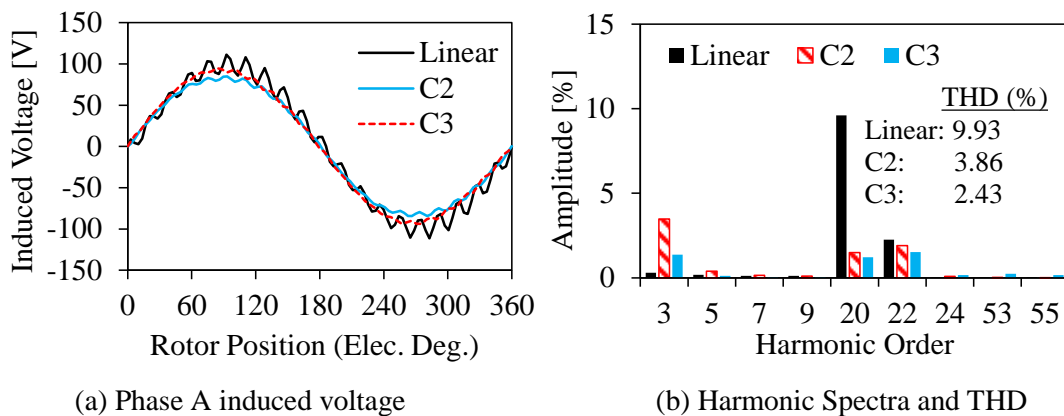
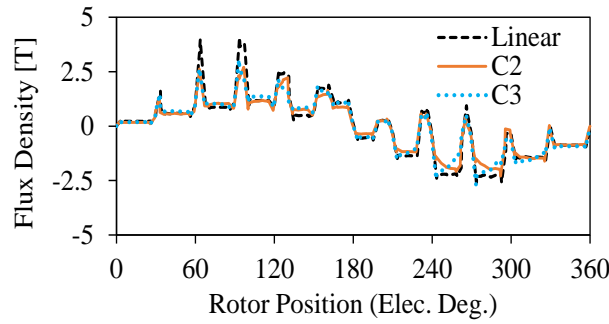
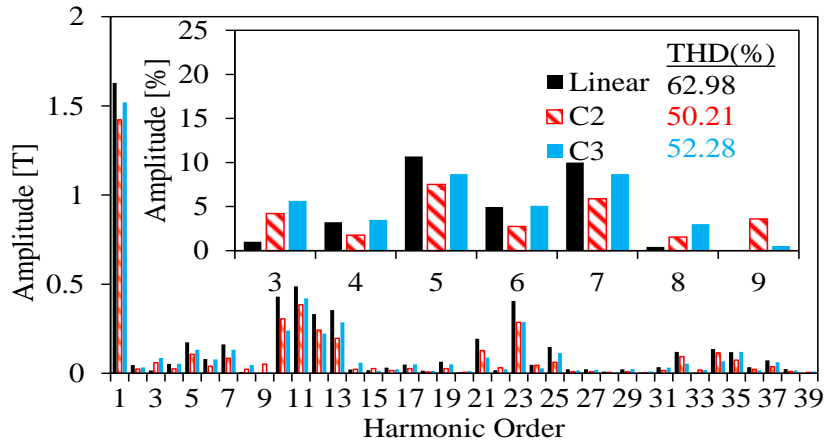


Fig. 5.4 Phase 'A' induced voltage waveforms (a), harmonic spectra and THDs for Linear case, C#2, and C#3 (b).



(a) Air-gap flux density variation with respect to rotor position.



(b) Harmonic spectrum of air-gap flux density.

Fig. 5.5 Air-gap flux density: (a) waveform and (b) harmonic spectra and THDs (b) for Linear case, C#2 and C#3.

The rotor and stator tooth flux density variations with respect to rotor position from the top to the bottom of a tooth are shown in Fig. 5.6. In order to verify that the distortion contributions coming from the rotor and stator yokes are the minimum, their flux density waveforms (see Fig. 5.6(g, h)) and harmonic spectra (see Fig. 5.7(g, h)) are also investigated. Considering the flux density harmonic spectra of the yoke parts, it may be concluded that their contributions to the bar current are negligible. Due to the higher reactance of the lower part of the bar, the flux is the highest at the top of the bar tips and diminishes to a minimum at the bottom. It means that the stator and rotor MMFs and permeances generate a large number of harmonics in the air-gap which generate a large number of harmonics at the top of the rotor tooth parts. Moreover, there are many field harmonics at the top of the tooth parts whilst they are very low at the bottom of the tooth due to the average effect (see (5.6)). The high-frequency field harmonic components in Fig. 5.6(a) are originated from the various frequencies induced in the rotor bars due to the combined effect of stator and rotor slotting effect and forward and backward MMF harmonics. Since on the slot area the flux is the integration of flux density. In other word, in the air-gap, the flux ϕ_t coming from the stator tooth parts (area of the studied core A) turns into the flux density B_t .

$$\phi_t = \int B_t dA \quad (5.6)$$

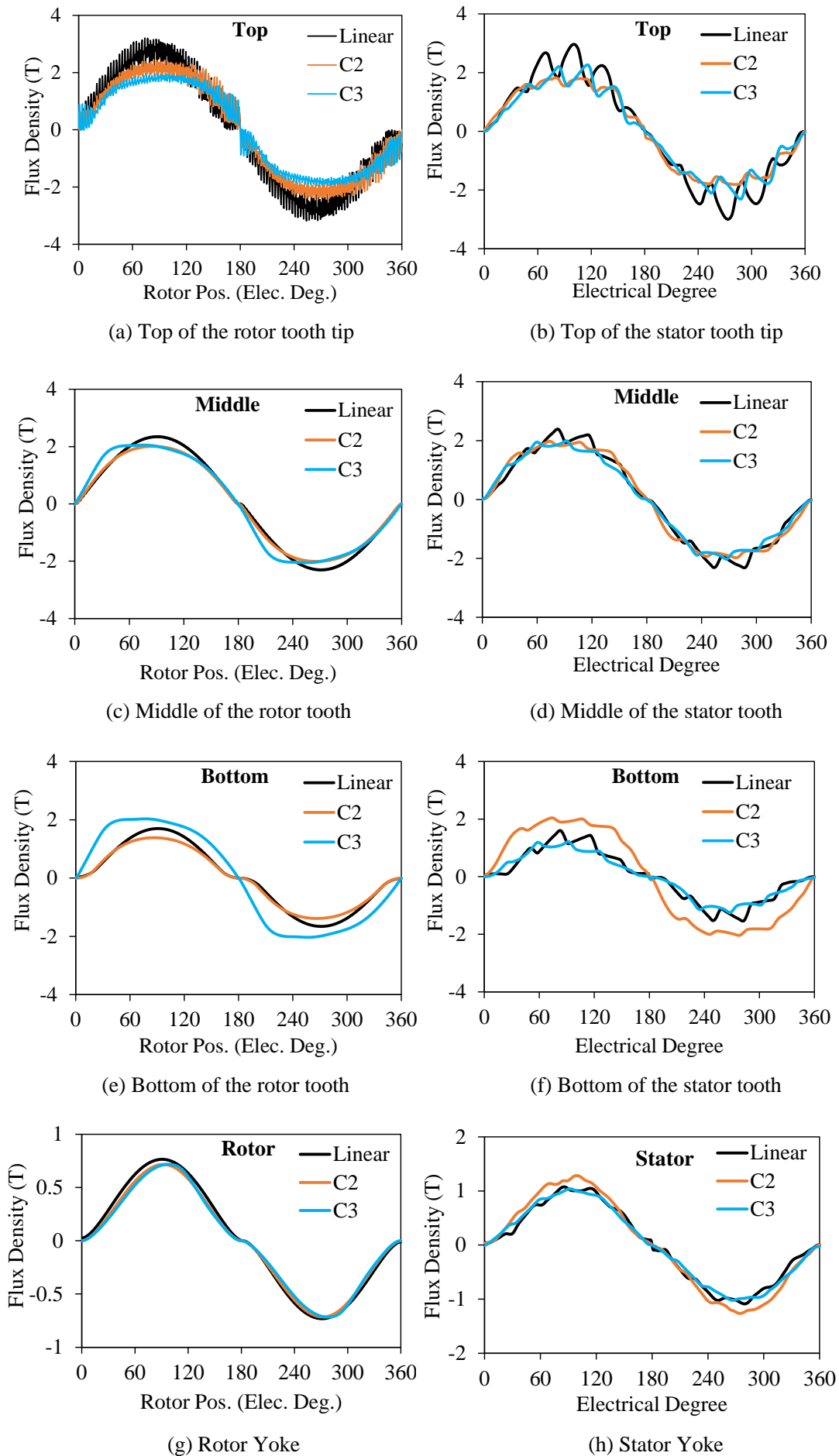
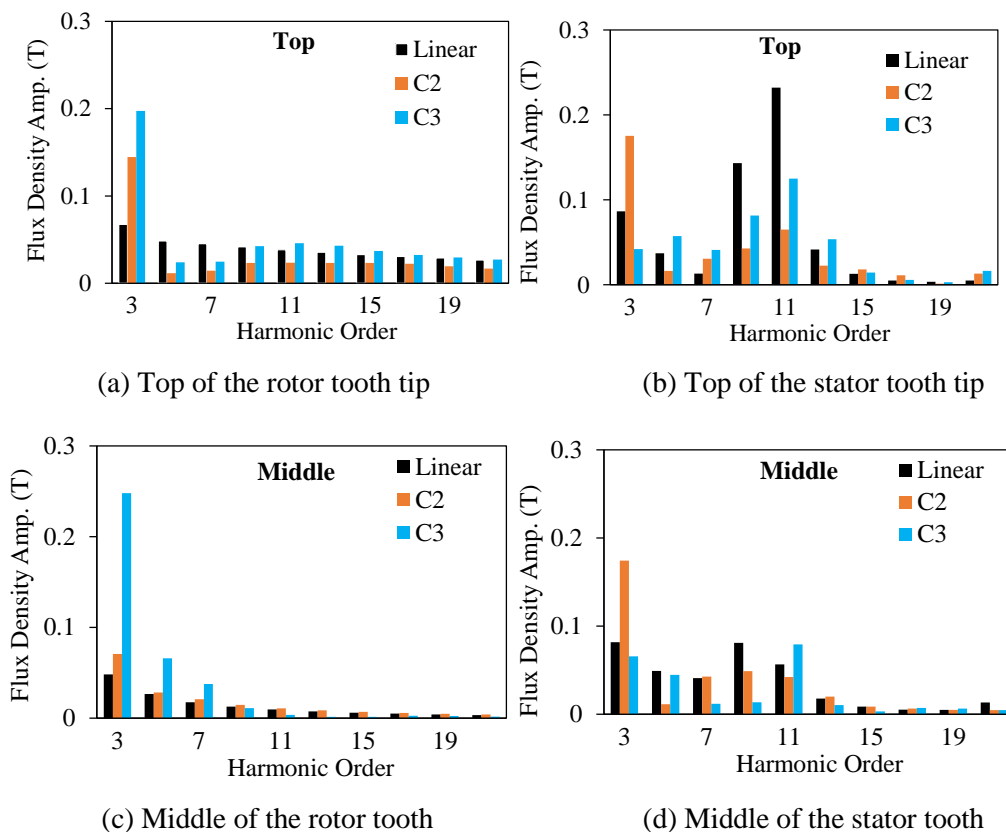


Fig. 5.6 Rotor and stator flux density waveforms at the top, middle, and bottom for Linear case, C#2, and C#3.

Furthermore, the flux density in the air-gap turns into the flux in the rotor tooth body again. Therefore, tooth parts can be imagined as an integration given in (5.6) acting as a low-pass filter (so called averaged effect) which makes the higher frequency harmonics gradually disappear. Therefore, as clearly seen in the upper sides of the tooth, there are a lot of high frequency harmonics on the waveforms (see Fig. 5.6(a, b)). These higher frequency harmonics gradually disappear due to the low slot reactance. In addition, it should be considered that because of the winding factor and slotting effects, the distortion on the stator tooth flux is larger than that of the rotor tooth flux. On the other hand, since there is no slip frequency effect on the stator side, the higher order harmonics have not been induced on the stator side whilst they have been induced significantly on the rotor side. In case of C#3, the flux waves have been more distorted since the non-linear material has been used on the rotor teeth and the same situation is valid for the C#2 (see Fig. 5.7(a, c, e)). Once non-linear material assigned for the stator teeth, its 3rd harmonic is always higher (see Fig. 5.7(b, c, d)). As seen in the rotor tooth flux waveforms (see Fig. 5.6(a, c, e)), even if only the stator tooth parts saturated (C#2), it has an effect on resultant main flux waveform. Therefore, its waveform has also large 3rd order harmonic. But it is not as high as the rotor tooth parts saturated only case (C#3). Based on Fig.6(c, d), Fig. 5.7(c, d) and (5.4), it is concluded that due to the highly saturated rotor tooth parts (C#3), the rotor bar current becomes non-sinusoidal. Further explanation are given in the following section.



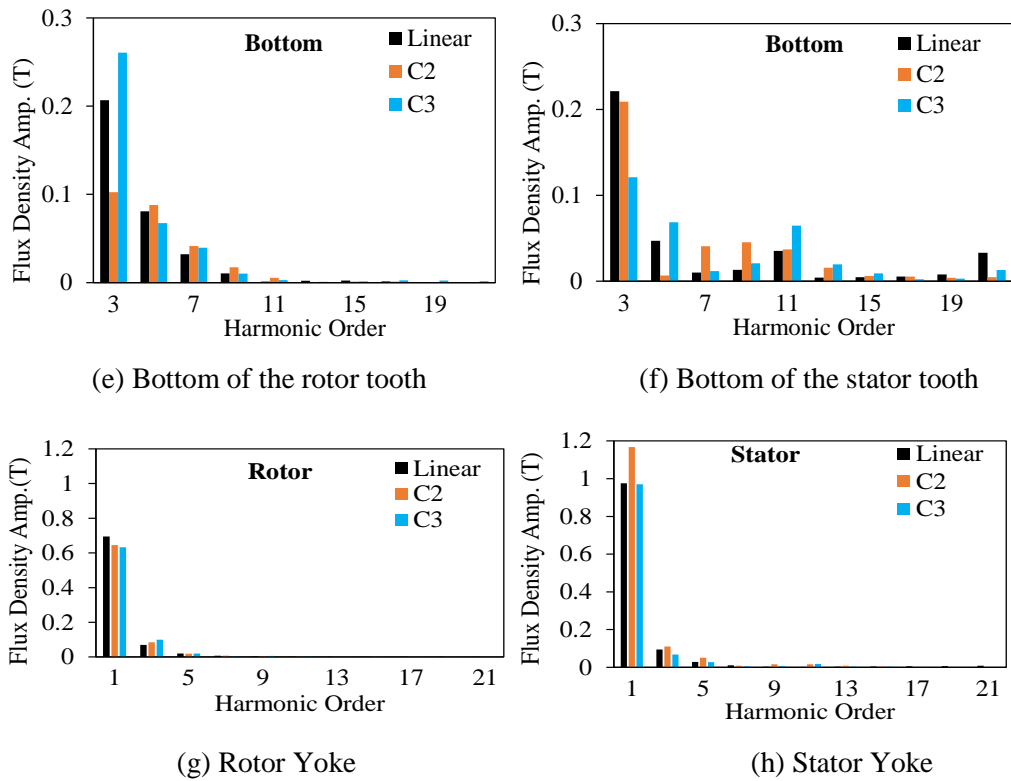


Fig. 5.7 Magnetic flux density harmonic spectra along the rotor and stator teeth for Linear case, C#2 and C#3.

5.5 Influence of Magnetic Saturation

As explained previously, the saturation effect is inevitable in the electrical machines. The tooth saturation is more important than the yoke saturation which is mainly because the tooth iron is smaller than the yoke in quantity and the flux density is not uniformly distributed around the iron cores of the machine. As shown foregoing, it is highly distorted on the tooth parts. In order to reveal why the rotor tooth saturation is more responsible for the non-sinusoidal bar current, relative permeability and slot flux lines including leakage and torque producing components should be investigated. Obtained flux line and relative permeability distributions for C#2 and C#3 are illustrated in Fig. 5.8. As clearly seen in Fig. 5.8, the influence of the slot leakage on this phenomenon is essential. In C#3, the fluxes coming from the tip parts (including zigzag and belt leakage) flow to the rotor tooth body parts and the same phenomenon is valid for case C#2. As explained, the flux at the tip parts are highly distorted.

Once this highly distorted flux at the tooth tip parts flows directly to the adjacent tooth body through the slot, a number of low and high order harmonic components are transferred to the main flux. Therefore, it has been revealed that the reason behind this phenomenon is the saturation of the tooth tip parts. Since the highly saturated parts cannot carry any more flux, those fluxes pass through to lower saturated parts of tooth bodies (see Fig. 5.8). However, in the linear case, those highly distorted fluxes of the tip parts will never be passed to the tooth body parts. Therefore, extra flux harmonics are not produced on the tooth body in the linear case. As well known, the more saturation on the tooth parts,

the more leakage in the slots [ANG63], [CHA69]. By using (5.2), leakage flux density (tangential component of the slot flux density) of the rotor (H_r) and stator (H_s) slot (including the slot opening) have been calculated and their variations with respect to rotor position are illustrated in Fig. 5.9. As expected, more slot leakage has occurred at the saturated parts and in Linear case it is always minimum.

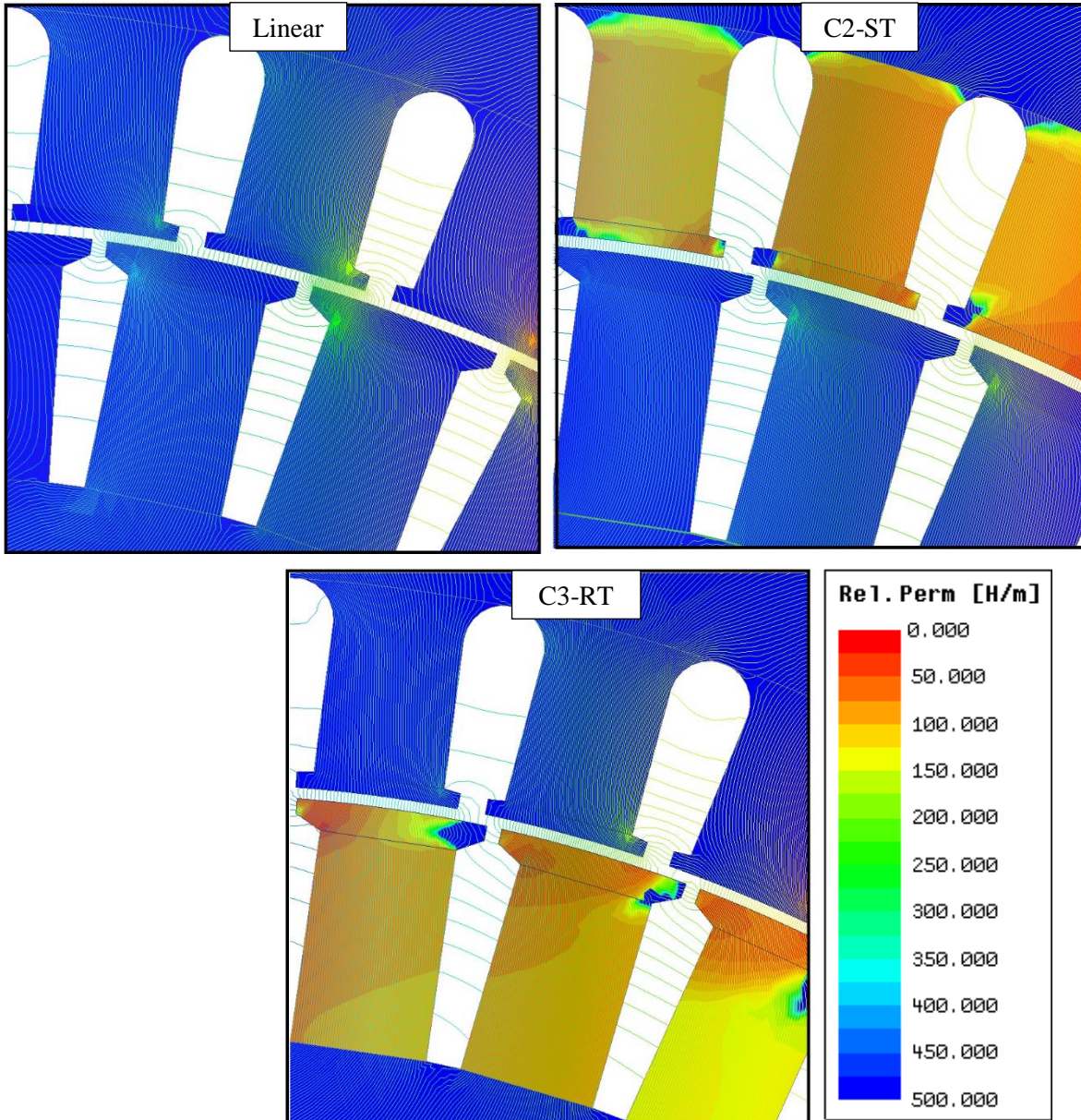
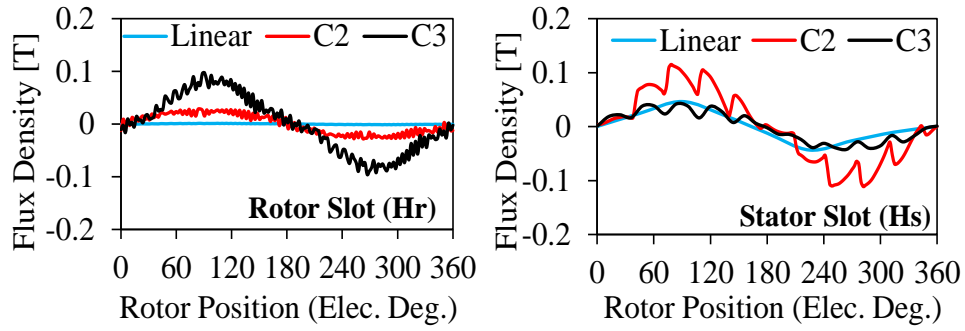


Fig. 5.8 Flux line and relative permeability distributions for different saturation cases.

In order to reveal that in which part of the rotor and stator slots the leakages are maximum, the leakages along the H_{x1} , H_{x2} and H_x have been calculated separately and compared as shown in Fig. 5.10. As clearly seen in Fig. 5.10, the leakage is significantly higher at the stator and rotor tooth tip parts. Furthermore, in order to reveal which part of the machine has the higher slot leakage percentage, the leakage flux percentages are calculated according to tangential components of the rotor and stator slot fluxes for Linear case, C#2 and C#3 as given in Table 5.2. Based on Table 5.2, it is obvious that if saturation is ignored (Linear case), the minimum slot leakage is obtained. However, if saturation is considered in that case significantly high slot leakages are obtained depending on the place of the

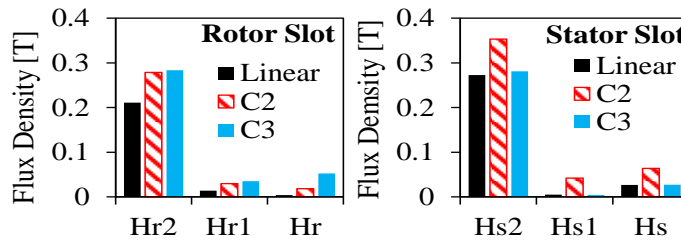
saturation. As expressed in (5.4), there is a direct correlation between the rotor tooth flux density and the rotor bar current. This relationship can also be presented in terms of saturation factor as expressed in (5.7) and (5.8) [BUC72], where m , f_s , N_s , k_{w1} , s , τ_p , R , k_{sat_n} , I_M , and α_r are the phase number, the synchronous (stator) frequency, the fundamental winding factor, the slip, the pole pitch in slot number, the rotor slot number, the saturation factor, the magnetizing current, and the phase shift between bars divided by pole pitch, respectively. In addition, in (5.8), MMF_{sn} , MMF_{Rn} , MMF_{gn} , and B_{gn} are the stator, rotor, and air-gap magneto motive forces, and the air-gap flux density amplitude, respectively.



(a) Leakage flux density of rotor slot

(b) Leakage flux density of stator slot

Fig. 5.9 Variation of the rotor and stator slot leakage flux densities with respect to rotor position.



(a) Amplitudes of leakage flux density of the rotor slot parts

(b) Amplitudes of leakage flux density of the stator slot parts

Fig. 5.10 Amplitudes of the leakage flux density of the rotor and stator at the slot opening (Hx2), slot home excluding the slot opening (Hx1), and average flux density in the slot including the slot opening (Hx) for all cases ($x=s$ for stator, $x=r$ for rotor, see Fig. 5.2(b) for the details of the slot parts).

Table 5.2 Slot Leakage Percentages

	Linear	C2	C3
Hr	1.79	6.85	23.63
Hs	12.38	38.96	12.27

As seen from (5.7), the bar current is inversely proportional to saturation factor. Therefore, in order to reveal its effect (saturation level of each part), the saturation factor is calculated by using (5.8) for Linear case, C#2 and C#3 and the results are illustrated in Fig. 5.11. The total saturation factor calculated for

C#2 is the highest and as for the Linear case, it is negligibly low. As clearly seen in Fig. 5.11, saturation factor of the rotor yoke (RY) and stator yoke (SY) is negligible whilst the rotor tooth (RT) and stator (ST) is significant. Considering the saturation factors and slot leakage fluxes, reconstructed bar current waveforms by ignoring the higher frequency harmonic components in order to clearly see the effect of the saturation harmonics are illustrated in Fig. 5.12(a).

$$I_{bn} = \left(\frac{4\sqrt{2}}{50^8} \right) \frac{m^2 \cdot f_s (N_s k_{w1})^3 s \cdot \tau_p \cdot l_s}{g_e \cdot P \cdot R \cdot k_{sat_n} \cdot \sqrt{R_{bns}^2 + X_{bns}^2}} \{I_M \sin(\alpha_r)\} \quad (5.7)$$

$$k_{sat_n} = 1 + \frac{MMF_{Sn} + MMF_{Rn}}{MMF_{gn}} = \frac{1}{2} \left[1 + \sqrt{1 + \frac{1.6\pi(MMF_{Sn} + MMF_{Rn})}{B_{gn} g}} \right] \quad (5.8)$$

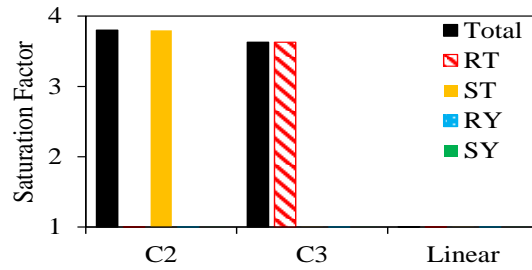


Fig. 5.11 Calculated saturation factors for C#2, C#3 and Linear case.

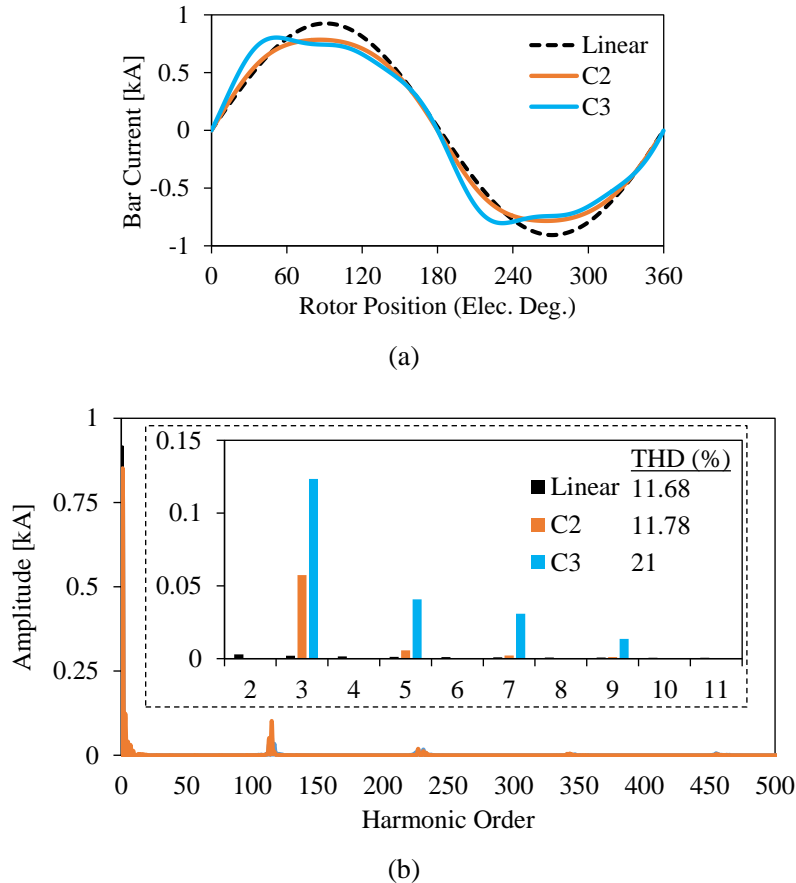
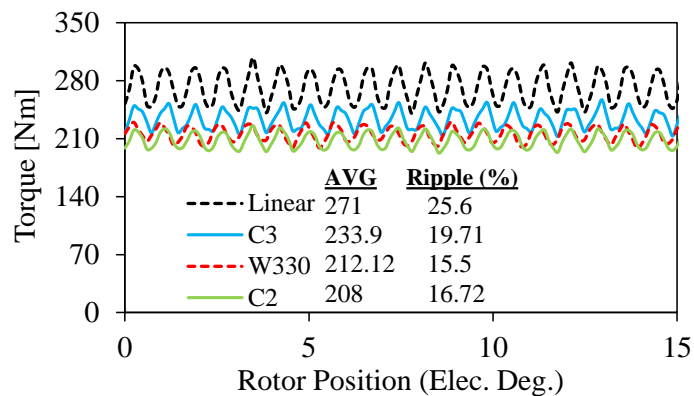
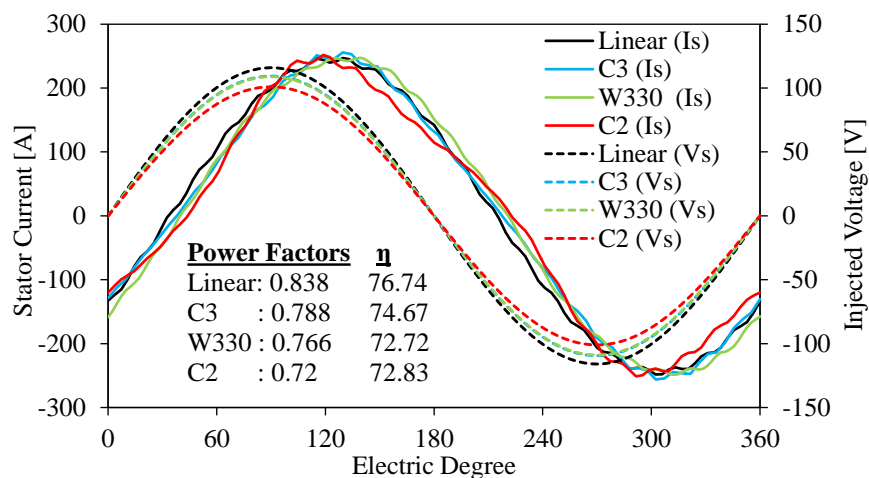


Fig. 5.12 Reconstructed bar current for Linear case, C#2, and C#3: (a) waveform and (b) harmonic spectra.

As expected the 3rd harmonic component has become the most dominant one due to the saturation (see Fig. 5.12(b)). As clearly seen in the figure, if the effect of the saturation, which limits the main flux amplitude, is neglected, the rms values of the maximum available bar current are 648.8A, 594.3A, and 609.28A for Linear, C#2, and C#3, respectively. This finding has revealed that even if the saturation factor is higher in case C#2 (due to highly saturated stator teeth), it does not cause rotor bar current to become non-sinusoidal. Furthermore, it is also obvious that if the stator tooth parts are highly saturated, it influences the overall machine performance since the maximum induced voltage decreases. Considering (5.4), (5.7), Fig. 5.6, and Fig. 5.10, it is concluded that due to the highly saturated rotor tooth parts, the bar current becomes non-sinusoidal. This is also the explanation for why the rotor bar current becomes non-sinusoidal in the extreme operating conditions such as fairly low slip or very significantly high electric loadings. Because under all these operating conditions, the rotor tooth parts are saturated highly due to the increase in the magnitude of the air-gap flux density. More details about the influence of electric loading and slip on the bar current waveform will be presented in Chapter 7. As previously explained, the magnetic saturation plays a very important role on the air-gap field and hence the performance characteristics of the machine. The influence of the saturation on the torque quality, power factor and efficiency is illustrated in Fig. 5.13.



(a) Torque density variation and torque ripple



(b) Injected voltage and induced currents in the Phase 'A' winding

Fig. 5.13 Performance characteristics: (a) torque quality and (b) power factor.

If the effect of the saturation is ignored, more torque would be obtained at the peak current in case of assigning linear material instead of non-linear material to the cores (see Fig. 5.13(a)). Because of the slot leakage increasing with the saturation (see Fig. 5.10), the torque amount decreases [LIP17]. However, depending on the highly saturated region around the IM, achieved torque density and percentage of the torque ripple change. It is a common knowledge that there is a direct correlation between the bar current and the torque. Since the saturation factor of C#2 is the maximum, its torque density is the minimum. Once the stator teeth are highly saturated (C#2), the achieved torque density is slightly higher than the case of rotor teeth which are highly saturated (C#3). However, torque ripple percentage is vice versa. In addition, the saturation causes the decrease of the power factor by much more lagging the current as clearly seen in Fig. 5.13(b). In Fig. 5.13(b), all obtained power factors including the original design (IM with W330 non-linear material) are illustrated. Note that, during the calculation of efficiency, the windage, friction and stray load losses were assumed to be 1% of the output power [BOL10]. There is a slightly difference between the efficiencies η . However, as expected, in the Linear case the achieved efficiency is the maximum since it has the highest output power and power factor. Since the stator core is highly saturated in C#2, the lowest torque density and output power has been achieved even if it has the same stator current magnitude as so in the other cases. Although the power factor of the C#2 is the lowest, its efficiency is slightly higher than that of the C#3. Its rotor bar and core losses are the lowest as well since the obtained torque density is the lowest in C#2. As a result, if the saturation occurs, all the machine performance characteristics are affected. It is proven that the saturation increases the magnitude of the 3rd harmonics of air-gap flux density and bar current. Furthermore, it has revealed that the influence of stator tooth saturation on the torque quality is higher while the influence of rotor saturation on the efficiency is higher.

5.6 Conclusion

In this chapter, the influence of the magnetic saturation on the rotor bar current waveform of a squirrel-cage IM has been investigated. The levels of iron saturation of each magnetic circuit components on the main flux path and their influences on the performance characteristics of the machine including the bar current waveform, torque quality, power factor, efficiency, etc., have been examined. It is concluded that, each part on the main flux path has a considerable effect on the bar current waveform. However, among these parts, the saturation of rotor tooth body parts has the most contribution to the distortion of rotor bar current.

This study has also revealed that the high saturation causes more slot leakage flux, especially in the tooth tip parts. The flux density of the tooth tip parts contain highly distorted flux components and those harmonics diminish to a minimum due to the average effect of the tooth body parts. It has also found that the saturation causes reduction in the output power, power factor, efficiency and also torque density.

In Chapters 6 and 7, the influences of design parameters and operating parameters on the rotor bar current waveform will be further investigated in detail.

6 Influence of Design Parameters on Non-Sinusoidal Bar Current Waveform

In this chapter, the influences of design parameters, such as air-gap length, stator slot/pole number combinations, rotor slot numbers, slot geometric parameters, rotor skew angle, and stator coil pitch on electromagnetic performance characteristics of conventional squirrel-cage IMs are examined in detail with particular reference to the bar current waveform. It has been revealed that each considered parameter has a significant effect on the bar current waveform and the key performance characteristics, such as torque, torque ripple, power losses, efficiency, etc. The conditions when the non-sinusoidal rotor bar current waveform occurs and the reasons behind this phenomenon are investigated by FEA.

6.1 Introduction

In Chapter 5, it has been shown that a 3rd harmonic flux component exists as a consequence of the magnetic saturation occurred in the rotor tooth body parts. Furthermore, it is found that because of this 3rd harmonic flux component, the bar current waveform becomes non-sinusoidal. In this chapter, the influences of the design parameters, which have a potential to cause magnetic saturation, on the electromagnetic performance and bar current waveform will be investigated systematically. In literature, there are several studies on the influence of design parameters:

- air-gap length on the machine characteristics [MOR92], [OSS94], [DOR99], [HIR07], [VAL08], [DAJ08], [AGU12], [GHO12], [ABD13], [JUA14], [ZHA14b], and some guidelines for selecting the proper length [ALG65], [LIP04], [PYR08], [GUN16c];
- slot/pole number (S/P) combinations on the performance characteristics, eccentricity issues and parasitic effects, such as noise, vibration, etc., in the IMs [KRO31], [CHA64], [LIA95], [MEL95], [HIR97], [NAN01], [WOL07], [BES09], [NAN09], [JOK13], [SED14], [TSO14], [AGA16], [GUN17a];
- rotor slot number on the electromagnetic force, unbalanced magnetic pull (UMP), vibration, and acoustic noise [KRO31], [ALG54], [ARK97], [HIR97], [KOB97], [KIM99], [HUA02], [LIP04], [AHO06], [FIR07], [VAL07], [MAR08], [BES09], [BOL10], [SOB11], [GYF13], [GUN17b];
- rotor skew on magnetic noise, magnetic saturation, vibration and acoustic noise, UMP, power losses [OST86], [DOR95], [NAU97], [MCC98], [WAN16].

However, a limited number of studies investigated the influence of various design parameters on the other performance characteristics, such as bar current, torque, efficiency, power factor, etc. in IMs [AHO06], [VAL07], [MAR08], [GYF13], [GUN16a], [GUN16b], [GUN16c], [GUN17a], [GUN17b], [GUN18a]. On the other hand, this thesis will be the first study investigating the non-sinusoidal bar current phenomenon in the IMs.

In this chapter, previously designed IM (see Appendix C for the specifications) has been employed and modified without changing the stack length and stator outer diameter in order to examine the influence of various design parameters. Since the bar current plays a substantial role in the torque production, power density, power losses, efficiency, etc., its accurate prediction is essential. Therefore, the design parameters given below, which have a direct effect on the magnetic saturation of the machine cores, should be identified with a special attention in order to predict the bar current with a high accuracy.

- Air-gap length;
- Stator slot/pole number (S/P) combinations with a specific rotor slot number;
- More common stator slot/rotor slot/pole number (S/R/P) combinations;
- Slot geometric parameters;
- Rotor skew angle;
- Stator coil pitch.

For each design parameter, the influence of the magnetic saturation on air-gap flux density, rotor bar current, rotor tooth flux densities, torque quality and also efficiency will be revealed. The levels of magnetic saturation in different parts, including stator and rotor back irons, tooth body and tooth tips etc., will be examined. In addition, the influences of the forgoing design parameters on the bar current waveform and performance have been investigated in [GUN16c], [GUN17a], [GUN17b], [GUN18a]. It has been revealed that the rotor bar current waveform becomes non-sinusoidal after exceeding a specific design parameter amount or slot number. In addition, it has also been revealed that each of the forgoing design parameter has a significant effect on the bar current waveforms and electromagnetic performance characteristics.

6.2 Air-Gap Length

IMs are one type of electric machines which are widely used in the traction systems of the electric vehicles (EVs) due to their advantages, such as simple, robust, reliable structure, and also cheaper and mature manufacturing technology [GUA14]. In the EV application, the torque density, torque ripple and efficiency are very important design considerations. In order to reduce the torque ripple and improve the torque density and efficiency in IMs, a lot of control methods have been investigated in literature [BAR97], [SUT13], [ISM13]. From design point of view, torque density and efficiency can be improved and torque ripple can be minimized by optimizing the slot geometries, the winding configuration [ALB13], and the number of rotor slots [VAL07] etc. In addition, the air-gap length is one of the main concerns for design process of any type of electrical machine since it has a significant influence on their performance characteristics. A longer air-gap length increases the magnetizing current and stator copper losses which cause the decrease in the power factor and efficiency. In addition, it also reduces the torque density since the air-gap flux density weakens. On the other hand, a shorter

air-gap causes higher eddy current losses because of the permeance harmonics produced by the slots. Therefore, a special care should be taken in the air-gap length selection in order to achieve better performance, particularly improved efficiency.

There are several different studies on the influence of air-gap length [MOR92], [OSS94], [DOR99], [HIR07], [DAJ08], [VAL08], [AGU12], [GHO12], [ABD13], [HAI14], [JUA14] and some guidelines for selecting the proper air-gap length [ALG65], [PYR08], [LIP17]. In order to reveal the relationship between the starting performance and the closure of the slots, the influence of the air-gap length on the leakage flux has been investigated [HAI14]. The air-gap length subject is also indirectly related with the non-uniform air-gap distribution (rotor eccentricity) which causes unbalanced magnetic pull (UMP). The parameters affecting the magnitude of the UMP generated in an IM have been investigated and it has also revealed that the tooth saturation may also cause a distribution of the flux because of the greatly increased reluctance path round the narrow airgap by the concentration of the flux. [DOR99]. In [OSS94], saturation of the magnetic cores has been investigated in some non-uniform air-gap conditions. It has been concluded that the saturation level varies along the machine periphery with respect to flux density value and is due to the non-uniformity of the air-gap and hence the narrower the air-gap the higher the saturation [OSS94]. In order to calculate some performance characteristics of AC machines by taking into the effect of the magnetic saturation, instead of having a variation in the iron permeability a winding function approach has been developed by assuming the air-gap length variable, being a function of position and level of the air-gap flux [MOR92]. In a similar study, a modified winding function approach has been utilized to calculate the inductances accurately by considering a linear rise of the saturation factor with respect to air-gap length [GHO12]. In another similar study, in order to model the saturation of the main flux path, the effect of eccentricity has also been taken into account by making the air-gap length a function of saturation level and spatial position [ABD13]. Furthermore, a study has been conducted on an axial-flux squirrel cage IM in order to investigate the influence of the air-gap length on the machine performance. It has been revealed that by changing the air-gap length, an optimal loss can be found between the rising stator copper loss and the decreasing rotor eddy current loss [VAL08]. The influence of the air-gap on the characteristic performances of different kind of electrical machines have been investigated in literature. For a large synchronous generator, the effect of the air-gap length on line current, flux density and core loss characteristics has been investigated [AGU12]. The influence of the effective air-gap length on the phase self- and mutual-inductances, flux linkage, line current magnitude and other performance characteristics such as rotor permeance harmonics have been investigated for a salient pole synchronous permanent-magnet machine [DAJ08]. The influences of air-gap length and pole number on the various losses under constant voltage and speed operation have been investigated for IMs [HIR07]. In a similar study, the influence of mechanical parameters including the air-gap length on the IM efficiency has been investigated in [JUA14]. It is concluded that an IM having narrower air-gap has more distorted waveforms than that of its counterpart having larger air-gap. The influence of the air-gap length on flux fringing has also been investigated

and it has been revealed that the longer the air-gap, the higher the fringing flux [ALG65]. These fringing flux causes additional copper and core losses and hence heat around the slot and tooth parts [ALG65].

In this section, the squirrel-cage IM whose stator outer diameter, stack length, slot/pole number, winding layout and rated operation parameters such as voltage, current, and speed are exactly the same as those of the Toyota Prius 2010 IPM machine which is designed and several FEA based magnetic and electrical analyses have been performed in order to reveal the influence of air-gap length on the rotor bar current waveform and some performance characteristics such as magnetizing current, torque density and ripple, power factor, machine losses, and efficiency. Moreover, the correlation between the non-sinusoidal bar current and magnetic saturation depending on the air-gap length will be explained in this section.

6.2.1 Importance of Air-Gap Length

In order to select the air-gap length which best suites to any rotating machine a few design guidelines exist in literature [ALG65], [PYR08], [LIP17]. Moreover, although the air-gap is of great significance, no theoretical optimum could have been directly solved. In principle, the air-gap length g varies as a function of the operating conditions and the air-gap length of a standard IM which has more than 1 pole pairs p can be calculated in mm as a function of power P_{out} in kW as given in (6.1) [PYR08].

$$g = 0.006(30 + 10^{1.2}P_{out}^{0.4}), \quad \text{when } p > 1 \quad (6.1)$$

The air-gap is affected considerably by thermal expansion of stator and rotor teeth, the centrifugal forces and the magnetic pull [VAL08]. For IMs, in power ratings from 0.75 to 750 kW, practical values from 0.2 to 5 mm are typical; the higher the motor speed, the longer the air-gap in order to avoid excessive iron losses in the teeth [PYR08]. However, there are also very special IMs with oversized air-gap length designed for rotating anode drive in X-ray tubes which requires noise, temperature, electrical/magnetic isolation and etc. [GER00]. Although increasing the air-gap increases magnetizing current and decreases the achievable flux density, it will also tend to decrease stray load loss [ALG65], [GER00]. On the other hand, a small length of the air-gap may lead to increase in magnetic losses on the surface of the rotor, due to increased permeance harmonics created by the stator and rotor slots. This requires thinner laminations to reduce the effect of eddy currents in the parts of the IM. Moreover, whatever gap is used, it must be uniform and large enough to ensure that eccentricity of the rotor with respect to the stator does not cause the shaft stiffness to be overcome by UMP, which may allow the rotor to strike the stator. It should be also considered that to be able to avoid the UPM, originated from the non-uniform air-gap flux distribution, odd combinations of slot/pole number ($gcd\{S, P\}$) should not be chosen. A non-uniform air-gap causes an increase in torque ripple and hence noise and vibration. Overall, all these mentioned factors should be considered carefully when dealing with the air-gap length design.

6.2.2 Investigation of Air-Gap Length

The 2-D FEAs under steady state operation condition at 950 rpm have been performed. For simplicity, during the analyses, all other machine specifications (see Appendix D) are fixed except for the supplied voltage in order to maintain the same stator currents and the air-gap length which has been changed from 0.1g to 5g ($g = 0.73 \text{ mm}$) with 0.1g step size from 0.1g to 0.5g and 0.5g step size from 0.5g to 5g.

6.2.3 Influence of Air-Gap Length on Electromagnetic Performance Characteristics

As known, the relationship between the induced voltages in a winding around a ferromagnetic core carrying a sinusoidal flux is linear. As expressed in (6.2) the voltage induced in the phase windings depends on the air-gap flux density B_{gh} , the number of turns per phase N_t , synchronous frequency f_s , fundamental winding factor k_{w1} , coil pitch τ_c in stator slot number, and stack length l_s . Therefore, as illustrated in Fig. 6.2(a), considering $B_{gh} = d\phi_{gh}/dA_g$, it is obvious that the induced voltage on the phase windings will reduce as the air-gap length increases. As clearly seen in the figure, when the air-gap length is very short (i.e. 0.1g) the level of the distortion is noticeably high.

$$E_s = 2\sqrt{2}N_t f_s k_{wh} \tau_c l_s B_{gh} \quad (6.2)$$

The saturation point of the assigned core material is close to 1.5T as illustrated in the BH curve of the material (see Fig. 6.1). The magnitudes of the flux densities in both the stator and rotor ferromagnetic core parts, especially in the tooth parts, decrease as the air-gap length increases. Air-gap flux density waveforms for different air-gap lengths are illustrated in Fig. 6.3(a). Due to the increasing effect of slotting and saturation, the distortion of the waveform increases as the air-gap length decreases. Under very tiny air-gap length (0.073mm) operation condition, THD of the air-gap flux density is about 90% (see Fig. 6.3(b)) and it has decreased to 18% at 3.65mm air-gap length. In addition as seen in Fig. 6.3(b), under the constant phase current operating condition, the magnitude of the air-gap flux density (radial component of the resultant air-gap flux density) increases substantially as the air-gap length is shortened. Therefore, more saturation at the rotor core and increase in the level of the effective armature reaction can be predicted for short air-gap lengths. The most dominant air-gap flux density harmonics which are the higher order harmonics including the 11th, 13th, 12th, and 23th have changed considerably while the lower order harmonics such as 5th and 7th have changed slightly.

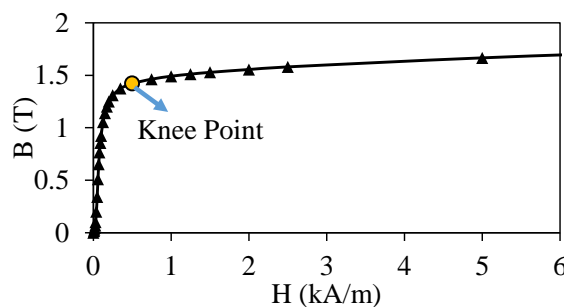


Fig. 6.1 BH curve of the core material (W330_35).

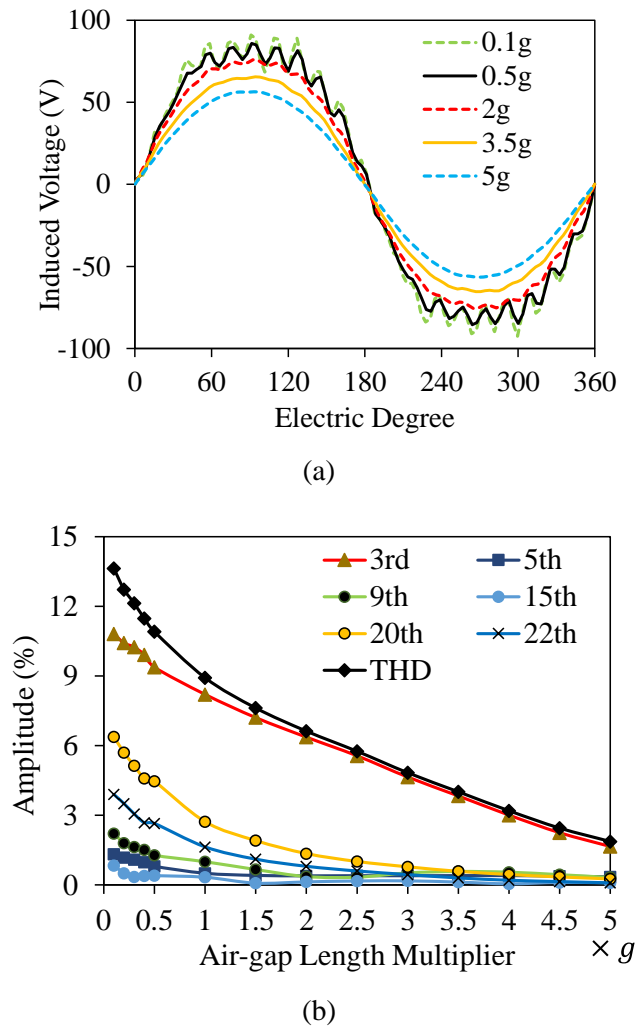


Fig. 6.2 Induced voltage of Phase ‘A’ for various air-gap lengths: (a) waveform and (b) variation of dominant harmonics with respect to air-gap length.

The influence of the air-gap length on the rotor bar current waveform has been illustrated in Fig. 6.4. As seen, when the air-gap length is the shortest the waveform of the current is the most distorted one. The bar current has become non-sinusoidal at 3.5g and the level of distortion has been increased significantly while approaching to 0.1g. Variation of the sub- and super-harmonics of the bar currents for various air-gap lengths and variation of the most dominant harmonic percentages with respect to air-gap length have been shown in Fig. 6.5. While the amplitude of the fundamental harmonic is decreasing with respect to air-gap length, their harmonics percentages are decreasing gradually. As clearly seen in the figures, the dominant harmonics are the 3rd, 5th and 7th. While shortening the air-gap length, the amplitude percentages of these harmonics have increased considerably after 3.5g. As explained in [GUN16a], [GUN16b], the 3rd harmonic of the bar current increases significantly if saturation has occurred partially on the cores especially the rotor tooth parts. Therefore, variation of the slope of the THD curve at 3.5g in Fig. 6.5(e) evidently indicates that the amplitude percentage of the 3rd harmonic has increased significantly due to that the level of the saturation has increased (flux density on rotor tooth area has exceeded its knee point on the BH curve) after 3.5g mm (see Fig. 6.1 and Fig.

6.8(d)). Amplitude percentages of the low order bar current harmonics have changed considerably with respect to air-gap length while the 11th harmonic stands still.

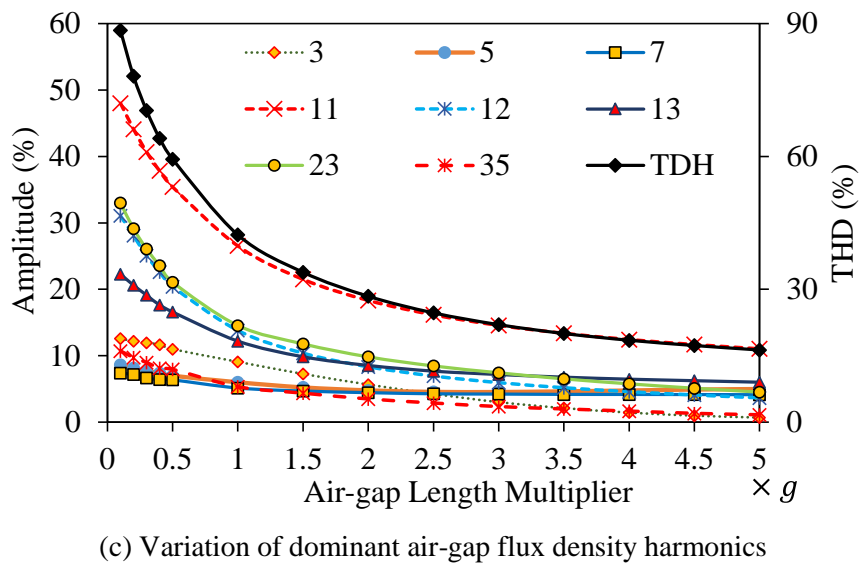
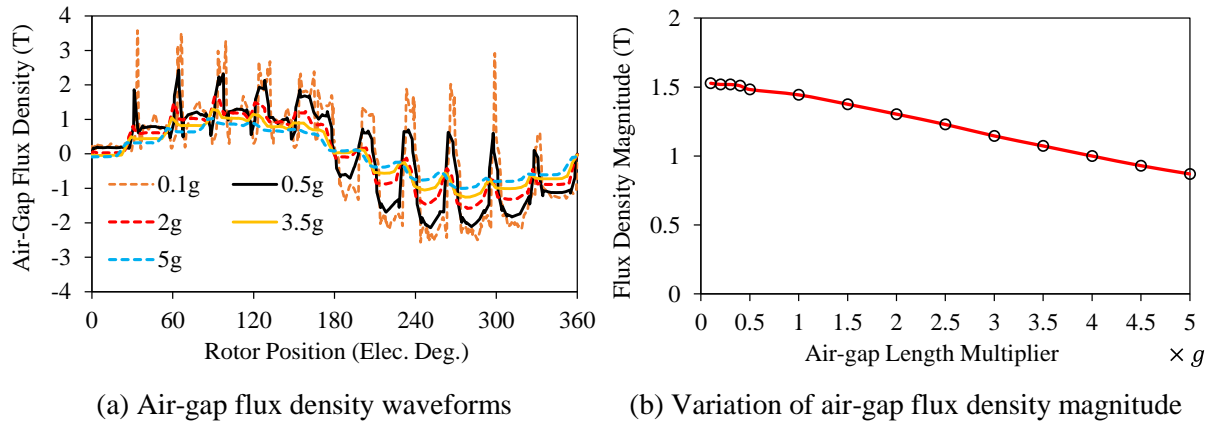
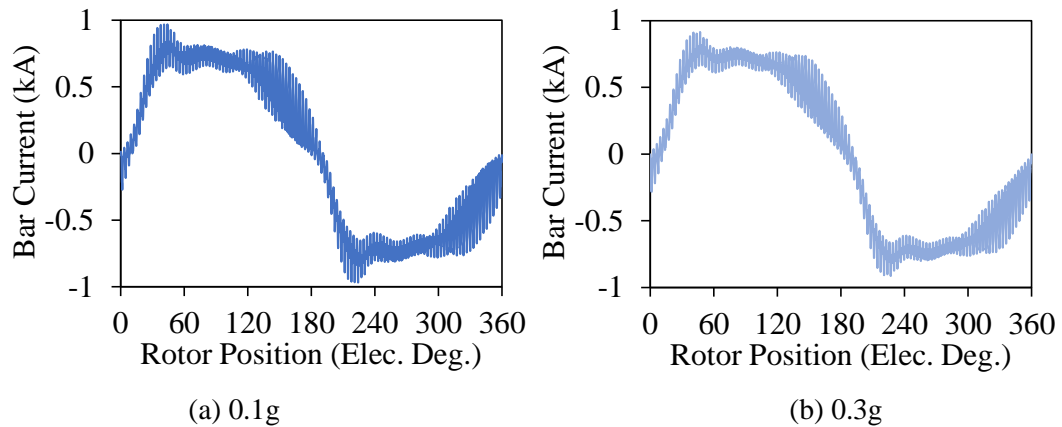


Fig. 6.3 Air-gap flux density for various air-gap lengths: (a) waveform, (b) variation of air-gap flux density magnitude with air-gap length and (b) variation of the dominant air-gap flux density harmonics and THD with air-gap length.



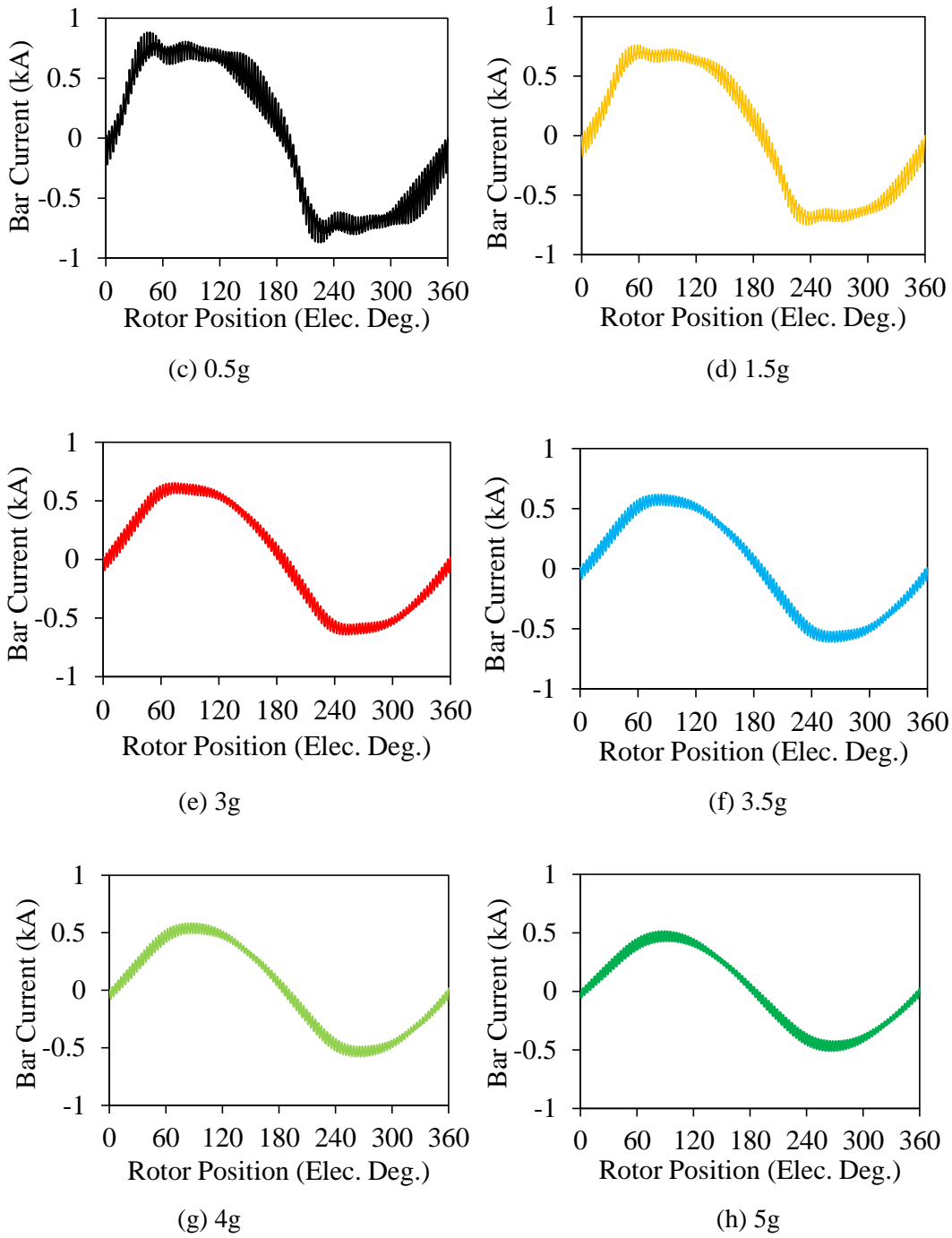
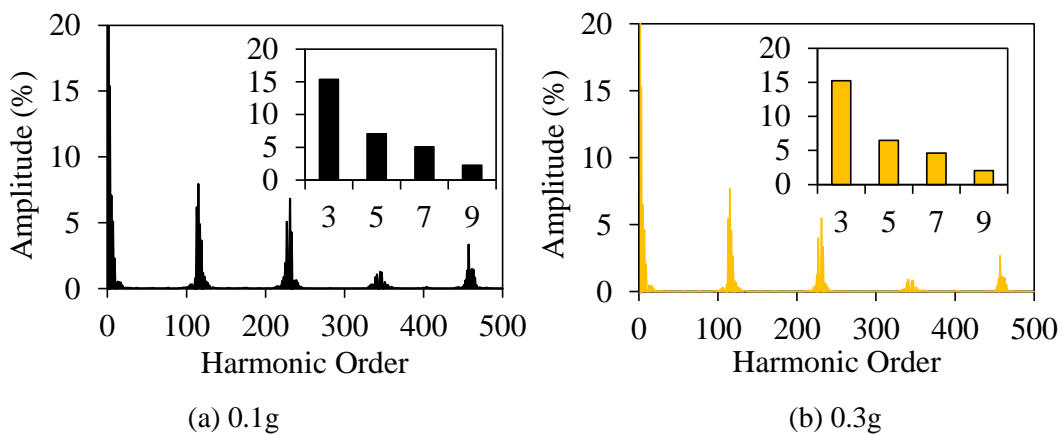
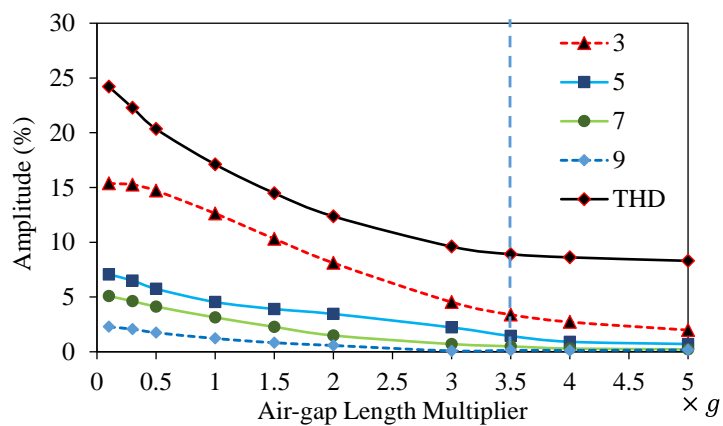
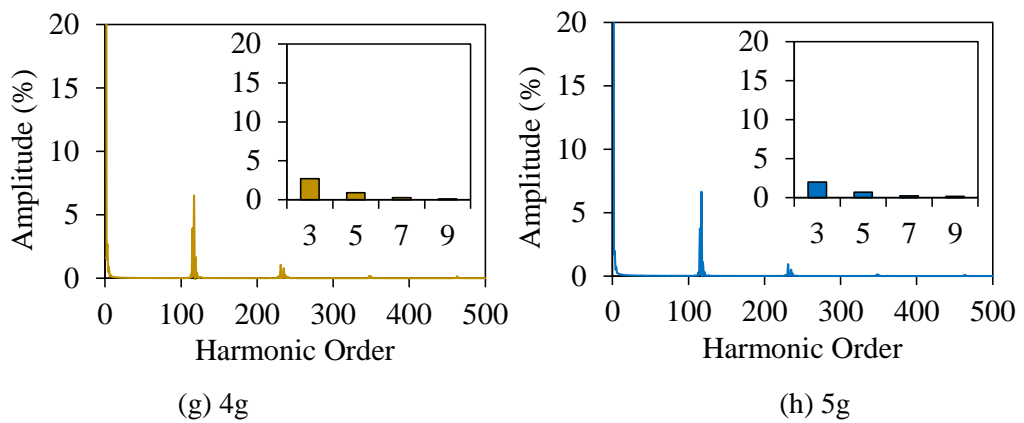
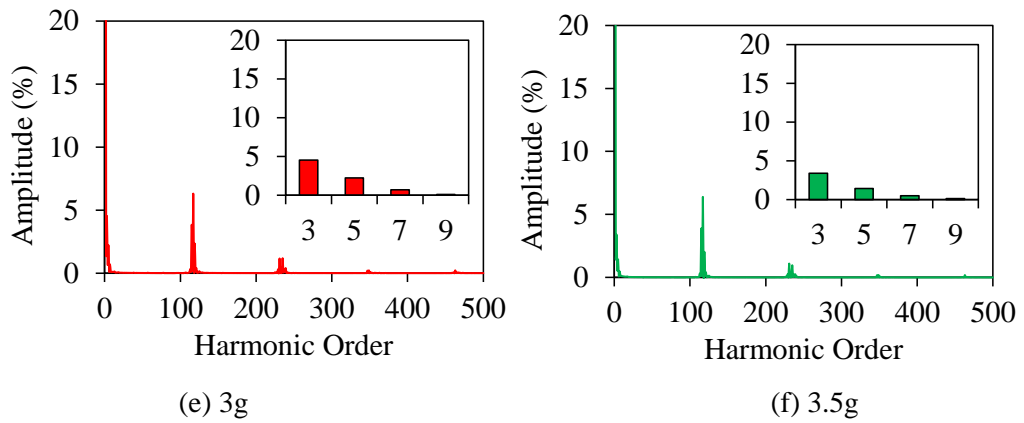
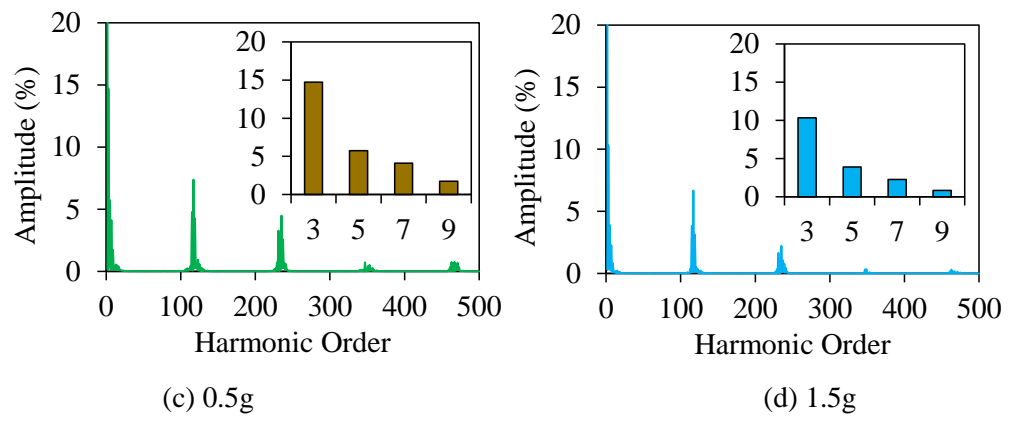


Fig. 6.4 Bar current waveforms for various air-gap lengths at constant rated speed (950 rpm).





(k)

Fig. 6.5 Harmonic spectra of the bar currents for various air-gap lengths: (a-h) lower and higher order harmonics (a-h) and (k) variation of the dominant harmonics and THD with respect to air-gap length.

At constant speed (950 rpm), average torque and ripple variation with respect to air-gap length is illustrated in Fig. 6.6. It is revealed that if the air-gap length is shortened, the torque ripple percentage increases significantly, especially after 1.5g, while the torque density reduces due to the weakening air-gap flux density. The variation of the various parameters such as magnetizing current, power factor, losses and efficiency have been illustrated in Fig. 6.7. As explained before, there is an inverse relation between the power factor and the magnetizing current as seen in Fig. 6.7(a). Due to the extremely high saturation of the cores, the power factor shows slightly increase until the 0.5g point while the magnetizing current decreases slightly. As explained in Chapter 5 and [GUN16b], the saturation reduces the power factor. This conclusion is true under the constant air-gap length, operation speed and excitation conditions. However, in this study, this finding is valid only under the extremely high saturation level conditions, i.e. 0.1g to 0.5g (while saturation factor is higher than 3). As seen in Fig. 6.7(a), even if the saturation level is higher in the cases of shorter air-gap lengths, the power factor decreases as the air-gap length is enlarged. It is obvious that considering the equivalent circuit of the IM, magnetizing current has a direct correlation with the phase current while saturation factor has indirect. Therefore, the influence of the magnetizing current on the phase current angle is much higher than the saturation factor.

The influence of the air-gap length on the machine losses and efficiency is shown in Fig. 6.7(b). Loss-efficiency graph has been divided to 3 sections according to saturation levels of the ferromagnetic cores: section 1 is the extremely high saturation region, section 2 is the medium-level saturation region and the section 3 is the no-saturation region. In the section 1, due to the increase in the power factor as seen in Fig. 6.7(b), the efficiency has increased. After 0.5g point, since the power factor starts to decrease considerably, efficiency decreases remarkably in section 2 and 3. The maximum efficiency (86.58 %) has been achieved at 0.4g length with 0.05 slip and the efficiency decreases exponentially with increasing air-gap length. Note that friction, windage and stray losses were assumed to be 1% of the output power [BOL10].

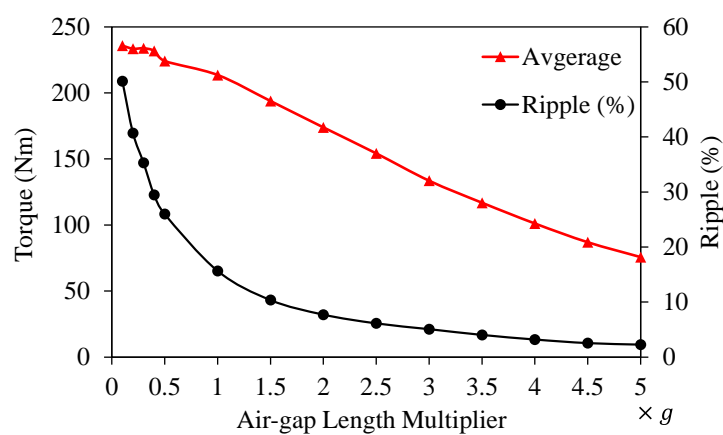
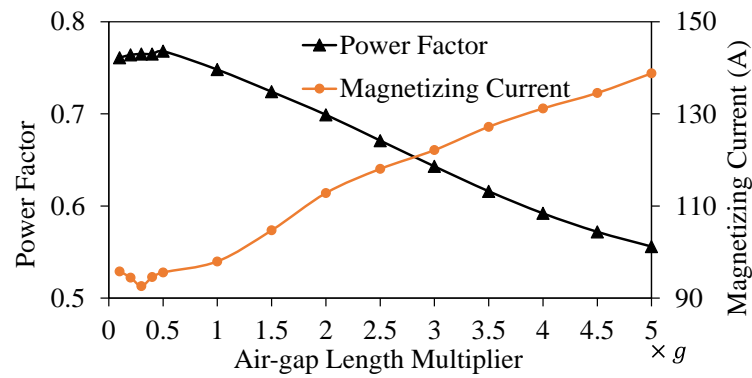
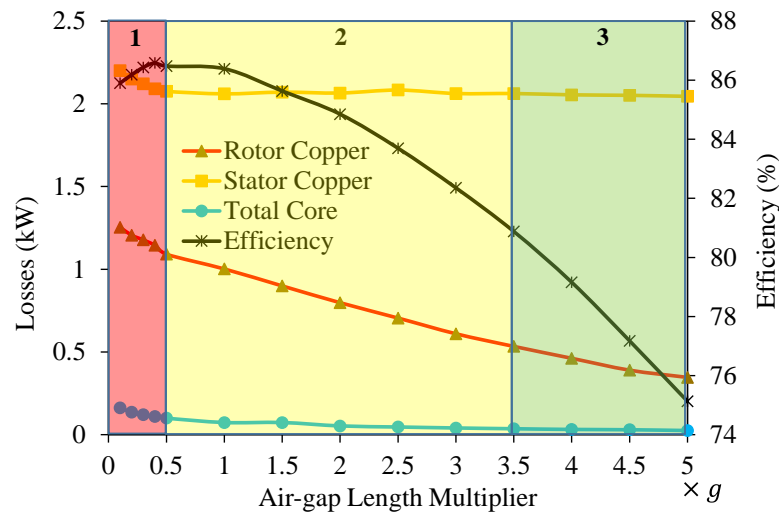


Fig. 6.6 Average torque and torque ripple variation with respect to air-gap length.



(a) Power factor and magnetizing current



(b) Losses and efficiency

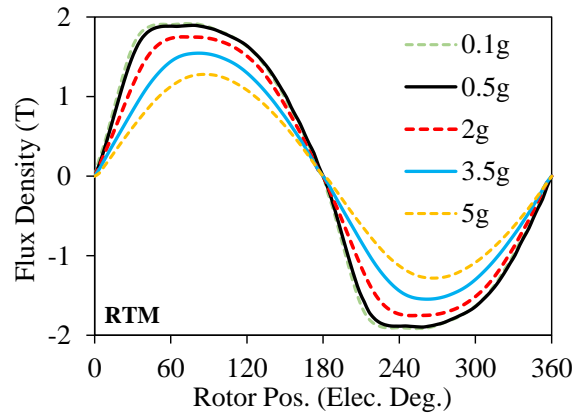
Fig. 6.7 Variation of the key electromagnetic performance characteristics with respect to air-gap length: (a) power factor and magnetizing current, (b) machine losses and efficiency.

Since the stator current is fixed at 250 A for each air-gap length case by changing the amplitude of the injected voltage, the stator copper loss has kept almost the same after the extremely saturation case. However, the rotor bar copper loss decreases due to the torque decreases as the air-gap is enlarged. The main reason behind of this phenomenon is the reduced induced voltage due to the reduced flux density with increasing air-gap length. The other reason is that due to the induced high amplitude of the 3rd harmonic component in the bar currents because of the saturation, extra copper losses are generated. As seen Fig. 6.7(b), as the air-gap length is increased the total magnitude of the iron core losses decreases slightly due to decreased eddy currents with decreasing saturation level. Furthermore, it has been revealed that the larger the air-gap, the lower the maximum achievable power density. As clearly seen in Fig. 6.6 and Fig. 6.7, the air-gap length has a significant effect on all the machine performance characteristics.

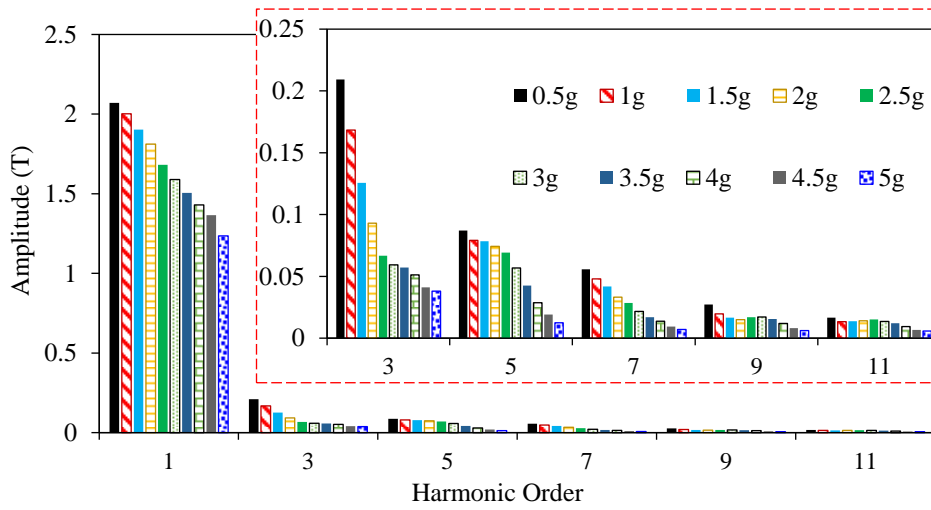
6.2.4 Influence of Air-Gap Length on Magnetic Characteristics

In order to reveal the reason behind the non-sinusoidal bar current phenomenon, the magnetic characteristics of the designed IM are investigated for each available air-gap length. It has been shown

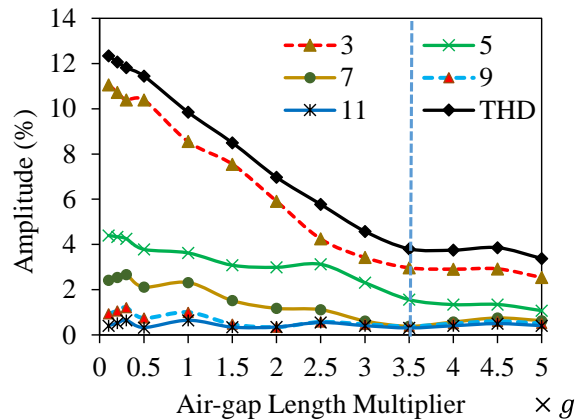
that with the increasing air-gap length, the characteristics of the magnetic circuit parameters change. As explained in Chapter 5, there is a direct correlation between the bar current and the rotor tooth flux density. Therefore, the flux density variation along the middle of the rotor tooth (RTM) with respect to rotor position for various air-gap lengths has been illustrated in Fig. 6.8(a). When the air-gap length is 0.1g, the flux density on the rotor tooth takes the maximum value and its waveform is the most distorted one as seen in Fig. 6.8(b, c). Furthermore, the slope of the THD curve has changed sharply after 3.5g point.



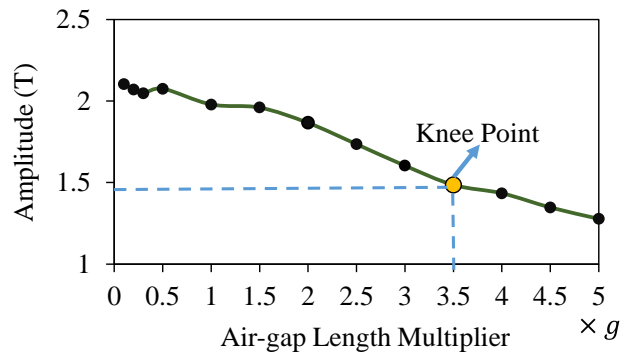
(a) Flux density variation along the middle of the rotor tooth (RTM).



(b) Harmonic spectra of the flux density at RTM.



(c) Harmonic spectra of RTM flux density.



(d) Variation of the flux density amplitudes at the RTM.

Fig. 6.8 Flux density waveforms at the middle of the rotor tooth for various air-gap lengths: (a) waveform, (b) harmonic spectra of the flux density at RTM, (c) variation of the dominant harmonics and THD of (a) with respect to air-gap length, and (d) variation of the flux density magnitude at the RTM with respect to air-gap length.

Therefore, as seen in Fig. 6.8(c), considering previously obtained bar current harmonic spectra and flux density of RTM harmonic spectra it can be concluded that until the 3.5g point the rotor teeth saturate highly (see Fig. 6.8(d)). Therefore, because of the highly saturated tooth parts, the bar current becomes non-sinusoidal. Comparing the BH curve of the core material and RTM flux density amplitude (see Fig. 6.1 and Fig. 6.8(d), respectively), it is obvious that the exact saturation point is about 1.48 T.

What is not yet clear is why saturation of the rotor tooth is more responsible for the non-sinusoidal bar current is as follows. As clearly explained in [MOR92] and [GUN16b], the degree of the saturation is related with the leakage flux along the slots. The waveform of the flux density on the rotor tooth tip (RTT) is shown in Fig. 6.9(a). As seen in the figure, the flux at tips are highly distorted. When this highly distorted flux at the tips flows directly to the adjacent tooth body through the slot, a number of low and high order harmonic components are injected to the main flux. In theory, as explained in Chapter 5, the cores act as a low pass filter which gradually diminishes the high order harmonics. This phenomenon can be observed from Fig. 6.8(a) and Fig. 6.9(a, b). The level of the distortion of the flux density is reduced as long as the flux approaches to the root of the tooth. Furthermore, this filtering effect starts to happen on the tooth tip parts. Here, when those highly saturated un-filtered fluxes directly pass to the tooth body, they cause to induce extra harmonics on the main flux. As explained before, since there is a direct correlation between the RTM flux and the bar current, the bar current became non-sinusoidal due to this phenomenon. Therefore, the results of this investigation reveals that the increasing leakage with increasing saturation is the reason behind the non-sinusoidal bar current phenomenon. The shorter the air-gap length, the more saturation on the teeth, and hence the more leakage in the slots (see Fig. 6.10) [ANG63].

Another major finding of this study is illustrated in Fig. 6.10. As air-gap length is enlarged, the slot leakage which causes the increase in magnetic saturation has been decreased remarkably as can be seen in Fig. 6.10. Moreover, it has also been revealed that the flux leakage is notably higher in the slot

opening area than those inside of the slot. In Fig. 6.10, total and teeth (stator and rotor) saturation factors are indicated by K_{sat_Total} and K_{sat_Tooth} , respectively. Note that these saturation factors have been calculated by (6.5). It is obvious that K_{sat_Total} consists of K_{sat_Tooth} mainly. The saturation factor is approximately unit until the 3.5g point, and it starts to increase considerably as the air-gap length approaches 0.1g.

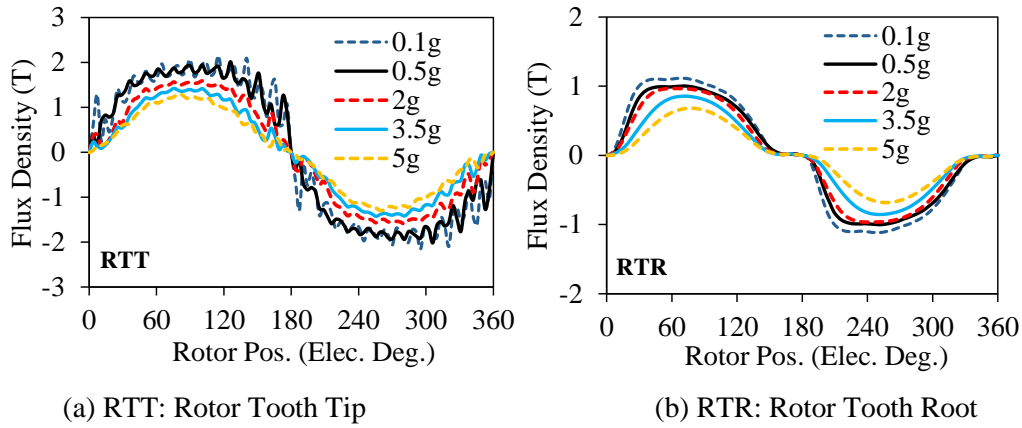


Fig. 6.9 Flux density variation: (a) along the RTT, (b) along the RTR, and (c) variation of the ratio of rotor slot opening (B_{rs0}) and average slot leakage flux density (B_{rs}) to air-gap flux density (B_g).

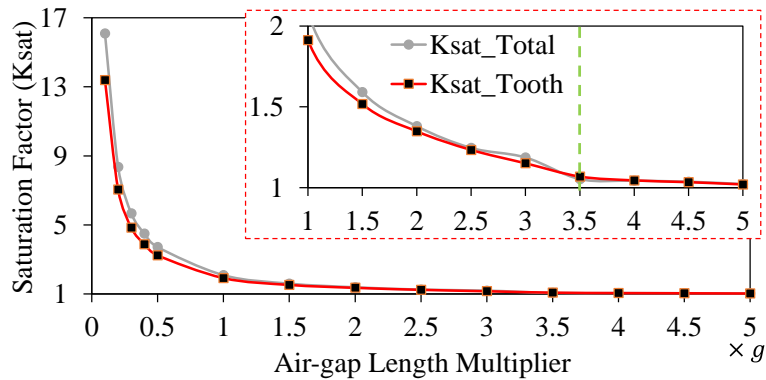


Fig. 6.10 Variation of the rotor tooth (K_{sat_Tooth}) and total (K_{sat_Total}) saturation factors with respect to air-gap length.

6.3 Rotor Slot Number

The performance characteristics of IMs strongly depend on the proper selection of stator and rotor slot combination. The vast majority of the studies in literature, which are related with the rotor slot number topics, are reported on the influence of rotor slot number on the electromagnetic force, unbalanced magnetic pull (UMP), vibration, and acoustic noise [KRO31], [ALG54], [ARK97], [KON97], [KIM99], [HIR97], [HUA02], [AHO06], [FIR07], [VAL07], [MAR08], [BES09], [BOL10], [SOB11], [GYF13], [LIP17]. In order to determine the proper slot combinations in terms of parasitic effects such as torque ripple, UMP, vibration, electromagnetic and acoustic noise, etc., some empirical rules and recommendations have been presented [KRO31], [KIM99], [HUA02], [MAR08], [BOL10], [LIP17]. Effect of three different slot combinations on the electromagnetic and acoustic noise has been investigated numerically in [KOB97]. The harmonics in the electromagnetic force, which are the source of mechanical vibrations and electromagnetic and acoustic noise, have been investigated and an approach to reduce these harmonics by changing the rotor slot number has been introduced [KIM99], [HUA02].

Relatively less papers have investigated the influence of rotor slot number on the other performance characteristics in IMs, such as losses, power factor, etc. [AHO06], [VAL07], [MAR08], [GYF13]. The effect of even and odd rotor slot numbers on the performance characteristics of a solid-rotor, 2-pole, 48-slot IM has been investigated in [AHO06]. The harmonic contents of air-gap flux density, torque and UMP at different rotor slot numbers are studied in detail. A similar study has been conducted for an axial-flux aluminium-cage solid-rotor IM in [VAL07]. In another similar study, the influences of different rotor slot number ranging from 24 to 48 on the air-gap flux density, torque, power density, power factor and efficiency have been investigated and some proper rotor slot numbers have been determined for a 4-pole, 36-slot IM [GYF13]. In [MAR08], a detailed study has been conducted on the effect of rotor slot number on the iron loss of IMs with various slot numbers. In addition, effect of the rotor slot number on the electromagnetic force in case of cage faults is also investigated [ARK97], [SOB11] and there are some studies on the optimal design of rotor slot geometry and optimal slot number for magnetic noise reduction in squirrel-cage IMs [FIR07], [BES09]. On the other hand, to the best of the authors' knowledge, there is no study related with the influence of rotor slot number on rotor bar current waveform in literature.

In this section, the influence of rotor slot number on the performance characteristics, such as phase winding induced voltage and current, air-gap flux density, rotor bar current, rotor tooth and slot flux densities, electromagnetic force, torque, torque ripple, losses, power factor and also efficiency are numerically studied for squirrel-cage IM having 48-stator slots and 8-poles. The harmonic content of air-gap flux density, tooth flux density, and slot leakage flux as well as radial and tangential components of the electromagnetic force are studied in detail for each rotor slot number. For different rotor slot numbers varying from 30 to 76, saturation factors and slot leakage flux density amplitudes are evaluated and their influence on the rotor bar current waveforms are investigated.

6.3.1 Determination of Rotor Slot Number

The different rotor designs are carried out to find out the influence of rotor slot number on the machine performance characteristics. In order to achieve comparable results, the same operation conditions (250A phase current at 950rpm speed) and the same rotor and stator geometric parameters and winding layout (5-slot pitch single layer), which are the same as the Toyota Prius 2010 IPM (see Appendix E), are used in all calculations. The numbers of stator slots and poles are fixed to 48 and 8, respectively. Only the number of rotor slots have been changed from 30 to 76. It is worth mentioning that as reported in [ARK97], [ALG54], and [HIR97], since the use of odd number of rotor slots in squirrel-cage IMs causes significantly high UMP and vibrations, only the even rotor slot numbers have been chosen in order to avoid the UMP and vibrations due to the asymmetric issues. The performance characteristics of the IM are evaluated by using a 2-D, non-linear, time-stepping finite element analysis (FEA) of the magnetic field.

Before the design procedure of an IM, there are a lot of design criteria in terms of cost and performance which should be taken into consideration. As well known, there is a correlation between cost and performance i.e. size and weight determined by the peak torque is directly related with material and manufacturing cost. Furthermore, the main machine parameters such as size, efficiency and peak torque are determined by the number of poles. Choosing the optimal number of poles and number of stator slots is very important issue in terms of cost and efficiency as reported in [GUN16a]. For instance, choosing higher number of poles provides less back iron requirement with the penalty on magnetizing current and efficiency [JUR15]. Likewise, choosing lower number of slots is advantageous in terms of slot filling factor, manufacturing and also cost while it is disadvantageous in terms of breakdown torque [LIP17]. In terms of torque density and torque quality, some key parameters such as stator slot number S and pole number P combinations considering the short- and long-pitch winding layout, stator/rotor slot opening should be optimized also. In the rotor design of a squirrel-cage IM, determinations of the number of rotor slots and their geometries are some of the most important aspects determining the noise, vibration, torque density and torque ripple characteristics. Considering these characteristics certain empirical rules have been proposed for choosing the number of rotor slots R in relation to the S , P , and phase number m [TOL04], [BES09], [GYF13]. Based on the experiments gained from the existing literature, the rotor slot number R can be chosen according to:

- (i) $0.8S < R < 1.25S$ or $R \approx 0.9S$;
- (ii) $R \neq S$, $R \neq S \mp m \mp 1, 2$ or $5P$;
- (iii) $R \neq S \mp P \mp 1, 2$.

For peak torque density (i) should be considered. In addition, to avoid large torque ripple, synchronous hooks and cusps and noisy operations (ii) and (iii) should be considered. Furthermore, a general equation estimating the optimal rotor slot number for any S/P combination at which the maximum torque and efficiency with fairly low torque ripple can be achieved, as will be derived in Section 6.4.

6.3.2 Influence of Rotor Slot Number on Performance Characteristics

The influence of rotor slot number can be investigated for variable and constant rotor resistance cases. In order to obtain constant rotor resistance, the rotor slot width, corresponding to slot area, should be changed with a constant ratio. On the other hand, in order to obtain variable rotor resistance, the rotor slot width should be fixed at constant length. For constant resistance, the optimal rotor slot opening and slot widths, which are ~4.4mm and 1mm, respectively, are used and for variable resistance, the rotor slot opening and width ratios given in (6.3) and (6.4) have been used for any rotor slot number and the calculated rotor resistance variation with respect to rotor slot number is illustrated in Fig. 6.11. The influence of the rotor slot number in both constant and variable rotor resistance cases on the electromagnetic characteristics, particularly bar current waveform, have been investigated in the following sections.

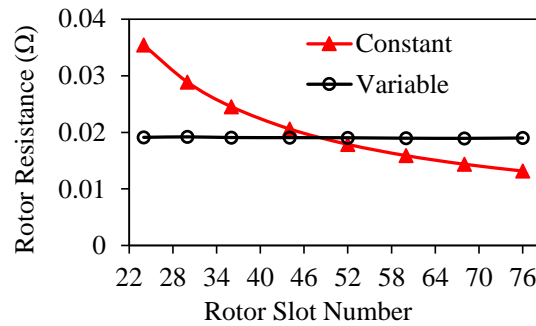


Fig. 6.11 Comparison of rotor resistance at 75°C for constant and variable rotor slot widths.

A. Constant Slot Width: Variable Rotor Resistance

The influence of the rotor slot number, on the bar current waveform, average torque, torque ripple, bar copper loss, and efficiency is investigated parametrically by a 2-D, non-linear, time-stepping FEA of the magnetic field. The number of rotor slots is varied from 24 to 76. In order to investigate the individual influence of the rotor slot number, the rotor slot width b_{tr} is fixed to 4.78mm and the rotor slot opening with b_{r0} is fixed to 1mm. Note that the amplitudes are determined by global optimization results of 48S/52R/8P combination. In addition, in order to achieve comparable results, the same operation conditions as 176.6Arms phase current and 950rpm imposed speed are assigned. It is worth mentioning that as mentioned above and reported in [ALG54], [ARK97], [HIR97], since the use of odd number of rotor slots in squirrel-cage IMs causes significantly high unbalanced magnetic pull (UMP) and vibrations, only the even rotor slot numbers have been chosen in order to avoid the UMP and vibrations due to the symmetry issues. In addition, in order to avoid the UMP and large parasitic effects, the multiply of the pole and phase numbers are not been considered as well. Note that the individual effect of any rotor slot parameter is investigated by keeping the other parameters at their optimal value given in the Appendix D. To be able to induce the same current amplitude in the stator windings of the IMs, different voltage amplitudes have been applied as seen in Fig. 6.12. This is because of the fact that the rotor resistance decreases with increasing rotor slot number as illustrated in Fig. 6.11 for the constant rotor slot width case. Thus, since the rotor resistance is decreased, the rotor circuit voltage and

consequently the input voltage decreases in order to induce the same phase current in the stator windings.

Obtained Phase ‘A’ current waveform and variation of its dominant harmonics with respect to rotor slot number is illustrated in Fig. 6.13. As clearly seen, the IM designed with 44 rotor slots has relatively higher distortion due to the significantly increased effect of armature reaction. However, the current THD percentage for each machine less than 3%. This is mainly due to the winding MMF harmonics illustrated in Fig. 6.14. As known, the performance of IMs is notably sensitive to the winding harmonics. The smoother the MMF in the air-gap the lower losses are induced into the surface layer of the rotor.

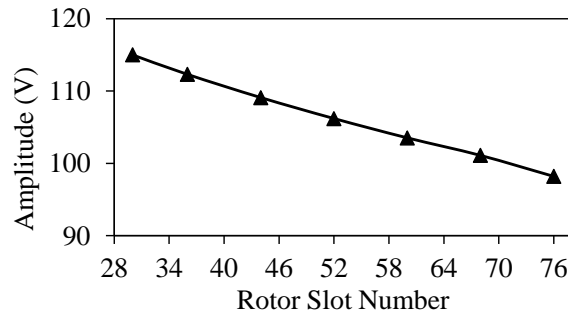


Fig. 6.12 Variation of the applied voltage amplitude.

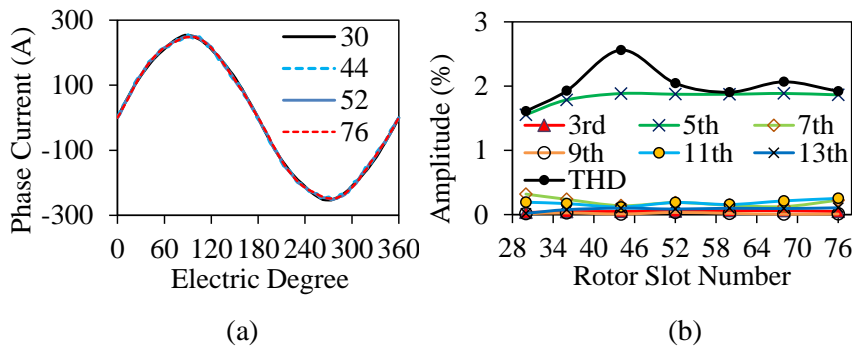


Fig. 6.13 Phase ‘A’ current: (a) waveform and (b) dominant harmonics against rotor slot number.

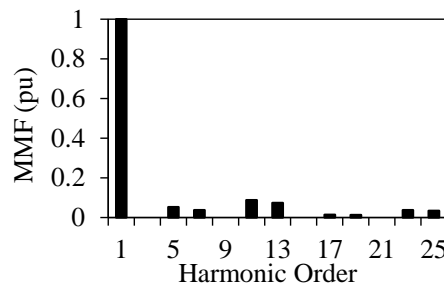


Fig. 6.14 MMF harmonics.

Phase ‘A’ induced voltage waveforms for IMs designed with various rotor slot numbers are illustrated in Fig. 6.15 (a). Furthermore, variation of dominant harmonics with respect to rotor slot number is shown in Fig. 6.15(b). Because of the combined effect of the MMF and slotting harmonics, the waveforms have been distorted. The 3rd harmonic is the most dominant harmonic which does not exist in the MMF harmonics. Therefore, as explained in Chapter 5, the 3rd harmonic became dominant due the effect of the magnetic saturation of the iron cores.

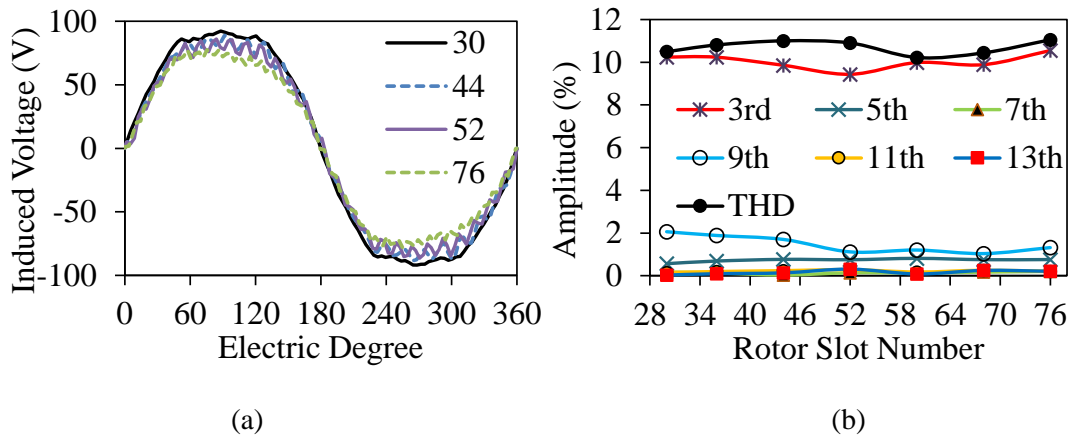


Fig. 6.15 Phase 'A' induced voltage: (a) waveform and (b) variation of voltage harmonics with respect to rotor slot number.

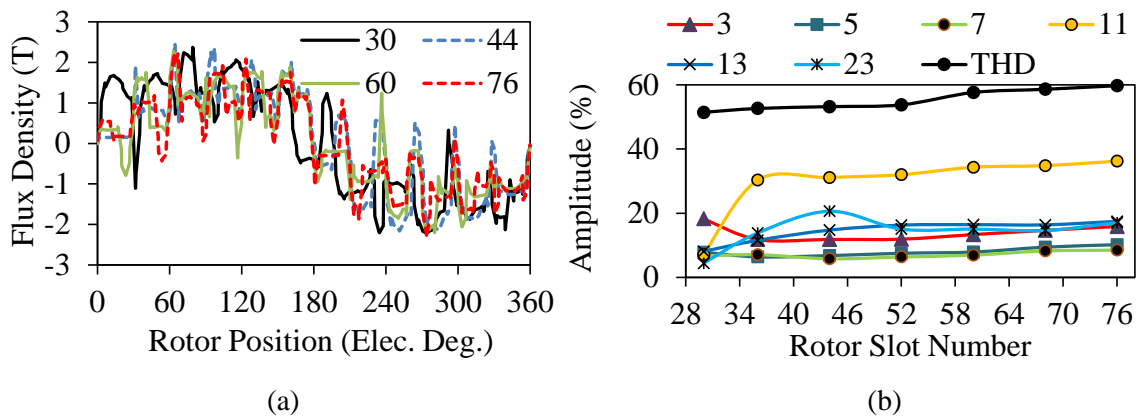


Fig. 6.16 Air-gap flux density: (a) waveform and (b) variation of flux density harmonics with respect to rotor slot number.

Harmonic content of the air-gap flux density includes both the stator and rotor MMF harmonics together. In fact, a major part of the bar copper loss at the surface layer of the rotor are due to the air-gap harmonics. The distortion waveform of the air-gap flux density for various rotor slots and the variation of the air-gap flux density harmonics with respect to slot number are shown in Fig. 6.16. As seen in Fig. 6.16(b), there has been sharp changes after 30 and 52 rotor slots. It is also known that the air-gap flux harmonics, produced due to the certain stator and rotor slot combinations, cause the torque ripple (see Fig. 6.18(a)) and vibration, which can cause mechanical stresses to rotor and serious bearing and noise problems. The magnitudes of the harmonic fields affecting the air-gap depend highly on the ratio of the slot numbers of the stator and the rotor. Rotor bar current waveform and variation of the bar current harmonics with respect to rotor slot number are illustrated in Fig. 6.17. In order to observe the bar current waveforms more clearly, their reconstructed versions by using the first ten harmonics are also shown in Fig. 6.17(b). As seen in Fig. 6.17(a, b), all the bar current waveforms are non-sinusoidal under the current operation conditions. However, it is obvious that the level of the distortion increases as the rotor slot number increases. Furthermore, the THD of the bar current has increased dramatically after 52 rotor slot (see Fig. 6.17(c)). Therefore, considering the variation of the air-gap flux density

harmonics shown in Fig. 6.16(b), it can be predicted the 52 rotor slot number is critical in terms of performance characteristics. The reason behind the non-sinusoidal bar current phenomenon is the saturation of iron cores, particularly the rotor teeth as explained in detail in Chapter 5. The other important details related with the non-sinusoidal bar current phenomenon will be explained in the following section.

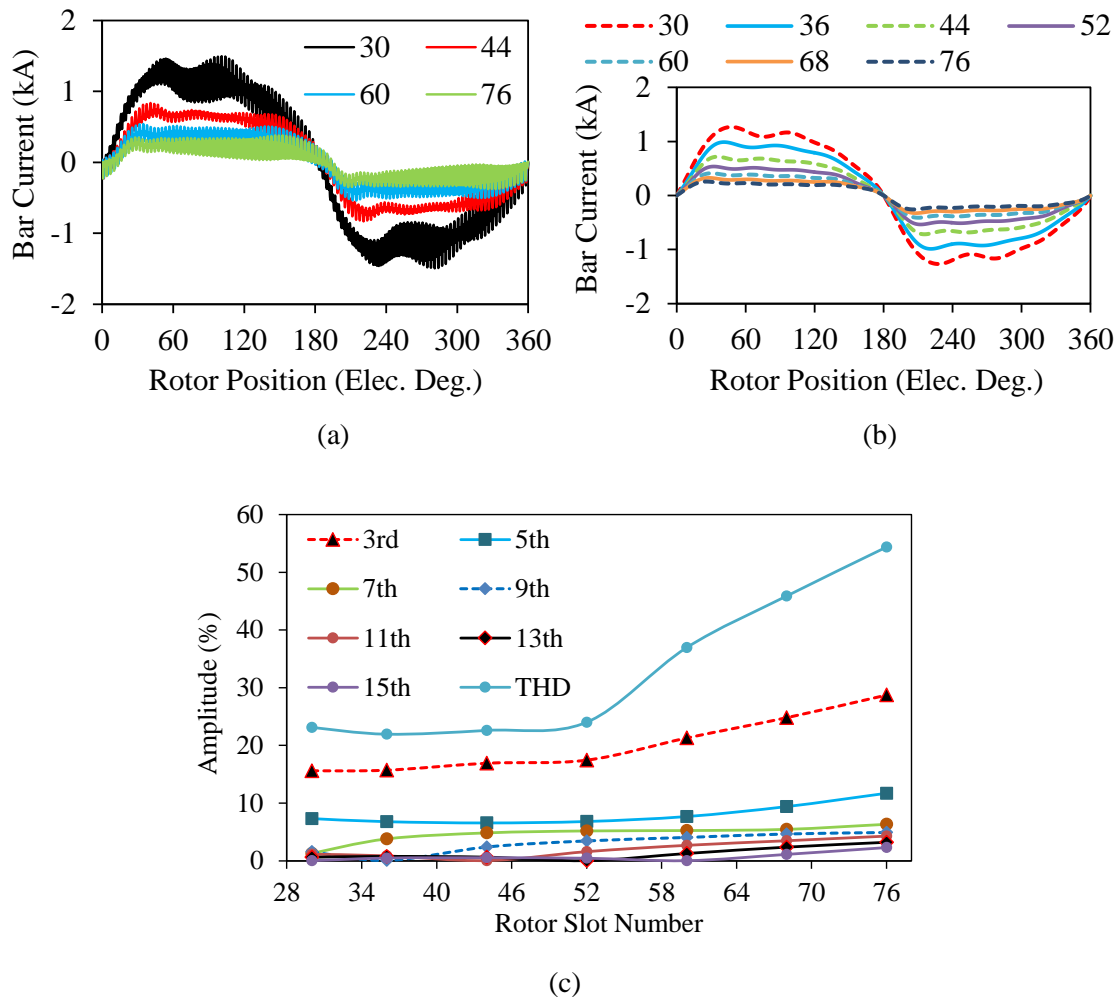


Fig. 6.17 Rotor bar current waveform: (a) original, (b) reconstructed by ignoring the higher order harmonics, and (c) harmonic spectra.

Some key performance characteristics of the IM designed with various rotor slot numbers are presented in Fig. 6.18. As clearly seen in Fig. 6.18(a), the time average torque at pullout slip of the analysed IM varies as a function of rotor slot number. The magnitude of torque ripple depends highly on the ratio of the stator and rotor slot numbers. Among these numbers, there is a critical combination which gives the maximum torque and minimum torque ripple. As seen in Fig. 6.18(a), this critical rotor slot number is 52. The correlation between the power factor, efficiency η and rotor slot number is also exponential as seen in Fig. 6.18(b, c). Since the same current is induced in windings in all cases, there is no change in the stator copper loss P_{scu} . On the other hand, the rotor bar current P_{rcu} and total iron loss P_c have changed slightly with respect to the rotor slot number. Considering these performance curves, it can be concluded that the optimal slot number for 48-stator slot and 8-pole IM is 52.

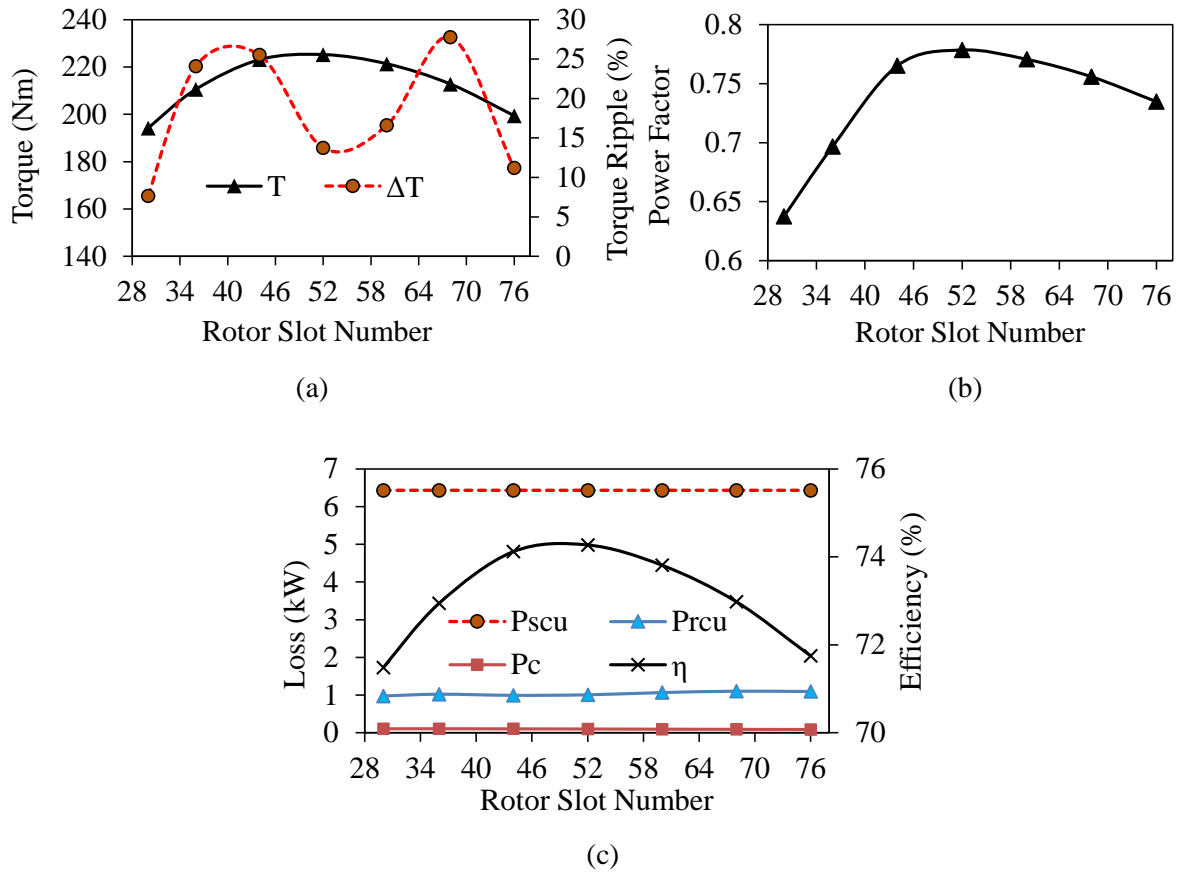


Fig. 6.18 Variation of performance characteristics as a function of rotor slot number: (a) time average torque at pullout slip and torque ripple, (b) power factor, and (c) power losses and efficiency.

B. Variable Slot Width: Constant Rotor Resistance

In order to investigate the individual influence of the rotor slot number, the ratio of the rotor slot width b_{tr} to the slot pitch τ_r and the ratio of the rotor slot opening width b_{r0} to rotor slot width are kept constant for any rotor slot number during the calculations as given in (6.3) and (6.4), respectively. Note that only the slot parameters given in (6.3) and (6.4) and the rotor slot number have been changed and all other parameters and operating specifications have been kept constant during parametric analyses.

The variation of b_{tr} and b_{r0} and corresponding rotor resistance variations with respect to rotor slot number have been shown in Fig. 6.19 and Fig. 6.11, respectively. Note that the constants given in (6.3) and (6.4) have been derived empirically as a consequence of a large number of parametric analyses and global optimizations.

$$\frac{b_{tr}}{\tau_r} = \frac{1}{\sqrt{2}} \quad (6.3)$$

$$\frac{b_{r0}}{b_{tr}} = \frac{1}{2\pi} \quad (6.4)$$

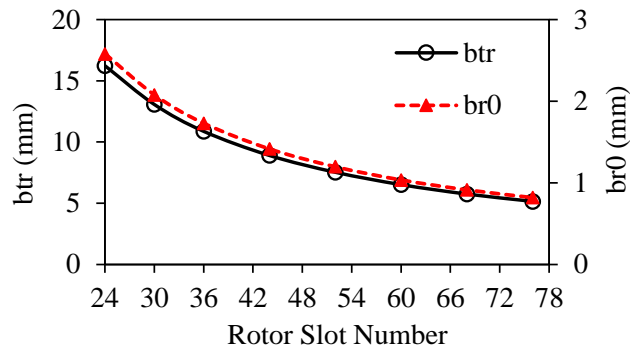


Fig. 6.19 Variation of rotor tooth b_{tr} and rotor slot opening b_{r0} widths with rotor slot number.

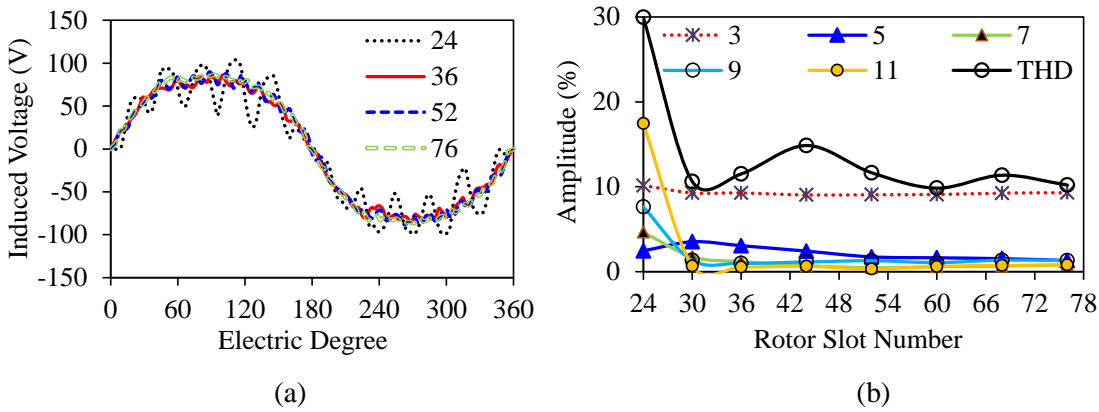


Fig. 6.20 Phase 'A' induced voltage: (a) waveform and (b) variation of voltage harmonics with respect to rotor slot number.

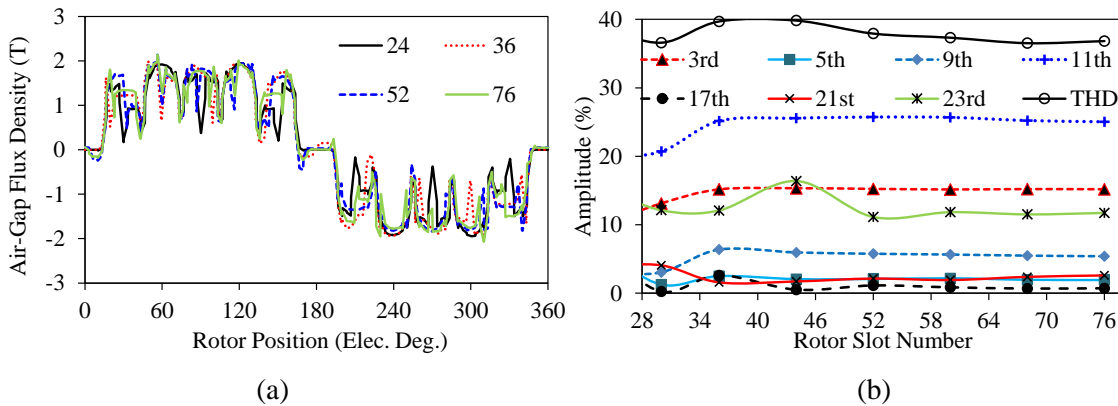


Fig. 6.21 Air-gap flux density: (a) waveform and (b) variation of flux density harmonics with respect to rotor slot number.

The variation of Phase 'A' induced voltage waveform and variation of dominant harmonics with respect to rotor slot number are illustrated in Fig. 6.20. As expected, amplitudes of the fundamental frequency are the same since the rotor resistances are the same. On the other hand, the induced voltage THD of the IM with 24 rotor slot is the highest while the IM with 60 rotor slot is the lowest. It can also be deduced for the case of constant rotor resistance that the higher the rotor slot number, the lower the phase induced voltage harmonic distortions. On the other hand, as can be seen from Fig. 6.21, rotor slot number has a negligible effect on the air-gap flux density distortion for the constant resistance case.

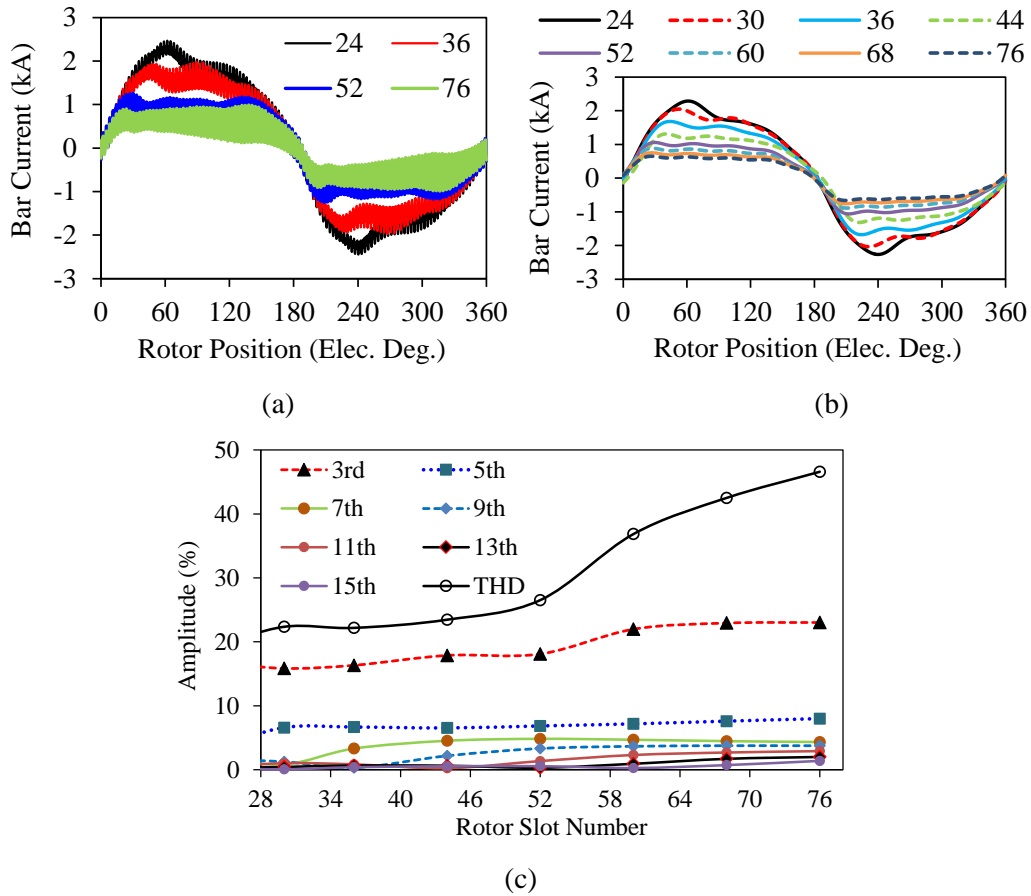


Fig. 6.22 Rotor bar current waveform: (a) original, (b) reconstructed, and (c) harmonic spectra.

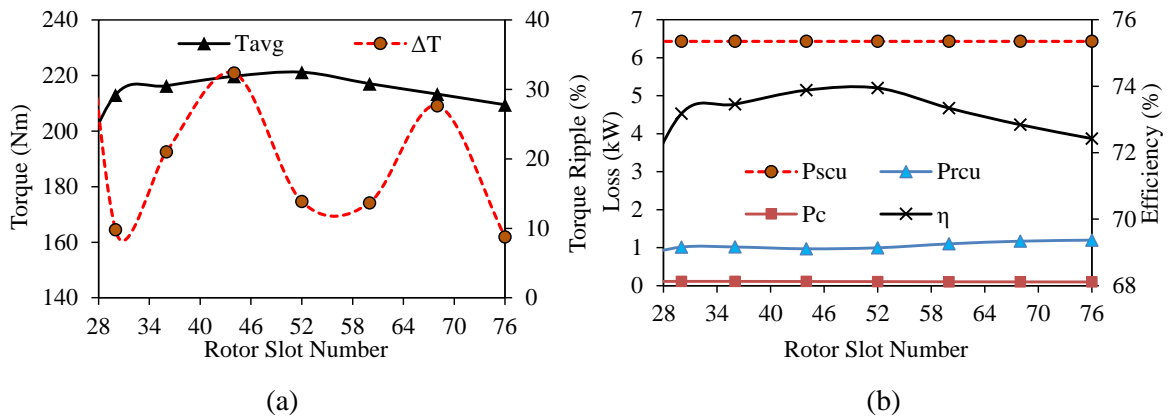


Fig. 6.23 Variation of performance characteristics as a function of rotor slot number: (a) time average torque at pullout slip and torque ripple and (b) power losses and efficiency.

As clearly seen in Fig. 6.17 and Fig. 6.22, regardless of the constant or variable rotor resistance, the rotor slot number has a significant effect on the bar current waveform. The THD level of the bar current has been sharply increased after 52 rotor slot number. The most dominant bar current harmonic is the 3rd harmonic and it has also been increased sharply after 52 rotor slot number. As explained before this is due to the increase in the saturation level of the rotor tooth body (see Fig. 6.25 and Fig. 6.28(b)). Therefore, considering the performance characteristics, illustrated in Fig. 6.23, it can be concluded that in terms of maximum torque and efficiency the 52 rotor slot is the optimal rotor slot number regardless of rotor resistance.

6.3.3 Investigation of Rotor Tooth Flux Density

There is a direct relationship between the bar current waveform and the rotor tooth flux density as explained in Chapter 5. This relationship can be explained by examining the flux density variations, slot leakage flux levels and saturation factors of different machine parts. Flux density distributions for various rotor slot numbers with variable and constant rotor resistance are illustrated in Fig. 6.24 and Fig. 6.25, respectively. Note that the knee point of the used core material is approximately 1.48T. As seen in the figures, the both stator and rotor tooth parts have been saturated highly. Since the saturation level of the rotor tooth body increases with the increasing rotor slot number, the saturation level of the stator tooth decreases since the coefficients of magnetic circuit parameters change for each case due to the change in the amount of the leakage flux (see Fig. 6.32). This finding is valid for both constant and variable rotor resistance cases. The reason behind the increase of the rotor leakage flux is the reduction of the total surface area of the rotor tooth parts, i.e., it can be clearly seen from Fig. 6.24 and Fig. 6.25 that the total tooth width inside one rotor pole pitch have been reduced as the rotor slot number is increased. In other words, the total rotor tooth width indicated with arrows between A and B reference line in Fig. 6.24(a) and (f) reduces as the rotor slot number is increased. The radial and tangential components of the rotor tooth parts including rotor tooth tips (RTT), rotor tooth middle (RTM), and rotor tooth root (RTR) have been examined as follows. As combined effect of air-gap flux harmonics originated from MMF and slotting harmonics, with saturation harmonics, a large number of low frequency harmonics are induced in the flux density of RTT parts as seen in Fig. 6.26(a) and Fig. 6.27(a) and the level of distortion increases with the increasing number of rotor slot.

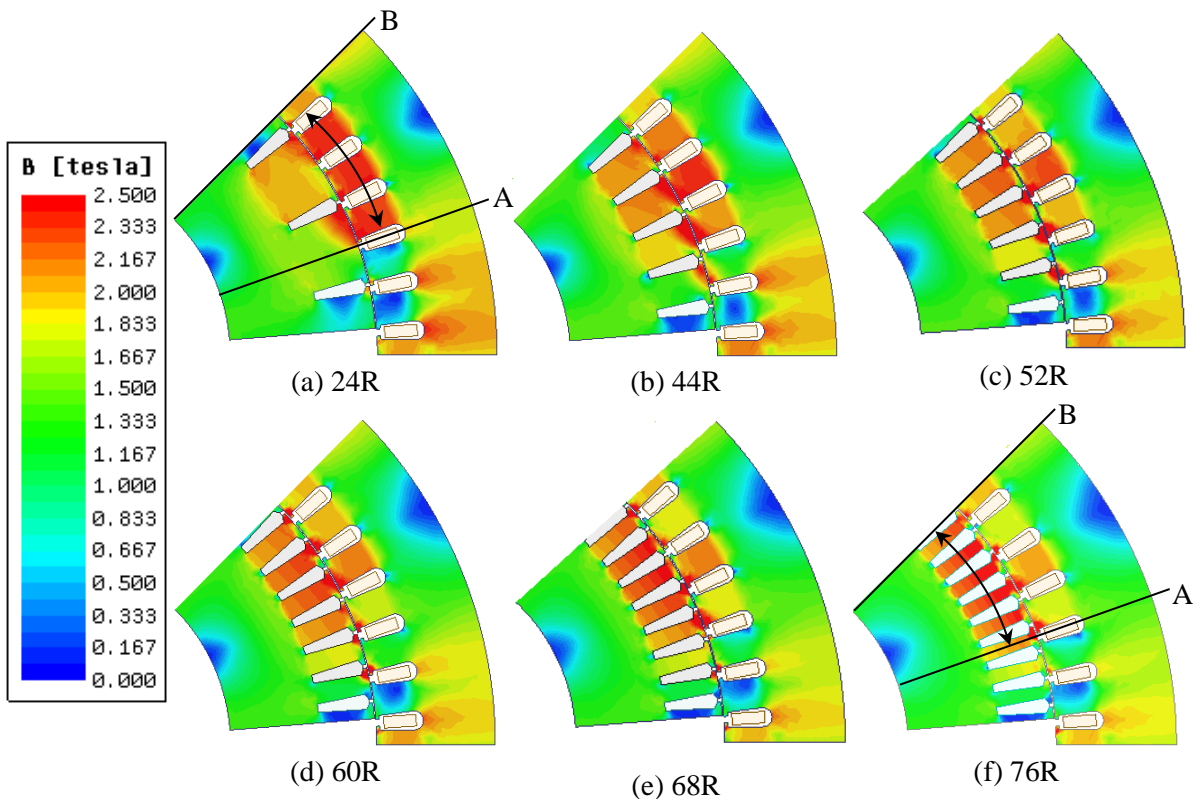


Fig. 6.24 Flux density distributions for different rotor slot numbers having constant rotor slot width.

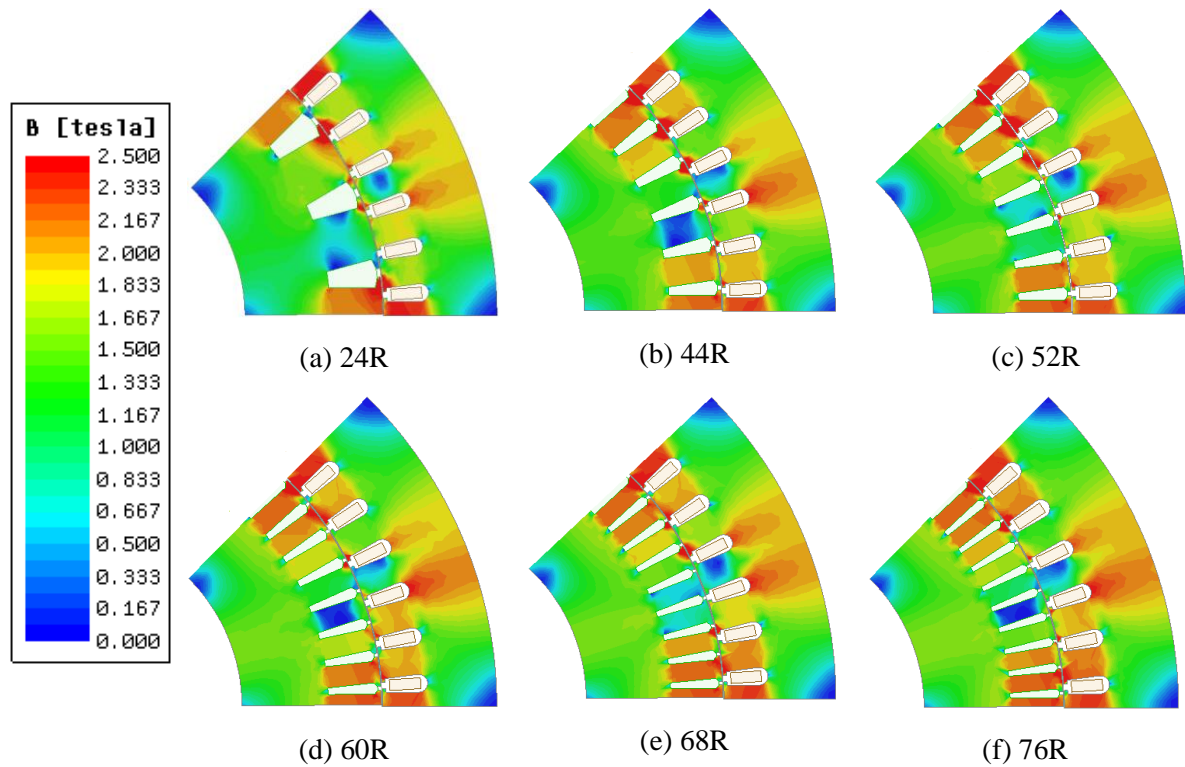


Fig. 6.25 Flux density distributions for different rotor slot numbers having variable rotor slot width.

In addition, the variation of the radial and tangential components of the flux density at the RTT with respect to rotor slot number is illustrated in Fig. 6.26(b) and Fig. 6.27(b) for variable and constant rotor resistance cases, respectively. As seen in the figure, the amplitudes of the flux density components are similar to each other. On the other hand, the same variation is illustrated for the flux density at the RTM as seen in Fig. 6.28. However, the differences between the radial and tangential components are considerably high and while the radial component increases with increasing rotor slot number, but the tangential component decreases.

In order to reveal the correlation between the bar current waveform and the flux density at the RTM, the variation and its harmonic spectra are illustrated in Fig. 6.29 and Fig. 6.30 for variable and constant rotor resistance cases, respectively. As explained in Chapter 5, this close relationship can be observed. On the other hand, it is also clear that the high frequency harmonics have been cancelled due to the filtering effect of the rotor teeth. The details related with this phenomenon can be found in Chapter 5. As seen in Fig. 6.29(b) and Fig. 6.30(b), the most dominant harmonic is the 3rd harmonic as being in the bar current waveform and the THD of the flux density increases with rotor slot number. As well known, iron saturation causes the increase of the 3rd harmonic of the flux density. Therefore, considering Fig. 6.24 and Fig. 6.25, it is obvious that the rotor teeth are saturated highly. Waveforms of the flux density at the RTR are illustrated in Fig. 6.31(b). It has been revealed that filtering affects only the higher order harmonics. The waveforms are still non-sinusoidal but their amplitudes are similar. Magnitudes of the radial and tangential components of the RTR flux density is illustrated in Fig. 6.31(b).

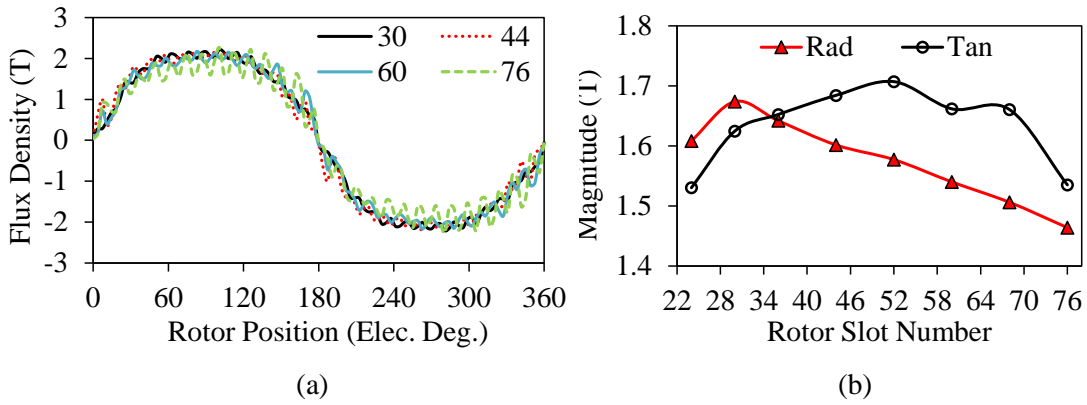


Fig. 6.26 Flux density at the RTT for constant rotor slot width: (a) waveforms for various rotor slot number and (b) variation of flux density components with respect to rotor slot number.

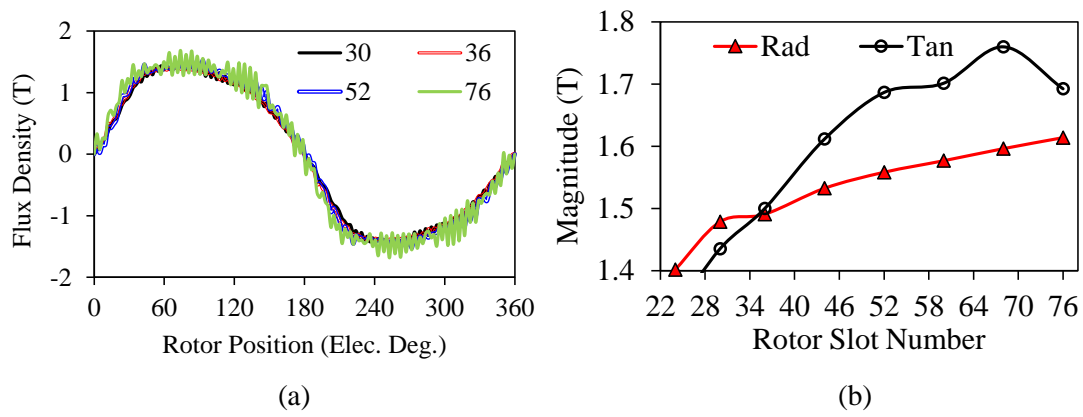


Fig. 6.27 Flux density at the RTT for variable rotor slot width: (a) waveforms for various rotor slot number and (b) variation of flux density components with respect to rotor slot number.

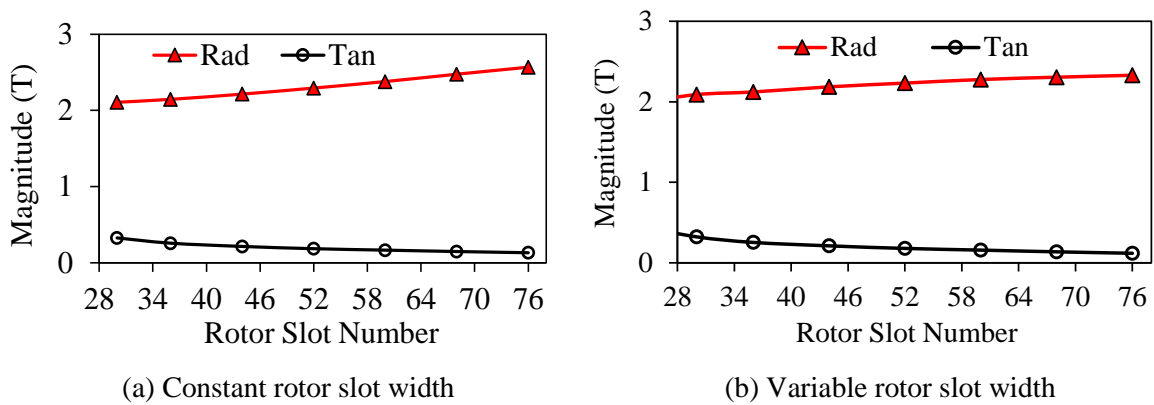


Fig. 6.28 Variation of the flux density components of the RTM with respect to rotor slot number.

As being in the RTM part (see Fig. 6.28), radial component increase with rotor slot number and the magnitude of the radial component is several times higher than the tangential component. Considering the figures between Fig. 6.28 and Fig. 6.31, it can be concluded that when compared to the other parts of the IM, the RTTs are the most saturated parts and since the filtering (averaging) effect is the minimum in this part, a large number of low frequency harmonics are induced in the flux density waveform. Furthermore, at the RTT parts, the amplitudes of the radial and tangential components are very close to

each other. On the other hand, from tooth tips to the root with increasing effect of the filtering phenomenon, the higher order harmonics are gradually diminished and the differences between the amplitudes of the radial and tangential components increase significantly.

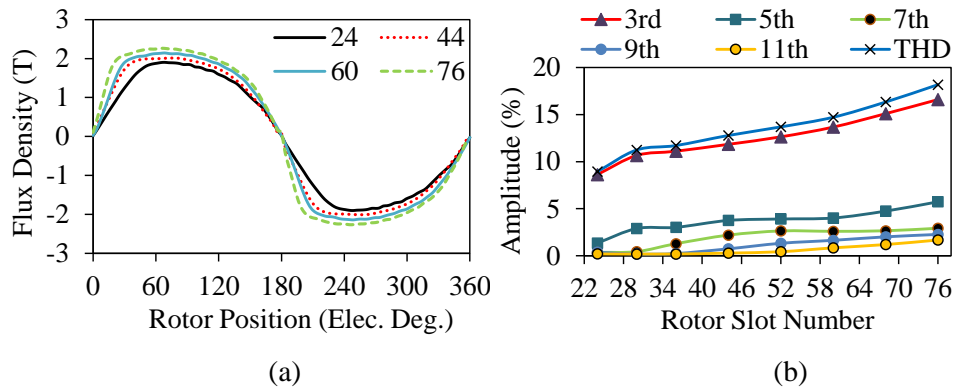


Fig. 6.29 Flux density at the RTM for constant rotor slot width: (a) waveforms for various rotor slot number and (b) variation of harmonics and THD with respect to rotor slot number.

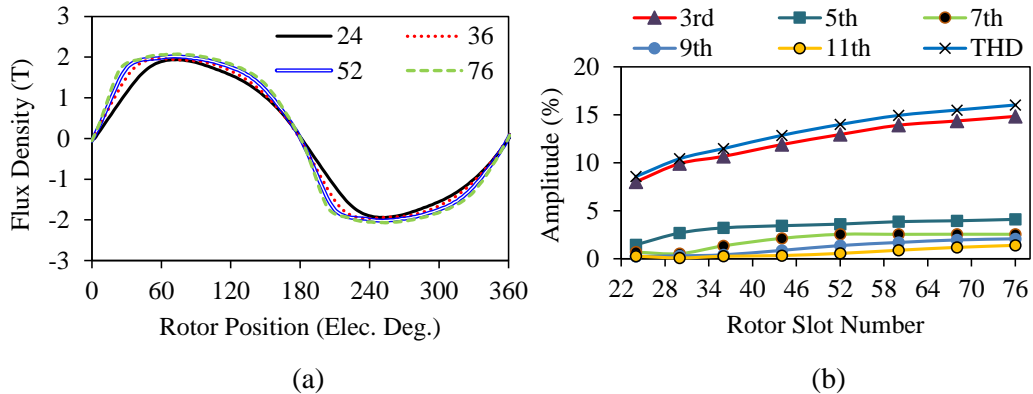


Fig. 6.30 Flux density at the RTM for variable rotor slot width: (a) waveforms for various rotor slot number and (b) variation of harmonics and THD with respect to rotor slot number.

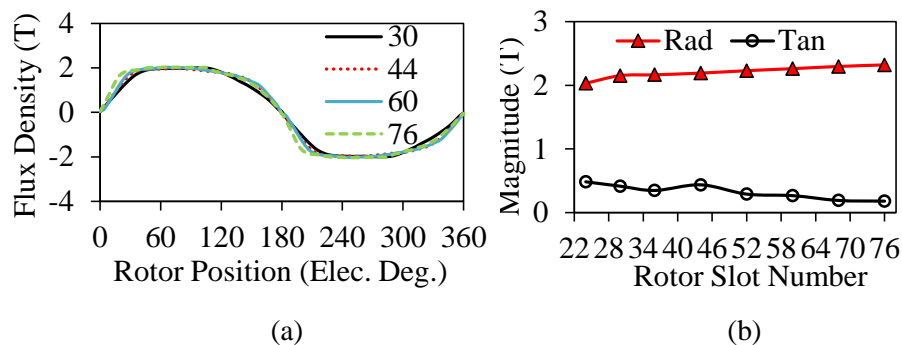


Fig. 6.31 Flux density at the RTR : (a) waveforms for various rotor slot number and (b) variation of flux density components with respect to rotor slot number.

6.3.4 Investigation of Rotor Slot Flux Density

It is a fact that the radial component of the air-gap flux density, which is generated due to the interaction between stator and rotor fields, is the torque producing field. On the other hand, the

tangential component of the rotor slot flux density is known as the leakage flux density which is a function of rotor slot geometric parameters and stator and rotor current [BOL10], [LIP17]. Therefore, radial and tangential components of the flux density at the rotor slot have been investigated with respect to rotor slot number for variable and constant rotor resistance cases as illustrated in Fig. 6.32(a) and (b), respectively.

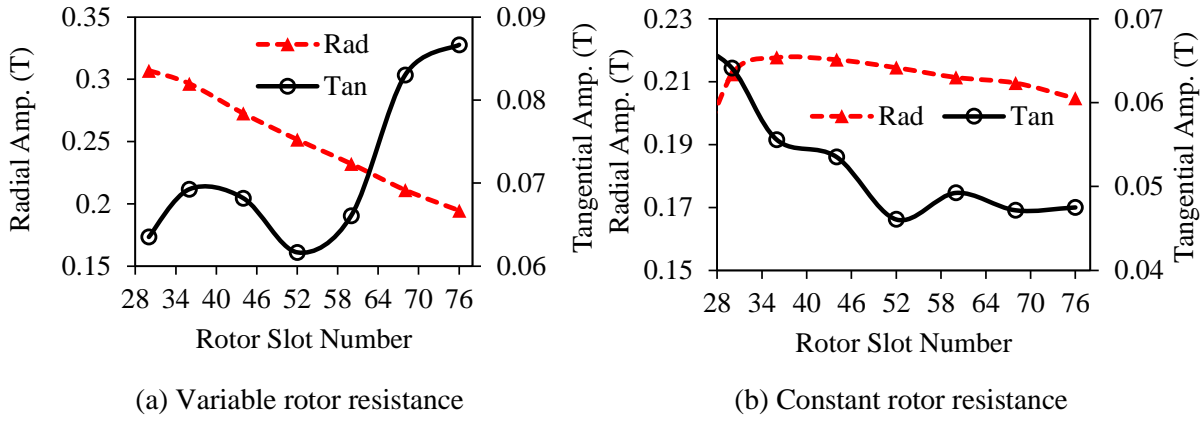


Fig. 6.32 Variation of the flux density components at rotor slot with respect to rotor slot number: (a) variable rotor resistance case and (b) constant rotor resistance case.

As seen in Fig. 6.32, the amplitude of the radial component of the rotor slot flux density decreases with increasing rotor slot number for both variable and constant rotor resistance cases. While there is a sharp drop at the amplitude of the radial flux density component for variable rotor resistance case, there is a smooth drop at the amplitude of the radial flux density component for constant rotor resistance case. On the other hand, the leakage (tangential) component sharply increases for variable rotor resistance case while it decreases smoothly for constant rotor resistance case. Since the rotor tooth body saturation level of the designs with constant rotor resistance is much lower than that of the design with variable rotor resistance (see Fig. 6.33), the amplitudes of the leakage flux density for any rotor slot number are lower in the cases of constant rotor resistance. From Fig. 6.32, it can be concluded that regardless of the design with constant or variable rotor resistance, the minimum leakage is achieved if the 48-stator slot IM is designed with 52 rotor slots. There is a linear correlation between the flux leakage and the saturation. To be able to reveal the level of saturation at the different parts of the rotor, the saturation factors are calculated by (6.5) and (6.6) and illustrated as shown in Fig. 6.33.

$$K_{sx} = \frac{1}{2} \left[1 + \sqrt{1 + \frac{1.6\pi \cdot H_x \cdot l_s}{B_g \cdot g}} \right] \quad (6.5)$$

$$K_s = \frac{1}{2} \left[1 + \sqrt{1 + \frac{1.6\pi \cdot MMF_R}{B_g \cdot g}} \right] \quad (6.6)$$

where $K_{sx \rightarrow x=t}$ is average rotor tooth saturation factor, $K_{sx \rightarrow x=c}$ is rotor yoke saturation, K_s is total rotor saturation factor, $H_{x \rightarrow x=t}$ is rotor tooth average filed intensity, $H_{x \rightarrow x=c}$ is rotor yoke average filed intensity, l_{stack} is machine stack length, B_g is air-gap flux density amplitude, g is air-gap length, and MMF_R is rotor magnetomotive force. As expected, flux leakage and saturation factors curves show similar trends. As seen in Fig. 6.33, the saturation factor increased sharply after 52 slot number for both variable and constant rotor resistance cases. However, the level of the saturation factors of the design with constant rotor resistance is lower than that of the design with variable rotor resistance. It has been revealed that in terms of leakage and saturation issues 52 rotor slot numbers are the optimum.

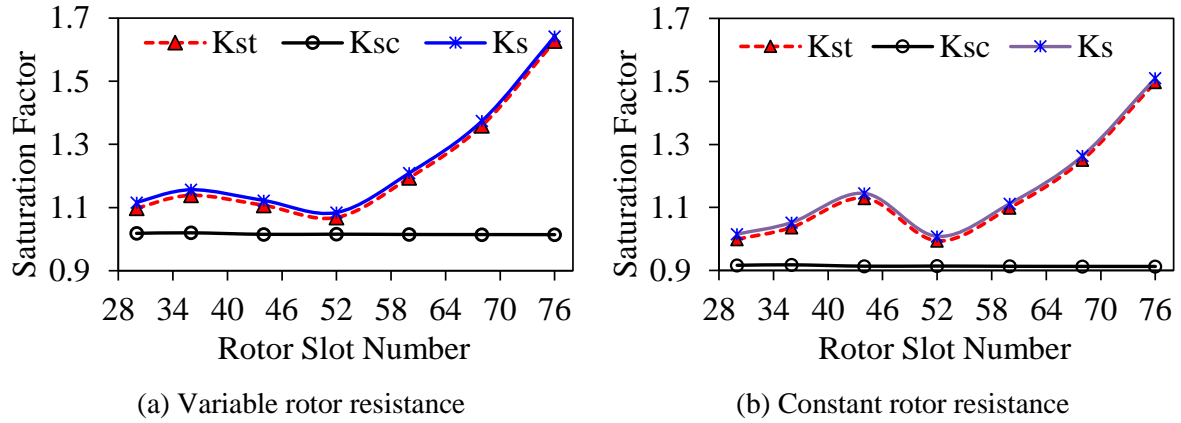


Fig. 6.33 Variation of the saturation factor of the various machine parts as a function of rotor slot number.

6.3.5 Investigation of Electromagnetic Force

The squirrel-cage IMs produce electromagnetic vibration and noise caused by interaction between stator and rotor harmonic fluxes in the air-gap. The tangential and radial component of the resultant force acting upon the stator surface can be calculated by integrating the Maxwell stress tensor over a closed surface as expressed in (6.7) and (6.8), respectively [KIM99].

$$\vec{F}_t = \oint_s \left[\vec{H}(\vec{B} \cdot \vec{n}_{12}) - \frac{1}{2} \vec{n}_{12}(\vec{B} \cdot \vec{H}) \right] ds \quad (6.7)$$

$$\vec{F}_r = \oint_s \left\{ \left[\vec{H}_1(\vec{B}_1 \cdot \vec{n}_{12}) - \left(\frac{\vec{B}_1 \cdot \vec{H}_1}{2} \right) \vec{n}_{12} \right] - \left[\vec{H}_2(\vec{B}_2 \cdot \vec{n}_{12}) - \left(\frac{\vec{B}_2 \cdot \vec{H}_2}{2} \right) \vec{n}_{12} \right] \right\} ds \quad (6.8)$$

where \vec{H}_i and \vec{B}_i are the magnetic field intensity and flux density vectors of surface element adjacent to the boundary. \vec{n}_{12} is the unit normal vector to the surface and goes to air-gap region from the higher permeability region. The electromagnetic forces acting on the stator surface illustrated from Fig. 6.34 to Fig. 6.36 have been calculated by using (6.7) and (6.8).

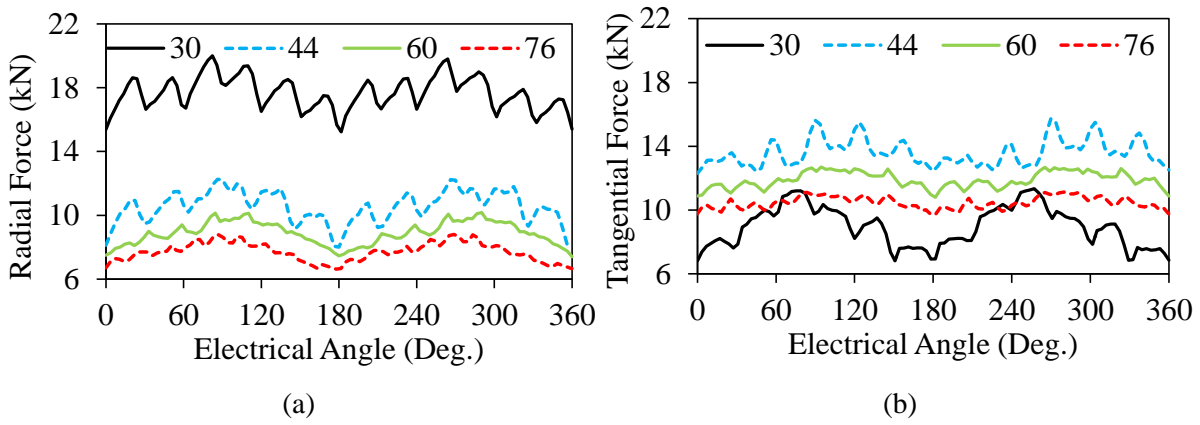


Fig. 6.34 Stator surface electromagnetic forces of IMs having variable rotor resistance for different rotor slot numbers: (a) radial component and (b) tangential component.

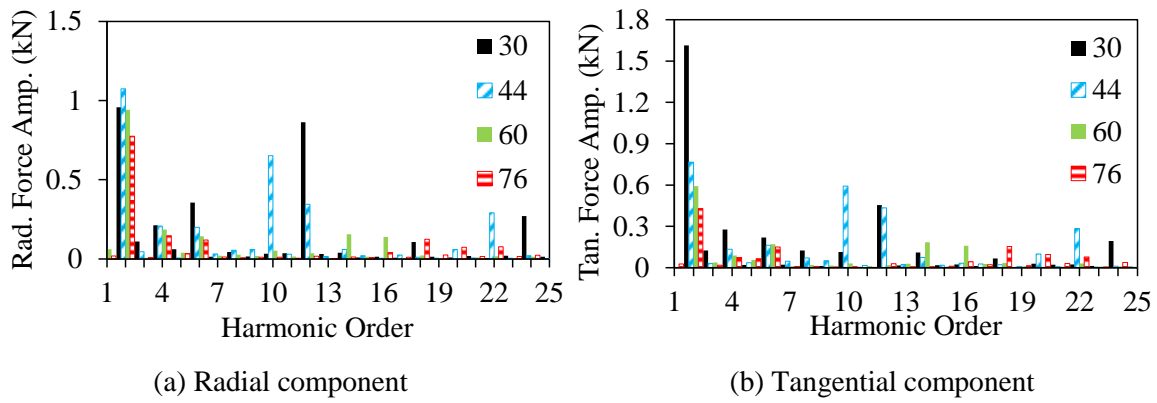


Fig. 6.35 Harmonic spectra of the electromagnetic forces acting on the stator core surface: (a) radial component and (b) tangential component.

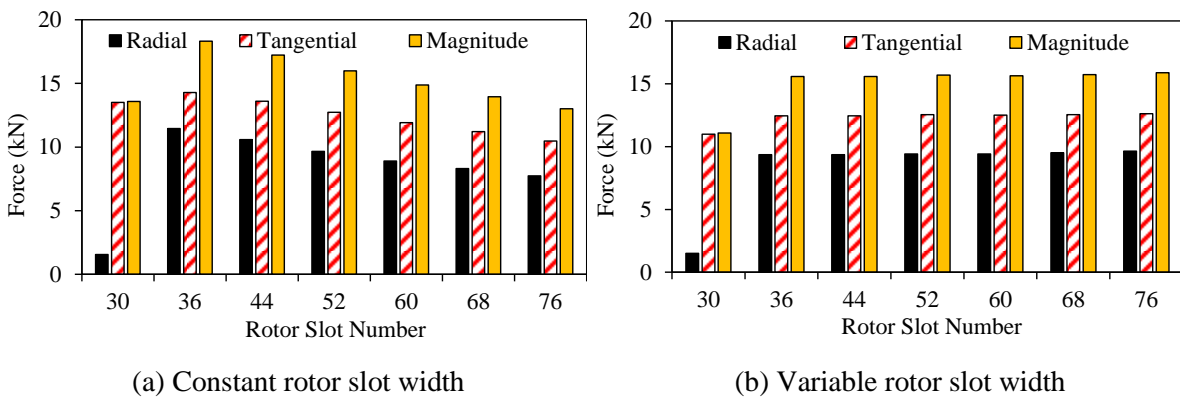


Fig. 6.36 Radial, tangential, and magnitude of the net forces affecting on the stator surface with different rotor slot number.

The electromagnetic force due to slot combinations has a significant effect on vibration and hence acoustic noise [KIM99], [KOB97], [AHO06], [HIR97]. The harmonics of the radial electromagnetic force cause the vibration [ALG54], [KOB97] and the vibration depends strongly on the stator and rotor slot combinations. As clearly seen in Fig. 6.34 and Fig. 6.35, radial and tangential components of the electromagnetic forces acting on the stator surface for 30, 44, 60, and 76 rotor slot numbers are

compared with each other and their harmonic components obtained from the discrete Fourier transform. As seen in Fig. 6.35(a), the radial force harmonics are maximum in case of 30 rotor slot, while it is minimum in case of 76 rotor slots. In addition, it is found that the 2nd harmonic is the most dominant harmonic in the harmonic spectra of the radial component which causes the vibration. Furthermore, the DC components of the radial, tangential and the magnitude of the electromagnetic force acting to stator core surface of IMs designed with constant and variable rotor slot widths are shown in Fig. 6.36 for each rotor slot number. As seen, as the rotor slot number is increased, the magnitude of the force decreases for the case of constant rotor slot width while it stands still for the case of variable rotor slot width. Since the 30 rotor slot number is not sub-multiple of the pole pair number, the radial component of the surface force is almost 9 times lower than the tangential force component.

6.4 Stator Slot and Pole Number Combination

In this section, unlike the individual influence of the rotor slot number on the performance characteristics and bar current waveform, the individual and common influences of S/P and S/R/P combinations, respectively will be investigated in depth. In literature, there are a lot of studies on the influence of S/P combinations on the performance characteristics, eccentricity issues and parasitic effects in the IMs, such as noise, vibration, etc. [KRO31], [CHA64], [LIA95], [MEL95], [HIR97], [NAN01], [WOL07], [BES09], [NAN09], [KOC09], [JOK13], [SED14], [TSO14], [AGA16]. However, to the best of the author's knowledge, there is no study related with the influence the stator slot number/pole number combination on the rotor bar current waveform in existing literature.

The importance of the S/P combination in terms of performance and parasitic effects has been investigated and very useful rules to predetermine the parasitic effects, such as crawling, vibration, noise and etc., has been presented in [KRO31]. In a similar study, some experimental results related with the characteristics of dominant electromagnetic vibration for various stator, rotor slot and pole number combinations have been presented and in terms of vibration some experimental results have also been presented for various slot/pole number combinations [HIR97]. In a more recent study, the influence of pole number on the acoustic noise of inverter-fed IMs has been examined and a number of parameters that generate noise and vibration have been revealed [TSO14]. A comprehensive performance comparison between 2-pole and 4-pole IMs has been presented and important trade-offs between IMs for variable speed drive applications and some general pole determination criteria have been presented [LIA95]. In a similar recently published paper, the influence of pole number on the steady-state performance of IMs has been investigated from the relationship between the key performance parameters of 2-pole reference IM and its 4-, 6-, and 8-pole counterparts [AGA16]. In [SED14], the influence of pole number of an IM, which is designed for an eco-urban electric car, on the performance characteristics in both propulsion and regenerative brake modes has been investigated by comparing the 2-, 4-, 6-, and 8-pole IMs and a suitable pole number has been defined for both normal and aggressive speed profiles. A study has been conducted in order to determine the optimum pole

number of IMs used on adjustable frequency applications by considering the machine losses, speed and torque [MEL95]. Influence of stator and rotor slot numbers on the magnetic noise and vibration has been analytically demonstrated and an analytical rule to avoid magnetic noise has been established [BES09]. General rules for the correlation between the numbers of stator slots, rotor slots and poles, and the rotor slot harmonics with saturation related harmonics in the stator current spectrum has been introduced. It has been concluded that saturation-related harmonics are shown to be the most dominant in IMs with a specific pole number for a certain combination of stator and rotor slots [JOK13]. Furthermore, the influence of the stator slot and pole numbers on the space harmonics generated by the MMF waveform has been investigated and the reduction methods of these harmonics are presented in [NAN01], [WOL07], [NAN09]. Furthermore, the influence of the stator slot and pole pair number on the space harmonics generated by the MMF waveform has been investigated and reduction methods of these harmonics are presented in [CHA64], [KOC09].

In this study, in order to reveal the influence of S/P combinations on the stator winding induced voltage and current, air-gap flux density, rotor bar current, stator and rotor tooth flux densities, torque and torque ripple, losses, power factor and also efficiency, 36S/6P, 48S/8P, and 60S/10P IMs have been designed by using the same geometric and operational parameters with the Toyota Prius 2010 IPM. In order to examine the individual influence of the S/P combinations on the bar current waveform and electromagnetic performance characteristics, 52 rotor slot has been assigned initially for each IM. Subsequently, the effect of the S/R/P combination with estimated optimal rotor slot numbers has been investigated. A general equation, giving the optimal rotor slot for maximum torque and efficiency with relatively low torque ripple, has been derived for squirrel-cage IMs with any S/P combination. The flux density waveforms in different parts of the stator and rotor tooth as well as relative permeabilities will be examined. Furthermore, for each S/P combination, saturation levels of the tooth parts and slot leakage flux density amplitudes will be determined and their influence on the bar current waveform will also be investigated.

6.4.1 Determination of Stator Slot and Pole Number Combination

The influence of stator slot/pole number combination on the electromagnetic performance and the bar current waveform are investigated by 2-D FEA under steady state operation condition. In order to observe the influences, 36S/6P, 48S/8P, and 60S/10P IMs all having a rotor slot number of 52 are designed preliminarily by using the geometrical and operation specifications which are the same as the Toyota Prius 2010 IPM (see Appendix D) and the same transient analysis has been conducted by using exactly the same FEA setup properties including the design considerations given as follows:

- The same winding layout with single-layer and 5 slot-pitch distributed windings has been utilized (the same fundamental winding factor);
- All machines have 52 slots initially in their rotors;
- All machines are operated with 176.6 Arms current at 950rpm;

- The W330 core material has been used (see Fig. 5.2 for the BH curve of the material).

Important stator slot/pole number selection criteria for the 3-phase IMs are: (a) maximum winding factor, (b) maximum fundamental MMF amplitude and minimum MMF harmonics, (c) high and even greatest common divisor (*gcd*), and (d) high least common multiplier (*lcm*). Here, (a) and (b) are related with the torque density and copper losses, while (c) and (d) are related with the unbalanced magnetic pull, torque ripple, acoustic noise and vibration issues. On the other hand, as investigated in [KRO31], [LIA95], [MEL95], [HIR97], [BES09], [SED14], [TSO14], [AGA16], the rotor slot number has also significant influence on the torque density and torque ripple.

6.4.2 Influence of Stator Slot and Pole Number on Performance Characteristics

As known very well, the MMFs produced by the stator windings play a very important role in distortion of the performance curves such as air-gap flux density, bar current, and the copper losses etc. Therefore, the distortion of the MMF waveform is of great importance in terms of performance and parasitic effects. The MMF harmonic spectra of the designed IMs are illustrated in Fig. 6.37.

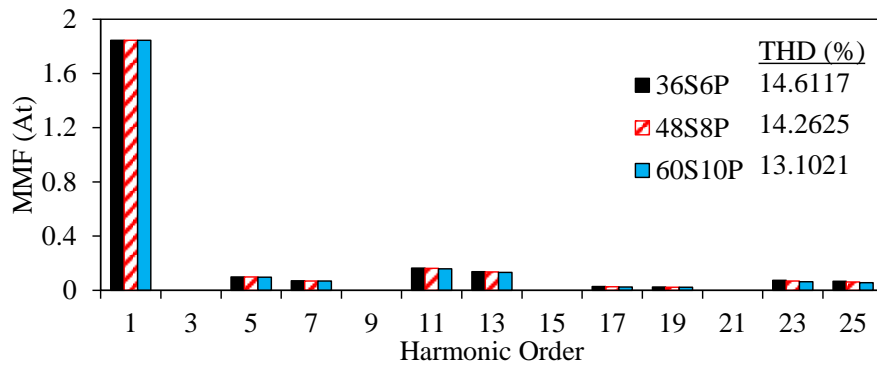


Fig. 6.37 Winding MMF harmonic spectra for one turn and one amp.

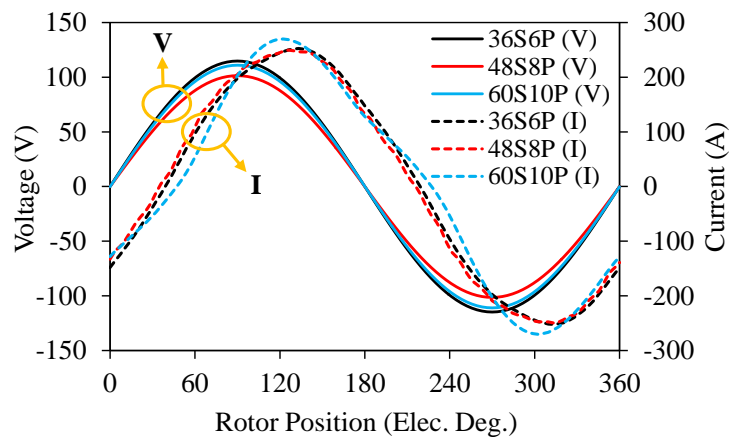


Fig. 6.38 Applied voltage and induced current in Phase ‘A’ winding for different S/P combinations.

As seen in the figure, even if the fundamental MMF for one turn and one ampere is almost the same for all IMs, the THD percentage is reduced as the stator slot and pole numbers are increased. Therefore, it can be predicted that the parasitic effects will be lower if the stator slot and pole numbers are increased together. To be able to induce the same current in the stator windings of the IMs, slightly different

voltage amplitudes have been applied as seen in Fig. 6.38. From this figure, it is also possible to see the power factor angles. Whilst the 60S10P IM has the highest angle (47.25°), the 48S8P IM has the lowest (35.045°) power factor angle (see also Table 6.1 for the power factors). The harmonic spectra of the phase currents are shown in Fig. 6.39. It is very interesting that the phase current THD of the 60S10P IM is several times higher than the other machines even if it has the lowest MMF THD percentage. Induced voltage waveforms and their harmonic spectra are illustrated in Fig. 6.40.

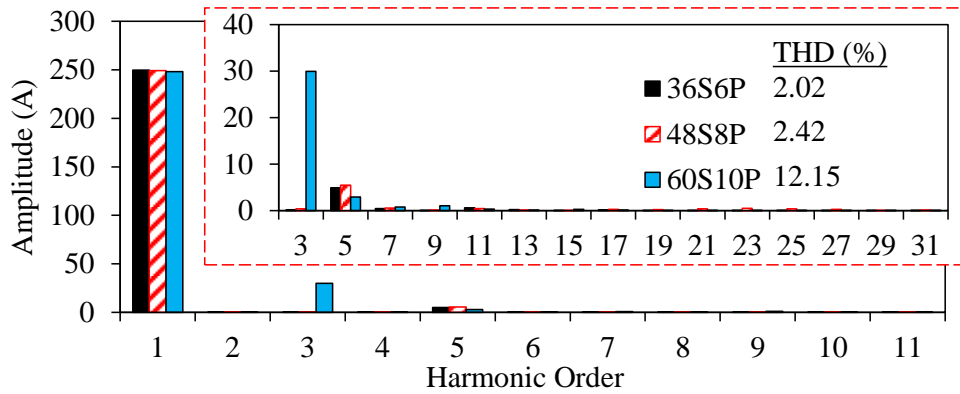
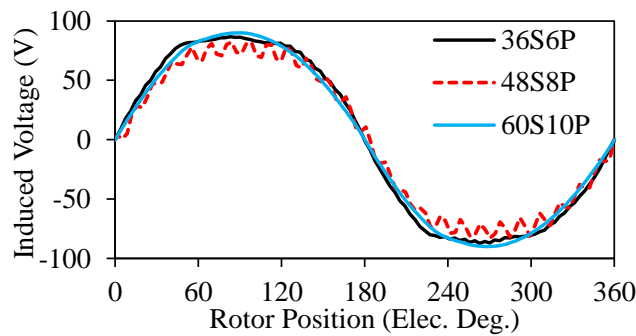
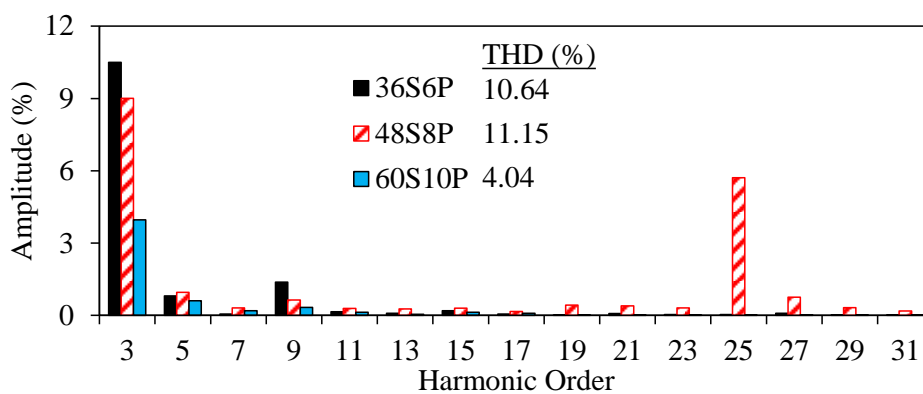


Fig. 6.39 Harmonic spectra of currents induced in Phase 'A' winding for different S/P combinations.

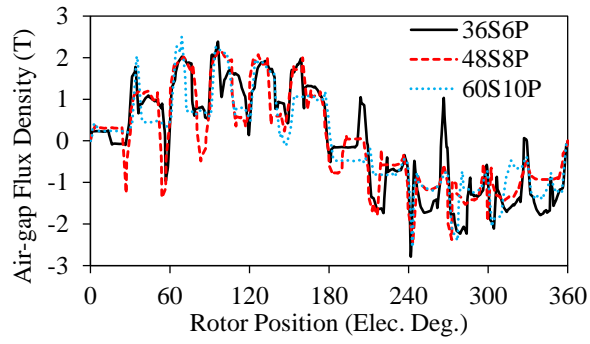


(a)

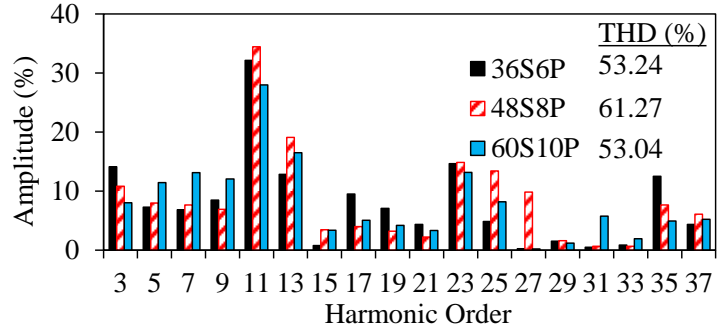


(b)

Fig. 6.40 Induced voltage in Phase 'A' of different S/P combinations: (a) waveform and (b) harmonic spectra.

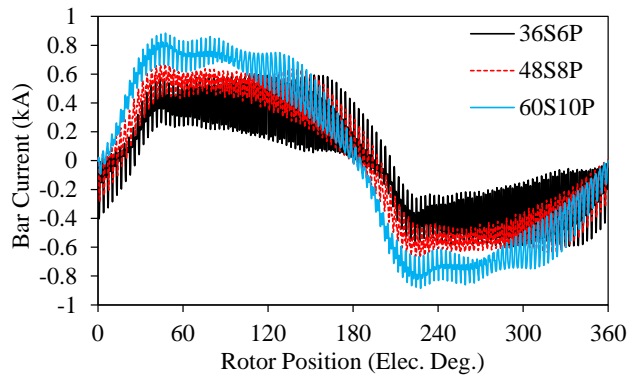


(a)

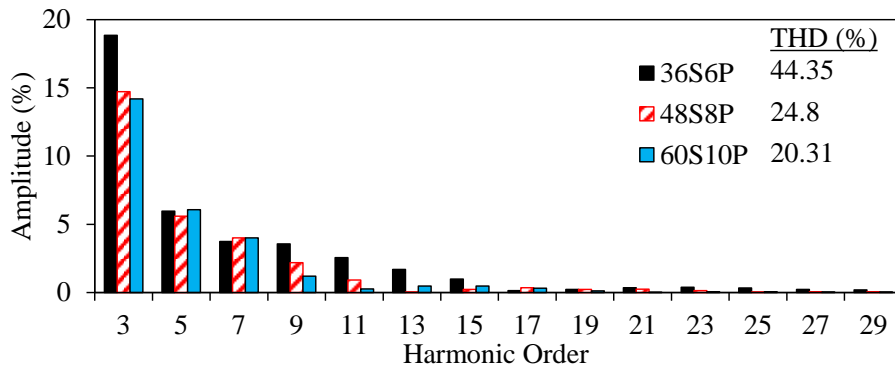


(b)

Fig. 6.41 Air-gap flux density of different S/P combinations: (a) waveform and (b) harmonic spectra.



(a)



(b)

Fig. 6.42 Rotor bar current of different S/P combinations: (a) waveform and (b) harmonic spectra.

In contrast with phase current waveform distortion, the voltage waveforms induced in 36S/6P and 48S/8P IMs have much higher distortion. This is due to the fact that each machine has different

magnitude of slotting and saturation harmonics. As explained in Chapter 5, the saturation affects mostly the 3rd harmonic of the examined curve. Therefore, it can be predicted that the 36S/6P IM will be the most saturated IM among the others, as will be shown in Fig. 6.43. Air-gap flux density waveforms and their harmonic spectra showing the distortion levels are illustrated in Fig. 6.41. As in the induced voltage, the 48S8P IM is the most distorted one while 36S/6P is the most saturated IM. The linear correlation between the induced voltage and the air-gap flux density can be observed from the THD percentages as explained in Chapter 5. Rotor bar current waveforms and their harmonic spectra are illustrated in Fig. 6.42(a) and (b), respectively. As clearly seen from the spectra and waveforms, although all obtained bar currents are non-sinusoidal, the bar current waveform of the 36S/6P IM has the highest distortion while the 60S/10P IM has the lowest. Therefore, it has been revealed that the stator slot/pole number combination has an effect on the rotor bar current waveform. The stator slot/pole number combination affects the saturation of iron cores, particularly in the tooth body of the rotor. As will be shown in the following section, the stator slot/pole number combination has a direct effect on the saturation of the iron cores. The flux density distribution for the designed IMs are illustrated in Fig. 6.43. The knee point of the assigned core material is determined as approximately at 1.48T from its BH curve. The calculated average flux densities of the stator and rotor tooth parts are indicated in the figures for each machine. Therefore, it is obvious that all of the stator and rotor tooth bodies are highly saturated. In addition, as predicted before, the 36S/6P IM has the highest saturation level.

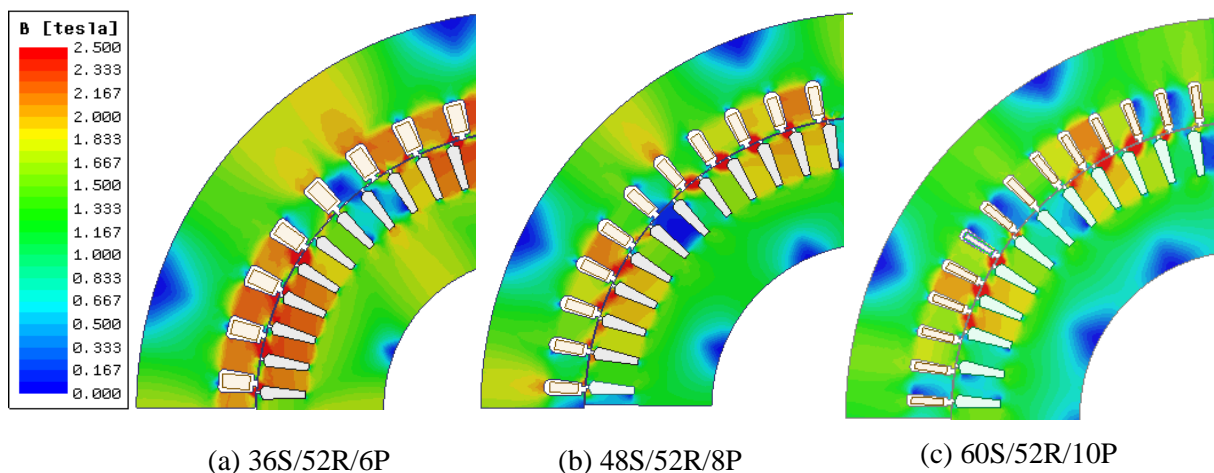


Fig. 6.43 Flux density distributions of IMs with different S/P and arbitrary rotor slot number.

The key performance characteristics of the designed IMs are summarized in Table 6.1. As seen in the table, although the rms values of the induced currents in the stator windings are the same, there is a slight difference between the achieved average torque T values. However, the torque ripple percentages ΔT are totally different due to the interaction between the slotting harmonics (including the rotor slotting effect) and the MMF harmonics. Stator winding copper loss P_{scu} , rotor bar copper loss P_{Rcu} , and core loss P_C in each machine are also given in Table 6.1. Since the 6P IM requires thicker yoke because of the saturation of the stator yoke, its split ratio is lower than the others. Therefore, to be able to achieve the similar average torque with the 8P and 10P IMs, the number of turns in 6P IM has been increased.

Therefore, the 36S6P IM has the highest P_{Scu} . There is a linear correlation between P_{Rcu} and the MMF harmonics in the air-gap and hence the rotor bar current. Therefore, as seen in the table, the higher the MMF harmonics, the higher the P_{Rcu} under the same torque density condition. In addition, as expected the higher the pole number, the higher the P_C . Output power P_{out} , power factor $P.F$ and efficiency η of each machine are also calculated. It is noted that additional losses are assumed to be 1% of the output power during the calculation of the efficiency. Even if the 36S/6P IM has higher $P.F$. than the 60S/10P IM, its efficiency is lower because of the higher copper losses. It has been revealed that in terms of efficiency the 8P IM is favourable whilst the 6P IM is favourable in terms of average torque.

Table 6.1 Performance characteristics of IMs with arbitrary rotor slot number

	T (Nm)	ΔT (%)	P_{Scu} (kW)	P_{Rcu} (kW)	P_C (kW)	P_{out} (kW)	$P.F.$	η (%)
36S/6P	236.3	5.7	8.32	1.478	0.08	23.51	0.773	69.93
48S/8P	230.68	15.9	6.55	1.2	0.1	22.95	0.814	73.96
60S/10P	235.7	5.23	6.79	1.19	0.12	23.45	0.707	73.78

6.4.3 Performance with Optimal Rotor Slot Numbers

In order to determine the optimal rotor slot number for any S/P combination a number of parametric analyses have been performed by considering (6.3) and the explanations given in Section 6.3.

A. 36S/6P IM

The influence of the rotor slot number on the performance characteristics of the 36S/6P IM is investigated and the obtained results are illustrated in Fig. 6.44 and Fig. 6.45. As the rotor slot number is reduced, the amplitude of the bar current is increased and the amplitude of the dominant harmonics and consequently the THD level is decreased as seen in Fig. 6.44(b). In addition, the average torque, torque ripple, and efficiency are decreased dramatically, while the bar copper loss is increased significantly for the rotor slot numbers larger than 40. Moreover, the maximum torque and efficiency and relatively low torque ripple are achieved for the 40 rotor slot number of the 36S/6P IM.

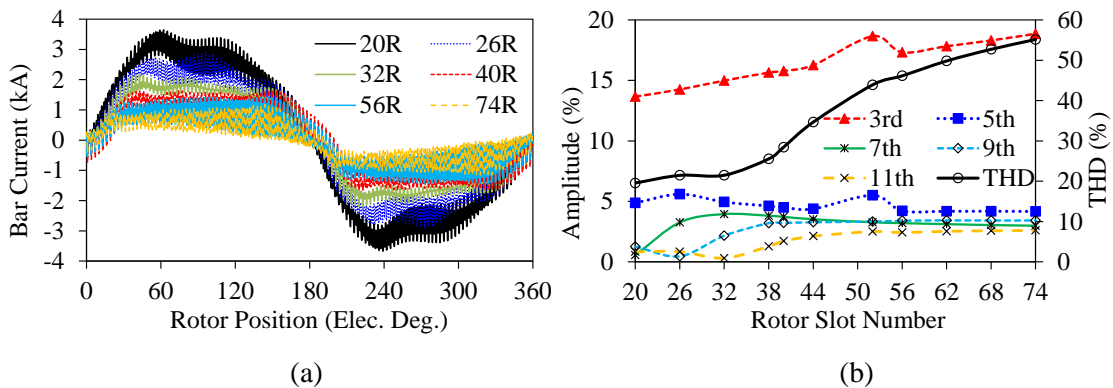


Fig. 6.44 Bar current for different rotor slot number of 36S/6P IM: (a) waveform and (b) variation of the dominant bar current harmonics and THD with respect to rotor slot number.

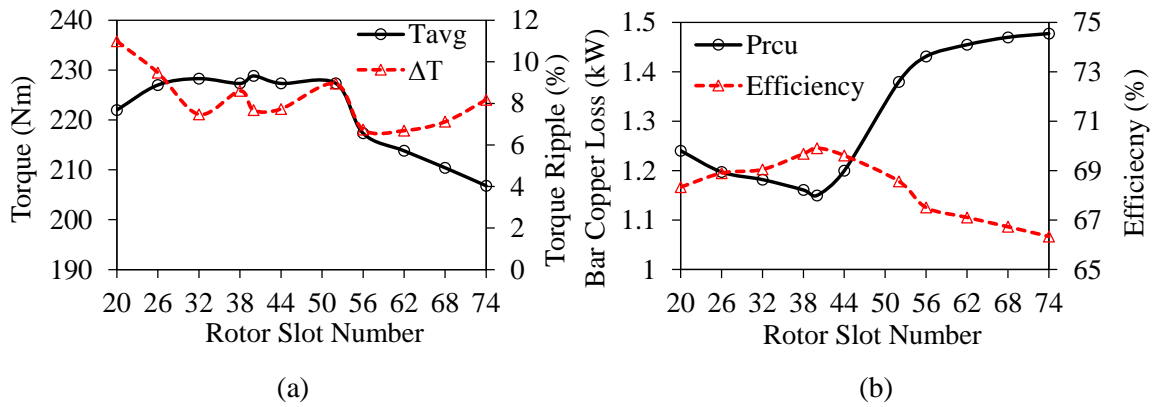


Fig. 6.45 Performance characteristics against rotor slot number of 36S/6P IM: (a) average torque and torque ripple, and (b) rotor copper loss and efficiency.

B. 48S/8P IM

The effect of the rotor slot number on some performance characteristics of the IM having 48S/8P is examined. The variation of the bar current waveform, dominant bar current harmonics, and the THD level with respect to rotor bar number are illustrated in Fig. 6.46. As seen, as the rotor slot number is increased, the distortion level is increased considerably whilst the fundamental bar current amplitude is decreased. Fig. 6.47 illustrates the variation of the average torque, torque ripple, bar copper loss, and efficiency with respect to rotor slot number. The maximum torque and efficiency is achieved at the 52 rotor slot number. It can be seen that the torque ripple and bar copper loss of the 48S/8P IM are very sensitive to the rotor slot number.

C. 60S/10P IM

The influence of the rotor slot number on some performance characteristics of the IM having 60S/10P is investigated in this section. The bar current waveforms for different rotor slot number is illustrated in Fig. 6.48(a). As seen in the figure, as the rotor slot number is increased, the fundamental amplitude of the bar current is decreased and the distortion level is increased remarkably (see Fig. 6.48(b)). It is shown that the most dominant harmonic is the 3rd harmonic as observed from the other S/P combinations. Variation of the average torque, torque ripple, bar copper loss, and efficiency are shown in Fig. 6.49. As the rotor slot number is increased, the average torque is increased whilst the torque ripple is decreased. Moreover, since the output power increases as the rotor slot number is increased, the bar copper loss and efficiency are also increased. The maximum average torque and efficiency are achieved for the 64 rotor slot number of the 60S/10P IM. Briefly, independent of the S/P combinations, as the rotor slot number is increased, the fundamental amplitude is decreased and the waveform starts to take top-flatted shape and consequently the bar current THD level is increased considerably. It has been validated that depending on the generated torque amount, the higher the pole number, the lower the bar copper loss. It can be concluded that the rotor slot number has a significant effect on the performance characteristics of IMs having different S/P combinations. Furthermore, there is a specific rotor slot number for any S/P combination at which the maximum torque and efficiency with relatively low torque

ripple might be achieved. Considering the figures between Fig. 6.44 and Fig. 6.49 , a general rule, estimating the optimal rotor slot number for any S/P combination, given in (6.9), is derived, where q is the stator slot/phase/pole number.

$$R \cong S + 2q \quad (6.9)$$

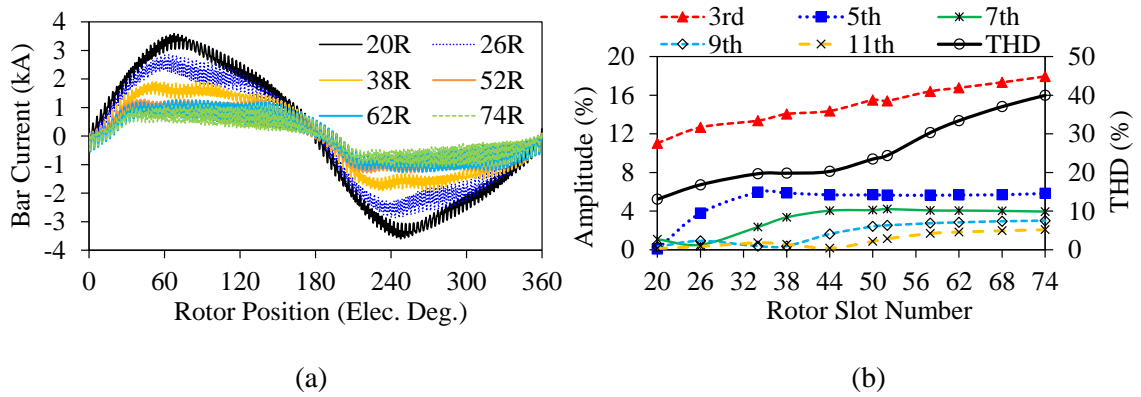


Fig. 6.46 Bar current for different rotor slot number of 48S/8P IM: (a) waveform and (b) variation of the dominant bar current harmonics and THD with respect to rotor slot number.

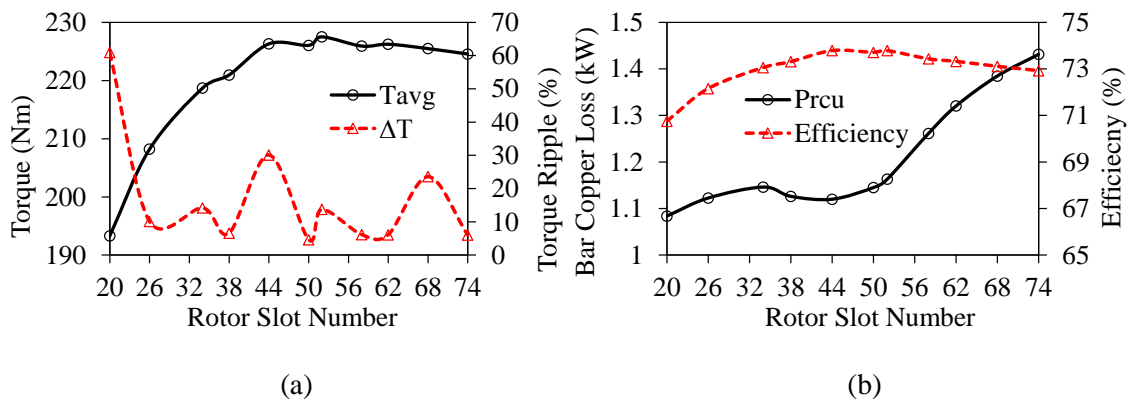


Fig. 6.47 Performance characteristics against rotor slot number of 48S/8P IM: (a) average torque and torque ripple, and (b) rotor copper loss and efficiency.

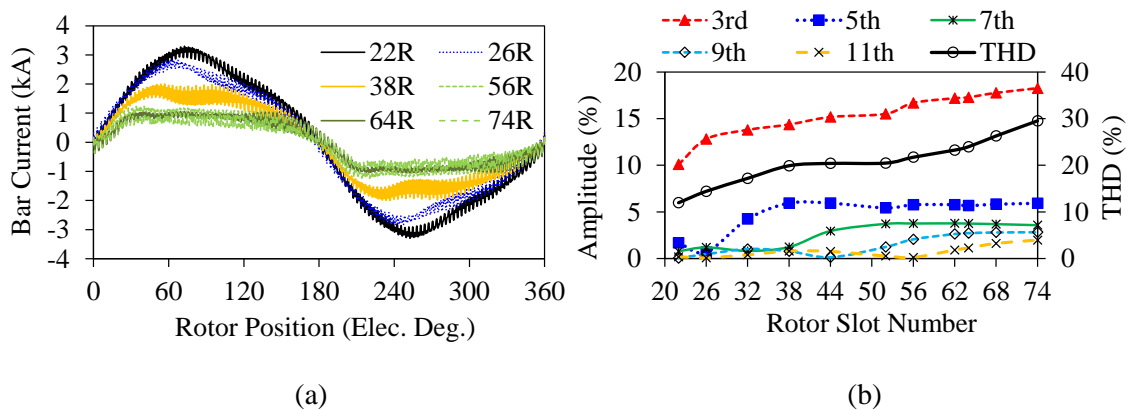


Fig. 6.48 Bar current for different rotor slot number of 60S/10P IM: (a) waveform and (b) variation of the dominant bar current harmonics and THD with respect to rotor slot number.

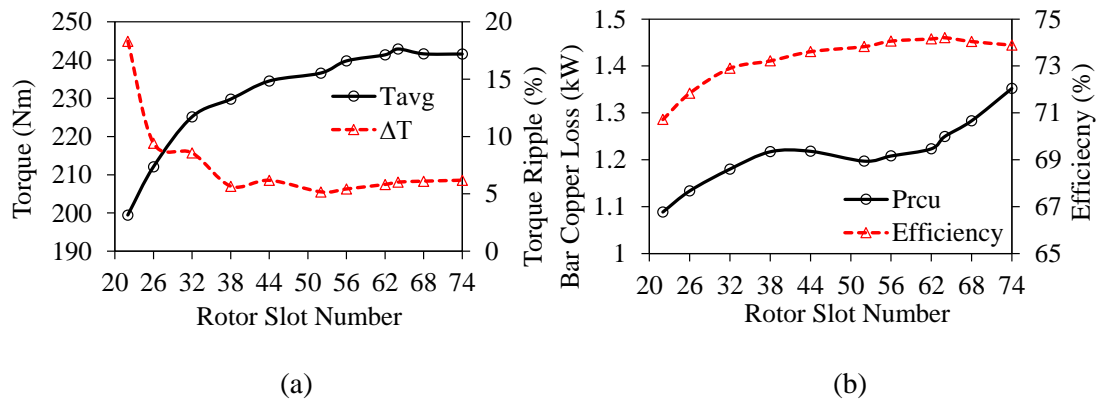


Fig. 6.49 Performance characteristics against rotor slot number of 60S/10P IM: (a) average torque and torque ripple, and (b) rotor copper loss and efficiency.

The bar current waveforms with the optimal rotor slot number is shown in Fig. 6.50(a). As seen in the figure, under the specified operation conditions (176.6 Arms @ 950rpm), none of the waveforms are sinusoidal. It can be observed that as the S/P number is increased, the fundamental amplitude of the bar current is reduced. The harmonic spectra of the bar currents, showing the low- and high-order harmonics, are illustrated in Fig. 6.50(b) and (c), respectively.

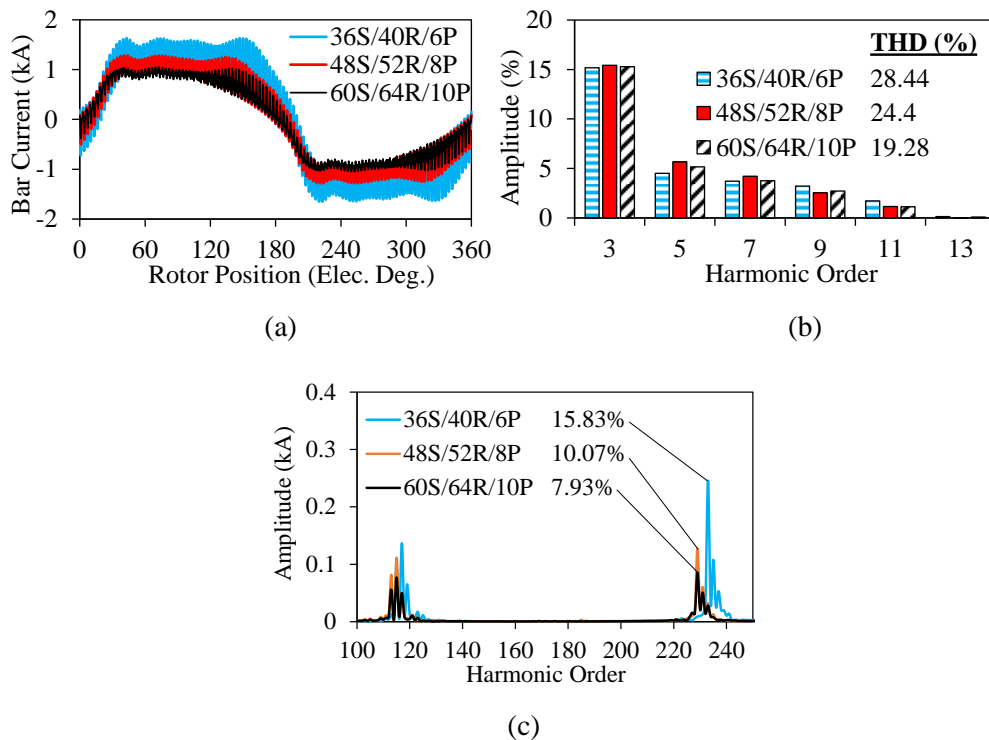


Fig. 6.50 Bar currents of IMs with different S/P combinations: (a) waveform, (b) the low-order harmonics, and (c) high-order harmonics.

As seen in the figures, the lower the pole number, the higher the bar current distortion. Moreover, it can be concluded that the bar current distortion level of IMs, designed with the optimal rotor slot number, is lower than those with arbitrary rotor slot numbers (see Fig. 6.42). It is also obvious that the high-order harmonics are reduced significantly thanks to designation of the optimal rotor slot number for 6P

IM (see Fig. 6.42(c)). On the other hand, when compared to design with the 52-rotor slots, the high-order bar current harmonic amplitudes of the 10P IM is increased considerably with the 64-rotor slots. In addition, the level of the flux density on the stator and rotor tooth parts are reduced substantially (see Fig. 6.43 and Fig. 6.51). Therefore, it can be concluded that the flux leakage (see Table 6.3) and consequently the saturation level of the machines are reduced by designing the IMs with optimal rotor slot number. Electromagnetic performance comparison of IMs having optimal rotor slots is given in Table 6.2. It can be concluded that the key performance characteristics; such as average torque, copper losses, output power, and efficiency are improved thanks to the determination of the optimal rotor slot number.

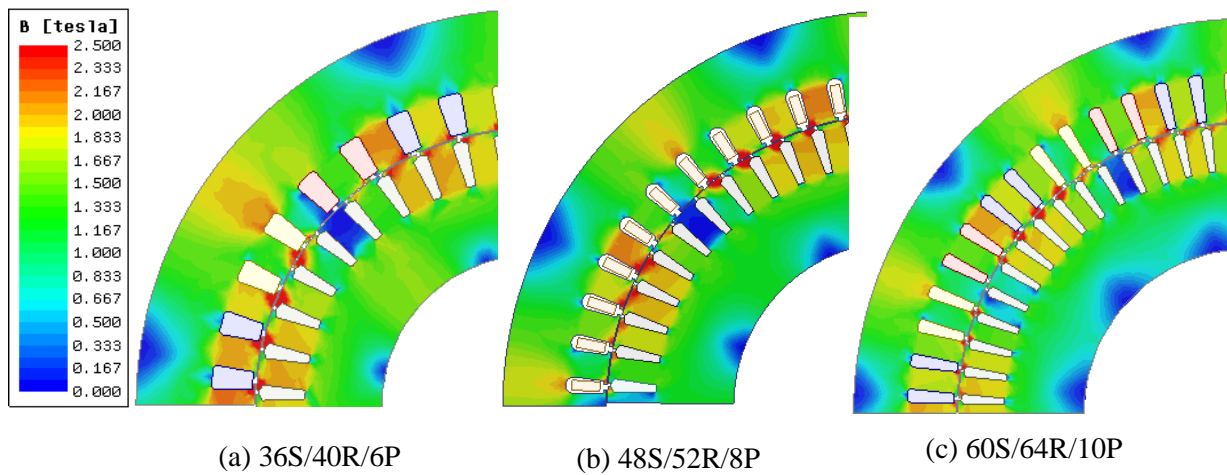


Fig. 6.51 Flux density distributions of different S/P and optimal rotor slot number.

In Table 6.2, P_{Scu_in} and P_{Scu_end} are the stator copper loss of the slot windings and the end-windings, respectively. Since the coil pitch (in mm) and consequently the end-winding radial length of the 10P is the shortest, its stator copper loss is the minimum. As shown, the average torque level of the 10P IM with the optimal rotor slot number is increased remarkably. In order to make a fair comparison, the number of turns per phase of the 10P is reduced from 6⁽¹⁾ to 5⁽²⁾ (see Table 6.2). Although the 10P IM is favorable in terms of torque and efficiency at the constant-torque region, the poorer flux-weakening capability than those of the 6P and 8P IMs can be predicted since its pole number is the highest. In the same manner, the highest torque and power at the high-speed operation region might be expected for the 6P IM.

Table 6.2 Performance characteristics of IMs with optimal rotor slot number

	T (Nm)	ΔT (%)	P_{Scu_in} (kW)	P_{Scu_end} (kW)	P_{Rcu} (kW)	P_c (kW)	P_{out} (kW)	η (%)
36S/40R/6P	228.83	7.67	2.16	6.17	1.17	0.088	22.76	69.92
48S/52R/8P	227.5	13.7	2.07	4.48	1.16	0.103	22.63	73.78
60S/64R/10P⁽¹⁾	242.9	6.02	2.47	4.31	1.25	0.12	24.16	74.21
60S/64R/10P⁽²⁾	228.4	4.64	1.77	3.13	1.14	0.11	22.72	78.06

6.4.4 Investigation of Tooth Flux Density

As explained in previously, there is a linear correlation between the bar current waveform and the rotor tooth flux density.

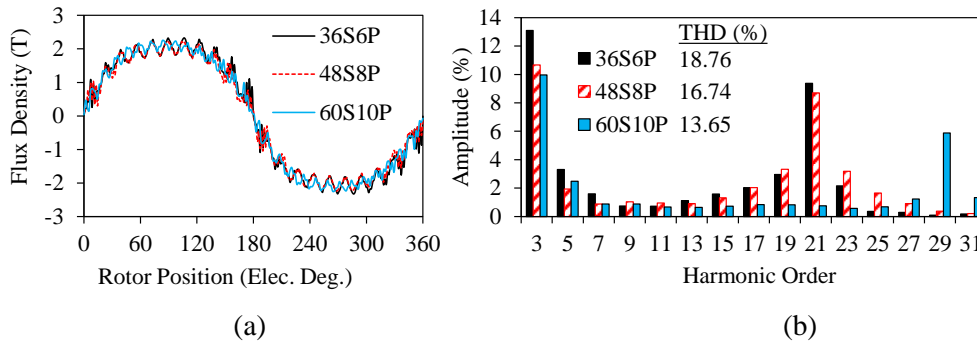


Fig. 6.52 Rotor tooth tip flux densities for different S/P combinations: (a) waveform and (b) harmonic spectra.

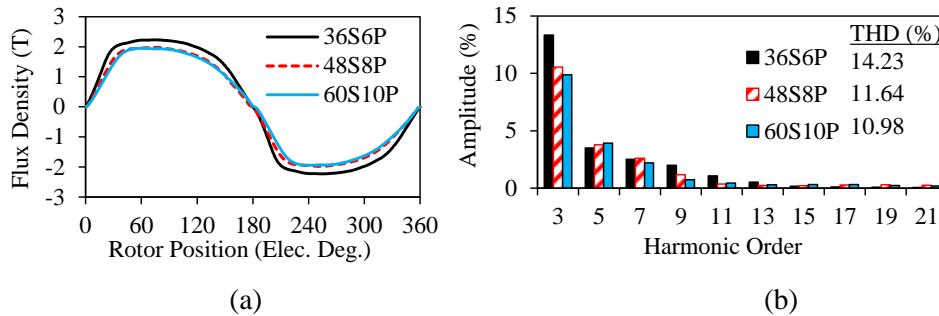


Fig. 6.53 RTM flux densities for different S/P combinations: (a) waveform and (b) harmonic spectra.

Therefore, in order to investigate this correlation, the flux densities on the rotor tooth tips and middle of the tooth parts have been calculated and the influence of the stator slot/pole number combination has been examined as follows. Variation of the flux densities on the rotor tooth tips with respect to rotor position and harmonic spectra are illustrated in Fig. 6.52. As clearly seen the rotor tooth tip flux densities have been highly distorted due to the combined effect of stator and rotor MMFs and permeances, saturation, and slotting. Among the designed IMs, while 60S/10P IM has the least distorted flux density on the tooth tips, the 36S6P IM has the most distorted waveform since it is the most saturated one (see Fig. 6.52(b)). Flux density variation in the middle of the rotor tooth bodies and their harmonic spectra are illustrated in Fig. 6.53. As seen in Fig. 6.53(b), the 3rd harmonic is the most dominant harmonic in the bar current. Considering Fig. 6.42 and Fig. 6.53, the close correlation between the bar current and flux density in the middle of the rotor tooth can be noticed easily. Furthermore, as explained in Chapter 5, due to the filtering (average) effect of the tooth body, the flux density is more distorted on the tips and it diminishes to minimum on the root of the tooth. However, as noticed, even if the higher order flux density harmonics are gradually disappear, the 3rd harmonic cannot be cancelled. The reason behind this phenomenon will be explained in the following section.

6.4.5 Influence of Core Saturation

As known, the air-gap flux density is generated due to the interaction between the stator and rotor magnetic fields and the radial component of the air-gap flux density is the torque producing flux density [BOL10], [LIP17]. On the other hand, the tangential component of the rotor and stator fields are the rotor and slot leakage components, respectively, and they depend on the slot geometries and the currents of the stator and rotor. Since the saturation is directly related with the leakage flux, the permeability of iron cores together with the slot leakage flux should be investigated in order to reveal the reasons behind the non-sinusoidal bar current. Therefore, in order to analyze the effect of the saturation and leakage flux, in addition to design by using non-linear material in both of the stator and rotor, another design is performed by using a linear material in the rotor only for the investigated IMs.

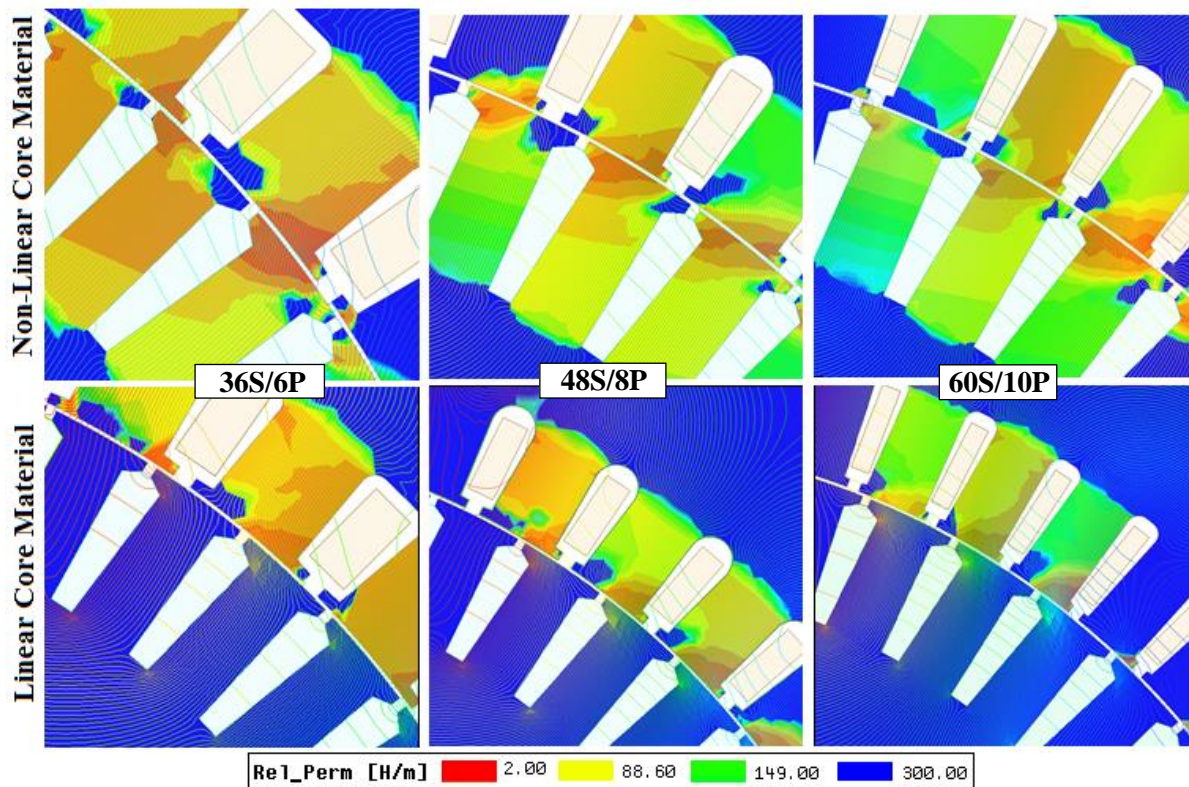


Fig. 6.54 Flux line and relative permeability distributions of IMs with non-linear core materials in both stator and rotor and with rotor only linear ($\mu_r = 10^5$) material.

The BH curve of the non-linear and linear material is given Chapter 5 (see Fig. 5.2). Flux line and relative permeability distributions of the IMs designed by using non-linear materials for stator and rotor and linear material for only rotor core are illustrated in Fig. 6.54. As seen in the figure, the permeability of the iron cores from the highest to lowest are 60S/10P, 48S/8P, and 36S/6P, respectively. As seen, the permeability of the tooth tips are almost zero. On the other hand, in the case of linear material usage in the rotor only, there is no saturation in the rotor and the flux lines coming from the rotor tooth tips never pass to the tooth bodies as shown in Fig. 6.54. As shown previously, these fluxes at the tips are highly distorted. When these highly distorted fluxes at the tooth tips flow directly to the adjacent tooth body, a lot of extra harmonics are transferred to the main flux at tooth body. That is why the filtering action

of the tooth body cannot filter the some certain harmonics. Owing to the fact that the highly saturated parts cannot carry any more flux, the highly distorted fluxes of the tips pass through to less saturated parts of tooth bodies (see Fig. 6.54). On the other hand, these fluxes never pass to the adjacent tooth bodies in the linear material rotor case. Therefore, extra harmonics are never produced on the tooth body. Furthermore, since each combination has different saturation level, they have different slot leakage flux magnitudes and hence different bar current distortions. The tangential components of the rotor slot flux density (leakage flux density) while both of the stator and rotor cores are assigned with non-linear material and their harmonic spectra are illustrated in Fig. 6.56. Since there is no filtering effect in the slot all the flux densities are distorted significantly. Among the IMs, the 36S/6P IM has the highest leakage flux density amplitude as seen in Fig. 6.56(b) and Table 6.3. Thus, its rotor bar current waveform is the most distorted one. It is also obvious that the more saturation on the teeth, the more leakage in the slots. Furthermore, independently of the S/P combination, the optimal rotor slot number leads to obtain low leakage flux density as given in Table 6.3.

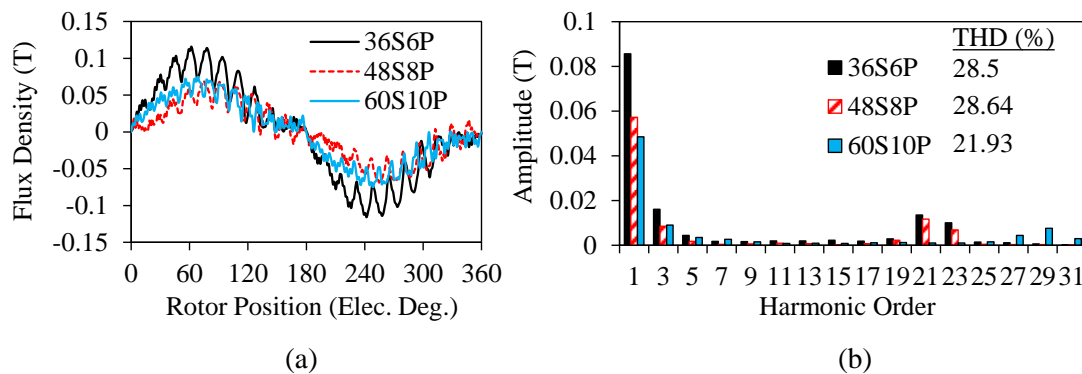


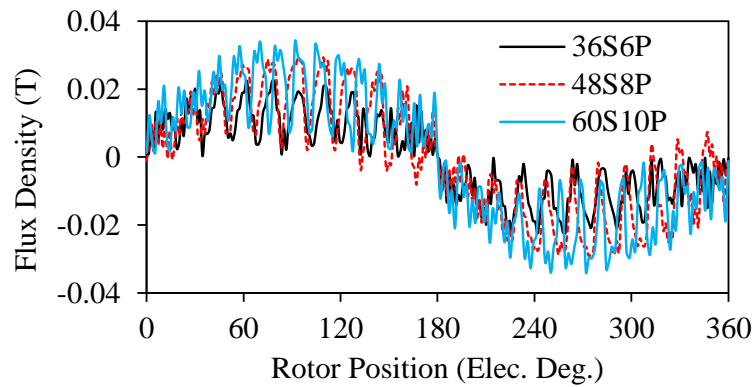
Fig. 6.55 Tangential components of the rotor slot flux densities for different S/P combinations whilst all the core materials are non-linear: (a) waveform and (b) harmonic spectra.

Table 6.3 Magnetic Flux Density Components of Rotor

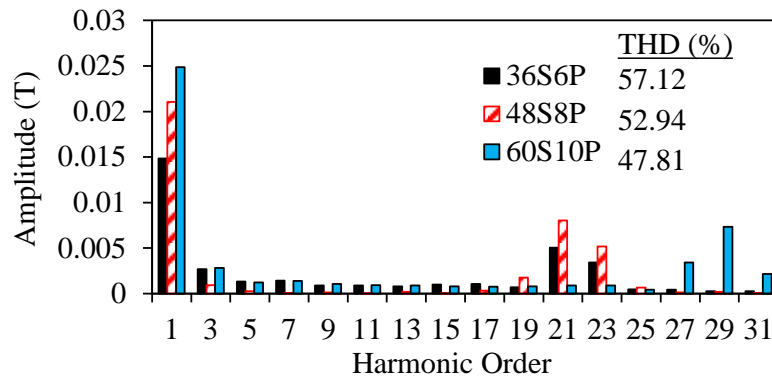
	Slot Leakage Flux Density Amp. (T)	Tooth Flux Density Amp. (T)	Tooth flux 3 rd Harm. (%)	Tooth Flux THD (%)
36S/52R/6P	0.086	2.496	13.338	14.229
36S/40R/6P	0.074	2.154	7.391	12.845
48S/52R/8P	0.057	2.132	9.455	13.138
60S/52R/10P	0.049	2.085	6.585	10.983
60S/64R/10P⁽²⁾	0.042	2.131	6.284	7.956

Rotor slot leakage flux density variations with respect to rotor position and harmonic spectra while the rotor core is assigned with the linear material are illustrated in Fig. 6.56. It has been revealed that although the level of the leakage flux depends of the level of the saturation, there are still leakage flux even if there is no saturation. This might be due to the effect of slot geometries including the slot opening and permeance. In addition, these effects are more dominant than the saturation in the 10P IM and it is obvious these effects are lower in the IMs which has lower pole number. Considering Fig. 6.55 and Fig.

6.56, the influence of saturation on the level of the leakage flux is significant. When compared the slot leakage percentages of the non-linear case with linear case, 82.67%, 63.22%, 48.71% more slot leakages have occurred for the 36S/6P, 48S/8P, and 60S/10P IMs, respectively.

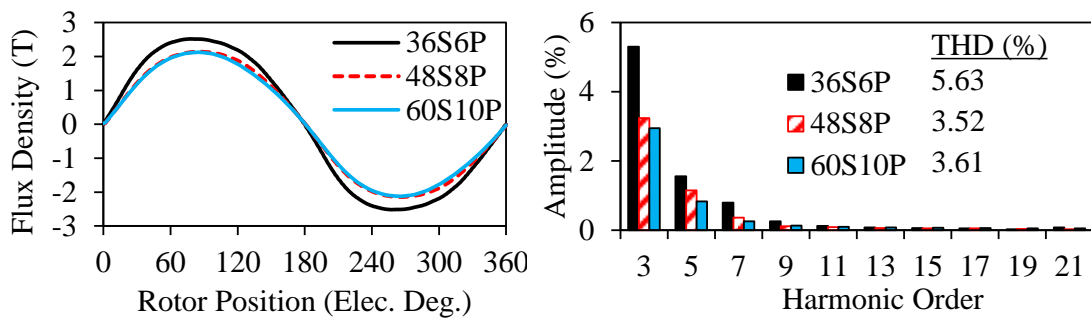


(a)

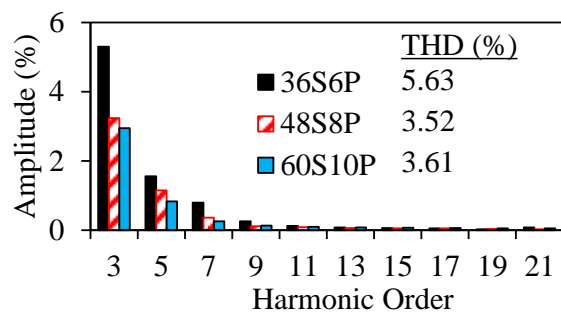


(b)

Fig. 6.56 Tangential components of the rotor slot flux densities for different S/P combinations whilst only the rotor core material is linear: (a) waveform and (b) harmonic spectra.



(a)



(b)

Fig. 6.57 Flux densities at the middle of the rotor tooth body whilst only the rotor core material is linear: (a) waveform and (b) harmonic spectra.

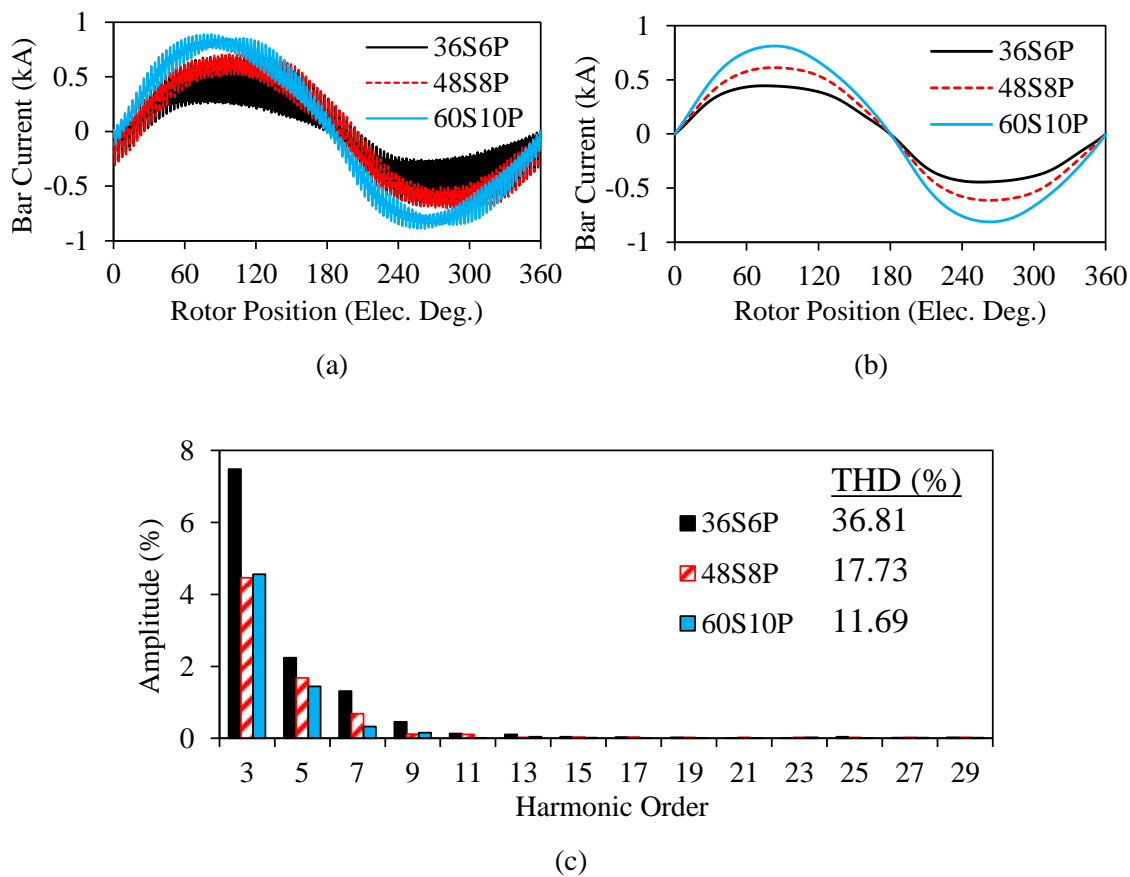


Fig. 6.58 Rotor bar current whilst only the rotor core material is linear: (a) original waveform, (b) reconstructed waveform, and (c) harmonic spectra.

In case of the saturation at the rotor, the obtained flux density waveform at the middle of the rotor tooth body and its harmonic spectra are illustrated in Fig. 6.57. Considering Fig. 6.53(b) and Fig. 6.57(b), it can be concluded that if there is no saturation in the rotor tooth body, the levels of the flux density waveform distortions have reduced significantly for all IMs. Similarly, as seen in Fig. 6.58, the distortion levels of the rotor bar currents have also reduced remarkably. The 3rd harmonic reduction percentages in case of preventing the saturation are 60.3%, 70%, 67.9% for 36S/6P, 48S/8P, and 60S/10P IMs, respectively.

Under the design considerations given in Section 6.4.1, the key findings can be summarized as follows:

- (1) Stator slot/pole number combination has an indirect effect on the bar current waveform;
- (2) The lower the pole number, the higher the saturation level and hence the higher the distortion of the bar current;
- (3) The lower the pole number, the lower the core losses;
- (4) If the saturation of rotor core is prevented or ignored, the higher the pole number, the higher the slot leakage flux;
- (5) Non-sinusoidal rotor bar current phenomenon occurs if the rotor tooth bodies are saturated.

6.5 Stator and Rotor Slot Geometric Parameters

In this section, in order to reveal the influence of stator and rotor slot geometric parameters on the machine characteristics, a conventional squirrel-cage IM with 48S/8P/52R is designed by using the same geometric and operational parameters as the Toyota Prius 2010 IPM. The investigated geometric parameters are indicated in Fig. 6.66.

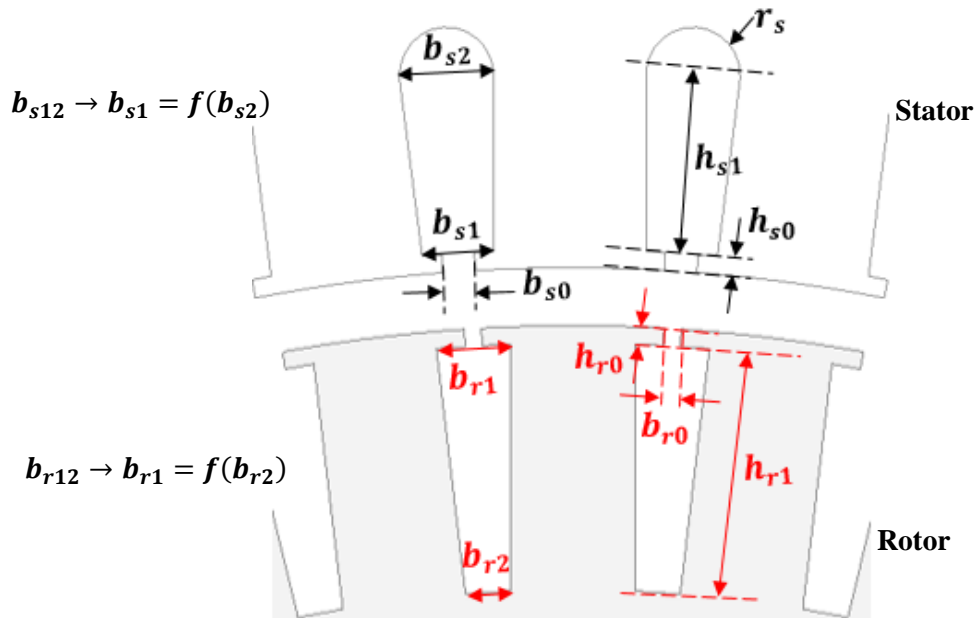


Fig. 6.59 Investigated stator and rotor slot geometric parameters.

As indicated in the figure, since parallel tooth structure is used for both the stator and rotor, slot width parameters b_{s1} and b_{r1} are functions of b_{s2} and b_{r2} , respectively. Therefore, in order to simplify the analyses and retain the parallel tooth structure, parameters b_{s12} and b_{r12} are used. Individual effect of each parameter illustrated in Fig. 6.66 is investigated by performing 2-D FEA under steady-state operation condition. While investigating the influence of any geometric parameter, other parameters are kept at their optimal values. It has been revealed that the rotor slot depth h_{r1} and stator slot width b_{s12} have the most dominant effect on the performance characteristics. They cause the bar current waveform to become non-sinusoidal. The parameters b_{r12} , h_{r0} , h_{s0} , and h_{s1} also have significant effect on the both distortion level of the bar current and performance characteristics while the slot opening parameters b_{r0} and b_{s0} have the least effect. The influence of each geometric parameter on the electromagnetic characteristics of the IM is examined in depth. Moreover, in order to explain the reason behind the non-sinusoidal bar current waveform, the harmonic content of air-gap flux density, saturation levels of the rotor and stator parts as well as flux density distributions are also presented in detail.

6.5.1 Influence of Stator Slot Geometric Parameters

The influence of the stator slot parameters on the bar current, torque, power losses, and efficiency has been investigated in this part. The IM specifications including the optimum slot geometric parameters are given in Appendix D.

A. Stator Slot Opening Width b_{s0}

The variation of the bar current waveform, the bar current fundamental and 3rd harmonic amplitudes, THD percentage, average torque T_{avg} , torque ripple ΔT , stator copper loss P_{scu} , rotor bar copper loss P_{rcu} , total core loss P_{core} , and efficiency with respect to b_{s0} is shown in Fig. 6.60 and Fig. 6.61. Note that 1% of the output power is taken into account as additional losses for the more accurate calculation of the efficiency. The influence of b_{s0} on the bar current waveform, power losses, and efficiency is very small. However, b_{s0} has a slight effect on the torque ripple as seen in Fig. 6.61(a).

B. Stator Slot Width b_{s12}

The influence of the stator slot width parameter b_{s12} on bar current waveform, harmonics and THD, torque, torque ripple, losses, and efficiency is shown in Fig. 6.62 and Fig. 6.63. Among the other stator slot parameters, b_{s12} is the most dominant parameter for the characteristics of the IM. The bar current waveform starts to become sinusoidal after 10mm of b_{s12} . As seen in Fig. 6.63, the peak torque can be achieved at 2mm of b_{s12} whilst the peak efficiency can be achieved at 7.2mm.

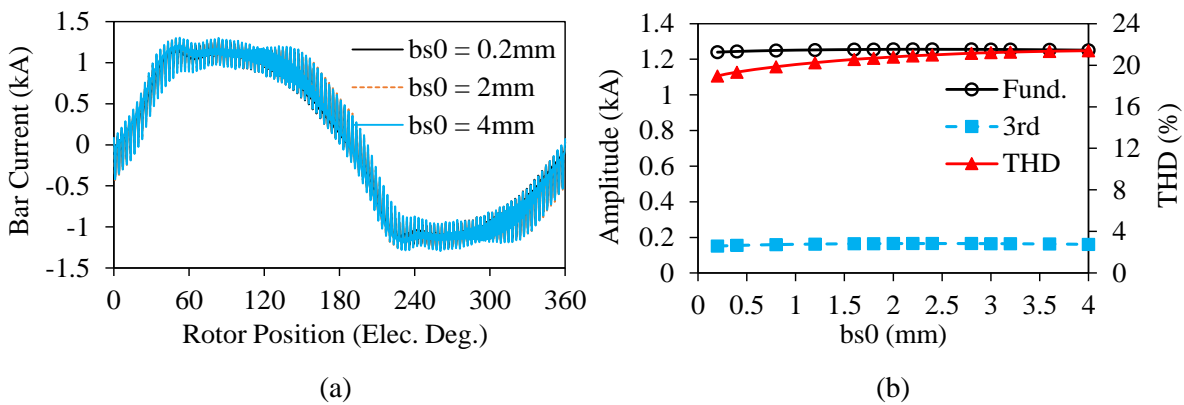


Fig. 6.60 Bar current for different b_{s0} : (a) waveform and (b) variation of harmonics and THD with respect to b_{s0} .

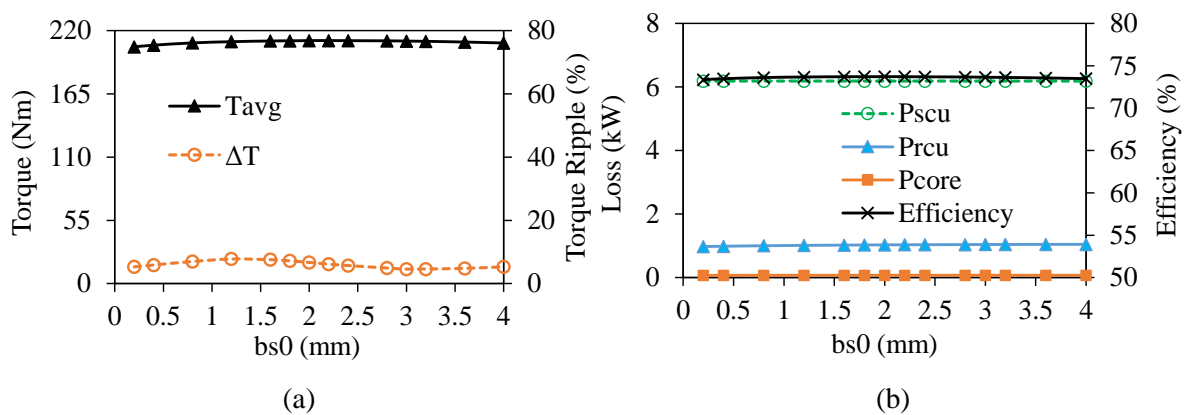


Fig. 6.61 Performance characteristics against b_{s0} : (a) average torque and torque ripple, and (b) power losses and efficiency.

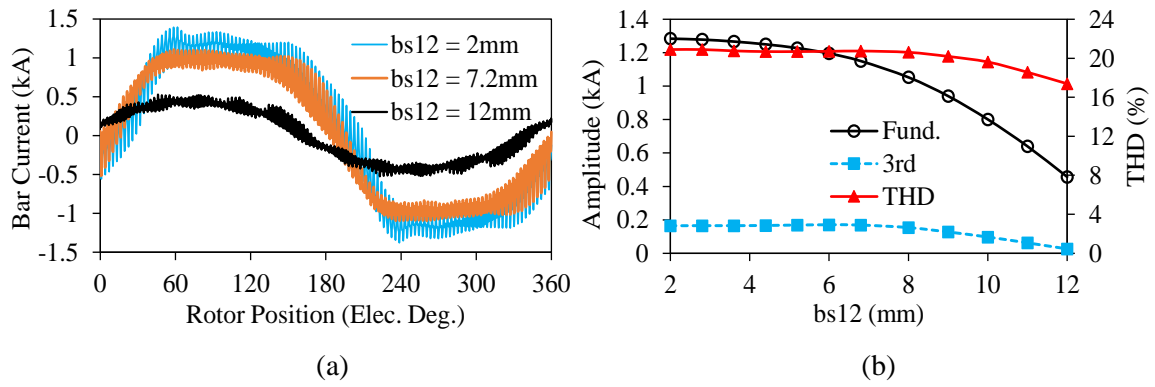


Fig. 6.62 Bar current for different b_{s12} : (a) waveform and (b) variation of harmonics and THD with respect to b_{s12} .

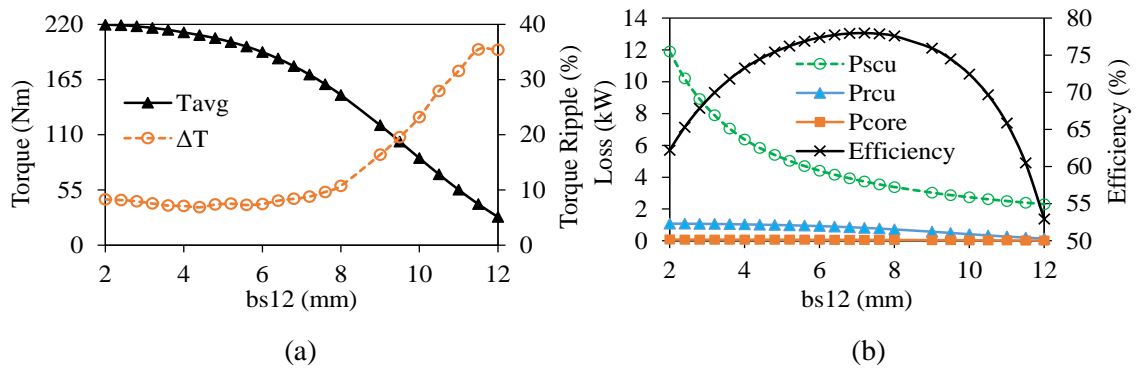


Fig. 6.63 Performance characteristics against b_{s12} : (a) average torque and torque ripple, and (b) power losses and efficiency.

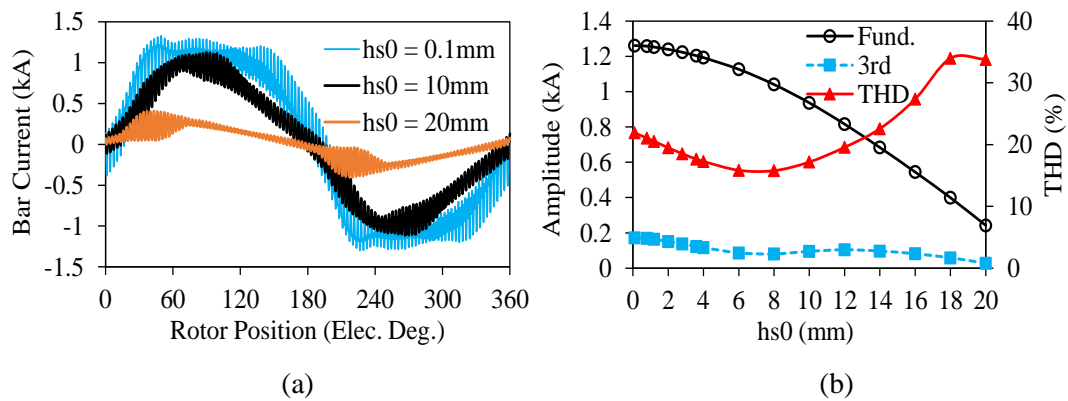


Fig. 6.64 Bar current for different h_{s0} : (a) waveform and (b) variation of harmonics and THD with respect to h_{s0} .

C. Stator Slot Opening Height h_{s0}

The influence of h_{s0} on the bar current waveform and performance characteristics is illustrated in Fig. 6.64 and Fig. 6.65, respectively. The bar current waveform is always non-sinusoidal for any value of h_{s0} . The higher the h_{s0} , the lower the bar current amplitude. The lowest bar current THD is obtained at 6mm of h_{s0} while the highest is obtained at 18mm. As seen in Fig. 6.65(a), the torque is very

sensitive to h_{s0} . In terms of high average torque, low torque ripple, and high efficiency, it is favourable to keep h_{s0} as small as possible.

D. Stator Slot Height h_{s1}

The influence of h_{s1} on the bar current waveform and performance characteristics is illustrated in Fig. 6.66 and Fig. 6.67, respectively. It is obvious that the change in the characteristics with respect to h_{s1} is quite similar to that of h_{s0} . As seen in figures, the torque, torque ripple, copper losses, and consequently the efficiency is very sensitive to h_{s0} . Considering Fig. 6.63, Fig. 6.65, and Fig. 6.67, it can be concluded that b_{s12} , h_{s0} , and h_{s1} are the most dominant stator slot parameters for the performance characteristics of the IM.

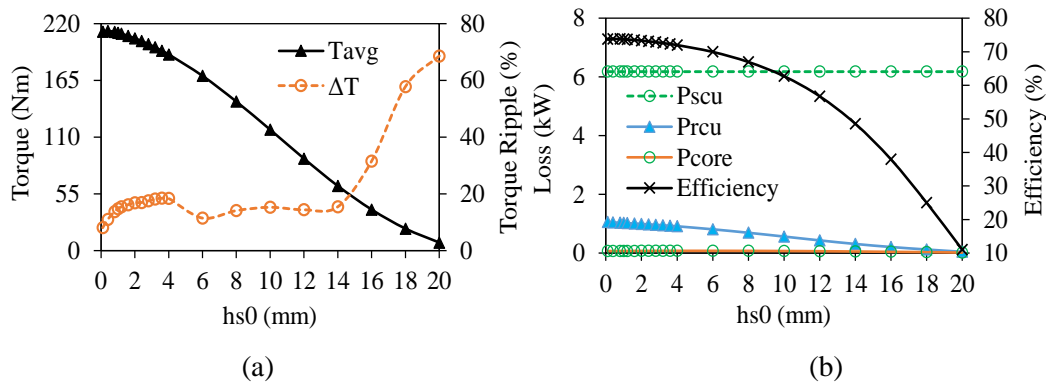


Fig. 6.65 Performance characteristics against h_{s0} : (a) average torque and torque ripple, and (b) power losses and efficiency.

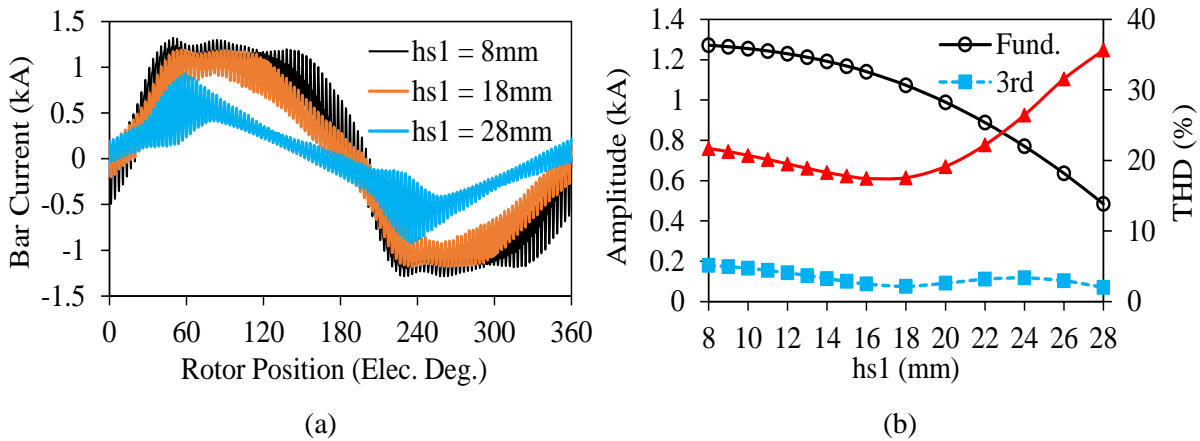


Fig. 6.66 Bar current for different h_{s1} : (a) waveform and (b) variation of harmonics and THD with respect to h_{s1} .

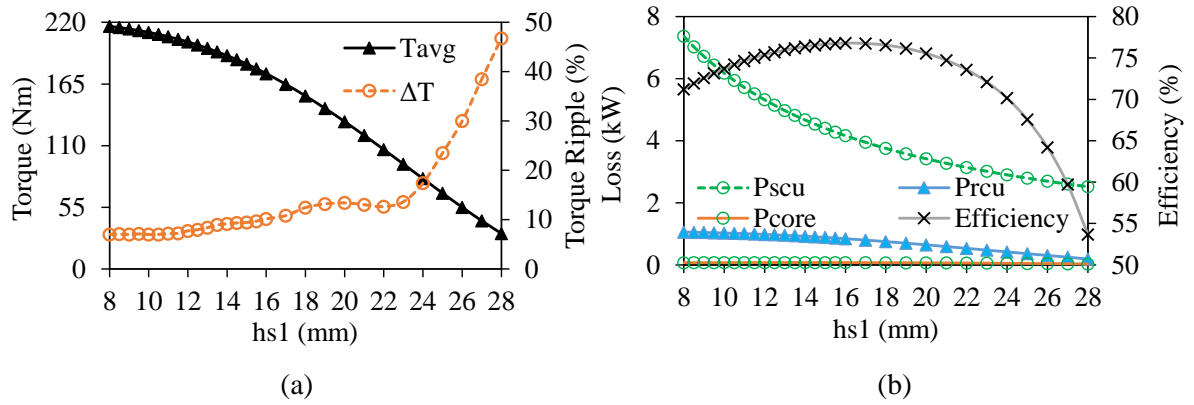


Fig. 6.67 Performance characteristics against h_{s1} : (a) average torque and torque ripple, and (b) power losses and efficiency.

6.5.2 Influence of Rotor Slot Geometric Parameters

In this part, the influence of the rotor slot parameters, illustrated in Fig. 6.59, on the bar current, torque, power losses, and efficiency will be investigated parametrically. Note that as conducted in the analyses of the influence of the stator slot geometric parameters, the individual effect of any rotor slot parameter is investigated by keeping the other parameters at their optimal value given in Appendix D.

A. Rotor Slot Opening Width b_{r0}

The influence of b_{r0} on the bar current, torque, power losses, and efficiency is illustrated in Fig. 6.68 and Fig. 6.69, respectively. Considering Fig. 6.60 and Fig. 6.61, it can be realized that b_{r0} has the same effect as b_{s0} . The influence of b_{r0} on the bar current waveform, power losses, and efficiency is insignificant. However, it has a considerable effect on the average torque and torque ripple as shown in Fig. 6.69(a).

B. Rotor Slot Width b_{r12}

The variation of bar current waveforms, bar current harmonics, and distortion level with respect to b_{r12} is shown in Fig. 6.70. As seen, even though the bar current waveform never becomes sinusoidal for any value of b_{r12} , it has a significant effect on the bar current harmonics. It is observed that even if b_{r12} takes its minimum value (the possible largest tooth body width), because of the high speed (950rpm) and high electric loading (250Apeak) operation conditions, the tooth body is saturated heavily. Therefore, under these conditions, the bar current waveform cannot be sinusoidal as shown in Chapter 5. The variation of the average torque, torque ripple, power losses, and efficiency is illustrated in Fig. 6.71. As seen in the figures, these characteristics are very sensitive to b_{r12} . The maximum torque, relatively low torque ripple, and maximum efficiency have been achieved at 4.35mm of b_{r12} .

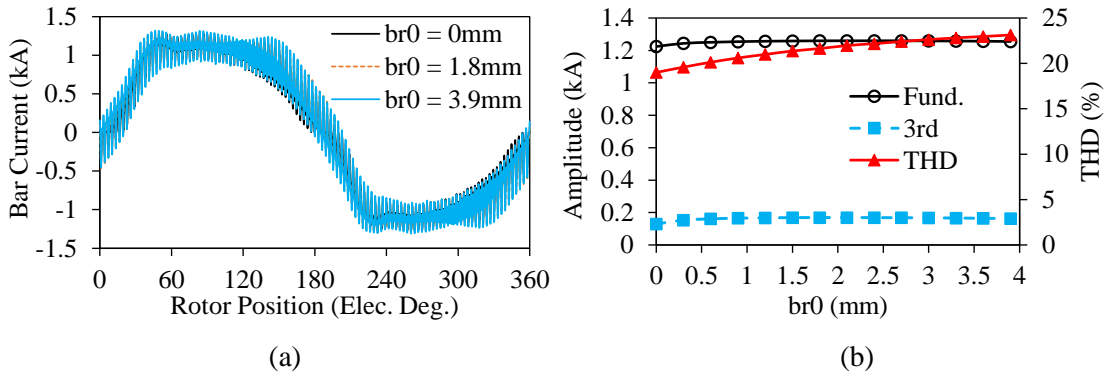


Fig. 6.68 Bar current for different b_{r0} : (a) waveform and (b) variation of harmonics and THD with respect to b_{r0} .

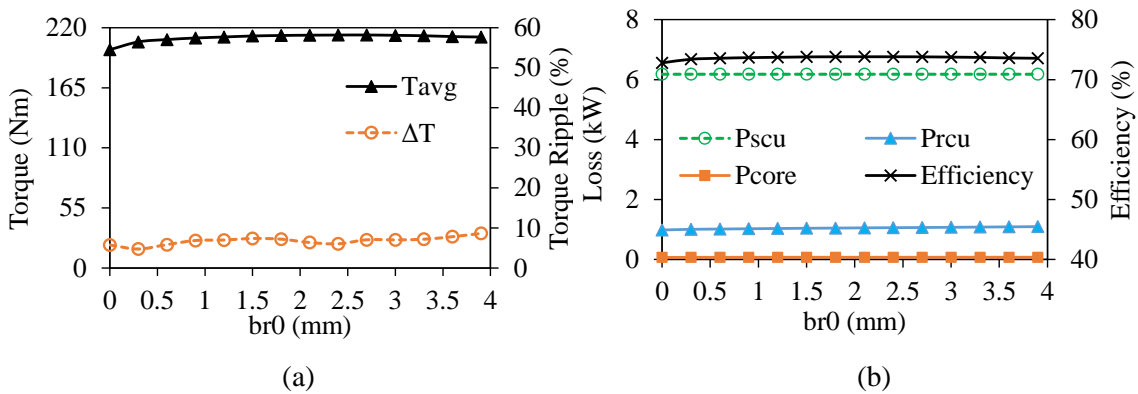


Fig. 6.69 Performance characteristics against b_{r0} : (a) average torque and torque ripple, and (b) power losses and efficiency.

C. Rotor Slot Opening Height h_{r0}

The influence of h_{r0} on the bar current waveform and variation of the bar current amplitude, the 3rd harmonic, and THD are shown in Fig. 6.72. As seen, the bar current waveform never becomes sinusoidal for any value of h_{r0} . The fundamental amplitude, the 3rd harmonic, and THD decrease until $h_{r0}=19\text{mm}$ and they dramatically increase after this value. The variation of the average torque, torque ripple, power losses, and efficiency is shown in Fig. 6.73. The larger the h_{r0} , the lower the average torque, the higher the torque ripple, the lower the bar copper loss, and the lower the efficiency. The reduction in the efficiency is due to remarkable reduction of the output power. In order not to sacrifice the average torque and efficiency, h_{r0} should be chosen as small as possible. From Fig. 6.70 to Fig. 6.73, it can be concluded that among the other rotor slot parameters, b_{r12} and h_{r0} are the most dominant parameters for the electromagnetic performance characteristics of the IM.

D. Rotor Slot Height h_{r1}

The effect of the rotor slot height parameter h_{r1} is investigated and the obtained results are illustrated in Fig. 6.74 and Fig. 6.75. As seen in the bar current waveform (see Fig. 6.74(a)), the rotor bar current waveform becomes non-sinusoidal for the values of h_{r1} lower than 30mm (see Fig. 6.74(b)) since the

3rd harmonic, which is responsible for the flat-topped curves as explained in [5-8], reduces sharply. As illustrated in Fig. 6.75, the influence of h_{r1} on T_{avg} , ΔT , P_{scu} , P_{rcu} , P_{core} , and efficiency is considerable. As can be realized, h_{r1} is the most dominant parameter for the bar current waveform of the IM among the other rotor slot parameters. The highest torque and efficiency can be obtained between 11-15mm of h_{r1} .

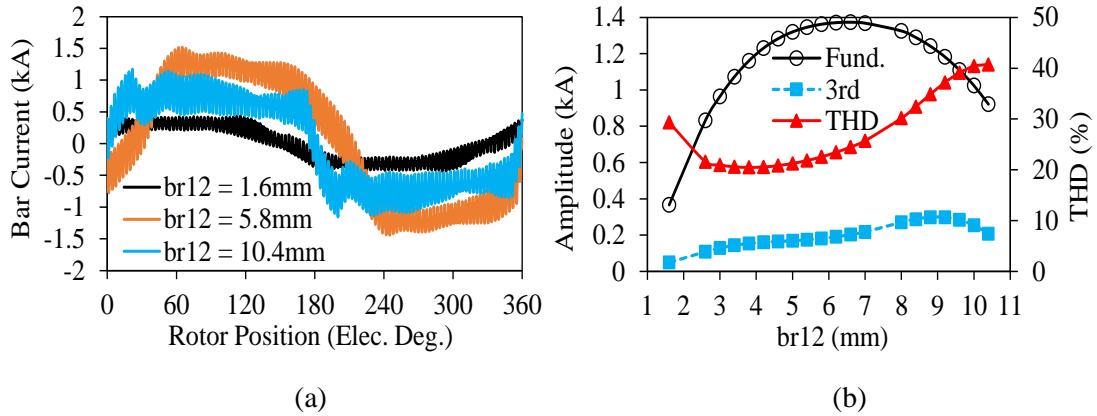


Fig. 6.70 Bar current for different b_{r12} : (a) waveform and (b) variation of harmonics and THD with respect to b_{r12} .

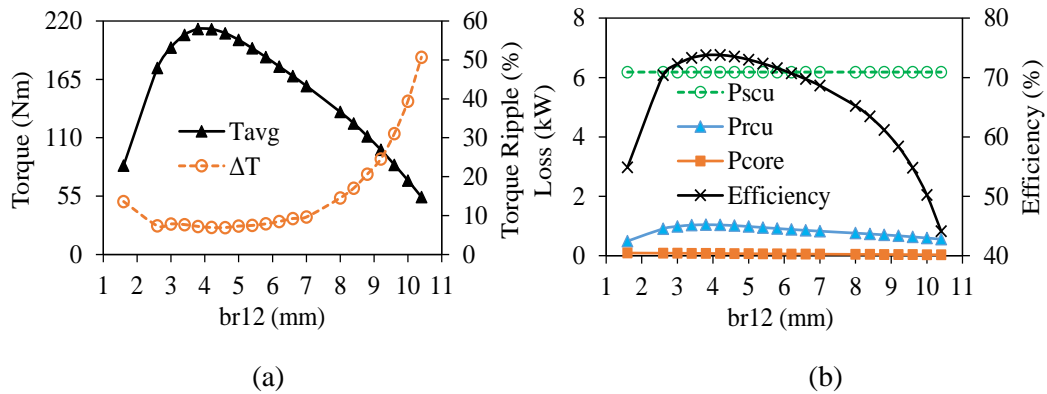


Fig. 6.71 Performance characteristics against b_{r12} : (a) average torque and torque ripple, and (b) power losses and efficiency.

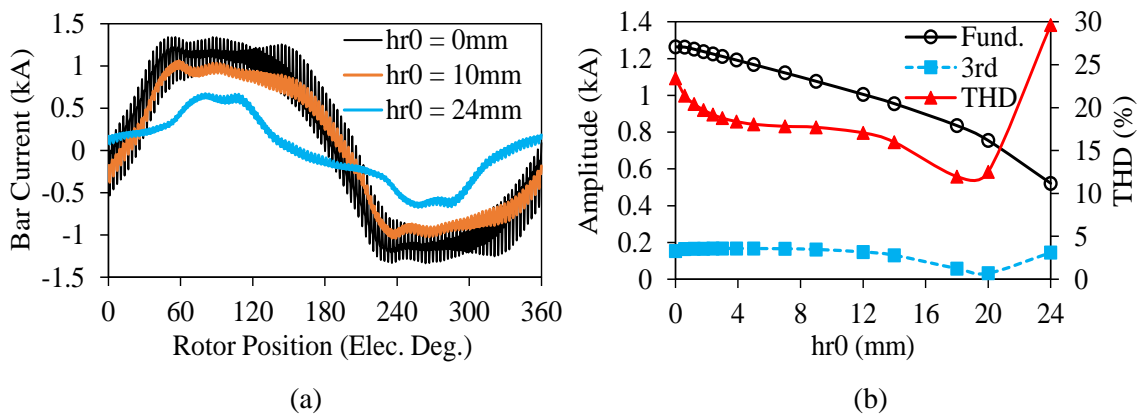


Fig. 6.72 Bar current for different h_{r0} : (a) waveform and (b) variation of harmonics and THD with respect to h_{r0} .

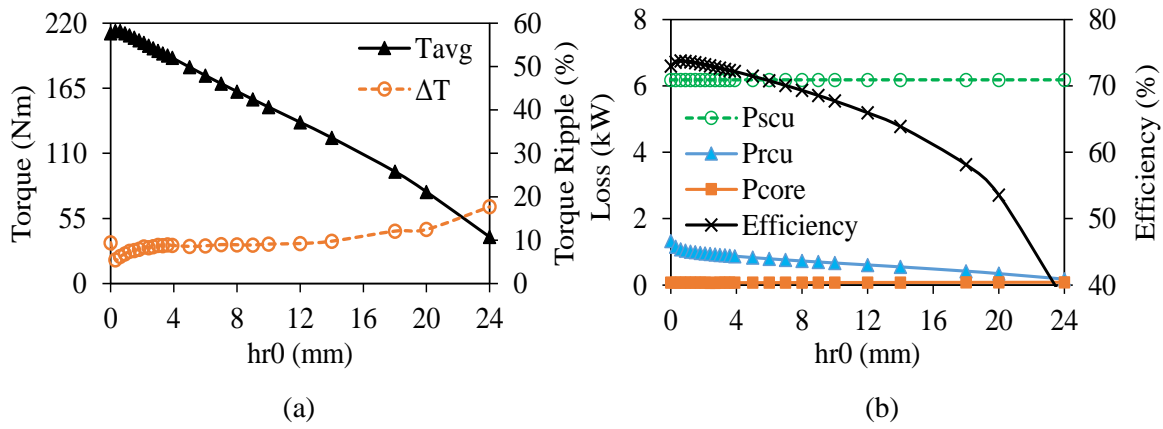


Fig. 6.73 Performance characteristics against h_{r0} : (a) average torque and torque ripple, and (b) power losses and efficiency.

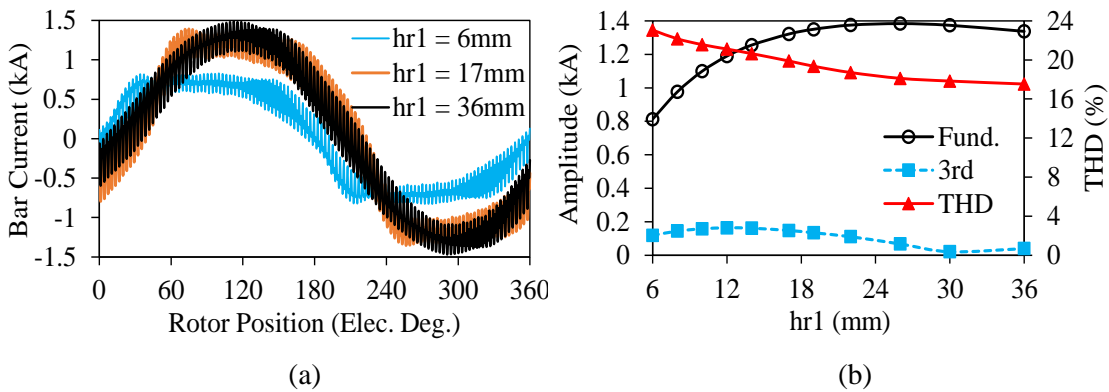


Fig. 6.74 Bar current for different h_{r1} : (a) waveform and (b) variation of harmonics and THD with respect to h_{r1} .

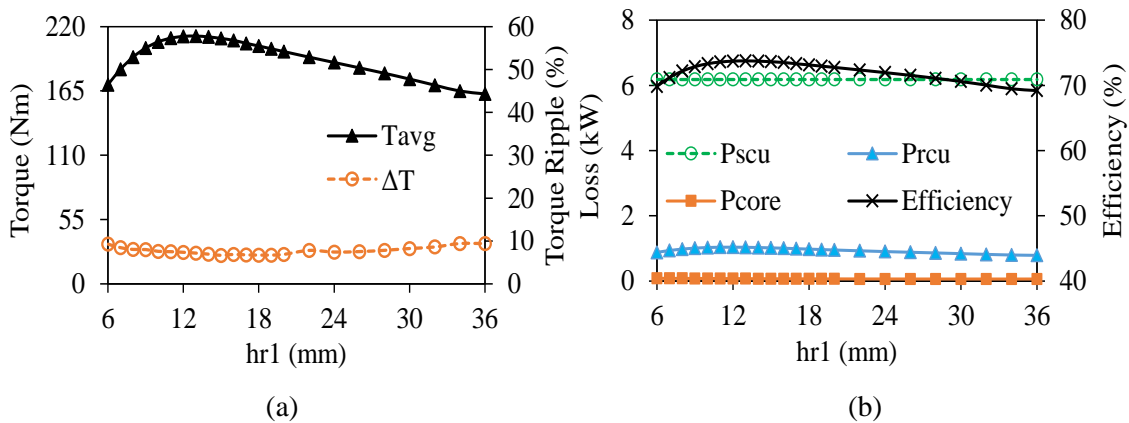


Fig. 6.75 Performance characteristics against h_{r1} : (a) average torque and torque ripple, and (b) power losses and efficiency.

6.5.3 Investigation of Magnetic Saturation

As explained in previously, the main reason behind the non-sinusoidal bar current waveform is the saturation of the rotor tooth body parts. Therefore, it can be predicted that the influence of b_{r12} on the bar current waveform should be significant. However, since the saturation level of the rotor tooth body

parts cannot be reduced sufficiently even if b_{r12} takes its minimum value, the bar current waveform is always non-sinusoidal for any value of b_{r12} parameter. Nevertheless, it is shown that the higher the b_{r12} , the higher the 3rd harmonic of the bar current. It has been revealed that among the investigated slot parameters, b_{s12} and h_{r1} have the most significant effect on the bar current waveform. As clearly seen from the reconstructed bar current waveforms (see Fig. 6.76), the bar current can become sinusoidal for some values of b_{s12} and h_{r1} . Therefore, the influence of b_{s12} and h_{r1} on the air-gap flux density, tooth body flux density, and saturation factor are investigated as follows.

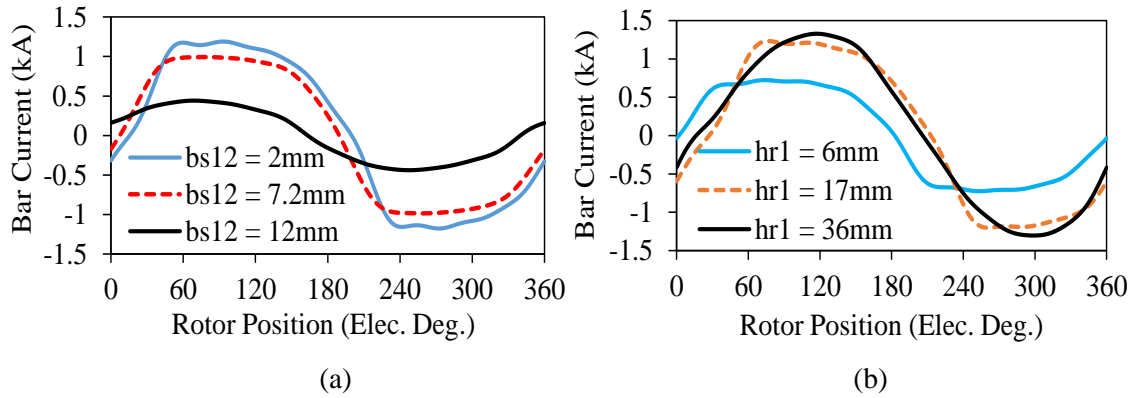


Fig. 6.76 Reconstructed bar current waveforms: (a) for various b_{s12} and (b) for various h_{r1} .

The air-gap flux density waveforms for various b_{s12} and h_{r1} and the variation of the dominant air-gap flux density harmonics are illustrated in Fig. 6.77 and Fig. 6.78. As seen in Fig. 6.77, as b_{s12} is increased, the fundamental amplitude of the air-gap flux density decreases because of increasing saturation level of the stator tooth parts (see Fig. 6.79). In the same manner, as shown in Fig. 6.78, as h_{r1} is increased, the fundamental amplitude of the air-gap flux density decreases because of increasing saturation level of the rotor yoke (see Fig. 6.80). As the slot parameters change, the air-gap flux density harmonics vary, some in a linear manner, others such as 3rd, 5th, 7th, etc. in a non-linear manner as seen in Fig. 6.77(b) and Fig. 6.78(b). The air-gap flux density distortion level does not change noticeably for b_{s12} , it increases remarkably as h_{r1} is increased.

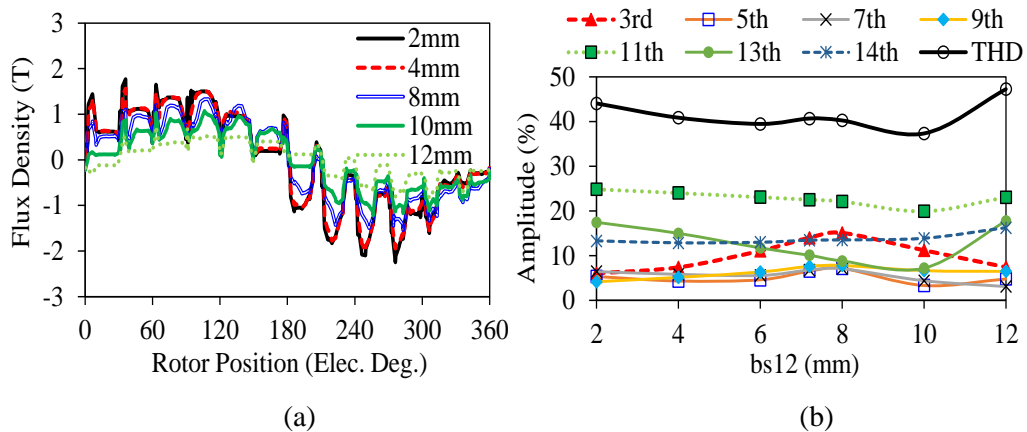


Fig. 6.77 Air-gap flux density for various b_{s12} : (a) waveform and (b) variation of the dominant harmonics and THD with respect to b_{s12} .

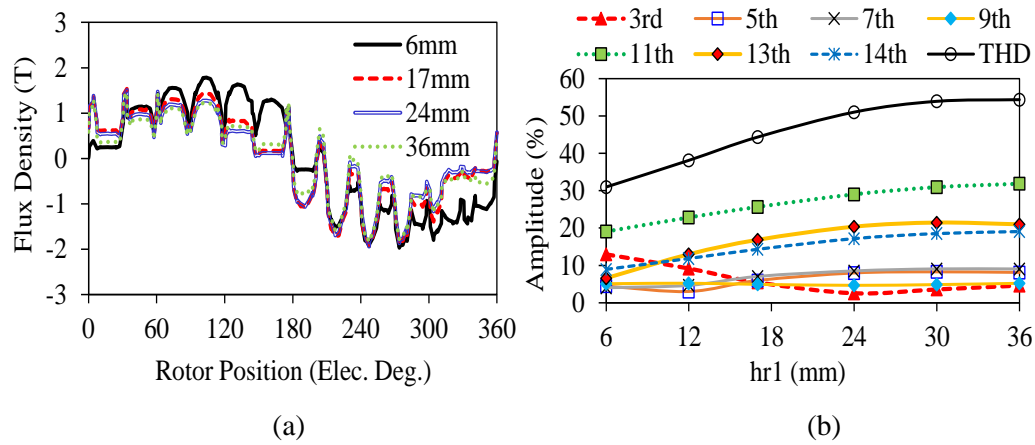


Fig. 6.78 Air-gap flux density for various h_{r1} : (a) waveform and (b) variation of the dominant harmonics and THD with respect to h_{r1} .

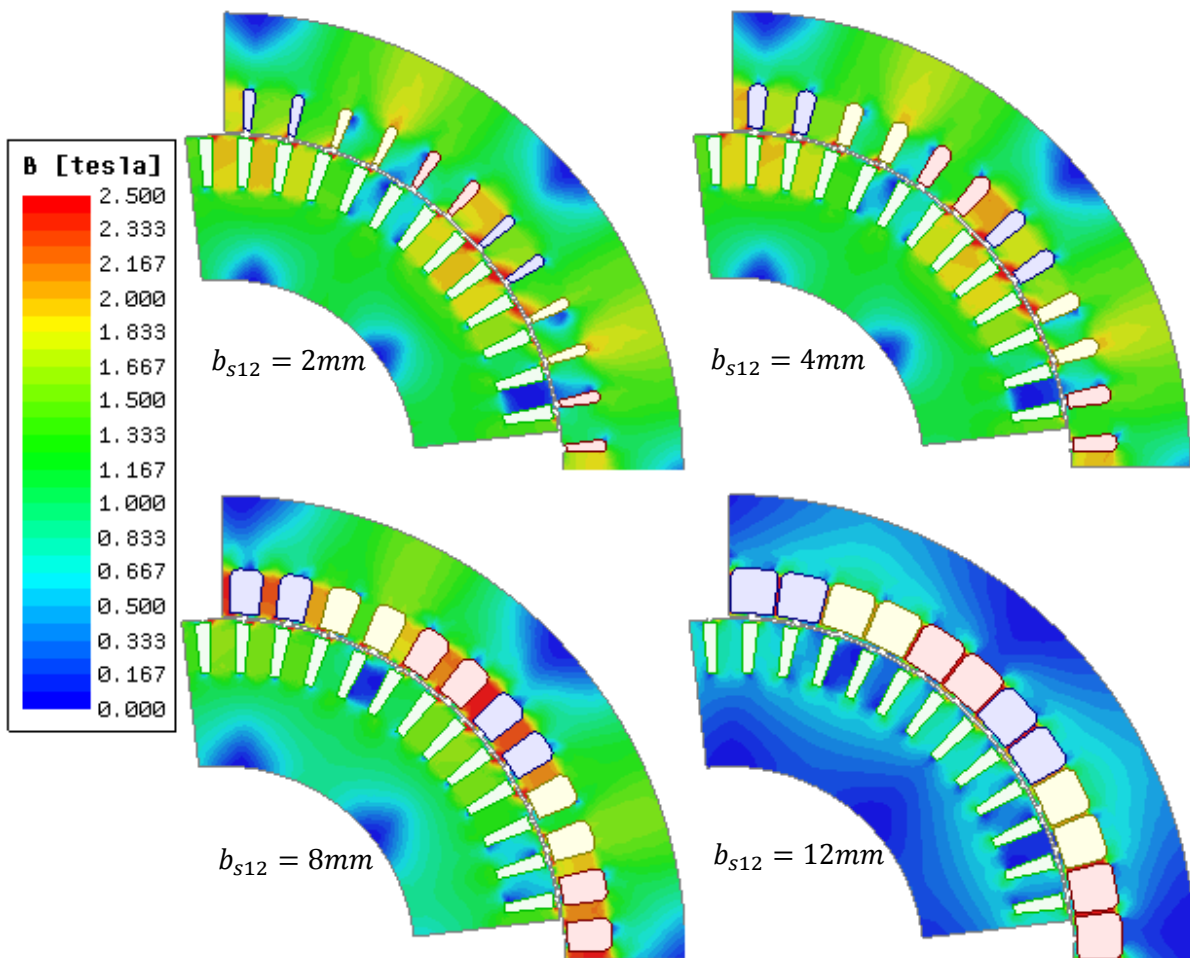


Fig. 6.79 Flux density distributions for various values of b_{s12} .

In Fig. 6.79, it can be observed that as b_{s12} is increased, the saturation level of the stator parts increases while the saturation level of the rotor parts decreases. On the other hand, as h_{r1} is increased, the saturation level of the stator parts and rotor tooth parts decreases while the saturation level of the rotor yoke part increases. If the stator tooth body part is saturated before the rotor tooth body part, i.e. the saturation level of the stator tooth body part is higher than that of the rotor tooth body part, then the

bar current waveform may become sinusoidal since the total flux level and consequently the saturation level of the rotor tooth body part is reduced. In the same manner, if the saturation level of the rotor yoke is saturated first, then again the bar current waveform may become sinusoidal as shown in Fig. 6.76. This phenomenon can be observed much clearer from Fig. 6.81. As seen in the figures, once the flux density of the rotor tooth body part is increased beyond the knee point of the core material BH-curve, the bar current waveform starts to take the form of non-sinusoidal wave (see Fig. 6.76). Therefore, it can be concluded that the critical width and height values of b_{s12} and h_{r1} are 10mm and 30mm, respectively.

As explained previously, there is a close relationship between the rotor tooth body flux density and the bar current waveforms. This close relationship can be observed from Fig. 6.76, Fig. 6.82, and Fig. 6.83. As seen in Fig. 6.82(a), as b_{s12} is increased, the rotor tooth body flux density waveform starts to change from sinusoidal to non-sinusoidal. As seen in Fig. 6.82(b), the most dominant harmonic order is the 3rd. After 8mm, the 3rd harmonic and consequently THD level decrease dramatically. In the same manner, as illustrated in Fig. 6.83(a), as h_{r1} is increased from 6mm to 36mm, the rotor tooth body flux density waveform changes from non-sinusoidal to sinusoidal due to the reduction of the tooth body saturation level. The reduction of the 3rd harmonic and hence the THD percentage stops at 30mm of h_{r1} as seen in Fig. 6.83(b).

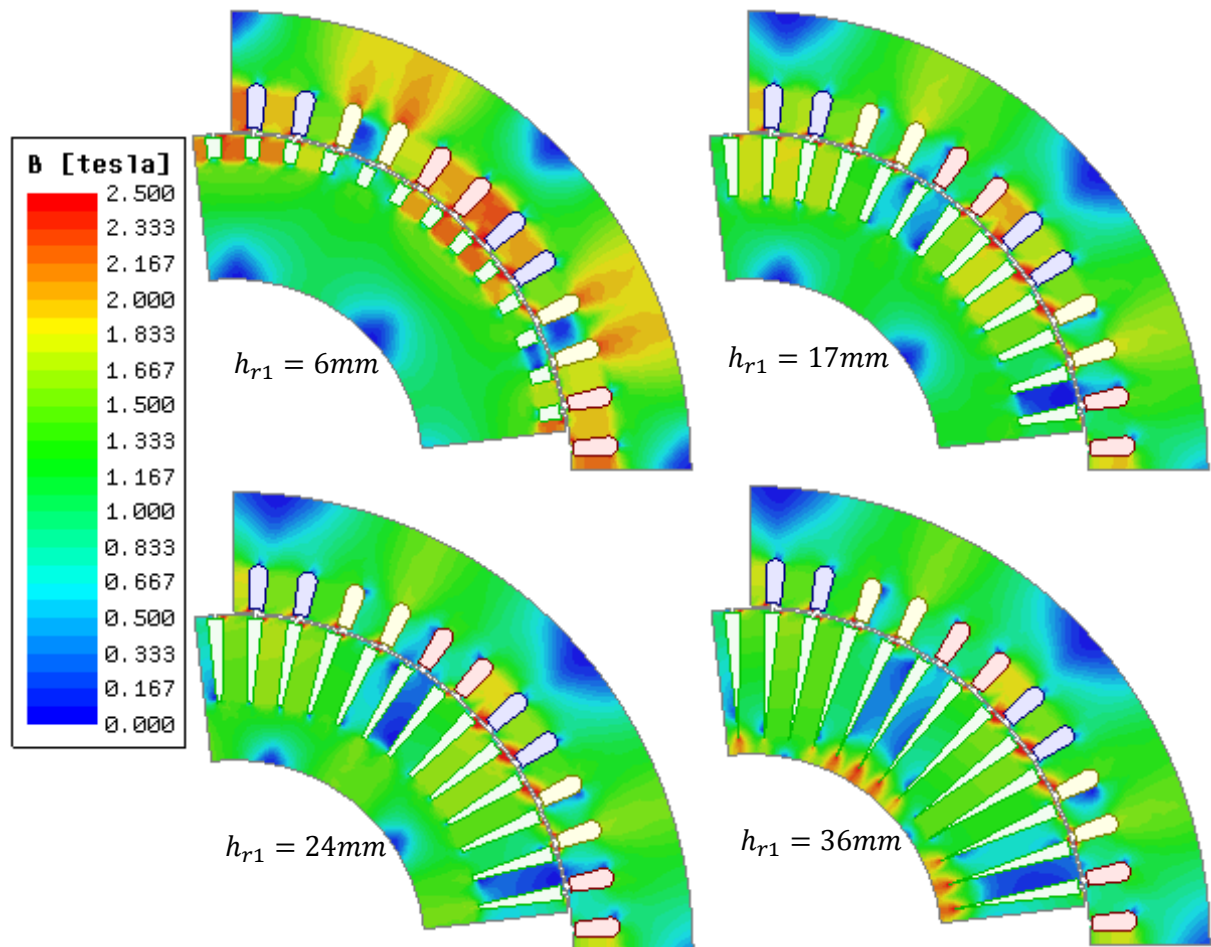


Fig. 6.80 Flux density distributions for different values of h_{r1} .

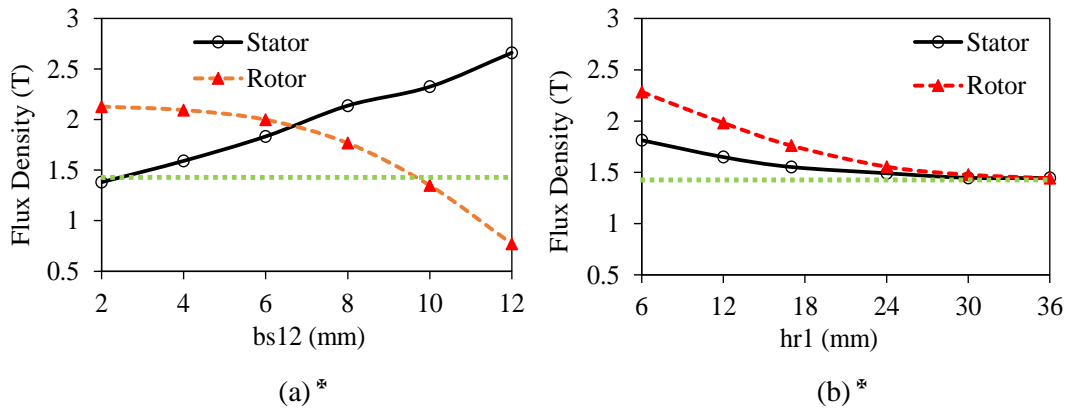


Fig. 6.81. Stator and rotor tooth body flux densities: (a) against b_{s12} and (b) against h_{r1} .

* The light green dots indicate the knee point of the BH-curve ($\sim 1.48\text{T}$).

To be able to reveal the level of the saturation at the stator and rotor parts analytically, the saturation factors are calculated and the variation of the stator and rotor saturation factors are illustrated in Fig. 6.84. Note that the details related with the calculation of the saturation factor has been given in Chapter 5 and Section 6.3. The saturation factor of the stator increases considerably as b_{s12} is increased whilst the saturation factor of the rotor decreases dramatically as seen in Fig. 6.84(a).

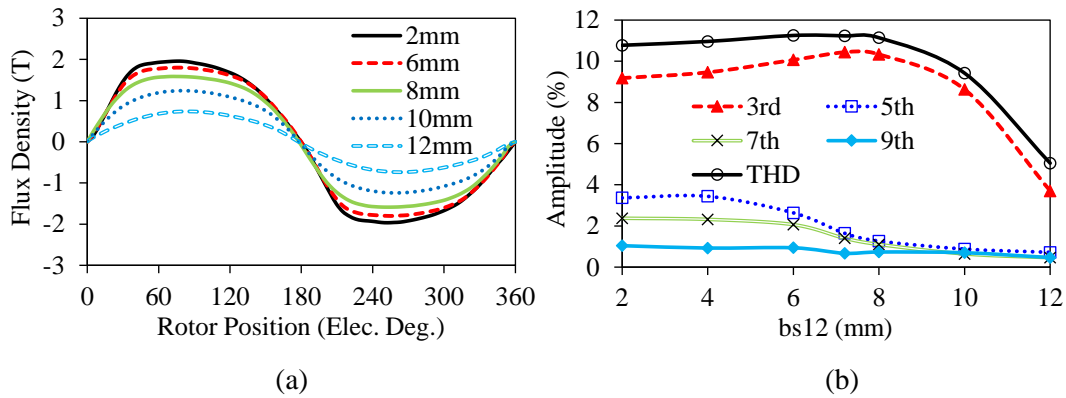


Fig. 6.82 Rotor tooth body flux density for various b_{s12} : (a) waveforms and (b) variation of the dominant flux density harmonics with respect to b_{s12} .

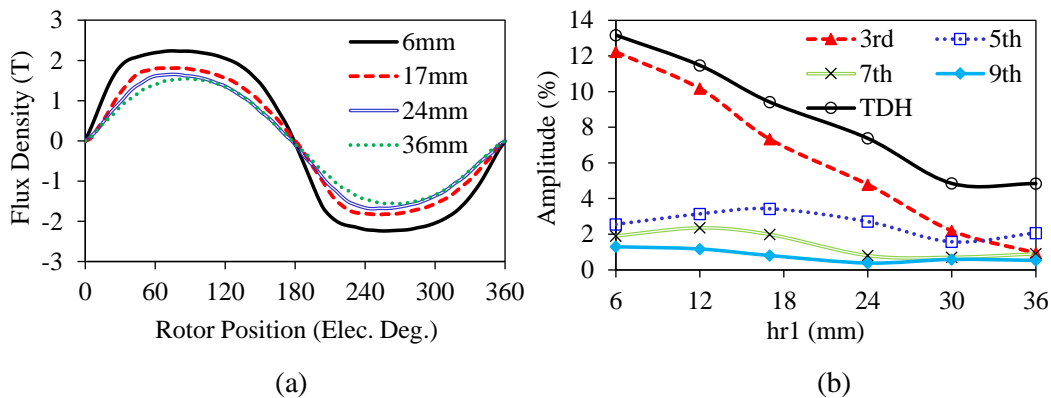


Fig. 6.83 Rotor tooth body flux density for various h_{r1} : (a) waveforms and (b) variation of the dominant flux density harmonics with respect to h_{r1} .

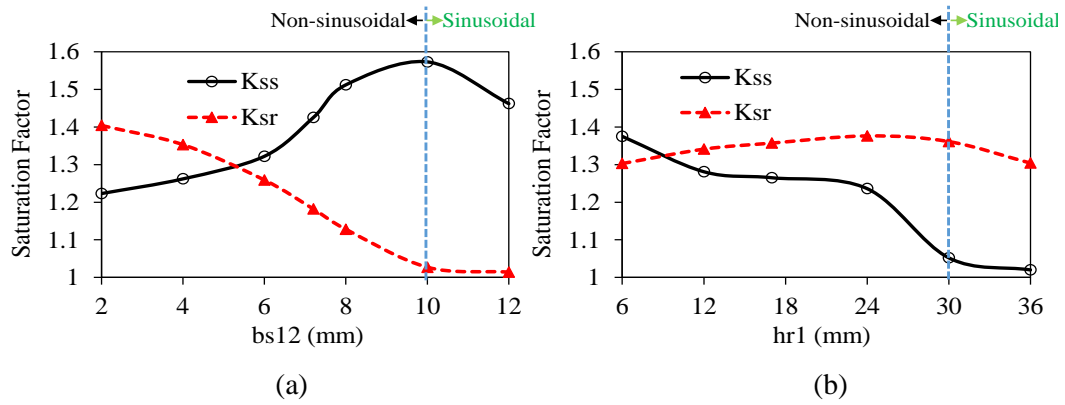


Fig. 6.84 Variations of stator and rotor saturation factors* with respect to (a) b_{s12} and (b) h_{r1} .

* K_{ss} : stator saturation factor; K_{sr} : rotor saturation factor.

On the other hand, the saturation factor of the stator decreases whilst the saturation factor of the rotor increases as h_{r1} increases as seen in Fig. 6.84(b). It can be realized that there has been notable saturation factor changes at the 10mm of b_{s12} and the 30mm of h_{r1} . These changes in the saturation factors indicate that the bar current waveforms become sinusoidal at these points. In addition, the waveforms retain sinusoidal for the larger values than those of the indicated values while they are non-sinusoidal for all the smaller values than those of the indicated values.

As evidenced by the magnetic analysis results, the verification of the reason behind the non-sinusoidal bar current phenomenon has been substantiated by different ways, i.e. variation of rotor tooth body flux density amplitudes with respect to stator slot width and rotor slot height parameters, rotor tooth flux density waveforms, and saturation factors of stator and rotor parts of the IM.

6.6 Rotor Skew

As well known, in order to improve the starting characteristics of grid connected IMs and reduce the torque ripple level, skewed rotors are employed [OST86], [DOR95], [NAU97], [MCC98], [WAN16]. In this section, the influence of the rotor skew angle on the bar current waveform and performance characteristics are investigated for IM with 48S/52R/8P designed by using the same operating and geometric specifications as the Toyota Prius 2010 IPM machine. The effect of rotor skew angle is investigated by performing 2-D FEA under steady-state operation condition. While investigating the influence of the skew angle, all other operating and geometric parameters are kept at their optimal values.

6.6.1 Rotor Skew Angle

In order to investigate the influence of rotor skew angle on the bar current waveform and performance, several parametric analyses have been conducted with different skew angles changing from 0° to 90° . The transient solver of the time-stepping, non-linear, 2-D FEA program can take into account the effects of skewed rotor slots by using a single- or multi-sliced model. However, since the 2-D models cannot account for the axial flux, the solver uses only the approximations for the calculation

of the magnetic field in the skewed slot modes. Therefore, the presented results in this section has been calculated by neglecting the 3-D effects such as end-effects, axial flux effects, etc. In addition, only single-sliced rotor model has been used in this thesis. Skewing of the rotor slots is illustrated in Fig. 6.85. Note that since the axial slots turn into tangential slots, the 90° skewing is practically not possible. It has been calculated theoretically for only completeness purpose.

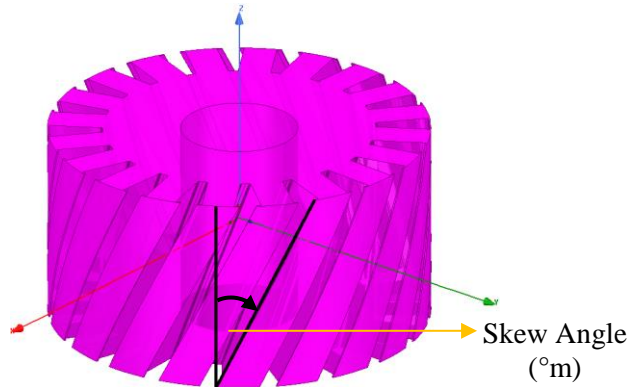


Fig. 6.85 Rotor skewing and skew angle in mechanical degree (°m).

6.6.2 Influence of Rotor Skew on Performance Characteristics

The air-gap flux density waveforms for various rotor skew angle and variation of the air-gap flux density dominant harmonics and THD rate are shown in Fig. 6.86.

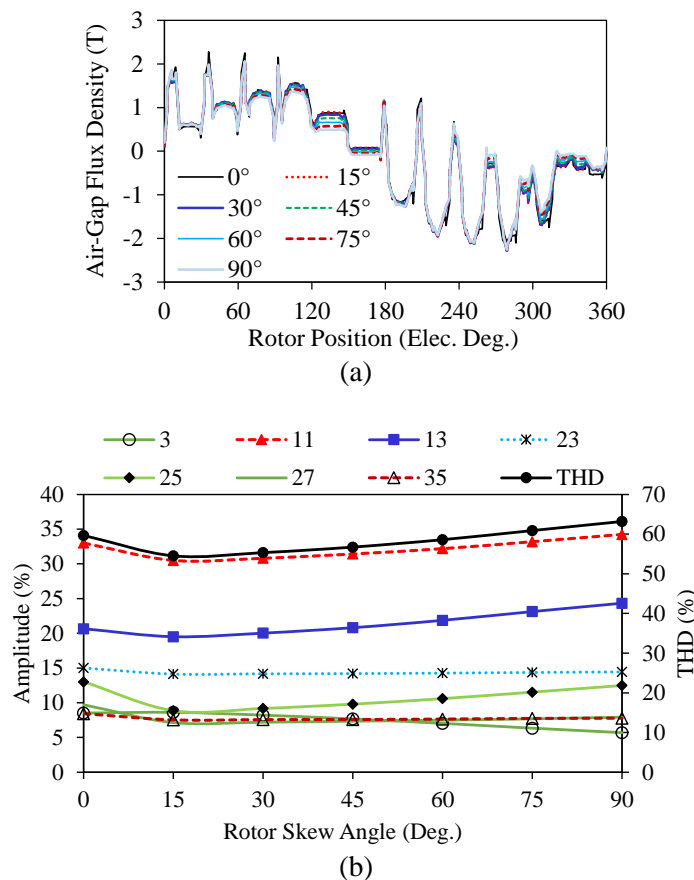
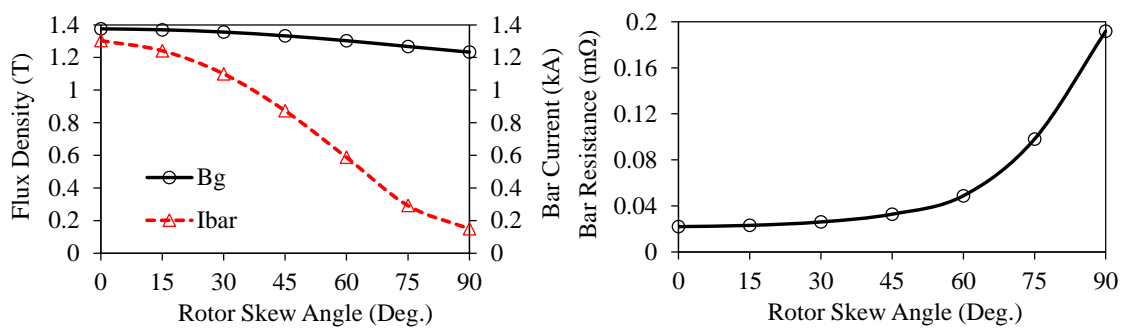


Fig. 6.86 Air-gap flux density for various skew angle (a) waveform and (b) variation of the dominant air-gap flux density harmonics and THD with respect to skew angle.

As seen, the air-gap flux density waveform is highly distorted because of the combined effect of the slotting and winding MMF harmonics. The influence of the skew angle on the air-gap flux density harmonics is considerable. It can be seen that the minimum air-gap flux density THD is obtained at 15° of the skew angle. The variations of the air-gap flux density B_g , bar current fundamental amplitude I_{bar} and bar resistance are illustrated in Fig. 6.87. As seen, although the air-gap flux density amplitude is reduced slightly, the bar current amplitude is reduced dramatically with increasing skew angle. The one of the reasons for this is that the higher the skew angle, the lower the interaction between the conductor bars and air-gap flux (armature reaction) and consequently the lower the induced EMF on the bar conductors. Another reason is that the bar resistance increases as the skew angle is increased as shown in Fig. 6.87(b). This phenomenon can be observed from Fig. 6.88. It is obvious that the higher the rotor skew angle, the lower the flux density in both stator and rotor parts of the IM.



(a) Air-gap flux density and bar current variation

(b) Bar resistance variation

Fig. 6.87 Air-gap flux density B_g , bar current amplitude I_{bar} and bar resistance against skew angle.

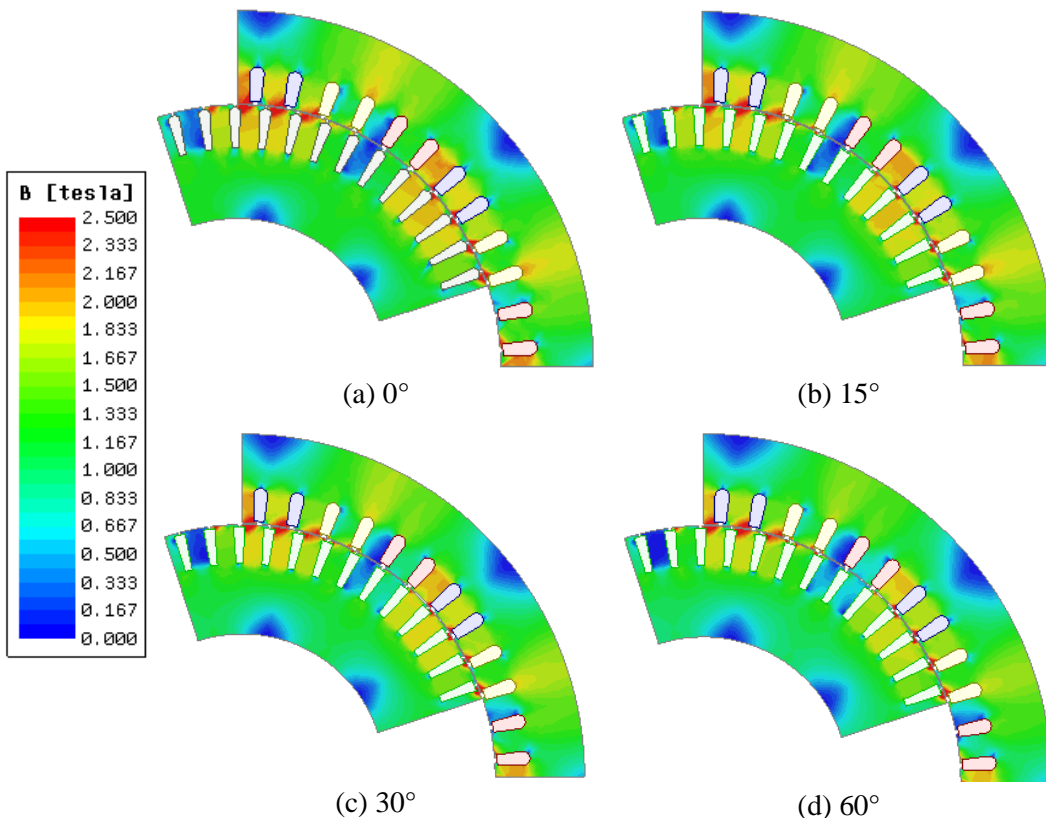


Fig. 6.88 Flux density distributions for different skew angles.

The variation of the rotor bar current waveform with respect to skew angle is shown in Fig. 6.89. As clearly seen, the skew angle has a significant effect on the bar current low- and high-frequency harmonics (see Fig. 6.90). Each skew angle affects the different harmonic order of the bar current. For instance, while the 15° of the skew angle is reduced the high order harmonics, the skew angle of 75° is increased the high order harmonics in the bar current. In addition, as seen in Fig. 6.91, the low-frequency harmonics and the THD level of the bar current became relatively low at the 30° of the skew angle. It can be observed that the higher the skew angle, the lower the fundamental amplitude of the bar current (see also Fig. 6.87).

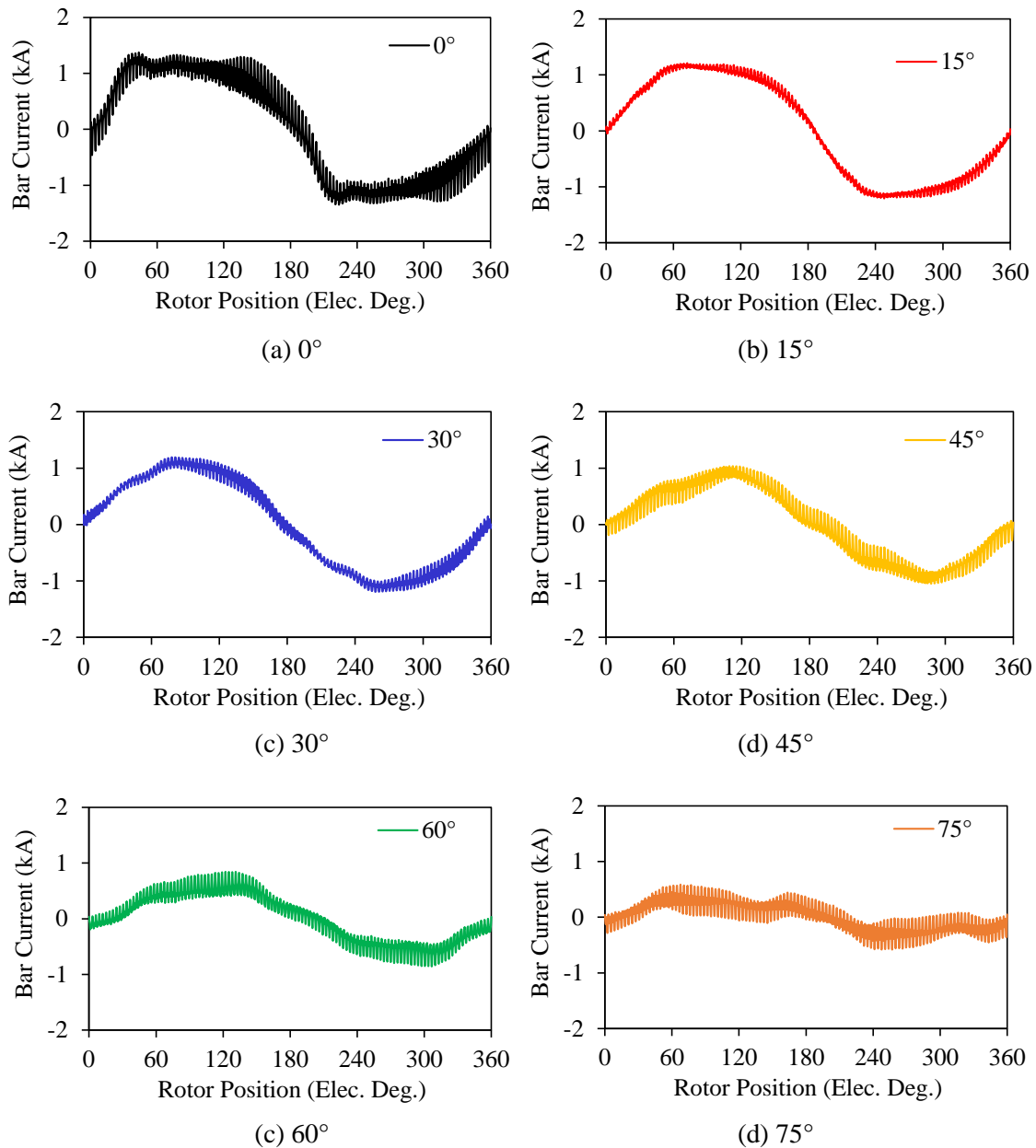


Fig. 6.89 Rotor bar current waveforms for various rotor skew angles.

The 3rd harmonic, which depends on the level of the magnetic saturation, becomes relatively low at the 15° and 30° of the skew angle. It can be concluded that the 30°, corresponding to 4 stator slot pitches, is the optimal skew angle in terms of the THD of the bar current. The variation of the average torque,

torque ripple, rotor bar copper loss, and efficiency with respect to skew angle is shown in Fig. 6.92. As seen in the figure, the average torque reduces slightly whilst the torque ripple reduces remarkably with the increased skew angle. On the other hand, the efficiency reduces slightly because of increasing rotor bar copper loss. It can be concluded that depending on the skew angle, the bar current harmonic distortion and torque ripple do not change linearly. In order to minimize the distortion level and torque ripple, an optimal skew angle should be calculated.

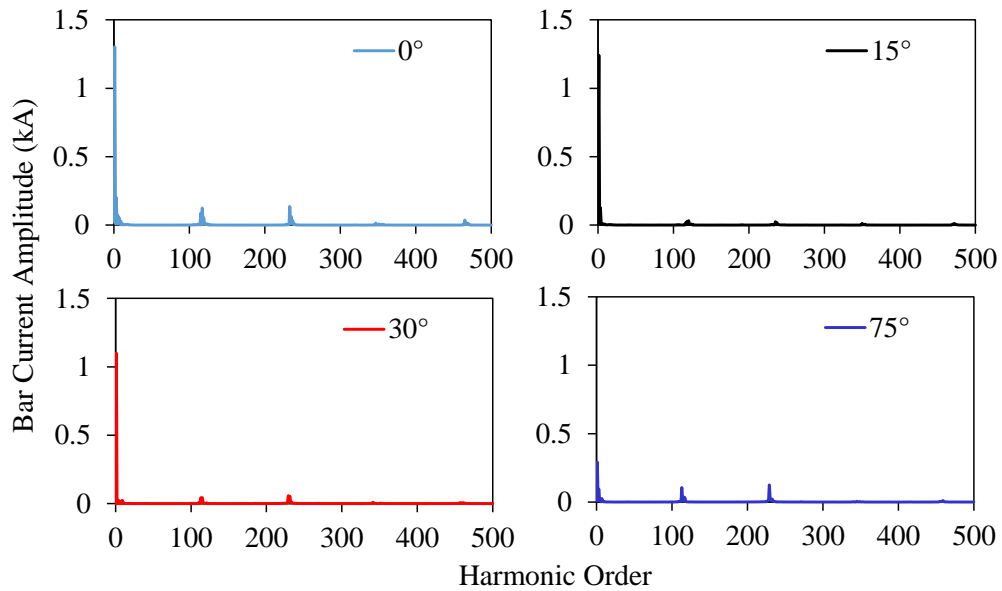


Fig. 6.90 Harmonic spectra of bar current for various rotor skew angle.

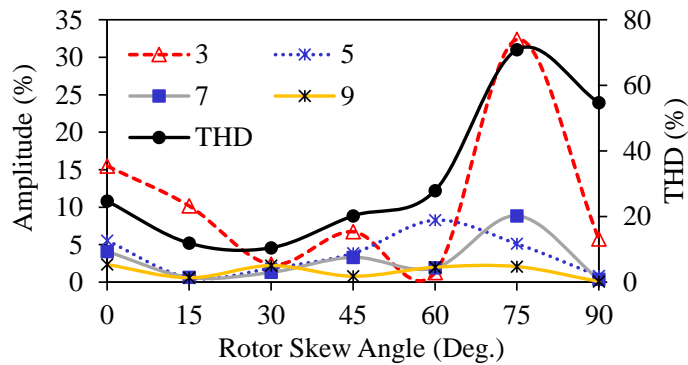


Fig. 6.91 Variation of dominant bar current harmonics and THD with respect to skew angle.

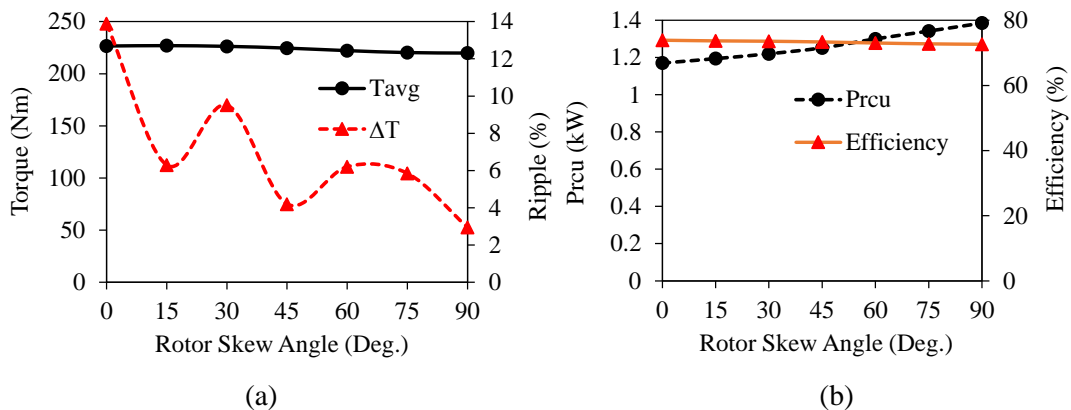


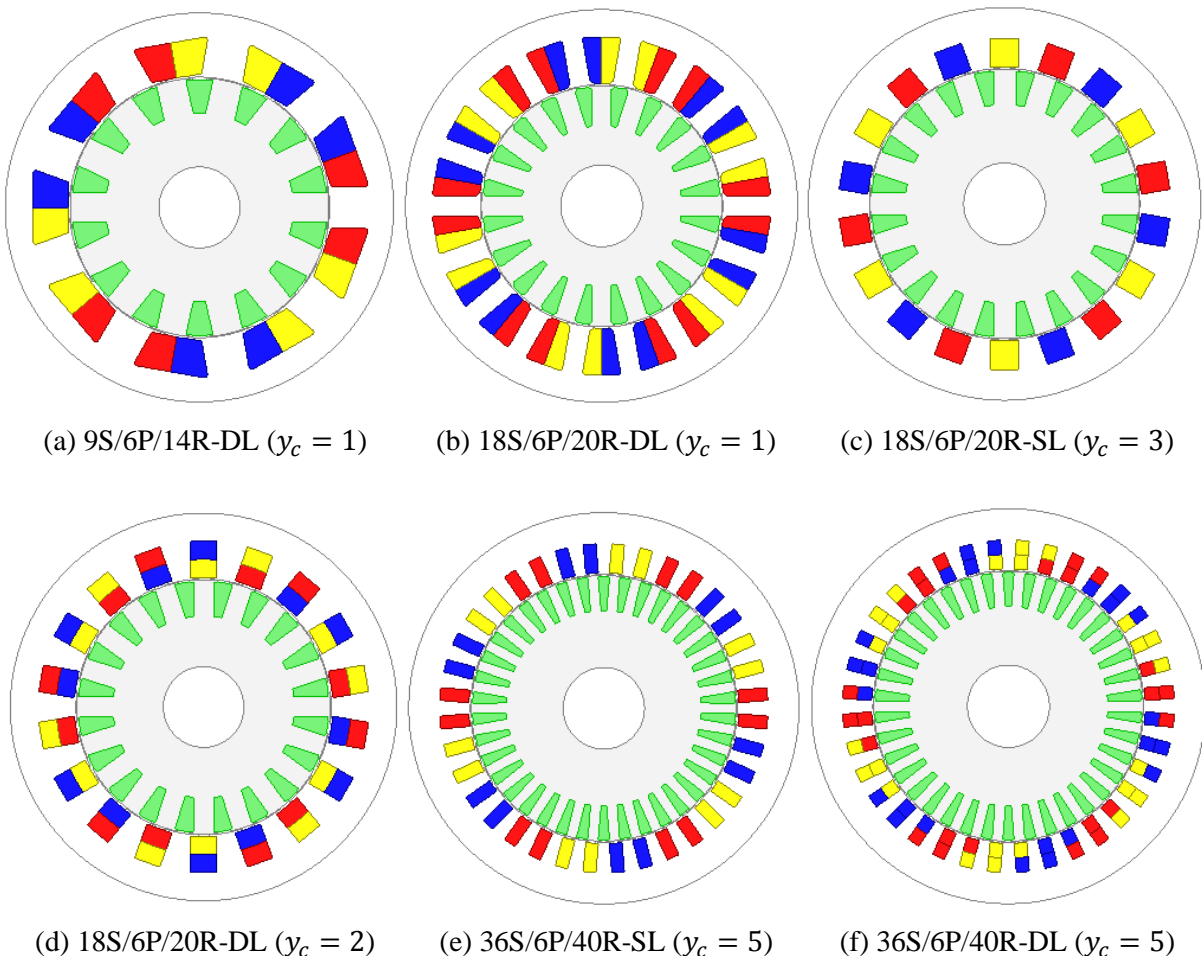
Fig. 6.92 Torque, torque ripple (a), and bar copper loss and efficiency (b) against skew angle.

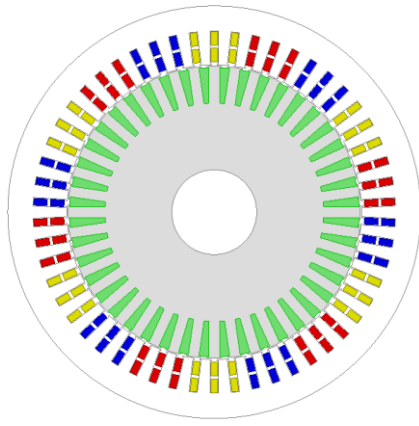
6.7 Stator Coil Pitch

In this section, influences of stator coil pitch on the electromagnetic performance of squirrel-cage IMs, designed by using the Value's specifications (see Chapter 2 and Appendix C), are investigated. Various coil pitches varying from 1 to 9 are studied considering the number of winding layers and slot/pole number combinations. Note that all the considered IMs have been globally optimized for maximum torque and minimum power losses by keeping the outer diameter and stack length fixed. In addition, optimal rotor slot number for $q \geq 1$ combinations have been estimated by (6.9). In addition, the optimal rotor slot number is estimated parametrically as for the $q = 0.5$ combination.

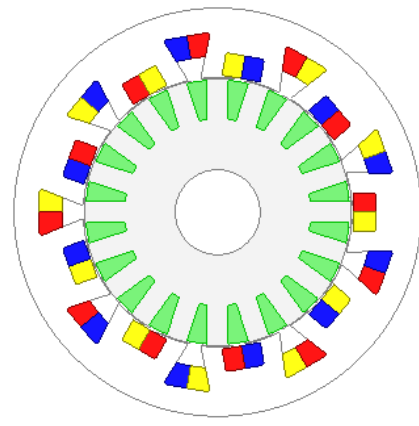
6.7.1 Design of IMs with Various Coil Pitches

In order to investigate the influence of coil pitch y_c on the bar current waveform and key performance characteristics, different S/R/P combinations and winding layers, namely single-layer SL and double-layer DL 2-D, has been studied. In addition, newly developed winding topology has also been investigated together with the conventional winding topologies. The 2-D cross-sections of the designed IMs are illustrated in Fig. 6.93. Note that the key specifications of the considered IMs are given in Table 2.4 (Chapter 2). It can be realized that the winding layout of the advanced IM is similar to the conventional IM with the 18S/6P/20R-DL ($y_c = 2$).





(g) 54S/6P/44R-DL ($\gamma_c = 9$)



(h) 18S/6P/20R-DL ($\gamma_c = 2$ -ANW)

Fig. 6.93 2-D view of designed IMs with various slot/pole numbers and winding layouts.

The MMF harmonic spectra of the considered winding topologies are illustrated in Fig. 6.94. As seen, the 54S/6P-DL configuration has the least MMF whilst the 9S/6P-DL configuration has the most. In addition, although the 18S configurations have different fundamental MMF amplitudes, their THD levels are the same. Considering Fig. 6.94, it can be predicted that the bar current distortion level of the 9S/6P-DL will be the highest whilst the 54S/6P-DL will be the lowest. Consequently, the rotor bar copper losses of the 9S/6P-DL will be the maximum whilst as for the 54S/6P-DL it will be the lowest. In addition, as seen Fig. 6.94, the THD level of the double-layer configuration is lower than that of its single-layer counterpart.

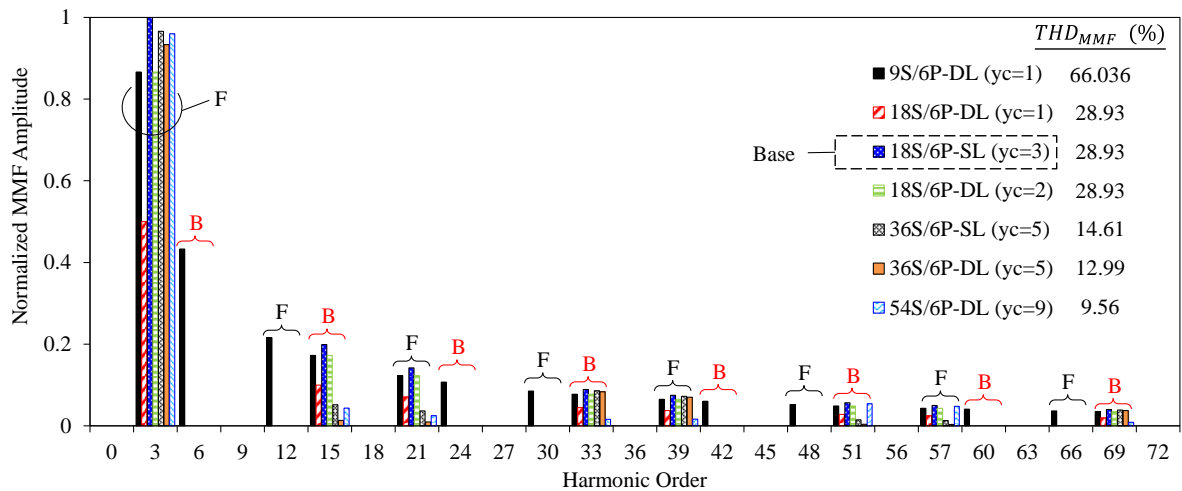


Fig. 6.94 Comparison of normalized MMF harmonics according to 18S/6P-SL and the MMF THDs.

6.7.2 Influence of Stator Coil Pitch on Performance Characteristics

The bar current waveforms for the considered IMs having different winding configurations are illustrated in Fig. 6.95. It is obvious that all the combinations have non-sinusoidal bar current waveform and all contain higher order harmonics. However, the amplitudes of these higher order harmonics are the minimum for the 36S/6P-DL IM having 5-slot pitch whilst it is maximum for the 9S/6P-DL IM

having 1-slot pitch. It is clear that, all rotor bar current waveforms are non-sinusoidal. As explained in Chapter 5, depending on the saturation level of rotor tooth body parts, the rotor bar current waveform becomes non-sinusoidal. Therefore, as illustrated in Fig. 6.98, the 9S/6P-DL IM has the highest flux density in the rotor tooth body part whilst the 54S/6P-DL has the minimum.

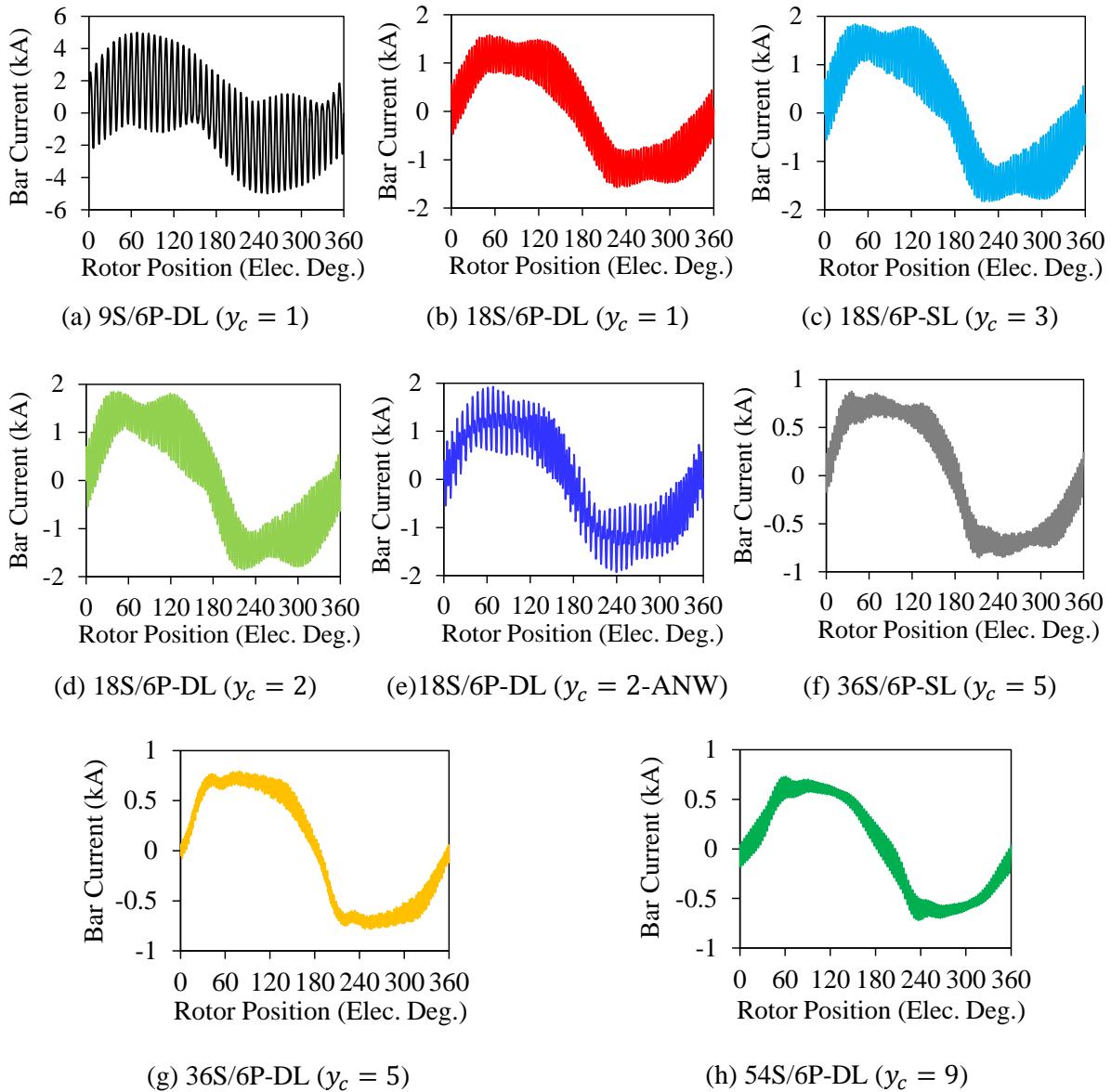


Fig. 6.95 Comparison of bar current waveforms.

The harmonic spectra of the bar currents showing the high-order and low-order harmonics are illustrated in Fig. 6.96 and Fig. 6.97, respectively. As seen in Fig. 6.96(a), the fundamental bar current harmonic amplitude is lower than that of the high-order harmonic. Therefore, as seen in Fig. 6.97, its distortion level is the highest one. As explained before, these harmonics, originated from the winding MMF harmonics, are induced in the bars. The amplitudes of these high order harmonics have been reduced as the stator coil pitch is increased. Therefore, it can be noticed that the bar current THD levels of the 36S combinations are almost 1/2 and 1/6 of the 18S and 9S combinations, respectively. As predicted previously, this highly distorted bar current causes a significant increase in the bar copper loss

as given in Table 6.4. In addition, as the coil pitch is increased, the magnitude of the low- and high-order harmonics are diminished to minimum. Moreover, the IMs designed with double-layer winding configurations have lower bar current distortion level than that of their single-layer winding counterparts.

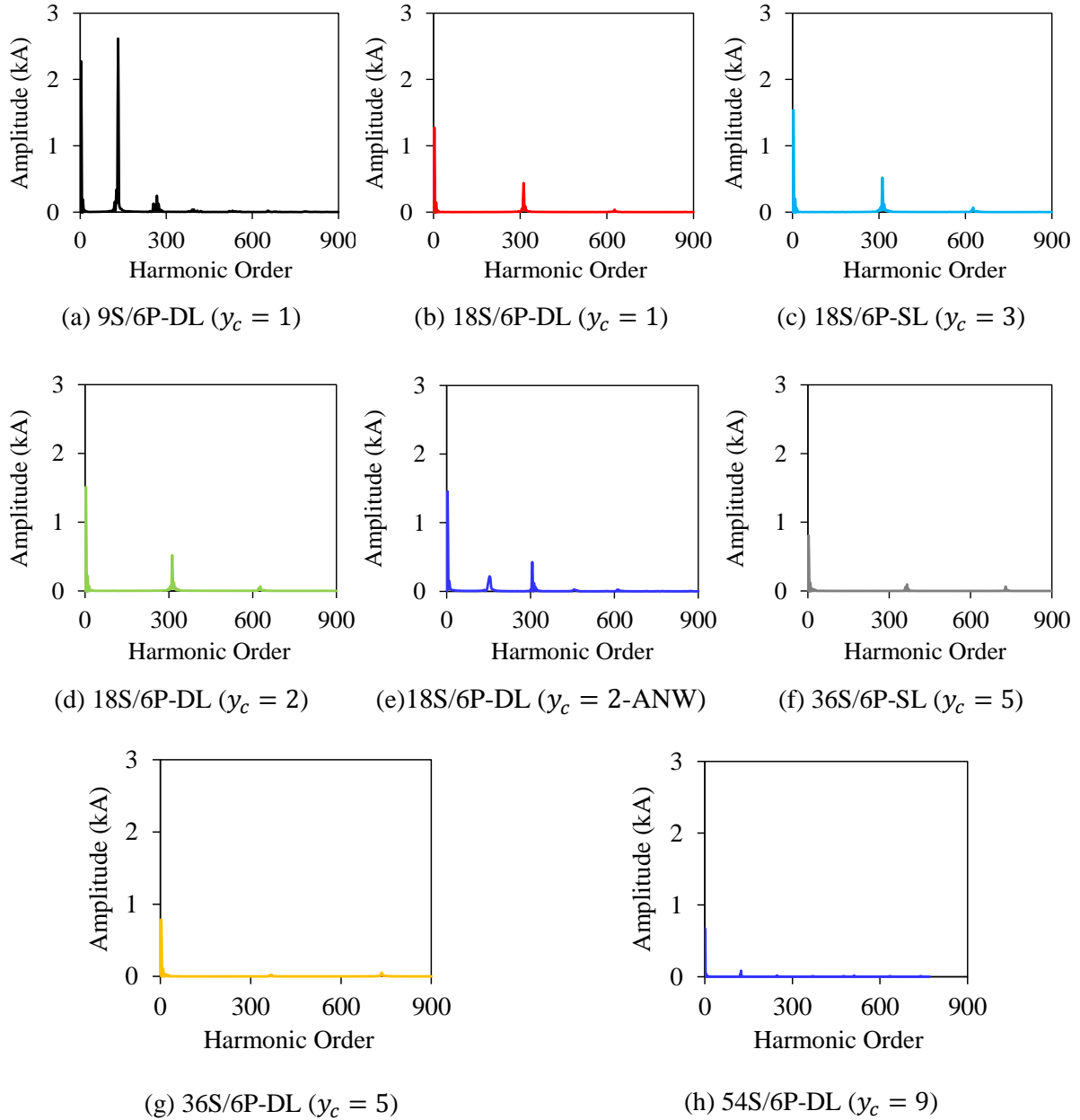


Fig. 6.96 Comparison of bar current harmonic spectra.

The key electromagnetic performance characteristics, including fundamental winding factor k_{w1} , total axial length l_a , average torque T , torque ripple ΔT , stator copper losses in the slots $P_{Scu.in}$, stator copper losses in the end-windings $P_{Scu.end}$, total stator copper loss P_{Scu} , rotor bar copper loss P_{Rcu} , total core loss P_C , output power P_{out} , and efficiency η , are listed Table 6.4 for the IMs designed with various coil pitches. As seen, the overall performance characteristics of IMs with $y_c = 5$ are the

best whilst IMs with $y_c = 1$ winding configurations are the worst. As expected, the higher the fundamental winding factor, the higher the average torque.

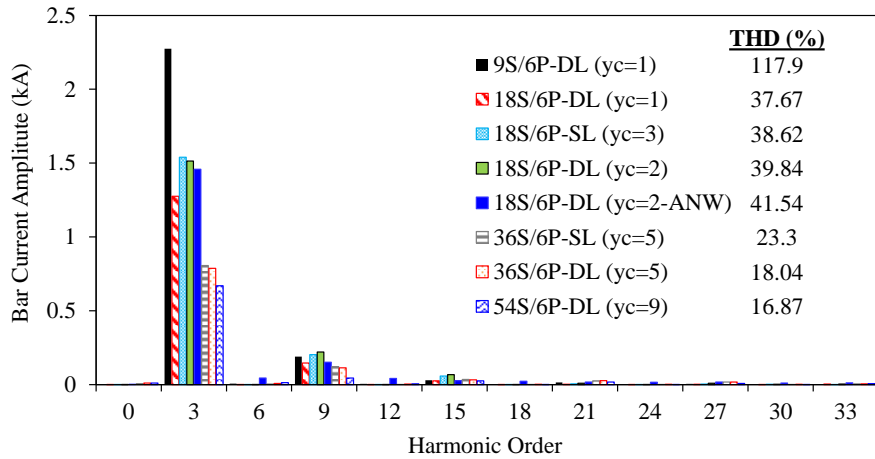


Fig. 6.97 Comparison of the bar current low-order harmonics and bar current THDs.

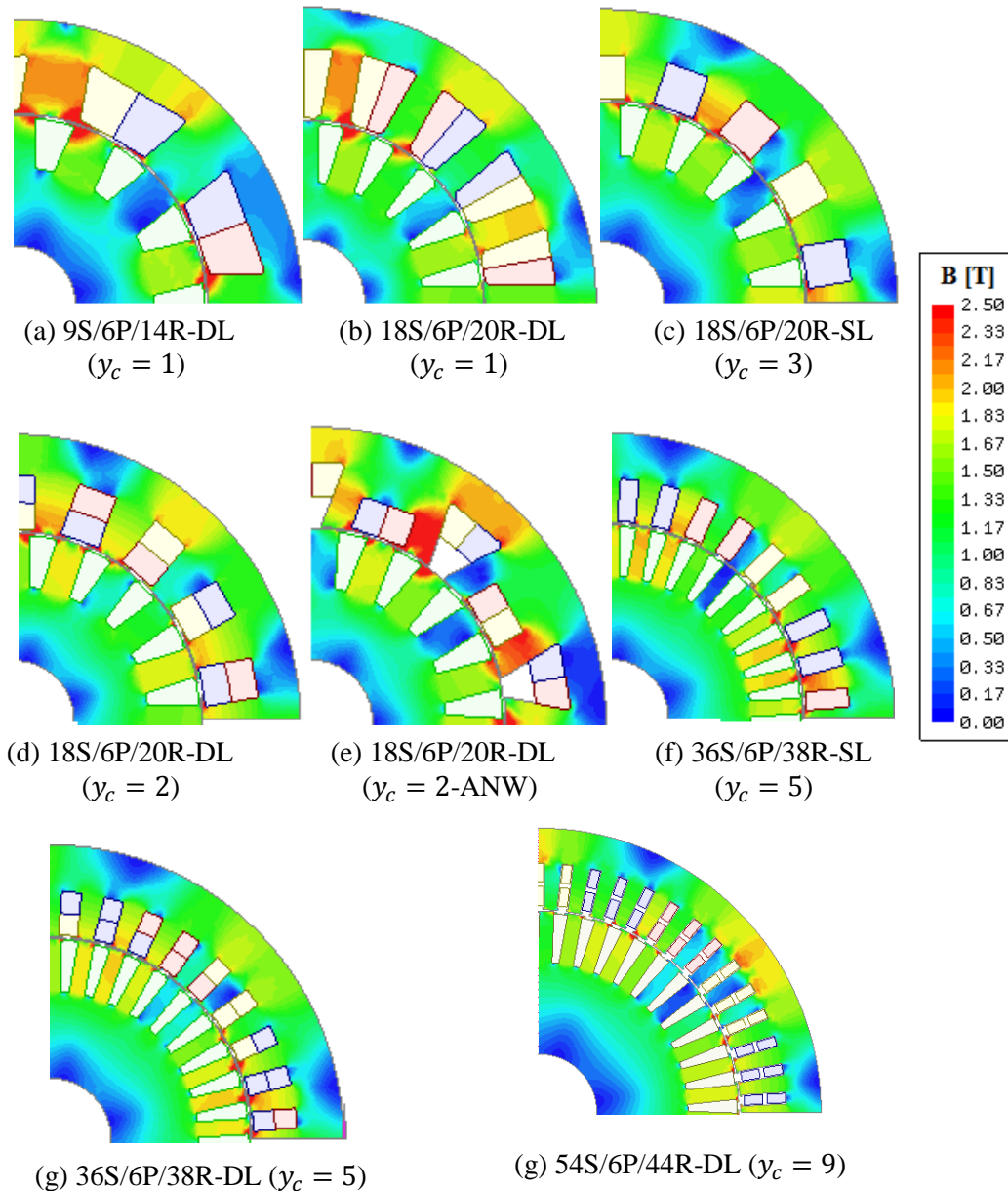


Fig. 6.98 Flux line density distributions of IMs with various winding topologies.

Even though, more number of turns per phase has been used in order to tolerate the low winding, comparable torque cannot be achieved for $y_c = 1$ winding configurations because of the significantly high leakage flux and small split ratio. In addition, because of the more number of turn requirements of the $y_c = 1$ winding configurations, the more stator copper losses are obtained. As seen in Table 6.4, since the coil pitch of 54S/6P combination is 1.8 times longer than that of the 36S/6P combinations, its P_{scu_end} is also ~ 1.8 times higher. Moreover, as predicted, because of the very high MMF harmonics induced in the bar current, the bar copper losses of the IMs designed with $y_c = 1$ winding configurations are significantly high. Thus, the efficiency of the IMs designed with $y_c = 1$ winding configurations are relatively low. Furthermore, it has been shown that the higher the coil pitch, the lower the torque ripple rate. The performances of the IMs designed with $y_c = 2$ winding configurations are between the IMs designed with $y_c = 1$ and $y_c = 5$. On the other hand, it has been revealed that the IMs designed with double-layer windings instead of single-layer windings have lower power losses, especially they have lower rotor bar copper losses because of the lower MMF harmonics. It can be also seen that thanks to the newly developed NW topology 27.1% shorter machine with 3.2% and 3.03% high torque and efficiency is obtained respectively, when compared to its conventional counterpart (18S/6P-DL).

Table 6.4 Performance comparison between IM with different winding topologies

	9S/6P DL ($y_c = 1$)	18S/6P DL ($y_c = 1$)	18S/6P SL ($y_c = 3$)	18S/6P DL ($y_c = 2$)	18S/6PDL ($y_c = 2$ - ANW)	36S/6P SL ($y_c = 5$)	36S/6P DL ($y_c = 5$)	54S/6P DL ($y_c = 9$)
k_{w1}	0.866	0.5	1	0.866	0.866	0.966	0.933	0.96
l_a (mm)	94.02	82.69	133.71	114.24	83.28	118.46	111	122
T (Nm)	43.613	37.953	55.12	52.33	54.01	55.78	54.104	52.21
ΔT (%)	28.792	20.528	10.667	9.112	18.145	6.605	3.887	4
P_{Scu_in} (kW)	1.88	2.24	1.33	1.59	1.3	1.2	1.2	1.2
P_{Scu_end} (kW)	0.94	0.59	1.74	1.36	0.66	1.25	1.26	2.27
P_{Scu} (kW)	2.82	2.83	3.07	2.95	1.96	2.45	2.45	3.46
P_{Rcu} (kW)	2.778	0.693	1.074	1.026	0.86	0.557	0.506	0.501
P_c (kW)	0.061	0.016	0.064	0.062	0.021	0.014	0.013	0.013
P_{out} (kW)	8.541	7.512	10.91	10.357	10.69	11.127	10.793	10.42
η (%)	59.8	67.5	71.64	71.42	74.96	78.04	77.78	71.83

6.8 Discussions and Conclusions

In this chapter, the influences of a number of design parameters; such as air-gap length, rotor slot number, stator slot/pole number, stator and rotor slot geometric parameters, rotor skew, and stator coil pitch on the bar current waveform and performance characteristics are investigated systematically. It is found that each design parameter has a substantial effect on the bar current waveform and performance characteristics. It has been verified though the parametric analyses for each design parameter that the

reasons behind the non-sinusoidal bar current of squirrel-cage IMs is found as the saturation of the rotor tooth body parts. The discussions and the key findings of this chapter are given as follows.

A. Air-Gap Length

In this section, the influence of air-gap length on performance characteristics including the rotor bar current waveform of a squirrel-cage IM with 48S/52R/8P has been investigated for different air-gap lengths. Based on the obtained results, important conclusions drawn from this work include:

- Under the fixed current excitation operating condition, the shorter the air-gap length, the higher the level of saturation (see Fig. 6.3(b) and Fig. 6.8);
- The high saturation due to the short air-gap causes more slot leakage flux especially in the slot openings;
- The flux density of the tooth tips contain highly distorted high frequency flux components and those harmonics diminish to minimum due to the filter effect of the teeth;
- The shorter the air-gap length, the more distorted performance curves is due to the saturation of the teeth;
- There is a critical air-gap length that causes to change some performance characteristics of the machine, i.e. rotor bar current waveform has become non-sinusoidal after these specific points;
- The larger air-gap length causes to decrease in efficiency by increasing the amplitude of the magnetizing current;
- The large air-gap length causes reduction in maximum achievable power and torque density, efficiency and also power factor by increasing the magnetizing current requirement of the IM.

In order to avoid lower efficiency, power and torque density, the air-gap length should not be designed very large. The harmonics of the air-gap flux density and hence the other parameters which depend on the air-gap flux density, such as stator current and induced voltage, rotor induced voltage and current, can be minimized by choosing a proper air-gap length. Furthermore, the distortion effect can be reduced effectively by enlarging the air-gap.

B. Rotor Slot Number

The influence of rotor slot number on the performance characteristics including the stator and rotor bar currents, torque, torque ripple, electromagnetic force acting on the stator core, machine losses, power factor, efficiency etc., of squirrel-cage IMs with 48S/52R/8P has been investigated in this part. It is shown that the number rotor slots has a significant effect on the performance characteristics of the IM. In order to avoid the disturbance caused by interacting fields of the rotor and stator, the rotor slot

number should be selected with a special care. Under the design considerations given in the Appendix D, the key findings can be summarized as follows:

- It is revealed that there is an optimal rotor slot number estimating by $R \cong S + 2q$, which is 52 for 48S/8P IM, at which the maximum torque, relatively low torque ripple, minimum saturation level, maximum power factor, and efficiency are achieved;
- The lower the rotor slot number, the lower the distortion on the rotor bar current waveform;
- The minimum slot leakage flux and saturation factor can be achieved for 52 rotor slots;
- The higher the rotor slot number, the lower the electromagnetic force acting on the stator core surface.

Moreover, it is also shown that the flux density at the rotor tooth tips contains a large number of high frequency harmonics depending on the rotor slot number and those harmonics have completely cancelled due to the filtering effect of the teeth. Because of the excessive flux leakage increases with the saturation in the rotor tooth parts, the flux density waveform of the rotor tooth becomes non-sinusoidal. Since the lower order harmonics, particularly the 3rd harmonic, cannot be cancelled by the filtering effect of the teeth, it is induced in the bar current and makes the bar current waveform non-sinusoidal.

C. Stator Slot/Pole Number Combinations

In this section, the influence of stator slot/pole number combinations on the performance characteristics including the stator and rotor bar currents, torque, torque ripple, losses, power factor, and efficiency of squirrel-cage IMs with 36S/6P, 48S/8P, and 60S/10P, all having 52 rotor slots, has been investigated. Furthermore, the levels of saturation and slot leakage flux and their influences on the bar current waveform have been examined in depth.

It is concluded that at the given operation conditions (at 176.6Arms stator current and 5% slip) the rotor bar current of all machines are non-sinusoidal. Besides, there is an indirect correlation between the pole number and the distortion level of the rotor bar current waveform and if the rotor core material is saturated then the higher the pole number, the lower the slot leakage flux and hence the lower the distortion on the rotor bar current. However, this relation is vice-versa in case of the rotor core material is un-saturated (linear).

This study has also revealed that depending on the pole number, the flux density of the tooth tips contains highly distorted flux components. The level of this distortion is higher in the IMs whose pole number is low. In addition, independent of the pole number, the higher order harmonics are completely cancelled due to the average effect of the teeth. Moreover, it has been revealed that it is possible to reduce the bar current distortion level and improve the performance characteristics simultaneously by selecting the optimal rotor slot number for any S/P combination.

D. Stator Slot and Rotor Slot Geometric Parameters

The influence of stator and rotor slot (corresponding to tooth) geometric parameters on the bar current waveform and performance characteristics of a squirrel-cage IM with 48S/8P/52R has been investigated in this section. It is concluded that while some of the geometric parameters have significant effect, some have negligible effect on the performance characteristics and the bar current I_{Bar} as given in Table 6.5. Note that the fractional degrees indicate that the influence of the geometric parameters is between the closed integer levels. As shown, the reason why different geometric parameters have different effects on the characteristics is due to change of the working point on the BH-curve of the core material.

Table 6.5 Comparison of the influence of geometric parameters on performance characteristics of the squirrel-cage IM

	I_{Bar}	T_{avg}	ΔT	P_{scu}	P_{rcu}	Eff.	
b_{s0}	1	1	1.5	0.5	1	1	
b_{s12}	3	3	3	3	2	3	
h_{s0}	2.5	3	3	0	3	3	0-Negligible
h_{s1}	2.5	3	3	3	3	3	1-Slight
b_{r0}	1	1	1.5	1	1	1	2-Moderate
b_{r12}	2.5	3	3	0	2	3	3-Significant
h_{r0}	2.5	3	2	0	3	3	
h_{r1}	3	2	1.5	0	1.5	1.5	

Based on the obtained results, the important key findings drawn from this study include:

- Among the other rotor slot parameters, b_{r12} and h_{r0} are the most dominant parameters in terms of electromagnetic performance while h_{r1} is the most dominant parameter in terms of the bar current waveform.
- Among the other stator slot parameter, h_{s0} , and h_{s1} are the most dominant stator slot parameters for the electromagnetic performance while b_{s12} is the most dominant parameter in terms of both electromagnetic performance and the bar current waveform.

In order to avoid lower efficiency, power and torque density;

- b_{s0} and b_{r0} should not be very small;
- The optimum b_{s12} , h_{s1} , b_{r12} and h_{r1} should be calculated;
- h_{s0} and h_{r0} should be as small as possible.

The average torque, output power, and efficiency can be maximized and the torque ripple and power losses can be minimized simultaneously by choosing the proper slot geometric parameters. This can be easily done by conducting a multi-objective global optimization.

E. Rotor Skew

In this section, the influences of rotor skew on the bar current waveform and key performance characteristics are investigated. It has been found that the rotor slot skew angle has a significant effect on the bar current waveform and performance characteristics. It is revealed that there is a critical skew angle making the torque ripple minimum and diminishing the bar current harmonic content to a minimum. It is found that with the critical skew angle of the studied IM, which is 30° , the 3rd harmonic content of the bar current, which is responsible for the flat-topped waveforms, become minimum. In addition, it is also shown that the higher the skew angle, the lower the saturation in machine cores, the lower the average torque and efficiency.

Although skewing of rotor slots in IMs helps to improve some performance characteristics such as, improve the starting characteristics of grid connected IMs, reduce the torque ripple level and permeance harmonics caused by slots, it is not preferred for the IMs used in the EV/HEV applications in order not to sacrifice the performance characteristics such as torque, power and efficiency. Because, as evidenced from Fig. 6.87(b), skewing causes an increase in the rotor resistance. As the rotor resistance increases, the torque and power will be drop. In addition, because of the increase in the rotor resistance, the bar copper loss will be increase and consequently the efficiency will decrease. Since the high power and efficiency are very challenging characteristics for IMs designed for the EV/HEV applications, the rotor slots are not skewed.

F. Stator Coil Pitch

The influences of stator coil pitches varying from $y_c = 1$ to 9 and number of winding layers on the electromagnetic performance are investigated with particular reference to the bar current waveform. It has been revealed that the stator coil pitch has also significant effect on the bar current waveform and performance characteristics. Some other key findings of this study is summarized as follows.

- The longer the slot pitch, the lower the bar current distortion level: The bar current THD of the 54S/6P-DL ($y_c = 9$) is 85.7% lower than that of the 9S/6P-DL ($y_c = 1$);
- The longer the slot pitch, the lower the rotor bar copper loss: The bar copper loss of the 54S/6P-DL ($y_c = 9$) is 81.67% lower than that of the 9S/6P-DL ($y_c = 1$);
- For $q \leq 2$ combinations, the longer the slot pitch, the lower the parasitic effects and the better the performance characteristics such as higher torque, higher efficiency, lower torque ripple etc. The average torque, torque ripple, and efficiency of the IM with 36S/6P-DL ($y_c = 5$) are

+24.05%, -86.5%, and +29.05%, respectively when compared to the IM with 9S/6P-DL ($y_c = 1$);

- The double-layer winding configurations lead to lower parasitic effects, such as lower torque ripple and lower bar current distortion rate, etc.
- The bar current distortion levels and performance characteristics of the IMs with ($y_c = 2$) are between the IMs with ($y_c = 1$) and ($y_c = 9$);
- Among the IMs with $y_c \leq 3$ configurations, the newly developed 18S/6P-DL ($y_c = 2$ -NWW) is favourable in terms of total axial length, average torque, output power, and efficiency.

In Chapter 7, the influences of operating parameters on the rotor bar current waveform and the key performance characteristics will be further investigated in detail.

7 Influence of Operating Parameters on Non-Sinusoidal Bar Current Waveform

In this chapter, the influences of operating parameters, including slip and electric loading on the electromagnetic performance characteristics of conventional squirrel-cage IMs, designed by using the same stator outer diameter, stack length, air-gap length, output power and rated speed as the Toyota Prius 2010 IPM machine, is investigated in detail with particular reference to the bar current waveform. It is observed that after exceeding the certain slip rate and electric loading level, the rotor bar current waveform becomes non-sinusoidal even if the stator windings are fed with a sinusoidal source. The conditions for such non-sinusoidal rotor bar current to occur and the reasons behind this phenomenon are investigated by FEA, with particular reference to the numerical verification of the obtained non-sinusoidal bar current waveforms by locked-rotor analyses.

7.1 Introduction

In Chapter 5, the main reason behind the non-sinusoidal bar current phenomenon, i.e. magnetic saturation of rotor teeth, has been explained. In Chapter 6, the design parameters causing the bar current waveform to become non-sinusoidal have been investigated in detail. In this chapter, influence of operating parameters, including slip and electric loading, on the bar current waveform will be investigated systematically.

In literature, although there are a large number of studies on the influence of some operating parameters on the stator current waveform, there are only a few studies on the influence of some operating parameters on the rotor bar current waveform of a squirrel-cage IM [HOO11], [WEI11], [DON05], [GAU41], [BUC72], [BRA74], [MUK89], [DON05], [PRE89], [BOG03], [BOT05], [BEL06], [BLA09], [GRA09]. Nevertheless, in these studies, the explanations related to the non-sinusoidal bar current have not given or are insufficient. It is possible to divide the studies on the rotor bar current waveforms into four cases, i.e. the performance of IM under:

- (a) Sinusoidal supply fed [WEI11], [HOO11], [GAU41], [BUC72], [BRA74], [MUK89], [DON05], [PRE89], [BOG03], [BOT05], [BEL06], [BLA09], [GRA09], [DAJ13a];
- (b) Non-sinusoidal supply fed [GYS00], [BOT04], [KUN12];
- (c) Faulty operating condition [BRU07], [SUN13], [MES14];
- (d) Saturated core operating condition [LEE61], [CHA71], [MOR92], [PER12].

Under both non-sinusoidal and sinusoidal supply conditions, the rotor bar current analysis has been performed by using the equivalent circuit of the IM [PRE89]. In order to numerically calculate the rotor bar current waveform and its harmonic spectrum, a study on electromagnetic design workflow for squirrel-cage IM has been conducted [GRA09]. To be able to determine the flux pattern accurately, a

method has been introduced to predict the instantaneous current distribution in a squirrel-cage IM of known geometry and winding design, based on a direct method of simulation [MUK89]. A similar method has been developed in [BEL06] in order to model the behaviour of the rotor quantities such as rotor frequency and current accurately by taking into account the magnetic and electric machine properties.

The stator current waveforms of a single phase IM are investigated and some analytical expressions have been derived for rotor bar currents taking into account the saturation effect [BRA74]. A similar study [BOG03] which presents a detailed analysis method, taking into account the hysteresis of magnetic material, the saturation effect, the induced currents in different rotor bars and the eddy currents in the laminations, has been introduced in order to calculate the machine losses accurately.

For different IMs which have different numbers of poles, coil slot pitches, different speeds and phases, the rotor bar current waveforms at the four different regions of the bar (top, quarter, half and bottom) has been analyzed in order to find out the components of the rotor bar current and the effect of the rotor bar current harmonics upon the efficiency of the motor [GAU41]. Another study on the components of the rotor bar current has been presented in [WEI11] for a single phase IM. In this study, the rotor bar current components have been determined as magnetizing, working and slip components.

In order to measure the rotor bar current online, a squirrel-cage IM has been built and some experimental data has been collected from the bars by using a type of current sensor assembled by soft ferrite rings wounded with a thin coil inserted in the rotor bars in order to measure the bar currents [DON05], [BOT05]. In [BLA09], in order to measure the rotor bar current of a special IM, the same measurement method has been used. In both of these studies only the waveforms have been showed but no explanation has been made on the origins of the non-sinusoidal waveforms.

The rotor bar current waveform has also been investigated under unconventional winding layout designs of IMs. By using Fractional Slot Concentrated Winding (FSCW) technique, an IM has been designed [DAJ13a] and according to the obtained analysis results the rotor bar current is not sinusoidal because of the very large rotor EMF harmonics due to the winding space harmonics.

Under non-sinusoidal voltage fed operating condition, an investigation has been conducted by [KUN12] on the impact of the voltage fluctuations on the performance of an IM, particularly the stator and rotor current variation characteristics by using a dynamic model. In a similar study [BOT04], it has been revealed that the Joule power loss, whose contribution is 10% of the total losses under the sinusoidal supply fed operating condition, increases dramatically under the non-sinusoidal operating condition because of the magnetic flux pulsations. The stator current has been calculated and compared with the measured stator current in order to verify an improved analytical method which has been used for the evaluation of the rotor bar current under non-sinusoidal supply fed condition [GYS00].

The rotor faults greatly affect the currents in the bars and in the end rings both in amplitude and in harmonic content depending on the relative position of the fault [MES14]. Generally, the rotor faults

consist of broken bars of the rotor cage. If the number of the broken bars decreases, the magnitude of the normalized stator current decreases while it is almost equal to unity under healthy operating condition [SUN13]. To be able to measure the bar current waveform under broken bar condition, IM with stranded isolated cables on the rotor has been prototyped and fed by sinusoidal voltage [BRU07] and the rotor bar current waveforms have been compared under healthy and broken bar operating conditions [SUN13] by performing different faulty scenarios in order to investigate the effects of broken bars on the performance of the IM [MES14]. In addition, some predictions have been made for the rotor circuit of the IM under saturated operating conditions [LEE61], [MOR92], [BOL10], [PER12].

In this chapter, previously designed IM by using the same stator outer diameter, stack length, slot/pole number, winding layout and rated operating parameters such as stator voltage, current and speed of Toyota Prius 2010 IPM machine (for the specifications see the Appendix D) has been employed in order to investigate the influence of slip and electric loading. Furthermore, the numerical verification of the non-sinusoidal bar current waveform by locked-rotor analyses has also been done on the same IM. Since the bar current plays a very important role in the torque production, the power density, and the efficiency of the IM, its accurate prediction is essential. Therefore, to be able to predict the rotor bar current accurately, the operating parameters such as slip and electric loading, which should be taken into account, has been investigated in depth in this chapter. Many different cases, such as different loading, slip, and saturation, have been conducted. It has been revealed that, the rotor bar current waveform does not only become non-sinusoidal under non-sinusoidal source fed or faulty bar operating conditions, but it also becomes non-sinusoidal after exceeding a specific slip and an electric loading operating range under sinusoidal operation. Moreover, the obtained non-sinusoidal bar current waveforms have been verified numerically by the locked-rotor analyses.

7.2 Electric Loading

The influence of electric loading on the bar current waveform is investigated by 2-D FEA under steady state operating condition. During the analysis, all other machine specifications (see Appendix E) are fixed except for the stator winding voltage and hence winding current (under 950 rpm imposed speed operating condition).

7.2.1 Influence of Electric Loading on Performance Characteristics

The variation of induced voltage of Phase 'A' winding with respect to stator current and the variation of their percentage of dominant harmonics and THD rate are shown in Fig. 7.1 and Fig. 7.2, respectively. These harmonics are due to the winding MMF harmonics (see Fig. 7.3), saturation and slotting effect. As seen from Fig. 7.1, the rms value of the induced voltage increases as expected. Whilst the high order harmonics (20th, 22th, and 24th) decrease with the increasing stator current, the low order harmonics (3rd and 5th) increase. Furthermore, whilst the THD of the induced voltage changes significantly before 175A, it does not change after exceeding 175A of phase current. Bar current

waveforms for various stator currents are shown in Fig. 7.6. The bar current becomes non-sinusoidal after exceeding 175A of stator current. The variation of the air-gap flux density with respect to rotor position for various stator current operating condition is illustrated in Fig. 7.4(a). Considering the variation of the low order harmonic percentages of the induced voltage (see Fig. 7.2) and air-gap flux density shown in Fig. 7.5, it can be deduced that the higher the electric loading, the higher the low order induced voltage harmonics and hence the air-gap flux density harmonics, and the lower the higher order harmonics. It is also predicted that these lower order harmonics in the air-gap field will pass through to the rotor side.

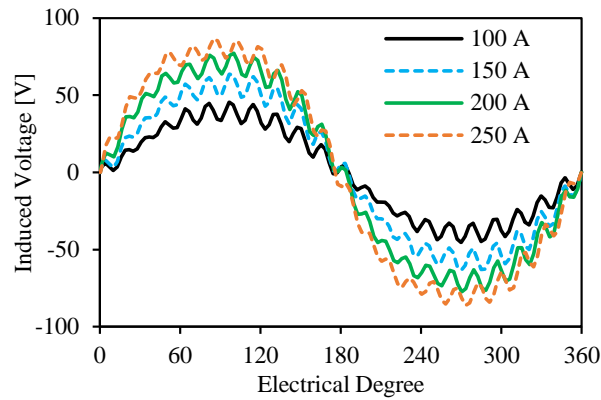


Fig. 7.1 Induced voltage waveforms for various stator currents.

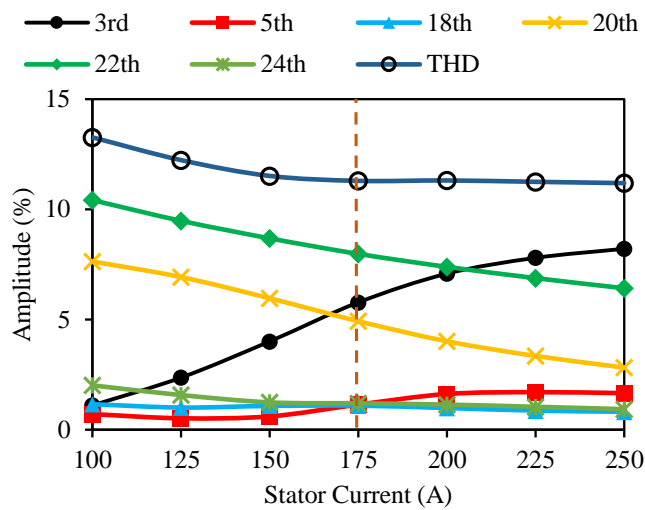


Fig. 7.2 Variation of induced voltage harmonics and THD with respect to stator current.

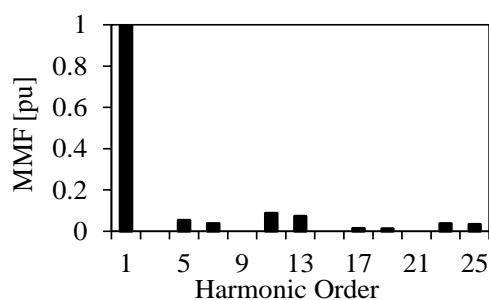
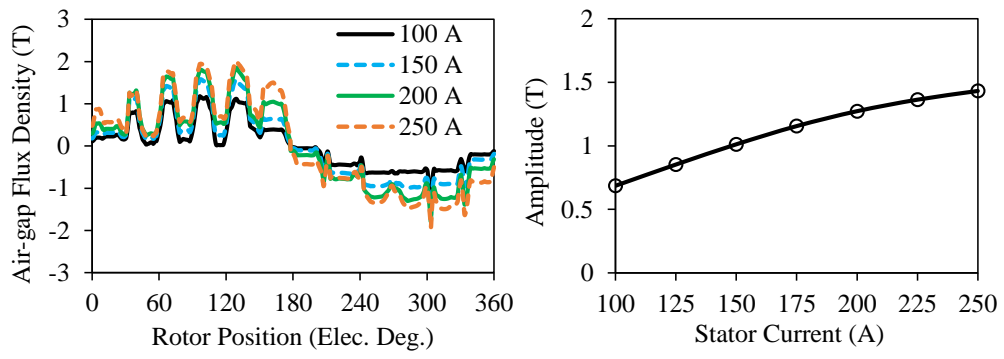
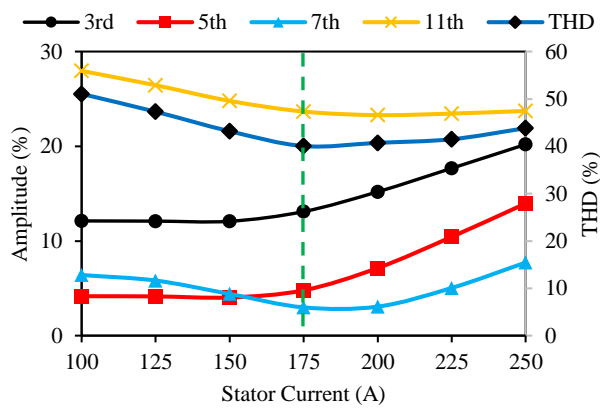


Fig. 7.3 Normalized MMF space harmonics of the designed 48S/52R/8P IM.



(a) Waveforms (b) Variation of fundamental amplitude

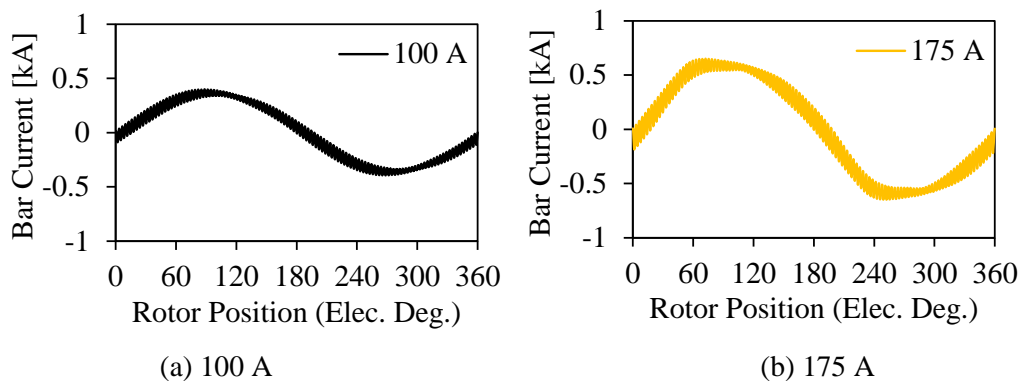
Fig. 7.4 Air-gap flux density: (a) waveforms for various stator currents and (b) variation of fundamental air-gap flux density with stator current.



(b)

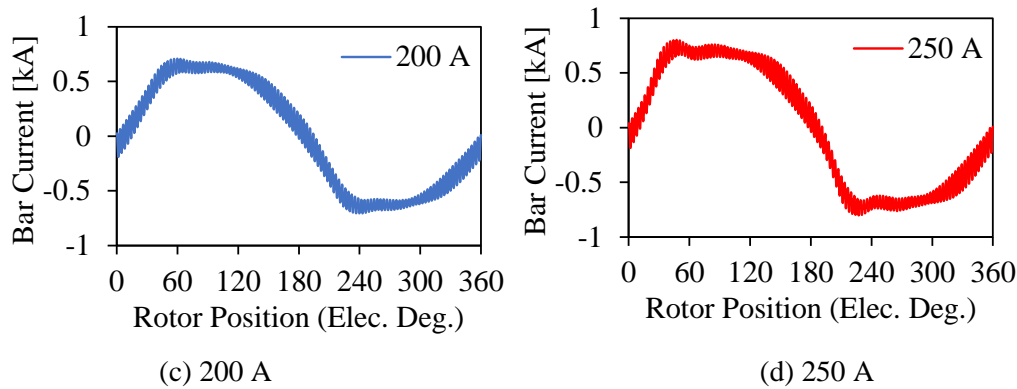
Fig. 7.5 Air-gap flux density for different stator currents: (a) waveforms and (b) variation of the percentage of the dominant harmonic magnitudes and THD with respect to stator current.

The higher order harmonics always exist in the bar currents because of the high frequency flux harmonics induced at the top of the rotor teeth. However, lower order harmonics change due to the stator current. The correlation between these lower order harmonics and stator current is shown in Fig. 7.6(e). The slope of the THD percentage increases significantly after exceeding 175 A which is the point where the sinusoidal bar current becomes non-sinusoidal. Therefore, considering the figures from Fig. 7.1 to Fig. 7.6 it can be concluded that after exceeding 175 A, the performance characteristic of the IM has changed.



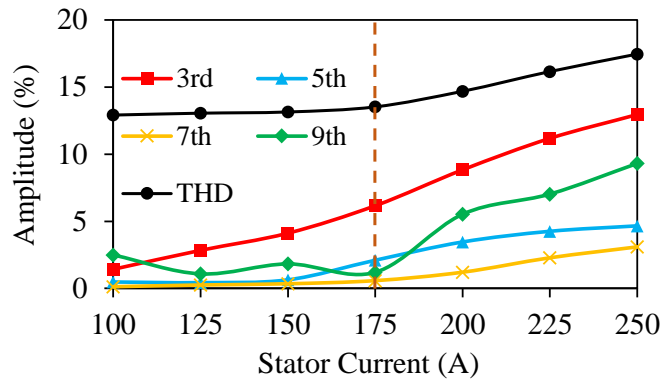
(a) 100 A

(b) 175 A



(c) 200 A

(d) 250 A



(e) Variation of dominant bar current harmonics and THD with respect to stator current.

Fig. 7.6 Rotor bar current for different stator current: (a-d) waveform and (b) variation of harmonic amplitude percentages and THD with respect to stator current (e).

7.2.2 Influence of Electric Loading on Magnetic Characteristics

To be able to reveal the reason behind this phenomenon, the magnetic characteristics of the designed IM have been investigated. It is obvious that with increasing loading the magnitudes of the magnetic circuit parameters change. It is very well known that the magnitude of the leakage flux increases with saturation of the magnetic cores. Therefore, by using (5.1), expressed in Chapter 5, the rotor slot leakage flux densities have been calculated and illustrated in Fig. 7.8. In the case of electrical loading, the slot leakages especially the rotor slot leakages increase considerably with the increasing stator current (see Fig. 7.8) due to the saturation of the rotor teeth as seen in Fig. 7.7. Fig. 7.8 shows that the leakage flux density magnitude is higher at the slot opening of both the rotor and the stator. In addition, there is an inverse correlation between saturation and equivalent rotor flux density as already proven in [BUC72].

The influence of the loading on the torque density and ripple has also been investigated. Variation of the torque density and its ripple with respect to stator current is illustrated in Fig. 7.9. Torque density shows linear growth while the torque ripple shows exponential decay, especially before the 175 A, this decay is very sharp. As mentioned previously, the magnetic saturation plays a very important role on the air-gap field [BOL10] and hence performance characteristics of the machine. Furthermore, the effect of the saturation can be determined by the saturation factor which is defined by the MMF in the total mutual flux path divided by MMF in air-gap as given in by using (5.8) expressed in Chapter 5 [BUC72].

By using this definition, it is possible to determine when the bar current waveform becomes non-sinusoidal. Fig. 7.10 shows the calculated saturation factor for various stator currents. As can be seen, as the load increases the saturation factor exhibits a peak, i.e. it increases first and then starts to decrease. Here, the current value associated with the peak value of the saturation factor indicates that the saturation starts after exceeding that point, and the bar current waveform starts to become non-sinusoidal, whilst the distortion of the air-gap flux increases as the current increases (see Fig. 7.5).

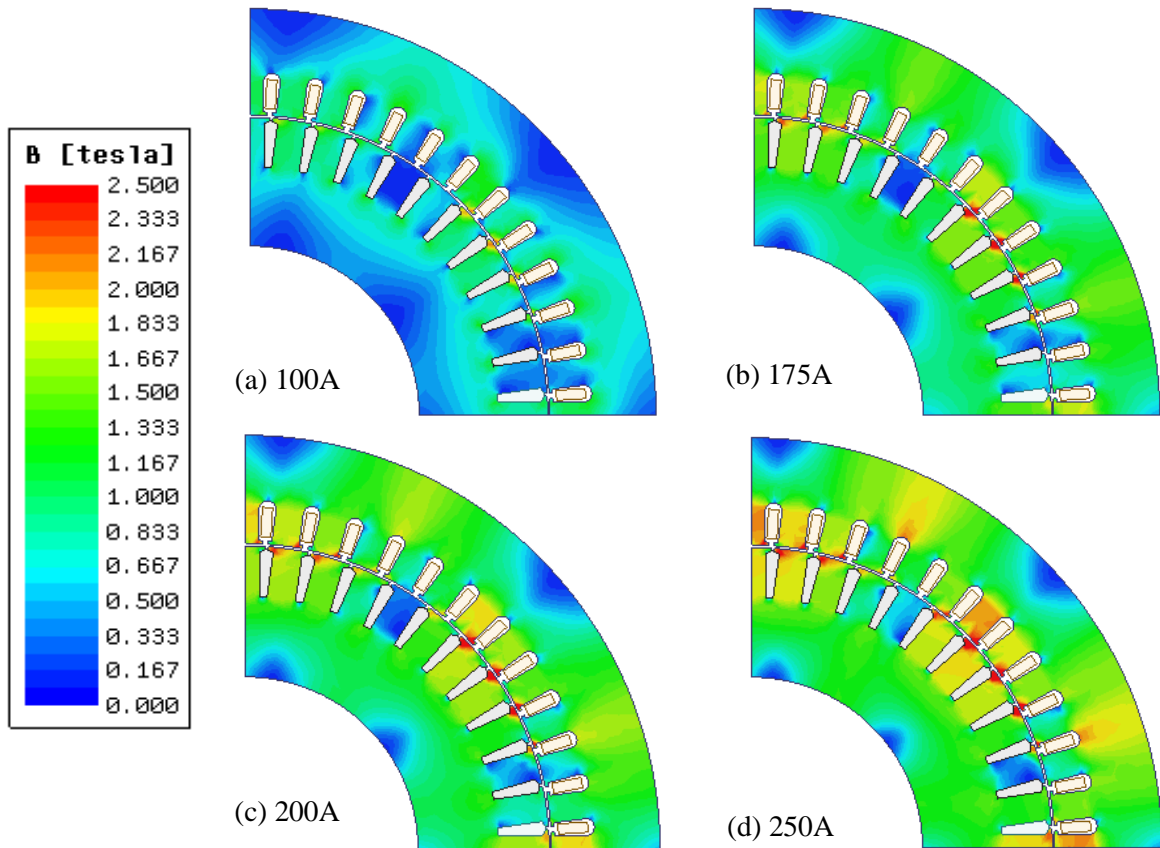


Fig. 7.7 Flux density distributions for various electric loadings.

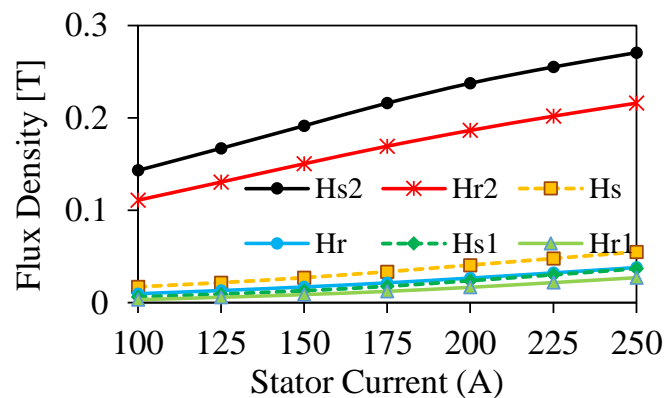


Fig. 7.8 Variation of slot leakage flux densities (Hs, Hr: whole slot length including the tips) with respect to stator current.

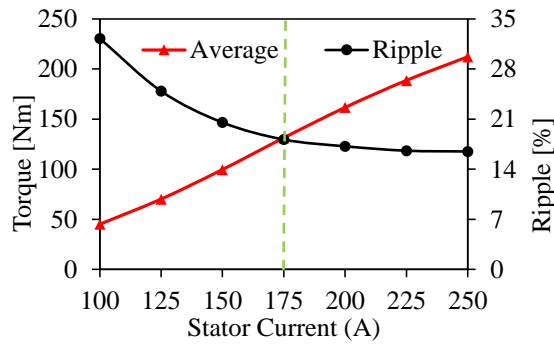


Fig. 7.9 Torque density and torque ripple percentage variation with respect to stator current.

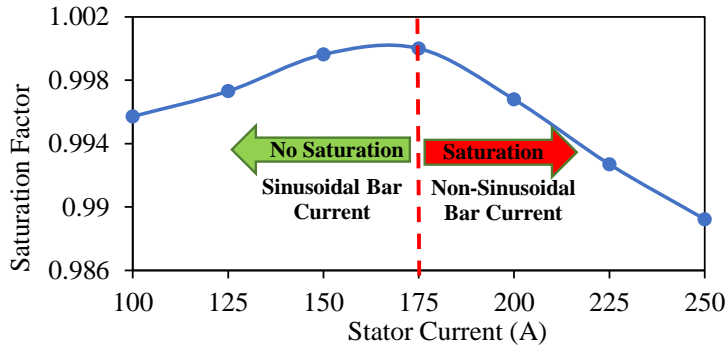


Fig. 7.10 Variation of normalized saturation factor with respect to stator current.

7.3 Slip

The influence of slip on the bar current waveform has been investigated by keeping all the parameters constant except for the rotor speed. The steady state results have been investigated under the peak injected voltage operating condition (102 V which generates 250 A).

7.3.1 Influence of Slip on Electromagnetic Performance Characteristics

With the increasing speed (decreasing slip), variation of the induced voltage in Phase ‘A’ winding is shown in Fig. 7.11. There is an inverse correlation between the slip and the induced voltage fundamental amplitude. The variation of the amplitudes of the lower and higher order harmonics of the stator induced voltages with respect to slip is shown in Fig. 7.12. The 3rd and 22nd harmonics are the most dominant ones and the amplitudes of harmonics have changed after exceeding 0.08 (920 rpm) of slip rate.

The influence of the slip on the air-gap flux density is shown in Fig. 7.13. Note that the air-gap flux density waveform is reconstructed due to the first 7 harmonic components. As seen in air-gap flux density variation which is reconstructed by using the first 7 harmonics, peak value of the flux density decreases with slip. Considering the variation of the amplitude percentages of the air-gap harmonics given in Fig. 7.14, the magnitude of the lower and higher frequency harmonics increase with increasing slip. As seen in Fig. 7.14, on the amplitude variation of the lower and higher order harmonics a deviation has been occurred near the 0.08 slip region again. Therefore, it is obvious that around this operating

point the performance characteristic of the IM has changed. To investigate the influence of the slip on the IM performance characteristics such as torque density, torque ripple, losses and efficiency, the bar current should be investigated in depth.

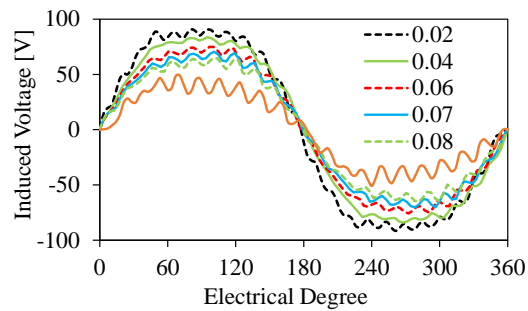


Fig. 7.11 Induced voltage waveforms for various slips.

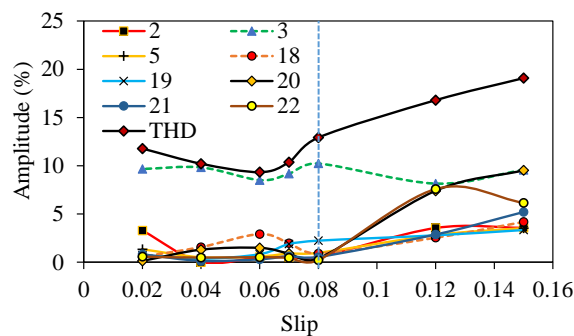


Fig. 7.12 Variation of the dominant induced voltage harmonics and THD with respect to slip.

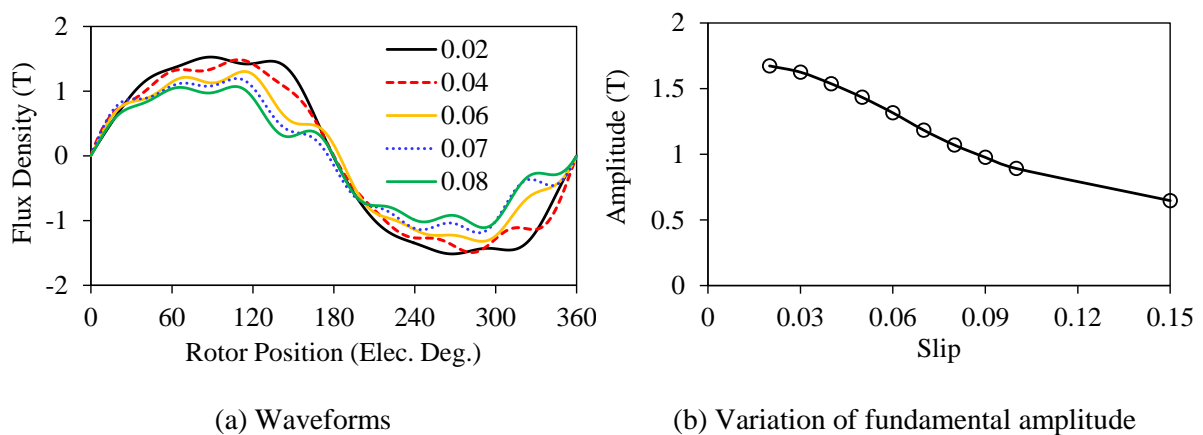


Fig. 7.13 Air-gap flux density: (a) Reconstructed air-gap flux density waveforms for various slip rates and (b) variation of fundamental air-gap flux density amplitude with slip.

The bar current waveforms have been evaluated by using (5.5). In order to calculate the bar current, the inter-bar ring currents have been calculated first as shown in Fig. 7.15 (see Fig. 5.1 for squirrel-cage construction and current components). Under 0.04 slip operating condition, by summing up the inter-bar ring currents point by point as given in (5.5), the bar current waveform which is non-sinusoidal at 0.04 slip has been obtained. By using this method, the bar current waveforms for various slips have been obtained in Fig. 7.16(a)-(f). The waveform of the bar current has become non-sinusoidal after exceeding 920 rpm (slip= 0.08), and the distortion level has increased with increasing speed. The

variation of the harmonic percentages of the bar current and THD value with respect to slip is shown in Fig. 7.16(g).

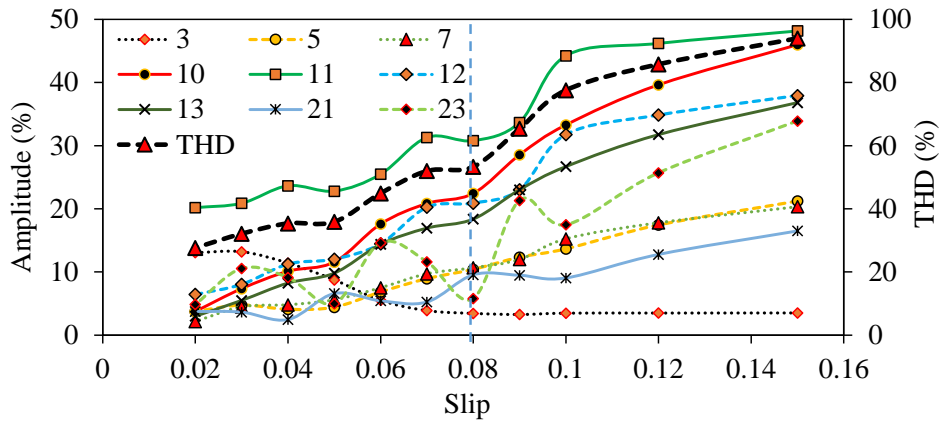


Fig. 7.14 Variation of the air-gap flux harmonics and THD with respect to slip.

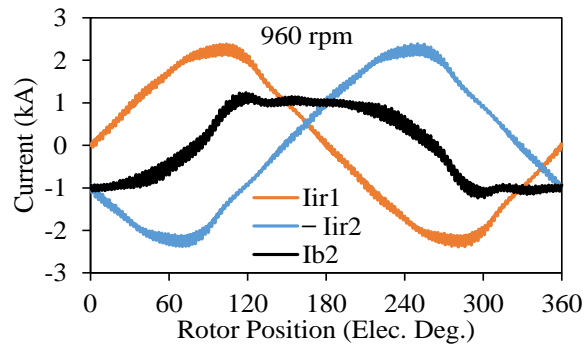
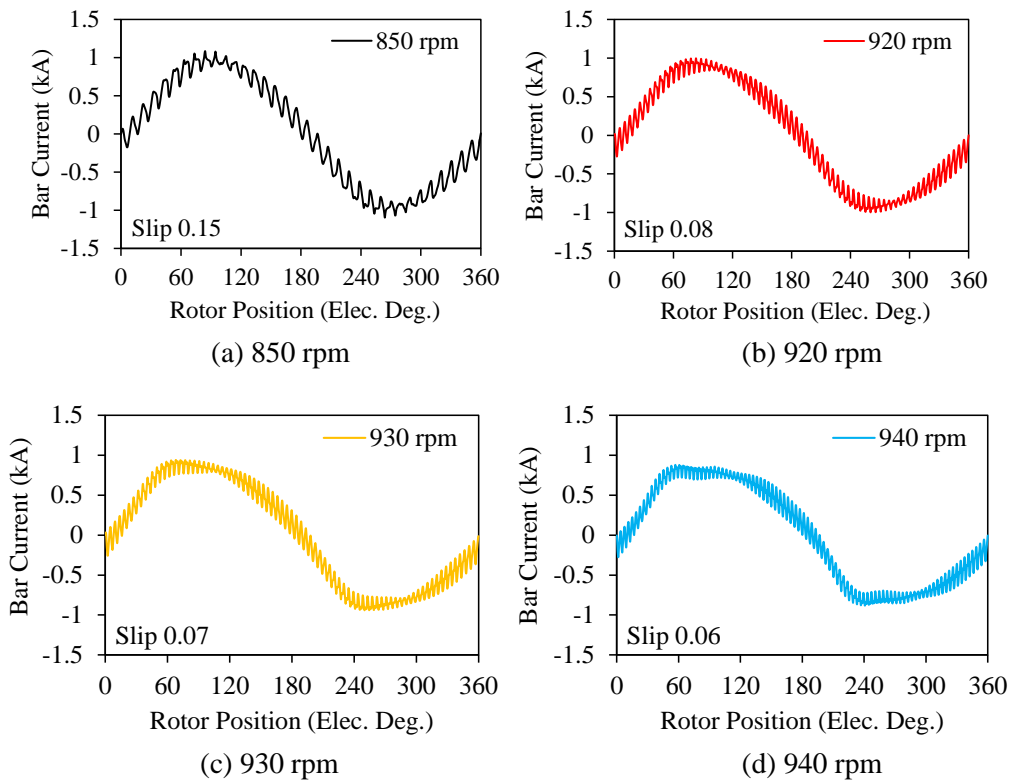


Fig. 7.15 Rotor bar (I_{b2}) current and inter-bar ring (I_{ir1} and I_{ir2}) current waveforms.



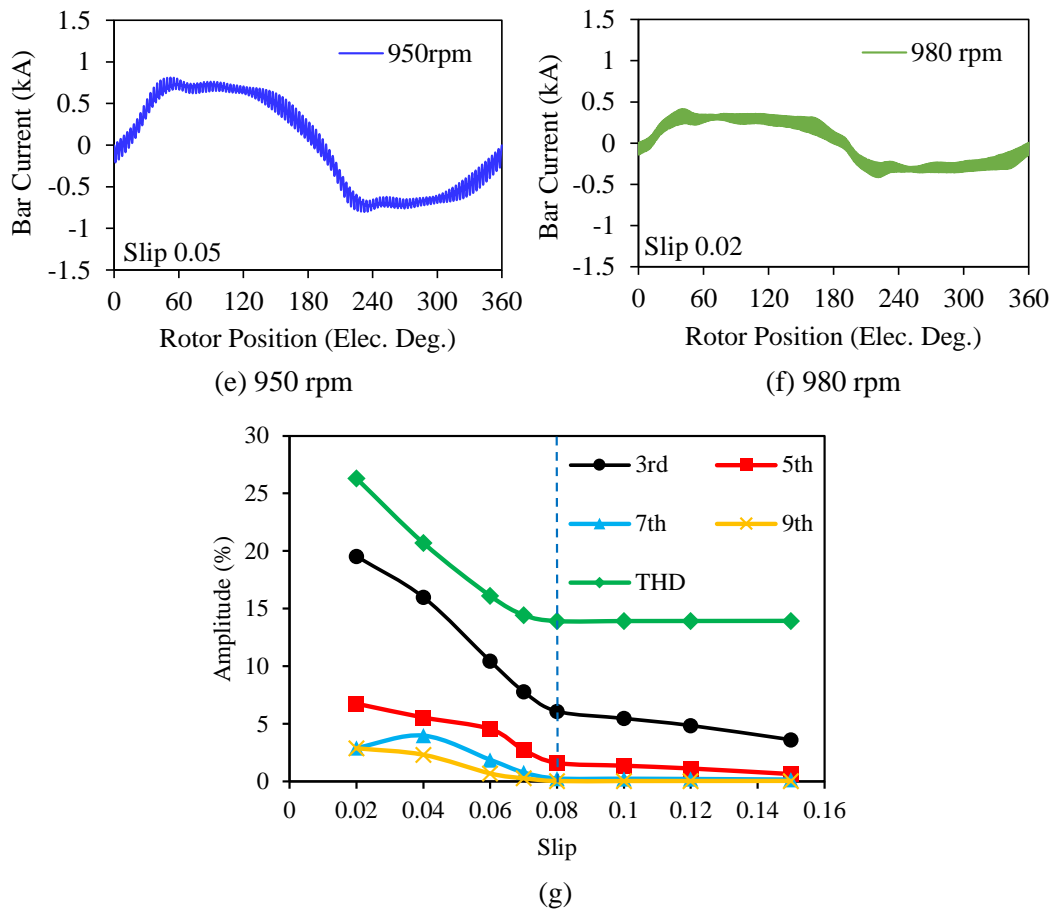


Fig. 7.16 Bar current waveforms for various slip values (a)-(f) and their harmonic amplitude percentages with reference to fundamental component and THD of the bar currents (g).

The dominant harmonic is the 3rd and after the 0.08 slip value the slope of each curve has changed significantly. Especially, the amplitude of the THD has doubled. It shows that the lower the slip, the higher the harmonic amplitude. It is very interesting that although the induced voltage in the stator windings increases and also the value of the rotor bar resistance decreases with increasing speed (see Fig. 7.11 and Fig. 7.16), the magnitudes of the bar currents decrease.

This phenomenon is due to the considerably increasing slot leakage with decreasing slip as seen in Fig. 7.19. The reason behind the increasing flux leakage is due to the saturation of the iron cores of the IM and the decreasing equivalent slot leakage and magnetizing reactance. As seen in Fig. 7.19, after exceeding the peak point of the saturation factor all reactances have decreased. To reveal the effect of the magnetizing reactance, (5.4) has been derived in terms of magnetizing reactance as expressed in (5.7). The bar current has a linear correlation with magnetizing reactance [BUC72]. As seen in Fig. 7.20, the saturation level of the iron cores has increased with the increasing speed due to the increase in the magnitude of the air-gap flux density (see Fig. 7.13(b)). As explained previously, since the magnetic core material of the IM cannot carry more flux than the amounts higher than its knee point in the BH curve (see Fig. 6.8(d)), the magnetic cores, particularly stator and rotor tooth parts, go to the saturation and the level of saturation increases as the magnitude of the air-gap flux increases (see Fig. 7.13(b) and Fig. 7.20). The saturation limits the fluxes on the rotor and stator teeth and causes more leakages. The

influence of the slip on the bar self-inductance and its ripple is shown in Fig. 7.19. As seen, there has been a considerable increase in the magnitude of the self-inductance ripple near the 0.08 slip region.

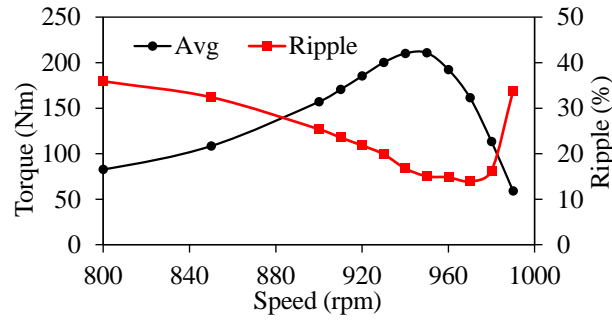


Fig. 7.17 Variation of torque and torque ripple rate with respect to speed.

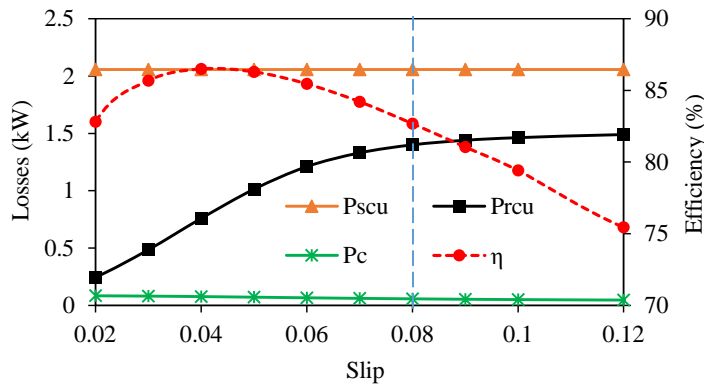


Fig. 7.18 Variation of power losses and efficiency with respect to slip.

The influences of slip on the torque-speed characteristic and efficiency performance are illustrated in Fig. 7.17 and Fig. 7.18, respectively. As seen in Fig. 7.17, the maximum torque (212 Nm) and the minimum torque ripple (15.5%) have been achieved at 950 rpm with 0.05 slip. However, the maximum efficiency η (86.5%) has been achieved at 960 rpm with 0.04 slip (see Fig. 7.18). Note that, during the calculation of efficiency the windage, friction and stray load losses were assumed to be 1% of the output power [BOL10], [LIP17]. Since the stator current is fixed at 250 A for each imposed speed by changing the amplitude of the injected voltage, the stator copper loss P_{Scu} has not changed. However, the rotor bar copper loss P_{Rcu} decreases as the slip decreases due to the decrease in the bar conductor impedance (see Fig. 7.19) and also the rotor frequency. Furthermore, the slope of P_{Rcu} has changed significantly after 0.08 slip rate. There is a slightly increase in the total magnitude of the iron core losses P_C due to increased eddy currents which increase with the total flux leakage of rotor side.

7.3.2 Influence of Slip on Magnetic Characteristics

The variation of the magnetic characteristics such as flux density, leakage reactance, saturation factor, etc. with respect to slip have been examined in this section. Considering (5.7) given in Chapter 5, and Fig. 7.19, it can be concluded that although the total impedance of the bar conductor decreases as the leakage and magnetizing reactance decrease the magnitude of the bar current also decreases because the decrease rate of the magnetizing reactance is higher than the bar impedance. Therefore, it can be concluded that considering the previous sections and obtained results, all evidences support each

other. It means, if saturation occurs, whole machine performance characteristics are affected.

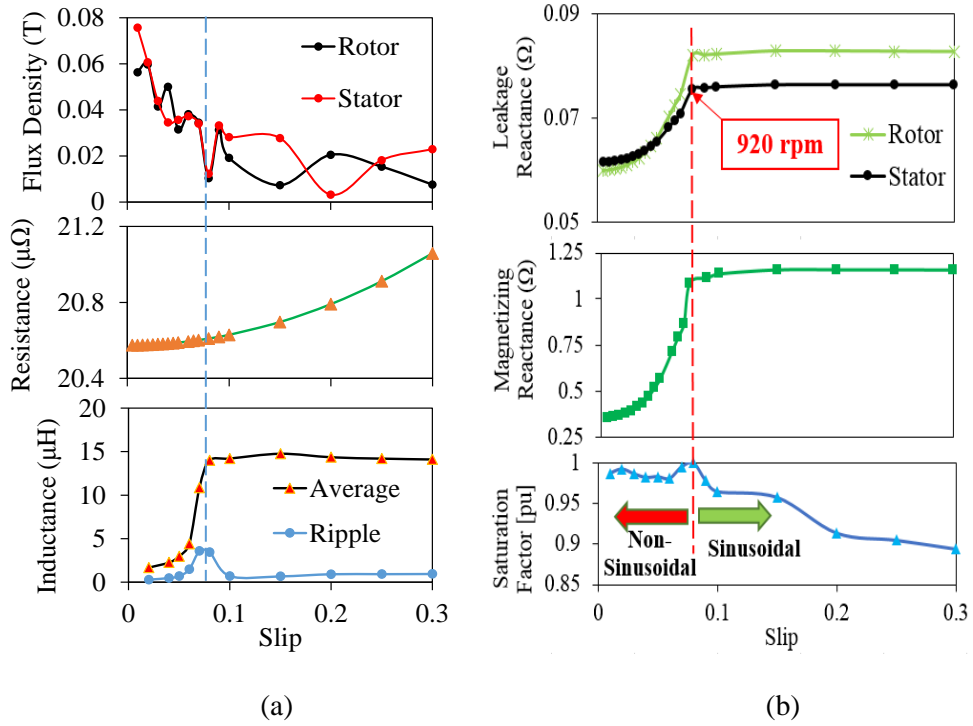


Fig. 7.19 (a) Flux leakage density of rotor and stator slots, rotor resistance and inductance variation with slip and (b) equivalent leakage reactance, magnetizing reactance, and normalized saturation factor variation with respect to slip.

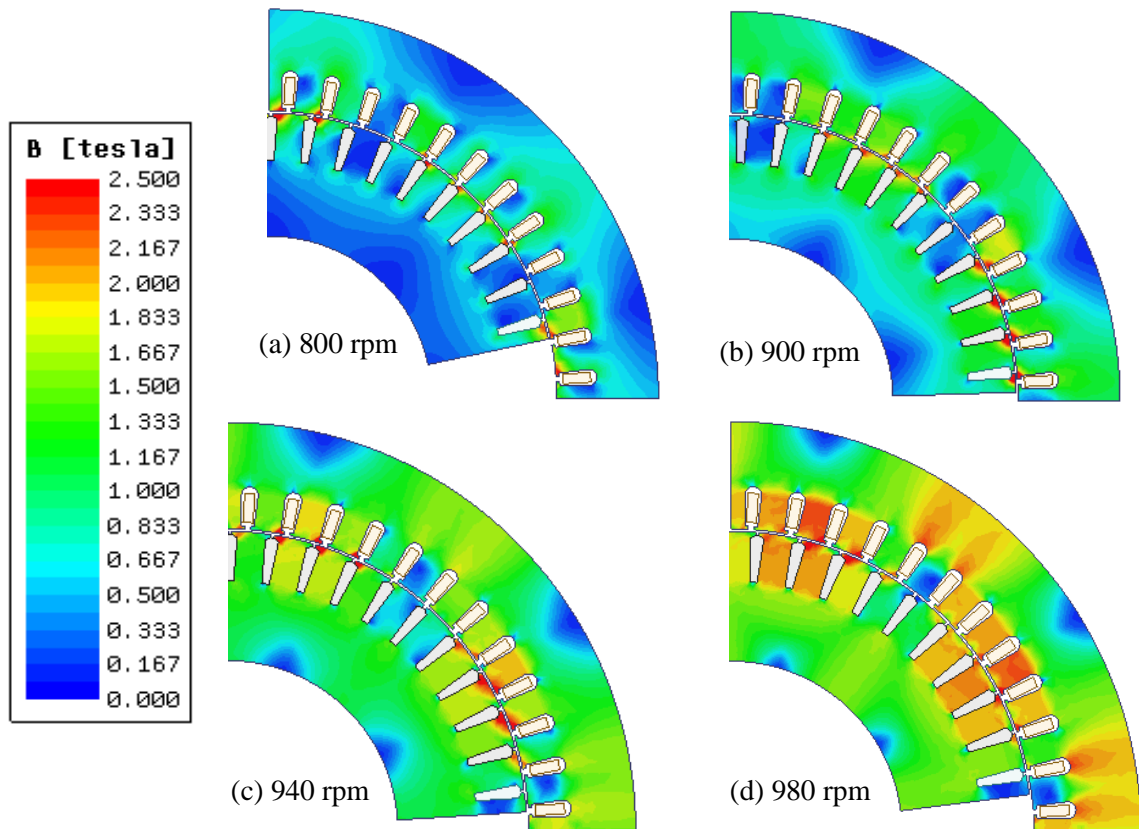


Fig. 7.20 Flux density distributions for different speed operations.

By calculating the saturation factor it can be realized that when the saturation occurs by performing an electrical loading or slip analysis. It is proven that the saturation increases the magnitude of the 3rd harmonics of air-gap flux density and consequently the bar current. Therefore, for the sake of accuracy, during the design and analysis stage, the rotor current of an IM should not always be considered as sinusoidal. Usually, not such assumption is made in the FEA but it is made in some other model based analysis and control design softwares such as Matlab/Simulink.

7.4 Verification of Non-Sinusoidal Bar Current Waveform by Locked-Rotor Analysis

In order to validate the non-sinusoidal bar current waveform in IMs, a numeric method has been presented in this section. Based on the transformer operating principle of the IM (locked-rotor (short-circuited rotor) operation condition), it is possible to observe the bar current waveform easily. In that case, the rotor frequency would be equal to the synchronous frequency since the slip is equal to one as expressed in (7.1),

$$f_r = sf_s \quad (7.1)$$

where f_r , s , and f_s are the rotor frequency, the slip, and the synchronous frequency, respectively. Therefore, by applying exactly the same excitation (current amplitude and frequency) of the rotor to the stator windings when the bar current is non-sinusoidal, it is possible to observe the same phenomenon.

In terms of the bar current waveform, only the difference between the rated and locked-rotor operating conditions will be the absence of the high-frequency harmonics due to the absence of the slotting effect and slip harmonics. In other words, both space and time harmonics will still present but there will be no high-frequency harmonics because of the absence of slotting effect and slip harmonics as a consequence of the stationary rotor. Therefore, by either varying the phase current or synchronous frequency, it is possible to observe the non-sinusoidal bar current waveform. Furthermore, as verified in Sections 7.2 and 7.3, the high-order harmonics are not involved, but only the low-order harmonics are involved while investigating the non-sinusoidal bar current phenomenon. It is shown in Chapter 5 and Chapter 6 that the bar current waveform became non-sinusoidal because of the saturation of the rotor tooth body parts. In addition, this affects only the 3rd harmonic. As a consequence, neglecting of the space harmonic would not affect the non-sinusoidal bar current phenomenon in IMs.

7.4.1 Constant Frequency and Variable Current

In order to observe the bar current waveform variation under the short-circuited rotor operating with constant synchronous frequency and variable current, several parametric analyses are performed. The obtained bar current waveforms for low- and high-frequency operations are illustrated in Fig. 7.21 and Fig. 7.23, respectively. As seen in Fig. 7.21, for 1 Hz synchronous frequency, the bar current waveform starts to become flat-topped after exceeding 100 A stator current. It can also be observed from Fig. 7.22.

As seen, the most dominant harmonic is the 3rd harmonic and it increases dramatically after exceeding 100A of electric loading. Moreover, as predicted previously, there is no high frequency harmonics in the bar current waveforms.

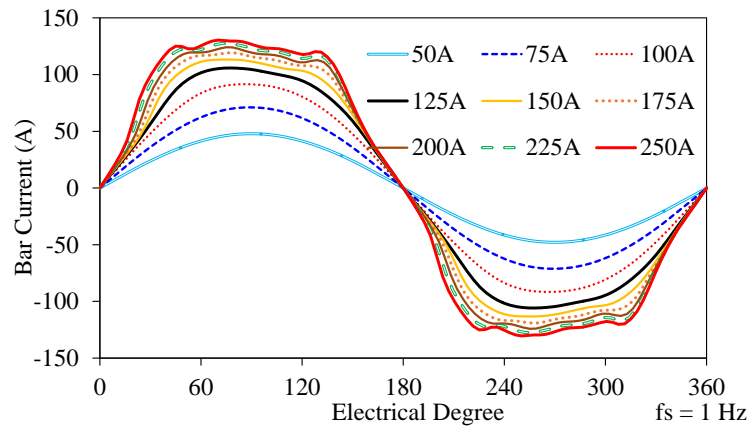


Fig. 7.21 Bar current waveforms for various phase currents at 1 Hz synchronous frequency.

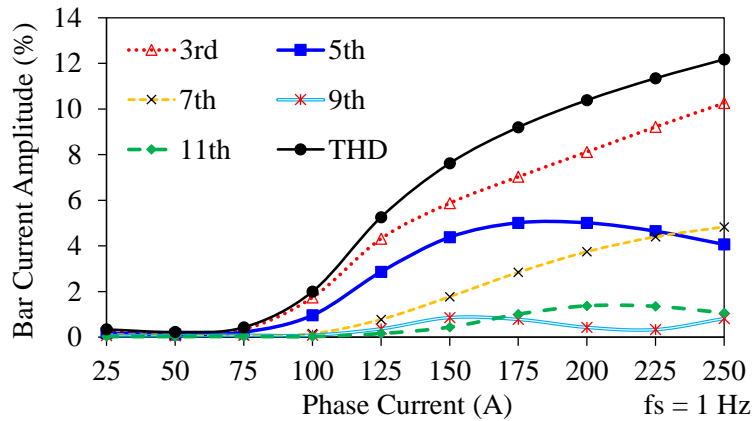


Fig. 7.22 Variation of the dominant bar current harmonics and THD rate with respect to phase current for 1 Hz synchronous frequency.

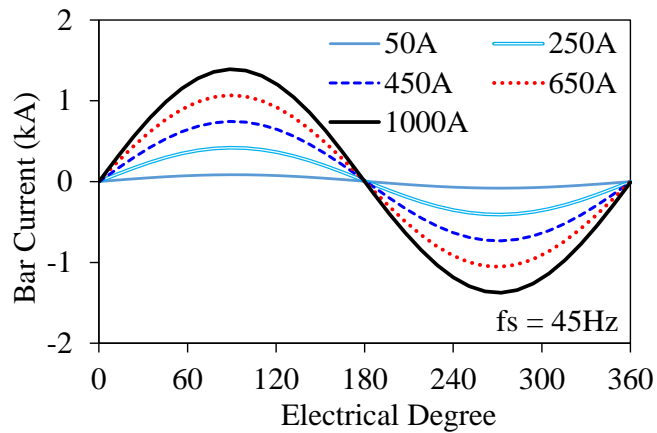


Fig. 7.23 Bar current waveforms for various phase currents at 45 Hz synchronous frequency.

If the frequency is increased from 1 Hz to 45 Hz, the phase current range should be increased dramatically in order to observe the non-sinusoidal bar current waveform as illustrated in Fig. 7.23. As

seen Fig. 7.23 and Fig. 7.24, even if the 1 kA phase current is not enough to make the bar current non-sinusoidal for the 45 Hz frequency. Note that the fundamental amplitude of the bar current is decreased considerably during the locked rotor operation when compared to 250A at 950rpm operating condition (see Fig. 7.6(d)). This is because of the frequency drop of the stator circuit causing the voltage to drop in stator circuit and consequently in rotor circuits. However, as shown before, even if the fundamental amplitude of the bar current is reduced, the waveform has not changed.

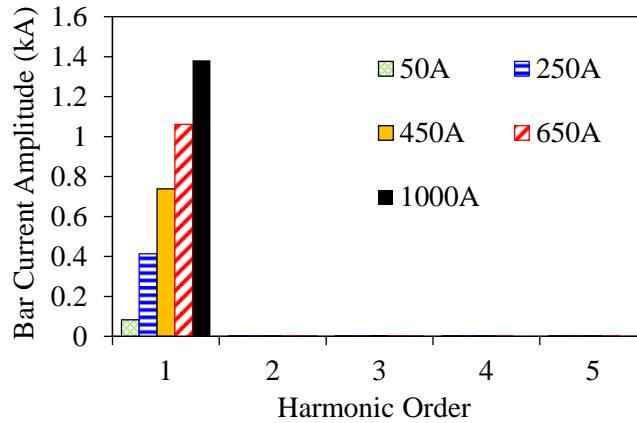


Fig. 7.24 Harmonic spectra of the bar currents for various stator currents at 45 Hz synchronous frequency.

7.4.2 Constant Current and Variable Frequency

In order to investigate the influence of the frequency on the bar current waveform under the short-circuited rotor operation with maximum phase current (250A), several parametric analyses are performed and the obtained bar current waveforms are illustrated in Fig. 7.25. At 250A and 950rpm operating, the rotor frequency is $\sim 3.33\text{Hz}$ and the bar current waveform is non-sinusoidal (see Fig. 7.16(e)). As shown in the Fig. 7.26, the waveform starts to become non-sinusoidal at $\sim 3.4\text{Hz}$ ($THD \geq \sim 5\%$). Thus, the non-sinusoidal bar current phenomenon has been validated by performing the locked-rotor analyses.

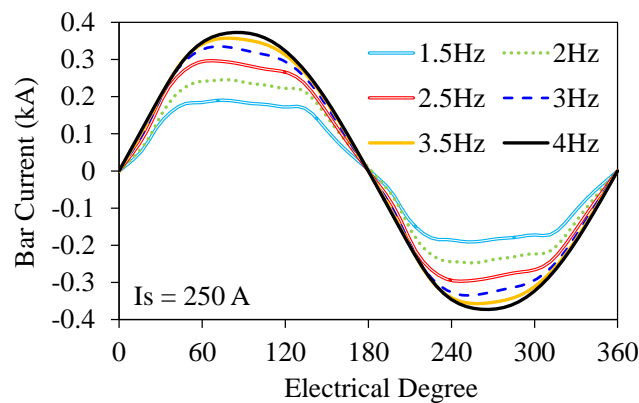


Fig. 7.25 Bar current waveforms for various synchronous frequencies at 250 A stator current.

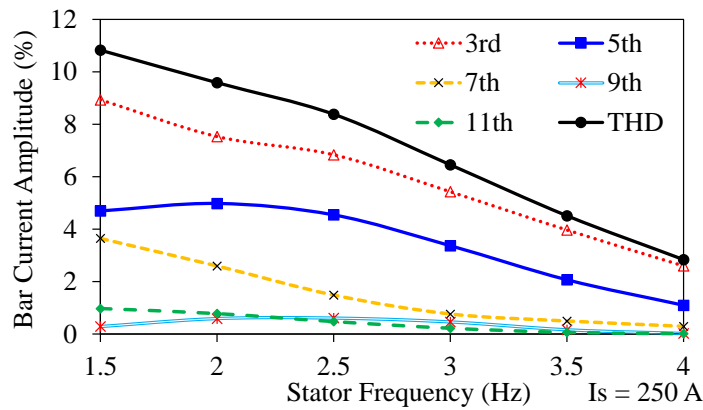


Fig. 7.26 Variation of the dominant bar current harmonics and THD rate with respect to synchronous frequency at 250 A stator current.

7.5 Conclusion

In this chapter, influence of the slip and electric loading on the performance characteristics have been examined with particular reference to bar current waveform and the reason behind the non-sinusoidal bar current of a squirrel-cage IM is explained in detail. It is concluded that, the electric loading and the slip have a significant influence on the bar current waveform. After exceeding the specific stator current and the imposed speed, the bar current becomes non-sinusoidal. The main reason for all cases is the slot leakages due the saturation of the rotor tooth parts. Moreover, the non-sinusoidal bar current phenomena have been validated numerically by locked-rotor simulations.

It is demonstrated through Chapters 5, 6, and 7 that the magnetic saturation of the tooth parts increases the amplitudes of the low-order harmonic components, particularly the amplitude of the 3rd harmonic, which is the dominant harmonic component of the air-gap flux density and consequently the bar current. In the circumstances, since the bar current waveform is not sinusoidal (flat-topped), the amplitude of the bar current is different from that of the sinusoidal bar current. Consequently, the average torque, torque ripple, output power, efficiency, bar current density, etc. cannot be calculated accurately. Therefore, for the sake of accuracy, the rotor current of an IM should not always be considered as sinusoidal during the design and analysis stages.

8 General Conclusions and Future Work

8.1 Summary

This thesis investigates the advanced IM topologies with reduced size, cost, and improved performance, with particular reference to the non-sinusoidal bar current phenomenon in squirrel-cage IMs. Firstly, alternative methodologies for the size reduction of IMs have been investigated. The most promising topology is identified as FSCW technique due to its significantly short-end windings. However, it is found that due to the highly distorted MMF created by the FSCWs, adopting FSCWs into the IMs results in a large amount of rotor bar copper losses. In order to reduce the MMF harmonics without increasing the size of the machine, a new technique, called “non-overlapping winding”, is developed. Basically, this technique consists of the combination of the auxiliary tooth (doubled stator slots) technique and phase shifting technique, i.e. short-pitched windings with a coil pitch of two slot pitches together with an adapted non-overlapping technique. Thanks to this method more than 42% of the MMF harmonics are cancelled. As an inevitable consequence of non-overlapping winding technique, half of the stator slots left unfilled. In order to improve the performance of the machine, half of the unfilled slots are utilized by core material and a unique slot shape with lower leakage flux has been obtained as a result of multi-objective global optimization by genetic algorithm. As a consequence, a unique stator structure with non-overlapping windings has been obtained. Thus, a 25% axially shorter IM with improved performance is designed when compared to its conventional counterpart.

The influences of a number of design parameters; such as number of turns, rotor slot number, stator slot/rotor slot/pole number combinations, stator and rotor slot geometric parameters, and stack length on the performance and flux-weakening characteristics have been investigated. It is shown that each design parameters has a significant effect on the performance characteristics of the AIMs. It is also found that increasing the stack length from 70mm to 105mm leads to 41.55% increase in the peak power in the constant power region. Furthermore, the peak power has been increased up to 408% in the deep flux-weakening region (i.e. 20krpm). It is found that to be able to mitigate the parasitic effects and overall performance of AIMs, simultaneously, the rotor slots with closed slots, particularly with u-shaped bridges can be adopted. By adopting the u-shaped rotor slot bridges to a AIM, ~30% and ~50% reductions in bar copper loss and torque ripple have been achieved, respectively. In addition, ~1.08 increase in the maximum efficiency and ~6% reduction in the rotor bar current density are obtained. However, since some of the flux are short-circuited through the bridges, it has a 3.8% reduction in the average torque.

The comparative analysis between the CIM and AIMs shows that the overall performances of the AIMs are competitive and even better than CIM under high electric loadings and mid-constant power operation region, in terms of torque, power, and efficiency. In addition, in the deep flux-weakening

region, although the flux-weakening performance of the AIM is poorer than that of the CIM, it is possible to increase it significantly by appropriately increasing the stack length of the AIM.

In this thesis, the rotor bar current waveform, which is usually assumed to be sinusoidal, has also been investigated in detail. It is shown that the bar current waveform can become non-sinusoidal under some certain design and operating conditions; such as very low slip operating, very high electric loading operating, very narrow air-gap length designs, design with inappropriate stator slot/rotor slot/pole number combinations, design with inaccurate rotor skew angle, and design with inappropriate stator slot and/or rotor slot geometric parameters. Moreover, the iron saturation levels in different parts of the IM are examined and their influences are also investigated, while the dominant part causing the non-sinusoidal rotor bar current waveform is identified. It is found that the magnetic saturation, particularly in the rotor tooth tip parts and rotor tooth body parts, has a significant effect on the bar current waveform; and the phenomenon has been explained in detail.

8.2 Importance of MMF Harmonics for Squirrel-Cage IMs

Since the air-gap flux density is mainly produced by the stator windings, their influence on the performance of IMs is of great importance. The quality of the air-gap flux density depends on the distribution of the phase windings and consequently the quality of the MMF waveform. This distribution may be integer or fractional and the windings can be concentrated or distributed. Each winding configuration has its own merits and demerits. However, as shown in Chapter 2, the FSCW topologies are not suitable for the EV/HEV applications because of their insufficient performance and low efficiency due to the highly distorted MMF waveform. Some key properties corresponding to the importance of the MMF harmonics can be summarised as follows:

- Although the FSCWs provide quite shorter axial end-winding lengths, which is favourable in terms of compactness and lower stator copper loss, their MMF waveforms are highly distorted, causing a significant increase in the bar copper loss and parasitic effects, such as torque ripple, acoustic noise, vibration, etc.
- Although compactness is essential for the EV/HEV applications, it is not appropriate to employ FSCWs in the IMs because of the insufficient performance and unwanted parasitic effects.
- Increasing the stator slot number and pole number of any q family leads to a reduction in the magnitude of the MMF harmonics.
- Utilizing double-layer windings rather than single-layer windings leads to low parasitic effects since the harmonic winding factors and MMF harmonic contents of the double-layer configurations are lower than those of the single-layer configurations.

8.3 Developed Non-Overlapping Winding Topology

8.3.1 MMF Harmonic Reduction Method

An adapted non-overlapping winding configuration with an unconventional stator has been developed for a squirrel-cage IM in order to reduce the total axial length and improve the performance characteristics at the same time. Basically, the developed method consists of the combination of auxiliary/doubled stator slot approach and correspondingly the phase shifting method. As presented in Chapter 3, if the second set of winding is shifted by 3 stator slots and the polarization of the windings are reversed according the first set of winding, the resultant stator being short-pitched windings with a coil pitch of two slot pitches, it is possible to cancel the 6th and 12th winding harmonics. Therefore, comparing to initial FSCW topology, it is possible to reduce the winding harmonic index by ~42.6% by adopting the proposed ANW technique. Since the coils of the phases are non-overlapped, half of the stator slots cannot be fully filled. However, in order to improve the effectiveness of the proposed winding topology, the unfilled stator slots have been utilized with iron core material and the slot geometry has been optimized for achieving the minimum slot flux leakage by genetic algorithm.

8.3.2 Key Properties of the Developed Winding Topology

The primary function of the proposed methodology is to reduce the harmonic content of the MMF waveform without increasing the total axial length and sacrificing the performance characteristics. The key properties of the proposed ANWs are compared with ISDW and FSCW configurations in Table 8.1.

Table 8.1 Comparison of properties of different winding configurations

Characteristic	Relation	ISDW	ANW	FSCW
MMF harmonic content	Number of stator slot/phase/pole (q)	Lowest	Low	Highest
Magnitude of fundamental MMF	Slot-pitch number (y_c)	Highest	High	Lowest
Rotor copper loss Eddy current loss Parasitic effects	MMF harmonics	Lowest	Low	Highest
Leakage inductance	Contact among the phases through the coil	Low	Moderate	High
	Space requirement	More	Less	Less
End-winding	Axial end-winding length	Long	Short	Short
	Stator end-winding copper loss	High	Low	Low
	Easy of assemble	Difficult	Easy	Easy
Stator slot fill factor	Efficiency Current Density Thermal conductivity	Low	High	High

Other important properties of the proposed winding topology can be listed as follows:

- ✘ Advantages of using ANWs instead of ISDWs:
 - Relatively high efficiency;
 - Short total axial length;
 - Simplicity in manufacturing.
- ✘ Disadvantages of using ANWs:
 - Relatively high torque ripple;
 - Relatively high rotor bar current density;
 - Low winding factor (0.866).

8.3.3 Design of IMs with Adapted Non-Overlapping Winding Topology

As explained in Chapter 3, since the coils of the windings are single lap-coil, it is possible to design lap-coil windings with any slot pitch without sacrificing the fundamental winding factor. Then, the number of the overlay would be equal to number of coil pitch. However, the proposed winding configuration is not applicable for any stator slot/pole number combinations. It is applicable only for the $q = 1$ combinations.

The key findings obtained from an IM, whose stator windings are designed with ANWs, are given as follows.

- Thanks to the proposed method, ~42.6% of the MMF harmonics are cancelled. Consequently, the rotor bar copper loss is reduced more than ~70% comparing to its FSCW counterpart.
- Thanks to the proposed method, the total axial length is reduced ~ 25% comparing to its ISDW counterpart. Furthermore, torque and power densities are improved remarkably.

Furthermore, even if the stator slots, which cannot be fully filled, seem to exhibit disadvantage in terms of space utilization, they actually may help improving the thermal characteristics of the IM by introducing extra air-cooler canals into the stator.

In order to validate the FEA predictions of the AIMs, a 70mm 18S/44R/6P AIM and 90mm 18S/20R/6P AIM are decided to prototype, and the manufacturing of the stator stacks have been completed. The photos of the manufactured stator stacks are shown in Fig. 8.1. Since prototyping of IMs is much more complicated, particularly the rotors, the prototypes are still in the process of manufacturing. The torque/power characteristics, power factor, and efficiency predictions will be validated by the experimental measurements in the future. Note that the FEA predictions have been validated on CIM in Chapter 2.

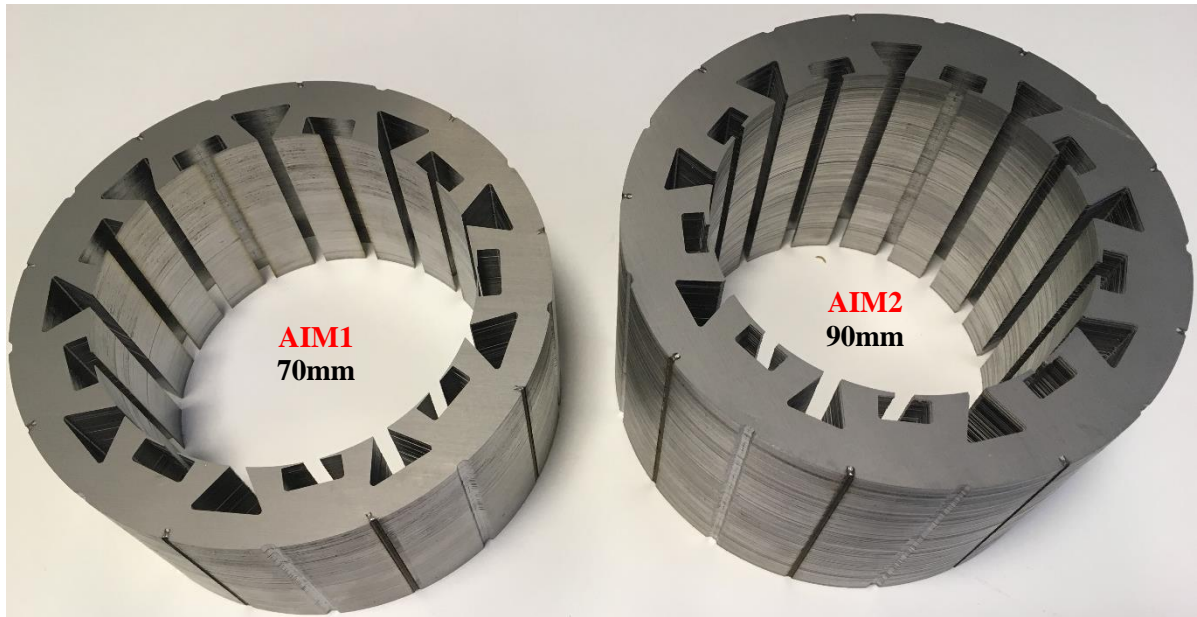


Fig. 8.1 Prototyped stator stacks with 70mm and 90mm stack lengths.

8.3.4 Influence of Design Parameters

It is shown in Chapters 3 and 4 that the major machine parameters, such as rotor slot number for a specific stator slot and pole numbers, stator slot/rotor slot/pole number combinations, stack length, number of turns per phase, slot geometry parameters, etc. have a significant influence on the electromagnetic and flux-weakening performance characteristics. Useful design guidelines for AIMs obtained from a large number of parametric analyses are summarised as follows.

- The influence of stator slot and pole number combination on the performance and characteristics of the AIMs:
 - The high-pole and correspondingly high-stator slot number for lower MMF harmonics and consequently lower bar copper loss and parasitic effects;
 - Low-pole number for higher torque and hence high power in the constant power region;
 - Low-pole number for lower skin and proximity effect loss of the windings and total core losses.

- The influence of the rotor slot number on the performance and characteristics of the AIMs:
 - Phase, pole, and stator slot numbers should be considered for the minimization of the parasitic effects and UMP;
 - Low-rotor slot number for lower bar copper loss and bar current density;
 - The proposed empirical formula, $R \approx S + 2q$, for the optimal rotor slot number in terms of minimal torque ripple, bar copper loss, and bar current density.

- The influence of stack length on the performance and characteristics of the AIMS:
 - The longer stack length leads to a low number of turns requirement and consequently high torque at high-speed operations;
 - Lower stator and rotor copper losses and current densities, high efficiency, and higher power can be achieved by designing the stack length relatively longer.
 - The longer the stack length, the lower the stator current density and the copper losses, the higher the efficiency;
 - The longer the stack length, the higher the material cost, weight, volume and consequently the more space requirement.

Moreover, if the flux-weakening and efficiency characteristics are more critical restrictions than the compactness, then, it is possible to improve the overall electromagnetic and flux-weakening characteristics of an IM by increasing the stack length. The key idea that makes the overall performance improvement possible by increasing the stack length is to reduce the number of turns per phase in order to keep the torque at the same level. Thus, since the number of turns and consequently the main flux is reduced, the flux-weakening performance increases significantly. In addition, since the output power is increased and the stator copper loss is reduced by adopting the reduced number of turns per phase, the efficiency of the machine increases remarkably. It should be noted that for constant torque region, the higher the number of turns, the higher the power. However, as for the constant power region, the lower the number of turns, the higher the power. Moreover, each slot geometry parameter has a significant effect on the performance characteristics individually. Therefore, in order to achieve the best performance characteristics, the carefully selected geometric parameters of the IMs should be optimized globally.

8.3.5 Influence of Rotor Type/Slot Opening Effect

Depending on the manufacturing process, time, and cost, it is possible to design the rotor as open slot with insert-bars or closed slot with die-casting bars. In Chapter 4, the influence of rotor slot opening on the average torque, torque ripple, bar copper loss, and efficiency is investigated. It is shown in Chapter 4 that the parasitic effects and the bar copper loss may be reduced significantly by utilizing closed rotor slots with u-shaped slot bridges. The main advantage of the open-slot rotor type is that it has a slightly better flux-weakening capability than that of the closed-slot rotor types. However, the bar copper loss and parasitic effects of the open-slot rotor types are considerably high. In addition, manufacturing of the open-slot (insert-bar) rotor types is more difficult than that of the cast-rotor types. The benefits of utilizing rotor with a u-shaped bridge structure are summarised as follows:

- ✧ Since the high-order air-gap flux density harmonics are filtered by the rotor bridges, ~30% in bar copper loss and ~50% reduction in torque ripple are achieved;

- ✘ The maximum efficiency is increased by $\sim 1.08\%$;
- ✘ Die-casting manufacturing method may be utilized easily;
- ✘ Slip is reduced by $\sim 0.53\%$;
- ✘ Since $\sim 6\%$ reduction in the rotor bar current density is achieved, smaller cooling equipment may be used.

On the other hand, some drawbacks of the u-shaped bridges are given as follows.

- A slight reduction in the flux-weakening performance;
- There is a 3.8% reduction in the average torque at the constant torque region, because of the short-circuited flux through the rotor bridges;
- Reduction in the mechanical resilience on the rotor part because of the quite thin rotor bridges.

8.4 Comparison between CIM and AIM

In order to reveal the advantages of the ANW topology, the IM designed by employing the ANWs is compared with the CIM having ISDW configuration. To be able to conduct a fair comparison, all the machines have been designed with the same stator outer diameter, stack length, materials, and inverter current and voltage ratings. In order to show that the performance of the AIMS can be increased by increasing the stack length, AIM1 and AIM2, whose stack length and total axial length equal to the CIM, respectively, have been designed. The key characteristics of the machines are compared as listed in Table 8.2. Note that in order to simplify the comparison, the CIM is chosen as the basis and the performance parameters of all other machines are normalized correspondingly. As seen in Table 8.2, the overall performances of the AIMS are competitive. Note that the material costs, mass densities and mass calculation method are presented in Appendix E.4.

It has also been revealed that thanks to the flexible design options provided by the AIM topology, it is possible to design compact and high efficiency IMs. On the other hand, if the high electromagnetic performance and efficiency are considered as more important design criteria, then it is also possible to meet these criteria by extending the stack length without exceeding the total axial length of the corresponding CIM design.

8.5 Non-Sinusoidal Bar Current Phenomenon in IMs

Detailed investigations on the non-sinusoidal bar current waveform have been carried out. The influence of design and operating parameters, such as; slip, electric loading, air-gap length, rotor slot number, stator slot/pole number combinations, rotor skew angle, and coil pitches on the electromagnetic performance with a particular reference to bar current waveform has been presented. It is found that

since there is a direct correlation between all these parameters and the saturation level of the machine, all the considered parameters have a significant effect on the performance and rotor bar current waveform.

8.5.1 Influence of Saturation

In Chapter 5, the levels of iron saturation in different parts, including the stator and rotor back iron, tooth body and tooth tips etc., are examined in order to identify the dominant part causing the non-sinusoidal bar current waveform. It is found that although each part on the main flux path has a considerable effect on the bar current waveform, among these parts, the saturation of the rotor tooth body parts has the most contribution to the distortion of rotor bar current. This study has also revealed that the high saturation causes more slot leakage flux, especially in the tooth tip parts. The flux density of the tooth tip parts contain highly distorted flux components and those harmonics diminish to the minimum due to the average effect of the tooth body parts.

Table 8.2 Normalized electromagnetic performance, mass, and cost comparison under different operation conditions (The baseline: CIM)

	CIM (Absolute Values)	AIM1	AIM2
Stack Length	50.8mm	1	1.425
Total Axial Length	101.24mm	0.786	1
Torque (~1krpm) @100A	85.31Nm	0.876	0.975
Torque (~1krpm)@250A	220.75Nm	0.992	0.989
Torque (~1krpm) @500A	462.713Nm	1.085	1.151
Torque @8krpm	109.82Nm	0.785	0.983
Torque @16krpm	15.83Nm	0.853	0.905
Torque Ripple @100A	11.85%	1.424	0.979
Torque Ripple @250A	10.15%	1.934	1.005
Torque Ripple @500A	9%	2.055	1.022
Output Power (Rated)	33.52kW	0.981	0.99
Output Power (Max)	110.08kW	0.816	1.038
Output Power @8krpm	92.2kW	0.785	0.981
Output Power @16krpm	26.57kW	0.853	0.988
Efficiency (Rated)	83%	0.956	1.015
Efficiency (Max)	95%	1	1.01
Efficiency @8krpm	94%	1.011	1.021
Efficiency @16krpm	87%	1.035	1.08
Stator Current Density (~1krpm)	28.52A/mm ²	1.008	0.839
Rotor Current Density (~1krpm)	18.17A/mm ²	0.919	0.735
Total Mass	25.22kg	0.963	1.23
Total Cost	£48.05	0.975	1.025

8.5.2 Influence of Design and Operating Parameters

The influences of a number of design and operating parameters; such as slip, electric loading, air-gap length, rotor slot number, stator slot/pole number, stator and rotor slot geometric parameters, rotor skew, and stator coil pitch on the bar current waveform and performance characteristics are investigated in Chapters 6 and 7. It is found that each design and operating parameter have a substantial effect on the saturation level of the machine parts and consequently on the bar current distortion level and performance characteristics. It has been verified through the parametric analyses for each design and operating parameters that after exceeding a critical amount of the considered parameter, the bar current becomes non-sinusoidal (flat-topped). The findings of influence of slip and electric loading analyses have also been numerically verified through the locked-rotor analyses.

It is demonstrated in Chapters 5, 6, and 7 that the magnetic saturation of the tooth parts increases the amplitudes of the low-order harmonic components, particularly the amplitude of the 3rd harmonic. Depending on the distortion level of the bar current, the bar current waveform and consequently the amplitude are different from those of the sinusoidal bar current. In conclusion, if the bar current is always assumed as being sinusoidal, the average torque, torque ripple, output power, bar current density, rotor bar copper loss, efficiency, etc. cannot be calculated accurately. Therefore, for the sake of accuracy, the rotor current of an IM should not always be considered as sinusoidal during both design and analysis stages.

8.6 Future Work

Following the research presented in this thesis, the proposed future research includes:

- Investigation of thermal characteristics of the AIMs and potential utilization of not fully filled slots for ventilation;
- Investigation of rotor bridge mechanical stress;
- Investigation of multi-phase ($m > 3$) non-overlapping winding configurations;
- Investigation of asymmetric non-overlapping winding configurations;
- Investigation of new squirrel-cage rotor structures on the performance of the AIMs;
- Experimental investigation of AIMs;
- Investigation of non-sinusoidal bar current phenomenon under no-load operating condition;
- Corresponding to the locked-rotor analyses, the development of a practical method for the online measurement of the rotor bar current.

References

- [ABD12] A. S. Abdel-Khalik and S. Ahmed, "Performance evaluation of a five-phase modular winding induction machine," *IEEE Trans. Ind. Electron.*, vol. 59, no. 6, pp. 2654 - 2669, Jun. 2012.
- [ABD13] C. Abdellah and B. Azeddine, "Spectral analysis to detect mixed eccentricity fault in saturated squirrel cage induction motor," in *IEEE Int. Signal Process. Comput. Control Conf. (ISPCC'13)*, 2013, pp. 1-6.
- [ABD15a] A.S. Abdel-Khalik, S. Ahmed, and A. M. Massoud, "Low space harmonics cancelation in double-layer fractional slot winding using dual multiphase winding," *IEEE Trans. Magn.*, vol.51, no.5, pp.1-10, May 2015.
- [ABD15b] A. S. Abdel-Khalik, M. S. Diab, S. Ahmed, and A. M. Massoud, "A new single tooth winding layout for a single-phase induction motor with segmented stator," in *IEEE Ind. Electron. Soc. Annu. Conf. (IECON'15)*, Yokohama, 2015, pp. 102-107.
- [AGA16] E. B. Agamloh, A. Cavagnino, and S. Vaschetto, "Impact of number of poles on the steady-state performance of induction motors," *IEEE Trans. Ind. Appl.*, vol. 52, no. 2, pp. 1422-1430, Mar. 2016.
- [AGU12] A. B. M. Aguiar, A. Merkhouf, and K. Al-Haddad, "Influence of the air gap length on the magnetic core loss in large hydro generator," in *Int. Conf. Elect. Mach. (ICEM'12)*, 2012, pp. 328-332.
- [AHO06] T. Aho, J. Nerg, and J. Pyrhonen, "The effect of the number of rotor slits on the performance characteristics of medium-speed solid rotor induction motor," in *Int. Conf. Power Electron., Mach. Drives, (PEMD'06)*, Dublin, 2006, pp. 515-519.
- [ALB08] L. Alberti, N. Bianchi, and S. Bolognani, "A very rapid prediction of im performance combining analytical and finite-element analysis," *IEEE Trans. Ind. Appl.*, vol. 44, no.5, pp. 1505-1512, Sept. 2008.
- [ALB09a] L. Alberti, N. Bianchi, and S. Bolognani, "A finite-element procedure to compute variable speed induction machine performance," in *IEEE Energy Convers. Congr. Expo. (ECCE'09)*, 2009, pp. 20-24.
- [ALB09b] L. Alberti and N. Bianchi, "Analysis of asynchronous machines for direct drive wind power generation," in *Int. Elect. Mach. Drives Conf. (IEMDC'09)*, Miami, 2009, pp. 1838-1843.
- [ALB11] L. Alberti, N. Bianchi, and S. Bolognani, "Variable-speed induction machine performance computed using finite-element," *IEEE Trans. Ind. Appl.*, vol. 47, no. 2, pp. 789-797, Apr. 2011.
- [ALB12] L. Alberti and N. Bianchi, "Design and tests on a fractional-slot induction machine," in *IEEE Energy Convers. Congr. Expo. (ECCE'12)*, 2012, pp. 166-172.
- [ALB13] L. Alberti and N. Bianchi, "Theory and design of fractional-slot multilayer windings," *IEEE Trans. Ind. Appl.*, vol. 49, no. 2, pp. 841-849, Jan. 2013.
- [ALG54] P. L. Alger, "The magnetic noise of polyphase induction motors," *Trans. American Inst. Elect. Eng., Part III: Power App. Syst.*, vol. 73, no. 1, pp. 118-125, Jan. 1954.
- [ALG65] P.L. Alger, *Induction Machines – Their Behavior and Uses*, 2nd ed. NY: Gordon and Breach Science Pub. Ltd., 1965, pp.181-188.

- [ALG76] P. L. Alger and R. E. Arnold, "The history of induction motors in America," *IEEE Proc.*, vol. 64, no. 9, pp. 1380-1383, Sept. 1976.
- [ALM14] A. T. D. Almeida, F. J. T. E. Ferreira and D. A. Quintino, "Technical and economical considerations on super high-efficiency three-phase motors," *IEEE Trans. Ind. Appl.*, vol.50, no.2, pp.1274-1285, Apr. 2014
- [AMO95] A. H. Amor, P. L. Timar, and M. Poloujadoff, "Induction squirrel cage machine design with minimization of electromagnetic noise," *IEEE Trans. Energy Convers.*, vol. 10, no. 4, pp. 681-687, Dec 1995.
- [ANG63] G. Angst, "Saturation factors for leakage reactance of induction motors with skewed rotors," *IEEE Trans. Power App. Syst.*, vol. 82, no. 68, pp. 716-725, Oct. 1963.
- [APP87a] J. Appelbaum, E. F. Fuchs, and J. C. White, "Optimization of three-phase induction motor design part I: Formulation of the optimization technique," *IEEE Trans. Energy Convers.*, vol. EC-2, no. 3, pp. 407-414, Sept. 1987.
- [APP87b] J. Appelbaum, I. A. Khan, E. F. Fuchs, and J. C. White, "Optimization of three-phase induction motor design part II: The efficiency and cost of an optimal design," *IEEE Trans. Energy Convers.*, vol. EC-2, no. 3, pp. 415-422, Sept. 1987.
- [ARA10] H. Arabaci and O. Bilgin, "Effects of rotor faults in squirrel-cage induction motors on the torque-speed curve," in *Int. Conf. Elect. Mach. (ICEM'10)*, Rome, 2010, pp. 1-5.
- [ARK97] A. Arkkio, "Unbalanced magnetic pull in cage induction motors with asymmetry in rotor structures," in *Int. Conf. Elect. Mach. Drives, (IEMDC'97)*, Cambridge, 1997, pp. 36-40.
- [BAC15] J. P. Bacher and A. Mütze, "Comparison of an induction machine with both conventionally distributed and fractional-slot concentrated stator windings," *e & i Elektrotechnik und Informationstechnik*, vol. 132, no. 1, pp. 39-45, 2015.
- [BAR56] T. H. Barton, O. I. Butler and H. Sterling, "The theory and characteristics of the 3:1 pole-changing induction motor," in *Proc. IEE - Part A: Power Eng.*, vol. 103, no. 9, pp. 285-294, Jun. 1956.
- [BAR97] R. Barro and P. Hsu, "Torque ripple compensation of induction motors under field oriented control," in *Applied Power Electron. Conf. (APEC'97)*, 1997, pp. 527-533.
- [BEE08] J. Beerten, J. Verweckken, and J. Driesen, "Prediction-based ripple reduction in direct torque control of an induction machine," in *Int. Conf. Elect. Mach. (ICEM'08)*, Vilamoura, 2008, pp. 1-6.
- [BEL06] A. Bellini, O. Bottauscio, M. Chiampi, C. Tassoni, and M. Zuca, "Induction motor rotor quantities at load conditions: finite element analysis and experimental validation," *IEEE Trans. Magn.*, vol. 42, no. 10, pp. 3476-3478, Oct. 2006.
- [BEL08] A. Bellini, F. Filippetti, C. Tassoni, and G. A. Capolino, "Advances in diagnostic techniques for induction machines," *IEEE Trans. Ind. Electron.*, vol. 55, no. 12, pp. 4109-4126, Dec. 2008.
- [BEN98] A. Benoudjit and N. Nait Said, "New dual-airgap axial and radial-flux induction motor for on wheel drive electric propulsion systems," in *Int. Conf. Power Syst. Technol. (POWERCON'98)*, 1998, pp. 615-619.
- [BES08a] J. L. Besnerais, V. Lanfranchi, M. Hecquet, and P. Brochet, "Multiobjective optimization of induction machines including mixed variables and noise minimization," *IEEE Trans. Magn.*, vol. 44, no. 6, pp. 1102-1105, Jun. 2008.

- [BES08b] J. L. Besnerais, V. Lanfranchi, M. Hecquet, and P. Brochet, "Acoustic noise of electromagnetic origin in a fractional-slot induction machine," *COMPEL - Int. J. Comput. Math. Elect. Electron.*, vol. 27, no. 5, pp. 1033-1052, Feb. 2008.
- [BES09] J. L. Besnerais, V. Lanfranchi, M. Hecquet, and P. Brochet, "Optimal slot numbers for magnetic noise reduction in variable-speed induction motors," *IEEE Trans. Magn.*, vol. 45, no. 8, pp. 3131-3136, Aug. 2009.
- [BIA00] N. Bianchi and S. Bolognani, "Reducing torque ripple in PM synchronous motors by pole-shifting," in *Int. Conf. Elect. Mach. (ICEM'00)*, Helsinki, Finland, 2000, pp. 1222-1226.
- [BIA04] N. Bianchi and T. Jahns, "Design, analysis, and control of interior PM synchronous machines," *IEEE Ind. Appl. Soc.*, 2004, ch. 3, pp. 3.1-3.66.
- [BIA08] N. Bianchi, S. Bolognani, D. Bon, and M. D. Pre, "Torque Harmonic Compensation in a Synchronous Reluctance Motor," *IEEE Trans. Energy Convers.*, vol. 23, no. 2, pp. 466-473, Jun. 2008.
- [BIA09] N. Bianchi, S. Bolognani, D. Bon, and M. D. Pre, "Rotor flux-barrier design for torque ripple reduction in synchronous reluctance and PM-assisted synchronous reluctance motors," *IEEE Trans. Ind. Appl.*, vol. 45, no. 3, pp. 921-928, Jun. 2009.
- [BIA12] N. Bianchi, D. Durello, and E. Fornasiero, "Multi-objective optimization of a PM Assisted Synchronous Reluctance Machine, including torque and sensorless detection capability," in *IET Int. Conf. Power Electron., Mach. Drives (PEMD'12)*, Bristol, 2012, pp. 1-6.
- [BIA97a] N. Bianchi and S. Bolognani, "Parameters and volt-ampere ratings of a field-oriented induction motor drive for flux-weakening applications," in *Proc. Int. Conf. Elect. Mach. Drives (IEMDC'97)*, 1997, pp. 46-50.
- [BIA97b] N. Bianchi and S. Bolognani, "Design procedure of a vector controlled induction motor for flux-weakening operations," in *Conf. Rec. 32nd IEEE IAS Annu. Meeting*, New Orleans, LA, 1997, pp. 104-111.
- [BIA98] N. Bianchi and S. Bolognani, "Unified approach to the analysis and design of an AC motor drive for flux-weakening operations," in *Rec. 33rd IEEE IAS Annu. Meeting Ind. Appl. Conf.*, 1998, pp. 95-102.
- [BIA99] N. Bianchi, S. Bolognani, and G. Comelato, "Finite element analysis of three-phase induction motors comparison of two different approaches," *IEEE Trans. Energy Convers.*, vol. 14, no.4, pp. 1523-1528, Dec. 1999.
- [BLA03] S. T. Blazek, J. W. Sliwa, and A. F. Kolesnichenko, "Asynchronous motors having rotor structures". U. S. Patent 6,531,801 B1, Mar. 11, 2003.
- [BLA09] F. Blazquez, C. Vezanones, D. Ramirez, and C. Platero, "Characterization of the rotor magnetic field in a brushless doubly-fed induction machine," *IEEE Trans. Energy Convers.*, vol. 24, no. 3, pp. 599-607, Sept. 2009.
- [BOG03] A. Boglietti, O. Bottauscio, M. Chiampi, and M. Lazzari, "Modelling high frequency phenomena in the rotor of induction motors under no-load test conditions," *JMMM-J. Magnetism Mag. Mat.*, vol. 254-255, no. 0, pp. 244-246, Jan. 2003.
- [BOG11] A. Boglietti, A. Cavagnino, and M. Lazzari, "Computational algorithms for induction-motor equivalent circuit parameter determination—part I: resistances and leakage reactances," *IEEE Trans. Ind. Electron.*, vol. 58, no. 9, pp. 3723-3733, Sep. 2011.

- [BOG13] A. Boglietti, A. Cavagnino, M. Popescu, and D. Staton, "Thermal model and analysis of wound-rotor induction machine," *IEEE Trans. Ind. Appl.*, vol. 49, no. 5, pp. 2078-2085, Sept./Oct. 2013
- [BOG92] A. Boglietti, P. Ferraris, M. Lazzari, and F. Profumo, "A new design criteria for spindles inductance motors controlled by field-oriented technique," in *Proc. Int. Conf. Elect. Mach. (ICEM'92)*, pp. 356-360, 1992.
- [BOL01] I. Boldea, and S. A. Nasar, *The Induction Machine Handbook*, FL:CRC Press LLC, pp. 28-30, 2001.
- [BOL10] I. Boldea, and S. A. Nasar, *The Induction Machine Design Handbook*, 2nd ed. FL:CRC Press LLC, pp.513-537, 2010.
- [BOL14] I. Boldea, L. Tutelea, L. Parsa, and D. Dorrell, "Automotive electric propulsion systems with reduced or no permanent magnets: An overview," *IEEE Trans. Ind. Electron.*, vol. 61, no. 10, pp. 5696-5711, Oct. 2014.
- [BON08] A. H. Bonnett and C. Yung, "Increased efficiency versus increased reliability," *IEEE Ind. Applicat. Mag.*, vol. 14, no. 1, pp. 29-36, Jan. 2008.
- [BOT04] O. Bottauscio, M. Chiampi, A. Manzin, and M. Zucca, "Additional losses in induction machines under synchronous no-load conditions," *IEEE Trans. Magn.*, vol. 40, no. 5, pp. 3254-3261, Sept. 2004.
- [BOT05] O. Bottauscio, M. Chiampi, L. Donadio, and M. Zucca, "Experimental setup for the measurement of induction motor cage currents," *JMMM-J. Magnetism Mag. Mat.*, vol. 290-291, Part 2, no. 0, pp. 1322-1325, Apr. 2005.
- [BRA74] J. R. Brauer, "Saturation harmonics and current waveforms of single-phase induction motors," *IEEE Trans. Power App. Syst.*, vol. PAS-93, no. 1, pp. 40-44, Jan. 1974.
- [BRU07] C. Bruzzese, O. Honorati, and E. Santini, "Evaluation of classic and innovative sideband-based broken bar indicators by using an experimental cage and a transformed (n, m) complex model," in *IEEE Int. Symp. Ind. Electron. (ISIE'07)*, pp. 1264-1269, 2007.
- [BU03] L. Bu, C. Li, J. Krukowski, W. Xu, and X. Liu, "A new energy recovery double winding cage-rotor induction machine," *IEEE Trans. Energy Convers.*, vol. 18, no. 2, pp. 315-320, 2003.
- [BUC72] L. W. Buchanan and K. L. Cation, "Rotor current and magnetic field variations in induction motors with skewed rotors," *IEEE Trans. Power App. Syst.*, vol. PAS-91, no. 5, pp. 1803-1811, Sept. 1972.
- [BUS16] J. Buschbeck, M. Vogelsberger, A. Orellano, and E. Schmidt, "Pareto optimization in terms of electromagnetic and thermal characteristics of air-cooled asynchronous induction machines applied in railway traction drives," *IEEE Trans. Magn.*, vol. 52, no. 3, pp. 1-4, Mar. 2016.
- [CAR14] E. Carraro, N. Bianchi, S. Zhang, and M. Koch, "Permanent magnet volume minimization of spoke type fractional slot synchronous motors," in *IEEE Energy Convers. Congr. Expo. (ECCE'14)*, Sept 2014.
- [CAR95] F. Caricchi, F. Crescimbeni, and E. Santini, "Axial flux electromagnetic differential induction motor," in *Int. Elect. Mach. Drives Conf. (IEMDC'95)*, Durham, 1995, pp. 1-5.
- [CHA02] C. C. Chan, "The state of the art of electric and hybrid vehicles," *Proc. IEEE*, vol. 90, no. 2, pp. 247-275, Feb. 2002.

- [CHA06] H. R. Cha, C. H. Yun, T. U. Jung, H. M. Kim, J. C. Kim, S. H. Baek, and K. H. Kim, "A control of the mmf space harmonic parasitic torques in the concentrated winding ac machine using skew angle optimization," in *IEEE Ind. Electron. Conf. (IECON'06)*, Paris, 2006, pp. 1018-1022.
- [CHA07] C. C. Chan, "The state of the art of electric, hybrid, and fuel cell vehicles," *IEEE Proc.*, vol. 95, no. 4, pp. 704-718, Apr. 2007.
- [CHA64] B. J. Chalmers, "A.C. machine windings with reduced harmonic content," in *Proc. Inst. Elect. Eng.*, vol. 111, no. 11, pp. 1859-1863, Nov. 1964.
- [CHA69] B. J. Chalmers and R. Dodgson, "Saturated leakage reactances of cage induction motors," *Proc. Inst. Elect. Eng.*, vol. 116, no. 8, pp. 1395-1404, Aug. 1969.
- [CHA71] B. J. Chalmers and R. Dodgson, "Waveshapes of flux density in polyphase induction motors under saturated conditions," *IEEE Trans. Power App. Syst.*, vol. 90, no. 2, pp. 564-569, Mar. 1971.
- [CHE02] S. Chen, B. Lequesne, R. R. Henry, Yanhong Xue, and J. J. Ronning, "Design and testing of a belt-driven induction starter-generator," *IEEE Trans. Ind. Appl.*, vol. 38, no. 6, pp. 1525-1533, Nov. 2002.
- [CHE13] X. Chen, J. B. Wang, P. Lazari, and L. Chen, "Permanent-magnet assisted synchronous reluctance machine with fractional-slot winding configurations," in *IEEE Int. Elect. Mach. Drives Conf. (IEMDC'13)*, Chicago, May. 12-15, 2013, pp. 393-400.
- [CHE14] M. Cheng and P. Han, "A dual-stator brushless doubly-fed induction motor for EV/HEV applications," in *Int. Conf. Intell. Green Build. Smart Grid (IGBSG'14)*, Taipei, 2014.
- [CHE14b] X. Chen, J. Wang, and V. I. Patel, "A generic approach to reduction of magnetomotive force harmonics in permanent-magnet machines with concentrated multiple three-phase windings," *IEEE Trans. Magn.*, vol. 50, no. 11, pp. 1-4, Nov. 2014.
- [CHE17] X. Chen and J. Wang, "Magnetomotive force harmonic reduction techniques for fractional-slot non-overlapping winding configurations in permanent-magnet synchronous machines," *Chinese J. Elect. Eng.*, vol. 3, no. 2, pp. 102-113, Sep. 2017.
- [CHI08] R. K. S. Chitroju and C. Sadarangani, "Design and analysis of asymmetrical rotor for induction motors," in *Int. Conf. Elect. Mach. (ICEM'08)*, Vilamoura, 2008, pp. 1-6.
- [CHO16] P. K. Choudhary and S. P. Dubey, "Efficiency optimization of induction motor drive in steady-state using artificial neural network," in *Int. Conf. Comput. Power, Energy Inform. Commun. (ICCPEIC'16)*, Chennai, 2016, pp. 295-302.
- [CIS10] M.V. Cistelecan, F.J.T.E. Ferreira, M. Popescu, "Three phase tooth-concentrated interspersed windings with low space harmonic content," in *Int. Conf. Elect. Mach. (ICEM'10)*, Rome, Italy, 2010, pp.1-6.
- [COW03] J. G. Cowie and D. T. Brender, "Die-cast copper rotors for improved motor performance," in *Pulp Paper Ind. Tech. Conf.*, SC, USA, 2003, pp. 42-49.
- [COX08] T. Cox, F. Eastham, and J. Proverbs, "End Turn Leakage Reactance of Concentrated Modular Winding Stators," *IEEE Trans. Magn.*, vol. 44, no. 11, pp. 4057-4061, Nov. 2008.
- [COX11] T. Cox and J. F. Eastham, "Multi layer planar concentrated windings," in *IEEE Int. Elect. Mach. Drives Conf. (IEMDC'11)*, Niagara Falls, 2011, pp. 1439-1444.
- [CRO02] J. Cros and P. Viarouge, "Synthesis of high performance PM motors with concentrated windings," *IEEE Trans. Energy Convers.*, vol. 17, no. 2, pp. 248-253, Jun 2002.

- [CUI06] S. Cui, Y. Cheng, and C. C. Chan, "A basic study of electrical variable transmission and its application in hybrid electric vehicle," in *IEEE Veh. Power Propul. Conf. (VPPC '06)*, Windsor, 2006.
- [CUN06] M. Cunkas and R. Akkaya, "Design optimization of induction motor by genetic algorithm and comparison with existing motor," *Math. Comput. Applicat.*, vol. 11, no. 3, pp. 193–203, 2006.
- [CUN08] M. Cunkas, "Intelligent design of induction motors by multiobjective fuzzy genetic algorithm," *J. Intell. Manuf.*, vol. 21, no. 4, pp. 393-402, Nov. 2008.
- [DAI98] A. Daidone, F. Parsasiliti, M. Villani, and S. Lucidi, "A new method for the design optimization of three-phase induction motors," *IEEE Trans. Magn.*, vol. 34, no. 5, pp. 2932-2935, 1998.
- [DAJ08] G. Dajaku and D. Gerling, "Influence of the air-gap permeance harmonics on the performances of the salient pole synchronous PM machines," in *Int. Conf. Elect. Mach. (ICEM'08)*, 2008, pp. 1-6.
- [DAJ11a] G. Dajaku and D. Gerling, "Eddy current loss minimization in rotor magnets of PM machines using high-efficiency 12-teeth/10-slots winding topology," in *Int. Conf. Elect. Mach. Syst. (ICEMS'11)*, Beijing, 2011.
- [DAJ11b] G. Dajaku and D. Gerling, "A novel 24-slots/10-poles winding topology for electric machines," in *IEEE Int. Elect. Mach. Drives Conf. (IEMDC)*, pp.65-70, 2011.
- [DAJ12a] G. Dajaku and D. Gerling, "A novel 12-teeth/10-poles PM machine with flux barriers in stator yoke," in *Proc. 20th Int. Conf. Electr. Mach. (ICEM'12)*, Marseille, Sep. 2–5, 2012, pp. 36–40.
- [DAJ12b] G. Dajaku and D. Gerling, "Low costs and high-efficiency electric machines," in *Int. Elect. Drives Production Conf. (EDPC'12)*, Nuremberg, 2012, pp. 1-7.
- [DAJ13a] G. Dajaku and D. Gerling, "Different novel electric machine designs for automotive applications," in *Int. Elect. Veh. Symp. Exhib. (EVS'27)*, Barcelona, 2013, pp. 1-7.
- [DAJ13b] G. Dajaku and D. Gerling, "A novel tooth concentrated winding with low space harmonic content," in *IEEE Int. Electr. Mach. Drives Conf. (IEMDC'13)*, Chicago, IL, 2013, pp. 821–826.
- [DAJ13c] G. Dajaku and D. Gerling, "Novel Winding Topologies for Synchronous and Asynchronous Machines," *Haus der Technik*, Vol. 1, no. 14., pp. 26-40, 2013.
- [DAJ14a] G. Dajaku and D. Gerling, "Low costs and high efficiency asynchronous machine with stator cage winding," in *IEEE Int. Electric Veh. Conf. (IEVC'14)*, Florence, 2014, pp. 1-6.
- [DAJ14b] G. Dajaku, W. Xie, and D. Gerling, "Reduction of low space harmonics for the fractional slot concentrated windings using a novel stator design," *IEEE Trans. Magn.*, vol. 50, no. 5, pp. 1-12, May 2014.
- [DAJ15] G. Dajaku, F. Bachheibl, A. Patzak, and D. Gerling, "Intelligent stator cage winding for automotive traction electric machines," in *Int. Elect. Veh. Symp. Exhib. (EVS'28)*, Kintex, 2015, pp. 1-8.
- [DAJ16] G. Dajaku, S. Spas, X. Dajaku, and D. Gerling, "An improved fractional slot concentrated winding for low-poles induction machines," in *Int. Conf. Elect. Mach. (ICEM'16)*, Lausanne, 2016, pp. 114-119.

- [DAS16] P. P. Das and S. N. Mahato, "Design optimization of a six-phase induction motor by flower pollination and modified artificial bee colony algorithms," in *IEEE Region 10 Conf. (TENCON'16)*, Singapore, 2016, pp. 3313-3317.
- [DAU91] R. H. Daugherty and C. U. Wennerstrom, "Need for industry standards for AC induction motors intended for use with adjustable-frequency controllers," *IEEE Trans. Ind. Appl.*, vol. 27, pp. 1175-1185, Dec. 1991.
- [DEB02] K. Deb, A. Pratap, S. Agarwal, and T. Meyarivan, "A fast and elitist multiobjective genetic algorithm: NSGA-II," *IEEE Trans. Evol. Comput.*, vol. 6, no. 2, pp. 182-197, Apr 2002.
- [DEM14] M. Dems and K. Komez, "Performance characteristics of a high-speed energy-saving induction motor with an amorphous stator core," *IEEE Trans. Ind. Electron.*, vol. 61, no. 6, pp. 3046-3055, Jun. 2014.
- [DIA16] S. Diaz, U. Tietge, and P. Mock, "CO₂ emissions from new passenger cars in the EU: Car manufacturers' performance in 2015," The Int. Council on Clean Transport., June 2016.
- [DIA72a] P. Diamant, "A new approach to multi-segmented rotor slot design for induction motors Part I," *IEEE Trans. Power App. Syst.*, vol. PAS-91, no. 6, pp. 2383-2389, Nov. 1972.
- [DIA72b] P. Diamant, "A new approach to multi-segmented rotor slot design for induction motors Part II," *IEEE Trans. Power App. Syst.*, vol. PAS-91, no. 6, pp. 2390-2396, Nov. 1972.
- [DIA72c] P. Diamant, "A new approach to multi-segmented rotor slot design for induction motors Part III," *IEEE Trans. Power App. Syst.*, vol. PAS-91, no. 6, pp. 2397-2404, Nov. 1972.
- [DOG11] H. Dogan, F. Wurtz, A. Foggia, and L. Garbuio, "Performance analysis and comparison of three IPMSM with high homopolar inductance for electric vehicle applications," in *Proc. Eur. Conf. Power Electron. Appl.*, Birmingham, Sep. 2011, pp. 1-10.
- [DON05] L. Donadio, M. Zucca, A. Bellini, C. Concar, and E. Lorenzani, "Time harmonics investigation of stator and rotor currents of a dedicated induction machine," in *IEEE Int. Conf. Elect. Mach. Drives (IEMDC'05)*, San Antonio, 2005, pp. 1820-1825.
- [DON99] V. Donescu, A. Charette, Z. Yao, and V. Rajagopalan, "Modeling and simulation of saturated induction motors in phase quantities," *IEEE Trans. Energy Convers.*, vol. 14, no. 3, pp. 386-393, Sept. 1999.
- [DOR11] D. G. Dorrell, M. F. Hsieh, M. Popescu, L. Evans, D. A. Staton, and V. Grout, "A review of the design issues and techniques for radial-flux brushless surface and internal rare-earth permanent-magnet motors," *IEEE Trans. Ind. Electron.*, vol. 58, no. 9, pp. 3741-3757, Sep. 2011.
- [DOR12] D. G. Dorrell, A.M. Knight, L. Evans and M. Popescu, "Analysis and design techniques applied to hybrid vehicle drive machines—Assessment of alternative IPM and induction motor topologies," *IEEE Trans. Ind. Electron.*, vol. 59, no. 10, pp. 3690-3699, 2012.
- [DOR13] D. G. Dorrell, J. K. H. Shek, M. A. Mueller, and M. F. Hsieh, "Damper windings in induction machines for reduction of unbalanced magnetic pull and bearing wear," *IEEE Trans. Ind. Appl.*, vol. 49, no. 5, pp. 2206 - 2216, 2013.
- [DOR95] D. G. Dorrell, "The influence of rotor skew on unbalanced magnetic pull in cage induction motors with eccentric rotors," in *Int. Conf. Elect. Mach. Drives (Conf. Publ. No. 412)*, Durham, 1995, pp. 67-71.
- [DOR99] D. G. Dorrell, "Experimental behavior of unbalanced magnetic pull in 3-phase induction motors with eccentric rotors and the relationship with tooth saturation," *IEEE Trans. Energy Convers.*, vol. 14, no. 3, pp. 304-309, 1999.

- [DUA11a] S. Duan and L. Zhou, "Influence of parameters on field weakening performance of induction motor," in *Int. Conf. Elect. Mach. Syst. (ICEMS'11)*, Beijing, 2011, pp. 1-5.
- [DUA11b] Y. Duan and R. G. Harley, "A novel method for multiobjective design and optimization of three phase induction machines," *IEEE Trans. Ind. Appl.*, vol. 47, no. 4, pp. 1707-1715, Jul. 2011.
- [EAS08] F. Eastham, T. Cox, P. Leonard, and J. Proverbs, "Linear induction motors with modular winding primaries and wound rotor secondaries," *IEEE Trans. Magn.*, vol. 44, no. 11, pp. 4033-4036, Nov. 2008.
- [EAS10] J. F. Eastham, T. Cox and J. Proverbs, "Application of planar modular windings to linear induction motors by harmonic cancellation," in *IET Electric Power Appl.*, vol. 4, no. 3, pp. 140-148, Mar. 2010.
- [ERL65] M. S. Erlicki and J. Appelbaum, "Optimized parameter analysis of an induction machine," *IEEE Trans. Power App. Syst.*, vol. 84, no. 11, pp. 1017-1024, Nov. 1965.
- [EST16] S. Estenlund, M. Alaküla, and A. Reinap, "PM-less machine topologies for EV traction: A literature review," in *Int. Conf. Elect. Syst. Aircraft Railway Ship Propul. Road Veh. Int. Transport. Electrification Conf. (ESARS-ITEC)*, Toulouse, 2016, pp. 1-6.
- [FEI89] R. Fei, E. F. Fuchs, and H. Huang, "Comparison of two optimization techniques as applied to three-phase induction motor design," *IEEE Trans. Energy Convers.*, vol. 4, no. 4, pp. 651-660, Dec. 1989.
- [FIR07] V. Fireteanu, T. Tudorache, and O. A. Turcanu, "Optimal design of rotor slot geometry of squirrel-cage type induction motors," in *IEEE Int. Elect. Mach. Drives Conf. (IEMDC'07)*, Antalya, 2007, pp. 537-542.
- [FRE03] M. A. A. Freitas, D. A. Andrade, H. Paula, and J. L. Domingos, "Effects of magnetic saturation on induction machines driven by static converters," in *IEEE Int. Elect. Mach. Drives Conf. (IEMDC'03)*, pp. 1026-1031, 2003.
- [FRE07] M. Freddy and L. Heinz, "Parasitic effects in PM machines with concentrated windings," *IEEE Trans. Ind. Appl.*, vol. 43, no. 5, pp. 1223-1232, Sep./Oct. 2007.
- [FRI09] G. Friedrich and A. Girardin, "Integrated starter generator," *IEEE Ind. Appl. Mag.*, vol. 15, no. 4, pp. 26-34, Jul. 2009.
- [FUN15] Y. Funaki, N. Watanabe, M. Nakamura, I. Hirotsuka, K. Tsuboi, and M. Yoshida, "A study of the effect of the stator tooth shape on the characteristics of three-phase induction motor with concentrated windings," in *Int. Conf. Elect. Mach. Syst. (ICEMS'15)*, Pattaya, 2015, pp. 150-155.
- [GAU41] J. S. Gault, "Rotor-bar currents in squirrel-cage induction motors," *Elect. Eng.*, vol. 60, no. 7, pp. 784-791, Jul. 1941.
- [GER00] D. Gerling, "Design of an induction motor with multilayer rotor structure and large gap," in *Int. Conf. Elect. Mach. (ICEM'00)*, 2000, pp. 458-461.
- [GER05] A. Di Gerlando, G. M. Foglia, R. Perini, and M. Ubaldini, "Design and operation aspects of field regulated PM synchronous machines with concentrated armature windings," in *IEEE Int. Elect. Mach. Drives Conf. (IEMDC'05)*, San Antonio, 2005, pp. 1165-1172.

- [GER11] D. Gerada, A. Mebarki, N. L. Brown, K. J. Bradley, and C. Gerada, "Design aspects of high-speed high-power-density laminated-rotor induction machines," *IEEE Trans. Ind. Electron.*, vol. 58, no. 9, pp. 4039-4047, Sept. 2011.
- [GHO12] A. Ghoggal, S. E. Zouzou, M. Sahraoui, H. Derghal, and A. Hadri-Hamida, "A winding function-based model of air-gap eccentricity in saturated induction motors," in *Int. Conf. Elect. Mach. (ICEM'12)*, 2012, pp. 2739-2745
- [GIE12] J. F. Gieras and J. Saari, "Performance calculation for a high-speed solid-rotor induction motor," *IEEE Trans. Ind. Electron.*, vol. 59, no. 6, pp. 2689-2700, Jun. 2012.
- [GIE14] J. F. Gieras and G. I. Rozman "Reduction of leakage flux in electrical machines". U.S. 2014/0,354,106 A1, Dec. 04, 2014.
- [GOR13] H. Gorginpour, B. Jandaghi, and H. Oraee, "A novel rotor configuration for brushless doubly-fed," *IET Electric Power Appl.*, vol. 7, no. 2, p. 106–115, 2013.
- [GOR14] H. Gorginpour, H. Oraee, and E. Abdi, "Calculation of core and stray load losses in brushless doubly fed induction generators," *IEEE Trans. Ind. Electron.*, vol. 61, no. 7, pp. 3167-3177, Jul. 2014.
- [GOS13] J. Goss, M. Popescu, and D. Staton, "A comparison of an interior permanent magnet and copper rotor induction motor in a hybrid electric vehicle application," in *Int. Elect. Mach. Drives Conf. (IEMDC'13)*, Chicago, IL, 2013, pp. 220-225.
- [GRA09] C. Grabner and J. Bacher, "Electromagnetic design workflow for squirrel cage induction machines," in *Int. Conf. Power Eng., Energy Elect. Drives (POWERENG '09)*, 2009, pp. 72-77.
- [GUA14a] Y. Guan, Z. Q. Zhu, I. A. A. Afinowi, J. C. Mipo, and P. Farah, "Comparison between induction machine and interior permanent magnet machine for electric vehicle application," in *Int. Conf. Elect. Mach. and Syst. (ICEMS'14)*, Hangzhou, 2014, pp. 144-150.
- [GUA14b] Y. Guan, Z. Q. Zhu, I. A. A. Afinowi, J. C. Mipo, and P. Farah, "Difference in maximum torque-speed characteristics of induction machine between motor and generator operation modes for electric vehicle application," in *Int. Conf. Elect. Mach. (ICEM'14)*, Berlin, 2014, pp. 130-136.
- [GUA15] Y. Guan, Z. Q. Zhu, I. Afinowi, and J. C. Mipo, "Influence of machine design parameters on flux-weakening performance of induction machine for electrical vehicle application," in *IET Elect. Syst. Transport.*, vol. 5, no. 1, pp. 43-52, 3 2015.
- [GUA15b] Y. Guan, "Torque-speed characteristics of induction machine and hybrid permanent magnet assisted synchronous reluctance machine for electric vehicle application," Ph.D. dissertation, Dept. Electron. Elect. Eng., Sheffield Univ., Sheffield, UK, 2015.
- [GUA16] Y. Guan, Z.Q. Zhu, I.A.A. Afinowi, J.C. Mipo, and P. Farah, "Comparison between induction machine and interior permanent magnet machine for electric vehicle application", *COMPEL-Int. J. Comput. Math. Elect. Electron. Eng.*, vol. 35, issue. 2, pp.572-585, 2016.
- [GUE08] J. M. Guerrero and O. Ojo, "Air-gap flux density optimization in dual stator winding induction machines," in *IEEE Power Electron. Specialists Conf.*, Rhodes, 2008, pp. 3767-3773.
- [GUN12] T. Gündoğdu and G. Kömürköz, "Technological and economical analysis of salient pole and permanent magnet synchronous machines designed for wind turbines," *JMMM-J. Magnetism Mag. Mat.*, vol. 324, no. 17, pp. 2679-2686, 2012.

- [GUN14] T. Gundogdu, G. Komurgoz, and B. Mantar, "Implementation of fractional slot concentrated windings to induction machines," in *IEEE Int. Conf. Power Electro., Mach. Drives (PEMD'14)*, 2014, pp. 1-6.
- [GUN16a] T. Gundogdu, Z. Q. Zhu, J. C. Mipo and P. Farah, "Investigation of non-sinusoidal rotor bar current phenomenon in induction machines—Influence of slip and electric loading," in *Int. Conf. Elect. Mach. (ICEM'16)*, Lausanne, 2016, pp. 419-425.
- [GUN16b] T. Gundogdu, Z. Q. Zhu, J. C. Mipo and P. Farah, "Influence of magnetic saturation on rotor bar current waveform and performance in induction machines," in *Int. Conf. Elect. Mach. (ICEM'16)*, Lausanne, 2016, pp. 391-397.
- [GUN16c] T. Gundogdu, Z. Q. Zhu, J. C. Mipo and P. Farah, "Influence of air-gap length on rotor bar current waveform of squirrel-cage induction motor," in *Int. Conf. Elect. Mach. and Syst. (ICEMS'16)*, Chiba, 2016, pp. 1-6.
- [GUN17a] T. Gundogdu, Z. Q. Zhu, and J. C. Mipo, "Influence of stator slot and pole number combination on rotor bar current waveform and performance of induction machines", in *Int. Conf. Electr. Mach. and Syst. (ICEMS'17)*, Sydney, 2017.
- [GUN17b] T. Gundogdu, Z. Q. Zhu, and J. C. Mipo, "Influence of rotor slot number on rotor bar current waveform and electromagnetic performance of induction machines", in *Int. Conf. Electr. Mach. and Syst. (ICEMS'17)*, Sydney, 2017.
- [GUN18a] T. Gundogdu, Z. Q. Zhu, J. C. Mipo, and S. Personnaz, "Influence of stator and rotor geometric parameters on rotor bar current waveform and electromagnetic performance of induction machines", in *Int. Conf. Power Electron. Mach. Drives (PEMD'18)*, Liverpool, UK, 2018.
- [GUO07] Z. Guowei, W. Fengxiang, and S. Yongshan, "Reduction of rotor loss and cogging torque of high speed PM machine by stator teeth notching," in *Int. Conf. Elect. Mach. Syst. (ICEMS'07)*, 2007, pp. 856-859.
- [GYF13] K. N. Gyftakis and J. Kappatou, "The impact of the rotor slot number on the behavior of the induction motor," *Advances Power Electron., Hindawi Pub. Corp.*, vol. 2013, pp. 1-9, 2013.
- [GYS00] J. J. C. Gyselinck, L. Vandeveld, D. Makaveev, and J. A. A. Melkebeek, "Calculation of no load losses in an induction motor using an inverse vector Preisach model and an eddy current loss model," *IEEE Trans. Magn.*, vol. 36, no. 4, pp. 856-860, Jul. 2000.
- [HAF15] S. Haffner, L. A. Pereira, and L. F. A. Pereira, "A method for optimization of five-phase induction machines based on genetic algorithms," *J. Control, Automation and Elect. Syst.*, vol. 26, no. 5, pp. 521-534, Oct. 2015.
- [HAI14] Z. Haisen, Z. Jian, W. Xiangyu, W. Qing, L. Xiaofang, and L. Yingli, "A design method for cage induction motors with non-skewed rotor bars," *IEEE Trans. Magn.*, vol. 50, no. 2, pp. 769-772, 2014.
- [HAR95] A. Harson, P. H. Mellor, and D. Howe, "Design considerations for induction machines for electric vehicle drives," in *Int. Conf. Elect. Mach. and Drives (IEMDC'95)*, Durham, 1995, pp. 16-20.
- [HAS08] N. Hashemnia and B. Asaei, "Comparative study of using different electric motors in the electric vehicles," in *Int. Conf. Elect. Mach.*, Sept. 2008, pp. 1-5
- [HEI15] G. Heins, D.M. Ionel, and M. Thiele, "Winding factors and magnetic fields in permanent-magnet brushless machines with concentrated windings and modular stator cores," *IEEE Trans. Ind. Applicat.*, vol.51, no.4, pp.2924-2932, 2015.

- [HIR07] I. Hirotaka, K. Kawakami, K. Tsuboi, H. Matura, and T. Mizuno, "Characteristics of high-speed constant-voltage operation of squirrel-cage induction motors -the influence of gap length in 4- and 8-pole induction motors," in *Int. Conf. Elect. Mach. Syst. (ICEMS 07)*, 2007, pp. 1094-1098.
- [HIR97] I. Hirotaka, K. Tsuboi, and F. Ishibashi, "Effect of slot-combination on electromagnetic vibration of squirrel-cage induction motor under loaded condition," in *Proc. Power Convers. Conf.*, Nagaoka, 1997, pp. 843-848.
- [HOF97] H. Hofmann, S. R. Sanders, and C. R. Sullivan, "Stator-flux-based vector control of induction machines in magnetic saturation," *IEEE Trans. Ind. Applicat.*, vol. 33, no. 4, pp. 935-942, Jul. 1997.
- [HOO11] T. Hooek, "Discussion on "Wave shape of currents in an individual rotor conductor of a single-phase induction motor." Chicago, June 30, 1911," *Trans. American Ins. Elect. Eng.*, vol. 30, no. 6, pp. 2125-2126, Jun. 1911.
- [HUA02] K. S. Huang, Z. G. Liu, H. Li, J. Yang, D. R. Turner, L. Jiang, and Q. H. Wu, "Reduction of electromagnetic noise in three-phase induction motors," in *Int. Conf. Power Syst. Tech.*, 2002, pp. 745-749.
- [HUA88a] H. Huang, E. F. Fuchs, and Z. Zak, "Optimization of single-phase induction motor design. I. Formulation of the optimization technique," *IEEE Trans. Energy Convers.*, vol. 3, no. 2, pp. 349-356, Jun. 1988.
- [HUA88b] H. Huang, E. F. Fuchs, and J. C. White, "Optimization of single-phase induction motor design. II. The maximum efficiency and minimum cost of an optimal design," *IEEE Trans. Energy Convers.*, vol. 3, no. 2, pp. 357-366, Jun. 1988.
- [HUY10] D. C. Huynh, M. W. Dunnigan, and S. J. Finney, "Energy efficient control of an induction machine using a chaos particle swarm optimization algorithm," in *IEEE Int. Conf. Power Energy*, Kuala Lumpur, 2010, pp. 450-455.
- [IDI97] K. Idir, C. Liuchen, and D. Heping, "A new global optimization approach for induction motor design," in *IEEE Canadian Conf. Elect. Comp. Eng., Eng. Innovation: Voyage of Discovery*, Newfoundland, 1997, pp. 870-873.
- [IKE07] M. Ikeda and T. Hiyama, "Simulation studies of the transients of squirrel-cage induction motors," *IEEE Trans. Energy Convers.* vol. 22, no. 2, pp. 233-239, Jun. 2007.
- [ISH05] D. Ishak, Z. Q. Zhu, and D. Howe, "Eddy-current loss in the rotor magnets of permanent-magnet brushless machines having a fractional number of slots per pole," *IEEE Trans. Magn.*, vol. 41, no. 9, pp. 2462-2469, Sep. 2005.
- [ISH06] D. Ishak, Z. Q. Zhu, and D. Howe, "Comparison of PM brushless motors, having either all teeth or alternate teeth wound," *IEEE Trans. Energy Convers.*, vol. 21, no. 1, pp. 95-106, Mar. 2006.
- [ISL10] R. Islam and I. Husain, "Analytical model for predicting noise and vibration in permanent-magnet synchronous motors," *IEEE Trans. Ind. Appl.*, vol. 46, no. 6, pp. 2346-2354, Nov. 2010.
- [ISM13] M. M. Ismail, "Direct torque control of induction machine based on fuzzy logic algorithm," in *Int. Conf. Control Decision Inform. Technol. (CoDIT'13)*, 2013, pp. 224-230.
- [ITO09] K. Ito, K. Naka, M. Nakano, and M. Kobayashi, "Electric machine," U.S. Patent 7,605,514 B2, Oct. 20, 2009.

- [JAB07] H. M. Jabr and N. C. Kar, "Starting performance of saturated induction motors," in *IEEE Power Eng. Soc. General Meeting*, pp. 1-7, 2007.
- [JAC00] A. G. Jack, B. C. Mecrow, P. G. Dickinson, D. Stephenson, J. S. Burdess, J. N. Fawcett, and T. Evans, "Permanent magnet machines with powdered iron cores and pressed windings," *IEEE Trans. Ind. Appl.*, vol. 36, no. 4, pp. 1077–1084, Aug. 2000.
- [JAC04] A. G. Jack, B. Mecrow, and O. Krogen, "Induction machine stator". U.S. Patent 6,815,863 B1, Nov. 9, 2005.
- [JAC05] A. G. Jack, B. Mecrow, and O. Krogen, "Electrical machine stator and rotor". U. S. Patent 6,849,985 B2, Feb. 1, 2005.
- [JAC99] A. G. Jack, B. C. Mecrow, P. G. Dickinson, D. Stephenson, J. S. Burdess, J. N. Fawcett, and T. Evans, "Permanent magnet machines with powdered iron cores and pre-pressed windings," in *IEEE Ind. Appl. Conf. Annu. Meeting*, Phoenix, 1999, pp. 97-103.
- [JAN95] P. L. Jansen, L. J. Li, and R. D. Lorenz, "Analysis of competing topologies of linear induction machines for high-speed material transport systems," *IEEE Trans. Ind. Appl.*, vol. 31, no. 4, pp. 925 - 932, 1995.
- [JAZ89] W. Jazdzynski, "Multicriterial optimisation of squirrel-cage induction motor design," *IEE Proc. B - Electric Power Appl.*, vol. 136, no. 6, pp. 299-307, Nov. 1989.
- [JEN12] B. Jensen, A. Jack, G. Atkinson, and B. Mecrow, "Performance of a folded-strip toroidally wound induction machine," *IEEE Trans. Ind. Electron.*, vol. 59, no. 5, pp. 2217 - 2226, 2012.
- [JIN14] X. Jin, Y. Xidang, M. Weiming, Z. Yuxing, and S. Zhaolong, "Nonlinear calculation methods of long primary double-sided linear induction motor," in *Int. Conf. Elect. Mach. Syst. (ICEMS'14)*, Hangzhou, 2014.
- [JOK13] G. M. Joksimović, J. Riger, T. M. Wolbank, N. Perić, and M. Vašak, "Stator-current spectrum signature of healthy cage rotor induction machines," *IEEE Trans. Ind. Electron.*, vol. 60, no. 9, pp. 4025-4033, Sep. 2013.
- [JUA14] L. Juan and J.X. Shen, "Influence of mechanical parameters on power efficiency of induction motors," in *Int. Conf. Elect. Mach. Syst. (ICEMS 14)*, 2014, pp. 2555-2560.
- [JUN07] T. U. Jung, C. H. Yun, H. R. Cha, M. G. Chae, and H. M. Kim, "Improved design for driving characteristics in single phase induction motor with concentrated winding," in *IEEE Power Electron. Spec. Conf.*, Orlando, 2007, pp. 2418-2422.
- [JUR15] S. Jurkovic, K. M. Rahman, J. C. Morgante, and P. J. Savagian, "Induction machine design and analysis for general motors e-assist electrification technology," *IEEE Trans. Ind. Appl.*, vol. 51, no. 1, pp. 631-639, Feb. 2015.
- [KAB16] M. A. Kabir and I. Husain, "New multilayer winding configuration for distributed MMF in AC machines with shorter end-turn length," in *IEEE Power Energy Soc. General Meeting (PESGM'16)*, Boston, 2016, pp. 1-5.
- [KAW09] Y. Kawase, T. Yamaguchi, Z. Tu, N. Toida, N. Minoshima, and K. Hashimoto, "Effects of skew angle of rotor in squirrel-cage induction motor on torque and loss characteristics," *IEEE Trans. Magn.*, vol. 45, no. 3, pp. 1700-1703, Mar. 2009.
- [KEL03] J. W. Kelly, E. G. Strangas, and J. M. Miller, "Control of a continuously operated pole-changing induction machine," in *Int. Elect. Mach. Drives Conf. (IEMDC'03)*, Madison, 2003, pp. 211-217.

- [KHA12] A. S. Abdel-Khalik and S. Ahmed, "Performance evaluation of a five-phase modular winding induction machine," *IEEE Trans. Ind. Electron.*, vol. 59, no. 6, pp. 2654-2669, Jun. 2012.
- [KHA15a] A. S. Abdel-Khalik, M. S. Diab, S. Ahmed and A. M. Massoud, "A new single tooth winding layout for a single-phase induction motor with segmented stator," in *IEEE Ind. Electron. Soc. Conf. (IECON'15)*, Yokohama, 2015, pp. 102-107.
- [KHA15b] A. S. Abdel-Khalik, S. Ahmed and A. Massoud, "A five-phase linear induction machine with planar modular winding," in *IEEE Int. Conf. Ind. Technol. (ICIT'15)*, Seville, 2015, pp. 580-585.
- [KIM15] K. Kim, "Optimal design of rotor slot shape of induction motor for electric vehicle," in *IEEE Magn. Conf. (INTERMAG'15)*, Beijing, 2015, pp. 1-1.
- [KIM95] S.H. Kim and S.K. Sul, "Maximum torque control of an induction machine in the field weakening region," *IEEE Trans. Ind. Appl.*, vol. 31, no. 4, pp. 787-794, Jul. 1995.
- [KIM98] M. K. Kim, C. G. Lee, and H. K. Jung, "Multiobjective optimal design of three-phase induction motor using improved evolution strategy," *IEEE Trans. Magn.*, vol. 34, no. 5, pp. 2980-2983, Sep 1998.
- [KIM99] B. T. Kim, B. I. Kwon and S. C. Park, "Reduction of electromagnetic force harmonics in asynchronous traction motor by adapting the rotor slot number," *IEEE Trans. Magn.*, vol. 35, no. 5, pp. 3742-3744, Sep. 1999.
- [KIR07] J. L. Kirtley, J. G. Cowie, E. F. Brush, D. T. Peters, and R. Kimmich, "Improving induction motor efficiency with die-cast copper rotor cages," in *IEEE Power Eng. Soc. General Meeting*, Tampa, 2007, pp. 1-6.
- [KOB97] T. Kobayashi, F. Tajima, M. Ito, and S. Shibukawa, "Effects of slot combination on acoustic noise from induction motors," *IEEE Trans. Mag.*, vol. 33, no. 2, pp. 2101-2104, Mar. 1997.
- [KOC09] D. A. Kocabas, "Novel winding and core design for maximum reduction of harmonic magnetomotive force in ac motors," *IEEE Trans. Magn.*, vol. 45, no. 2, pp. 735-746, Feb. 2009.
- [KOM00] H. Kometani, Y. Asao, and K. Adachi, "Dynamo-electric machine," U.S. Patent 6,166,471, Dec. 26, 2000.
- [KON09] M. Kondo, R. Ebizuka, and A. Yasunaga, "Rotor design for high efficiency induction motors for railway vehicle traction," in *Int. Conf. Elect. Mach. Syst.*, Tokyo, 2009, pp. 1-4.
- [KOR18] W.C. Korthals-Altes, "Motor winding," U.S. Patent 1,267,232 A, May. 21, 1918.
- [KRO31] G. Kron, "Induction motor slot combinations rules to predetermine crawling, vibration, noise and hooks in the speed-torque Curve," *Trans. American Ins. Elect. Eng.*, vol. 50, no. 2, pp. 757-767, Jun. 1931.
- [KUN12] K. Zhao, P. Ciufu, and S. Perera, "Induction motors subject to regular voltage fluctuations: Stator and rotor current analysis from a heating perspective," in *IEEE Int. Conf. Harmonics Quality of Power (ICHQP'12)*, pp. 642-648, 2012.
- [KUN17] N. Kunihiro, K. Nishihama, M. Iizuka, K. Sugimoto, and M. Sawahata, "Investigation into loss reduced rotor slot structure by analyzing local behaviors of harmonic magnetic fluxes in inverter-fed induction motor," *IEEE Trans. Ind. Appl.*, vol. 53, no. 2, pp. 1070-1077, Mar. 2017.

- [LAC08] S. Lachecinski and M. Dems, "Optimization of big power low voltage induction motor using hybrid optimization algorithms," in *Int. Conf. Elect. Mach.*, Vilamoura, 2008, pp. 1-6.
- [LAI82] E. R. Laithwaite and S. B. Kuznetsov, "Cage-rotor induction motor with unity power factor," *IEE Proc. B – Elect. Power Appl.*, vol. 129, no. 3, pp. 143-150, May 1982.
- [LAN77] C. F. Landy, "Analysis of rotor bar currents as a means of evaluating torque produced in a squirrel-cage induction motor," *Proc. Elect. Eng. Inst.*, vol. 124, no. 11, pp. 1078, Nov. 1977.
- [LEE13] G. Lee, S. Min, and J. P. Hong, "Optimal shape design of rotor slot in squirrel-cage induction motor considering torque characteristics," *IEEE Trans. Magn.*, vol. 49, no. 5, pp. 2197-2200, May 2013.
- [LEE61] C. H. Lee, "Saturation harmonics of polyphase induction machines," *IEEE Trans. Power App. Syst.*, vol. 80, no. 3, pp. 597-603, Apr. 1961.
- [LI05] J. Li and Y. R. Zhong, "Efficiency optimization of induction machines based on fuzzy search controller," in *Int. Conf. Machine Learning and Cybernetics*, Guangzhou, China, 2005, pp. 2518-2522.
- [LI10] W. Li, J. Cao and X. Zhang, "Electrothermal analysis of induction motor with compound cage rotor used for PHEV," *IEEE Trans. Ind. Electron.*, vol. 57, no. 2, pp. 660-668, Feb. 2010.
- [LI14] Q. Li, T. Fan, X. Wen, T. Xiang, and L. Ye, "A novel multi-layer winding design method for fractional-slot concentrated-windings permanent magnet machine," in *IEEE Transp. Electrific. Asia-Pacific Conf. and Expo (ITEC Asia-Pacific)*, 2014, pp. 1-5.
- [LI16] H. Li and K. W. Klontz, "Rotor design to reduce secondary winding harmonic loss for induction motor in hybrid electric vehicle application," in *IEEE Energy Convers. Cong. and Expo. (ECCE'16)*, Milwaukee, WI, 2016, pp. 1-6.
- [LI17] H. Li and K. W. Klontz, "An investigation of current harmonic influence on induction motor in hybrid electric vehicle application," in *IEEE Int. Elect. Mach. Drives Conf. (IEMDC'17)*, Miami, FL, 2017, pp. 1-6.
- [LIA11] Y. Liao, X. Feng, Z. Wang, and Q. Ni, "Reduction of torque ripple of VSI-fed induction machine controlled by direct torque control method," in *Int. Conf. Elect. Mach. Syst.*, Beijing, 2011, pp. 1-4.
- [LIA94] Y. Liao and T. A. Lipo, "Effect of saturation third harmonic on the performance of squirrel-cage induction machines," *Elect. Mach. Power Syst.*, vol. 22, no. 2, pp. 155-171, May. 1994.
- [LIA95] F. Liang, D. W. Novotny, R. W. Fei, and X. Xu, "Selection of the pole number of induction machines for variable speed applications," *IEEE Trans. Ind. Applicat.*, vol. 31, no. 2, pp. 304-310, Mar. 1995.
- [LIN16] C. H. Lin and C. C. Hwang, "Multiobjective optimization design for a six-phase copper rotor induction motor mounted with a scroll compressor," *IEEE Trans. Magn.*, vol. 52, no. 7, pp. 1-4, July 2016.
- [LIN76] C. E. Linkous, "High efficiency induction motor with multi-cage rotor". U.S. Patent 3,987,324, Oct. 19, 1976.
- [LIP17] T. A. Lipo, *Introduction to AC Machine Design*. Hoboken, NJ: John Wiley & Sons, Inc., IEEE Press, 2017, ch. 3-5.
- [LIP84] T. A. Lipo and A. Consoli, "Modeling and simulation of induction motors with saturable leakage reactances," *IEEE Trans. Ind. Appl.*, vol. 20, no. 1, pp. 180-189, Jan. 1984.

- [LIU03] G. Liuzzi, S. Lucidi, F. Parasiliti, and M. Villani, "Multiobjective optimization techniques for the design of induction motors," *IEEE Trans. Magn.*, vol. 39, no. 3, pp. 1261-1264, May. 2003.
- [LIW05] S. Liwei, D. Ying, C. Shumei, and C. Shukang, "Constant-power operation performance improvement of the induction machine drives for hybrid electric vehicle applications," in *Int. Conf. Elect. Mach. and Syst. (ICEMS'05)*, 2005, pp. 818-821.
- [LME17] LME Material Market, [Online]. (2017, Aug. 08). *Material market priced for Aug. 08, 2017*, [Online]. Available: <https://www.lme.com/>
- [LUN36] E. O. Lunn, "Induction motors under unbalanced conditions," *Elect. Eng.*, vol. 55, no. 4, pp. 387-393, Apr. 1936.
- [MAD98] G. Madescu, I. Boldea, and T. J. E. Miller, "The optimal lamination approach to induction machine design global optimization," *IEEE Trans. Ind. Appl.*, vol. 34, no. 3, pp. 422-428, 1998.
- [MAG03] F. Magnussen and C. Sadarangani, "Winding factors and joule losses of permanent magnet machines with concentrated windings," in *IEEE Int. Elect. Mach. Drives Conf. (IEMDC'03)*, Madison, 2003, pp. 333-339.
- [MAG07] F. Magnussen and H. Lendenmann, "Parasitic effects in PM machines with concentrated windings," *IEEE Trans. Ind. Appl.*, vol. 43, no. 5, pp. 1223-1232, 2007.
- [MAL16] J. A. Malagoli, J. R. Camacho, and M. V. F. da Luz, "Optimal design variables to minimize the cost of materials the stator of asynchronous machine," *J. Control, Autom. Elect. Syst.*, vol. 27, no. 2, pp. 157-168, Apr. 2016.
- [MAR08] T. Marčić, B. Štumberger, G. Štumberger, M. Hadžiselimović, and I. Zagradišnik, "The impact of different stator and rotor slot number combinations on iron losses of a three-phase induction motor at no-load," *JMMM-J. Magnetism Mag. Mat.*, vol. 320, no. 20, pp. e891-e895, Oct. 2008.
- [MAT01] F. Matter, *Review of the research program of the partnership for a new generation of vehicles: 7th report*, Washington, DC: The National Academies Press, Tech. Rep., 2001.
- [MAU13] T. Mauffrey, J. F. Pradurat, L. Durantay, and J. Fontini, "Comparison of 5 different squirrel cage rotor designs for large high speed induction motors," in *Petroleum and Chemical Ind. Committee (PCIC Europe)*, Istanbul, 2013, pp. 1-9.
- [MCC98] C. I. McClay and S. Williamson, "Influence of rotor skew on cage motor losses," *IEE Elect. Power Appl.*, vol. 145, no. 5, pp. 414-422, Sep. 1998.
- [MEL83] J. A. A. Melkebeek and D. W. Novotny, "The influence of saturation on induction machine drive dynamics," *IEEE Trans. Ind. Appl.* vol. 19, no. 5, pp. 671-681, Sept. 1983.
- [MEL95] M. J. Melfi, "Optimum pole configuration of AC induction motors used on adjustable frequency power supplies," in *Ind. Applicat. Soc. Petroleum Chemical Ind. Conf.*, Denver, 1995, pp. 237-242.
- [MES14] A. Mesbeh, M. Jarboui, and A. Masmoudi, "Graphical investigation of the induction motor rotor cage currents under faulty operation," in *Int. Conf. Ecolog. Veh. Renewable Energies (EVER'14)*, pp. 1-9, 2014.
- [MIL14] J. M. Miller, *Propulsion Systems for Hybrid Vehicles*, 1st ed. The Institution of Engineering and Technology, London, UK, pp.191-254, 2004.
- [MIS14] O. Misir and B. Ponick, "Analysis of three-phase induction machines with combined Star-Delta windings," in *IEEE Int. Symp. Ind. Electron. (ISIE'14)*, Istanbul, 2014.

- [MOL16] A. Mollaeian, S. M. Sangdehi, A. Balamurali, G. Feng, J. Tjong and N. C. Kar, "Reduction of space harmonics in induction machines incorporating rotor bar optimization through a coupled IPSO and 3-D FEA algorithm," in *Int. Conf. Elect. Mach. (ICEM'16)*, Lausanne, 2016, pp. 557-563.
- [MON13] L. Monjo, F. Córcoles, and J. Pedra, "Saturation effects on torque- and current-slip curves of squirrel-cage induction motors," *IEEE Trans. Energy Convers.* vol. 28, no. 1, pp. 243-254, Feb. 2013.
- [MOR14] O. Moros and D. Gerling, "Geometrical and electrical optimization of stator slots in electrical machines with combined wye-delta winding," in *Int. Conf. Elect. Mach. (ICEM'14)*, Berlin, 2014, pp. 2026-2030.
- [MOR15a] O. Moros and D. Gerling, "New flexible harmonic cost effective concentrated winding topology," in *IEEE Ind. Electron. Soc. Annu. Conf. (IECON'15)*, Yokohama, 2015, pp. 427-432.
- [MOR15b] O. Moros, G. Dajaku, C. Klusmann, and D. Gerling, "New high voltage 2-pole concentrated winding and corresponding rotor design for induction machines," in *IEEE Ind. Electron. Soc. Annu. Conf. (IECON'15)*, Yokohama, 2015, pp. 2632-2637.
- [MOR36] W. J. Morrill, "Induction motor secondary". U. S. Patent 2,037,532, Apr. 14, 1936.
- [MOR92] J. C. Moreira and T. A. Lipo, "Modeling of saturated AC machines including air gap flux harmonic components," *IEEE Trans. Ind. Appl.*, vol. 28, no. 2, pp. 343-349, Apr. 1992.
- [MOR97] M. Mori, T. Mizuno, T. Ashikaga, and I. Matsuda, "A control method of an inverter-fed six-phase pole change induction motor for electric vehicles," in *Power Conversion Conf.*, Nagaoka, 1997, pp. 25-32.
- [MUK89] S. Mukherjee, G. E. Adams, and R. G. Hoft, "FEM analysis of inverter-induction motor rotor conduction losses," *IEEE Trans. Energy Convers.*, vol. 4, no. 4, pp. 671-680, Dec. 1989.
- [MUL89] E. Muljadi, T. A. Lipo, and D. W. Novotny, "Power factor enhancement of induction machines by means of solid-state excitation," *IEEE Trans. Power Electron.*, vol. 4, no. 4, pp. 409-418, Oct. 1989.
- [MUN08] A. R. Munoz, F. Liang and M. W. Degner, "Evaluation of interior PM and surface PM synchronous machines with distributed and concentrated windings," in *IEEE Ind. Electron. Annu. Conf.*, Orlando, 2008, pp. 1189-1193.
- [MUT12] M. Muteba, A. A. Jimoh, and D. Nicolae, "Torque ripple reduction in five-phase induction machines using mixed winding configurations," in *Int. Conf. Elect. Mach.*, Marseille, 2012, pp. 512-518.
- [MUT17] M. Muteba and D.V. Nicolae, "Influence of mixed winding arrangements on torque ripples of five-phase induction machines," *Electric Power Syst. Research*, vol. 151, pp. 154-165, Oct. 2017.
- [NAN01] S. Nandi, S. Ahmed, H. A. Toliyat, and R. Bharadwaj, "Selection criteria of induction machines for speed-sensorless drive applications," in *IEEE Ind. Applicat. Conf. Annu. Meeting*, Chicago, 2001, pp. 1131-1138.
- [NAN09] S. Nandi, T. Ilamparithi, S. B. Lee, and D. Hyun, "Pole pair and rotor slot number independent frequency domain based detection of eccentricity faults in induction machines using a semi on-line technique," in *IEEE Int. Symp. Diagnos. Elect. Mach. Power Electron. Drives, (SDEMPED'09)*, Cargese, 2009, pp. 1-7.

- [NAN99] S. Nandi and H. A. Toliyat, "Condition monitoring and fault diagnosis of electrical machines-A review," in *IEEE Ind. Applicat. Confe.*, Phoenix, 1999, pp. 197-204.
- [NAU97] S. L. Nau, "The influence of the skewed rotor slots on the magnetic noise of three-phase induction motors," in *Int. Conf. Elect. Mach. Drives (IEMDC'97)*, Cambridge, 1997, pp. 396-399.
- [NEE93] H. P. Nee and C. Sadarangani, "The influence of load and rotor slot design on harmonic losses of inverter-fed induction motors," in *Int. Elect. Mach. Drives Conf. (IEMDC'93)*, Oxford, 1993, pp. 173-178.
- [NEE95] H. P. Nee, "Rotor slot design of inverter-fed induction motors," in *Int. Conf. Electrical Machines and Drives (IEMDC'95)*, Durham, 1995, pp. 52-56.
- [OJO90] J. O. Ojo, A. Consoli, and T. A. Lipo, "An improved model of saturated induction machines," *IEEE Trans. Ind. Appl.*, vol. 26, no. 2, pp. 212-221, Mar/Apr. 1990.
- [OLS11] M. Olszewski, "Evaluation of the 2010 Toyota Prius hybrid synergy drive system," Oak Ridge Nat. Lab., U.S. Dept. Energy, 2011.
- [ONL17a] [Online]. (2017, Oct. 15). *Tesla Roadster*. Available: https://en.wikipedia.org/wiki/Tesla_Roadster
- [ONL17b] [Online]. (2017, Oct. 15). *Tesla Model S*. Available: https://en.wikipedia.org/wiki/Tesla_Model_S
- [ONL17c] [Online]. (2017, Oct. 15). *General Motors EV 1*. Available: https://en.wikipedia.org/wiki/General_Motors_EV1
- [ONL17d] [Online]. (2017, Oct. 16). *Fiat Seicento*. Available: https://en.wikipedia.org/wiki/Fiat_Seicento
- [ONL17e] [Online]. (2017, Oct. 16). *Think City*. Available: https://en.wikipedia.org/wiki/Think_City
- [ONL17f] [Online]. (2017, Oct. 16). *DaimlerChrysler to Offer New Hybrid Dodge Durango in 2003*. Available: <http://powerpulse.net/daimlerchrysler-to-offer-new-hybrid-dodge-durango-in-2003/>
- [ONL17g] [Online]. (2017, Oct. 16). *The BMW X5i Performance*. Available: http://www.bmw.co.uk/en_GB/new-vehicles/ipformance/x5/2015/introduction.html
- [ONL17h] [Online]. (2017, Oct. 16) *Chevrolet introduces 2016 Silverado with Eassist*. Available: <http://media.chevrolet.com/media/us/en/chevrolet/news.detail.html/content/Pages/news/us/en/2016/feb/0225-silverado-eAssist.html>
- [ONL17i] [Online]. (2017, Oct. 19) *Hybrid Cars*. Available: <http://www.hybridcars.com/history/history-of-hybrid-vehicles.html>
- [OSS94] M. Ossama and T.A. Lipo, "A new induction machine model for analysis of eccentric rotor magnetic pull," in *Int. Symp. Power Electron. Elect. Drives Autom. Motion (SPEEDAM'94)*, pp. 173-177, Jun. 1994.
- [OST86] V. Ostovic, "A method for evaluation of transient and steady state performance in saturated squirrel cage induction machines," *IEEE Trans. Energy Convers.*, vol. EC-1, no. 3, pp. 190-197, Sept. 1986.
- [PAR08] K. J. Park, Kwangsoo Kim, Sang-hoon Lee, Dae-Hyun Koo, Kwang-Cheol Ko, and Ju Lee, "Optimal design of rotor slot of three phase induction motor with die-cast copper rotor cage," in *Int. Conf. Elect. Mach. Syst. (ICEMS'08)*, Wuhan, 2008, pp. 61-63.

- [PAT14a] A. Patzak and D. Gerling, "Design of an automotive 48 V integrated starter-generator on the basis of an induction machine with concentrated windings," in *Int. Conf. Elect. Mach. Syst. (ICEMS'14)*, Hangzhou, 2014, pp. 2583-2589.
- [PAT14b] A. Patzak and D. Gerling, "Design of a multi-phase inverter for low voltage high power electric vehicles," in *IEEE Int. Elect. Veh. Conf. (IEVC'14)*, Florence, 2014, pp. 1-7.
- [PAT14c] V. I. Patel, J. Wang, W. Wang, and X. Chen, "Six-phase fractional-slot-per-pole-per-phase permanent-magnet machines with low space harmonics for electric vehicle application," *IEEE Trans. Ind. Appl.*, vol. 50, no. 4, pp. 2554-2563, Aug. 2014.
- [PER12] L. A. Pereira, C. C. Scharlau, L. F. A. Pereira, and S. Haffner, "Influence of saturation on the airgap induction waveform of five-phase induction machines," *IEEE Trans. Energy Convers.*, vol. 27, no. 1, pp. 29-41, Feb. 2012.
- [PER17] L. A. Pereira, S. Haffner, G. Nicol, and T. F. Dias, "Multiobjective optimization of five-phase induction machines based on NSGA-II," *IEEE Trans. Ind. Electron.*, vol. 64, no. 12, pp. 9844-9853, Dec. 2017.
- [PET03] D. T. Peters, J. G. Cowie, E. F. Brush, and D. J. Van Son, "Copper in the squirrel cage for improved motor performance," in *Int. Elect. Mach. Drives Conf. (IEMDC'03)*, WI, USA, 2003, pp. 1265-1271.
- [PET07] D. T. Peters, E. F. Brush, and J. L. Kirtley, "Die-cast copper rotors as strategy for improving induction motor efficiency," in *Elect. Insulation Conf. Elect. Manuf. Expo*, Nashville, TN, 2007, pp. 322-327.
- [PET16] I. Petrov, P. Lindh, W. Y. Peng, C. S. Jang, H. P. Yang, and J. Pyrhönen, "Improvement of axial flux single-rotor single-stator induction machine performance by applying semi-magnetic wedges," in *Int. Conf. Elect. Mach. (ICEM'16)*, Lausanne, 2016, pp. 1795-1800.
- [PIL97] P. Pillay, R. Nolan, and T. Haque, "Application of genetic algorithms to motor parameter determination for transient torque calculations," *IEEE Trans. Ind. Appl.*, vol. 33, no. 5, pp. 1273-1282, Sep. 1997.
- [PLA93] D. Platt and B. Smith, "Twin rotor drive for an electric vehicle," *IEE Proc. B – Elect. Power Appl.*, vol. 140, no. 2, pp. 131 - 138, 1993.
- [POU15] A. A. Pourmoosa and M. Mirsalim, "Design optimization, prototyping, and performance evaluation of a low-speed linear induction motor with toroidal winding," *IEEE Trans. Energy Convers.*, vol. 30, no. 4, pp. 1546-1555, Dec. 2015.
- [PRE89] W. Prescott, D. G. Watterson, M. Bradford, and M. Lockwood, "Computational methods for the steady-state performance prediction of cage induction machines fed from nonsinusoidal supplies," in *Int. Conf. Elect. Mach. Drives (IEMDC'89)*, London, 1989, pp. 271-274.
- [PRO97] F. Profumo, Z. Zhang, and A. Tenconi, "Axial flux machines drives: A new viable solution for electric cars," *IEEE Trans. Ind. Electron.*, vol. 44, no. 1, pp. 39 - 45, 1997.
- [PYR08] J. Pyrhonen, T. Jokinen, and V. Hrabovcova, *Design of Rotating Electrical Machines*, Sussex, UK:Wiley, pp. 297-300, 2008.
- [RAM71] R. Ramarathnam and B. G. Desai, "Optimization of polyphase induction motor design: a nonlinear programming approach," *IEEE Trans. Power App. Syst.*, vol. PAS-90, no. 2, pp. 570-578, Mar. 1971.
- [RAM73] R. Ramarathnam, B. G. Desai, and V. S. Rao, "A comparative study of minimization techniques for optimization of induction motor design," *IEEE Trans. Power App. Syst.*, vol. PAS-92, no. 5, pp. 1448-1454, Sept. 1973.

- [RED11] P. B. Reddy, A. M. EL-Refaie, and K.-K. Huh, "Effect of number of layers on performance of fractional-slot concentrated-windings interior permanent magnet machines," in *IEEE Int. Conf. Power Electron. & Energy Conver. Cong. Expo. Asia (ICPE & ECCE)*, Korea, 2011.
- [RED12] P. B. Reddy, K.-K. Huh and A. El-Refaie, "Effect of stator shifting on harmonic cancellation and flux weakening performance of interior PM machines equipped with fractional-slot concentrated windings for hybrid traction applications," in *IEEE Energy Conver. Cong. Expo. (ECCE'12)*, Raleigh, NC, 2012.
- [RED14] P. B. Reddy, H. Kum-Kang, and A. M. El-Refaie, "Generalized approach of stator shifting in interior permanent-magnet machines equipped with fractional-slot concentrated windings," *IEEE Trans. Ind. Electron.*, vol. 61, no. 9, pp. 5035-5046, 2014.
- [REF05a] A. M. El-Refaie and T. M. Jahns, "Comparison of synchronous PM machine types for wide constant-power speed range operation," in *IEEE Ind. Appl. Annu. Meeting*, 2005, pp. 1015-1022.
- [REF05b] A. EL-Refaie and T. Jahns, "Optimal flux weakening in surface PM machines using fractional-slot concentrated windings," *IEEE Trans. Ind. Appl.*, vol. 41, no. 3, pp. 790–800, 2005.
- [REF08] A. M. El-Refaie and M. R. Shah, "Comparison of induction machine performance with distributed and fractional-slot concentrated windings," in *IEEE Ind. Appl. Soc. Annu. Meeting*, 2008, pp. 1-8.
- [REF10] A. M. El-Refaie, "Fractional-slot concentrated-windings synchronous permanent magnet machines: opportunities and challenges," *IEEE Trans. Ind. Electron.*, vol. 57, no. 1, pp. 107-121, Jan. 2010.
- [REF11] A. EL-Refaie and M. Shah, "Induction machine performance with fractional-slot concentrated windings," *COMPEL - The Int. J. Comp. Math. Elect. Electron. Eng.*, vol. 31, no. 1, pp. 119-139, 2011.
- [REF12] A. EL-Refaie and M. Shah, "Induction machine performance with fractional-slot concentrated windings," *COMPEL-Int. J. Comput. Math. Elect. Electron. Eng.*, vol. 31, no. 1, pp. 119-139, 2012.
- [REF13] A. M. El-Refaie, "Motors/generators for traction/propulsion applications: A review," *IEEE Veh. Technol. Mag.*, vol. 8, no. 1, pp. 90-99, Mar. 2013.
- [ROS62] G. M. Rosenberry, "Squirrel cage induction motor rotor". U. S. Patent 3,027,474, Mar. 27, 1962.
- [SAK11] V. P. Sakthivel and S. Subramanian, "Using MPSO algorithm to optimize three-phase squirrel cage induction motor design," in *Int. Conf. Emerging Trends Elect. Comput. Technol.*, Tamil Nadu, 2011, pp. 261-267.
- [SAK17] K. Sakai, M. Suzuki, and K. Takishima, "Induction machines with novel concentrated windings," in *IEEE Int. Elect. Mach. Drives Conf. (IEMDC'17)*, Miami, FL, 2017, pp. 1-7.
- [SAL05] P. Salminen, T. Jokinen and J. Pyrhonen, "Pull-out torque of fractional-slot PM-motors with concentrated winding," in *IEE Proc. – Elect. Power Appl.*, vol. 152, no. 6, pp. 1440-1444, 4 Nov. 2005.
- [SAL94] S. Salon, D. Burow, M. DeBortoli, and C. Slavik, "Effects of slot closure and magnetic saturation on induction machine behaviour," *IEEE Trans. Magn.*, vol. 30, no. 5, pp. 3697-3700, Sept. 1994.

- [SED14] K. Sedef, A. Maheri, M. Yilmaz and A. Daadbin, "Performances of AC induction motors with different number of poles in urban electric cars," in *Int. Symp. Environ. Friendly Energies Appl. (EFEA'14)*, St. Ouen, 2014, pp. 1-5.
- [SEI97] B. J. Seibel, T. M. Rowan, and R. J. Kerkman, "Field-oriented control of an induction machine in the field-weakening region with DC-link and load disturbance rejection," *IEEE Trans. Ind. Appl.*, vol. 33, no. 6, pp. 1578-1584, Nov. 1997.
- [SEK12] D. Sekiguchi, T. Nakamura, S. Misawa, H. Kitano, T. Matsuo, N. Amemiya, Y. Ito, M. Yoshikawa, T. Terazawa, K. Osamura, Y. Ohashi, and N. Okumura, "Trial test of fully hts induction/synchronous machine for next generation electric vehicle," *IEEE Trans. Appl. Supercond.*, vol. 22, no. 3, pp. 5200904-5200904, Jun. 2012.
- [SHI02] M. H. Shin, D. S. Hyun, and S. B. Cho, "Maximum torque control of stator-flux-oriented induction machine drive in the field-weakening region," *IEEE Trans. Ind. Appl.*, vol. 38, no. 1, pp. 117-122, Jan. 2002.
- [SHU06] C. Shumei, D. Ying, and S. Liwei, "Rotor slots design of induction machine for hybrid electric vehicle," in *IEEE Veh. Power Propul. Conf. (VPPC'06)*, Windsor, 2006, pp. 1-3.
- [SID05] A. Siddique, G. S. Yadava, and B. Singh, "A review of stator fault monitoring techniques of induction motors," *IEEE Trans. Energy Convers.*, vol. 20, no. 1, pp. 106-114, Mar. 2005.
- [SIN83] B. Singh, B. P. Singh, S. S. Murthy, and C. S. Jha, "Experience in design optimization of induction motor using 'SUMT' algorithm," *IEEE Trans. Power App. Syst.*, vol. PAS-102, no. 10, pp. 3379-3384, Oct. 1983.
- [SIN92] C. Singh and D. Sarkar, "Practical considerations in the optimisation of induction motor design," *IEE Proc. B – Elect. Power Applicat.*, vol. 139, no. 4, pp. 365-373, July 1992.
- [SMI66] B. H. Smith, "Theory and performance of a twin stator induction machine," *IEEE Trans. Power App. Syst.*, vol. PAS-85, no. 2, pp. 123-131, Feb. 1966.
- [SOB11] T. J. Sobczyk and W. Maciołek, "Influence of pole-pair number and rotor slot number on effects caused by cage faults," in *IEEE Int. Symp. Diagnostics Elect. Mach., Power Electron. Drives (SDEMPED'11)*, Bologna, 2011, pp. 199-204.
- [SOO02] W. L. Soong and N. Ertugrul, "Field-weakening performance of interior permanent-magnet motors," *IEEE Trans. Ind. Appl.*, vol. 38, no. 5, pp. 1251-1258, Oct. 2002.
- [SOU07] D. A. Souza, W. C. P. A. Filho, and G. C. D. Sousa, "Adaptive fuzzy controller for efficiency optimization of induction motors," *IEEE Trans. Ind. Electron.*, vol. 54, no. 4, pp. 2157-2164, Aug. 2007.
- [SPE92] R. Spee and A. K. Wallace, "Comparative evaluation of power factor improvement techniques for squirrel cage induction motors," *IEEE Trans. Ind. Appl.*, vol. 28, no. 2, pp. 381-386, Mar. 1992.
- [STA05] S. Staton, A. Boglietti, and A. Cavagnino, "Solving the more difficult aspects of electric motor thermal analysis in small and medium size industrial motors," *IEEE Trans. Energy Convers.*, vol. 20, no. 3, pp. 620-628, Sept. 2005.
- [STE12] A. Stening and C. Sadarangani, "Reduction of synchronous torques in induction machines using asymmetrical rotor slots," in *Int. Conf. Elect. Mach. Syst. (ICEMS'12)*, Sapporo, 2012, pp. 1-6.
- [SUN13] L. Sungho, J. Hong, S. B. Lee, E. J. Wiedenbrug, M. Teska, and H. Kim, "Evaluation of the influence of rotor axial air ducts on condition monitoring of induction motors," *IEEE Trans. Ind. Appl.*, vol. 49, no. 5, pp. 2024-2033, Apr. 2013.

- [SUN15] V. M. Sundaram and H. A. Toliyat, "A fractional slot concentrated winding (FSCW) configuration for outer rotor squirrel cage induction motors," in *IEEE Int. Elect. Mach. Drives Conf. (IEMDC'15)*, Coeur d'Alene, ID, 2015, pp. 20-26.
- [SUT13] T. Sutikno, N. R. N. Idris, A. Jidin, and M. N. Cirstea, "An improved FPGA implementation of direct torque control for induction machines," *IEEE Trans. Ind. Informat.*, vol. 9, no. 3, pp. 1280-1290, Aug. 2013.
- [TAM99] I. Tamrakar and O. P. Malik, "Power factor correction of induction motors using PWM inverter fed auxiliary stator winding," *IEEE Trans. Energy Convers.*, vol. 14, no. 3, pp. 426-432, Sep. 1999.
- [TAN02] L. Tang, L. Zhong, A. F. Rahman, and Y. Hu, "An investigation of a modified direct torque control strategy for flux and torque ripple reduction for induction machine drive system with fixed switching frequency," in *IEEE Ind. Appl. Conf.*, PA, 2002, pp. 837-844.
- [TAN11] J. K. Tangudu and T. M. Jahns, "Comparison of interior PM machines with concentrated and distributed stator windings for traction applications," in *IEEE Veh. Power Propul. Conf. (VPCC'11)*, Chicago, 2011, pp. 1-8.
- [TES88] N. Tesla, "A new system of alternate current motors and transformers," *Trans. American Inst. Elect. Eng.*, vol. 5, no. 10, pp. 308-327, Jul. 1888.
- [TOL04] H. A. Toliyat and G. B. Kliman, *Handbook of electric motors*, 2nd Ed., CRC Press, 2004.
- [TOL91a] H. A. Toliyat, T. A. Lipo, and J. C. White, "Analysis of a concentrated winding induction machine for adjustable speed drive applications. I. Motor analysis," *IEEE Trans. Energy Convers.*, vol. 6, no. 4, pp. 679-683, Dec. 1991.
- [TOL91b] H. A. Toliyat, T. A. Lipo, and J. C. White, "Analysis of a concentrated winding induction machine for adjustable speed drive applications. II. Motor design and performance," *IEEE Trans. Energy Convers.*, vol. 6, no. 4, pp. 684-692, Dec. 1991.
- [TOL94] H. A. Toliyat and T. A. Lipo, "Analysis of concentrated winding induction machines for adjustable speed drive applications-Experimental results," *IEEE Trans. Energy Convers.*, vol. 9, no. 4, pp. 695-700, Dec. 1994.
- [TOL95] H. A. Toliyat and T. A. Lipo, "Transient analysis of cage induction machines under stator, rotor bar and end ring faults," *IEEE Trans. Energy Convers.*, vol. 10, no. 2, pp. 241-247, Jun. 1995.
- [TOL98] H. A. Toliyat, "Analysis and simulation of five-phase variable-speed induction motor drives under asymmetrical connections," *IEEE Trans. Power Electron.*, vol. 13, no. 4, pp. 748-756, Jul. 1998.
- [TSO14] I. P. Tsoumas, H. Tischmacher and B. Eichinger, "Influence of the number of pole pairs on the audible noise of inverter-fed induction motors: Radial force waves and mechanical resonances," in *Int. Conf. Elect. Mach. (ICEM'14)*, Berlin, 2014, pp. 1811-1817.
- [TUT10] L. Tutelea and I. Boldea, "Induction motor electromagnetic design optimization: Hooke Jeeves method versus genetic algorithms," in *Int. Conf. Optim. Elect. Electron. Equip.*, Basov, 2010, pp. 485-492.
- [UKR17] UK RS Electroics, [Online]. Available: <http://uk.rs-online.com/web/p/magnets/6950188/>, last access: 21/08/2017.
- [US11] US Department of Energy. (2011) Final report on assessment of motor technologies for traction drives of hybrid and electric vehicles. [Online]. Available: <http://info.ornl.gov/sites/publications/files/pub28840.pdf>

- [UZH17a] N. Uzhegov, J. Barta, J. Kurfürst, C. Ondrusek, and J. Pyrhönen, "Comparison of high-speed electrical motors for a turbo circulator application," *IEEE Trans. Ind. Appl.*, vol. 53, no. 5, pp. 4308-4317, Oct. 2017.
- [UZH17b] N. Uzhegov, A. Smirnov, C. H. Park, J. H. Ahn, J. Heikkinen, and J. Pyrhönen, "Design aspects of high-speed electrical machines with active magnetic bearings for compressor applications," *IEEE Trans. Ind. Electron.*, vol. 64, no. 11, pp. 8427-8436, Nov. 2017.
- [VAL07] M. Valtonen, A. Parviainen, and J. Pyrhonen, "The effects of the number of rotor slots on the performance characteristics of axial-flux aluminium-cage solid-rotor core induction motor," in *IEEE Int. Elect. Mach. Drives Conf. (IEMDC'07)*, Antalya, 2007, pp. 668-672.
- [VAL08] M. Valtonen, A. Parviainen, and J. Pyrhonen, "Influence of the air-gap length to the performance of an axial-flux induction motor," in *Int. Conf. Elect. Mach. (ICEM'08)*, 2008, pp. 1-5.
- [VAS75] P. Vas, "Investigation of squirrel cage induction motors with concentrated rotor asymmetries," *Electrotechnika*, vol. 68, pp. 461-463, 1975.
- [VAS90] P. Vas, *Vector Control of AC Machines*, Oxford: Clarendon Press, 1990, pp. 124-130.
- [VAS93] P. Vas, *Parameter Estimation, Condition Monitoring, and Diagnosis of Electrical Machines*, Oxford: Clarendon Press, 1993.
- [VAT07] M. Valtonen, A. Parviainen, and J. Pyrhonen, "The effects of the number of rotor slots on the performance characteristics of axial-flux aluminium-cage solid-rotor core induction motor," in *Int. Elect. Mach. Drives Conf.*, 2007, pp. 668-672.
- [VEI56] C. G. Veinott, "Induction machinery design being revolutionized by the digital computer," *Trans. American Inst. Elect. Eng. Part III: Power App. Syst.*, vol. 75, no. 3, pp. 1509-1517, Jan. 1956.
- [VER17] C. Verucchi, C. Ruschetti, E. Giraldo, G. Bossio, and J. Bossio, "Efficiency optimization in small induction motors using magnetic slot wedges," *Elect. Power Syst. Res.*, vol. 152, pp. 1-8, Nov. 2017.
- [VIR12] B. Virlan, A. Simion, L. Livadaru, S. Benelghali, and R. Outbib, "Analysis of a three phase induction motor with outer rotor for multi-speed applications," in *Int. Conf. Elect. Mach.*, Marseille, 2012, pp. 411-417.
- [VOL07] R. Vollmer, "Electric machine with an induction rotor". U.S. Patent 2007/0040466 A1, Feb. 22, 2007.
- [WAN05] T. Wang, P. Zheng, Q. Zhang, and S. Cheng, "Design characteristics of the induction motor used for hybrid electric vehicle," *IEEE Trans. Magn.*, vol. 41, no. 1, pp. 505-508, Jan. 2005.
- [WAN06] J. Wang, Z. P. Xia, D. Howe, and S. A. Long, "Comparative study of 3-phase permanent magnet brushless machines with concentrated, distributed and modular windings," in *IET Int. Conf. Power Electron. Mach. Drives (PEMD'06)*, Dublin, 2006, pp. 489-493.
- [WAN08] J. Wang, K. Atallah, Z. Q. Zhu and D. Howe, "Modular three-phase permanent-magnet brushless machines for in-wheel applications," *IEEE Trans. Veh. Technol.*, vol. 57, no. 5, pp. 2714-2720, Sept. 2008.
- [WAN13] K. Wang, Z. Q. Zhu, G. Ombach, M. Koch, S. Zhang, and J. Xu, "Optimal slot/pole and flux-barrier layer number combinations for synchronous reluctance machines," in *Int. Conf. and Exhib. Ecological Veh. Renewable Energies*, 2013, pp. 1-8.

- [WAN14a] K. Wang, Z. Q. Zhu, G. Ombach, M. Koch, S. Zhang, and J. Xu, "Electromagnetic performance of an 18-slot/10-pole fractional-slot surface-mounted permanent-magnet machine," *IEEE Ind. Appl.*, vol. 50, no. 6, pp. 3685-3696, 2014.
- [WAN14b] K. Wang, Z. Q. Zhu, and G. Ombach, "Synthesis of high performance fractional-slot permanent-magnet machines with coil-pitch of two slot-pitches," *IEEE Trans. Energy Convers.*, vol. 29, no. 3, pp. 758-770, 2014.
- [WAN14c] K. Wang, Z. Q. Zhu, G. Ombach, M. Koch, S. Zhang, and J. Xu, "Design and experimental verification of an 18-slot/10-pole fractional-slot surface-mounted permanent-magnet machine," in *Proc. IEEE Int. Electr. Mach. Drives Conf.*, Chicago, 2014, pp. 300–307.
- [WAN14d] J. Wang, V. I. Patel, and W. Wang, "Fractional-slot permanent magnet brushless machines with low space harmonic contents," *IEEE Trans. Magn.*, vol. 50, no. 1, pp. 1-9, Jan. 2014.
- [WAN16] L. Wang, X. Bao, C. Di and Y. Zhou, "Influence on vibration and noise of squirrel-cage induction machine with double skewed rotor for different slot combinations," *IEEE Trans. Magn.*, vol. 52, no. 7, pp. 1-4, Jul. 2016.
- [WAN17] C. Wang, X. Bao, S. Xu, Y. Zhou, W. Xu, and Y. Chen, "Analysis of vibration and noise for different skewed slot type squirrel-cage induction motor," *IEEE Trans. Magn.*, vol. PP, no. 99, pp. 1-6, May. 2017.
- [WEI11] H. Weichsel, "Wave shape of currents in an individual rotor conductor of a single phase induction motor," in *Proc. American Inst. Elect. Eng.*, vol. 30, no. 6, pp. 1023-1044, Jun. 1911.
- [WIE92] J. Wiesing and H. Grotstollen, "Field oriented control of an asynchronous motor with a very wide region of flux weakening," in *Proc. IEEE Int. Symp. Ind. Electron.*, Xian, 1992, pp. 606-610.
- [WOL07] T. M. Wolbank and P. E. Macheiner, "Detection of airgap asymmetry in induction machines with different pole pair number using the current step response," in *IEEE Int. Electr. Mach. Drives Conf.*, (IEMDC'07), Antalya, 2007, pp. 1177-1182.
- [XIA08] T. Xiaoping, L. A. Dessaint, R. Champagne, and K. Al-Haddad, "Transient modeling of squirrel-cage induction machine considering air-gap flux saturation harmonics," *IEEE Trans. Ind. Electron.*, vol. 55, no. 7, pp. 2798-2809, Jul. 2008.
- [XU88a] X. Xu, R. D. Doncker, and D. W. Novotny, "A stator flux oriented induction machine drive," *IEEE Power Electron. Specialists Conf.*, Kyoto, Japan, 1988, pp. 870-876.
- [XU88b] X. Xu, R. Doncker, and D. W. Novotny, "Stator flux orientation control of induction machines in the field weakening region," *IEEE Ind. Appl. Soc. Annu. Meeting Conf. Rec.*, Pittsburgh, PA, USA, 1988, pp. 437-443 vol.1.
- [XUE11] P. Xue and J. Lin, "Discussion on the rare earth resources and its development potential of Inner Mongolia of China," in *Int. Conf. Mat. Renewable Energy Environment*, 2011, pp. 9–12.
- [YAM13] K. Yamazaki and K. Kanbayashi, "Shape optimization of induction machines by using combination of frequency- and time-domain finite element methods," *IEEE Trans. Magn.*, vol. 49, no. 5, pp. 2185-2188, May. 2013.
- [YAN15] Z. Yang, F. Shang, I. P. Brown, and M. Krishnamurthy, "Comparative study of interior permanent magnet, induction, and switched reluctance motor drives for EV and HEV applications," *IEEE Trans. Transport. Electrific.*, vol. 1, no. 3, pp. 245-254, Oct. 2015

- [YAN17] Y. Yang, S. M. Castano, R. Yang, M. Kasprzak, B. Bilgin, A. Sathyan, H. Dadkhah, and A. Emadi, "Design and comparison of interior permanent magnet motor topologies for traction applications," *IEEE Trans. Transport. Electrific.*, vol. 3, no. 1, pp. 86-97, Mar. 2017.
- [YAO16] Y. Yao, A. Cosic, and C. Sadarangani, "Power factor improvement and dynamic performance of an induction machine with a novel concept of a converter-fed rotor," *IEEE Trans. Energy Convers.*, vol. 31, no. 2, pp. 769-775, Jun. 2016.
- [YAO17] Y. Yao, C. Sadarangani, and H. Zhang, "Efficiency improvement of a 12-pole 17.5 kW induction motor using converter-fed wound rotor," in *Int. Conf. Elect. Mach. Syst. (ICEMS'17)*, Sydney, 2017, pp. 1-6.
- [YON15] P. Yongsoo, J.M. Yoo, S.K. Sul, "Double-delta sourced winding for dual winding induction machine," in *Int. Conf. Power Electron. ECCE Asia (ICPE-ECCE Asia)*, Seoul, 2015, pp. 77-85.
- [YUB07] Y. Yang, X. Wang, X. Leng, D. Wang, and S. Liu, "Reducing cogging torque in surface-mounted permanent magnet motors by teeth notching," in *IEEE Conf. Ind. Electron. Applicat. (ICIEA'07)*, Harbin, 2007, pp. 265-268.
- [ZER06] M. Zeraoulia, M. E. H. Benbouzid, and D. Diallo, "Electric motor drive selection issues for HEV propulsion systems: A comparative study," *IEEE Trans. Veh. Technol.*, vol. 55, no. 6, pp. 1756-1764, Nov. 2006.
- [ZHA00] Z. M. Zhao, S. Meng, C. C. Chan, and E. W. C. Lo, "A novel induction machine design suitable for inverter-driven variable speed systems," *IEEE Trans. Energy Convers.*, vol. 15, no. 4, pp. 413-420, Dec. 2000.
- [ZHA14a] Y. Zhang, C. Lin, J. Xu, and Z. Sun, "Analysis of coupling effect of double-side linear induction motor with shielding structure," in *Int. Conf. Elect. Mach. Syst. (ICEMS'14)*, Hangzhou, 2014.
- [ZHA14b] Z. Haisen, Z. Jian, W. Xiangyu, W. Qing, L. Xiaofang, and L. Yingli, "A design method for cage induction motors with non-skewed rotor bars," *IEEE Trans. Magn.*, vol. 50, no. 2, pp. 769-772, 2014.
- [ZHA16] M. Zhang, F. Eastham, and W. Yuan, "Design and modeling of 2G HTS armature winding for electric aircraft propulsion applications," *IEEE Trans. Appl. Supercond.*, vol. 26, no. 3, pp. 1-5, Apr. 2016.
- [ZHA96] Y. Zhao and T. A. Lipo, "Modeling and control of a multi-phase induction machine with structural unbalance," *IEEE Trans. Energy Convers.*, vol. 11, no. 3, pp. 570-577, Sep. 1996.
- [ZHE11] P. Zheng, W. J. Ke, Q. B. Zhao, and J. G. Bai, "Torque ripple reduction in an interior permanent-magnet synchronous motor for servo applications," in *Proc. Int. Conf. Electr. Mach. Syst.*, Beijing, 2011, pp. 1-5.
- [ZHU07] Z. Q. Zhu and D. Howe, "Electrical machines and drives for electric, hybrid, and fuel cell vehicles," *Proc. IEEE*, vol. 95, no. 4, pp. 746-765, Apr. 2007.
- [ZHU08] Z. Q. Zhu and C. C. Chan, "Electrical machine topologies and technologies for electric, hybrid, and fuel cell vehicles," in *IEEE Veh. Power Propul. Conf. (VPPC'08)*, Harbin, 2008, pp. 1-6.
- [ZHU11] Z. Q. Zhu and X. Liu, "Individual and global optimization of switched flux permanent magnet motors," in *Int. Conf. Elect. Mach. Syst. (ICEMS'11)*, Beijing, 2011, pp. 1-6.

Appendix A Modelling of Induction Machine in dq -axis Reference Frame and Calculation of Flux-Weakening Characteristic

In the field-weakening region, the dynamic performance of the IM is affected by the current rating and the maximum voltage of the inverter. In order to obtain the maximum torque in the constant power region, many efforts have been made [XU88a], [XU88b], [KIM95], [SEI97], and [HOF97]. In a rotor-flux-oriented IM drive, a maximum torque control method of an IM in the field-weakening region is proposed [KIM95]. In this method, maximum torque capability is obtained by considering the voltage and current limits. However, this method has a disadvantage in that a rotor-flux-oriented drive is sensitive to variations in leakage inductances. Therefore, when the leakage inductance is increased at the high speed, high electric loading, or very high frequency operations, poorer torque generation is resulted [XU88b]. On the other hand, the stator-flux-oriented control drive is not sensitive to the variations in the parameters of the machine. The selection of the flux reference is important to obtain maximum torque capability in the field-weakening region. The optimal flux reference can be selected by considering voltage, torque, and current limits [SHI02]. The onset of the field-weakening region is automatically determined according to the rated flux reference.

A.1 Voltage Limit

The steady state voltage equations for the stator-flux-oriented IM in the rotating d - q axis reference frame are calculated by (A.1) and (A.2).

$$v_{ds} = R_s i_{ds} \quad (\text{A.1})$$

$$v_{qs} = R_s i_{qs} + \omega_e \psi_{ds} \quad (\text{A.2})$$

where v_{ds} is the d -axis component of stator voltage, v_{qs} is the q -axis component of stator voltage, R_s is the stator resistance, i_{ds} is the d -axis component of stator current, i_{qs} is the q -axis component of stator current, ω_e is the excitation angular frequency, and ψ_{ds} is the d -axis component of the stator flux, which can be calculated by (A.3).

$$\psi_{ds} = L_s i_{ds} \quad (\text{A.3})$$

where L_s is the stator self-inductance. The maximum stator voltage V_{sm} is determined from the available dc-link voltage V_{dc} and PWM strategy. In this study, PWM strategy based on voltage space vector is used, and then $V_{sm} = V_{dc}/\sqrt{3}$ [BRO88]. Then, v_{ds} and v_{qs} should satisfy (A.4).

$$v_{ds}^2 + v_{qs}^2 \leq V_{sm}^2 \quad (\text{A.4})$$

Therefore, the limits of the current components can also be calculated by using the equations from (A.1) to (A.4) as follows.

$$i_{qs} \leq \frac{\sqrt{V_{sm}^2 - (R_s i_{ds})^2 - \omega_e \psi_{ds}}}{R_s}, \quad \text{if } R_s i_{ds} + \omega_e \psi_{ds} \geq 0 \quad (\text{A.5})$$

$$i_{qs} \geq \frac{-\sqrt{V_{sm}^2 - (R_s i_{ds})^2 - \omega_e \psi_{ds}}}{R_s}, \quad \text{if } R_s i_{ds} + \omega_e \psi_{ds} < 0 \quad (\text{A.6})$$

The $(R_s i_{ds})^2$ term in the relation (A.5) and (A.6) can be ignored if $(R_s i_{ds})^2 \ll V_{sm}^2$, respectively. If the current command i_{qs}^* does not remain in the voltage-limit boundary, the inverter runs out of voltage, and current relation is lost. Therefore, i_{qs}^* should remain inside the voltage-limit boundary for satisfying the voltage-limit constraints at each given operation frequency.

A.2 Current Limit

The maximum stator current I_{sm} is usually limited to 1.5 ~ 2 times the rated current provide higher acceleration torque during transients. The limit expressed in (A.7) should be satisfied.

$$i_{ds}^2 + i_{qs}^2 \leq I_{sm}^2 \quad (\text{A.7})$$

A.3 Torque Limit

The steady state torque T_e of a stator-flux-oriented IM is calculated by (A.8), where p is the number of the pole pairs [XU88a].

$$T_e = \frac{3}{2} p \psi_{ds} i_{qs} \quad (\text{A.8})$$

The condition for stability of a stator-flux-oriented IM is given by (A.9) from the steady state equation [XU88a].

$$T_e^* = \frac{3}{2} p \frac{(1-\sigma)}{2\sigma L_s} \psi_{ds}^{*2} \quad (\text{A.9})$$

where “*” is the command value, L_s is the stator self-inductance, σ is the total leakage factor which is expressed in (A.10), where L_m is the mutual inductance between the stator winding and the rotor winding (magnetizing inductance) and L_r is the rotor self-inductance. Torque-limit constraint can be derived from (A.8) and (A.9).

$$\sigma = 1 - \frac{L_m^2}{L_s L_r} \quad (\text{A.10})$$

The torque-limit constraint should not be violated to make the system stable under any circumstances. The torque limit boundary is influenced by the leakage factor of the machine and the stator flux reference. The torque-limit boundary of the machine with large leakage factor is smaller than that of the machine with small leakage factor at each given stator flux reference.

A.4 Optimal Flux for Maximum Torque

The flux-weakening performance of the IMs presented in this thesis have been calculated by using the optimal flux method for maximum torque at any operation speed proposed by [SHI02]. The maximum torque T_{e_v} considering only the voltage-limit boundary can be calculated by (A.11) at a given flux reference. The maximum torque T_{e_t} considering only the torque-limit boundary can be calculated by using (A.12) at a given flux reference.

$$T_{e_v} = \frac{3}{2} p \psi_{ds} i_{qs} = \frac{3}{2} p \frac{V_{sm} \psi_{ds} - \omega_e \psi_{ds}^2}{R_s} \quad (\text{A.11})$$

$$T_{e_t} = \frac{3}{2} p \psi_{ds} i_{qs} = \frac{3}{2} p \frac{(1-\sigma)}{2\sigma L_s} \psi_{ds}^2 \quad (\text{A.12})$$

Variations of T_{e_v} and T_{e_t} with flux are illustrated in Fig. A.1. As seen in the figure, T_{e_v} is decreased by the increment of frequency at a given flux. The flux that generating the maximum point of T_{e_v} at each operating frequency can be written as (A.13) with the condition of $\frac{dT_{e_v}}{d\psi_{ds}} = 0$. The maximum torque $T_{e_v,m}$ of T_{e_v} at each operating frequency can be given as (A.14) by substituting ω_e of (A.13) into (A.11). Critical flux $\psi_{ds,c}$ at the intersection (Point J) of T_{e_t} and $T_{e_v,m}$ can be given as (A.15) by equating $T_{e_v,m}$ to T_{e_t} . The torque command is limited by the torque-limit constraints given in (A.9). In the case where T_{e_t} is lower than T_{e_v} , the command torque and output torque become T_{e_t} at a given flux level and a given operating frequency. In the case where T_{e_v} is lower than T_{e_t} , the torque command is T_{e_t} by torque limiter at a given flux level and a given operating frequency. However, the output torque cannot become T_{e_t} but becomes T_{e_v} because voltage and current regulation is lost due to the exceeded voltage limit. In the case where the operating frequency ω_e is higher than the ω_c , the maximum torque becomes the intersections (K, L) of T_{e_v} and T_{e_t} at each given operating frequency. At the same time, the current i_{qs} is maximized at the intersections. In the case where the operating frequency ω_e is lower than ω_c , the current i_{qs} is maximized at the intersections (H₁, I₁). However the maximum torque becomes maximum points (H, I) of T_{e_v} at each operating frequency. If the operating frequency ω_e is lower than ω_c , the optimal flux reference $\psi_{ds,opt1}^*$ for maximum torque can be written as (A.16).

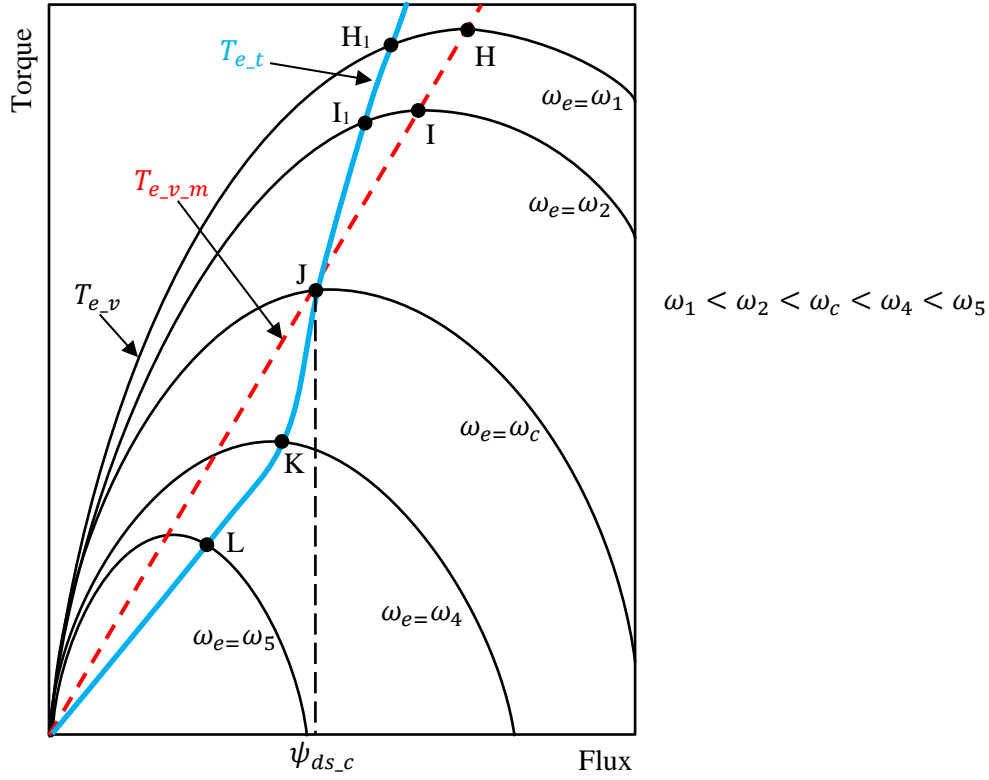


Fig. A.1 Maximum torque capability considering voltage limit and torque limit [SHI02].

$$\psi_{ds} = \frac{V_{sm}}{2\omega_e} \quad (\text{A.13})$$

$$T_{e_v_m} = \frac{3}{2}p \frac{V_{sm}}{2R_s} \psi_{ds} \quad (\text{A.14})$$

$$\psi_{ds_c} = \frac{\sigma L_s V_{sm}}{R_s(1-\sigma)} \quad (\text{A.15})$$

$$\psi_{ds_opt1}^* = \frac{V_{sm}}{2\omega_e}, \text{ if } \omega_e < \omega_c \quad (\text{A.16})$$

Once the operating frequency ω_e becomes higher than ω_c , (A.17) is valid. The optimal flux reference $\psi_{ds_opt2}^*$ for maximum torque can be calculated by using (A.18) derived from (A.17).

$$\frac{3}{2}p \frac{V_{sm}\psi_{ds} - \omega_e \psi_{ds}^2}{R_s} = \frac{3}{2}p \frac{(1-\sigma)}{2\sigma L_s} \psi_{ds}^2 \quad (\text{A.17})$$

$$\psi_{ds_opt2}^* = \frac{2\sigma L_s V_{sm}}{R_s - \sigma R_s + 2\sigma L_s \omega_e}, \text{ if } \omega_e > \omega_c \quad (\text{A.18})$$

Appendix B Drive Requirements and Lamination Specifications

B.1 Specification Limits

The specification limits are listed in Table B.1. It is expected that the designed AIMs should meet the given specifications. Note that due to commercial sensitivity, demanded torque/power-speed curves have been removed.

Table B.1 Specification limits

Specifications	Min. Value	Max. Value
Total Axial Length (mm)	—	120
Outer Diameter (mm)	—	144
Slot Filling Factor	0.45	0.65
Average Torque (Nm)	5	55.2
Output Power (kW)	8	12
Phase Current (Arms)	—	500

B.2 Lamination Specifications

The BH and loss specification of lamination M330-35 assigned for the Toyota Prius 2010 IPM machine is listed and shown in Table B.2 and Table B.4, respectively. In addition, the BH and loss specification of lamination M270-35 assigned for IMs is listed and shown in Table B.3 and Table B.5, respectively.

Table B.2 BH curve of lamination M330-35A

H (A/m)	B (T)	H (A/m)	B (T)	H (A/m)	B (T)
10	0.016	90	0.855	1000	1.491
15	0.029	100	0.922	1250	1.511
20	0.045	125	1.054	1500	1.528
25	0.068	150	1.139	2000	1.555
30	0.101	175	1.202	2500	1.580
40	0.200	200	1.250	5000	1.666
50	0.340	250	1.309	7500	1.730
60	0.509	350	1.374	10000	1.777
70	0.653	500	1.421		
80	0.765	750	1.463		

Table B.3 BH curve of lamination M270-35A

H (A/m)	B (T)	H (A/m)	B (T)	H (A/m)	B (T)
0	0	0.125	1.015	2	1.535
0.01	0.018	0.15	1.108	2.5	1.560
0.02	0.048	0.175	1.172	5	1.654
0.03	0.097	0.2	1.218	7.5	1.720
0.04	0.175	0.25	1.279	10	1.769
0.05	0.292	0.35	1.346		
0.06	0.436	0.5	1.394		
0.07	0.573	0.75	1.439		
0.08	0.690	1	1.466		
0.09	0.788	1.25	1.489		
0.1	0.870	1.5	1.505		

Table B.4 Loss characteristic of lamination M330-35A

B (T)	W/kg 50Hz	W/kg 100Hz	W/kg 200Hz	W/kg 400Hz	W/kg 700Hz	B (T)	W/kg 1000Hz	W/kg 1200Hz
0.10	0.022	0.049	0.115	0.304	0.70	0.02	0.006	0.089
0.15	0.049	0.110	0.260	0.67	1.53	0.05	0.037	0.341
0.20	0.084	0.188	0.447	1.16	2.62	0.1	1.083	1.538
0.25	0.125	0.282	0.67	1.74	3.95	0.15	2.478	3.250
0.30	0.171	0.387	0.93	2.39	5.4	0.2	4.193	5.621
0.35	0.221	0.50	1.21	3.14	7.2	0.25	6.352	8.362
0.40	0.276	0.63	1.53	3.98	9.1	0.3	8.963	11.474
0.50	0.397	0.92	2.24	5.9	13.4	0.35	11.602	15.034
0.60	0.53	1.24	3.06	8.1	18.7	0.4	14.765	18.839
0.70	0.68	1.60	3.99	10.7	24.9	0.5	21.854	29.294
0.80	0.85	2.00	5.0	13.7	32.2	0.6	30.187	40.032
0.90	1.03	2.44	6.2	17.0	41	0.7	40.795	55.102
1.00	1.23	2.93	7.5	20.8	50	0.8	53.749	
1.10	1.46	3.47	8.9	25.0	61	0.9	68.647	
1.20	1.71	4.09	10.5	29.7	73	1	86.284	
1.30	2.01	4.8	12.3	35	91			
1.40	2.40	5.7	14.6	41	115			
1.50	2.87	6.9	17.6	50	131			
1.60	3.37	8.0	20.9	60				
1.70	3.75	8.9	24.8	73				
1.75	3.91	9.7						
1.80	4.19							

Table B.5 Loss characteristic of lamination M270-35A

B (T)	W/kg 50Hz	W/kg 100Hz	W/kg 200Hz	W/kg 400Hz	W/kg 700Hz	B (T)	W/kg 1000Hz	B (T)	W/kg 1200Hz
0.10	0.018	0.041	0.098	0.256	0.59	0.10	0.886	0.02	0.094
0.15	0.043	0.095	0.227	0.58	1.31	0.15	1.764	0.05	0.352
0.20	0.075	0.167	0.398	1.01	2.27	0.20	3.763	0.1	1.326
0.25	0.113	0.253	0.60	1.53	3.44	0.25	5.867	0.15	3.082
0.30	0.157	0.350	0.84	2.13	4.74	0.30	8.079	0.2	5.073
0.35	0.204	0.46	1.10	2.80	6.26	0.35	10.733	0.25	7.692
0.40	0.256	0.58	1.39	3.56	7.96	0.40	13.213	0.3	10.591
0.50	0.370	0.84	2.04	5.26	11.7	0.50	21.271	0.35	14.089
0.60	0.50	1.13	2.78	7.17	16.2	0.60	27.908	0.4	17.359
0.70	0.64	1.46	3.62	9.41	21.5	0.70	36.751	0.5	26.902
0.80	0.79	1.82	4.52	11.9	27.6	0.80	48.094	0.6	37.094
0.90	0.96	2.22	5.53	14.8	34.6	0.90	60.143	0.7	49.153
1.00	1.14	2.65	6.66	18.0	42.8	1.00	75.708	0.8	66.369
1.10	1.35	3.13	7.89	21.7	52.1	1.10	92.695	0.9	85.012
1.20	1.58	3.68	9.30	25.8	62.9	1.20	114.869	1	105.062
1.30	1.86	4.3	10.9	30.5	79.5	1.30	138.441	1.1	126.653
1.40	2.19	5.1	12.9	36.4	103	1.40	176.609		
1.50	2.57	6.0	15.5	43.6	134				
1.60	2.94	7.0	18.5	53.0					
1.70	3.29	8.0	22.2	65.6					
1.75	3.50	8.7							
1.80	3.71								

Appendix C Specifications and Winding Properties of IMs Designed for Valeo

C.1 Specifications of Conventional Induction Machine

The specifications of the conventional IMs examined in Chapter 2 have been presented in this appendix. The optimization parameters mentioned in Chapter 2 are split ratio, stator and rotor slot geometric parameters, including b_{r1} , b_{r2} , h_{r1} , b_{s1} , b_{s2} , h_{s1} , and h_{s2} (see Fig. C.1). The rotor and stator slot parameters indicated in Table C.1 are given in Fig. C.1.

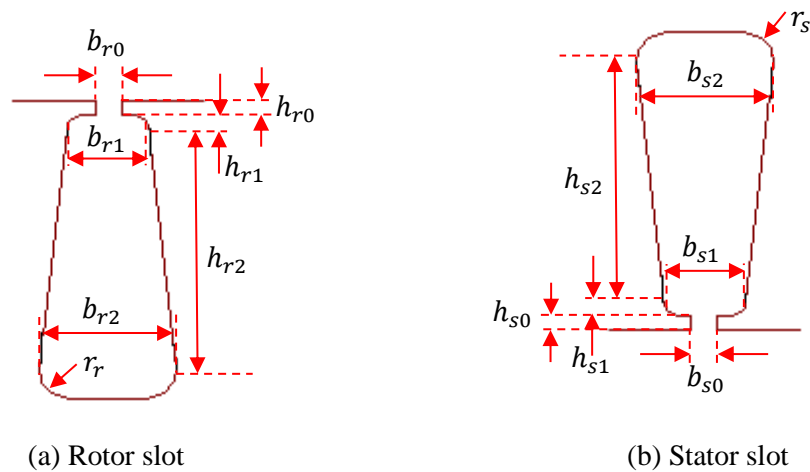


Fig. C.1 Rotor (a) and stator slot (b) parameters.

Table C.1 Specifications of 6-pole conventional IMs

<i>Parameter</i>	<i>9S/6P-DL</i> $y_c = 1$	<i>18S/6P-DL</i> $y_c = 1$	<i>18S/6P-SL</i> $y_c = 3$	<i>18S/6P-DL</i> $y_c = 2$	<i>36S/6P-SL</i> $y_c = 5$	<i>36S/6P-DL</i> $y_c = 5$	<i>54S/6P-DL*</i> $y_c = 9$
Rated speed (rpm)	1870	1890	1890	1890	1905	1905	1905
Slot number S	9	18	18	18	36	36	56
Rotor slot number R	14	20	20	20	38	38	44
Number of coils per phase	3	6	3	6	6	12	18
Number of turns per coil	14	17	10	2	9	9	1
Number of parallel branch	3	6	3	1	6	12	2
Coil pitch (y_c)	1	1	3	2	5	5	9
Air-gap length (mm)				0.35			0.4
Stator outer diameter (mm)				144			146
Stator inner diameter (mm)	96.48	88.992	99.36	95.04	98.496	99.072	140.2
Rotor outer diameter (mm)	95.78	88.292	98.66	94.34	97.796	98.372	103.4
Split ratio	0.67	0.618	0.69	0.66	0.684	0.688	0.7137
b_{s0} / b_{r0} (mm)	8 / 5.5	5.5 / 4	3.5 / 4	4 / 4	2 / 1.5	1.75 / 1.5	1 / 2
b_{s1} / b_{r1} (mm)	19 / 10	8.6 / 6.2	10.5 / 7	10 / 7	4.7 / 4.2	4.74 / 4.1	2.94 / 3.58
b_{s2} / b_{r2} (mm)	27 / 11.9	14 / 2.12	10.5 / 3.2	10 / 3.2	4.7 / 2.0	4.74 / 2.0	2.94 / 1.78
h_{s0} / h_{r0} (mm)	0.5 / 0.5	5.5 / 4	0.5 / 0.4	0.6 / 0.4	0.6 / 0.4	0.5 / 0.3	0.5 / 0.5
h_{s1} / h_{r1} (mm)	0.3 / 0.4	1 / 1	0.3 / 0.4	0.3 / 0.5	0.3 / 0.5	0.3 / 0.5	0 / 0
h_{s2} / h_{r2} (mm)	11.9 / 10	15.1/12.8	10 / 11.9	12.8/12.2	10.1/11.9	10 / 11.9	11.49 / 12.6
r_s / r_r (mm)	1.2 / 0.2	1 / 0.5	0.3 / 0.2	0.3 / 0.2	0.3 / 0.2	0.3 / 0.2	0 / 0
Stator slot filling factor				0.64			
Stack length (mm)				70			
Bar material				Copper 75_C			
Core material				M270-35A			

*Tested IM. The test results have been obtained from [GUA15b].

C.2 Specifications of the Proposed AIMs

The specifications of laminations of 18S/44R/6P AIM with 70mm and 90mm stack lengths are illustrated in Fig. C.2 and Fig. C.3, respectively. In addition, other specifications of the prototyped AIMs are listed in Table C.2.

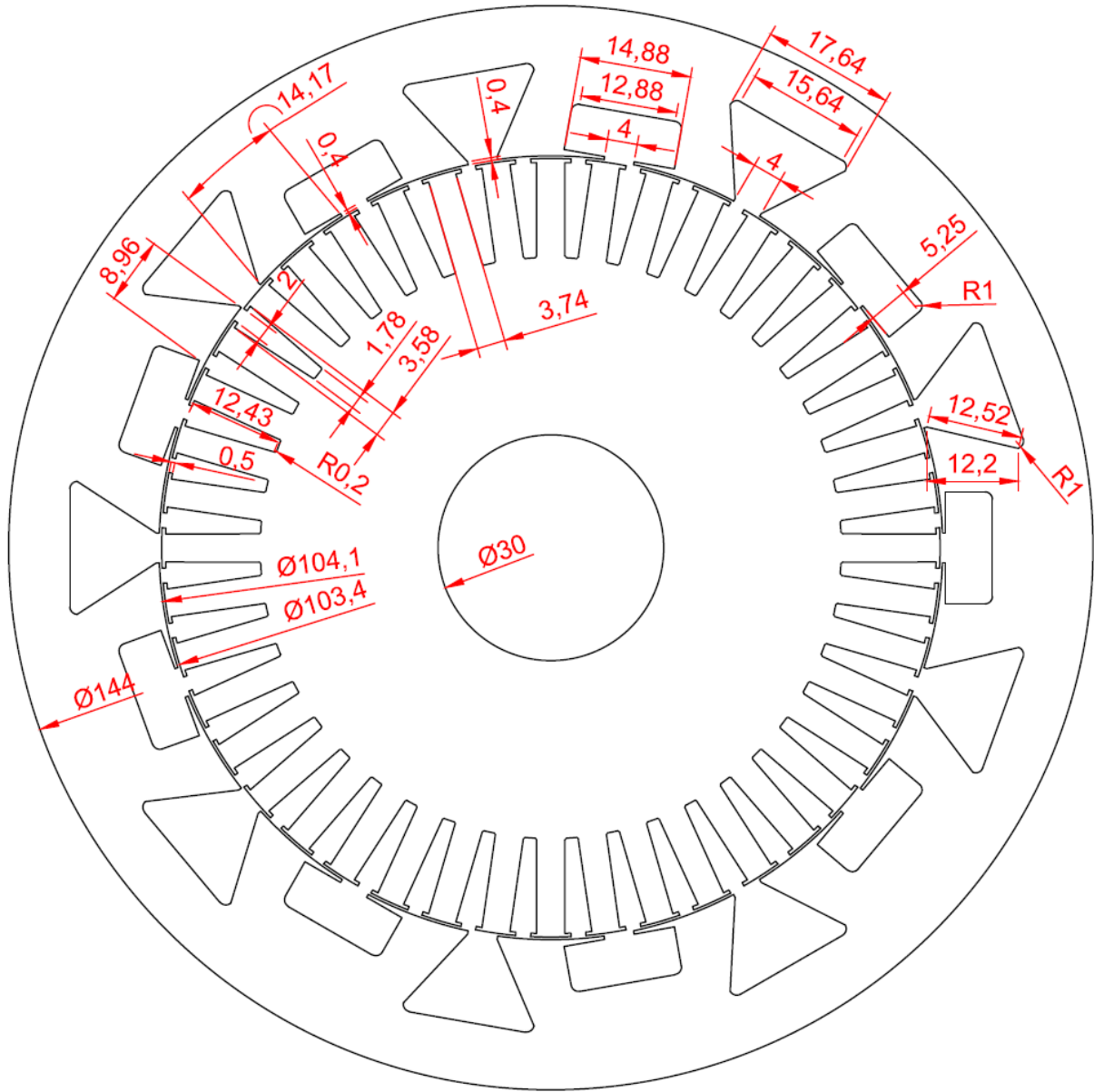


Fig. C.2 18S/44R/6P AIM with 70mm stack length.

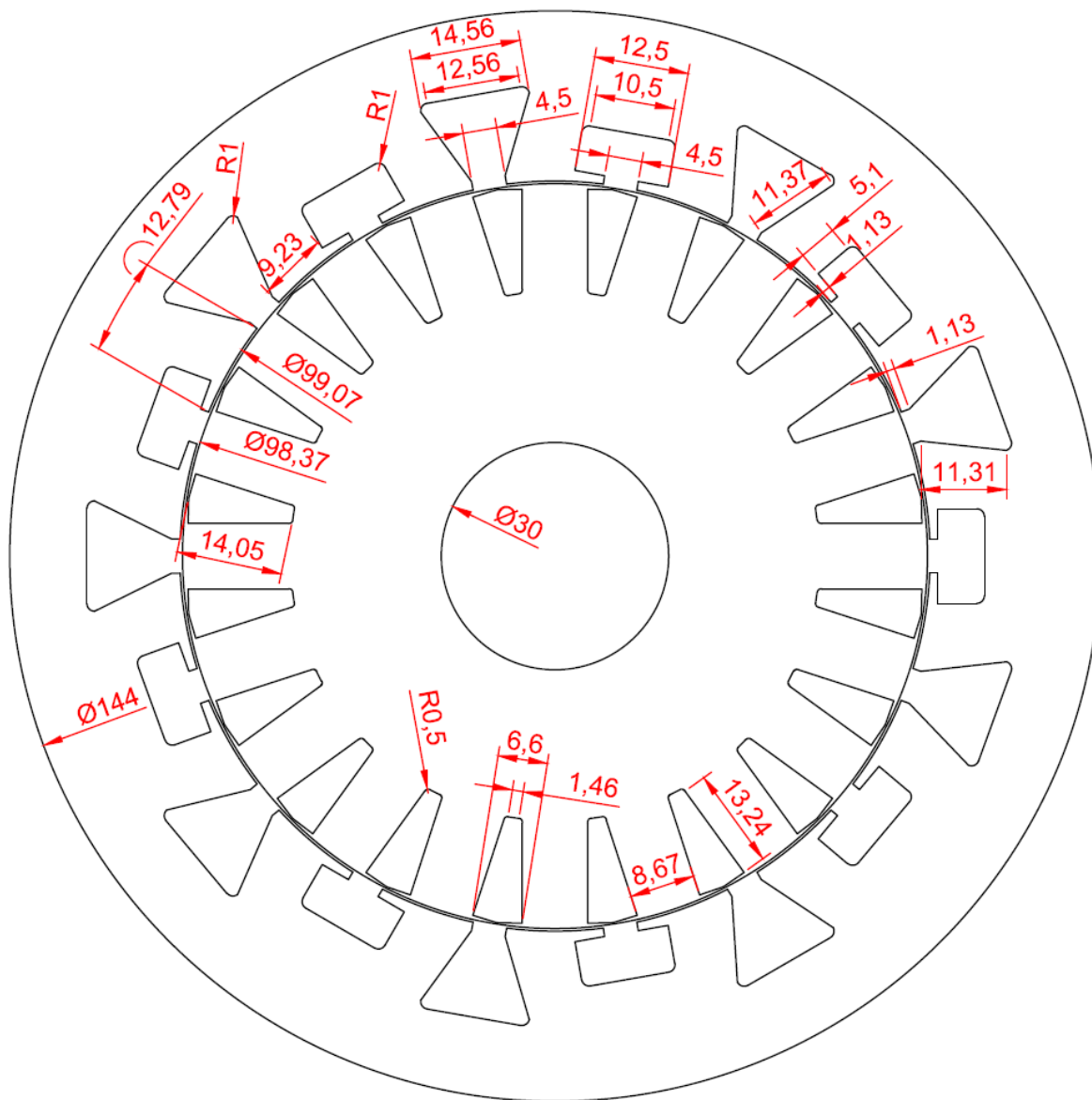


Fig. C.3 18S/20R/6P AIM with 90mm stack length.

Table C.2 Design specifications

Machine	18S/20R/6P – 70mm	18S/20R/6P – 90mm
Wire dimension (mm×mm)	AWG12	AWG3
Number of coils per slot	2	2
Number of turns per coil	11	9
Number of parallel branches	6	2
Number of series turns per phase	11	9
Slot filling factor	0.65	0.65
Stator resistance at 20°C (Ω)	0.00282	0.002524
Rotor resistance at 75°C (mΩ)	0.741	0.8711
End ring area (mm ²)	170	185
Iron grade	M270-35	M270-35

C.3 Winding Layout and Coil Connections of the 18S/6P AIMs

In this appendix, winding layout and coil connections of AIMs is presented for 18S/6P AIM. Since each phase has 6 coils, in order to maintain the required torque it is possible to use several parallel branches such as 1, 2, 3, and 6 for 6-pole AIM. The winding layout and coil numbers are given in Fig. C.4.

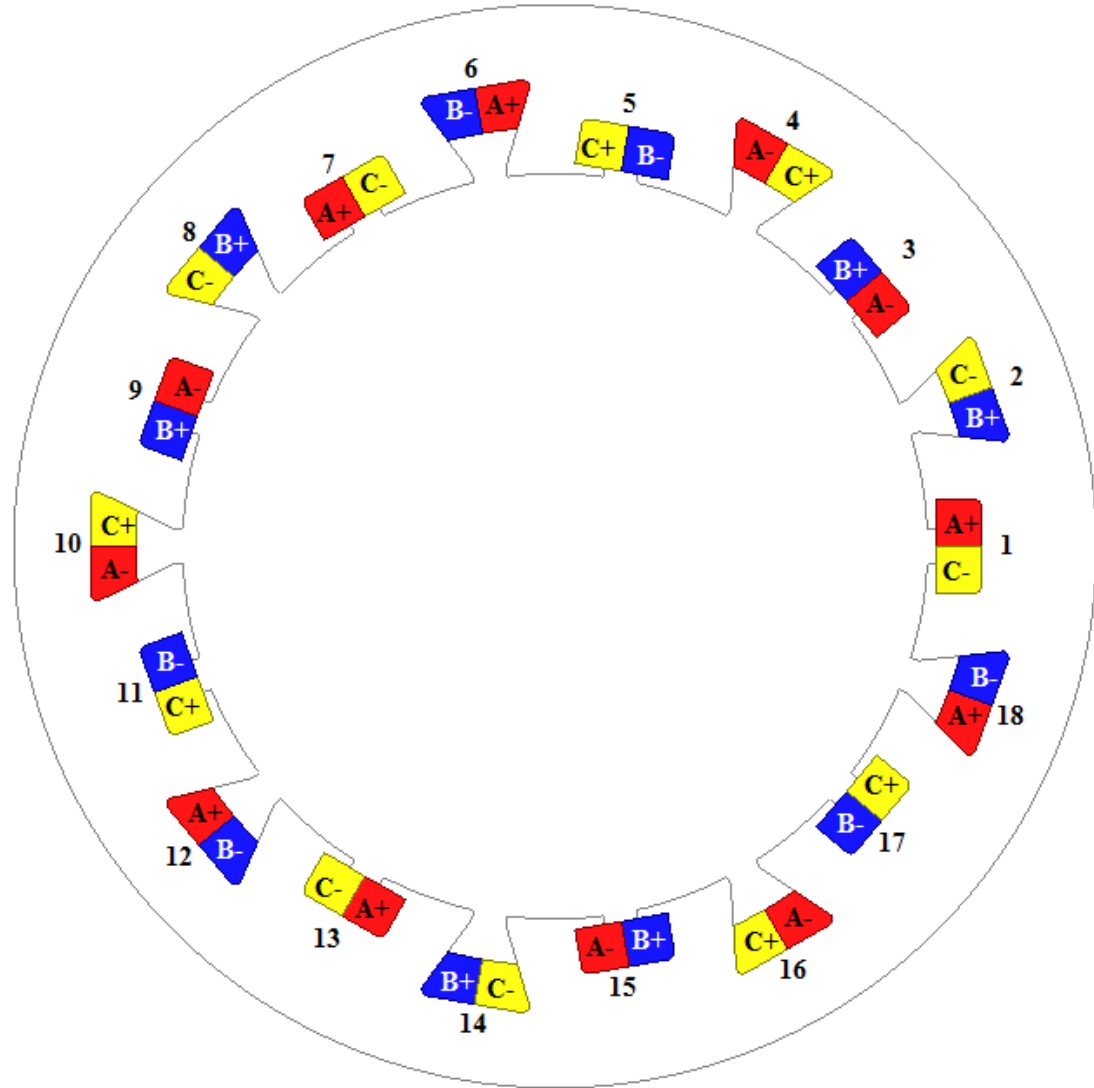
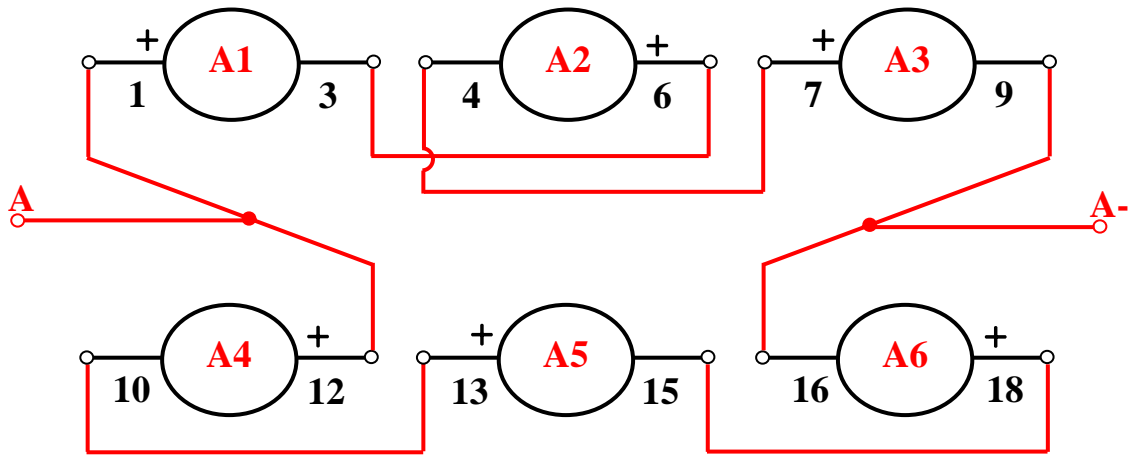


Fig. C.4 Winding layout of 18S/6P AIM.

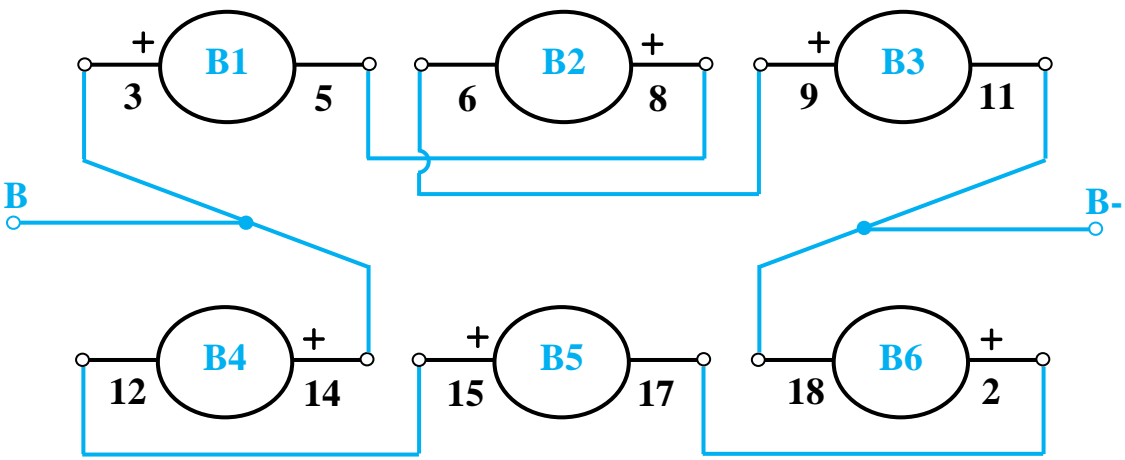
A. 18S/6P AIM with 90mm

The number of serial turns per phase is determined by the number of turns N_t and the number of parallel branch a as given in (C.1).

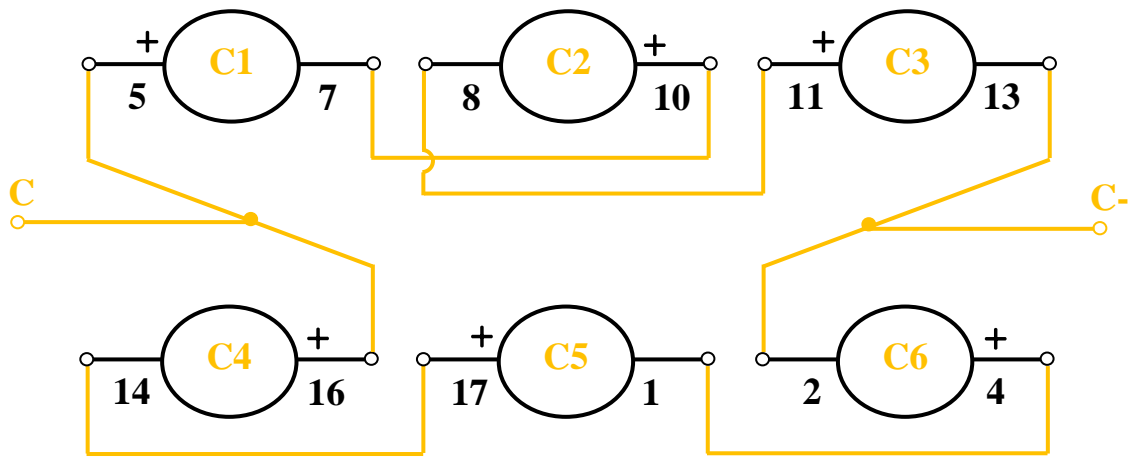
$$N_{st} = \frac{N_t}{a} = \frac{9}{6} = \frac{3}{2} \quad (\text{C.1})$$



(a) Phase A



(b) Phase B



(c) Phase C

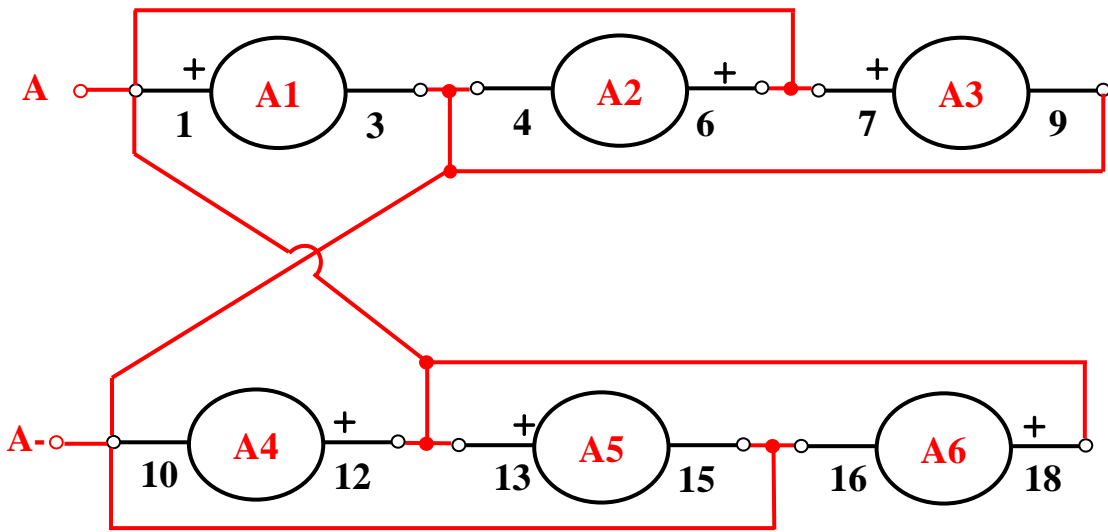
Fig. C.5 Coil connections of the phase windings for 90mm AIM with 2-parallel branches.

Winding layout of the 18S/20R/6P AIM with 90mm stack length is illustrated in Fig. C.5. Since there are 9-turns per coil and 6-parallel branches per phase, in order to simplify the manufacturing of windings, it is reasonable to use 3-turns per coil and 2-parallel branches per phase as shown in Fig. C.5. Thus, each phase consists of 6-coils with 3-turns and 2-parallel branches.

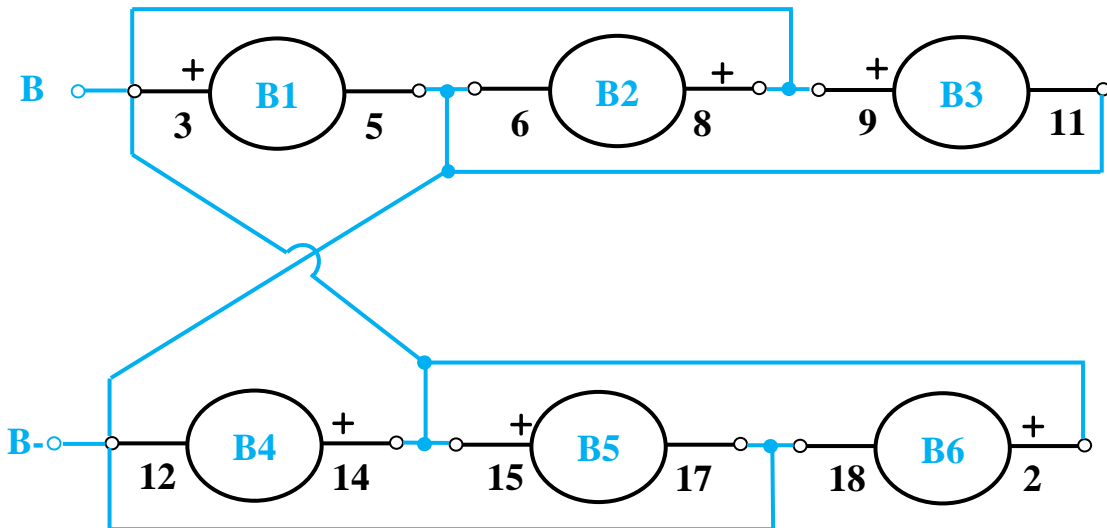
B. 18S/6P AIM with 70mm

Winding layout of 18S/6P AIM with 70mm is as exactly same as the 90mm AIM (see Fig. C.4). As for the 70mm AIM, there is no possible way to simplify the number of turns or parallel branch number since there are 11-turns per coil and 6-parallel branches per phase as given in (C.2). Therefore, all the coils of one phase should be connected in parallel as shown Fig. C.6. Thus, each phase consists of 6-coils with 11-turns and 6-parallel branches.

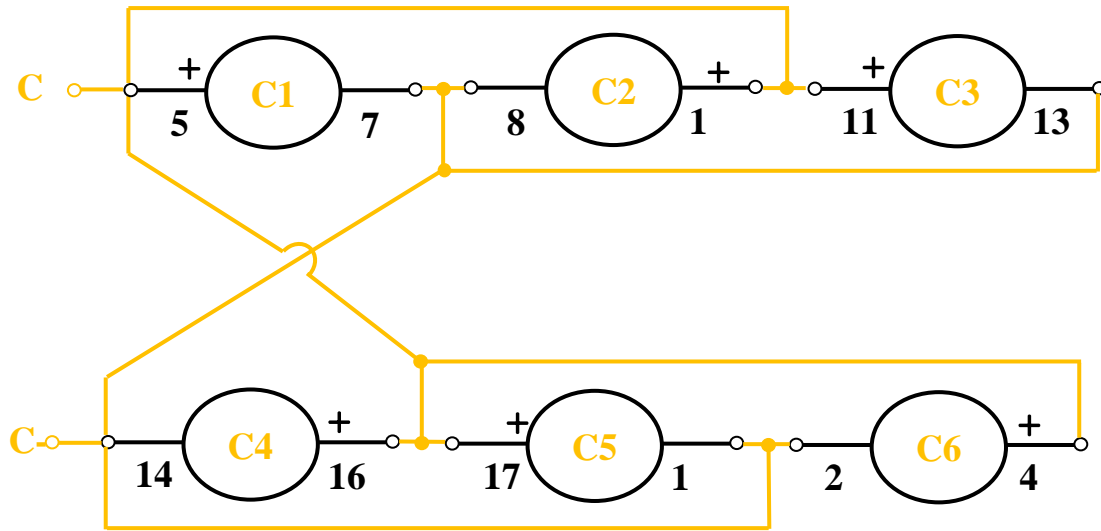
$$N_{st} = \frac{N_t}{a} = \frac{11}{6} \quad (C.2)$$



(a) Phase A



(b) Phase B



(c) Phase C

Fig. C.6 Coil connections of the phase windings for 70mm AIM with 6-parallel branches.

Appendix D Specifications of Toyota Prius 2010 IPM Machine

A 48 stator slots, 8 poles, and 44 rotor slots squirrel-cage IM whose main specifications and 2-D cross-sectional view are given in Table D.1 and Fig. D.1, respectively, has been designed in order to investigate the rotor bar current.

Table D.1 IM Design Specifications

Parameters	Value	Parameters	Value
Peak Power	60 kW	Wire Size, AWG	21
Peak Phase Current	250 A	Slot Fill Factor	0.5
Stator Outer Diameter	264 mm	CIM Winding Factor	0.966
Stator Inner Diameter	195 mm	AIM Winding Factor	0.866
Air-gap Length	0.4 mm	Iron Core Material	W330_35
Shaft Diameter	100 mm	Core Loss coefficients	
Stack Length	50.8 mm	Hysteresis (K_h)	126.904
Turns per Coil		Classical (K_c)	0.761
CIM: (36S6P/48S8P/60S10P ⁽¹⁾⁽²⁾)	10/7/6 ⁽¹⁾ /5 ⁽²⁾	Excess (K_e)	0
AIM: (186P/24S8P/30S10)	14/12/10	Stacking Factor	0.92
CIM Coil Pitch	5	Rotor Bar Material	Copper
AIM Coil Pitch	2	End-Ring Material	Copper
Optimum b_{s0}	1.88 mm	Optimum b_{r0}	1 mm
Optimum b_{s12}	4.13 mm	Optimum b_{r12}	4.35 mm
Optimum h_{s0}	1.02 mm	Optimum h_{r0}	1 mm
Optimum h_{s1}	10 mm	Optimum h_{r1}	14.06mm

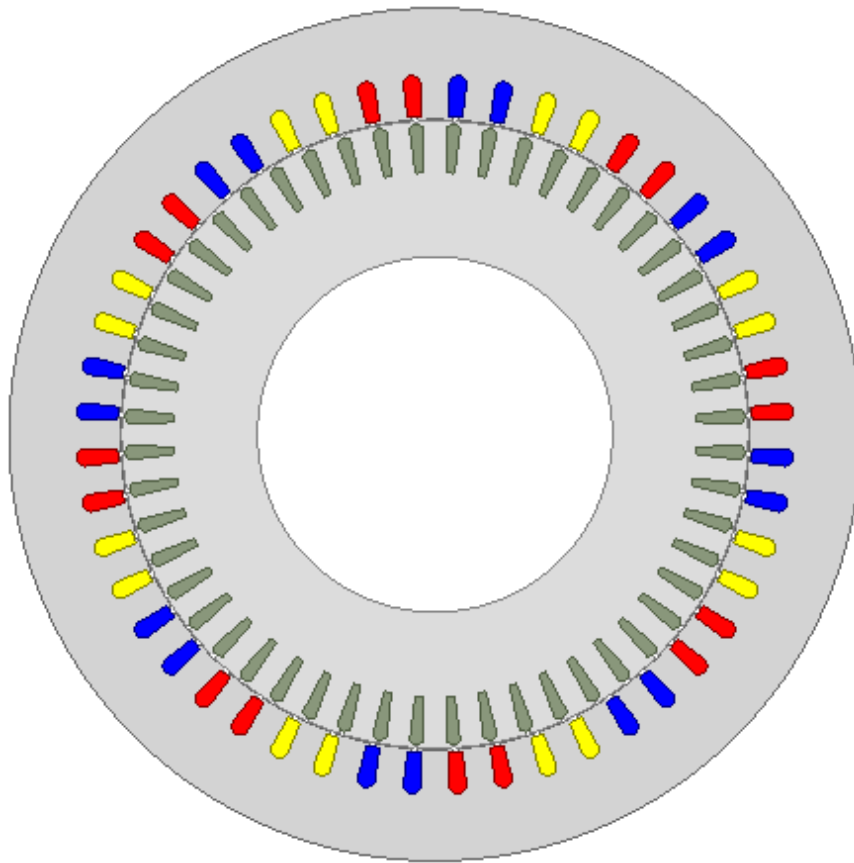


Fig. D.1 Cross-sectional views of the 48S/52R/8P CIM.

Appendix E Design Optimization of AIMs

The classical optimization methods have been utilized for the design optimization of the IMs since the beginning of the computer science [VEI56], [ERL65] and IM optimal design issue is receiving much more attention every passing day. In the existing literature, there are a large number of studies on the optimization of conventional IMs with wound or squirrel-cage rotor. It is possible to group these studies into several main categories as follows:

- (a) Design optimization;
 - Cost: volume, weight, material usage, material type, etc. [ERL65], [RAM71];
 - Performance characteristics: air-gap flux, efficiency, torque, torque ripple, acoustic noise, etc. [AMO95], [MOL16], [BUS16], [DAS16];
 - Cost and performance: [SIN83], [APP87a], [APP87b], [JAZ89], [SIN92], [AMO95], [KIM98], [LIU03], [BES08a], [CUN06], [CUN08], [DUA11b], [HAF15], [MAL16], [PER17];
- (b) Utilization/Comparison of different optimization algorithms: [RAM73], [HUA88a], [HUA88b], [FEI89], [IDI97], [DAI98], [LAC08], [TUT10], [DUA11b], [SAK11], [YAM13], [BUS16], [LIN16];
- (c) Drive/Control algorithm optimization [LI05], [SOU07], [GUE08], [HUY10], [CHO16].

In this appendix, feasible stator structures have been considered. As an inevitable consequence of employing non-overlapping winding topology, half of the stator slots cannot be fully filled as seen in Fig. E.1(a). These unfilled-slots can be utilized by using additional iron core material in order to reduce the saturation level of the stator teeth. Therefore, a better slot utilization might be achieved via using zig-zag slot structure as shown in Fig. E.1(b). Influence of these additional stator tooth pieces on the performance has been investigated by comparing the obtained characteristics with the straight-slot stator structure. The aim of this appendix is to present the optimization of AIM with different optimization approaches, namely, individual optimization, single-objective global optimization (SOGO) and multi-objective global optimization (MOGO). Genetic Algorithm (GA) has been used as optimization tool for SOGO and MOGO approaches. The effectiveness of each optimization approach has been investigated by comparing the optimal solutions. The determination and justification of optimization parameters has also been presented.

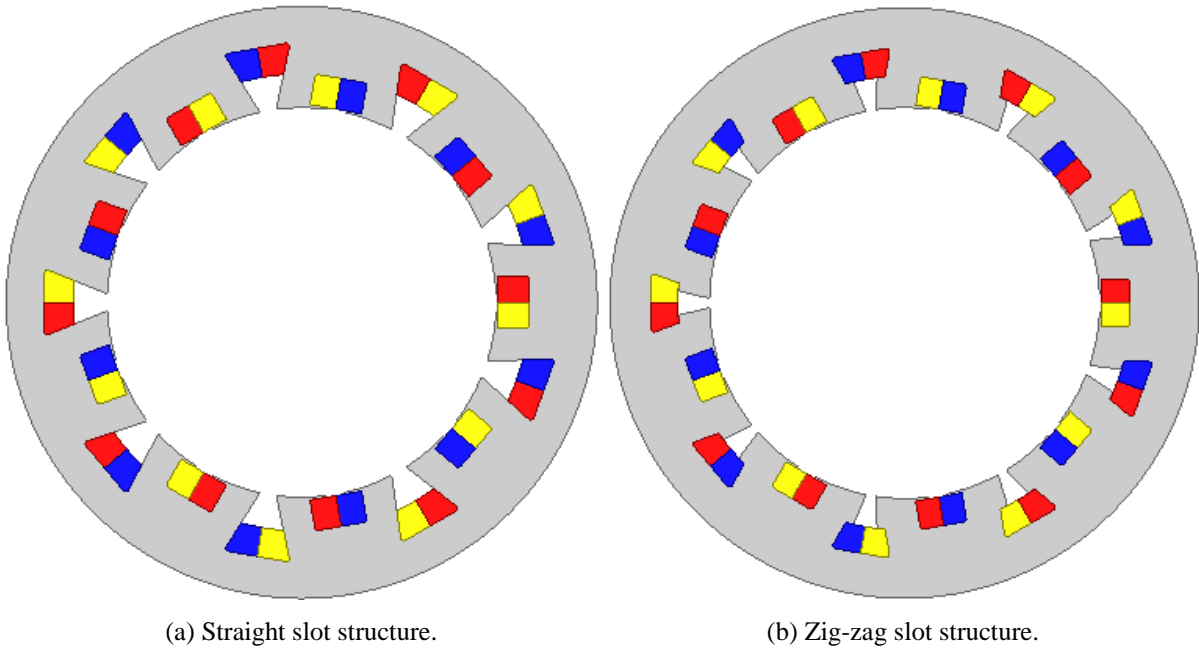


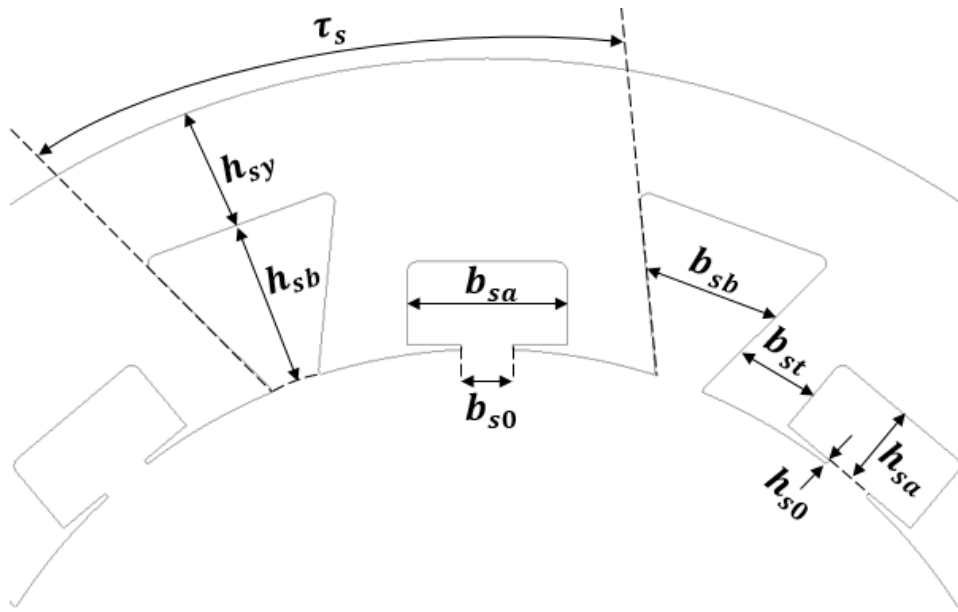
Fig. E.1 Feasible stator structures for non-overlapping winding topology.

E.1 Individual Optimization of AIM

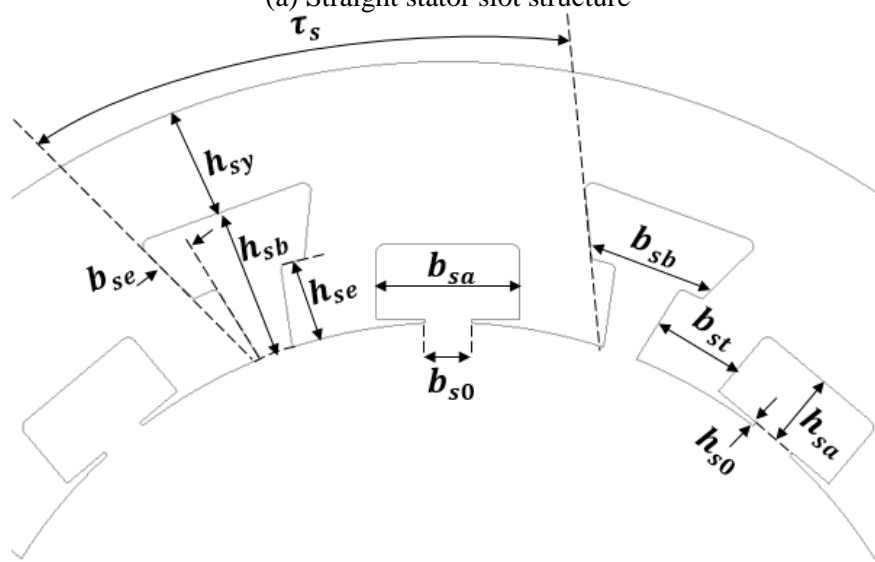
It is possible to optimize the machine by using individual and global optimization approach [ZHU11]. On the other hand, initially, it is quite reasonable to find the optimum geometrical parameters of the machine by using individual optimization method, which means, for each geometry parameter an individual optimization is required. Afterwards, multiple geometric parameters, which are previously optimized by using individual optimization approach, can be optimized by using the global optimization approach with the aid of GA. In order to initially determine the accurate constraints of the global optimization, conducting an individual optimization is very useful. On the other hand, the effectiveness of the global optimization approach can be validated via individual optimization approach. One of the important consideration that should be taken into account is that since the appropriate sequence is vital in the individual optimization approach, the sequence of the design parameters should follow their sensitivity [ZHU11].

E.1.1 Determination of Optimization Parameters

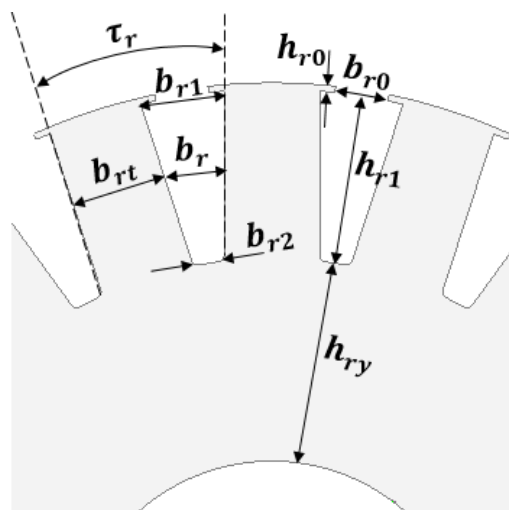
The design parameters are shown in Fig. E.1. As seen in the figure, in addition to straight slot the zig-zag slot has two additional width (b_{se}) and height (h_{se}) parameters. The same rotor structure (see Fig. E.1(c)) is used in both topologies during the optimization progress.



(a) Straight stator slot structure



(b) Zig-zag stator slot structure



(c) Rotor structure

Fig. E.2 Design variables of the NWIM.

Apart from the optimization parameters (geometric parameters), other specifications (non-participating directly with the optimization procedure) such as number of turns, stack length, air-gap

length, stator slot, rotor slot number, etc. should also be determined. It is a common knowledge that the number of turns per phase can be determined by considering the stack length, torque- and power-speed characteristics and stator current density limit. Torque- and power-speed curves of the AIMs with various slot/pole number combinations, number of turns per phase, and stack length are calculated by considering the stator current density as constant (31A/mm²).

Table E.1 Main and Initial Parameters of AIM*

Number of phases, m	3
Pole number, P	6
Active stack length, l_s	50.8
Stator Parameters	
Stator slot number, S	18
Outer diameter of stator, D_{so}	264
Inner diameter of stator, D_{si}	174
h_{sy}	19.28
h_{s0}	0.73
h_{sa}	12
$h_{sb} = 2h_{sa}$	24
b_{s0}	8
b_{sa}	24.85
b_{sb}	30.83
b_{st}	13.45
b_{se}	9.1
h_{se2}	10
Air-gap length, g	0.4
Rotor Parameters	
Rotor slot number, R	20
Inner diameter of rotor	60
h_{r0}	0.9
h_{r1}	24
h_{ry}	30.3
b_{r0}	8.06
b_r	12.6
b_{rt}	14.23

* All dimensions are in mm.

The initial design parameters for the AIMs with straight and zig-zag slot topologies are listed in Table E.1. As mentioned previously, outer diameter and stack length parameters are the same as the Toyota Prius 2010 IPM machine. The definitions and the individual optimization sequence of the design parameters are listed in Table 3.1. Note that the slip is not an actual optimization parameter. However, the slip delivering the peak torque should be determined before the individual optimization of each

parameter. Moreover, during the optimization progress the determined slip value should be kept constant. Note that, IMs, used for the variable speed applications, may be optimized according to different operation points. However, they are usually optimized in the constant torque operation region.

Another condition that should be considered during the optimization process is to determine the excitation. This can be phase current, stator current density, or stator copper loss. One of these parameters should be fixed during the individual optimization progress. In this study, fixed stator copper loss is chosen as excitation constant. Furthermore, the rotor bar copper loss is considered by limiting the rotor slot constraints in the GO sections. The calculation of stator copper loss is expressed in (E.1), where I_s , R_{phase} , J_s , N_t , a , k_f , N_c , A_s , ρ_{cu} , l_s , and τ_s denote the phase current, phase resistance, stator current density, number of turns per coil, parallel branch number, slot filling factor, number of coils, slot area, resistivity of the copper, active stack length, and stator slot pitch in mm respectively. To be able to keep the stator copper loss fixed during the individual optimization, the injected current is evaluated by using a copper loss coefficient k_c as expressed in (E.2) [ZHU11]. Actually, this coefficient, calculated by (E.3), is necessary in order to evaluate the torque production under fixed copper loss condition. Therefore, the torque and the copper loss are directly proportional to this coefficient as expressed in (E.4).

$$P_{scu} = 3 \frac{I_s^2}{a^2} R_{phase} = \frac{6J_s^2 N_t^2}{a^2 k_f} N_c A_s \rho_{cu} \left[l_s + \tau_s - \left(\frac{b_{sa} + b_{sb}}{4} \right) \right] \quad (E.1)$$

$$I_s = \frac{k_c \sqrt{A_s}}{N_t} \quad (E.2)$$

$$k_c = J_s \sqrt{A_s} = \frac{I_s N_t}{\sqrt{A_s}} = \frac{I_s N_t}{\sqrt{b_{sa} h_{sa}}} \quad (E.3)$$

$$P_{scu} = 3 \frac{I_s^2}{a^2} R_{phase} = \frac{6k_c^2 N_t^2}{a^2 k_f} N_c \rho_{cu} \left[l_s + \tau_s - \left(\frac{b_{sa} + b_{sb}}{4} \right) \right] \quad (E.4)$$

By using the equations from (E.1) to (E.4), variation of average torque and stator copper loss is illustrated in Fig. E.3. With the slot filling factor of 0.6, i.e. $k_f = 0.6$, as indicated in Fig. E.3, the copper loss of 5.64kW @80°C, which is equivalent to $k_c = 205.78$, is assumed during the individual optimization. As mentioned previously, before initiating the individual optimization, the slip delivering the peak torque for each topology should be determined. As illustrated in Fig. E.4, the slip values delivering the peak torque is determined as 4.13 (1438rpm) and 3.73 (1444rpm) for straight and zig-zag slot topology, respectively. Since using more parameters costs a huge time consumption, the number of parameters should be chosen as less as possible. Therefore, it is reasonable to choose the parameters which have the most significant effect on the torque density. Under these conditions, the

design parameters are optimized according to the following sequence (see Table 3.1): (1) stator split ratio; (2) stator slot width ratio; (3) stator yoke thickness ratio; (4) rotor slot width ratio; (5) rotor yoke thickness ratio; (6) stator slot opening ratio; (7) rotor slot opening ratio. The variation of the calculated average torque with respect to the defined design parameters for both straight and zig-zag slot AIMs are illustrated between Fig. E.5 and Fig. E.7. As clearly seen in the figures, the parameters delivering the maximum torque is chosen as individual optimized value. It is also clear that the average torque of the NWIM with straight slot structure is quite higher than the AIM with zig-zag slot structure. The reason behind this phenomenon can be revealed by investigating the figures from Fig. E.8 to Fig. E.10.

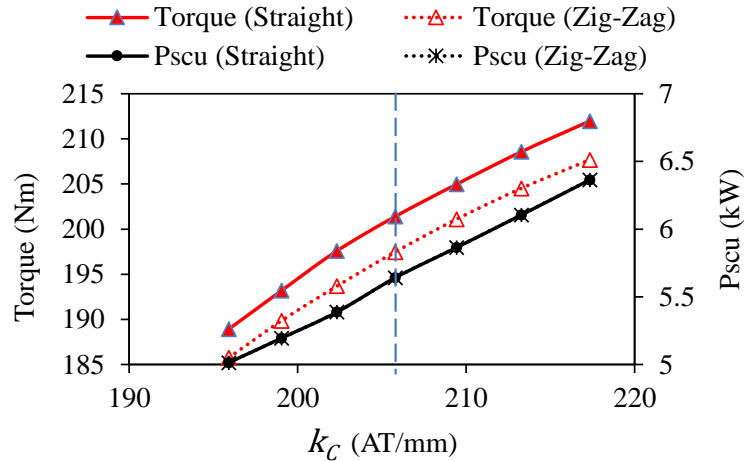


Fig. E.3 Average torque and stator copper loss against stator copper loss coefficient.

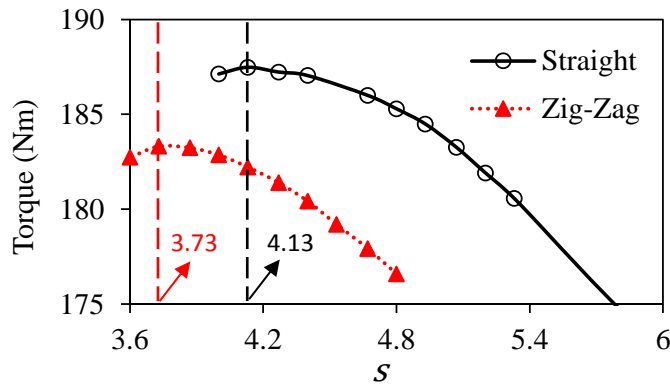


Fig. E.4 Average torque against slip percentage.

As seen in Fig. E.8(a), the higher the additional stator slot width parameter ratio b_{ser} , the higher the torque. In the same manner, the longer the h_{se} height parameter, the lower the torque. Actually, once b_{ser} is equal to one, or consequently h_{ser} is equal to zero, the structure of the zig-zag slot turns into the straight slot structure (see Fig. E.9). Therefore, it can be deduced that the addition tooth parameters of the zig-zag slot cause an increase in the stator slot leakage flux. This phenomenon is visible in Fig. E.9. The shorter the b_{ser} ratio, the higher the short-circuited flux. Moreover, the radial and tangential components of the stator slot flux density are illustrated in Fig. E.10.

Table E.2 Definition of the stator and rotor geometric parameters according to order of sensitivity

#	Explanation	Equation	Equation for additional parameters (Zig-Zag only)
–	Slip	$s = 100 \cdot \left(1 - \frac{n_s}{n_r}\right)$	
1	Stator split ratio	$\lambda_s = \frac{D_{si}}{D_{so}}$	
2	Stator slot width ratio	$b_s = 1 - \frac{2b_{st}}{\tau_s} = \frac{b_{sa} + b_{sb}}{\tau_s}$	$b_{ser} = 1 - \frac{2b_{se}}{b_{sb}}$
3	Stator yoke thickness ratio	$h_s = \frac{h_{sy}}{h_{sy} + h_{sb}} = \frac{h_{sy}}{h_{sy} + 2(h_{sa} + h_{s0})}$	$h_{ser} = \frac{h_{se}}{h_{sb}}$
4	Rotor slot width ratio	$b_{rr} = \frac{b_r}{\tau_r}$	
5	Rotor yoke thickness ratio	$h_r = \frac{h_{ry}}{h_{ry} + h_{r1} + h_{r0}}$	
6	Stator slot opening ratio	$b_{sor} = \frac{2b_{s0}}{\tau_{sb}}$	
7	Rotor slot opening ratio	$b_{ror} = \frac{b_{r0}}{b_r}$	

As explained in [BOL10], the tangential component of the slot flux density is the leakage component, whilst the radial component is the torque production component. As clearly seen in Fig. E.10, once the b_{ser} parameter is one, the leakage flux is the minimum and the useful flux is the maximum. Therefore, with the light of these findings, it can be concluded that zig-zag slot structure is not feasible for the AIM topology in terms of electromagnetic performance and also manufacturing issues since manufacture of straight slot is simpler and cheaper than the zig-zag slot. Consequently, since the torque is sacrificed significantly in case of the AIM with zig-zag slot design, only the optimization of the AIM with straight slot will be carried out in the following sections.

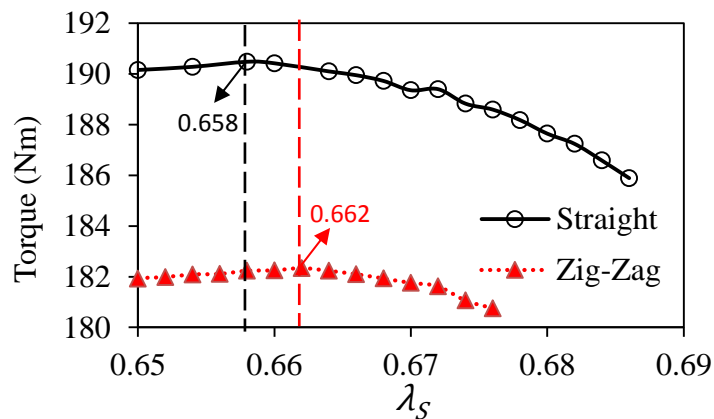


Fig. E.5 Average torque against split ratio.

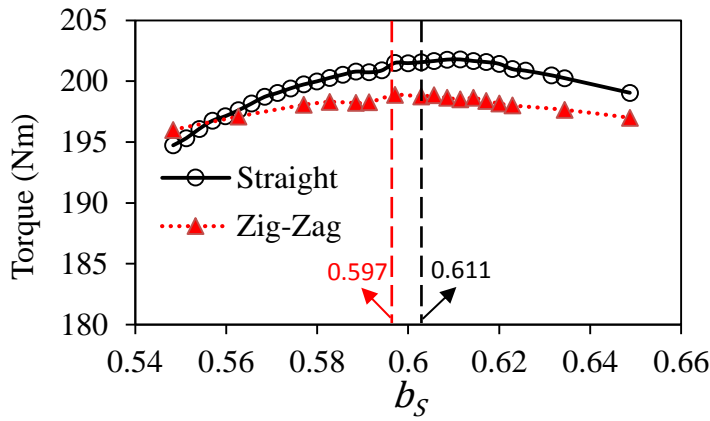


Fig. E.6 Average torque against stator slot width ratio.

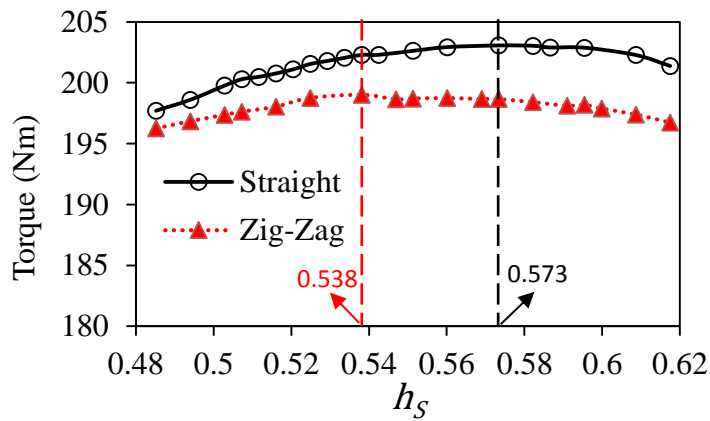
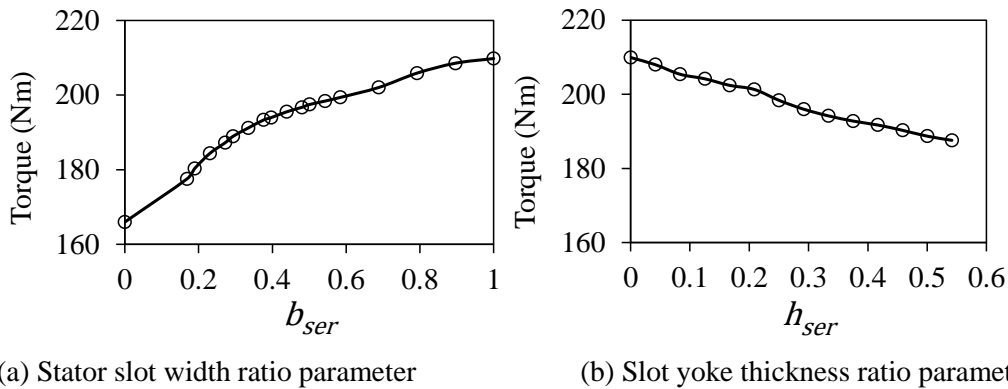


Fig. E.7 Average torque against stator yoke thickness ratio.



(a) Stator slot width ratio parameter

(b) Slot yoke thickness ratio parameter

Fig. E.8 Average torque against stator slot width ratio and stator yoke thickness ratio of the NWIM with zig-zag slot structure.

The results of individual optimization of the rotor parameters of the AIM with straight slot structure are illustrated from Fig. E.11 to Fig. E.14. The ratios delivering the maximum torque have been chosen as the individual optimum. Since the slot opening parameters have a significant effect on the torque ripple, the variation of torque ripple percentages are also calculated and shown in Fig. E.13 and Fig. E.14. As seen in the figures, apart from the ratios delivering the maximum torque, there are different optimum ratios delivering the minimum torque ripple. Since the torque is optimized in this part, the

ratios delivering the maximum torque have been chosen as optimum parameter. Because of the coupling effect among the design parameters, the maximum torque might not increase during the optimization. However, as shown in this paper, the maximum torque is increased significantly thanks to individual optimization approach. After the individual optimization, approximately 13% higher torque is achieved according to the initial design.

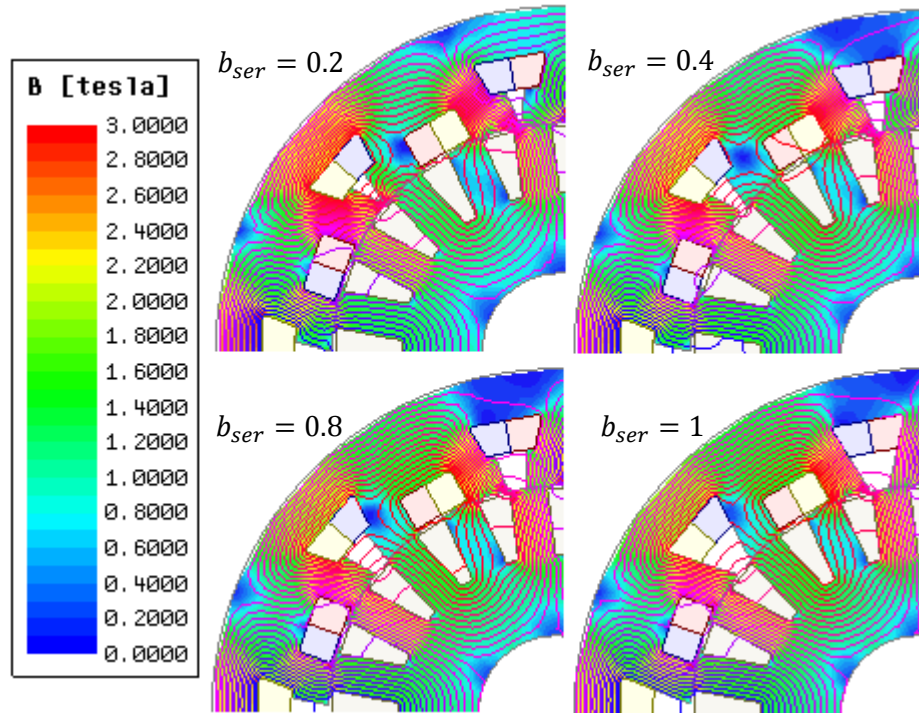


Fig. E.9 Flux density and line distributions of zig-zag slot AIM with various stator slot width ratio.

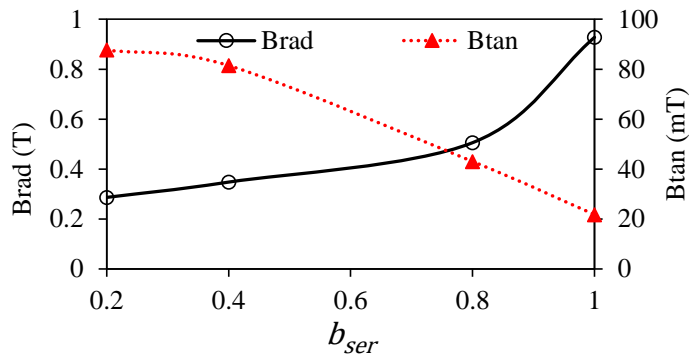


Fig. E.10 Radial and tangential components of the stator slot flux density.

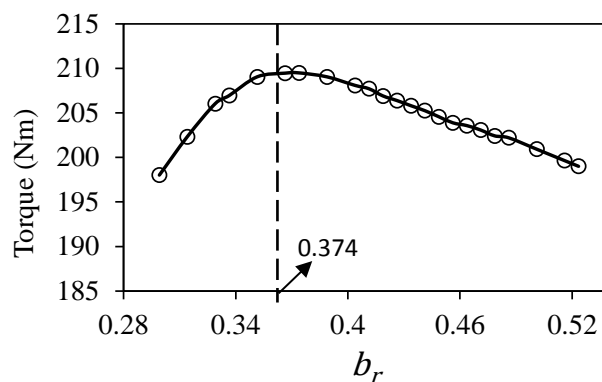


Fig. E.11 Average torque against rotor slot width ratio.

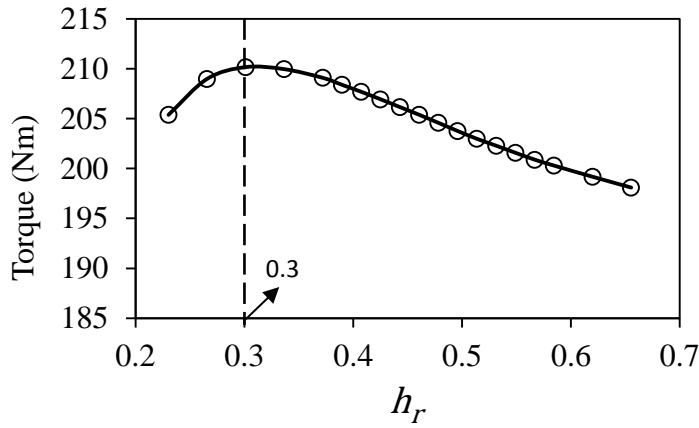


Fig. E.12 Average torque against rotor yoke thickness ratio.

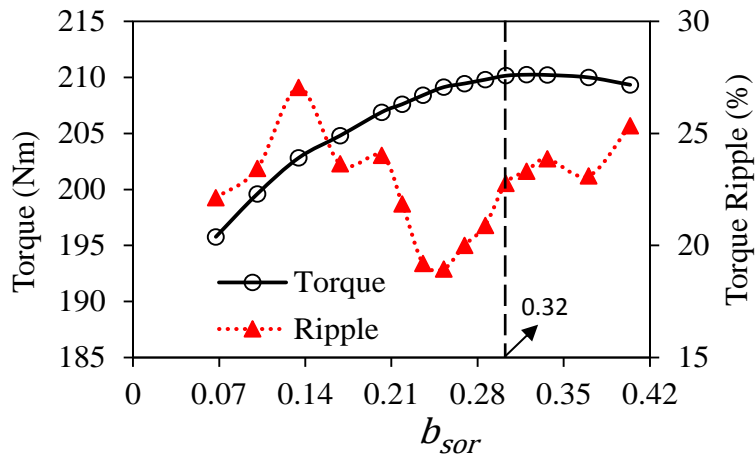


Fig. E.13 Average torque and torque ripple against stator slot opening ratio.

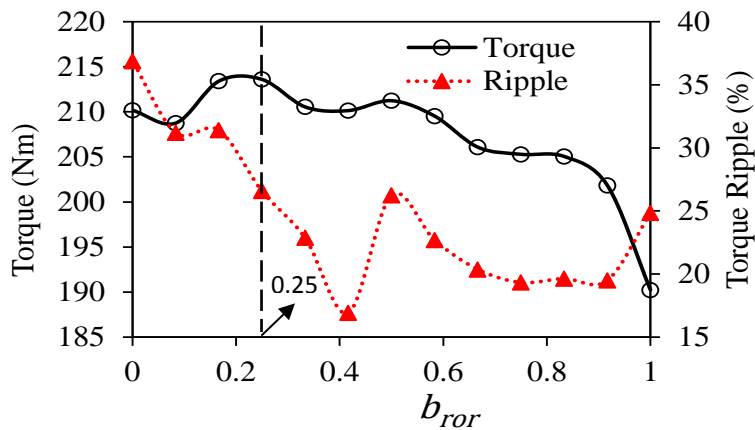


Fig. E.14 Average torque and torque ripple against rotor slot opening ratio.

In this study h_{s0} and h_{r0} parameters have not been optimized since their influence on the performance is negligible once the values of these parameters are minimum [GUN18a]. In other words, the longer the h_{s0} and h_{r0} parameters, the lower the average torque. Therefore, they have been fixed at their mechanically allowed values.

E.1.2 Determined Topology and Optimization Parameters

Because of the significantly sacrificed average torque of the AIM with zig-zag slot structure, the AIM with straight slot structure is chosen. The 2-D views of the initial and individually optimized AIMS with straight slot are shown in Fig. E.15. Initial and optimized values of the optimization parameters are listed in Table E.3. It has been revealed that compared with the initial design, wider stator slot tooth width, thinner yoke thickness, wider stator slot opening with, narrower and shallower rotor slot, and narrower rotor slot opening width are preferred to produce higher torque for the given specifications and copper loss.

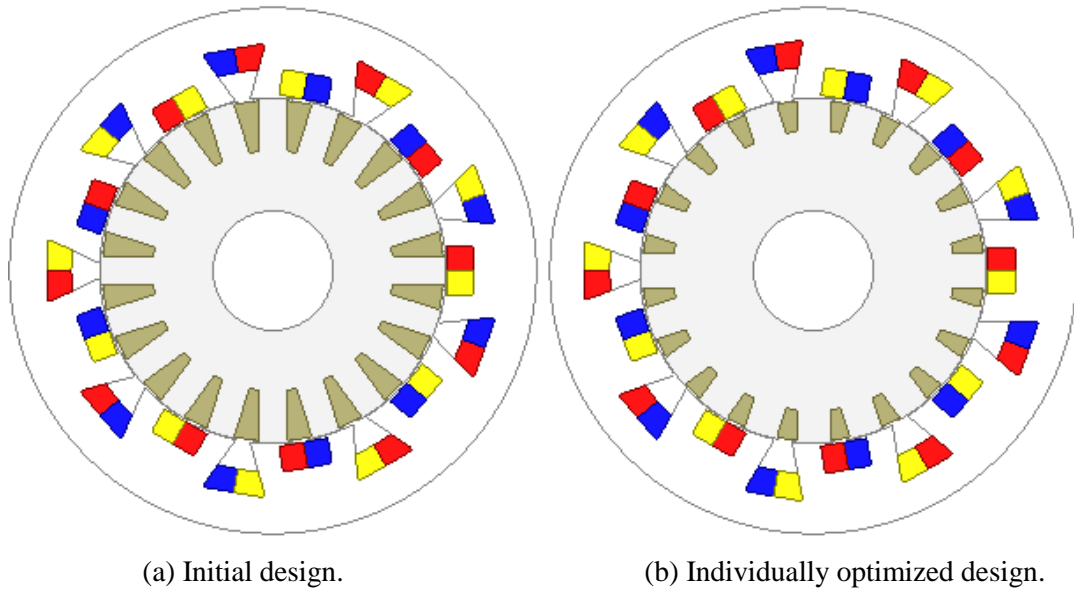


Fig. E.15 2-D view of initial and individually optimized AIM with straight slot designs.

Table E.3 Comparison between initial and individual optimized variables

#	Parameters	Initial value	Individual Optimized
-	s	4.8	4.13
1	λ_s	0.686	0.658
2	b_s	0.63	0.611
3	h_s	0.53	0.573
4	b_r	0.471	0.374
5	h_r	0.478	0.302
6	b_{sor}	0.27	0.32
7	b_{ror}	0.33	0.25

E.2 Single-Objective Global Optimization (SOGO) by GA

The Genetic Algorithm (GA) is a search procedure, which explores the solution space using mechanisms that emulates natural selection including next generations and mutilations for optimization analysis. Some new individuals (Children) are created and the grown population participates in a

natural-selection process that consecutively reduces the size of the population to a desired level (Next Generation) in each generation. The GA, which is known as the one of the effective numerical optimization methods, has been extensively used for exploring the optimized solution of the IMs. Moreover, as explained previously, torque, acoustic noise, material cost, efficiency and/or weighted combinations of these parameters (multi-objective optimization) are often adopting as the objective of the optimization [IDI97], [DAI98], [MAD98], [LIU03], [CUN06], [CUN08], [LAC08], [DUA11b], [HAF15], [PER17].

Because of the significant influence of objective function on the optimization results, the global optimization of the AIM is accomplished with two different restrictions as maximum current density and maximum stator copper loss. The settings of single-objective GA for both optimizations are as follows: parent size (population size), mating pool size, children size, Pareto Front size (number of survivors), population size of next generation, roulette selection, crossover probability, and mutation probability size are 30, 30, 30, 10, 30, 10, 1, and 2 respectively. Maximum number of generations (iteration number) is chosen as 1000. In order to achieve the highest torque, which is feasibly available, at the given specific outer diameter and stack length, it is intended to optimize the AIM. Therefore, the goal of the single-objective optimizations are to maximize the average torque at steady-state operation region. Note that, all the IMs considered in this section are optimized for the constant torque region. The actual cost functions are adopted as the sum of absolute weighted values w_i of the individual goal errors e_i at specific slip value for both of the single-optimizations as expressed in (E.5).

$$Cost = - \sum_{i=1}^N w_i e_i \quad (E.5)$$

E.2.1 With the Restriction of Maximum Current Density

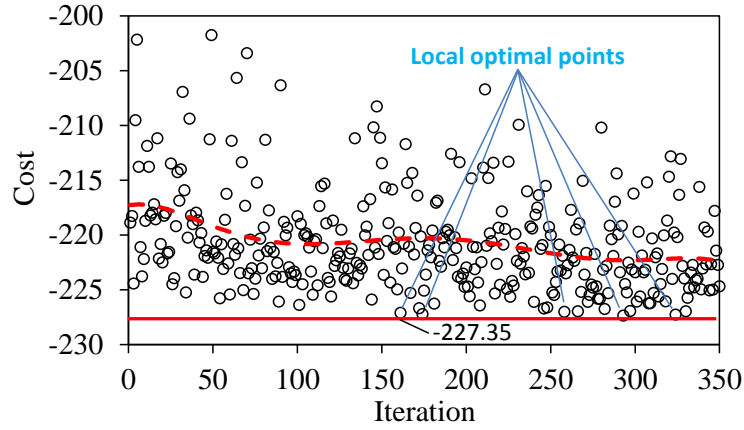
Typical allowable continuous current densities for IMs with liquid cooling in ducts is determined as 23 to 31A/mm² [LIP17]. Therefore, the maximum current density is assigned with the copper loss coefficient $k_c = 217.33$ whose equivalent current density is calculated as $J_s = 31A/mm^2$. Single-objective optimization procedure for the maximum current density is illustrated in Fig. E.16(a) and the solutions together with the individual optimization results are listed in Table E.4.

E.2.2 With the Restriction of Maximum Stator Copper Loss

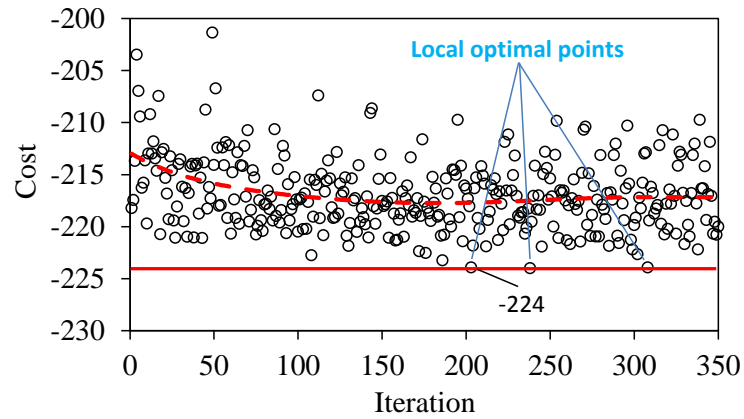
As known, the stator copper loss is the most dominant power loss in IMs. The stator copper loss is restricted as maximum 6.1kW with 0.6 stator slot filling factor via the copper loss coefficient $k_c = 213.27$. In order to perform a fair analysis, the assigned maximum stator copper loss value has been determined approximately same as the Toyota Prius IPM machine's copper loss at full load operation [OLS11]. Single-objective optimization procedure for the specified stator copper loss is illustrated in Fig. E.16(b). Moreover, the solutions of the optimized parameters together with the individual optimization results are listed in Table E.4. In addition, the total copper loss ($P_{scu} + P_{rcu}$) is limited by the constraints of the rotor slot.

E.2.3 SOGO Produced by GA

The calculated cost against iteration together with the determination of the local optimal points for both maximum current density and maximum copper loss density restrictions are illustrated in Fig. E.16. As seen in the figures, in the beginning of the optimization procedure the cost is high and it is considerably decreasing with the increasing iteration number.



(a) With the restriction of maximum current density (SOGO-R1)



(b) With the restriction of maximum stator copper loss (SOGO-R2)

Fig. E.16 Optimization produced by single-objective GA for AIM.

Table E.4 Global optimization variables with stator current density and stator copper loss restrictions

Parameters	Initial value	Individual Optimized	Constraints for J_s Rest.	Global Optimized for J_s Rest.	Constraints for P_{scu} Rest.	Global Optimized for P_{scu} Rest.
λ_s	0.686	0.658	[0.65:0.69]	0.651	[0.645:0.67]	0.65
b_s	0.63	0.611	[0.541:0.634]	0.577	[0.507:0.618]	0.584
h_s	0.53	0.573	[0.463:0.595]	0.518	[0.507:0.618]	0.554
b_r	0.471	0.374	[0.374:0.561]	0.393	[0.374:0.523]	0.39
h_r	0.478	0.302	[0.266:0.478]	0.335	[0.266:0.478]	0.336
b_{sor}	0.27	0.32	[0.28:0.48]	0.312	[0.28:0.48]	0.322
b_{ror}	0.33	0.25	[0.05:0.42]	0.262	[0.05:0.42]	0.249

However, it is also realised that due to the random characteristics of the GA, it jumped out the local optimal points as clearly seen in the figures. Although the same number of variables have been changing during the optimization procedures, the optimal torque has been obtained in a shorter time in the case of the restriction of the maximum current density. On the other hand, the time consumption of the GO with any restriction is not always shorter than without any restriction because of the random characteristics of the GA. Considering cost values, the optimal average torque obtained from the restriction with maximum current density optimization is slightly higher than the maximum stator copper loss optimization. The obtained solutions are listed in Table E.4 and the optimum values are shown in Table E.7 and Table E.8.

E.3 Multi-Objective Global Optimization (MOGO) by GA

The design optimization of the IMs involves compromising between disparate objectives such as high torque, high efficiency, and high power factor, low cost, small size, etc. Owing to such many conflicting optimization objectives, multi-objective optimization techniques are required to meet the design goals.

Multi-objective optimization approach is concerned with optimizing a number of objectives simultaneously. Once multi-objective optimization is considered, the problem presents a set of solutions known as Pareto Front, which incorporates the optimal solution of each individual objective and also the solutions representing the best compromise satisfying all objectives. One of the important difference between single-objective and multi-objective optimization is that in multi-objective optimization, the objective functions create a multi-dimensional space in addition to the natural decision variable space. The optimization of IMs by GA with multi-objective global optimization (MOGO) has been reported in several papers [LIU03], [CUN06], [CUN08], [LAC08], [TUT10], [DUA11b], [HAF15], [PER17]. As will be explained in detail in the following section, torque, stator copper loss and rotor bar copper loss have been chosen as objectives to be optimized. Since the objective function has a significant influence on the optimization results, the multi-objective global optimization (MOGO) of AIM is accomplished with and without restriction of rotor bar current density. The same GA settings of the SOGO is employed for the MOGO in order to optimize the determined objectives.

E.3.1 Determination of Objectives and Goals

For a given specific outer diameter and stack length, the most attractive objectives are to maximize the feasibly available torque and efficiency or minimize the dominant machine losses. As known well, the most dominant losses of an IM are stator and rotor copper losses. Depending on the utilized core material, the core losses are not dominant as in the PM synchronous machines. Moreover, as stated previously, it is intended to optimize the IMs at the constant torque region. Since the frequency is

remarkably low at the constant torque region, the core loss percentage when compared with the copper losses percentage is significantly low.

Another important subject which should be considered is time consumption. Particularly, once the IM is considered, because of the natural behaviour of the inductance phenomenon between stator and rotor coppers, to obtain the steady-state result from any simulation takes quite long time. Therefore, it is expected that with fewer variables and objectives the optimization solution may be found more quickly. Therefore, the objectives for the both of the optimizations, namely with and without the restriction of the rotor bar current density, are determined as follows.

- Torque;
- Stator copper loss;
- Rotor bar copper loss.

E.3.2 Justification of Objectives and Weights

In order to obtain the optimization solution more quickly, a special care should be taken while justifying the objectives and their weights. Considering the previously obtained individual and global optimization solutions and calculated copper losses, the objectives are justified as follows. The feasibly available torque is calculated approximately as 230 Nm by using the traditional torque equation expressed in (E.6).

$$S_{fa} = 11k_{w1}B_g a_c D_{so}^2 l_s n_r \quad (E.6)$$

$$P_{fa} = T_{fa} \omega_r \rightarrow T_{fa} = \frac{S_{fa} \cos \varphi}{\frac{2\pi n_r}{60}} = \frac{330}{\pi} D_{so}^2 l_s a_c k_{w1} B_g \cos \varphi$$

where S_{fa} , P_{fa} , T_{fa} , D_{so} , l_s , a_c , k_{w1} , B_g , n_r , ω_r , and $\cos \varphi$ are the feasibly available apparent power, active power, and average torque, stator outer diameter, stack length, electric loading, fundamental winding factor, average air-gap flux density, rotor speed, angular speed, and power factor, respectively. Considering the current density, efficiency, and the average torque of the Toyota Prius IPM machine at 250A, the torque objective is justified as 222 Nm as given in Table E.5. Furthermore, the analytically calculated torque value is validated as presented in the previous optimization solutions. Since the optimization has been performed by using 2-D FEA, only the stator slot copper losses can be calculated during the optimization procedure. Therefore, the stator slot copper loss for both optimizations are justified by using (E.10), where $P_{scu(SOGO-R1)}$ and $P_{scu(SOGO-R2)}$ are the stator slot copper loss obtained from the SOGO solution in case of maximum stator current density restriction and in case of maximum stator copper loss restriction, respectively. Note that P_{scu} does not include the end-winding copper loss. It includes only total stator slot copper loss.

$$P_{scu(SOGO-R1)} < P_{scu(MOGO12)} < P_{scu(SOGO-R2)} \rightarrow$$

$$P_{scu(MOGO12)} \approx \frac{P_{scu(SOGO-R1)} + P_{scu(SOGO-R2)}}{2} \quad (E.7)$$

In the same manner, the average rotor copper losses with and without the restriction of rotor bar current density are justified by considering the (E.8) and (E.9), respectively. In (E.8), $P_{rcu(Max_Sbar)}$ and $P_{rcu(Min_Sbar)}$ indicate the maximum and the minimum rotor bar losses obtained in case of maximum and minimum rotor bar surface area, respectively. In (E.9), $P_{rcu(Max_Cost)}$ and $P_{rcu(Min_Cost)}$ indicate the rotor bar copper losses in case of the maximum cost and minimum cost obtained from the SOGO-R2, respectively. Therefore, after the evaluation of the justified objective values, their weights, used for assigning higher or lower priority to a goal, are also calculated and listed together with the all the justified objectives as given in Table E.5.

$$P_{rcu(Max_Sbar)} < P_{rcu(MOGO1)} < P_{rcu(Min_Sbar)} \rightarrow$$

$$P_{rcu(MOGO1)} \approx \frac{P_{rcu(Max_Sbar)} + P_{rcu(Min_Sbar)}}{2} \quad (E.8)$$

$$P_{rcu(Min_Cost)} < P_{rcu(MOGO2)} < P_{rcu(Max_Cost)} \rightarrow$$

$$P_{rcu(MOGO2)} \approx \frac{P_{rcu(Min_Cost)} + P_{rcu(Max_Cost)}}{2} \quad (E.9)$$

Table E.5 Justified objectives and their weights

Variable	With J_r Restriction		Without J_r Restriction	
	Condition	Weight	Condition	Weight
Average torque (Nm)	≥ 222	0.41	≥ 222	0.41
Average stator slot copper loss (kW)	≤ 2.4	0.26	≤ 2.4	0.29
Average rotor copper loss (kW)	≤ 2.1	0.32	≤ 2.4	0.30

In the HEV/EV applications, both torque and efficiency are vital parameters that should be ideally as high as possible during any driving cycle. However, in some of the cases such as to obtain the maximum torque and efficiency simultaneously is not possible, the high torque is preferred instead of high efficiency. Considering this information, the weight of the torque is assigned as to be slightly higher in both optimizations.

E.3.3 Cost Function for MOGO

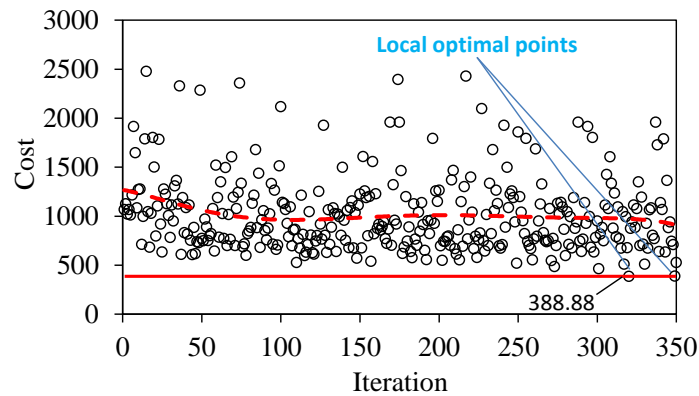
The cost function is determined as weighted sum of the sub-goal errors. Each sub-goal gives rise to an error value that represents the divergence between the simulated reaction and the goal value constrain. If the simulation response satisfies the goal limit, the cost value becomes zero. Alternatively, the error

value depends on the differences between the simulated response and the specific goal constrain. Therefore, the cost function is defined by (E.10), where G , w_j , N_j , e_i are the number of sub-goals, the weight factor related with the j^{th} sub-goal, the number of iterations for the j^{th} sub-goal, and the error contribution from the j^{th} sub-goal at the i^{th} iteration, respectively. Here, the value of e_i is determined by the band characteristics (conditions), target value, and the simulated response value.

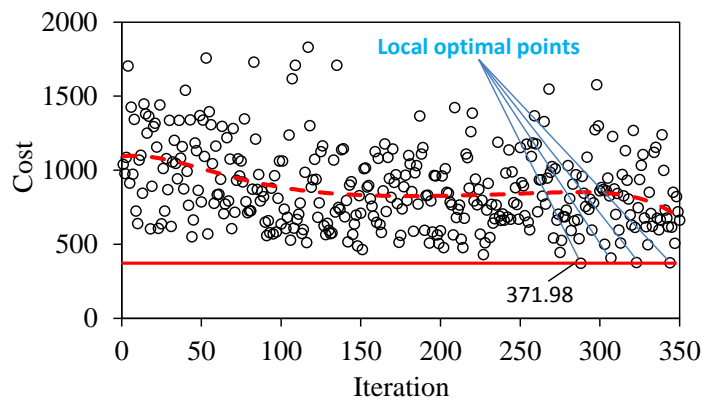
$$Cost = \sum_{j=1}^G \frac{w_j}{N_j} \sum_{i=1}^{N_j} e_i \quad (E.10)$$

E.3.4 MOGO Procedure by GA

After a large number of iteration, the optimal solutions with and without the bar current density restrictions are obtained as illustrated in Fig. E.17. As seen in the figures, compared to the SOGO, much longer time is consumed in order to obtain the optimal solutions. In addition, although the GA is a random search process, the solution without restriction has been obtained earlier than the solution with restriction as expected. However, in terms of cost value, the difference is not significant as seen in the figures. Determined constrains and the optimized values of the parameters are listed in Table E.6. Calculated material mass, cost and the electromagnetic performance values are given in Table E.7 and Table E.8.



(a) With rotor bar current density restriction



(b) Without rotor bar current density restriction

Fig. E.17 Optimization produced by single-objective GA for AIM.

Table E.6 Comparison between initial and individual optimized values

Parameters	Initial value	Individual Optimized	Constraints with J_r Rest.	Global Optimized with J_r Rest.	Constraints without J_r Rest.	Global Optimized without J_r Rest.
λ_s	0.686	0.658	[0.65:0.678]	0.667	[0.65:0.678]	0.668
b_s	0.63	0.611	[0.563:0.649]	0.565	[0.563:0.649]	0.564
h_s	0.53	0.573	[0.507:0.606]	0.49	[0.507:0.606]	0.497
b_r	0.471	0.374	[0.374:0.598]	0.393	[0.25:0.6]	0.373
h_r	0.478	0.302	[0.319:0.478]	0.353	[0.26:0.52]	0.312
b_{sor}	0.27	0.32	[0.28:0.5]	0.362	[0.28:0.5]	0.361
b_{ror}	0.33	0.25	[0.18:0.52]	0.236	[0.15:0.55]	0.245

E.4 Design and Performance Comparison

E.4.1 Design Comparison

The 2-D cross-sectional views of the optimized AIMs with the SOGO and MOGO are illustrated in Fig. E.18. As seen in the figures, although the stator slot/rotor slot/pole number (18S/20R/6P), the outer diameter, and the stack lengths are kept the same, depending on the constraints, restrictions and optimization method, the geometric shapes of the slots are different from each other. The machine masses and the costs for each machine are evaluated by using the expression given in (E.11), where D_{M330} , A_{Score} , A_{Rcore} , D_{CuS} , D_{CuR} , N_c , A_c , R , A_{Bar} , A_{Ring} , l_{Ring} are mass density of steel material, surface area of stator core, surface area of the rotor core, mass density of stator winding copper, mass density of rotor bar copper, total number of coils, surface area of the stator slot area with fill factor, rotor slot number, surface area of the bar and ring copper, and axial length of the one ring piece, respectively. The cost of the materials are evaluated by using the data provided by the London Metal Exchange (LME) as expressed in (E.11) [LME17].

- Copper: 4.815 £/kg - mass density: 7400 (kg/m³)
- Steel: 0.42 £/kg - mass density: 8933 (kg/m³)

$$M_{Tot} = D_{M330}(A_{Score} + A_{Rcore})l_s + 2D_{CuS}N_cA_c \left[l_s + \tau_s - \left(\frac{b_{sa} + b_{sb}}{4} \right) \right] + D_{CuR}(RA_{Bar}l_s + 2A_{Ring}l_{Ring}) \quad (E.11)$$

Calculated masses for different parts of the machine and total cost are listed in Table E.7. As seen in the table, there is no significant difference between the IMs in terms of mass. On the other hand, since per kilo cost of the copper is almost 11.5 times expensive than the core material, the IMs which require more copper is a bit expensive than the others. As clearly seen in the table, thanks to the global optimization method, the total has been reduced remarkably when compared with the initial design's cost.

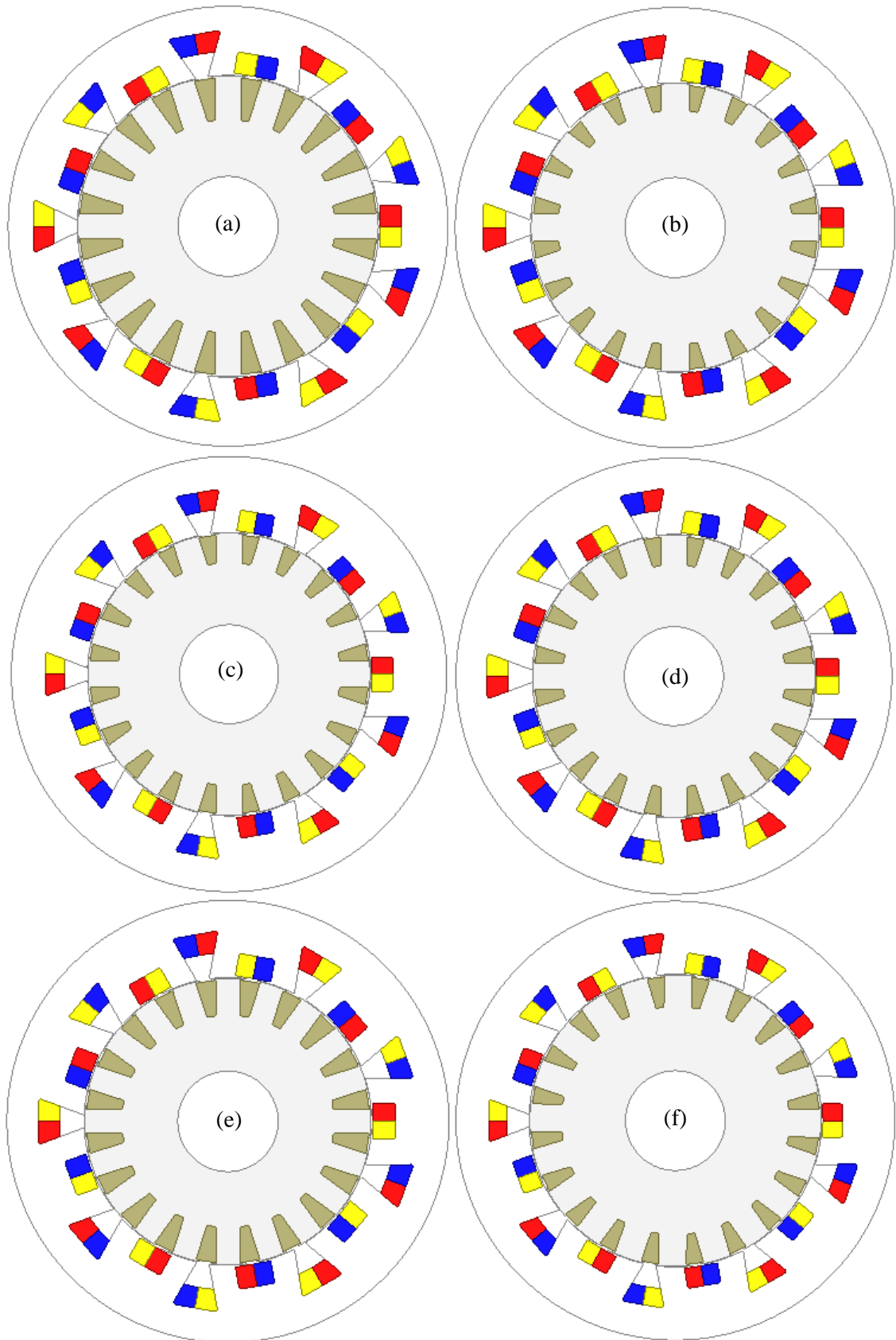


Fig. E.18 2-D views of 18S/20R/6P AIMs: (a) initial; (b) individual optimized; (c) SOGO with J_S restriction; (d) SOGO with P_{Scu} restriction; (e) MOGO with J_R restriction; (f) MOGO without J_R restriction.

If the IMs are optimized without any restriction (except for the maximum stator current density restriction), it is possible to reduce cost furthermore. As seen in Table E.7(f), since the stator copper usage is reduced, the cheapest NWIM is achieved. However, as will be shown, since the reduction of stator copper usage causes to increase the current density, more cooling requirement may be needed. This extra cooling requirement may increase the total cost.

Table E.7 Mass and cost comparison

	Design	Core Mass (kg)		Copper Mass (kg)		Total Mass (kg)	Total cost (£)
		Stator	Rotor	Stator	Rotor		
(a)	Initial	8.316	7.07	5.7	3.6	24.69	51.26
(b)	Individual Opt.	9.0	7.052	5.74	2.68	24.46	47.26
(c)	SOGO with J_s Rest.	9.774	6.74	4.65	2.84	24.01	43.02
(d)	SOGO with P_{Scu} Rest.	9.578	6.734	5.08	2.83	24.22	44.93
(e)	MOGO with J_r Rest.	9.578	6.33	5.08	3.29	24.28	46.98
(f)	MOGO without J_r Rest.	9.53	7.136	4.3	2.89	23.85	41.6

E.4.2 Electromagnetic Performance Comparison

In this section, electromagnetic performance characteristics, such as back-EMF, air-gap flux density, bar currents, torque, losses, efficiency, etc. are compared. The electromagnetic performance characteristics are investigated by performing 2-D FEA under steady-state operation condition at 1500rpm synchronous speed and 250A peak rated stator current.

In this section, all the obtained design and electromagnetic characteristics of the initial and optimized AIMs are summarized in order to reveal the effectiveness of the optimization methods and determine the most favourable candidate. In the HEV/EV applications, the most challenging parameters are higher torque, higher efficiency, light-weight and minimum space requirement. In addition, thermal characteristics of the machine should also be considered in terms of size of the cooling equipment. Therefore, considering the size of the cooling equipment, the current density levels of preferred machine should be as low as possible in order to save more space in the vehicle.

It has been revealed that although the individual optimization with appropriate sequence method is not good enough compared with the global optimization approaches, it is a very useful tool for the determination of the initial parameters, accurate constraints, and conditions/limits of the objectives. It has also shown that depending on the determination of the objective conditions, SO and MO global optimization methods are good enough to find the optimal solution. On the other hand, considering the simulation/optimization time consumption issues of the IM analyses, if the variable constraints and the objective conditions are determined accurately with the individual optimization method, the optimum solution can be found faster with SOGO method without needing the MOGO method. It is also shown that the optimal solution can be found more quickly with some restrictions such as stator copper loss, rotor bar current density, etc.

Table E.8 General comparison of the results of the optimized IMs with different approaches

Parameters	(a)	(b)	(c)	(d)	(e)	(f)
			SOGO	SOGO	MOGO	MOGO
Optimization objectives	Initial	Individual	with J_s Rest.	with P_{Scu} Rest.	with J_r Rest.	without J_r Rest.
Slip ratio λ_s	0.69	0.66	0.65	0.65	0.67	0.67
Stator slot width ratio b_s	0.63	0.61	0.58	0.58	0.57	0.56
Stator slot height ratio h_s	0.53	0.57	0.52	0.55	0.49	0.5
Rotor slot width ratio b_r	0.47	0.37	0.39	0.39	0.39	0.37
Rotor slot height ratio h_r	0.48	0.3	0.34	0.34	0.35	0.31
Stator slot opening ratio b_{sor}	0.27	0.32	0.31	0.32	0.36	0.36
Rotor slot width ratio b_{ror}	0.33	0.25	0.26	0.25	0.24	0.25
Torque (Nm)	184.89	206.38	231.34	229.65	219.15	221.88
Torque ripple (%)	27.64	34.19	19.46	21.17	19.63	19.89
Slip (%)	4.8	4.13	4.8	5.06	4.4	4.53
Output power (kW)	27.65	31.078	34.59	34.25	32.91	33.28
Stator slot copper loss (kW)	2.02	2.23	2.48	2.4	2.4	2.33
Stator end-winding copper loss (kW)	3.16	3.45	3.8	3.71	3.71	3.63
Total stator copper loss (kW)	5.18	5.68	6.27	6.12	6.12	5.97
Core loss (W)	0.06	0.07	0.06	0.08	0.08	0.07
Rotor copper loss (kW)	2.08	2.62	2.44	2.51	2.34	2.16
Efficiency (%)	78.59	78.3	79.247	79.24	79.32	79.73
Total axial length (mm)	80.91	79.05	76.07	76.72	76.77	75.11
Total mass (kg)	24.69	24.47	24.00	24.22	24.28	23.85
Total cost (£)	51.26	47.26	43.02	44.93	46.98	41.6
Stator current density (A/mm ²)	25.01	26.11	31	28.76	28.76	31
Rotor current density (A/mm ²)	14.08	15.94	21.94	22.68	16.69	20.06

If the AIMs are compared in terms of electromagnetic performance, it is possible to summarize Table E.8 as follows.

- Although the optimal design (c) has the highest torque and output power, the optimal design (f) has the highest efficiency;
- The optimal design (c)'s torque ripple is the minimum.

If the NWIMs are compared in terms of design characteristic, it is possible to summarize Table E.8 as follows.

- Although the optimal design (f) has the shortest axial length and total mass and hence cost, the initial design (a) has the minimum current densities;
- Although it seems like that the optimal design (f) is the most compact and cheapest candidate, because of the requirement of the more cooling equipment due to the higher stator and rotor current densities, the length and cost of the machine will be increased.

In conclusion, if the space (including the size of the cooling equipment) is the most important criteria, the most favourable candidate is the optimal design (e). On the other hand, if the electromagnetic performance is the most important criteria, the most favourable candidate is the optimal design (c).

Appendix F Influence of Rotor Slot Opening Parameters on the Electromagnetic and Flux-Weakening Performance Characteristics

In this section, the influence of rotor geometric parameters for a specific slot/pole number combination and stack length has been investigated considering different rotor topologies. Considered rotor slot parameters are illustrated in Fig. F.1. It is possible to change the topology of the rotor by changing the rotor slot opening parameters which are b_{r0} , h_{r0} , and h_{r1} . The considered rotor topologies are shown in Fig. F.2. Note that, since the performance of the AIM with u-shaped closed slot rotor topology is very similar to the closed slot with straight bridge topology, in order to simplify the electromagnetic performance comparisons, it has not been considered in this section. The main difference between the u-bridge and straight bridge is the amount of the bar copper loss.

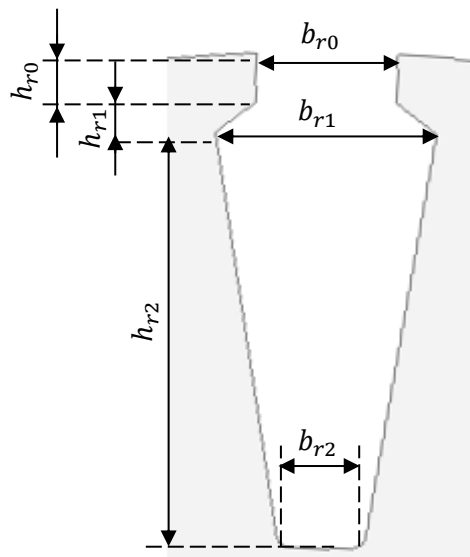


Fig. F.1 Rotor slot parameters.

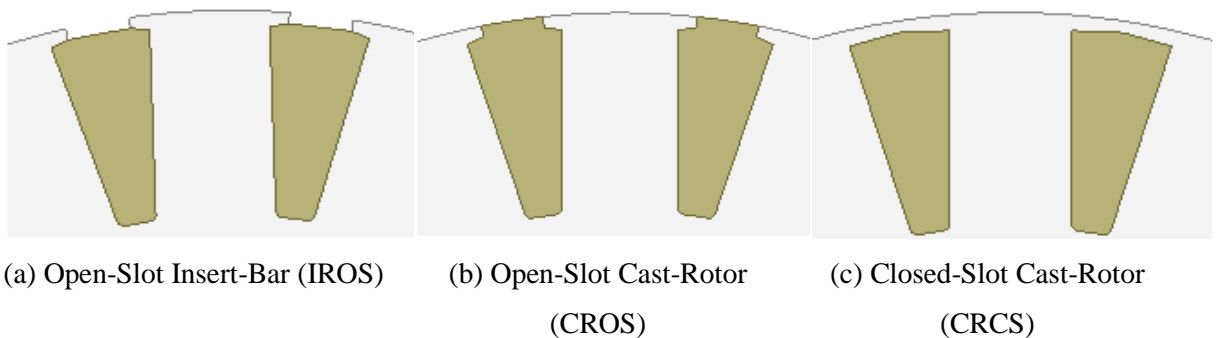


Fig. F.2 Various rotor slot shapes.

According to rotor manufacturing ways, it is possible to design the rotor in three different way as illustrated in Fig. F.2. Constitutively, there is two different ways to manufacture the rotor: insert-bar and cast-rotor. Manufacturing of cast-rotor type squirrel-cage rotor is simpler than the insert-bar. Cast-rotor type can be manufactured as open-slot and closed-slot as shown in Fig. F.2(b) and (c), respectively.

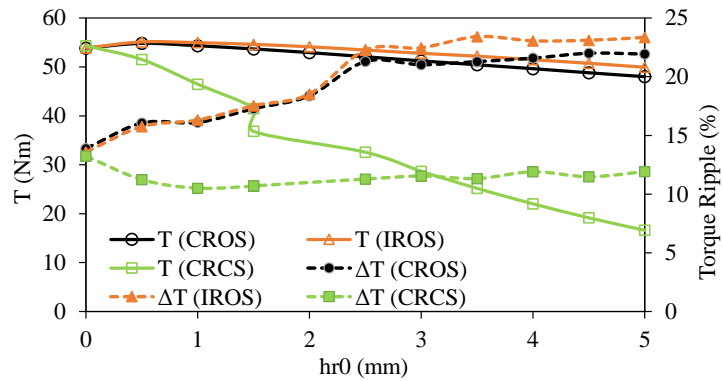
Investigated parameters are illustrated for three different types of rotor namely insert-rotor open-slot (IROS), cast-rotor open-slot (CROS), and cast-rotor closed-slot (CRCS). Therefore, in order to investigate the influence of the rotor slot-geometry parameters on the electromagnetic performance, the 18S/20R/6P AIM with 9-turn per phase and 90 mm stack length is adopted. Each parameter has been investigated individually except for the b_{r1} parameter. Since parallel rotor tooth is to be used in all the analyses, in order to keep the rotor tooth body parallel b_{r2} should be a function of b_{r1} as given in (F.1). Therefore, b_{r1} will be indicated as b_{r12} in this section. Note that, the imposed speed and stator current have been kept at their rated magnitudes during the analyses.

$$b_{r2} = f(b_{r1}) \rightarrow b_{r12} \quad (F.1)$$

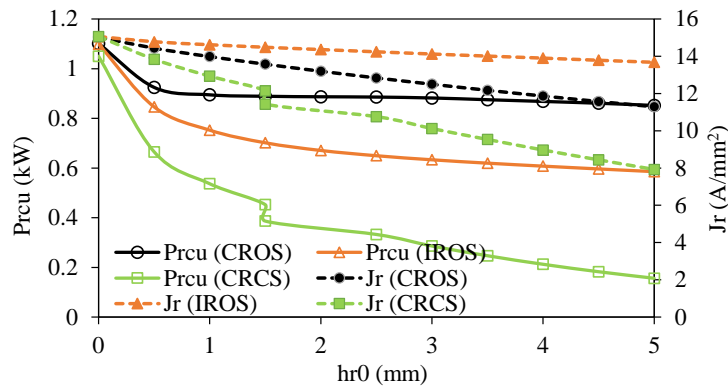
G.1 Electromagnetic Performance Characteristics

A. Slot Opening Height Parameter h_{r0}

The influence of the slot opening height parameter on torque T , torque ripple ΔT , rotor bar copper loss P_{rcu} , and bar current density J_r is illustrated in Fig. F.3. As seen in Fig. F.3(a), the open slot topologies CROS and IROS show very similar characteristics while closed slot CRCS quite different characteristics.



(a)



(b)

Fig. F.3 Variation of performance characteristics with h_{r0} : (a) average torque and torque ripple, and (b) rotor bar copper loss and bar current density.

The average torque reduces gradually for open slot topologies while it reduces significantly for closed slot topology because of the ever-increasing amplitude of the short-circuited flux through the rotor slot bridge (see Fig. F.4). On the other hand, the torque ripple of the open slot topologies increases considerably with increasing h_{r0} parameter while it is almost constant for the closed slot topology. It is also obvious that the torque ripple percentage of the CRCS is quite lower than that of the CROS and IROS topologies. Consequently, in terms of average torque and torque ripple, for all the rotor topologies it is reasonable to design the h_{r0} minimum as much as possible. The bar copper loss and rotor current density decrease with increasing h_{r0} as shown in Fig. F.3(b). This is because of the fact that the longer the h_{r0} , the farther away the bar from the air-gap. Thus, the amplitude of the field harmonics, bar current, and consequently rotor copper loss are reduced. However, as clearly seen, the reduction rate of the CRCS is quite higher than that of the IROS and CROS. On the other hand, since the bars of IROS is farther away from the air-gap than that of the CROS, its bar copper loss is lower.

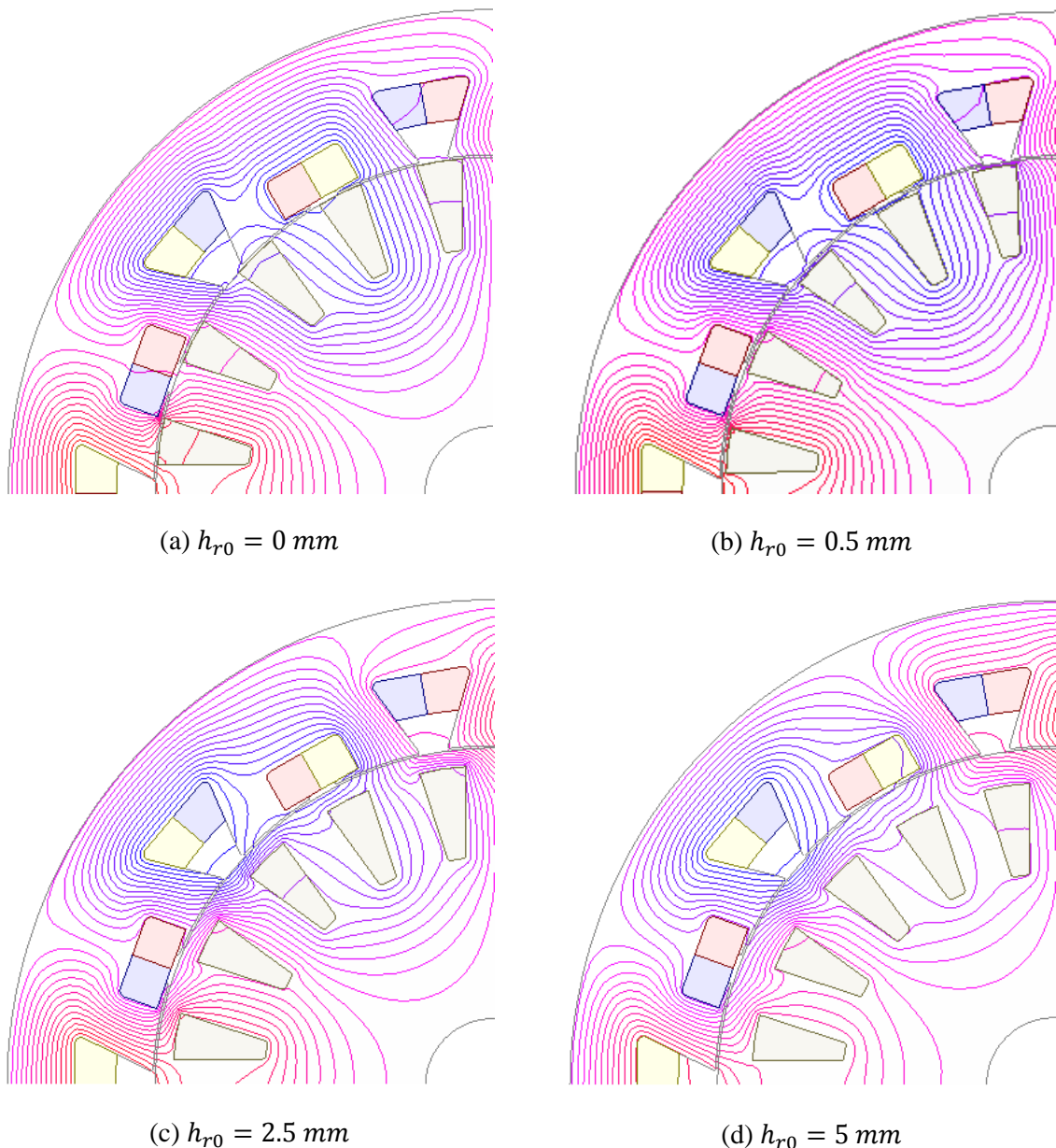
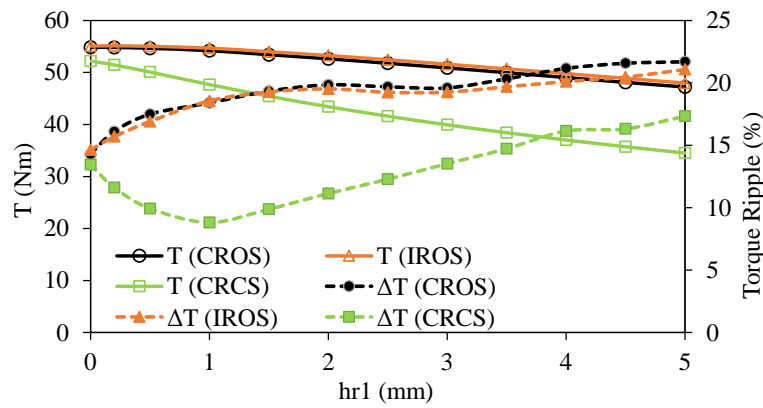


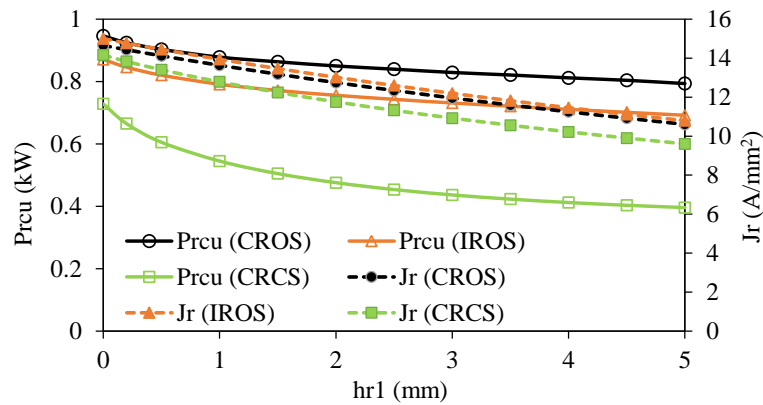
Fig. F.4 Flux line distributions showing the short-circuited fluxes through the rotor slot-bridge.

B. Slot Opening Chamfer Parameter h_{r1}

The influence of h_{r1} parameter on the some performance characteristics of the AIM with different rotor topologies is illustrated in Fig. F.5. As seen in Fig. F.5(a), the average torque is reduced with increasing h_{r1} parameter for all the topologies. However, the CRCS topology is more sensitive to h_{r1} . Increasing h_{r1} results in increasing torque ripple. Therefore, as evidenced from the influence of h_{r0} in terms of torque and torque ripple, it is reasonable to choose h_{r1} as minimum as possible. Fig. F.5(b) shows the variation of rotor bar copper loss and current density with h_{r1} . As seen, copper loss and current density of all the topologies reduce with increasing h_{r1} . Since some of the air-gap flux density harmonics are filtered by the rotor slot bridge, the bar current amplitude, current density, and bar copper loss of the CRCS topology is lower than that of the other topologies. As a result, whilst it is favorable to design the h_{r1} with minimum amount in terms of higher torque, it is reasonable to design it with maximum amount in terms of lower current density and copper loss.



(a)

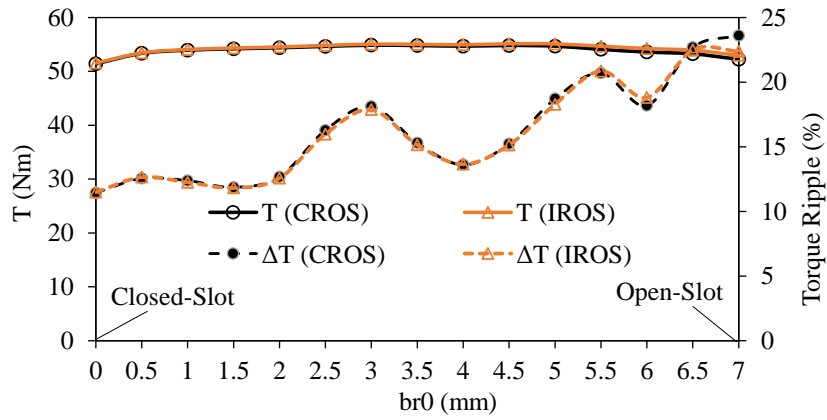


(b)

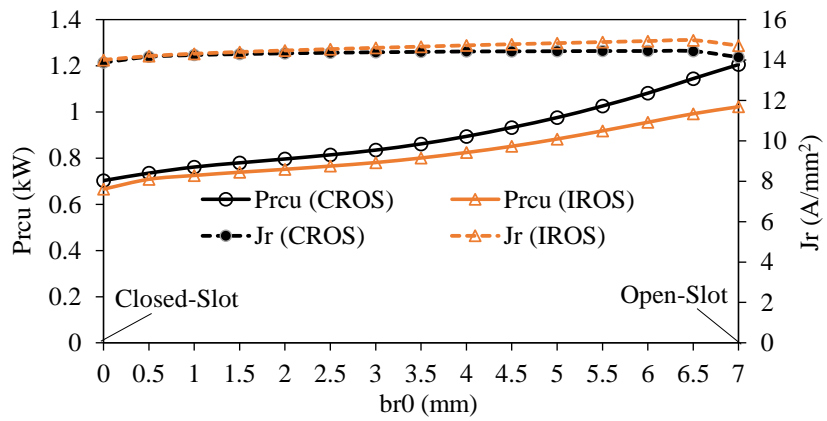
Fig. F.5 Variation of performance characteristics with h_{r1} : (a) average torque and torque ripple, and (b) rotor bar copper loss and bar current density.

C. Slot Opening Width Parameter b_{r0}

The variation of the torque, torque ripple, bar copper loss, and bar current density with respect to b_{r0} parameter is illustrated in Fig. 4.35. Note that since the CRCS has no slot opening, only the IROS and CROS topologies have been considered in this section.



(a)



(b)

Fig. F.6 Variation of performance characteristics with b_{r0} : (a) average torque and torque ripple, and (b) rotor bar copper loss and bar current density.

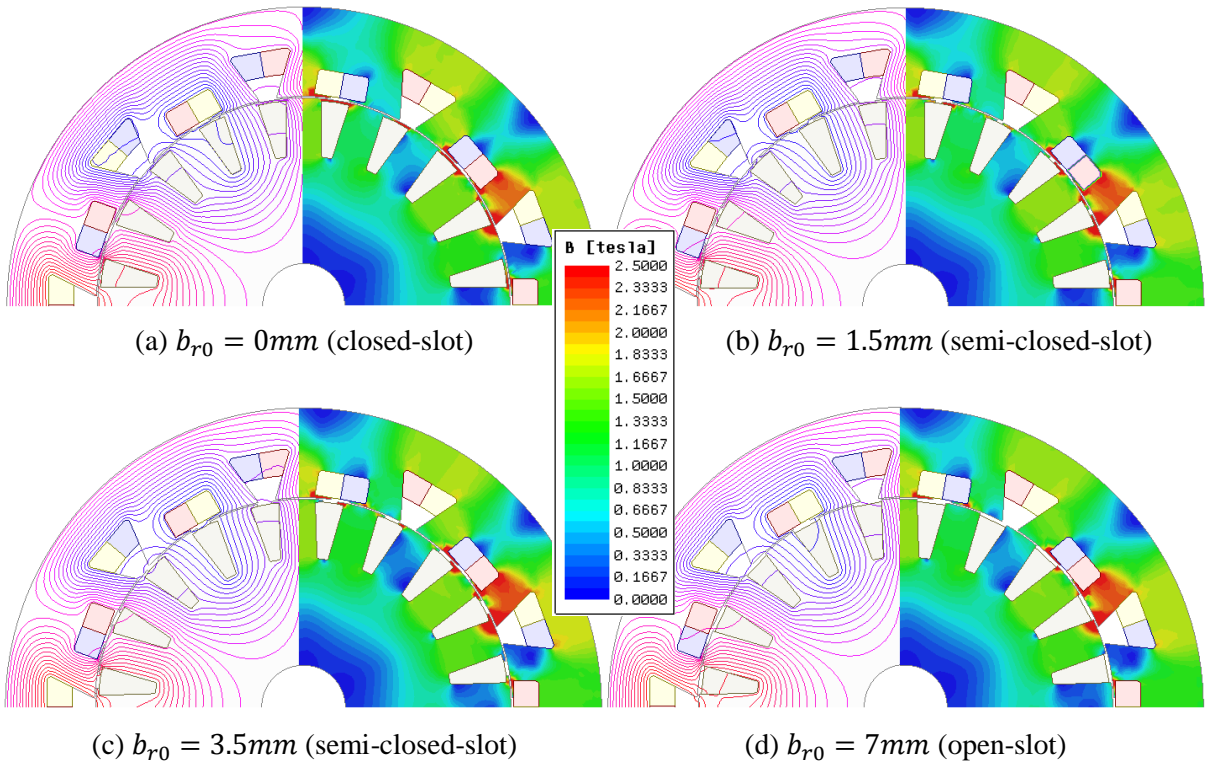
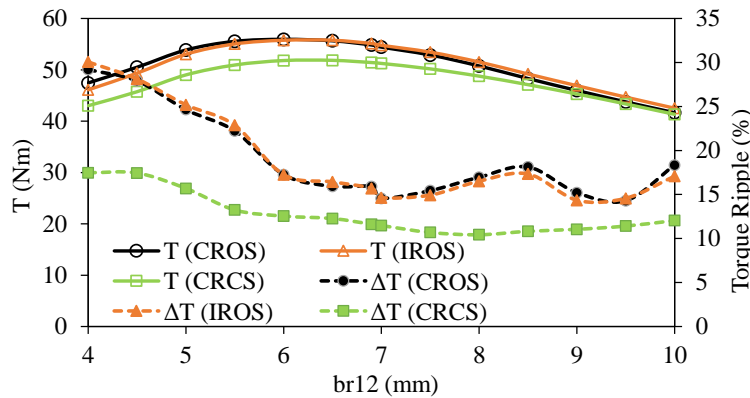


Fig. F.7 Flux line and flux density distributions for various widths of b_{r0} .

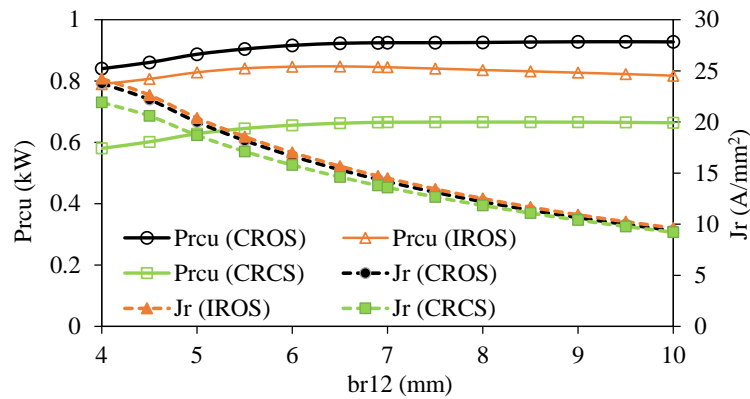
As seen in the figures, the average torque and rotor current density amplitudes are not changed significantly with b_{r0} . However, the torque ripple and bar copper loss are increased considerably with increasing b_{r0} . Considering the obtained results, it can be concluded that it is favourable to keep b_{r0} at the minimum in order to keep the bar copper loss and the torque ripple percentage at minimum. The flux line and flux density distributions for various values of b_{r0} are shown in Fig. 4.36. As seen, stator and rotor tooth tip parts are highly saturated. As seen in Fig. 4.36(a), some of the flux are short-circuited through the bridges. On the other hand, since the open-slot rotor cannot collect flux as much as the semi-closed-slots, the flux density on its rotor reduced (see Fig. 4.36(d)). As a consequence, as shown in Fig. 4.35(a), the average torque has reduced for the closed- and open-slot rotors.

D. Slot Width Parameter b_{r12}

The variation of some performance characteristics with respect to b_{r12} parameter is illustrated in Fig. F.8. As seen in Fig. F.8(a), the maximum torque has been obtained between 6 and 7 mm of b_{r12} . In addition, the torque ripple is quite low in this region. The rotor current density decreases with increasing b_{r12} parameter while the bar copper loss does not show significant change. It is very interesting that although the slot area is increased as b_{r12} is increased, the bar copper loss does not decrease. The reason behind this phenomenon can be seen from Fig. F.9. Although the bar diameter is increased and the rotor resistance is decreased, the bar copper loss is kept the constant since the bar current amplitude is increased.



(a)



(b)

Fig. F.8 Variation of performance characteristics with b_{r12} : (a) average torque and torque ripple, and (b) rotor bar copper loss and bar current density.

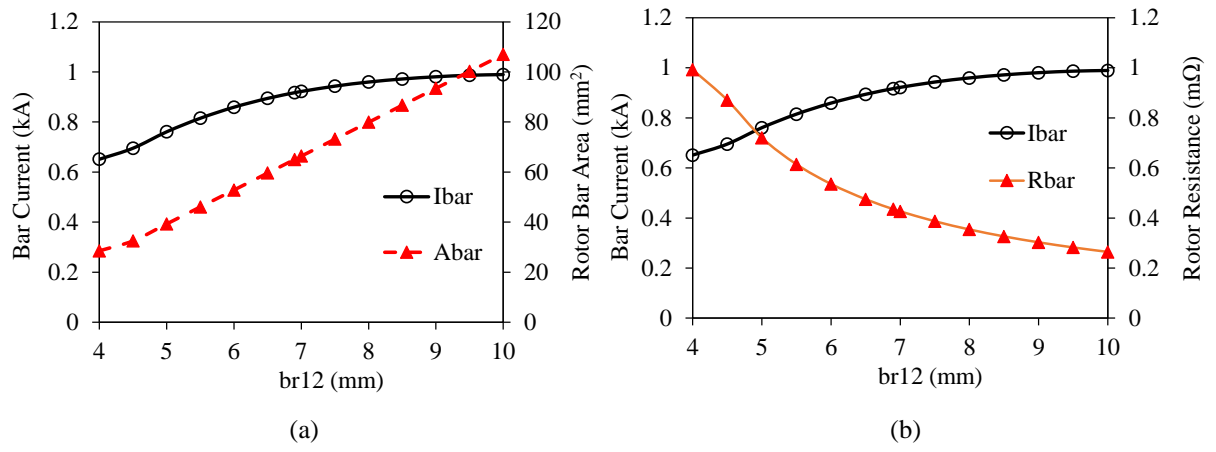


Fig. F.9 Variation of bar current, rotor slot area, and bar resistance with b_{r12} .

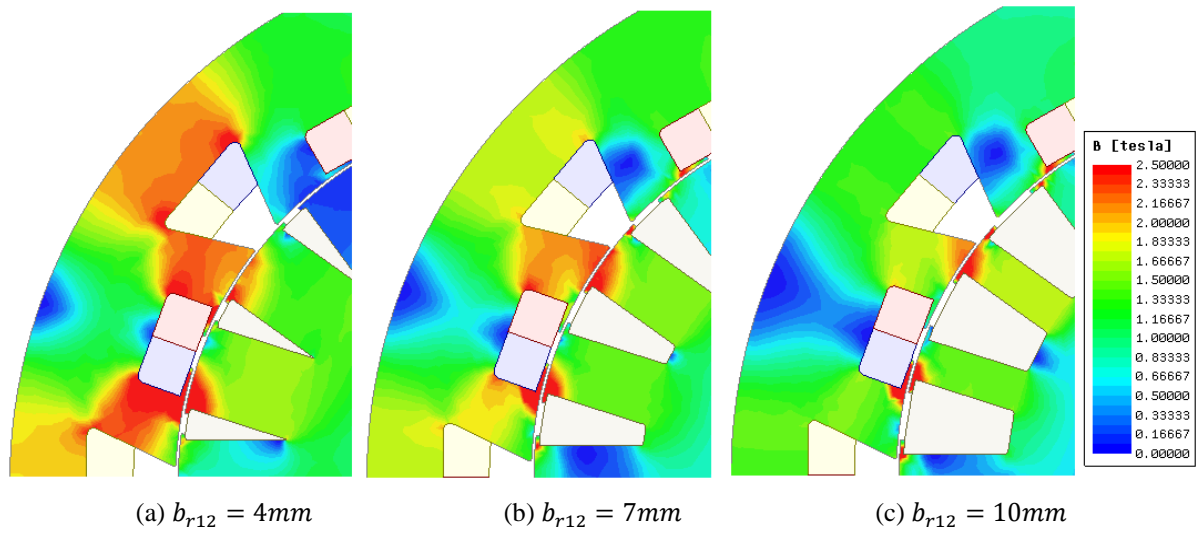


Fig. F.10 Flux density distributions of the AIMs designed with IROS type rotor for various values of b_{r12} .

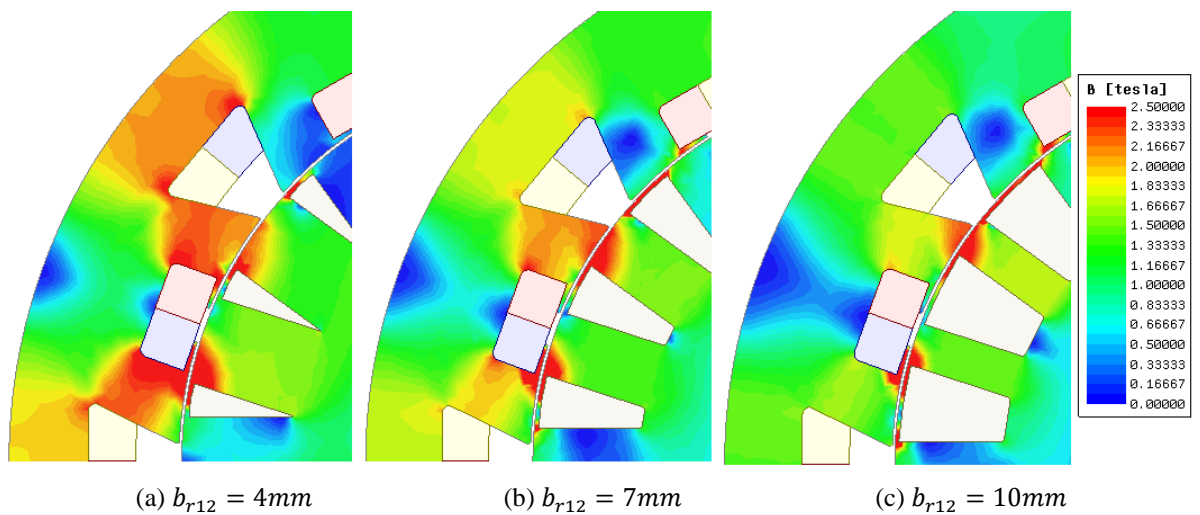


Fig. F.11 Flux density distributions of the AIMs designed with CRCS type rotor for various values of b_{r12} .

As expected, the average torque, torque ripple, and bar copper loss of the closed slot topology is lower than that of the open slot topologies. The reduction of the average torque of the IMs can be

explained by considering the flux density distributions illustrated in Fig. F.10 and Fig. F.11 for open and closed slot topologies, respectively. As seen, when b_{r12} becomes very small, the stator tooth parts are highly saturated. On the other hand, if b_{r12} becomes larger, then the rotor tooth parts start to saturate. Therefore, it can be concluded that the reduction in the torque for small values of b_{r12} parameter is due to the increase in saturation level of the stator tooth parts while the reduction in the torque for high values of b_{r12} parameter is due to the increase in the saturation level of the rotor tooth parts.

E. Slot Height Parameter h_{r2}

The influence of h_{r2} on the electromagnetic performance of the AIMs with different rotor topologies are presented in this section. Fig. F.12(a) shows the variation of torque and torque ripple against h_{r2} . As seen, the average torque increases significantly from 4mm to 8mm but after 8mm decreases gradually. In addition, torque ripple reduces considerably with increasing h_{r2} parameter. As expected, average torque and torque ripple of the closed slot topology is lower than that of the open slot topologies. The bar copper losses do not change significantly with h_{r2} whilst the rotor current densities decrease gradually. It is obvious that h_{r2} parameter has a dominant effect on the average torque, torque ripple, and current density rather than bar copper loss.

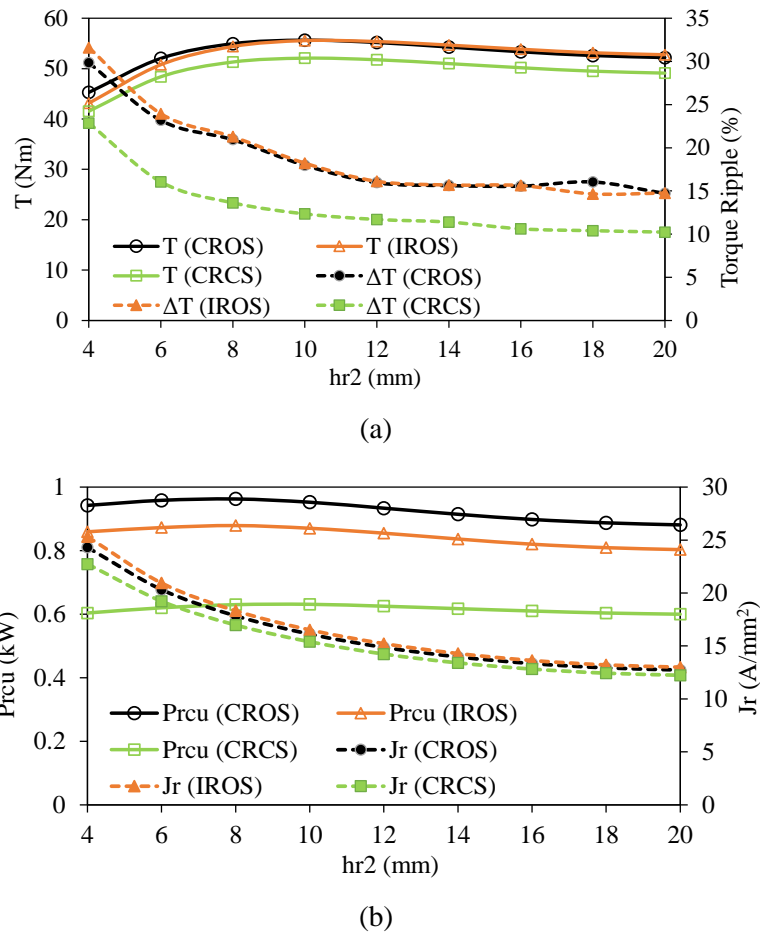


Fig. F.12 Variation of performance characteristics with h_{r2} : (a) average torque and torque ripple, and (b) rotor bar copper loss and bar current density.

In Table F.1, individual influence of each rotor slot parameter on the key performance characteristics and the proposed optimal values are summarized. It can be concluded that in order to design a AIM with high torque, low torque ripple, and high efficiency: (1) h_{r0} should be relatively high; (2) h_{r1} and b_{r0} should be low as much as possible; (3) b_{r12} and h_{r2} should be moderate (can be determined as between the maximum and minimum limits or an optimal value can be determined by conducting parametric analyses). In addition, among the rotor slot parameters, b_{r12} and h_{r2} have more dominant effect on the electromagnetic performance characteristics.

Table F.1 Comparison of influence of rotor slot parameters on the performance

Parameter	Average Torque	Torque Ripple	Bar Copper Loss	Bar Current Density	Optimal Value
h_{r0}	↓	↑	↓	↓	Relatively High
h_{r1}	↓	↑	↓	↓	Minimum
b_{r0}	—	↑	—	↑	Minimum
b_{r12}	∩	↓	—	↓	Moderate
h_{r2}	∩	↓	—	↓	Moderate

G.2 Flux-Weakening Performance Characteristics

The influence of dominant rotor slot geometry parameters on the flux-weakening performance of the 18S/20R/6P AIM is presented. Since the effect of slot width b_{r12} and slot height h_{r2} parameters are more dominant than that of the slot opening parameters, only the influence of slot width parameters on the flux-weakening performance is investigated in this section. In addition, since performance characteristics of closed slot topology is the best among the other topologies, the flux-weakening calculations have been made only for this topology.

A. Slot Width b_{r12} Parameter

The influence of b_{r12} parameter on the torque-speed and power-speed characteristics are illustrated in Fig. F.13 and Fig. F.14, respectively. As seen in the figures, the influence is not significant. Adopting larger b_{r12} leads to slightly lower torque at the constant torque region while it leads slightly higher power at deep flux weakening region. In addition, influence of b_{r12} on the efficiency is illustrated in Fig. F.15. As seen in the figures, adopting smaller b_{r12} parameter leads to larger maximum efficiency region.

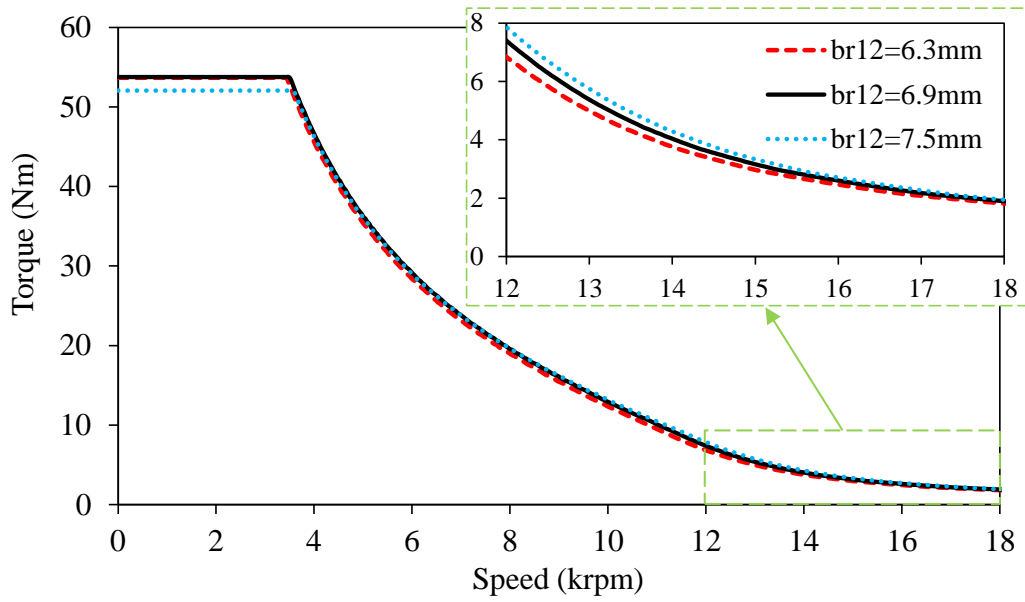


Fig. F.13 Torque-speed characteristics for various b_{r12} parameter of CRCS topology.

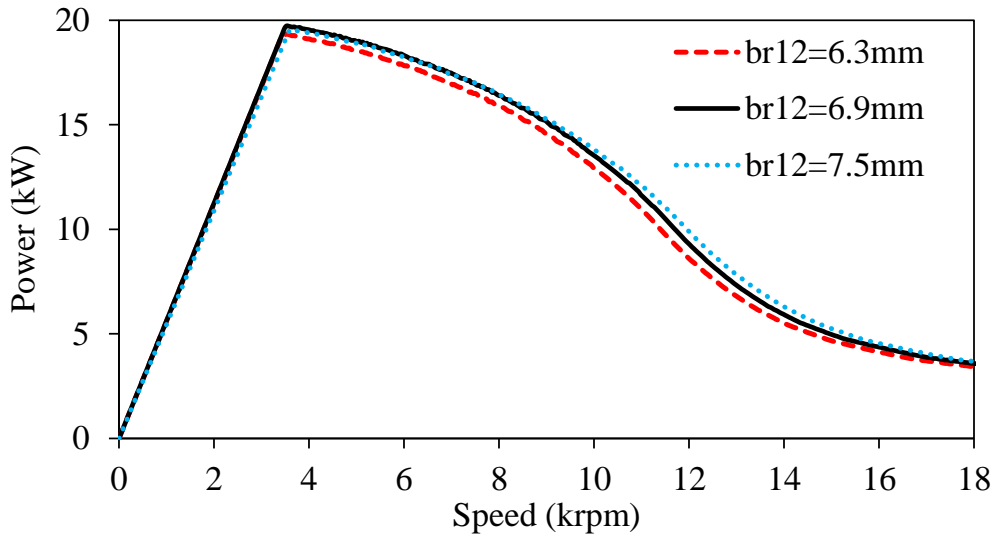
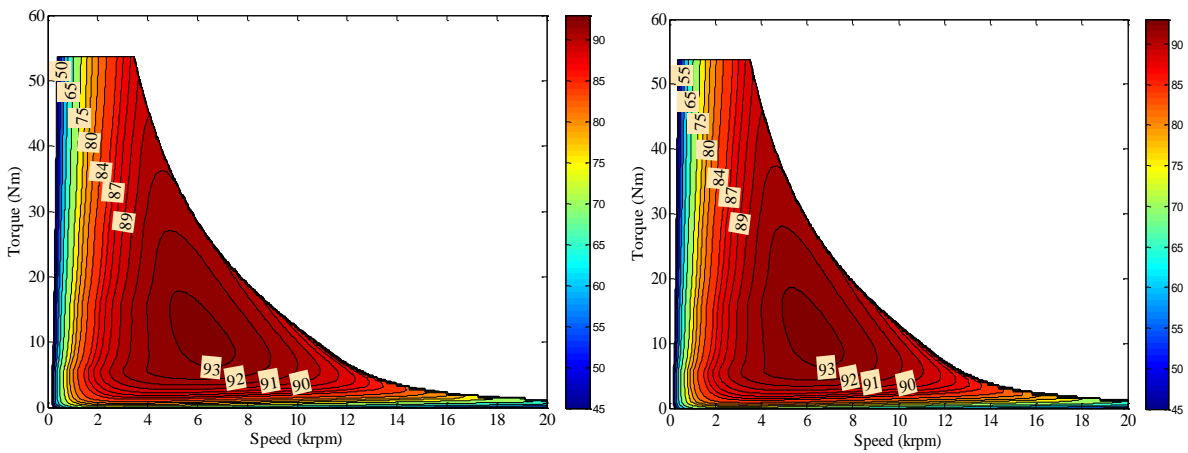
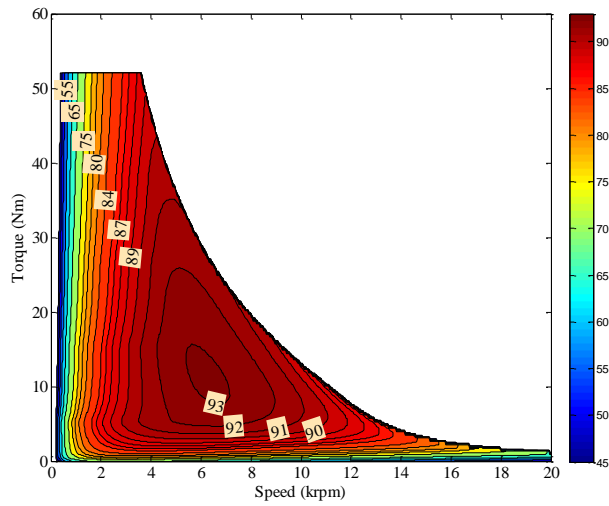


Fig. F.14 Power-speed characteristics for various b_{r12} parameter of CRCS topology.



(a) $b_{r12} = 6.3mm$

(b) $b_{r12} = 6.9mm$



(c) $b_{r12} = 7.5\text{mm}$

Fig. F.15 Efficiency maps for different b_{r12} parameter of CRCS topology.

B. h_{r2} Parameter

The influence of h_{r2} parameter on the torque-speed and power-speed characteristics are illustrated in Fig. F.16 and Fig. F.17, respectively. As seen in the figures, the influence of h_{r2} on the flux-weakening characteristics is considerable. Adopting smaller h_{r2} leads higher torque in the constant torque region and higher power in deep flux weakening region. This is because of the increased mutual inductance between the stator and rotor windings. In addition, influence of h_{r2} on the efficiency is illustrated in Fig. F.18. As seen, adopting larger h_{r2} leads higher maximum efficiency with larger region.

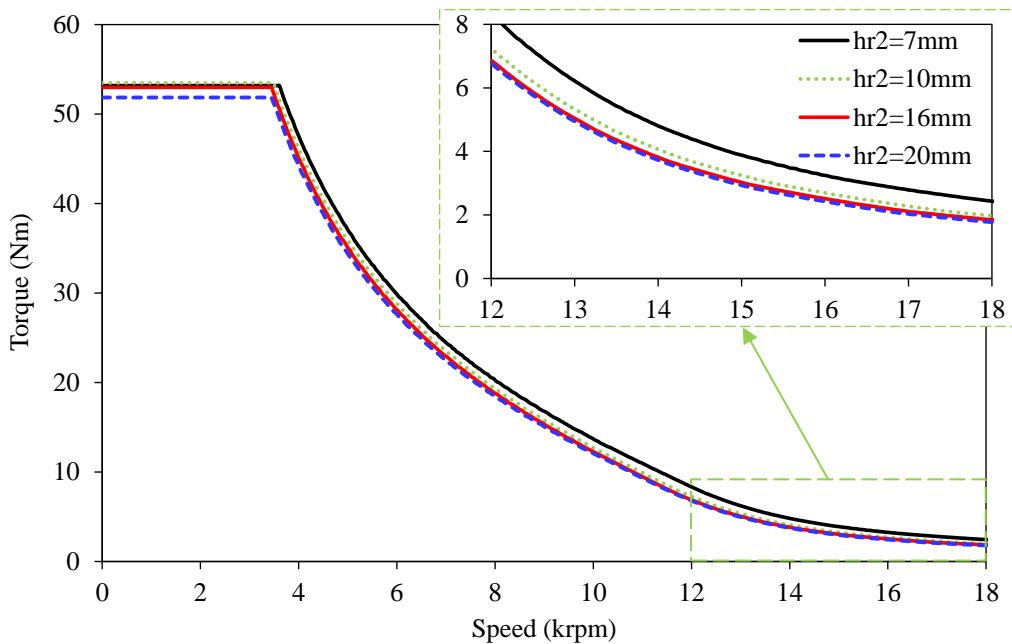


Fig. F.16 Torque-speed characteristics for various h_{r2} parameter of CRCS topology.

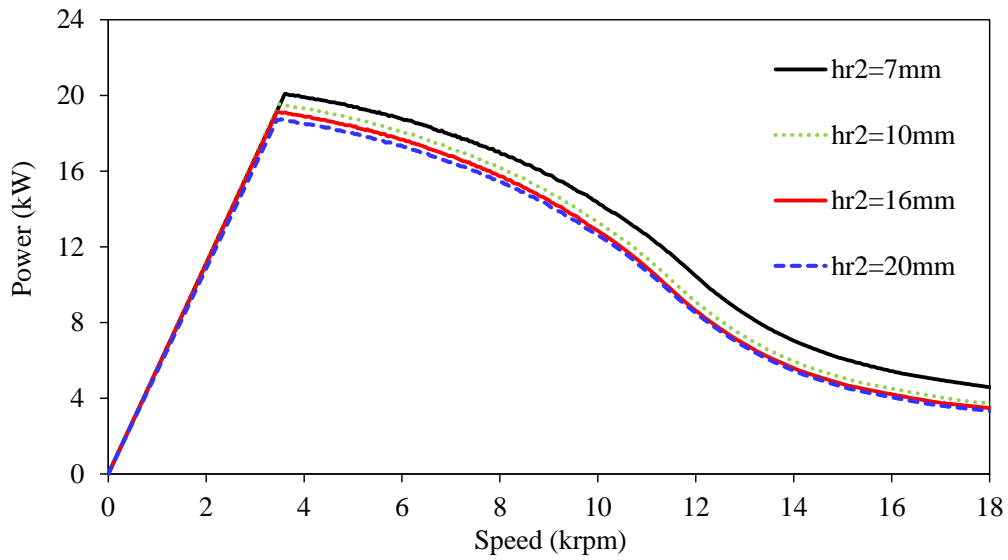


Fig. F.17 Power-speed characteristics for various h_{r2} parameter of CRCS topology.

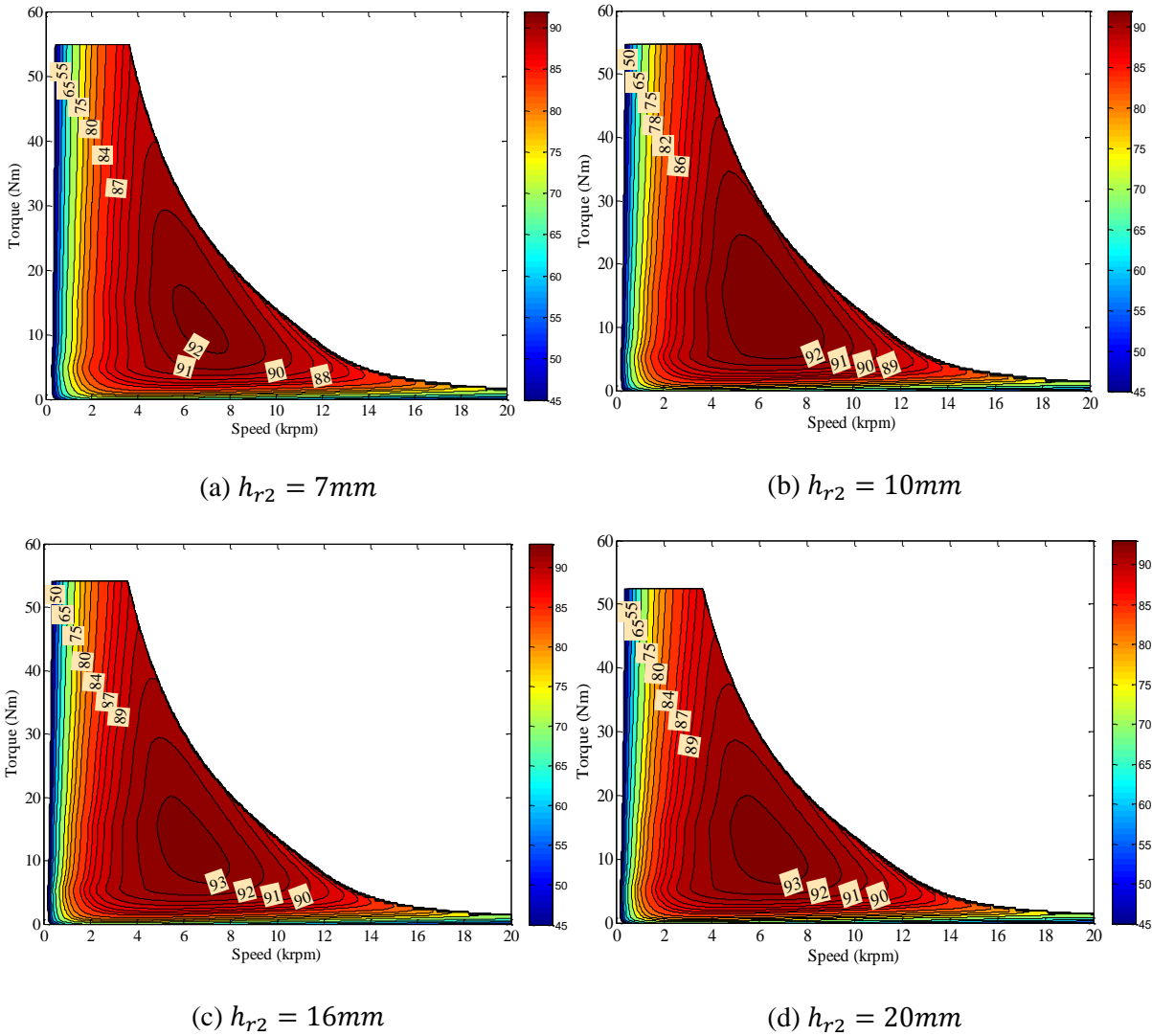


Fig. F.18 Efficiency maps for different h_{r2} parameter of CRCS topology.

Appendix G Generator Mode Operating Characteristics

As known, it is necessary that the electrical machines designed for EV/HEV applications should work in both motor and generator modes. However, as explained in [FRI09] [GUA14b], the maximum flux-weakening characteristics of IM in different operation modes are quite different. Therefore, it is necessary to investigate the generator mode operation of the proposed IMs. The influence of stator resistance, rotor resistance, variable inductance produced by saturation of the iron core, and iron loss parameters on the flux-weakening performance of a CIM have been investigated in [GUA15b]. It has been revealed that the lower the stator and/or rotor resistance, the better the flux-weakening performance in both motor and generator mode operation conditions. In addition, it has been revealed that if the variable inductance (iron saturation) is considered, the power factor is improved, but the flux-weakening performance is not changed. It has been concluded that the difference in flux-weakening characteristic is mainly influenced by both the stator and rotor resistances, but the difference in output power-speed characteristic is mainly influenced by the rotor resistance.

In this appendix, the difference between the flux-weakening characteristics of AIMS in the motor and generator operation modes have been investigated. The analysed characteristics include torque/power-speed performances, inverter drive characteristics, and differences in efficiency maps.

G.1 Circle Diagram of IMs

The operating performance of an IM drive can be easily performed by using a circle diagram which points out the available current and voltage limits at different synchronous angular frequencies in the $i_d - i_q$ plane [BIA97a], [BIA97b], [CHE02], [ALB11]. The circle diagram typically divides the torque-speed characteristics into three regions, namely constant torque, constant power, and high speed (or deep-flux weakening) [CHA02]. A typical circle diagram and corresponding torque-speed characteristics of an IM are illustrated in Fig. G.1. As seen in the figure, each region has been determined by a critical operation point, viz. A, A', B, B' . Note that apostrophe indicates the generator mode operation. Therefore, a quantitative behaviour of whole torque limit characteristics of AIM in both motor and generator modes can be defined by considering Fig. G.1.

From (A.7) the constant-torque curves are hyperbolas in the $i_d - i_q$ plane, the current limit (A.6) defines a circle, which is centred in the plane origin, and the voltage limit (A.3) defines an ellipse centred in the plane origin. As illustrated in Fig. G.1(b), the points A and A' define the rated torque obtained by the drive from zero to base angular frequency ω_A or ω'_A , at which the nominal voltage is reached. The current limit circle from points A or A' to B, B' defines the constant-power region and the line starting from B or B' to origin O defines the maximum torque to voltage ratio locus. As seen in Fig. G.1, IM in generator mode has better flux-

weakening characteristic than in motor mode. The reason behind this phenomenon is that the frequency of voltage limit ellipse in generator mode is larger than that in motor mode for the same current vector as seen in Fig. G.1(a). Because of the same i_d and i_q ($-i_q$ in generator mode) amplitudes, the identical torque value is obtained in the constant torque region. However, since the terminal voltage in generator mode is increased due to the super-synchronous speed (minus slip) operation, the longer constant torque and constant power regions are obtained. The frequency difference of the voltage limit ellipse of IM in different modes, for the same i_d and i_q , has been explained in detail [GUA15b] by using voltage vector diagram.

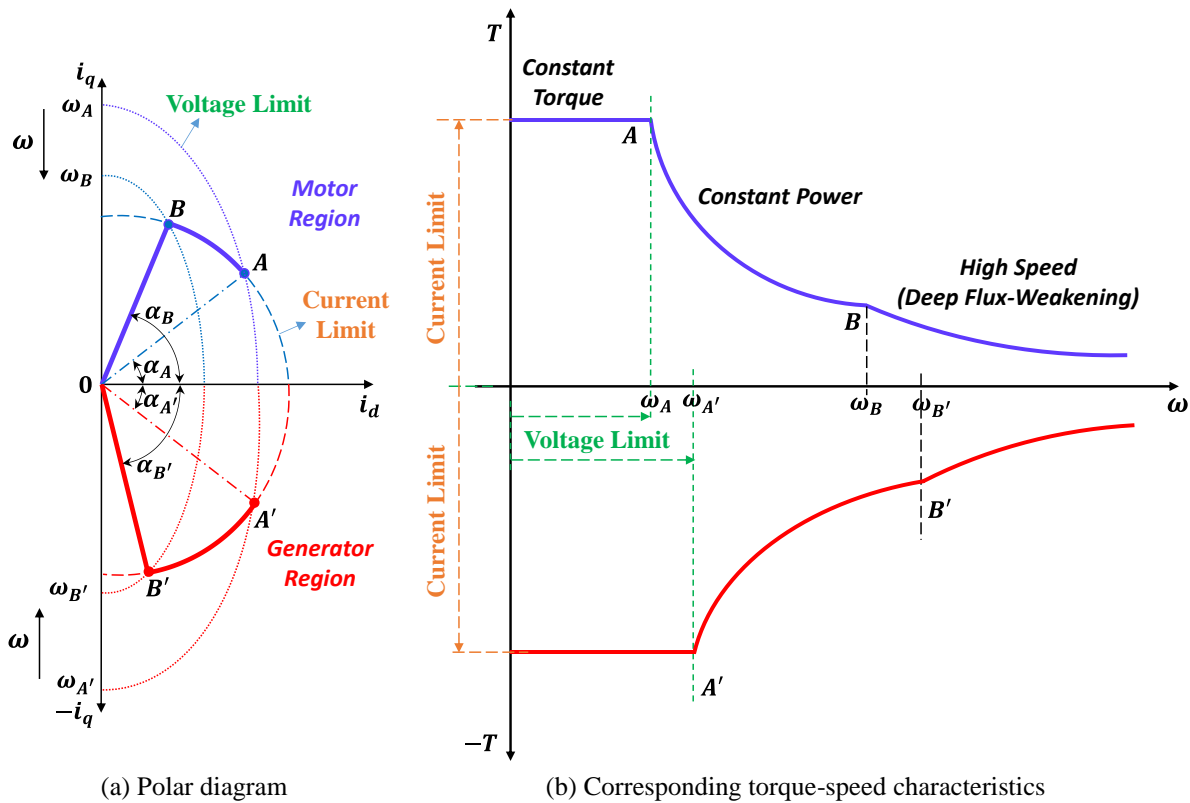
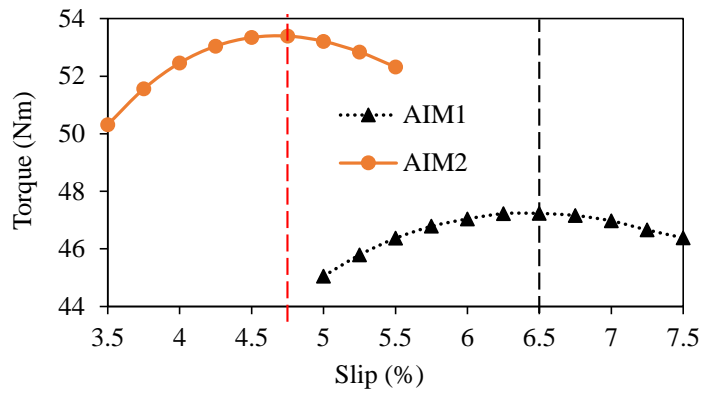


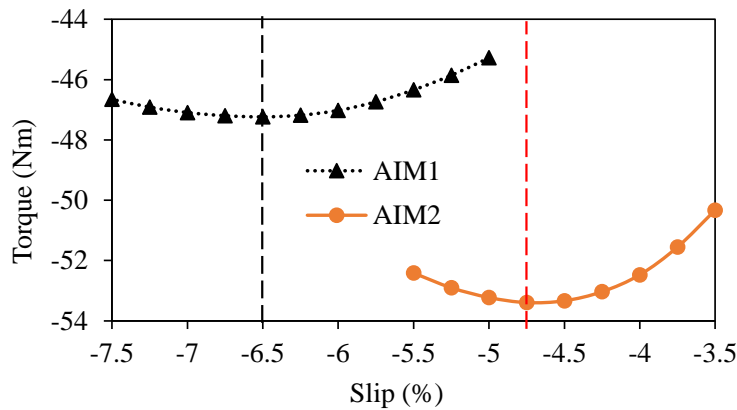
Fig. G.1 Circle diagram and corresponding torque-speed characteristics of IM in motor and generator modes: (a) current and voltage trajectories under the maximum torque control and (b) the corresponding torque-speed characteristics for both motor and generator operation modes.

G.2 Motor and Generator Mod Operation Characteristics of the AIMS

In order to operate the IM in the generator mode, the rotor speed should exceed the synchronous speed. The generator mode operation speed is called as super-synchronous speed. As known, at this speed the slip is negative. Constant torque region slip percentages for the AIM1 and AIM2 in motor and generator mode operations are illustrated in Fig. G.2. It is obvious that the value of the slip delivering the maximum torque has not changed in the generator mode operation. Therefore, it can be deduced that the slip delivering the maximum torque is independent of the operation mode.



(a) Motor mode

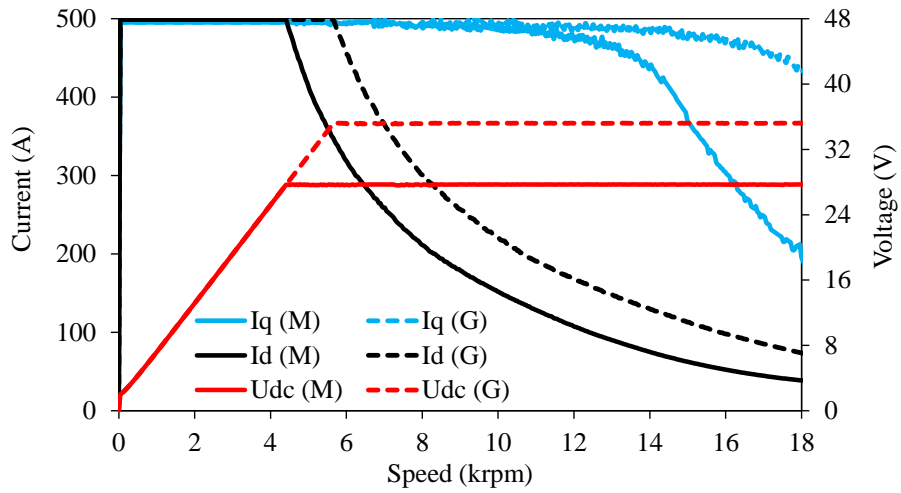


(b) Generator mode

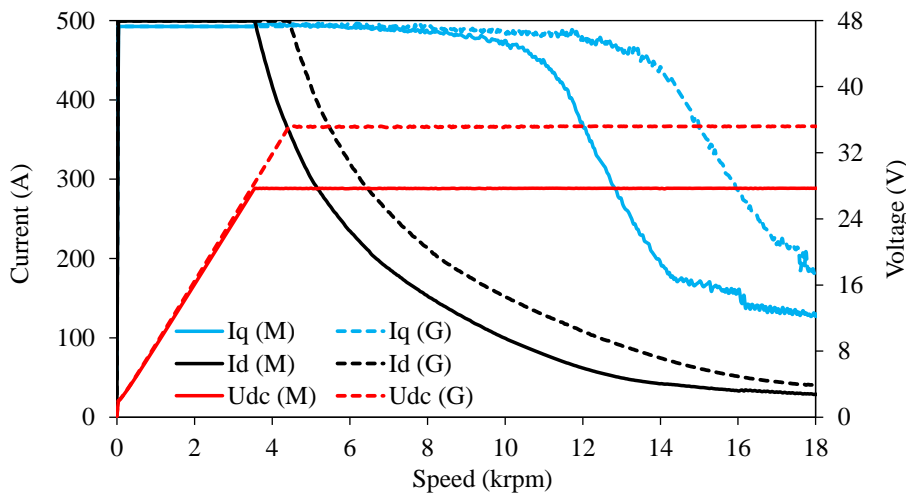
Fig. G.2 Comparison of slip percentages delivering the maximum torque.

The generator mode operation of the AIM1 and AIM2 have been calculated and in order to reveal the difference between the operation modes, calculated generator mode flux-weakening characteristics have been compared with the motor mode operation flux-weakening characteristics. Note that, torque/power-speed characteristics in generator mode are obtained in the 4th quadrant of the coordinate system as seen in Fig. G.1. However, the minus values have been transformed to positive values (transferred to 1st quadrant of the coordinate system) in order to make operation mode comparison much clearer. The drive characteristics of the AIMS in motor M and generator G modes are illustrated in Fig. G.3. The maximum current and voltage limits of the inverter are 500Arms and 48Vrms. Therefore, it has been ensured that the maximum current and voltage limits have not been exceeded. As expected, since the terminal voltage has been increased from 27V to 35V from motor to generator mode operation, respectively, better flux-weakening performance has been achieved in the generator mode for both AIMS. Note that, for the maximum torque operation, the maximum current limit of the inverter has not changed (fixed at 500Arms for the rated speed). The calculated flux-weakening characteristics of the AIMS for motor and generator modes have been compared in Fig. G.4. As expected, better flux-weakening characteristics have been achieved in the generator mode operation for both AIMS. The efficiency maps of the AIMS in motor and generator modes are illustrated in Fig. G.5. As clearly seen in the figures, in generator mode operation higher efficiency than in motor mode operation has been

achieved for both machines. Therefore, it can be concluded that during the generator mode operation, a better flux-weakening and higher efficiency characteristics than in the motor mode operation can be achieved.

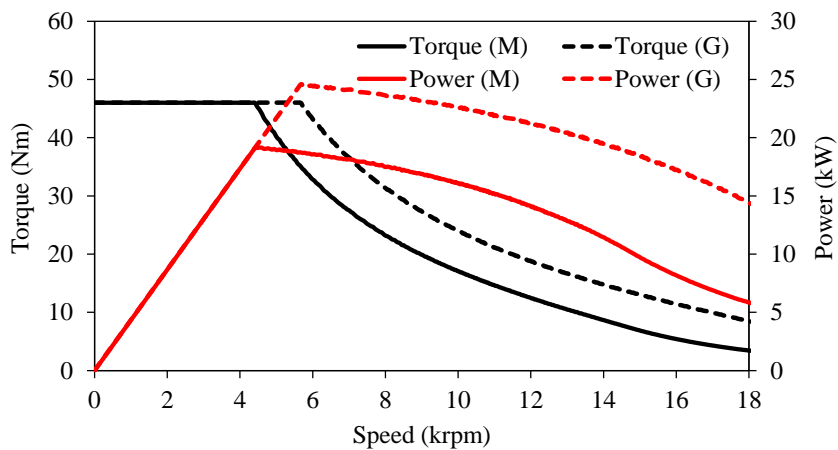


(a) AIM1

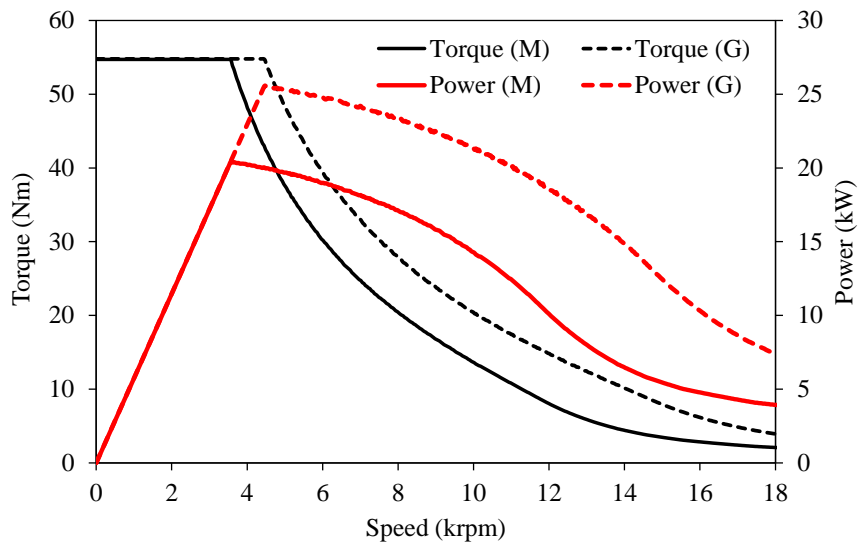


(b) AIM2

Fig. G.3 Comparison of inverter drive characteristics.

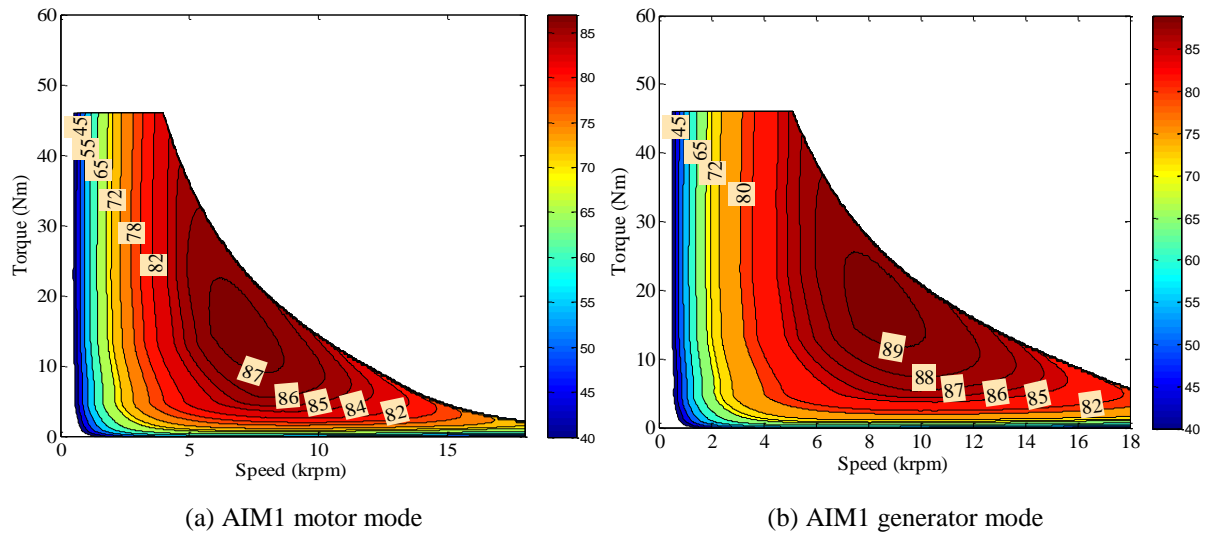


(a) Motor and generator mode operations of AIM1



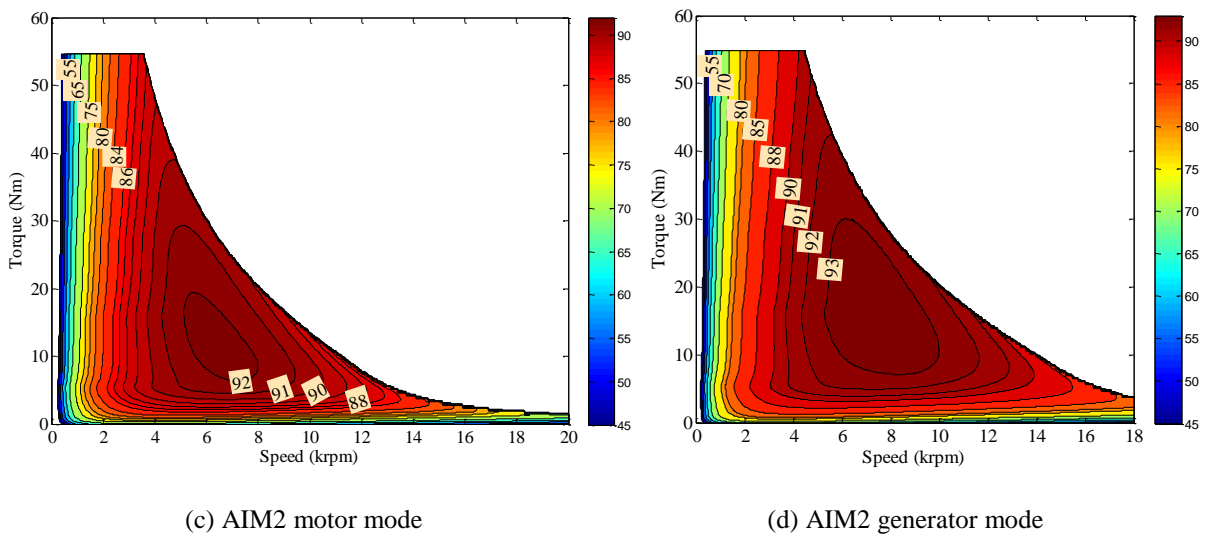
(b) Motor and generator mode operations of AIM2

Fig. G.4 Comparison of motor and generator modes flux-weakening characteristics of the AIM1 and AIM2.



(a) AIM1 motor mode

(b) AIM1 generator mode



(c) AIM2 motor mode

(d) AIM2 generator mode

Fig. G.5 Efficiency maps for motor and generator mode operations. (a), (b): AIM1; (c), (d): AIM2.

Publications

Journal papers published or in press:

- [J1] **T. Gundogdu**, Z. Q. Zhu, and J. C. Mipo, "Influence of Stator Slot and Pole Number Combination on Rotor Bar Current Waveform and Performance of Induction Machines," *IEEE Trans. Ind. Appl.*, (submitted in Jul. 2018).
- [J2] **T. Gundogdu**, Z. Q. Zhu, and J. C. Mipo, "Influence of Rotor Slot Number on Rotor Bar Current Waveform and Performance in Induction Machines," *IEEE Trans. Ind. Appl.*, (submitted in Jul. 2018).

Conference papers published or in press:

- [C1] **T. Gundogdu**, Z. Q. Zhu, J. C. Mipo, and S. Personnaz, "Influence of rotor skew on rotor bar current waveform and performance in induction machines," in *Int. Conf. Elect. Mach. Syst. (ICEMS'18)*, Jeju, 2018, (Accepted).
- [C2] **T. Gundogdu**, Z. Q. Zhu, J. C. Mipo, and S. Personnaz, "Influence of stator and rotor slot geometric parameters on rotor bar current waveform and performance in induction machines," in *Int. Conf. Power Electron, Mach. Drives (PEMD'18)*, Liverpool, 2018.
- [C3] **T. Gundogdu**, Z. Q. Zhu, and J. C. Mipo, "Influence of rotor slot number on rotor bar current waveform and performance in induction machines," in *Int. Conf. Elect. Mach. Syst. (ICEMS'17)*, Sydney, 2017, pp. 1-6.
- [C4] **T. Gundogdu**, Z. Q. Zhu, and J. C. Mipo, "Influence of stator slot and pole number combination on rotor bar current waveform and performance of induction machines," in *Int. Conf. Elect. Mach. Syst. (ICEMS'17)*, Sydney, 2017, pp. 1-6.
- [C5] **T. Gundogdu**, Z. Q. Zhu, J. C. Mipo, and P. Farah, "Influence of air-gap length on rotor bar current waveform of squirrel-cage induction motor," in *Int. Conf. Elect. Mach. Syst. (ICEMS'16)*, Chiba, 2016, pp. 1-6.
- [C6] **T. Gundogdu**, Z. Q. Zhu, J. C. Mipo, and P. Farah, "Investigation of non-sinusoidal rotor bar current phenomenon in induction machines — Influence of slip and electric loading," in *Int. Conf. Elect. Mach. (ICEM'16)*, Lausanne, 2016, pp. 419-425.
- [C7] **T. Gundogdu**, Z. Q. Zhu, J. C. Mipo, and P. Farah, "Influence of magnetic saturation on rotor bar current waveform and performance in induction machines," in *Int. Conf. Elect. Mach. (ICEM'16)*, Lausanne, 2016, pp. 391-397.